OECD

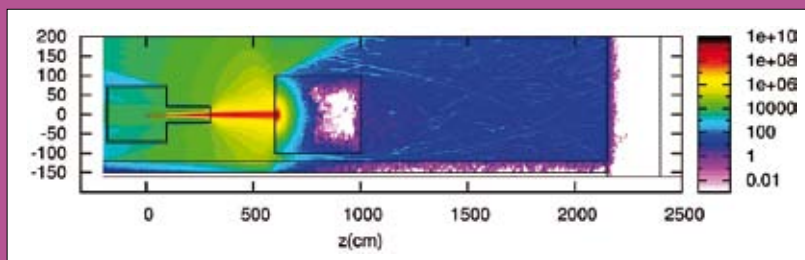# Shielding Aspects of Accelerators, Targets and Irradiation Facilities – SATIF-10

Workshop Proceedings
Geneva, Switzerland
2–4 June 2010

AEN NEA

N U C L E A R   E N E R G Y   A G E N C Y

Shielding Aspects of Accelerators, Targets and Irradiation Facilities – SATIF-10

10th Workshop Proceedings

Hosted by the
European Organization for Nuclear Research (CERN)
Geneva, Switzerland
2-4 June 2010

NUCLEAR ENERGY AGENCY
Organisation for Economic Co-operation and Development

ORGANISATION FOR ECONOMIC CO-OPERATION AND DEVELOPMENT

The OECD is a unique forum where the governments of 33 democracies work together to address the economic, social and environmental challenges of globalisation. The OECD is also at the forefront of efforts to understand and to help governments respond to new developments and concerns, such as corporate governance, the information economy and the challenges of an ageing population. The Organisation provides a setting where governments can compare policy experiences, seek answers to common problems, identify good practice and work to co-ordinate domestic and international policies.

The OECD member countries are: Australia, Austria, Belgium, Canada, Chile, the Czech Republic, Denmark, Finland, France, Germany, Greece, Hungary, Iceland, Ireland, Israel, Italy, Japan, Korea, Luxembourg, Mexico, the Netherlands, New Zealand, Norway, Poland, Portugal, the Slovak Republic, Slovenia, Spain, Sweden, Switzerland, Turkey, the United Kingdom and the United States. The European Commission takes part in the work of the OECD.

OECD Publishing disseminates widely the results of the Organisation's statistics gathering and research on economic, social and environmental issues, as well as the conventions, guidelines and standards agreed by its members.

> *This work is published on the responsibility of the Secretary-General of the OECD.*
> *The opinions expressed and arguments employed herein do not necessarily reflect the official*
> *views of the Organisation or of the governments of its member countries.*

NUCLEAR ENERGY AGENCY

The OECD Nuclear Energy Agency (NEA) was established on 1st February 1958 under the name of the OEEC European Nuclear Energy Agency. It received its present designation on 20th April 1972, when Japan became its first non-European full member. NEA membership today consists of 28 OECD member countries: Australia, Austria, Belgium, Canada, the Czech Republic, Denmark, Finland, France, Germany, Greece, Hungary, Iceland, Ireland, Italy, Japan, Korea, Luxembourg, Mexico, the Netherlands, Norway, Portugal, the Slovak Republic, Spain, Sweden, Switzerland, Turkey, the United Kingdom and the United States. The European Commission also takes part in the work of the Agency.

The mission of the NEA is:

– to assist its member countries in maintaining and further developing, through international co-operation, the scientific, technological and legal bases required for a safe, environmentally friendly and economical use of nuclear energy for peaceful purposes, as well as

– to provide authoritative assessments and to forge common understandings on key issues, as input to government decisions on nuclear energy policy and to broader OECD policy analyses in areas such as energy and sustainable development.

Specific areas of competence of the NEA include safety and regulation of nuclear activities, radioactive waste management, radiological protection, nuclear science, economic and technical analyses of the nuclear fuel cycle, nuclear law and liability, and public information.

The NEA Data Bank provides nuclear data and computer program services for participating countries. In these and related tasks, the NEA works in close collaboration with the International Atomic Energy Agency in Vienna, with which it has a Co-operation Agreement, as well as with other international organisations in the nuclear field.

Foreword

The transport of radiation through shielding materials is a major consideration in the safety design studies of nuclear power plants, and the modelling techniques used may be applied to many other types of scientific and technological facility. Accelerator and irradiation facilities represent a key capability in R&D, medical and industrial infrastructures. The range of scientific, medical and industrial applications is very wide. High-energy ion accelerators, for example, are now used not only in fundamental research, such as the search for new super-heavy nuclei, but also for therapy as part of cancer treatment.

While the energy of the incident particles on the shielding of these facilities may be much higher than those found in nuclear power plants, much of the physics associated with the behaviour of secondary particles produced is similar, as are the computer modelling techniques used to quantify key safety design parameters, such as radiation dose and activation levels. For these reasons, there are clear synergies with other technical work being carried out by the OECD Nuclear Energy Agency (NEA), and its Nuclear Science Committee continues to sponsor activities in this domain.

One of these activities concerns "Shielding Aspects of Accelerators, Targets and Irradiation Facilities" (SATIF). A series of workshops has been held over the last decade: SATIF-1 was held on 28-29 April 1994 in Arlington, Texas; SATIF-2 on 12-13 October 1995 at CERN in Geneva, Switzerland; SATIF-3 on 12-13 May 1997 at Tohoku University in Sendai, Japan; SATIF-4 on 17-18 September 1998 in Knoxville, Tennessee; SATIF-5 on 17-21 July 2000 at the OECD in Paris, France; SATIF-6 on 10-12 April 2002 at the Stanford Linear Accelerator Center (SLAC), Menlo Park, California; SATIF-7 on 17-18 May 2004 at ITN, Sacavém, Portugal; SATIF-8 on 22-24 May 2006 at the Pohang Accelerator Laboratory in the Republic of Korea; and SATIF-9 on 21-23 April 2008 at Oak Ridge National Laboratory (ORNL), Oak Ridge, Tennessee.

SATIF-10 was jointly organised by the following bodies:

- OECD Nuclear Energy Agency (NEA) and its Nuclear Science Committee (NSC);
- Radiation Safety Information Computational Center (RSICC) of ORNL;
- Division of Radiation Science and Technology of the Atomic Energy Society of Japan;
- CERN.

The current proceedings provide a summary of the discussions, decisions and conclusions as well as the text of the presentations made at the tenth SATIF workshop.

Acknowledgements

Dedicated to Lutz Moritz, 1943-2008

Table of contents

---

*   The full paper being unavailable at the time of publication, only the abstract is included.

---

*   The full paper being unavailable at the time of publication, only the abstract is included.

---

*   The full paper being unavailable at the time of publication, only the abstract is included.

Executive summary

The tenth SATIF workshop (SATIF-10) took place at CERN, Geneva (Switzerland) on 2-4 June 2010. This was the second time that SATIF was hosted by CERN, after SATIF-2 in October 1995. The workshop was chaired by Marco Silari and was the most attended meeting of the series, with 65 participants from 34 institutions and 14 countries.

The SATIF community welcomed Jim Gulliford, the NEA representative replacing Enrico Sartori who retired last year. SATIF forms part of the activities of the newly formed Expert Group on Radiation Transport and Shielding (EGRTS) which reports to the Nuclear Science Working Party on Scientific Issues of Reactor Systems (WPRS). The EGRTS also co-ordinates maintenance and development of the SINBAD database of Reactor Shielding, Fusion Neutronics and Accelerator Shielding benchmark experiments. More information on the activities of the WPRS can be found at: *http://home.nea.fr/science/wprs/index.html.*

The objectives of the SATIF meetings are:

- to promote the exchange of information amongst experts in the field of accelerator shielding and related topics;

- to identify areas where international co-operation can be fruitful, and recommend actions with strong need for international work on theoretical models, experimental work and benchmarking;

- to carry on a programme of work in order to achieve progress in specific priority areas;

- to present and assess achievements on actions agreed upon previously.

The SATIF-10 programme was organised in six sessions. Each session was opened by an invited talk to provide a review of the session topic, followed by contributed presentations. At the end of each session half an hour was allocated for general discussion. The meeting closed with a two-hour discussion session to provide a summary of the meeting and revise the topics where future actions are needed. Interesting presentations, productive discussions and constructive dialogue characterised all six sessions, and numbered to a total of 44 talks (6 invited and 38 contributed):

1) source term and related topics (1 invited + 8 contributions);

2) induced radioactivity (1 + 10);

3) benchmarking (1 + 7);

4) dosimetry (1 + 2);

5) medical and industrial accelerators (1 + 5);

6) present status of codes and code libraries (1 + 4).

There was also a one-hour session devoted to discussing the opportunity of setting up a network amongst the radiation protection groups of major accelerator laboratories in order to ease the exchange of information on topics of common interest like training, procedures, shielding assessments, instrumentation development and calibration, and so on.

Session 1 on source terms and related topics was opened by T. Nakamura, who gave an excellent overview of experimental data (until 2008) on neutron distributions and spallation products from thick and thin targets for p, d, He and HI beams (MeV to GeV). These data are an invaluable asset for the community and should possibly be included in SINBAD if/when digitised. For the first time in a SATIF meeting, discussion was started on what level of agreement between data and simulations

should be regarded as satisfactory. A very interesting set of results on radiation fields induced by 243 and 390 MeV quasi-monoenergetic neutrons was presented, which is another good candidate for inclusion into SINBAD.

Systematic studies of thick target yields (TTY), radiation fields in thick shielding, activation, muon-induced spallation reactions and radiation effects, all induced by proton beams with E up to 120 GeV were undertaken within the Japan-Fermilab JASMIN collaboration, again certainly of interest for inclusion in SINBAD when the analysis is finished. A talk was presented on considerations of dark current-induced radiation in superconducting RF cavities and shielding around. An interesting sensitivity analysis was presented of effects of cryogenic moderator, reflector, decoupler and temperature on radiation field at ESS. Other contributions discussed shielding and activation study for a high-intensity laser facility and neutron yield and nuclear transmutation at a photo-neutron source.

Megawatt beams were again a hot topic at the meeting. A new generation of accelerators, extremely high peak specific energy (up to ~0.1 MJ/g) and specific power (up to ~1 TW/g) in beam interactions with matter make design of such critical systems as targets, absorbers and collimators very challenging, requiring novel approaches. This also puts unprecedented requirements on the accuracy, capability and reliability of the simulation codes used in the designs. Particle production, DPA, nuclide inventory, energy deposition and hydrodynamics coupling are the modules of special importance. Benchmarking is absolutely crucial. Justified emulation of extreme conditions at existing lower energy and beam power facilities is the way to go. The JASMIN, BLIP (BNL) and HiRadMat (CERN) activities are excellent examples. Joint efforts with material experts are needed.

Session 2 on induced radioactivity was opened by a review talk by F. Gallmeier, who discussed the pros and cons of the two possible approaches: all-in-one, *i.e.* direct prediction by plugging in activation modules into transport codes solving for the radionuclide build-up and decay on-line on a per-event basis, versus modular, *i.e.* sampling fluxes and radionuclides in transport analysis and feeding the information into external activation codes. He stressed the need for realistic simulations to avoid unnecessary costs. His talk was followed by presentations discussing the use of Monte Carlo codes for generic activation studies, for both proton and ion accelerators, to predict the variation of ambient dose equivalent rate as a function of material irradiated and of cooling time. The activation properties of an element are an important factor to be taken into account in the choice of a material for any given application (*e.g.* beam dump). A conclusion drawn for ions is that the radionuclide inventory does not depend on the projectile species and that the induced activity decreases with increasing ion mass and with decreasing energy. A number of talks described various ongoing activation studies for present and future facilities such as SPES in Legnaro (Italy), CLIC, n_TOF, EURISOL and Beta Beams. The importance of benchmarking code predictions versus experimental data was underlined.

The proposal was made to create a database of reaction cross-sections:

- thermal to TeV (at least to 1 GeV);
- hadron, photon and heavy-ion projectiles;
- accelerator-relevant target materials.

with focus on:

- calculation of radioactive inventory for transport, handling and waste;
- ground and sump water activation;
- air activation;
- cooling water activation.

Session 3 on benchmarking was introduced by a review by P. Sala, who stressed that computing tools for accelerator radiation shielding are faced with new challenges from the present and next generation of particle accelerators. The Japan-Fermilab JASMIN collaboration has carried out experimental studies with the aim of benchmarking simulation codes and studying irradiation effects for upgrade and design of new high-energy accelerator facilities. Neutron production and propagation are reasonably well understood by most codes (with some caveats). Deep penetration is surprisingly well predicted but further benchmarks are welcome. There have been huge steps forward in the last

ten years on residual nuclei predictions, but still a lot of work is needed: new data and comparisons are welcome for both thin and thick targets, with particular emphasis on special cases (*e.g.* production of rare isotopes through (α,x) reactions by secondary α particles). Light (composite) charged particle production is a big challenge, which could also be relevant for radiation protection applications. There are not too many data available at medium/high energies for photonuclear reactions, so that new data are welcome.

As for code benchmarking for heavy ions, there are many experiments on neutron production (mostly by Japanese groups), but there is still a room for improvements in codes (*e.g.* forward angles) and almost no data are available above 1 GeV/A. Projectile fragmentation is a very important issue for particle therapy and not only: both experimental data and benchmarking are welcome (the FIRST experiment at GSI should provide data in the near future). A lot of interesting data came from GSI/FAIR, with also some unexpected challenges (*e.g.* range calculations). Radionuclide production distributions are of great interest. In general all sort of data for heavy ions are welcome, but perhaps there is a need to establish priorities.

The role of Λ hyperons in thick shielding calculations was discussed. Recent results by the PHITS code showed that their effect can be substantial, while there is no such evidence from the mature codes, FLUKA, MARS and GEANT, where this particle is always taken into account. Although a deeper look should be taken at this issue, it seems unlikely that Λ hyperons with their $c\tau$ = 7.89 cm and an inelastic cross-section comparable with that for nucleons and pions would become a driver in hadronic cascade development. Some discussion was devoted to calculation of scintillator efficiencies for high-energy neutrons, and to biasing (*i.e.* variance reduction techniques). It was stressed that there is no chance to make meaningful calculations for specific studies (*e.g.* deep penetration in shields) without biasing.

For the first time at a SATIF meeting, the issue of DPA in radiation damage to materials and electronics was specifically discussed. This is a very important problem for present and future projects. There is unfortunately a very complex physics background, which together with the impossibility of direct measurements generates different and confusing results. The practical implementation as well as the calculation methods can vary from very naïve to extremely complex. More in general, predictions relevant for material properties are becoming more and more essential for future projects. The idea was presented to plan a future SATIF session (or even a dedicated workshop) where every code presents how its DPA is computed and where to compare results on simple cases.

Session 4 on dosimetry was short as compared to previous SATIF meetings. The session was introduced by a comprehensive review by T. Sato of recent dosimetric studies, both computational (comparison of fluence-to-dose conversion coefficient, updated w_R and w_T, authorised voxel phantoms, neutron dose estimates) and experimental (JASMIN and KEK experiments, neutron measurements and the challenge of measuring in pulsed fields). A talk provided comprehensive FLUKA calculations of the radiation levels (prompt dose rate in service caverns and on the surface) around the ATLAS detector in the LHC. The session closed with an interesting discussion on dose, its definitions and "ingredients", phantoms and their description correlated with computer power and detectors.

Session 5 on medical and industrial accelerators was mostly devoted to particle therapy accelerators. It was opened by a review by G. Fehrenbacher on radiation protection issues at particle therapy facilities. There are a growing number of proton and ^{12}C ion medical accelerators, essentially synchrotrons and cyclotrons employing passive and active beam shaping systems in conjunction with fixed beams and isocentric gantries. The main radiation source at these machines is neutrons, for which source terms (neutron energy distributions) are needed (experimental data and Monte Carlo predictions). A peculiarity of these facilities is that many radiation sources are present, in the accelerator and treatment rooms, patient included. Various approaches are used to radiation shielding, both Monte Carlo and analytical using attenuation curves. Shielding materials employed at these facilities are concrete, combined low-Z + high-Z materials, and a sandwich technology recently introduced, which allows saving time and construction costs. Activation issues are present in the accelerator, energy degrader, beam transport and passive beam shaping system. In particular, cyclotron systems using an energy degrader and passive scattering techniques implicate higher activation and radiation exposure of personnel working on activated components in contrast to synchrotron based facilities. More shielding data are generally needed for light-ion facilities, as the available experimental data are essentially from measurements at HIMAC. Improvements are desirable, in particular for the lowest angles (0°-15°). There is also room for improvement in models.

Although most of the focus at the session on medical accelerator shielding (introduced for the first time at SATIF-6) has always been on proton accelerators, one presentation was on seismic base-isolation structure for a conventional electron linac, where alternative solutions to pure shielding have to be found to reduce costs. Calculations validated by measurements were presented to predict dose rates due to radiation scattered and streaming underneath the treatment room, taking into account multiple beams due to rotating gantry.

Finally, high-current, low-energy accelerators for novel applications such as material testing in strong neutron field, as well as a high-intensity laser facility and photo-neutron source presented in Session 1, pose new challenges (*e.g.* the dump must withstand high particle current and becomes a very intense neutron source) requiring novel shielding solutions.

Session 6 on the present status of codes and code libraries started with a comprehensive review by B. Kirk of nuclear computational information, followed by talks on modern activation-transmutation systems, on the impressive performance of the improved INCL4 and ABLA models, on radiation protection and safety issues in IFMIF, and on a "physics list" in Geant4 where the user defines all the particles, physics processes and cut-off parameters for his/her application. Preparing a physics list is not a simple job even for non-novice users. A debate followed, as this offer by the code seems appropriate for expert HEP users, whereas for radiation protection calculations it seems much safer not to let the user "play" with models but rather to provide a set of "defaults" adapted to the problem.

In summary, the main questions raised at the meeting were:

- What calculations are we not happy with?

  DPA, heavy ions at low energies, light fragment yields, nuclide yields (in some cases), consistency in deep penetration benchmarking, model performance at intermediate energies, dose conversion coefficients at E > 1 GeV.

- What level of agreement between data and simulations is satisfactory?

  Depending on a quantity or/and application it can be from a few % to a rather big factor.

- What data are needed?

  Material damage tests in nuclear and electromagnetic dominated cases at room and cryo temperatures. Low-energy pion spectra. Light-, heavy-ion and photon-induced particle production, radiation effects and radiation fields. Continue with JASMIN and HIMAC experiments.

- Shall SATIF help in pursuing the organisation of RP network amongst the accelerator laboratories?

- Shall we have a dedicated DPA session at SATIF-11?

The publication of the Accelerator Shielding Handbook was also discussed. The handbook was first proposed at SATIF-8 and since then some contributions have been provided, but much still has to be written. It has been agreed to look for a person who has sufficient available time to solicit the missing contributions to the various chapters and take up on the editing work.

Jim Gulliford (NEA), Nikolai Mokhov (Fermilab), Marco Silari (CERN)

Session I

Source term and related topics

Chair: Nikolai Mokhov

Production of neutrons and spallation products by high-energy particle beams

Takashi Nakamura
Prof. Emeritus of Tohoku University
Institute of Technology, Shimizu Corporation
Etchujima, Koto-ku, Tokyo, Japan

Abstract

This review summarises the experimental data up to 2008 on energy and angular distributions of neutrons produced from thick targets of various materials bombarded by protons, deuterons, He and heavier ions having a wide energy range from MeV to GeV. Total neutron yields and the moving source model approximations are also presented. Production cross-section data for spallation by proton to Ar ion are summarised in this paper, as well as excitation functions, mass-yield distributions and induced activities. Very recent results on induced activities are included for Ar and U ions.

Introduction

Thick target yield (TTY) generally means the angular-energy distribution of secondary neutrons produced from a thick target which is sufficiently thick to fully stop the incident particles. The TTY data are indispensable for estimating source terms used in accelerator shielding design. A number of experiments to give the TTY data have never been published. Although it is difficult to survey all papers on TTY, the TTY papers up to 2000 have been collected in a Japanese book written by Nakamura [1], and the TTY papers up to 2008 were added as much as possible in this survey. Although the TTY data for projectile ions heavier than He ions of energies above about 100 MeV/nucleon have been published as the handbook written by Nakamura and Heilbronn [2], here in this paper, the TTY data for light projectiles, mainly protons and deuterons are summarised, together with the TTY data for heavier projectiles of energies below about 100 MeV/nucleon.

In addition to TTY data, spallation product production cross-section data up to 2010 are summarised together with excitation functions, mass-yield distributions and induced activities for various projectiles from proton to U ion. They are the basic data for induced activity estimation in high-energy accelerator facilities. A systematic study has been done by Michel, *et al.* for protons [3], and for heavy ions from He to Ar ions, a comprehensive work has been done by a Japanese group and an American group using the Heavy Ion Medical Accelerator in Chiba (HIMAC), National Institute of Radiological Sciences (NIRS), Japan. These results are also cited in the handbook [2].

Thick target yield

Thick target yield by protons

Thick target yield by protons is summarised in Table 1. Many experimental results for various targets from Li to U are obtained for proton energy of 15 MeV up to 1.6 GeV at various accelerator facilities. The neutron detectors are mostly NE-213 organic liquid scintillator coupled with the TOF method and some with the unfolding technique. Activation detectors are also used in a few experiments. Typical experimental results are cited here for three proton energy regions of several tens of MeV, a few hundred MeV and above 500 MeV.

Figure 1 gives the neutron spectra at 0° to 150° in C, Al, Cu and Pb targets bombarded by 22, 30 and 40 MeV protons by Amos, *et al.* [6]. All spectra have two components; one below about 10 MeV especially for heavier target corresponds to neutrons produced almost isotropically through the equilibrium/evaporation process from a compound nucleus having a nuclear temperature of 1 to 2 MeV; the other above 10 MeV corresponds to neutrons having forward-peaked at higher energies, produced by the pre-equilibrium and direct reaction (usually in cascade) processes. The neutron spectra become softer at large emission angle for heavier target where the evaporation process through a larger number of target nucleons is prominent. The neutron spectra therefore become harder for lighter target like carbon. This can be explained by noting that the energy E_i transferred from a projectile to a target by one collision is proportional to $4M_pM_tE_0/(M_p + M_t)^2$, where M_p and M_t are the atomic masses of the projectile and target nuclei, respectively, and E_0 is the projectile kinetic energy. As a result, the sum of the transferred energies is greater for lighter target nuclei, and it is more likely that a nucleon receive a greater part of this transferred energy and that the fraction of the evaporation process is smaller, since the lighter target nucleus has a smaller number of nucleons. This implies that lighter target nuclei are excited in a state of higher nuclear temperature.

Figure 2 shows the neutron spectra at 0° to 110° in Fe target bombarded by 210 MeV protons by Yonai, *et al.* [20]. The measured spectra are compared with various calculations, MCNPX [31], and NMTC/JAM [32] coupled with several intranuclear cascade models, Bertini [33], CEM [34] and ISOBAR [35]. The calculation/experiment (C/E) ratios are also shown in these figures for the four calculation methods. Reasonably good agreement between all calculations and measurements is obtained, except at forward angles. At 0 and 7.5°, all calculations underestimate the measured spectra above 20 MeV, especially the MCNPX-CEM calculation. At 110°, only the NMTC/JAM-Bertini results overestimate the data. In the energy region below about 20 MeV, all calculations agree with measurements within a factor of 2. In the energy region above about 40 MeV, the agreement between measurements and all calculations is very good at large angles.

In order to check this disagreement of the TTY spectrum at 0°, the TTY experiment was done for C, Al, Fe and Pb targets using 140, 250 and 350 MeV protons. Figure 3 show the neutron spectra at 0° in C, Al, Fe, Pb targets bombarded by 140 MeV protons by Iwamoto, *et al.* [21]. The measured spectra are compared with Monte Carlo calculations, PHITS [36] and MCNPX. In the PHITS calculation, evaluated nuclear data libraries JENDL-HE [37] and LA150 [38] are used. For comparison, the nuclear reaction models ISOBAR and LAHET [39] are also used for PHITS and MCNPX calculations, respectively. The calculated spectra of JENDL-HE and LA150 agree well with the measured spectra above 10 MeV, while ISOBAR underestimates the Pb spectrum and LAHET overestimates all target spectra above 110 MeV.

Figure 4 gives the neutron energy spectra at 15 to 150° in Pb target by 0.5 and 1.5 GeV protons by Meigo, *et al.* [23]. The neutron spectra also have two components, an evaporation component below 10 MeV and a pre-equilibrium/cascade component above 10 MeV, but the ratio between these two components is quite prominent. The ratio between evaporation and pre-equilibrium/cascade neutrons is almost equal for Fe especially at forward angles, and the fraction of evaporation neutrons is much higher for Pb, which has a much larger numbers of nucleons. The measured spectra are compared with the NMTC/JAERI [40] and MCNP-4A [41] in Figure 4 using free nucleon-nucleon cross-section (NNCS) and in-medium NNCS [42]. Generally speaking, the agreement between experiment and calculation is good within a factor of 2.

Thick target yield by deuterons

Thick target yields by deuterons are summarised in Table 2. Many experimental results for various targets from Li to U are obtained for a deuteron energy of 8 MeV up to 200 MeV at various accelerator facilities, but mostly for Be target by 15 to 50 MeV deuteron bombardment.

Figure 5 gives the neutron spectra at 0 to 90° in Li and Be targets by 25 MeV deuterons by Aoki, *et al.* [45]. Except a big broad peak at the forward emission angle, all neutron spectra also have two components; one below about 10 MeV especially for heavier target corresponds to neutrons produced almost isotropically by the equilibrium/evaporation process; the other above 10 MeV corresponds to neutrons having forward-peaked at the higher energies produced by the pre-equilibrium/cascade process. Only in Figure 5(a), the Li(d,n) spectra extend up to around 42 MeV, which is consistent with the Q-value of 15.7 MeV of the Li(d,n) reaction.

In the forward direction, a broad peak is due to the stripping/break-up reaction of deuteron and the peak energy is about half of the incident deuteron energy. Considering the energy degradation in a thick target, the peak energy is about 40% of the incident deuteron energy, around 10 MeV for 25 MeV incident deuteron energy. This broad peak has a very strong angular dependence, because the stripping reaction is strongly forward-peaked.

The neutron energy spectrum based on the stripping reaction can be simulated on the basis of the Serber model [52], an elegantly simple semi-classical theory for deuteron stripping. The generalisation of the Serber model is given by effecting averages over the target thickness and emission angles by Menard, *et al.* [44]. The simulated results are compared with the measured results, as shown for Be target bombarded by 50 MeV deuterons in Figure 6. In the figure, the right flanks of the spectra above 25 MeV for 50 MeV deuterons are well reproduced by the Serber model. The neutron peak energies and production yields given by the model are lower than the experimental results. This behaviour is due to the fact that the evaporated neutrons are also considered to be emerging from the stripping and direct nuclear collisions. The shape of the theoretical distribution exhibits a maximum at an energy of neutrons lower than that given by the experiment by approximately 2 MeV.

Thick target yields by He and heavier ions of energies lower than 100 MeV/nucleon

Thick target yields by He and heavier ions of energies lower than 100 MeV/nucleon are summarised in Table 3. Projectiles are ^{3}He, ^{4}He (α), ^{6}Li, ^{7}Li, ^{11}B, ^{12}C and Ar of total energies from 40 MeV to 460 MeV, and targets are from Be to Pb.

Very few results are given for ^{3}He projectile and Figure 7 gives the neutron spectra at 0 to 135° in C, Cu and Pb targets injected by 65 MeV ^{3}He ions by Shin, *et al.* [46]. The neutron spectra also have two components of evaporation and pre-equilibrium/cascade processes, but in the forward direction, a broad peak is also shown due to the break-up reaction of ^{3}He nuclei (^{3}He,n2p). The most probable

energies of these peaked spectra are about 26 MeV for C and about 22 MeV for Cu, which are close to 1/3 of the incident kinetic energy of the ^{3}He projectile. This implies that the one neutron and two protons are emitted from ^{3}He nucleus having almost the same kinetic energies.

Among many experimental results on TTY by ^{4}He(α) and heavier projectiles, the Ta target results with 50 MeV ^{4}He(α) ions by Sarkar, et al. [54] are shown in Figure 8. In Figure 8, the spectra also have two components of evaporation and pre-equilibrium/cascade processes and the latter component decreases with increasing angles. The measured spectra are compared with the calculated spectra with the exciton model formalism [59] including the statistical multistep direct and the statistical multistep compound processes. The agreement between experiment and calculation is poor at 0° but becomes better at a larger angle.

Thick target yields by He and heavier ions of energies higher than 100 MeV/nucleon

Table 4 contains a list of the secondary neutron thick-target data sets by He and heavier ions of energies higher than 100 MeV/nucleon. Unless otherwise noted, all targets are thick enough to stop the primary beam. The first column contains the beam ion species and beam energy in MeV/nucleon. The second column lists the targets used with each beam. The third column lists the spectra that were measured. TTY indicates that double-differential thick target yields were measured, n/dΩ indicates that angular distributions were measured, and "total" indicates that total neutron yields were extracted. The total yields were usually limited to the angular range used in the measurements, so in most cases the total yields were not strictly "total" in the sense that they cover the distribution over all 4π steradians. The fourth column indicates the laboratory angles where spectra were measured. The fifth column lists the minimum neutron energy range measured. The last column indicates the accelerator facility where the measurements took place.

The double-differential thick-target yields (TTY) in the forward direction of 0 to 90° from the HIMAC series of experiments are shown in Figures 9 through 11 for 400 MeV/nucleon C, Fe, Xe ions, respectively, as examples, by Satoh, et al. [68], which have re-evaluated the former HIMAC experiments by Kurosawa, et al. [60-63] by changing the neutron detection efficiency calculation to a new code, SCINFUL-QMD [70] from the CECIL code [71]. The spectra have been obtained for neutron energy down to about 3 MeV, but the spectra above 10 MeV are shown in these figures. In general, the spectra in the forward direction have a broad peak at the high-energy end. The peak energy usually occurs at about 60 to 70% of the beam energy per nucleon. As the target mass becomes lighter and the projectile mass increases, the high-energy peak becomes more prominent. For example, the dependence on target mass can be clearly seen comparing the 400 MeV/nucleon C + C system with the 400 MeV/nucleon C + Pb system (Figure 9). Comparing the 400 MeV/nucleon C + Pb and Xe + Pb systems (Figures 9 and 11) shows a good example of the dependence on projectile mass. Most of the neutrons in this high-energy, forward region come from the break-up of the projectile and direct knock-on processes. The peak yield of the knock-on neutrons increases with decrease in the mass number of target nuclei. This is because the ratio of the cross-section of peripheral collision, which is a main source of the knock-on neutrons, to that of the central collision, which is a main source of evaporation process, is inversely proportional to the radius of the target nucleus.

At the high-energy end of the neutron spectra in the most forward direction, the high-energy tail spreads up to 2.5 times the incoming beam energy per nucleon, i.e. about 1 000 MeV for 400 MeV/nucleon. This can be explained by considering high-momentum components of a Fermi motion in a nucleus. The projectile nuclei are highly excited through the direct collision with some nucleons moving in the target nucleus to produce the projectile-like fragments. The high-energy neutrons are produced from the thus-excited projectile-like fragments.

At energies below 20 MeV, the spectra are dominated by the break-up of the target, evaporation process. Because the target remnant is moving slowly in the laboratory frame, that source of neutrons is essentially isotropic. As such, target-like neutrons can be seen at all angles. As target mass increases, the relative contribution to the overall spectra from target break-up increases. This feature can be seen by comparing 400 MeV/nucleon C + C and C + Pb spectra (Figure 9) at low energies.

At intermediate energies and intermediate angles, the spectra are dominated by the decay of the overlap region, where a sizeable number of projectile nucleons and target nucleons mix and can undergo several nucleon-nucleon collisions. As the impact parameter of the projectile-target interaction decreases, the likelihood of a surviving projectile source and target source also decreases, and the

contribution of the overlap region becomes the dominant source. Because interactions in a thick-target experiment occur over all projectile energies up to the incident beam energy, one cannot definitively say that an intermediate-energy neutron at forward angles comes from a projectile source or an overlap source, however.

As can be seen in Figures 9 to 11, PHITS calculation gives overall good agreement with the experimental data within a factor of three, except for a few cases. Uncertainties in the PHITS results are not plotted in the figures, and in general are of the order of about 5-15%, except for the highest energies, where the uncertainties can be greater than 50%. It is noted that the dropping curve at the high-energy end of neutron spectra in the most forward direction is reproduced well by PHITS. This means that the Quantum Molecular Dynamics (QMD) model is able to trace the behaviour of nucleons inside the nucleus including Fermi motion, and give proper relativistic correction for nucleus-nucleus interaction. A systematic underestimation, however, appears around the broad peak of knock-on neutrons. This deviation should be further revised by considering the nucleon-nucleon interaction.

Kurosawa, *et al.* [63] found that the HIMAC results verified the result found in Ref. [66] that the total yield shows very little dependence on target mass. Clearly, there is a dependence on projectile mass, and they found that the total yields above 5 MeV integrated between 0° and 90° could be estimated with the following formula:

$$Y = \frac{1.5 \times 10^{-6}}{N_T^{1/3}} E_P^2 \left(A_P^{1/3} + A_T^{1/3} \right)^2 N_P \frac{A_P}{Z_P^2} \tag{1}$$

where N_T and N_P are the neutron numbers of the target and projectile, A_T and A_P are the mass numbers of the target and projectile, Z_P is the atomic number of the projectile, and E_P is the incident energy per nucleon.

Figure 12 gives the normalised total yields using Eq. (1) by comparing the measured data above 5 MeV for C, Al, Cu and Pb targets. Eq. (1) gives in general good agreement with the measured data.

Moving-source model of thick-target neutron yield

The moving-source parameterisation has been used successfully in reproducing inclusive charged particle and neutron spectra from charged-particle interactions. The moving-source model assumes there are three thermal moving sources: One projectile-like source moving at a velocity near the incoming beam velocity; a second, target-like source moving very slowly in the laboratory frame; and a third "overlap" source moving 1/2 to 1/3 of the velocity of the beam. Each source is assumed to thermally emit nucleons with an isotropic distribution in its own rest frame. The spectrum of nucleons in the source's rest frame has the Maxwellian form:

$$\sqrt{E} e^{-E/T} \tag{2}$$

where E is the energy of the nucleon, and T is the temperature of the source.

Kato, *et al.* [72] fit the thick-target neutron yield data of Kurosawa, *et al.* [60-63] with the following moving source parameterisation:

$$\frac{d^2 Y}{dEd\Omega} = \left\{ \frac{N_0}{\sqrt{2\pi\sigma_c(\theta)^2}} \exp\left(-\frac{(E_n - E_c(\theta))^2}{2\sigma_c(\theta)^2} \right) \right\} + \left\{ \sum_{i=1}^{2} N_i \frac{\sqrt{E_n}}{2(\pi T_i)^{3/2}} \exp\left(-\frac{E_s}{T_i} \right) \right\} \tag{3}$$

where Y is the neutron fluence (neutron MeV^{-1} sr^{-1} ion^{-1}), E_n is the neutron energy in the laboratory reference frame, N is the source normalisation parameter (n MeV^{-1} sr^{-1} ion^{-1}), T is the source nuclear-temperature parameter (MeV), θ is the emission angle in the laboratory system (degrees), $E_c(\theta)$ is the peak energy fitting parameter (MeV), $\sigma_c(\theta)$ is the width (variance) fitting parameter (MeV), and E_s is the neutron energy in the source's rest frame, given by:

$$E_s = E_n + \varepsilon_i - 2\sqrt{\varepsilon_i E_n} \cos\theta \tag{4}$$

By studying the systematic trends in the fitting parameters, analytical forms of each parameter can be deduced. This allows for a reliable means to extend the moving source calculation beyond the

systems that were measured. Figure 13 exemplifies the fits to the neutron spectra from the Cu target with 100 MeV/nucleon He ion, and from the C target with 400 MeV/nucleon C ion, measured by Kurosawa, *et al.* [60,61] The fits using the moving source model well reproduce the measured spectra.

Spallation products production cross-section data

An important component in the design of heavy-ion accelerator facilities is an accurate estimation of the radioactivities induced by spallation products in accelerator components and in shielding materials. For this purpose, the production cross-sections for various spallation products have been measured from heavy-ion reactions by several groups. Table 5 shows the various beams, targets and facilities used in the experiments, along with the relevant references.

^{12}C + Cu excitation function

Using the data of Yashima, *et al.* [79-81], Kim, *et al.* [78], Titarenko, *et al.* [84], and Cumming, *et al.* [73-75], it is possible to plot the ^{12}C + Cu reaction cross-sections for various nuclides as a function of beam energy. Figure 14 exemplifies the excitation functions for some isotopes of four selected elements, Cr, Mn, Fe, Co. Only isotopes that were measured at all five energies are shown. The points at 100 MeV/nucleon, 230 MeV/nucleon and 400 MeV/nucleon come from Yashima, *et al.* [79-81], the points at 135 MeV/nucleon come from Kim, *et al.* [78], the points at 200 MeV/nucleon come from Titarenko, *et al.* [84], and the points at 2083 MeV/nucleon come from Cumming, *et al.* [74]. In general, as the beam energy increases, the cross-section decreases. This trend is especially evident for elements near the mass of the target (Cu).

Mass-yield distributions

The data can be summed over the same mass numbers to produce mass-yield (isobaric-yield) distributions. Figure 15 shows the mass-yield distributions (in mb) for the 230, 400 and 800 MeV/nucleon Ar, Ne, C and Si ions interacting in a Cu target, as examples by Yashima, *et al.* at HIMAC [80,81]. In general, as the mass of the beam increases, the yield also increases. In the figure, produced nuclides can be divided into the following three groups: (I) target fragmentation induced from a reaction of which the impact parameter is small or projectile fragmentation for heavy projectile; (III) target fragmentation induced from a reaction of which the impact parameter is almost equal to the sum of projectile radius and target radius; (II) target fragmentation induced from a reaction of which impact parameter is in the medium of (I) and (III). As can be expected from the trends noted in the excitation functions shown in Figure 14, the mass yields are somewhat independent of energy, although there appears to be a slight decrease in yield with increasing energy for the higher mass yields. Figure 15 also gives the comparison between the experimental results and the PHITS calculations. The C/E (calculation/experiment) ratios are shown in Figure 15(f). As shown in the figure, the PHITS calculations in general agree well with the experimental values within a factor of 2 except for several products. The PHITS calculation gives a large underestimation of the cross-sections, especially for the heavy-mass products. Figure 16 shows the experimental results for Cu target bombarded by 200 MeV/nucleon C ions by Titarenko, *et al.* at TWA-ITEP [84]. The experimental results are compared with the LAQGSM+GEM2 code [89] and the CASCADE code [90]. The LAQGSM+GEM2 code gives in general better agreement with the experimental data than the CASCADE code.

Induced activities

The spatial distributions of residual activities of isotopes produced in thick copper target by bombarding various ion beams are also measured. Figures 17(a) to 17(f) show the spatial distributions of residual activities of ^{7}Be, ^{22}Na, ^{38}Cl, ^{49}Cr, ^{56}Mn and ^{61}Cu isotopes produced in Cu target as a function of Cu depth in the unit of beam range for p, He, C, Ne, Si, Ar ion beams with different energies at HIMAC [82]. The feature of these figures can be summarised as follows. When the mass number difference between Cu and the produced nuclide is large, nuclides are produced dominantly by the primary projectile reaction. The reaction cross-sections therefore almost or slowly decrease with the target depth, according to the attenuation of projectile flux through the target. When the mass number difference between Cu and the produced nuclide is small, the fraction of nuclides produced

by secondary particles is large. With increasing mass number and projectile energy, the reaction cross-section increases with the depth of Cu target due to the increasing contribution of secondary particle reactions. In Figure 17, residual activity steeply increases near the projectile range in some cases. This is attributed to the projectile fragmentation just before stopping at the range. Since a projectile fragment has the same velocity and direction as the projectile ion, the projectile fragment stops at a slightly deeper point than the projectile range.

Summary

This review summarises the experimental data up to 2008 on energy and angular distributions of neutrons produced from thick targets of various materials bombarded by protons, deuterons, He and heavier ions having wide energy range from MeV to GeV. Total neutron yields and the moving source model approximations are also presented. Production cross-section data for spallation by proton to Ar ion are also summarised in this paper, as well as excitation functions, mass-yield distributions and induced activities. Very recent results on induced activities are included for Ar and U ions. These data will be very useful both as benchmark data for computer code validation and as source term data for accelerator shielding design calculation and induced activity evaluation.

Table 1: General information on thick-target neutron yield experiments by proton beams

Proj.	Energy (MeV)	Target	Emission angle (degree)	Facility	Neutron detection	Ref.
p	15	Li-7	0-45	Duke Univ.	NE218, TOF	4
	15, 18, 23	Li, Be	0 (0-40)	Chalk River	Stilben, TOF	5
	22, 30, 40	C, Al, Cu, Ta, Ag, Pb	0-150	NSCL	NE213, TOF	6
	25,35,45,55	Be	0-50	UC Davis	NE213, TOF	7
	30	C-13	0-120	Jyvaskira	Position Sensitive Detector, TOF	8
	30	C, Fe, Cu, Pb	0-135	INS	NE213, Unfolding	9
	35, 46	Be	0, 15, 45	Princeton	NE213, TOF	10
	35, 50, 70	Fe, Cu	0, 30, 60, 90, 110	CYRIC	NE213, TOF	11
	40	Al, Fe, Cu, Ta, SUS	0, 45, 90	Milano	Activation	12
	50	C, Al, Ta, W	0-90	CYRIC	NE213, TOF	13
	52	C, Fe, Cu, Pb	0-75	INS	NE213, Unfolding	14
	68	Be, C, Al, Cu, Au	0, 30, 60, 120	TIARA	NE213, TOF	15
	72	Cu	90-150	SIN(PSI)	Activation	16
	90	C-13	0-150	Groningen	NE213, TOF	17
	113	Be, C, Al, Fe, U	7.5-150	LAMPF	BC418, TOF	18
	140	C, Al, Fe, Pb	0, 90, 180	RCNP	NE213, TOF	19
	210	Fe	0-110	RIKEN	NE213, TOF	20
	250, 350	C, Al, Fe, Pb	0	RCNP	NE213, TOF	21
	256	C, Al, Fe, U	30-150	LAMPF	BC418, TOF	22
	500, 1 500	Pb	15-150	KEK	NE213, TOF	23
	500, 1 500	W	15-150	KEK	NE213, TOF	24
	590	Pb, U, Pb-Bi	30, 90, 150	SIN(PSI)	NE102, NE228, TOF	25
	660	Pb	60	JINR	NaI(Tl), TOF	26
	740	dep U + Steel	50, 130	LBL	NE102, NE228, TOF	27
	740	U	50, 130	LAMPF	NE213, Unfolding	28
	800, 1 200, 1 600	Pb, Fe, W, Al	0-160	SATURNE	NE213, TOF	29
	1 500	Fe	15, 30, 60, 90	KEK	NE213, TOF	30

Table 2: General information on thick-target neutron yield experiments by deuteron beams

Proj.	Energy (MeV)	Target	Emission angle (degree)	Facility	Neutron detection	Ref.
d	8,12,15	Li-7	0-45	Duke Univ.	NE218, TOF	4
	15, 18 23	Li, Be	0 (0-40)	Chalk River	Stilben, TOF	5
	16, 28	Be	0, 15, 45	Princeton	NE102A, TOF	10
	16, 33, 50	Be, C, Mo, Cu, Ta, Au	0-64	Louvain	NE111, TOF	43
	17, 20, 28	Be, C, U	0-20	IPN Orsay	NE213, TOF	44
	25	Li, Be	0-90	CYRIC	NE213, TOF	45
	33	C, Fe, Cu, Pb	0-135	INS	NE213, Unfolding	46
	40	Li	0-110	CYRIC	NE213, TOF	47
	40	C, Al	0-110	CYRIC	NE213, TOF	48
	40	Be	0-90	ORNL	NE213, TOF	49
	80, 160	Be, C	2.3-33.3	Groningen	NE213, TOF	50
	200	Be, U	0-84	Saturne	Activation	51

Table 3: General information on thick-target neutron yield experiments by He and heavier ion beams having lower than 100 MeV/nucleon energies

Proj.	Energy (MeV)	Target	Emission angle (degree)	Facility	Neutron detection	Ref.
³He	44	Be	0, 15, 45	Princeton	NE102A, TOF	10
	65	C, Fe, Cu, Pb	0-135	INS	NE213, Unfolding	46
α	30, 40 50	Al, Ti	0, 30, 45	VECC	NE213, Unfolding	53
	40, 50, 60	Be, Ta, Au	0, 30, 60, 90	VECC	NE213, Unfolding	54
	65	C, Fe, Cu, Pb	0-135	INS	NE213, Unfolding	46
	80	Ta	0, 60, 90	LBL	Activation	55
	100	C, Fe, Zr, Au	0-120	TIARA	NE213, TOF	16
⁶Li, ⁷Li	40	⁷Li, Be, C, Cu	0-120	Geel	NE213, TOF	56
¹¹B	42, 62	Al	0, 90	BARC-TIFR	BC501, TOF	57
¹²C	54, 65, 75, 84	Al	0, 90	BARC-TIFR	BC501, TOF	57
	220	C, Fe, Zr, Au	0-120	TIARA	NE213, TOF	58
Ar	95/nucleon	C	0, 20, 45, 90	Saturne	Activation	51
	460	C, Fe, Zr, Au	0-120	TIARA	NE213, TOF	58

**Table 4: General information on thick-target neutron yield experiments
by heavy ions having higher than 100 MeV/nucleon energies [2]**

Beam ion and energy (MeV/nucleon)	Targets	Measured spectra	θ (deg)	Emin (MeV)	Facility
He (100)	C, Al, Cu, Pb	TTY, n/dΩ total	0-90	3-5.5	HIMAC [60,61,68]
He (155)	Al	TTY, n/dΩ total	10-160	3-10	NSCL [65]
He (160)	Pb	TTY Total	0-150	3-13	SREL [66]
He (177.5)	C, H_2O, Steel, Pb	TTY Total	0-150	3-13	SREL [66]
He (180)	C, Al, Cu, Pb	TTY, n/dΩ total	0-90	3.5-17	HIMAC [60,61,68]
C (100)	C, Al, Cu, Pb	TTY, n/dΩ total	0-90	3-4	HIMAC [60,61,68]
C (155)	Al	TTY, n/dΩ total	10-160	3-10	NSCL [65]
C (180)	C, Al, Cu, Pb	TTY, n/dΩ total	0-90	2.5-5.5	HIMAC [60,61,68]
C (400)	C, Al, Cu, Pb	TTY, n/dΩ total	0-90	3-8.5	HIMAC [60,61,68]
Ne (100)	C, Al, Cu, Pb	TTY, n/dΩ total	0-90	5-6	HIMAC [62,68]
Ne (180)	C, Al, Cu, Pb	TTY, n/dΩ total	0-90	3-9.6	HIMAC [62,68]
Ne (400)	C, Al, Cu, Pb	TTY, n/dΩ total	0-90	3-6	HIMAC [62,68]
Si (800)	C, Cu	TTY, n/dΩ total	0-90	3.5-11	HIMAC [63,68]
Ar (400)	C, Al, Cu, Pb	TTY, n/dΩ total	0-90	3-10	HIMAC [63,68]
Fe (400)	C, Al, Cu, Pb	TTY, n/dΩ total	0-160	3-12	HIMAC [63,68,69]
Nb (272)	Nb, Al	TTY, n/dΩ n/dE, total	3-80	20 (all angles)	Bevalac [64]
Nb (435)	Nb	TTY, n/dΩ n/dE, total	3-80	20 (all angles)	Bevalac [64]
Xe (400)	C, Al, Cu, Pb	TTY, n/dΩ total	0-90	3.5-10	HIMAC [63,68]
[238]U-238 (1 000)	Fe (20)	TTY, n/dΩ	0-20	50	GSI [67]

**Table 5: Listing of the beams, energies (MeV/nucleon), targets and
facilities used to measure spallation product cross-sections and/or induced
activities [2]. The appropriate reference(s) for each entry is also listed.**

Beam	Energy	Target	Facility	Reference
^{14}N	278 AMeV	^{nat}Cu	PPA	[73]
^{12}C	2 083 AMeV	^{nat}Cu	Bevalac	[74]
^{40}Ar	2 000 AMeV	^{nat}Cu	Bevalac	[75]
^{12}C	2 100 AMeV	^{nat}Cu	Bevalac	[76]
^{20}Ne	211 AMeV	^{nat}Cu	Bevalac	[77]
^{20}Ne	377 AMeV	^{nat}Cu	Bevalac	[77]
^{12}C	135 AMeV	^{nat}Cu	RIKEN	[78]
^{4}He	100 AMeV	C, Al, Cr, Fe, Ni, Cu, Pb	HIMAC	[79,80]
^{12}C	100 AMeV	C, Al, Cr, Fe, Ni, Cu, Pb	HIMAC	[79,80]
^{20}Ne	100 AMeV	C, Al, Cr, Fe, Ni, Cu, Pb	HIMAC	[79,80]
^{4}He	230 AMeV	C, Al, Cr, Fe, Ni, Cu, Pb	HIMAC	[79,80]
^{12}C	230 AMeV	Al, Cr, Fe, Ni, Cu, Pb	HIMAC	[79,80]
^{20}Ne	230 AMeV	C, Al, Cr, Fe, Ni, Cu, Pb	HIMAC	[79,80]
^{40}Ar	230 AMeV	C, Al, Cr, Fe, Ni, Cu, Pb	HIMAC	[79,80]
^{12}C	400 AMeV	C, Al, Cr, Fe, Ni, Cu, Pb	HIMAC	[81,82]
^{20}Ne	400 AMeV	C, Al, Cr, Fe, Ni, Cu, Pb	HIMAC	[81,82]
^{40}Ar	400 AMeV	C, Al, Cr, Fe, Ni, Cu, Pb	HIMAC	[81,82]
^{28}Si	800 AMeV	C, Al, Cr, Fe, Ni, Cu, Pb	HIMAC	[81,82]
^{12}C	100 AMeV 200 AMeV	^{nat}Cu, Co ^{63}Cu, ^{65}Cu, Al, Co	GSI TWA-ITEP	[83] [84]
^{40}Ar	500 AMeV 800 AMeV 1 000 AMeV	Cu	GSI	[83] [85]
^{56}Fe	1 000 AMeV	Al, Pb, CH$_2$ PMMA	HIMAC	[86]
^{238}U	500 AMeV 950 AMeV	Cu Stainless steel	GSI	[87] [88]

Figure 1: Neutron yield spectra from stopping (a) Al, (b) Cu, and (c) Pb targets bombarded by protons at energies of 22, 30 and 40 MeV. Each energy group has spectra at 0, 30, 60, 90, 120, and 150°. Between the spectra labelled 0 and 150° are the other four spectra in monotonically descending order [6].
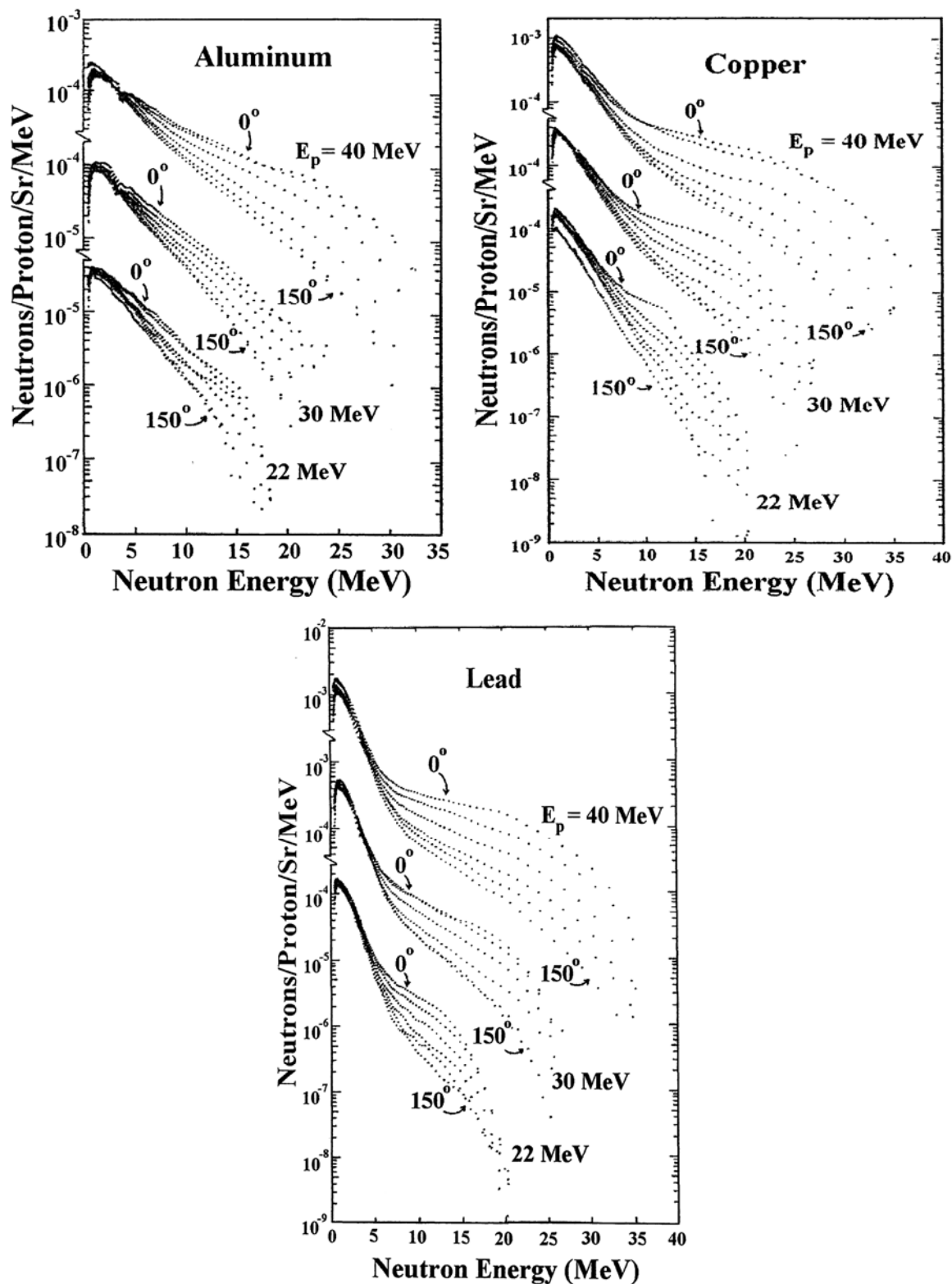
Figure 2: Neutron energy spectra from the iron target bombarded by 210 MeV proton compared with the calculations at angles of 0, 7.5, 15, 30, 60, 90 and 110° [20]
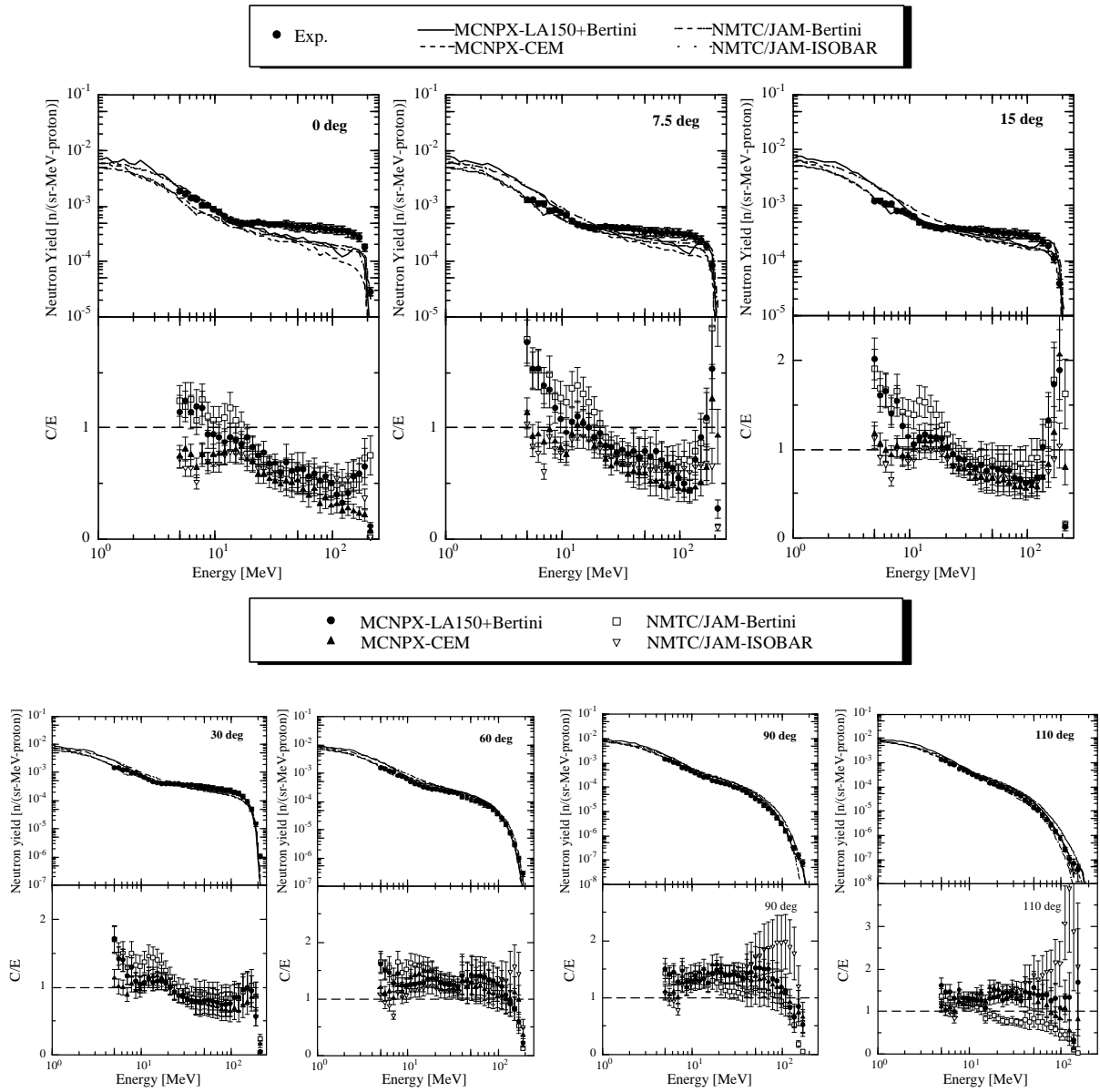
Figure 3: Neutron energy spectra for 140 MeV proton incidence on thick graphite, aluminium, iron and lead targets. The experimental results are compared with the calculated results as given in the text [21].
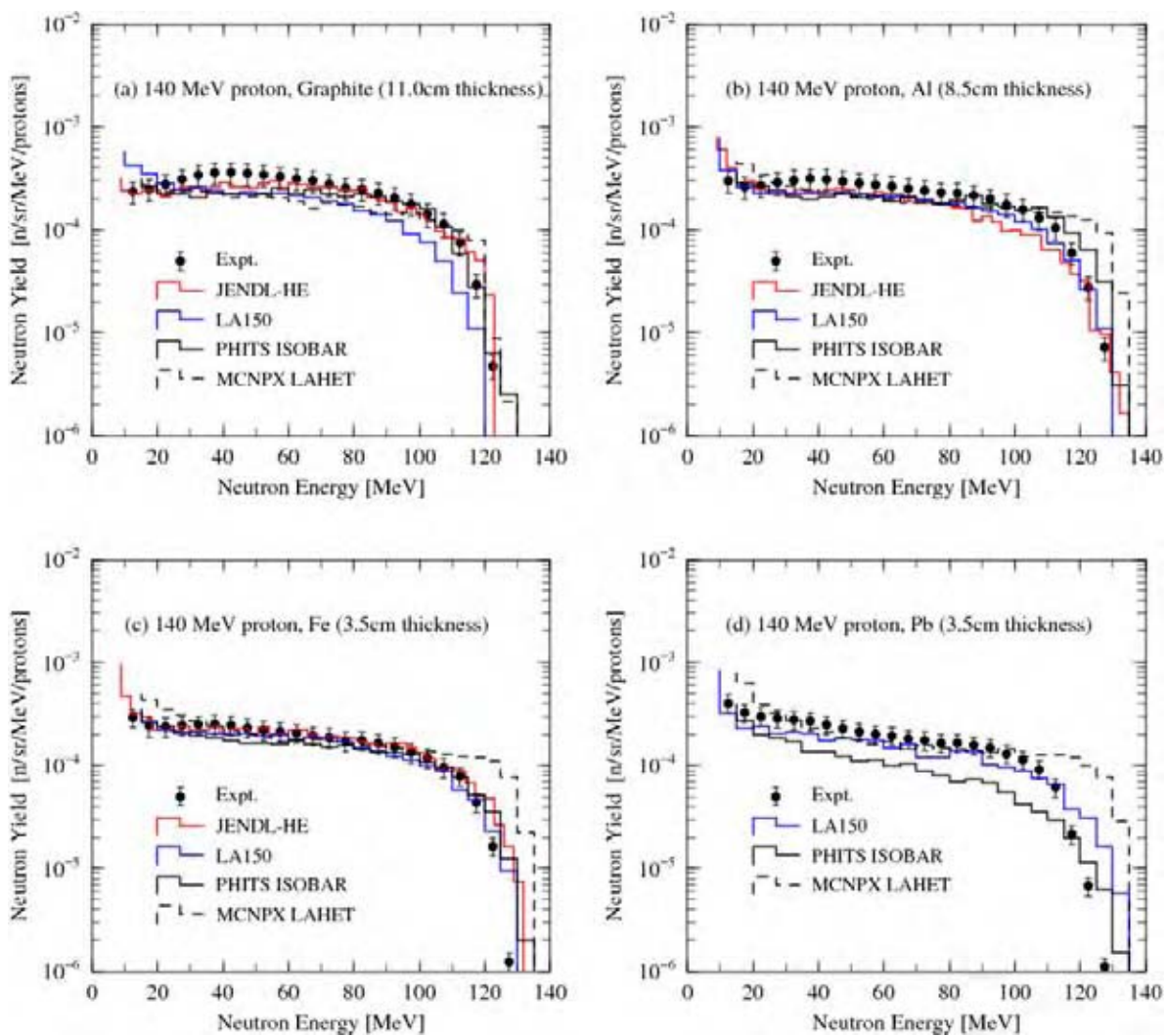
Figure 4: Neutron spectra for (a) 0.5 GeV and (b) 1.5 GeV protons incidence on thick lead target

Symbols stand for the experimental results, dashed and solid lines show results calculated with NMTC/JAERI
and MCNP-4A using free nucleon-nucleon cross-section (NNCS) and in-medium NNCS, respectively [23]
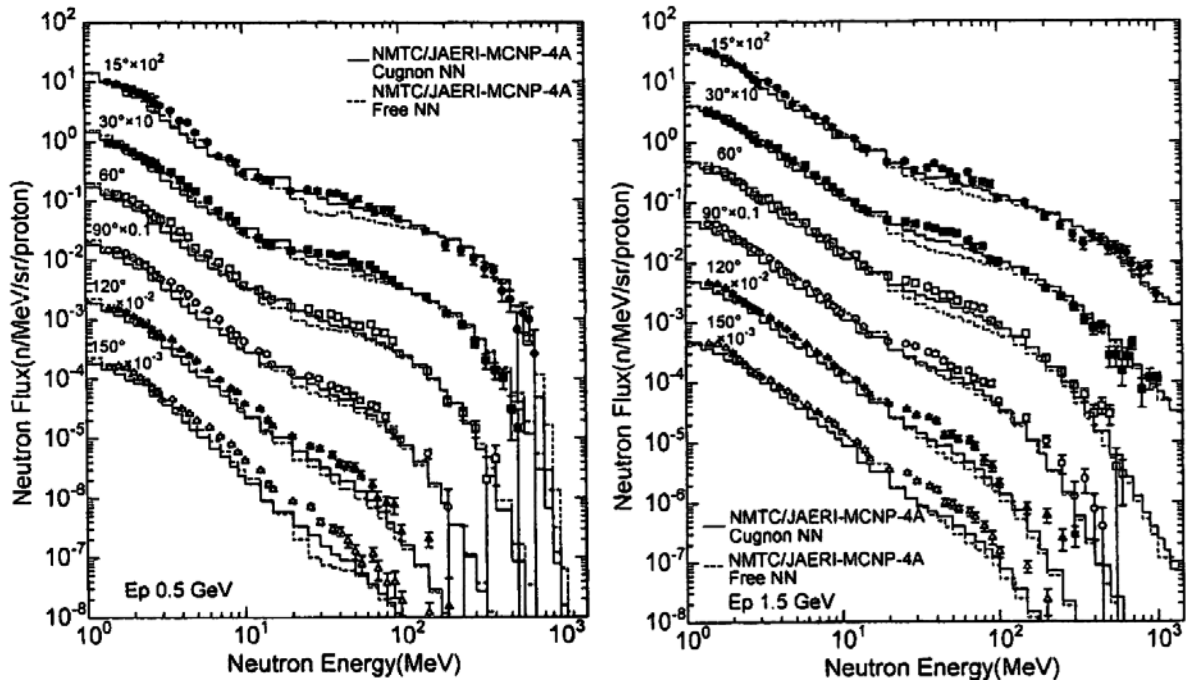
Figure 5: The results of thick-target neutron yields for (a) the Li(d,n) reaction and (b) the ^{9}Be(d,n) reaction for incident deuteron energy of 25 MeV [45]
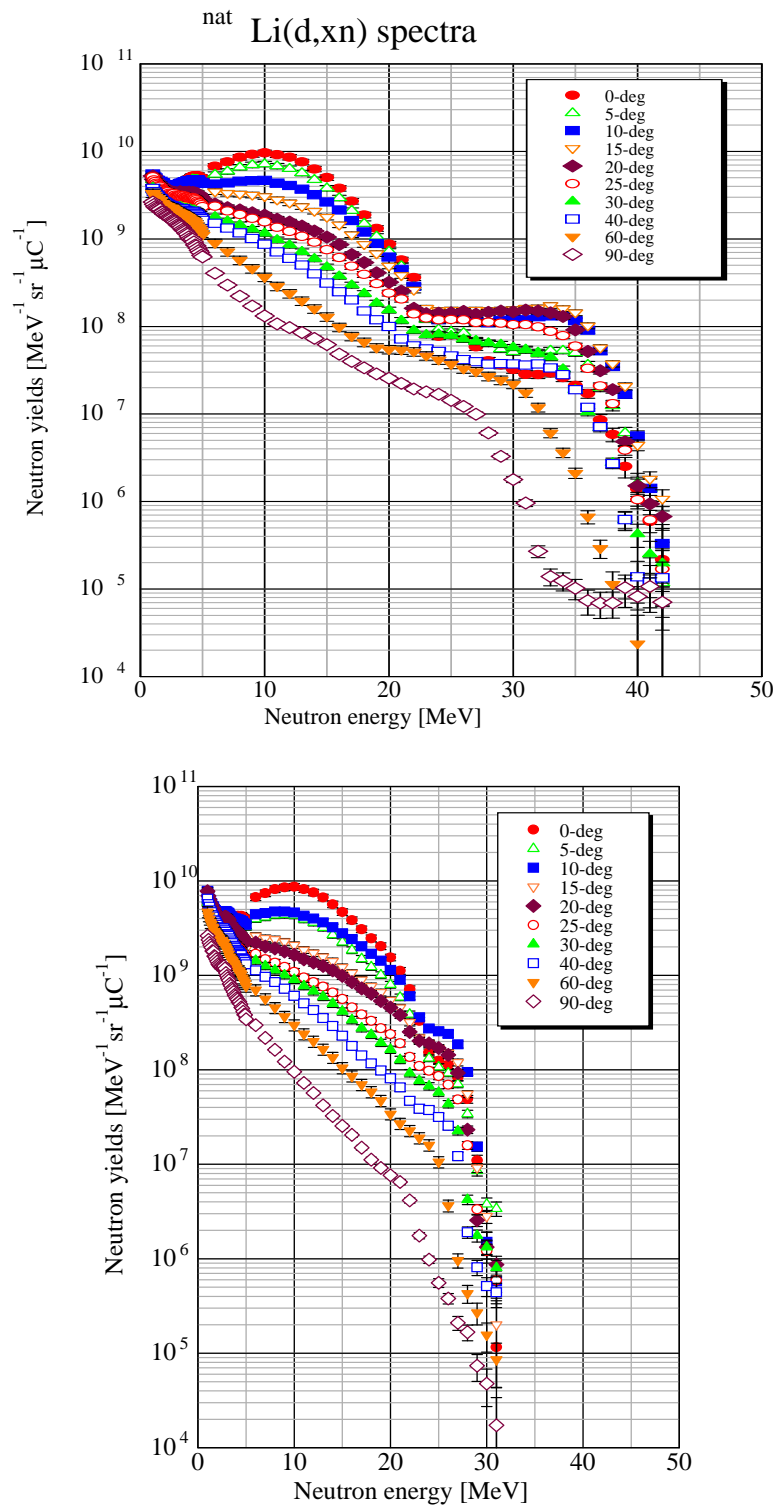
Figure 6: (a) Experimental energetic distributions of neutrons for 50 MeV ^{2}H incident energy on a thick Be target from Ref. [43]: filled circles at 0°, filled triangles with up-point at 5°, filled squares at 10°, and filled triangles with down-point at 25°. These distributions are compared with theoretical ones: (a) 0, (b) 5, (c) 10 and (d) 25°. The dotted lines are to guide the eye.
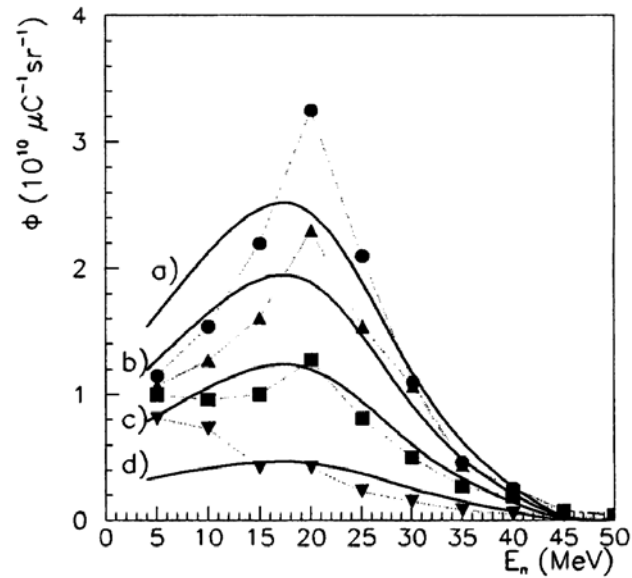
Figure 7: Neutron spectra of carbon, copper, and lead targets for 65-MeV ^{3}He injection at emission angles of 0, 15, 45, 75, and 135°. The spectra are normalised to one incident ^{3}He with a standard deviation. The solid curves indicate the Maxwellian distribution fitted to the neutron spectra [46].
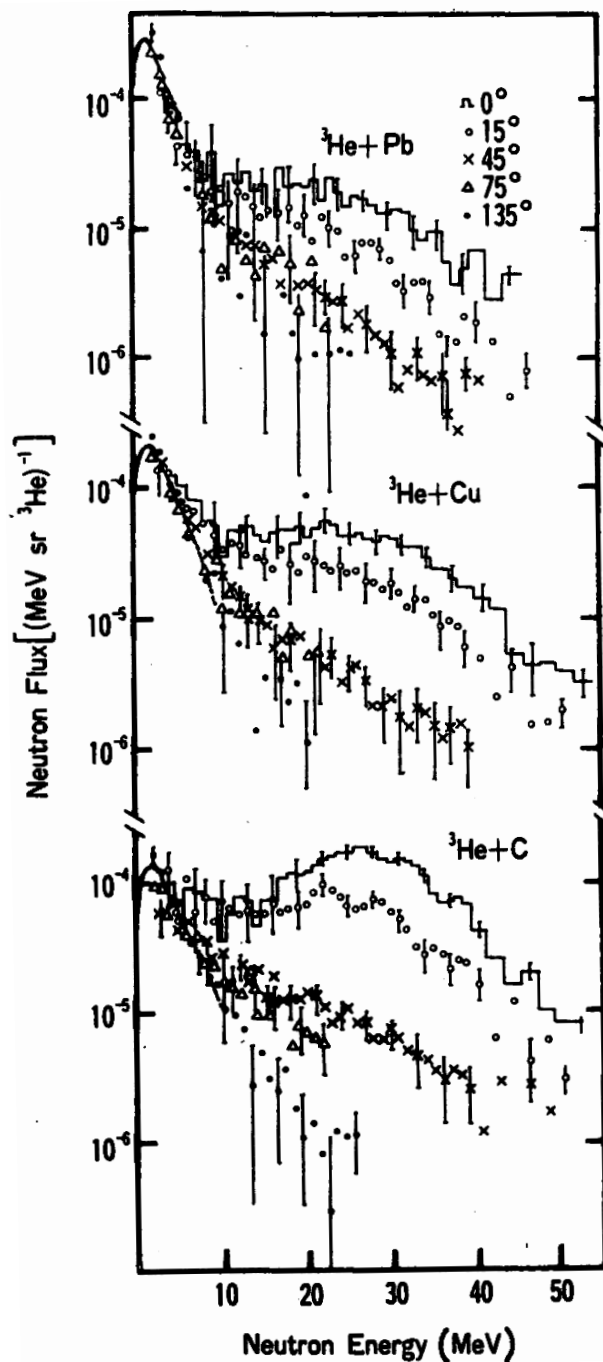
**Figure 8: Neutron spectra from ^{181}Ta target with 50 MeV alpha at 0, 30, 60, and 90°
emission angles. Experimental data are plotted in solid circles with error bars and
the solid lines are the theoretical calculations of the extended exciton model [54].**
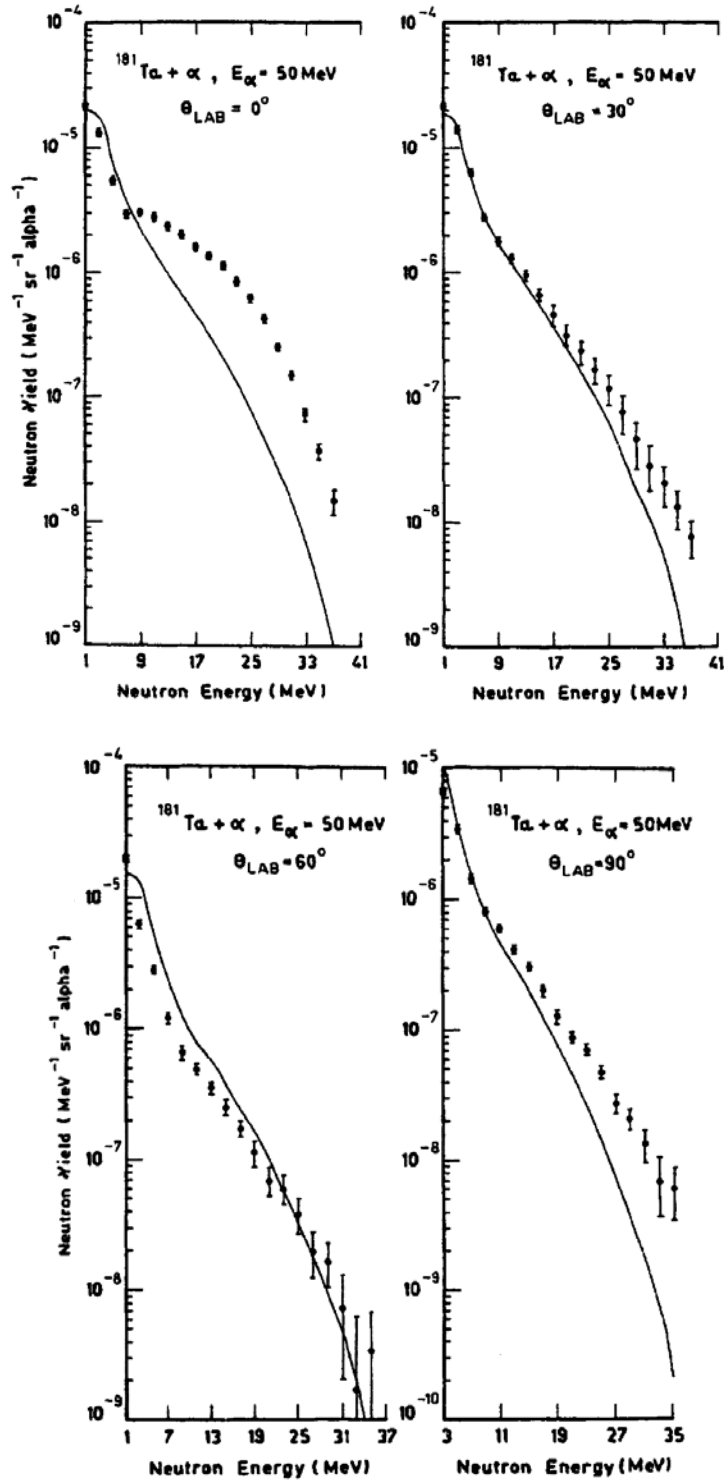
Figure 9: Neutron energy spectra for 400 MeV/nucleon C ion bombardment on thick C, Al, Cu and Pb targets. Marks indicate the experimental data and solid lines indicate the PHITS calculation [68].
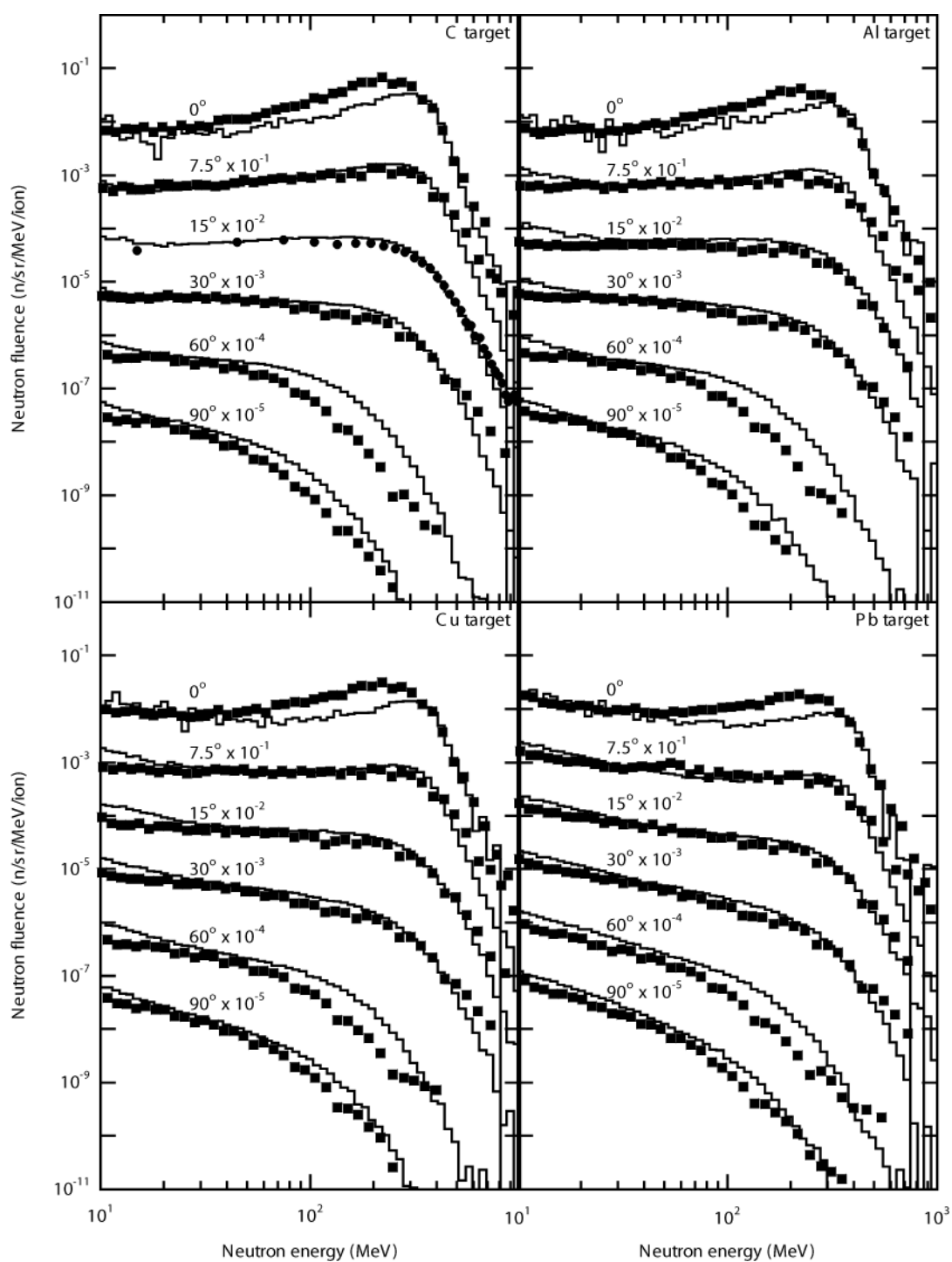
Figure 10: Neutron energy spectra for 400 MeV/nucleon Fe ion bombardment on thick C, Al, Cu and Pb targets. Marks indicate the experimental data and solid lines indicate the PHITS calculation [68].
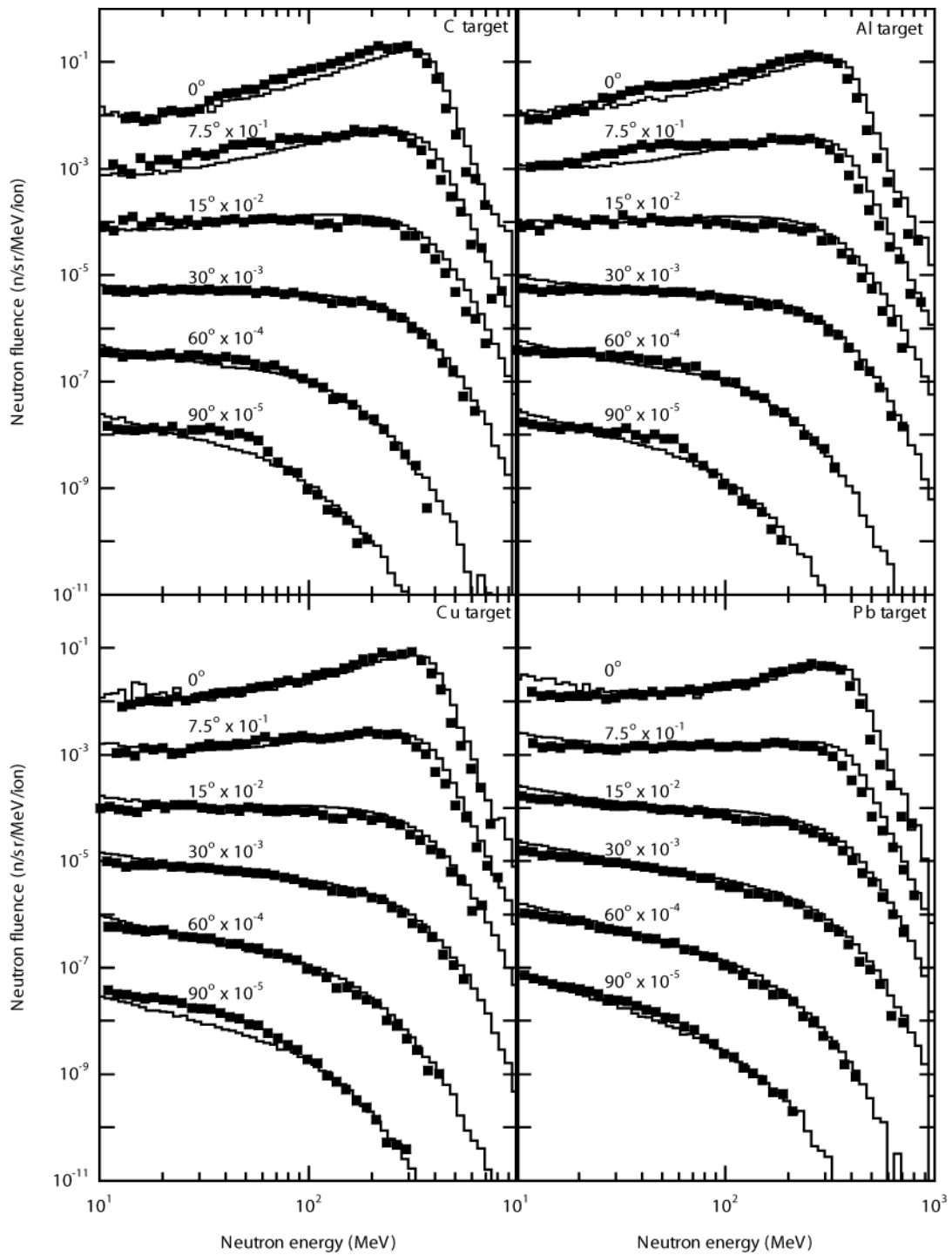
Figure 11: Neutron energy spectra for 400 MeV/nucleon Xe ion bombardment on thick C, Al, Cu and Pb targets. Marks indicate the experimental data and solid lines indicate the PHITS calculation [68].
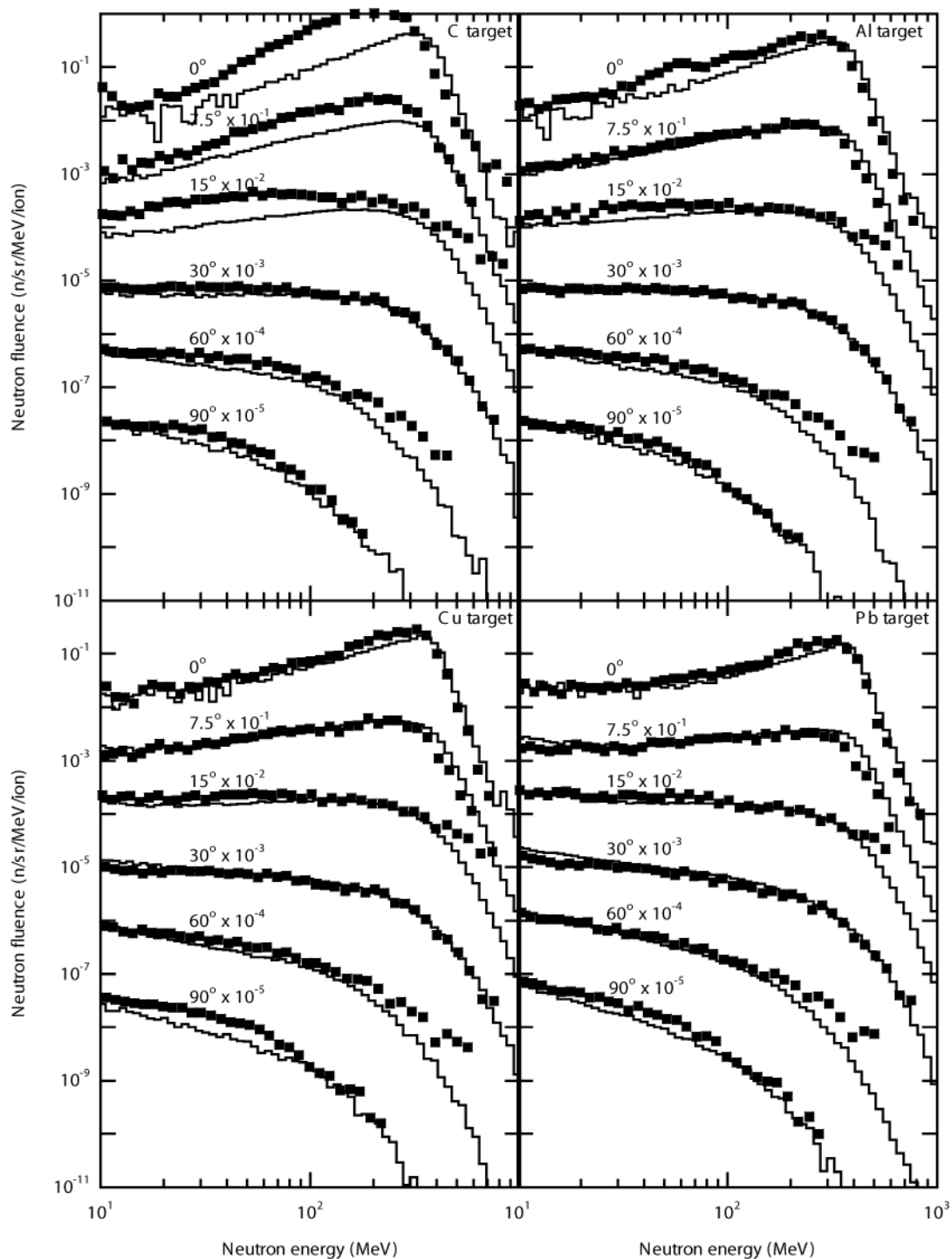
Figure 12: Normalised total neutron yield using Eq. (1) from the measured data which is shown by the symbols [63]. The solid lines are from the calculation using Eq. (1).
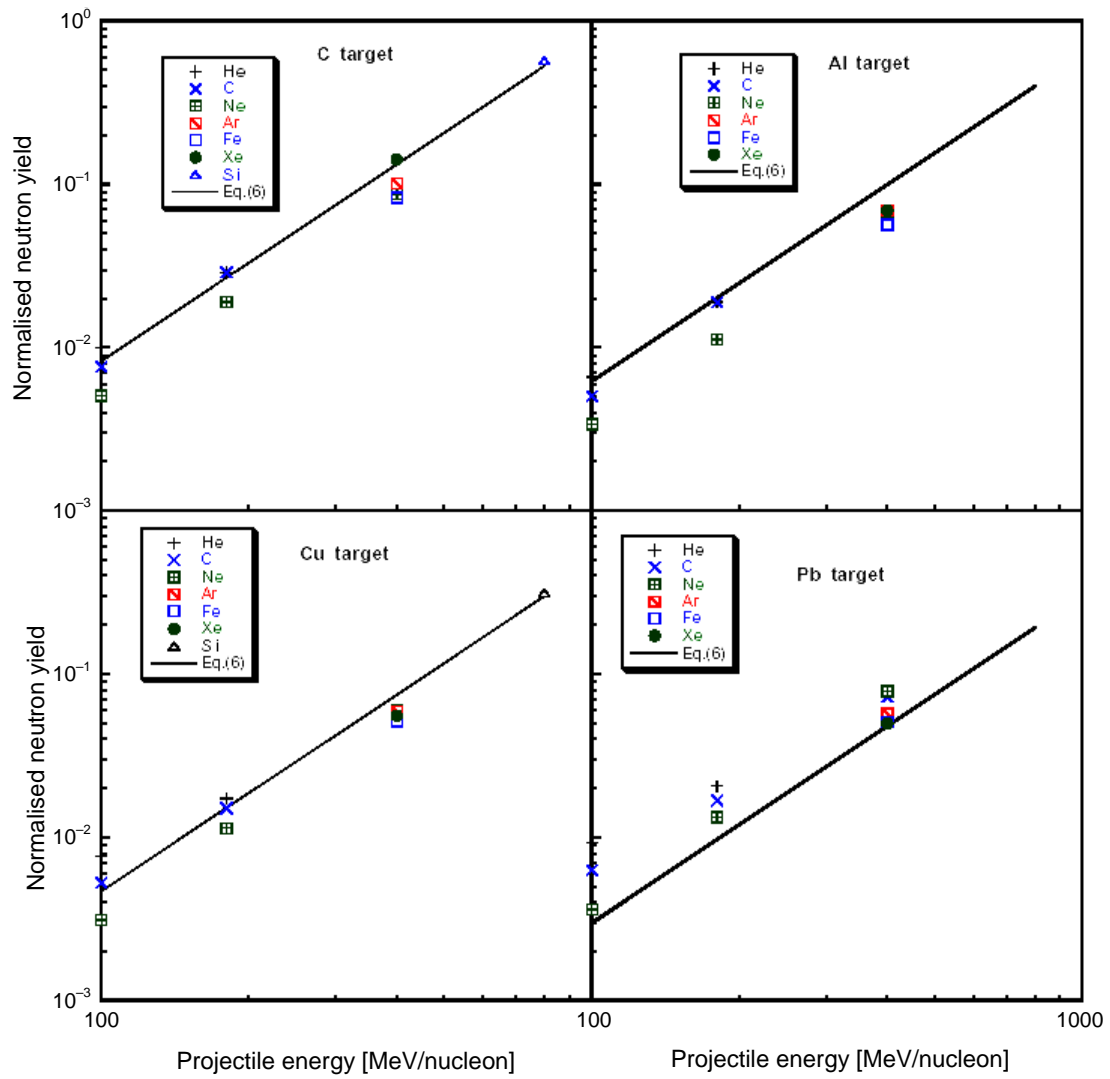
Figure 13: Moving source fits (solid lines) to data from (a) 100 MeV/nucleon He stopping in Cu and (b) 400 MeV/nucleon C stopping in C. Note the spectra are offset by the indicated factors of ten [2].
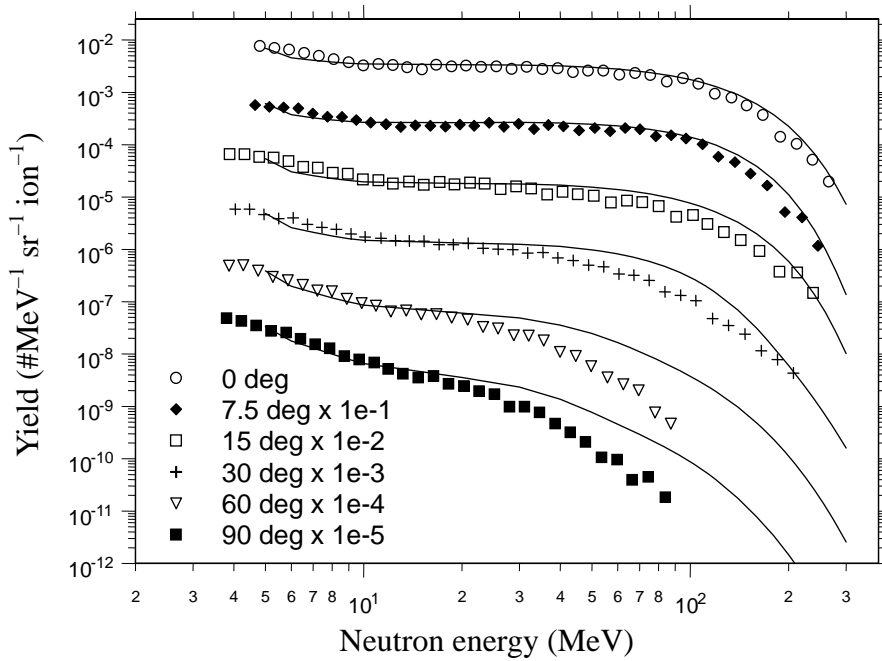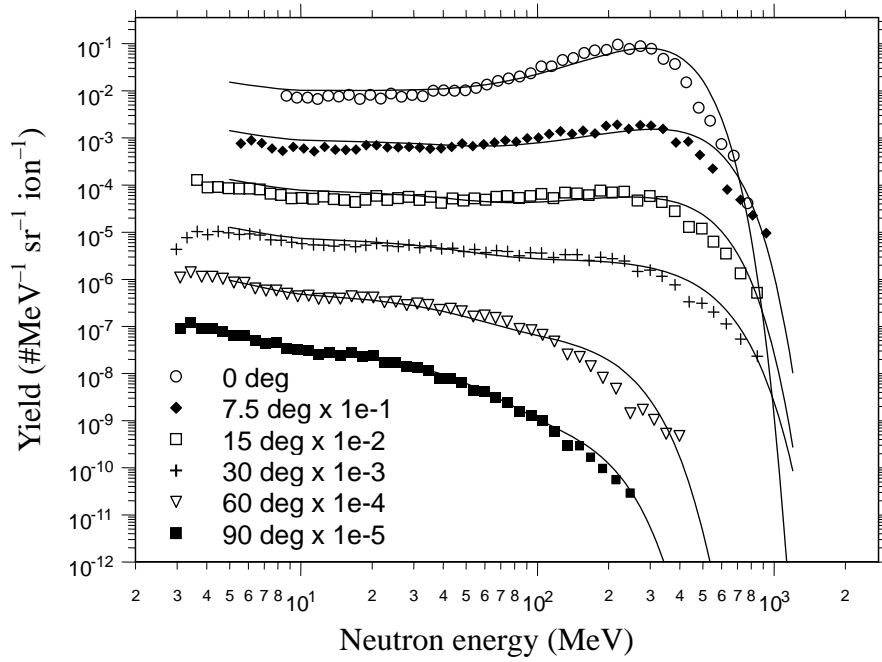
Figure 14: Excitation functions for various isotopes produced by ^{12}C interactions in Cu [2]

(a) Excitation function for ^{nat}Cu(^{12}C,x)Cr

(b) Excitation functions for ^{nat}Cu(^{12}C,x)Mn

(c) Excitation functions for ^{nat}Cu(^{12}C,x)Fe

(d) Excitation functions for ^{nat}Cu(^{12}C,x)Co
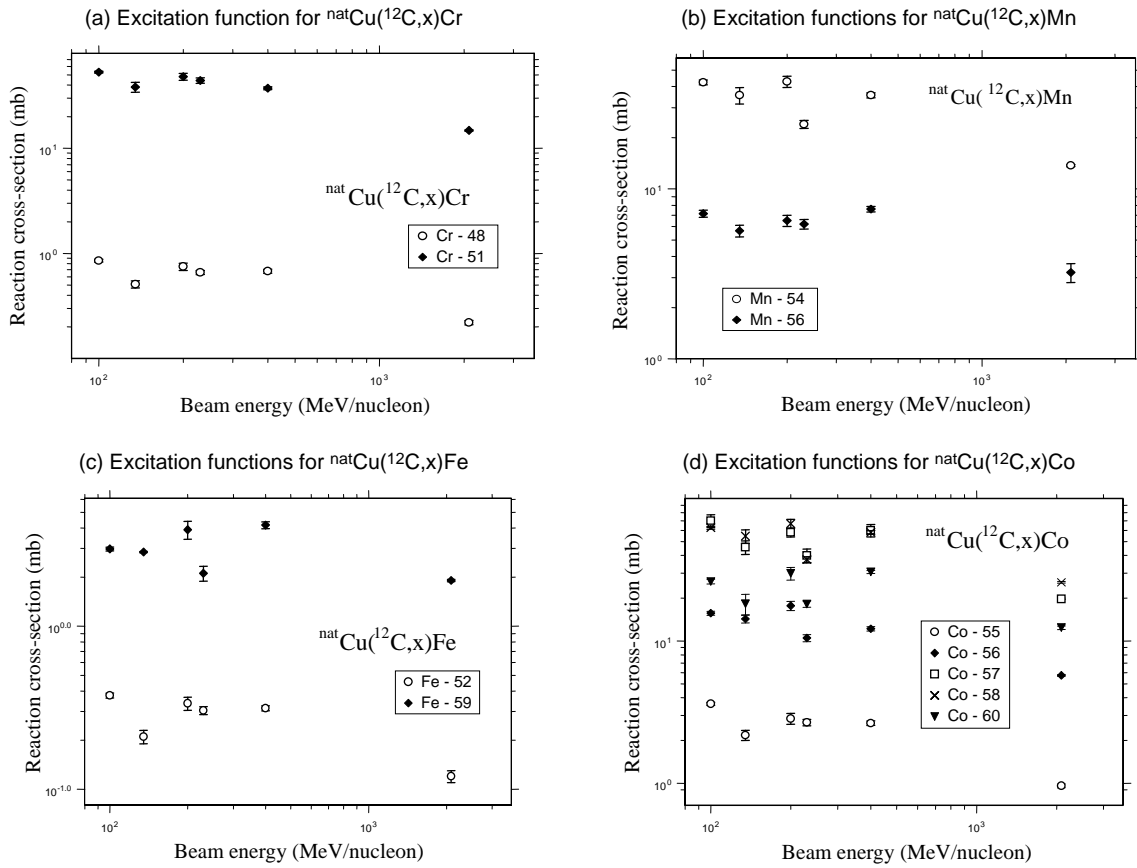
Figure 15: Comparison of measured cross-sections of radioactive nuclides produced in Cu for various projectiles with the PHITS Monte Carlo calculation [81]

(a) 230 MeV/nucleon Ar

(b) 400 MeV/nucleon Ar

(c) 400 MeV/nucleon Ne

(d) 400 MeV/nucleon C

(e) 800 MeV/nucleon Si

(f) C/E Value
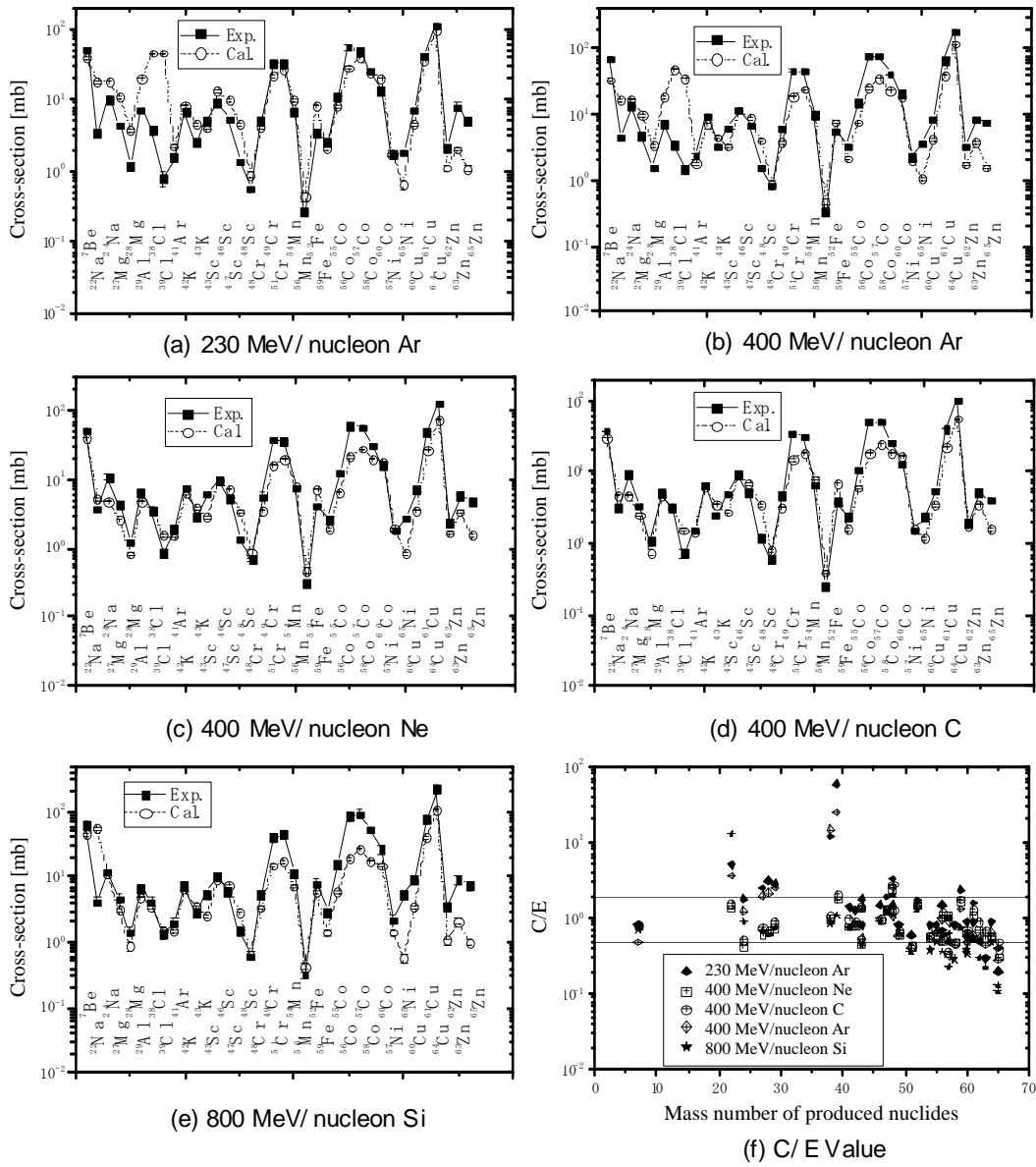
Figure 16: Comparison of measured cross-sections radioactive reaction products in Co and Cu induced by 200 MeV/nucleon C with the LAQGSM+GEM2 and CASCADE calculations [84]
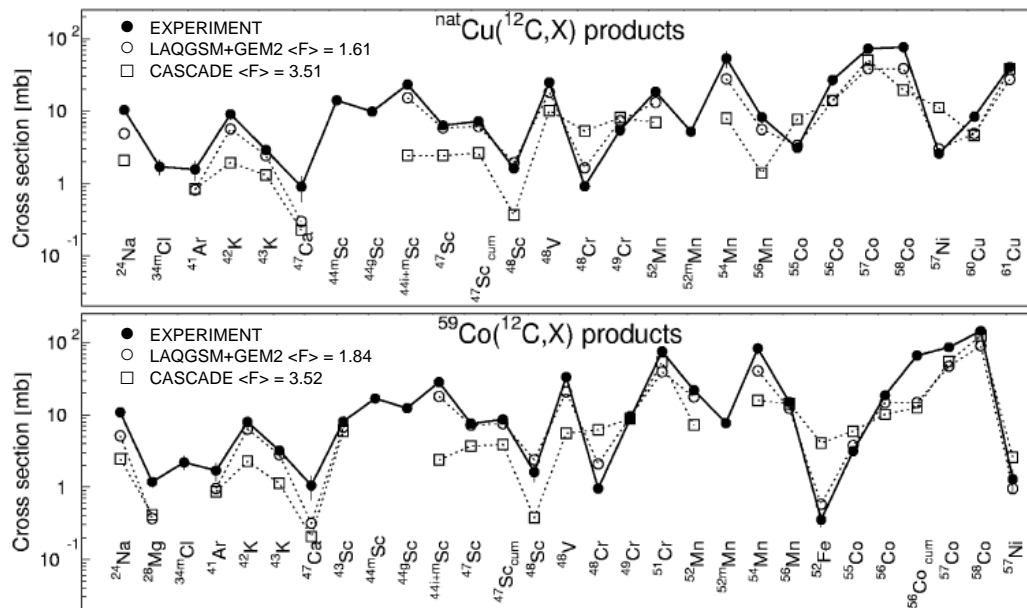
Figure 17: Spatial distribution of residual activities within Cu target depth.
For example, "Ne[230]" signifies 230 MeV/nucleon Ne irradiation [82].

(a) Residual activity of ^{7}Be

(b) Residual activity of ^{22}Na

(c) Residual activity of ^{38}Cl

(d) Residual activity of ^{49}Cr

(e) Residual activity of ^{56}Mn

(f) Residual activity of ^{61}Cu

Residual activity [Bq/ (ion g/ cm^2)]

Target depth normalised to beam range
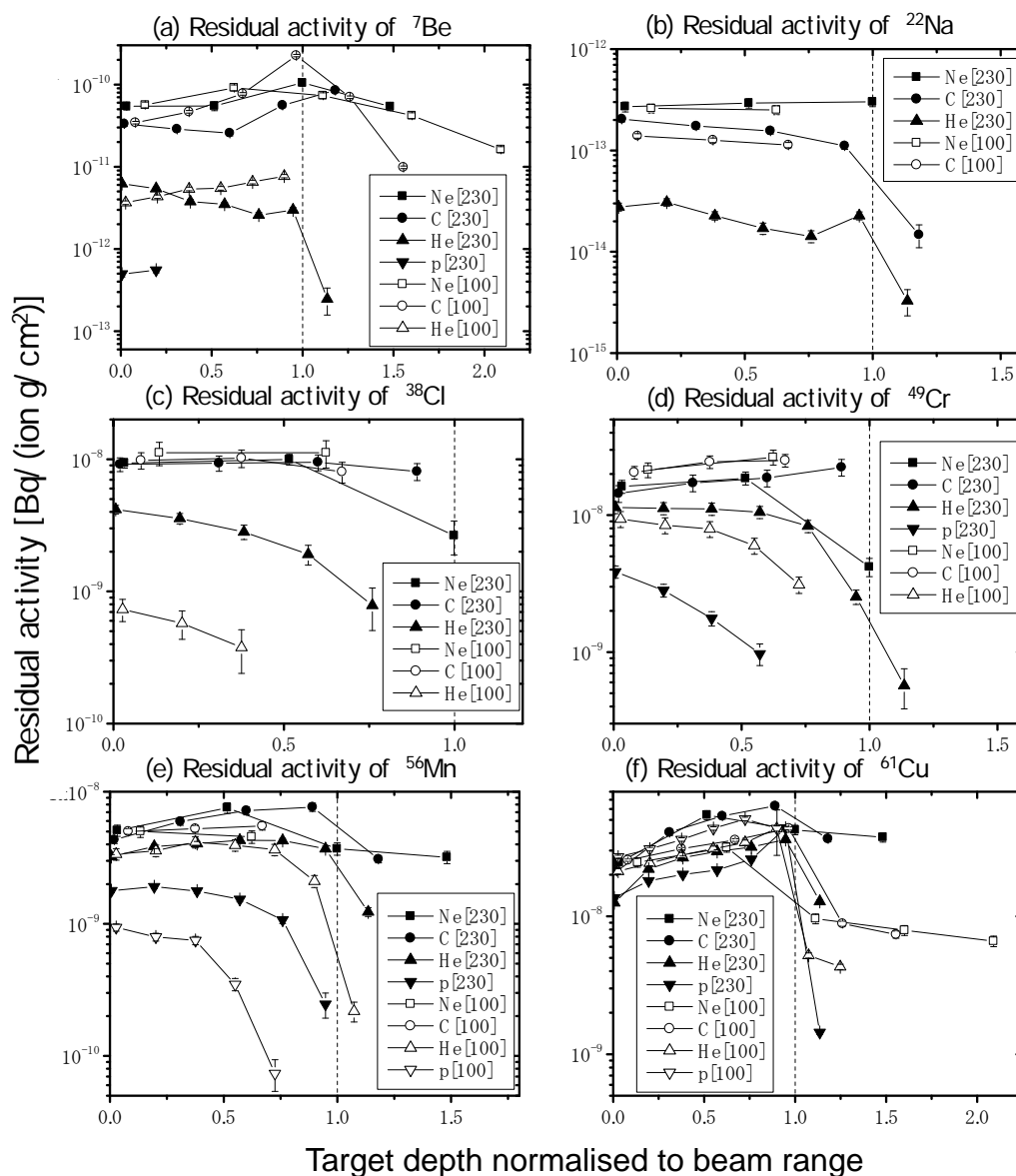
References

[1]   Nakamura, T., *Radiation Physics and Accelerator Safety Engineering*, 2nd Edition, Chijin Shokan, April 2001 (in Japanese).

[2]   Nakamura, T., L. Heilbronn, *Handbook on Secondary Particle Production and Transport by High-energy Heavy Ions*, World Scientific Publ. Co., January 2006.

[3]   Michel, R., *et al.*, *Nucl. Instr. and Meth. B 103*, 183 (1995); ibid. B 129, 153 (1997).

[4]   Nelson, C.E., *et al.*, *Phys. Med. Biol.*, 23, 39 (1978).

[5]   Lone, M.A., *et al.*, *Nucl. Instr. Meth.*, 143, 331 (1977).

[6]   Amos, T.M., *et al.*, *Nucl. Sci. Eng.*, 147, 73-82 (2004).

[7]   Johnson, S.W., *Med. Phys.*, 6, 432 (1979).

[8]   Radivojevic, Z., *et al.*, *Nucl. Instr. Meth.*, B194, 251 (2002).

[9]   Nakamura, T., *et al.*, *Nucl. Sci. Eng.*, 83, 444 (1983).

[10]   Waterman, F.M., *et al.*, *Med. Phys.*, 6, 432 (1979).

[11]   Itoga, T., *et al.*, *Proceedings of the International Conference on Nuclear Data for Science and Technology*, AIP Conference Proceedings, 769, 1568 (2005).

[12]   Birattari, C., *et al.*, *Health Phys.*, 49, 919 (1985).

[13]   Aoki, T., *et al.*, *Nucl. Sci. Eng.*, 146, 200 (2004).

[14]   Nakamura, T., *et al.*, *Nucl. Instr. Meth.*, 151, 493 (1978).

[15]   Meigo, S., *et al.*, *Proc. Int. Conf. on Nucl. Data*, 413-415 (1997).

[16]   Broome, T.A., *et al.*, *Health Phys.*, 44, 487 (1983).

[17]   Alyakrinskiy, O., *et al.*, *Nucl. Instr. Meth.*, A547, 616 (2005).

[18]   Meier, M.M., *et al.*, *Nucl. Sci. Eng.*, 102, 310 (1989).

[19]   Iwamoto, Y., *et al.*, ICRS-11, *Nucl. Technol.*, forthcoming.

[20]   Yonai, S., *et al.*, *Nucl. Instr. Meth.*, A515, 733 (2003).

[21]   Iwamoto, Y., *et al.*, *Nucl. Instr. Meth.*, A 593, 298 (2008).

[22]   Meier, M.M., *et al.*, *Nucl. Sci. Eng.*, 104, 339 (1990).

[23]   Meigo, S., *et al.*, *Nucl. Instr. Meth. A 431*, 521 (1999).

[24]   Meigo, S., *et al.*, *J. Nucl. Sci. Technol.*, Suppl. 2, 1252 (2002).

[25]   Cierjacks, S., *et al.*, *Proc. IV ICANS Meeting*, KEK (1980).

[26]   Arkhipin, D.A., *et al.*, *Nucl. Instr. Meth.*, A505, 397 (2003).

[27]   Madey, R., *et al.*, *Phys. Rev.*, C8, 2412 (1973).

[28]   Veeser, L.R., *et al.*, *Nucl. Instr. Meth.*, 117, 509 (1974).

[29]   David, J-C., *et al.*, private communication.

[30]   Meigo, S., *et al.*, *Proceedings of the International Conference on Nuclear Data for Science and Technology*, AIP Conference Proceedings, 769, 1513 (2005).

[31]   Waters, L.S. (Ed.), *MCNPX User's Manual Version 2.4.0*, LA-CP-02-408, Los Alamos National Laboratory, NM (2002).

[32]   Niita, K., *et al.*, *Nucl. Instr. Meth.*, B 184, 406 (2001).

[33]   Bertini, H.W., *Phys. Rev.*, 131, 1801 (1963); ibid. 188, 1711 (1969).

[34]   Mashnik, S.G., *et al.*, *Nucl. Instr. Meth.*, A 414, 68 (1998).

[35]   Chen, K., *et al.*, *Phys. Rev.*, 166, 949 (1968).

[36]   Iwase, H., K. Niita, T. Nakamura, *J. Nucl. Sci. Technol.*, 39, 1142 (2002).

[37]   Watanabe, Y., *et al.*, *AIP Conference Proceedings*, 769, 1646 (2005).

[38]   Chadwick, M.B., *et al.*, *Nucl. Sci. Eng.*, 131, 293 (1999).

[39]   Prael, R.E., H. Lichtenstein, *Users Guide to LCS: The LAHET Code System*, LA-UR-89-3014 (1989).

[40]   Nakahara, Y., T. Tsutsui, *A Code System for High Energy Nuclear Reactions and Nucleon-meson Transport Code*, JAERI-M 82-198 (1982) (in Japanese).

[41]   Briesmeister, J.F. (Ed.), *MCNP A General Monte Carlo N-Particle Transport Code Version 4A*, LA-12625 (1993).

[42]   Takada, H., *J. Nucl. Sci. Technol.*, 33, 275 (1996).

[43]   Meulders, J.P., *et al.*, *Phys. Med. Biol.*, 20, 35 (1975).

[44]   Menard, S., *et al.*, *Phys. Rev. Special Topics*, 2, 033501 (1999).

[45]   Aoki, T., *et al.*, *J. Nucl. Sci. Technol.*, 41, 399 (2004).

[46]   Shin, K., *et al.*, *Phys. Rev.*, C29, 1307 (1984).

[47]   Hagiwara, M., *et al.*, *Fusion Sci. Technol.*, 48, 1320 (2005).

[48]   Hagiwara, M., *et al.*, *J. Nucl. Mater.*, 329-333, 218 (2004).

[49]   Saltmarch, M.J., *et al.*, *Nucl. Instr. Meth.*, 145, 81 (1977).

[50]   Pauwels, N., *et al.*, IPNO 00-01 (2000).

[51]   Pauwels, N., *et al.*, *Nucl. Instr. Meth.*, B160, 315 (2000).

[52]   Serber, R., *Phys. Rev.*, 72, 1008 (1947).

[53]   Dhar, D., *et al.*, *Phys. Rev.*, C67, 024607 (2003).

[54]   Sarkar, P.K., *et al.*, *Phys. Rev.*, C43, 1855 (1991).

[55]   Wadman, W.W. III, *Nucl. Sci. Eng.*, 35, 220 (1969).

[56]   Schmieder, L., *et al.*, *Nucl. Instr. Meth.*, A256, 457 (1987).

[57]   Sunil, C., *et al.*, *Nucl. Instr. Meth.*, A534, 518 (2004).

[58]   Shin, K., *et al.*, *Proc. 1998 ANS Radiation Protection and Shielding Topical Conf.*, Nashville, TN, Vol. I, 207-214 (1998).

[59]   Kalbach, C., *Phys. Rev.*, C 23, 124 (1984); ibid. 24, 819 (1981).

[60]   Kurosawa, T., *et al.*, *Nucl. Instrum. Meth.*, A 430, 400 (1999).

[61]   Kurosawa, T., *et al.*, *Nucl. Sci. Eng.*, 132, 30 (1999).

[62]   Kurosawa, T., *et al.*, *J. Nucl. Sci. Tech.* 36, 41 (1999).

[63]   Kurosawa, T., *et al.*, *Phys. Rev.*, C 62, 044615 (2000).

[64]   Heilbronn, L, *et al.*, *Phys. Rev.*, C 58, 3451 (1998).

[65] Heilbronn, L., *et al.*, *Nucl. Sci. Eng.*, 132, 1 (1999).

[66] Cecil, R.A., *et al.*, *Phys. Rev.*, C 21, 2471 (1980).

[67] Yordanov, O., "Neutron Yields from 1 GeV/nucleon ^{238}U Ion Beams on Fe Target", *Nucl. Instrum. Method*, B 240, 863-870 (2005).

[68] Satoh, D., *et al.*, "Reevaluation of Secondary Neutron Spectra from Thick Targets upon Heavy-ion Bombardment", *Nucl. Instr. and Meth.*, A583, 507 (2007).

[69] Heilbronn, L., *et al.*, Neutron Production Yields from 400 MeV/nucleon Fe Stopping in C, Al, Cu and Pb Targets, private communication.

[70] Satoh, D., S. Kunieda, Y. Iwamoto, *et al.*, "Development of SCINFUL-QMD Code to Calculate the Neutron Detection Efficiencies for Liquid Organic Scintillator Up to 3 GeV", *J. Nucl. Sci. Technol.*, Suppl. 2, 657 (2002).

[71] Cecil, R.A., B.D. Anderson, R. Madey, *Nucl. Instr. Meth.*, 161, 439 (1979).

[72] Kato, T., T. Kurosawa, T. Nakamura, *Nucl. Instrum. Meth.*, A480, 571 (2002).

[73] Cumming, J.B., *et al.*, "Spallation of Cu by 3.9-GeV ^{14}N Ions and 3.9-GeV Protons", *Phys. Rev.*, C 10, 739 (1974).

[74] Cumming, J.B., R.W. Stoenner, P.E. Haustein, "Spallation of Copper by 25-GeV ^{12}C Ions and 28-GeV Protons", *Phys. Rev.*, C 14, 1554 (1976).

[75] Cumming, J.B., *et al.*, "Spallation of Copper by 80-GeV ^{40}Ar Ions", *Phys. Rev.*, C 17, 1632 (1978).

[76] Porile, N.T., G.D. Cole, C.R. Rudy, "Nuclear Reactions of Silver with 25.2 GeV ^{12}C Ions and 300 GeV Protons", *Phys. Rev.*, C 19, 2288 (1979).

[77] Hicks, K.H., *et al.*, "Interaction of 4.22-GeV and 7.54-GeV ^{20}Ne and Cu", *Phys. Rev.*, C 26, 2016 (1982).

[78] Kim, Y.K., *et al.*, "Heavy-ion Reactions of Cu with 135 MeV/nucleon ^{12}C", *Nucl. Phys.*, A578, 621 (1994).

[79] Yashima, H., *et al.*, "Measurement and Calculation of Radioactivities of Spallation Products by High-energy Heavy Ions", *Radio Chimica Acta*, 91, 689 (2003).

[80] Yashima, H., *et al.*, *Phys. Rev.*, C 66, 044607 (2002).

[81] Yashima, H., *et al.*, "Cross Sections for the Production of Residual Nuclides by High-energy Heavy-ions", *Nucl. Instrum. Meth.*, B, 226, No. 3, 243-263 (2004).

[82] Yashima, H., *et al.*, "Induced Radioactivity in Cu Targets Produced by High-energy Heavy Ions and the Corresponding Estimated Photon Dose Rates", *Radiat. Prot. Dosim.*, 112, 195-208 (2004).

[83] Fertman, A., *et al.*, "Induced Radioactivity Problem for High-power Heavy Ion Accelerators: Experimental Investigation and Long-time Predictions", *Laser and Particle Beams*, 20, 511 (2002).

[84] Titarenko, Yu.E., *et al.*, *Proceedings of AccApp'03*, San Diego, CA, USA, June 2003.

[85] Strasik, I., *et al.*, "Experimental Study and Simulation of the Residual Activity Induced by High-energy Argon Ions in Copper", *Nucl. Instr. Meth.*, B 268, 573 (2010).

[86] Zeitlin, C., *et al.*, "Comparisons of Fragmentation Spectra Using 1 GeV/amu ^{56}Fe Data and the PHITS Model", *Radiat. Meas.*, 43, 1242 (2008).

[87] Fertman, A., E. Mustafin, *et al.*, "First Results of an Experimental Study of the Residual Activity Induced by High-energy Uranium Ions in Steel and Copper", *Nucl. Instr. Meth.*, B 260, 579 (2007).

[88] Strasik, I., E. Mustafin, *et al.*, "Experimental Study of the Residual Activity Induced by 950 MeV/u Uranium Ions in Stainless Steel and Copper", *Nucl. Instr. Meth.*, B 266, 3443 (2008).

[89] Mashnik, S.G., *et al.*, "CEM03 and LAQGSM03: Extension of the CEM2k+GEM2 and LAQQGSM Codes to Describe Photo-nuclear Reactions at Intermediate Energies (30 MeV to 1.5 GeV)", *J. Nucl. Radiochem. Sci.*, 6 (2), A1-A19 (2005).

[90] Barashenkov, V.S., B.F. Kostenko, A.M. Zadorogny, *Nucl. Phys.*, A338, 413-420 (1980).

Shielding studies for superconducting RF cavities at Fermilab

Camille Ginsburg, Igor Rakhno
Fermilab, Batavia, Illinois, USA

Abstract

A semi-empirical method that allows us to predict the intensity of generated field emission in superconducting RF cavities is described. Spatial, angular and energy distributions of the generated radiation are calculated with the FISHPACT code. The Monte Carlo code MARS15 is used for modelling the radiation transport in matter. A comparison with dose rate measurements performed in the Fermilab Vertical Test Facility for ILC-type cavities with accelerating gradients up to 35 MV/m is presented as well.

Introduction

Test facilities for high-gradient superconducting RF cavities are usually strong sources of γ-radiation due to field-emitted electrons inside the cavities. The field-induced emission is generally the result of various imperfections, *e.g.* residual dust contamination, in the cavity. The imperfections can give rise to a significant enhancement of local electric field and, consequently, field emitted electrons which generate gammas in the surrounding material. The neutron component generated by the gammas is not negligible for accelerating gradients of above ~20 MV/m. The design of shielding for such facilities involves significant uncertainties because of the lack of a reliable model of the field emission.

We use a semi-empirical approach to predict the radiation source term in the superconducting RF cavities. It is based on realistic spatial, angular and energy distributions of field-emitted electrons modelled with the FISHPACT code [1] as well as dose rate measurements performed at the DESY Tesla Test Facility (TTF). Modelling of the interaction with and transport in matter for the generated radiation is performed with the Monte Carlo code MARS15 [2]. A comparison between predicted and measured dose rates for the Fermilab Vertical Test Facility is performed.

Source term issues

Field-induced dark current in superconducting RF cavities

Experimental observations of field-induced emission (in other words – dark current) in superconducting RF cavities can be summarised as follows: *i)* surface imperfections can happen anywhere, but field emission occurs mostly around irises – locations with the highest local electric field; *ii)* for a given superconducting RF cavity the emission usually does not occur at several sites; it usually happens at a single site and lasts until a significant amount of RF energy stored in the cavity is lost to the generated dark current. Therefore, in our model we focus on regions around the irises, and the field-emitted electrons are modelled inside the cavity until they hit the cavity surface. Phase-space co-ordinates of such events represent a digitised source term for subsequent modelling of secondary particle generation and transport in the entire system with the MARS15 code.

Dark current generation is assumed to be equiprobable for all regions around the irises. For a given region, however, the probability of field-induced emission depends greatly on the magnitude and RF phase of the surface electric field [3]. Therefore, the relative probabilities of possible electron trajectories differ significantly, and the most probable trajectories usually do not correspond to the highest electron energy gain in the accelerating field. In our model, the field emission is generated with azimuthal symmetry.

Trajectory analysis

A realistic two-dimensional model for the radiation source term was developed to describe the trajectories and energy distributions of field-emitted electrons generated in superconducting RF cavities at high accelerating gradients. The FISHPACT code used to model the electron trajectories is interfaced with the POISSON SUPERFISH fields. Although the simulation provides a field emission current, given input field emission parameters, code [4], a simulation package used to calculate RF electromagnetic only the electron trajectories and energies have been used here. The dose estimated in the simulation using standard parameters from literature [3] was found to be substantially higher than justified by existing data, so data have been used to normalise the predicted dose, as discussed later.

The cavity cell structure and simulated surface electric field are shown as a function of cavity Z in Figures 1 and 2. Electrons emitted from iris regions may be accelerated along the cavity axis and acquire significant energy. An example of simulated trajectories for an emission site, in which electrons can reach energy almost as high as the cavity accelerating gradient, is shown in Figure 3.

The maximum gradient of 30 MV/m has been chosen to correspond to the largest gradient at which field emission is likely to result in a substantial dose rate immediately above cryostat, as determined from data. In addition, this is approximately the largest gradient for which the Fermilab Vertical Test Facility must be able to test typical cavities without interrupting the RF system with radiation monitoring system trips.

Figure 1: The surface electric field of a nine-cell cavity (solid, normalised to 1 MV/m gradient), and the cavity cell structure (dashed) as a function of cavity Z from a SUPERFISH simulation. The electric field peaks in the cavity iris regions.
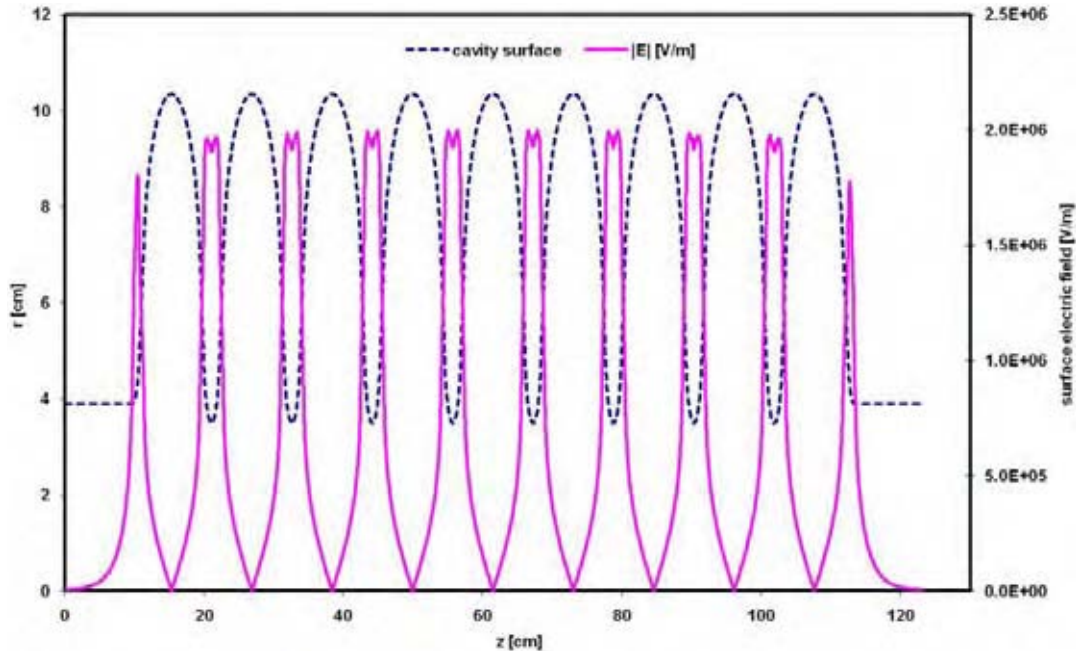
Figure 2: A zoomed view of the previous figure, showing detail around an iris in a nine-cell RF cavity
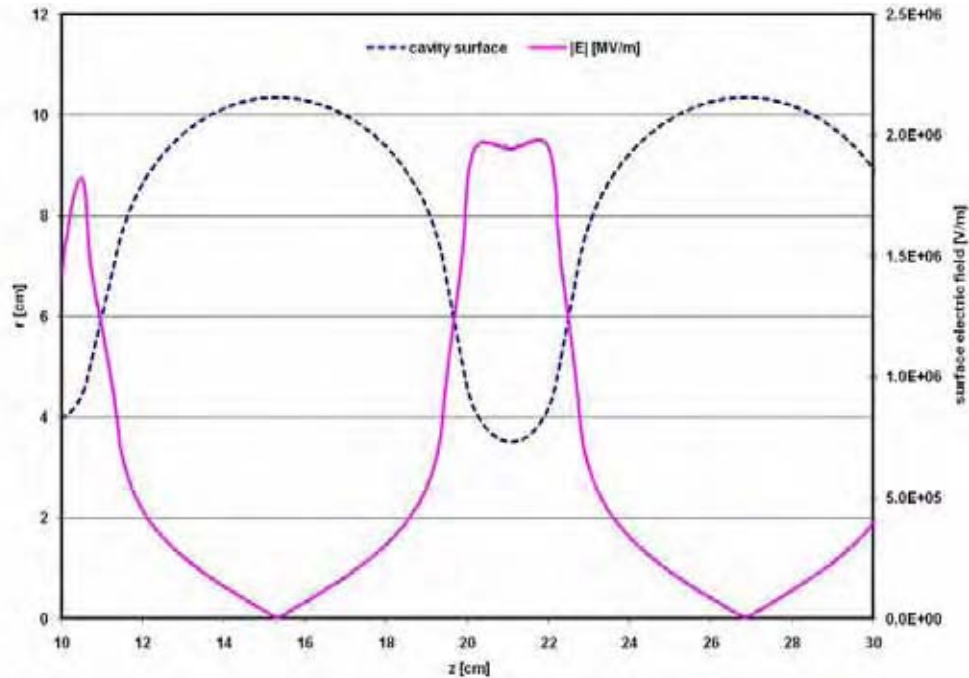
**Figure 3: Simulated electron trajectories generated in a nine-cell SRF cavity with
an accelerating gradient of 30 MV/m. The curves inside the cavity correspond
to electron trajectories for 10° increments in the RF phase, for the half period
in which the electric field has the correct sign to pull electrons from the surface.**
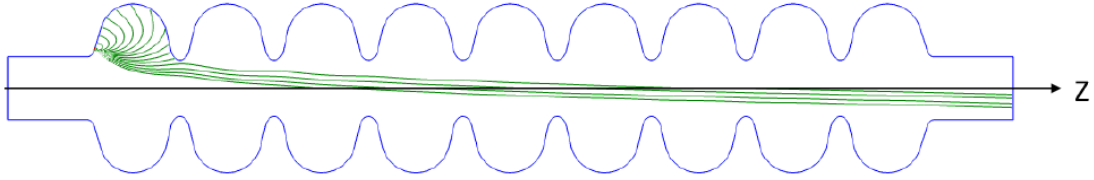
For every single iris, five emission sites were studied: the iris itself and four sites in its vicinity (two on each side). Emission sites near cavity beam pipes were taken into account as well. The surface electric field has the right sign to facilitate the electron quantum tunnelling under the surface potential barrier for 50% of the test time. The corresponding RF phase intervals were divided into eighteen (18) 10° bins, so that 17 sample trajectories with electric field greater than zero are generated for each emission site. The phase-space co-ordinates (**r**, **E**, Ω) of electrons when their trajectories hit the inner cavity surface were recorded for a subsequent modelling with the MARS15 code.

Fowler-Nordheim model

Fowler and Nordheim [3] were the first to provide a description of field emission as quantum mechanical tunnelling:

$$j \approx A(E)E^2 \exp\left(-\frac{B(E)\phi_e^{3/2}}{E}\right) \tag{1}$$

where j is the density of the generated electron dark current, E is the local electric field, A and B are slowly varying functions of E, and ϕ_e is work function of the emitting material. In practice, however, the field-induced emission was observed at much smaller fields than those compatible with Eq. (1). In order to better fit experimental results, the following expression was found to be more accurate:

$$j \approx SA(E)\beta^2 E^2 \exp\left(-\frac{B(E)\phi_e^{3/2}}{\beta E}\right) \tag{2}$$

Two new parameters are introduced in Eq. (2): *i)* the effective emitting area factor, *S*; *ii)* the local field enhancement factor, β. Eq. (2) implies that the emission occurs at small localised spots around imperfections and the local field at the imperfections can be significantly higher (by a factor of about 100 and more) than that predicted for an idealised cavity surface. The two parameters vary substantially and are usually determined from experimental data.

Intensity of the predicted dark current

Because of the variability in field emission parameters, experimental data from DESY/TTF are used to normalise the predicted dark current, as shown in Figure 4. From these data, we determined that for 90% of all measurements the dose rate measured under the external shielding did not exceed 5 R/hr.

Therefore, we assume that the total dark current generated in a superconducting RF cavity corresponds to the dose rate of 5 R/hr predicted at a similar location in Fermilab Vertical Test Facility, after controlling for differences in radiation shielding. Practically speaking, if the field emission is too high, cavities are removed from the test facility and undergo an extra cleaning procedure.

Vertical Test Facility at Fermilab

The Vertical Test Facility for superconducting RF cavities at Fermilab has been in operation since 2007. The facility currently consists of a single vertical test cryostat VTS1. Radiation shielding for VTS1 was designed for single nine-cell 1.3 GHz cavities using a very simple field emission model as the radiation

Figure 4: Measured maximum dose rates at DESY/TTF under the external shielding
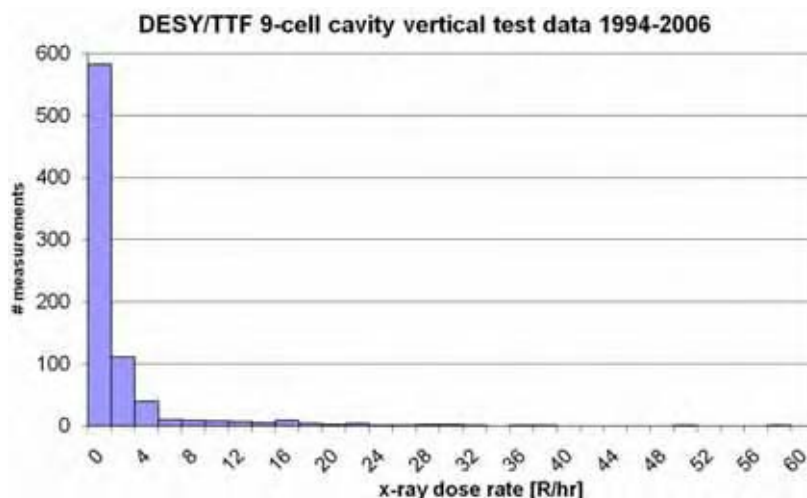
source [5]. The shielding consists of three parts: a plug internal to the cryostat, a movable shielding lid above the cryostat, and the concrete walls of the pit containing the cryostat. The internal shielding consists of a cylindrical assembly above the cavity containing layers of lead, steel and borated polyethylene. The external shielding consists of a concrete/steel movable shielding lid and borated polyethylene in instrumentation feedthrough regions. The RF system is interlocked through a radiation monitor outside of the shielding to maintain a controlled area designation.

Two additional cryostats with common design, VTS2&3, are being procured, and are sized such that six nine-cell cavities can be installed per cryostat. The test throughput will be gained through common cool-down and warm-up time, with cavities tested sequentially. Space for additional shielding, either internal or external to the cryostat, is limited. An evaluation of the radiation shielding was performed, to minimally extend the VTS1 shielding design to a six-cavity configuration in VTS2&3. The external shielding for VTS2&3 was unchanged. The internal shielding consists of cylindrical lead blocks above each of the cavities and cylindrical layers of steel and borated polyethylene above the upper cavities. The configuration of internal shielding with respect to the cavities is shown in Figure 5. Other cryostat components also serve as radiation shielding: *i)* layers of copper and G10 above the internal shielding and under the top plate; *ii)* the steel top plate; *iii)* several cylindrical shells around the superconducting RF cavities – magnetic shield of Cryoperm-10 with aluminium support liner, helium vessel, copper thermal shield and steel vacuum vessel. Various small components such as cables and pipes are not included in the model. The superconducting RF cavities are tested in a superfluid helium bath at 2 K. Measurements at VTS1 revealed that total cool-down time is about 180 minutes, and that cooling the internal shielding occupies about a third of that time. The estimated total cool-down time for VTS2&3 without the six internal shielding lead blocks, initially inherited from the VTS1 design, is about 240 minutes. Keeping all six lead blocks would increase the cool-down time by about 30%. Using an extra layer of external shielding on the movable lid, if necessary, is preferable in this case, and the extra mechanical load is expected to be well within the shield's load tolerance.

For VTS1, measured dose rates are shown in Figure 6. According to the described model, the predicted dose rate under the external shielding is < 0.250 R/hr 90% of the time. The measurements are well within this value, to within the limited statistics. The described approach to shielding design for test facilities is justified by the possibility of extra cleaning procedures for tested superconducting RF cavities.

Figure 5: A fragment of a model VTS2 or VTS3 insert with six RF cavities, showing a lead block above each cavity and a steel/borated polyethylene block above the entire cavity assembly
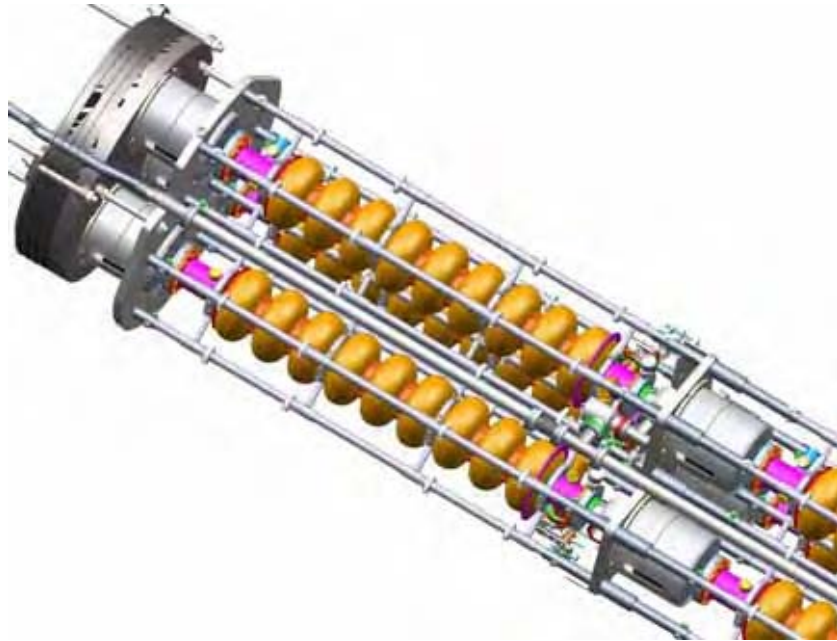
Figure 6: Dose rates measured at VTS1 for nine-cell superconducting RF cavities with various accelerating gradients
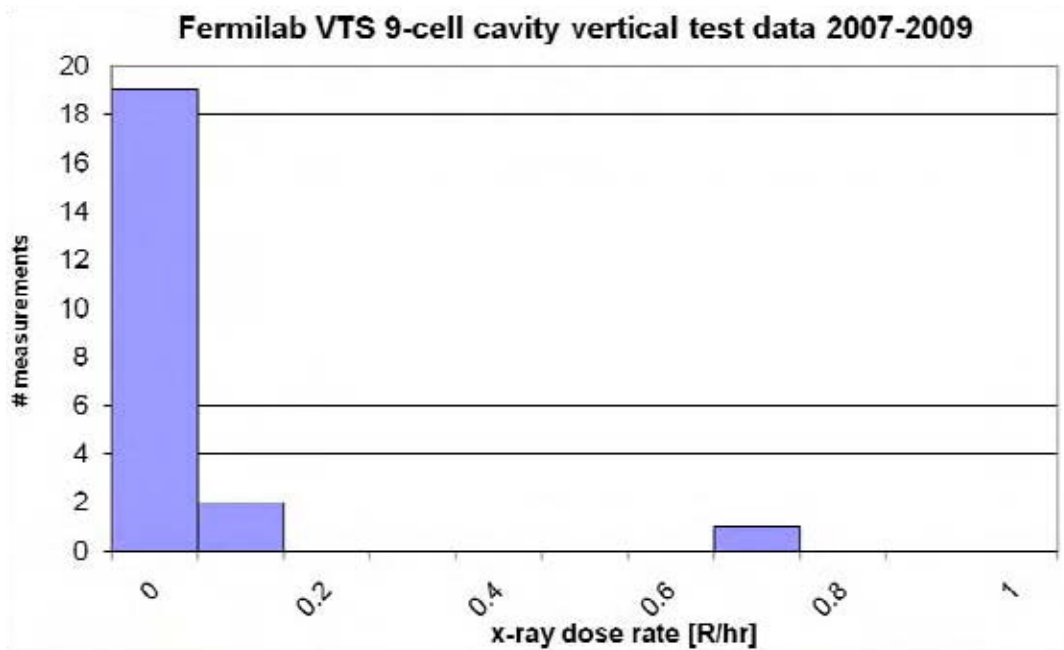
Acknowledgements

References

[1]   Donoghue, E., *et al.*, "Studies of Electron Activities in SNS-type Superconducting RF Cavities", *Proc. 12th Int. Workshop on RF Superconductivity (SRF2005)*, Ithaca, NY, USA, 10-15 July 2005.

[2]   Mokhov, N.V, S.I. Striganov, "MARS15 Overview", *Proc. Hadronic Shower Simulation Workshop*, Batavia, Illinois, USA, 6-8 September 2006.

[3]   Padamsee, H., J. Knobloch, T. Hays, *RF Superconductivity for Accelerators*, 2nd ed., Wiley and Weinheim (2008), pp. 230-242.

[4]   Halbach, K., R.F. Holsinger, "SUPERFISH – A Computer Program for Evaluation of RF Cavities with Cylindrical Symmetry", *Particle Accelerators*, 7, 213-222 (1976).

[5]   Rakhno, I., *Radiation Shielding Issues for SRF Cavity Test Facility at Fermilab*, Fermilab-TM-2367-AD (2006).

Characterisation of quasi-monoenergetic neutron energy spectra using [7]Li(p,n) reactions at 246-389 MeV

Y. Iwamoto[1], M. Hagiwara[2], D. Satoh[1], H. Iwase[2], H. Yashima[3], T. Itoga[4], T. Sato[1], Y. Nakane[1], H. Nakashima[1], Y. Sakamoto[1], T. Matsumoto[5], A. Masuda[5], J. Nishiyama[5], A. Tamii[6], K. Hatanaka[6], C. Theis[7], E. Feldbaumer[7], L. Jaegerhofer[7], C. Pioch[8], V. Mares[8], T. Nakamura[9]

[1]Japan Atomic Energy Agency, Japan
[2]High Energy Accelerator Research Organization (KEK), Japan
[3]Research Reactor Institute, Kyoto University, Japan
[4]RIKEN, Japan
[5]Natl. Metrology Inst. of Japan, Natl. Inst. of Advanced Industrial Sci. and Tech. (NMIJ/AIST), Japan
[6]Research Centre for Nuclear Physics, Osaka University, Japan
[7]European Organization for Nuclear Research (CERN), Geneva, Switzerland
[8]German Research Centre for Environmental Health, Germany
[9]Tohoku University, Japan

Abstract

We have measured neutron energy spectra of a quasi-monoenergetic [7]Li(p,n) neutron source with 246 and 389 MeV protons at seven angles (0°, 2.5°, 5°, 10°, 15°, 20° and 30°) using a time-of-flight (TOF) method employing organic scintillators NE213 at RCNP of Osaka university. We precisely deduced energy spectra of the source neutrons down to 2 MeV at 0° and 10 MeV at other angles. The cross-sections of the peak neutron production reaction at 0° are on the 35~40 mb line of other experimental data and the peak neutron angular distribution agrees well with the Taddeucci formula. Neutron energy spectra below 50 MeV at all angles are comparable, but the shape of the continuum above 100 MeV changes considerably with angle. The quasi-monoenergetic neutron beams are well suited to the calibration of detectors used in neutron spectrometry. In order to consider the correction required to derive the response in the peak region from the measured total response, we have proposed the synthetic energy spectra using the 10° and 30° spectra for the 246-389 MeV [7]Li(p,n) reactions. The proposed method enables the uncertainty of the response in the calibrations to be reduced.

Introduction

Radiation fields behind accelerator shielding and flight altitudes are characterised by a large contribution of neutrons with energies above 20 MeV. For investigating neutron fields at such places, integrating detectors such as Bonner spheres have been used with newly developed methods. Determination the reliability of Bonner sphere response matrices requires calculations using Monte Carlo codes and calibration measurements. Quasi-monoenergetic neutron reference beams are of special importance for calibrating the detectors.

Facilities such as TRIUMF [1], PTB [2], the National Accelerator Centre (NAC) [3] and RIKEN [4] have quasi-monoenergetic neutron fields with energies of up to 200 MeV employing ^{7}Li(p,n)^{7}Be (g.s. + 0.429 MeV, Q = -1.64 and -2.075 MeV). On the other hand, the RCNP facility [5] has neutron fields in energy regions up to 400 MeV and neutron energy spectra at 0° for 140-400 MeV protons have been measured [5,6]. These neutron energy spectra at 0° have not only peak neutrons but also low-energy continua caused by break-up and spallation reactions. In order to characterise the low-energy part of the neutron beam, the neutron spectra at larger angles should be measured and investigated. A similar investigation of the spectral fluence at low energies has already been made at NAC using the 100 MeV proton beam [7].

This report considers the measurement of neutron energy spectra at seven angles (0°, 2.5°, 5°, 10°, 15°, 20° and 30°) for the 246 and 389 MeV ^{7}Li(p,n) reactions at RCNP and the characterisation of the peak and low-energy continua of neutron energy spectra.

Measurement

The experiments were carried out in the 100 m tunnel at the RCNP ring cyclotron of Osaka University. A schematic view of the experimental arrangement is shown in Figure 1. The experimental set-up and electronic circuitry were almost the same as in Ref. [8].

Figure 1: Illustration of experimental set-up at the neutron experimental hall and the 100 m tunnel
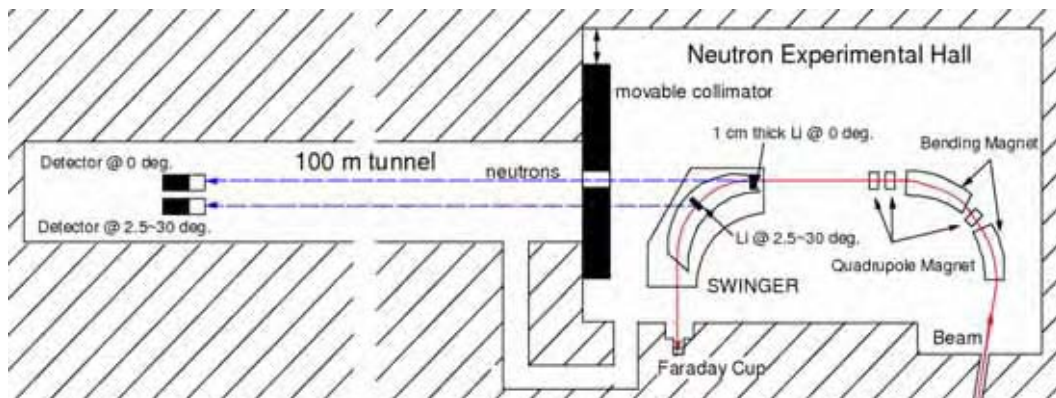
Proton beams extracted from the ring cyclotron at 246 and 389 MeV were transported to the neutron experimental hall and hit a 1.0 cm thick ^{nat}Li (^{6}Li 7.6% and ^{7}Li 92.4%) target placed in the swinger which was in a vacuum chamber. From the TRIM calculations [9], the energy lost by protons in the target is 0.87 MeV and 0.67 MeV for the 246 MeV and 389 MeV proton beams, respectively. Protons passing through a target were bent using a swinger magnet to the beam dump which measured the proton beam intensity with a Faraday cup. The beam current was kept at 10-60 nA. Neutrons produced at 0° from a target were extracted into the time-of-flight (TOF) tunnel through a 10×12 cm aperture in a 150 cm thick movable iron collimator embedded in a 150 cm thick concrete wall located 4.5 m away from the target. The neutron beam size is determined to be 3.88×10^{-4} sr by the 10×12 cm aperture. For example, the radius of the neutron beam at 20 m from the target is about 22 cm. The clearing magnet in the movable collimator served to reduce charged particles contaminating the neutron beam. The movable collimator and the swinger magnet allow neutron emissions to be measured through angles of 0°-30°.

The facility is perfectly suited for TOF study because the available flight path extends to about 100 m. Table 1 summarises the flight path, measured angles and neutron energy range.

Table 1: Flight path, measured angles and neutron energy range

Neutron energy	2 MeV < E_n < 10 MeV	10 MeV < E_n < 100 MeV	100 MeV < E_n
Detector diameter and thickness	5.08 cm	12.7 cm	25.4 cm
Distance between target and detector	6.4 m	15.5 m (246 MeV) 17.3 m (389 MeV)	60 m (246 MeV) 95.5 m (389 MeV)
Angle	0°	0°, 2.5°, 5°, 10°, 15°, 20°, 30°	0°, 2.5°, 5°, 10°, 15°, 20°, 30°

The neutron TOF measurements were performed using three sizes of NE213 organic liquid scintillator (25.4×25.4 cm, 12.7×12.7 cm and 5.08×5.08 cm in diameter and length) and each took measurements at three distances from the target to the surface of the detector. For the 6.4 m measurements, a 5 mm thick plastic scintillator, NE102A, placed in front of the detector tagged events induced by charged particles. Long path measurements using the 25.4×25.4 cm NE213 were performed to obtain good energy resolution in the high-energy region as mentioned in the next section. The time intervals between successive proton beam pulses can be enlarged from about 500 ns using a beam chopper to avoid contamination with lower-energy neutrons. These time intervals correspond to frame-overlap neutron energies of about 90 MeV at the maximum distances (60 m for 246 MeV and 95.5 m for 389 MeV), about 5 MeV at medium distances (15.5 m for 246 MeV and 17.3 m for 389 MeV) and about 1 MeV at 6.4 m, respectively.

Data analysis

In the TOF measurements, the total and slow components of the light outputs of NE213 were measured with two different timing gates put on the output signals of the NE213 to discriminate neutron events from photon events. The neutron events were clearly distinguished from the photon events using two-dimensional plots with total and slow components. The neutron flight time was measured as the time difference between the chopper signal and the neutron detector signal. These data were recorded with a conventional computer automated measurement and control system in an event-by-event mode.

The energy threshold of the detector was adjusted using the Compton edge by ^{137}Cs, ^{60}Co and ^{241}AmBe radioactive sources. The three energy thresholds, 0.494 MeVee (^{137}Cs) for 5.08×5.08 cm, 4.33 MeVee (^{241}AmBe) for 12.7×12.7 cm, and 43.3 MeVee (^{241}AmBe $\times$ 10) for 25.4×25.4 cm were employed in this analysis; 1 MeVee is the amount of light produced by an electron energy deposition of 1 MeV. This then allowed sufficiently well-defined neutron energies above 2.0, 10 and 100 MeV, respectively.

We calculated the neutron detection efficiency of NE213 using the SCINFUL-QMD code [10,11]. According to Refs. [10,11], this code can reproduce the experimental detection efficiency in the neutron energy region below 150 MeV using 12.7×12.7 cm and 5.08×5.08 cm NE213. For the 25.4×25.4 cm detector, the detection efficiency has not been sufficiently investigated. Therefore, the response function for 130-140 MeV and 200-250 MeV neutron incidences have also been measured and compared with the calculated results. Figure 2 shows a comparison of experimental data with calculated results. As SCINFUL-QMD successfully represents the experimental data of response functions, we conclude that calculated detection efficiency for the 25.4×25.4 cm detector is also reliable. The spectra separately obtained at the three flight distances were combined at 10 MeV and 100 MeV, and the neutron energy ranges are listed in Table 1. Finally, the energy spectra were divided by detection efficiency, detector solid angle and proton beam current.

The interaction of the monoenergetic neutrons at 246 and 389 MeV with the collimator, the wall and the floor were investigated using the PHITS code [12]. In the calculation, the monoenergetic neutrons had an angular distribution made by Taddeuchci [13] and JENDL-HE [14] was employed to transport all particles. Details about the angular distribution are in the next section. Figure 3 shows calculated neutron tracks using PHITS code. We can see that the peak neutrons expand with solid angle and include the low-energy neutrons produced from the collimator, the wall and the floor. Figure 4 shows the neutron energy spectra at 6.4 m and 60 m for 246 MeV incident protons. The peak

Figure 2: Response function using 25.4 × 25.4 cm NE213 for 135 and 250 MeV neutron incidences
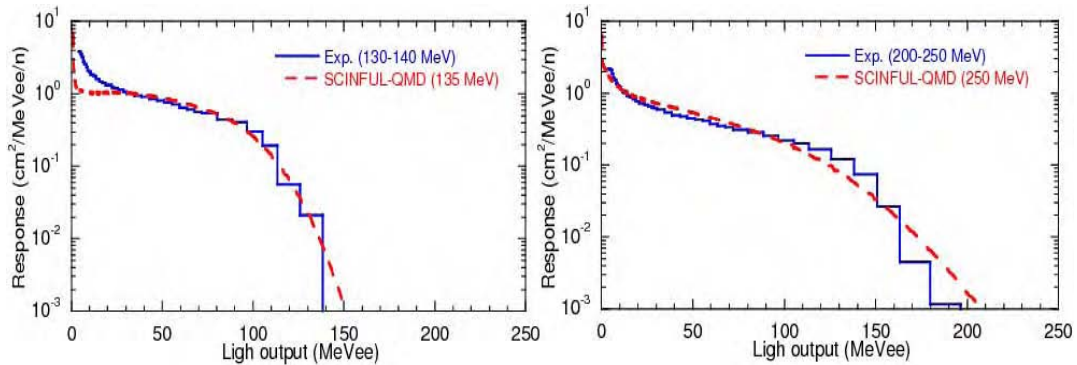
Figure 3: Neutron tracks for the 246 MeV monoenergetic neutron incidence in the PHITS calculation
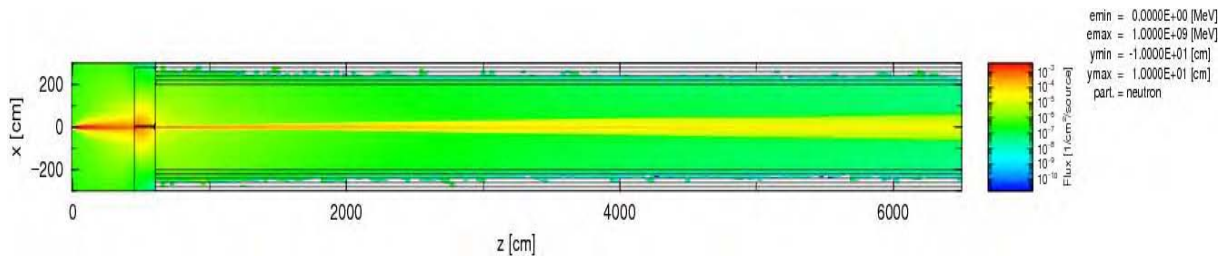
Figure 4: Calculated results of neutron energy spectra at 6.4 and 60 m in the 100 m tunnel for the 246 MeV neutron incidence
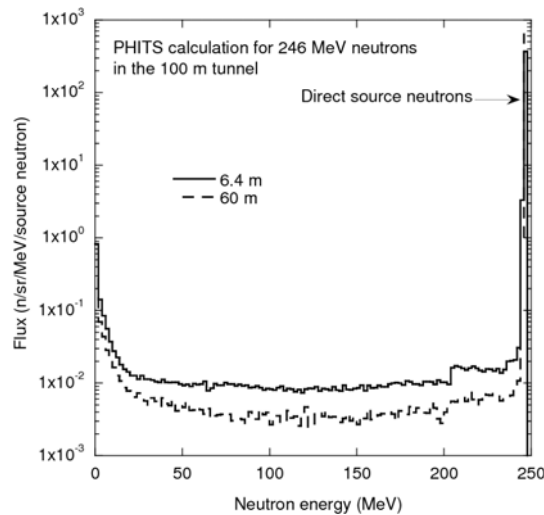
neutron presents the direct neutrons from a source; the room-scattered neutrons are indicated in the continuum part. The ratio of the continuum to the total, $\Phi_{continuum}/\Phi_{total}$ for the 246 and 389 MeV incident neutrons in the 100 m tunnel ranges from 0.3-1.5% and the contribution to the TOF measurement in the energy region above 1 MeV is almost negligible.

Uncertainties in the TOF measurements were due to statistical and systematic errors. The statistical uncertainties are below 0.16% for the peak neutrons and 1-3% for the continuum. The systematic error was mainly from the neutron detection efficiency and is estimated to be 15% [10,11].

The neutron energy resolution depends on the time and geometry, and can be expressed by [15]:

$$\frac{\Delta E}{E} = \gamma(\gamma + 1)\left[\frac{\Delta t}{t}\right] \tag{1}$$

where $\gamma = 1 + E/Mc^2$, E is the neutron kinetic energy, M the neutron rest mass, Δt the time resolution, and t the neutron flight time. The sources contributing to Δt are: *i)* the intrinsic time resolution of the neutron detector and the electronic circuit; *ii)* the time spread in the production of neutrons arising from the finite target thickness; *iii)* time dispersion arising from the incident beam spread; *iv)* the time spread resulting from finite thickness of neutron detectors. These four time-uncertainty components are not all normally estimated. The uncertainty *iii)* is negligible in this experiment. Thus, we approximate Δt as:

$$\Delta t = \sqrt{(\Delta\tau)^2 + (\Delta x/v)^2} \tag{2}$$

where $\Delta\tau$ is the time dispersion of the neutron detector and the electronic circuit, Δx the effective thickness of the neutron detector (half the value of length) plus the target (0.5 cm, half the value of thickness) and v the neutron velocity. The assumption in Eq. (2), that the time spread resulting from the detector plus target thickness is a Gaussian distribution with a full-width at half-maximum (FWHM) equal to Δx, overestimates the actual Δt. The time dispersion $\Delta\tau$ is taken as the FWHM of prompt gamma-ray peaks observed in each neutron TOF spectrum, which has been observed 0.7 ns. The maximum energy resolution is 2.3 MeV for 246 MeV neutrons at 60 m and 2.9 MeV for 389 MeV neutrons at 95.5 m.

Results

Figure 5 shows our neutron energy spectra for 246 and 389 MeV protons on ^{nat}Li and other spectra for 70 [16], 140 [6] and 350 MeV [5] protons on 99% enriched ^{7}Li. Peak neutrons are from transitions to the ground state and the first excited state of ^{7}Be and transitions to the ground state of ^{6}Be. The small peak 10 MeV lower than peak energy is from quasi free scattering and the transition to the high-energy

Figure 5: Neutron energy spectra for the Li(p,xn) reaction at 0°
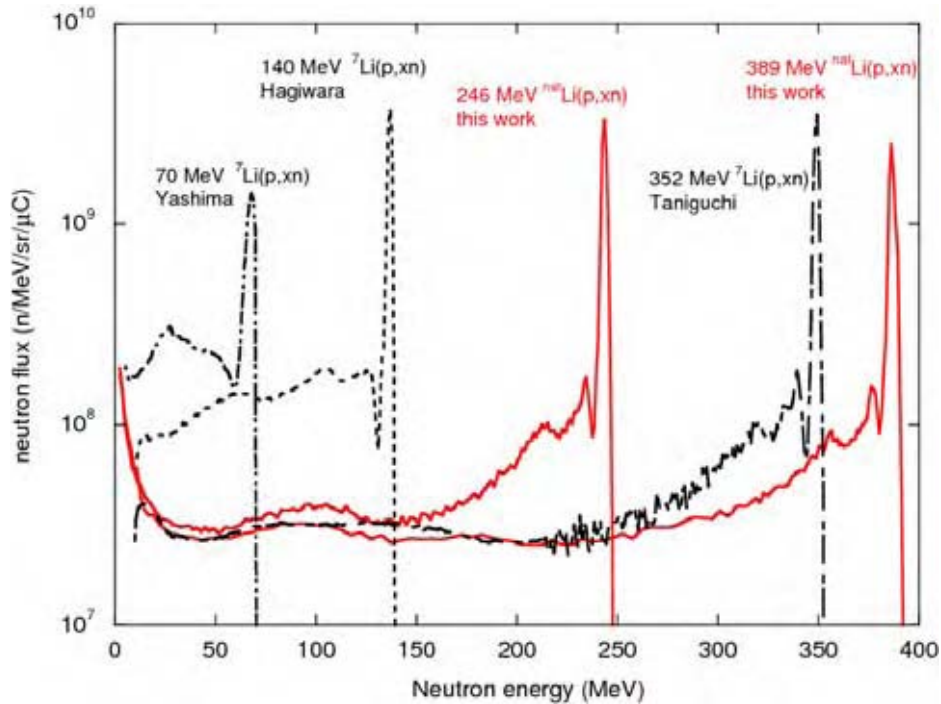
excited state of ^{7}Be. The continuum with $E_n > 20$ MeV is mainly from break-up and spallation reactions, and the low-energy part with $E_n < 20$ MeV is from evaporation processes. As mentioned earlier, most of the continuum of our data in Figure 5 comes directly from the ^{nat}Li(p,xn) reaction because there are very few room-scattered neutrons. In the neutron energy range 20-100 MeV, the continuum fluxes with 246, 350 and 389 MeV protons are comparable. On the other hand, the continua with 70 and 140 MeV protons increase with decreasing incident energy.

Table 2 shows the characteristics of the neutron energy spectra. Peak neutron intensities and cross-sections using ^{nat}Li were converted to the ^{7}Li data using the ratio $\sigma(^7\text{Li})$ to $\sigma(^{nat}\text{Li})$ for 160 MeV protons at $0°$, *i.e.* $\sigma(^7\text{Li})/\sigma(^{nat}\text{Li})$ is 1.04, if cross-sections are constant above 160 MeV, where $\sigma(^7\text{Li}) = 36.8$ mb, $\sigma(^6\text{Li}) = 19.5$ mb and $\sigma(^{nat}\text{Li}) = 35.5$ mb in the LAB system [17].

Table 2: Characteristics of the neutron energy spectra

	Hagiwara	This work	Taniguchi	This work
Proton energy [MeV]	140	246	352	389
Peak neutron energy [MeV]	137	244	350	387
Peak intensity of ^{7}Li(p,n) [n/sr/μC]	1.04×10^{10}	$(1.11 \pm 0.17) \times 10^{10}$	1.07×10^{10}	$(0.96 \pm 0.15) \times 10^{10}$
Peak cross-section of ^{7}Li(p,n) [mb]	35.8	38.2 ± 5.9	36.9	33.2 ± 5.1
Φ_{peak}/Φ_{total} (10 MeV < E_n)	0.38	0.5	0.44	0.4

Our neutron cross-sections for ^{7}Li(p,n) at $0°$ are on the 35~40 mb line of other experimental data. The contribution of peak fluence, Φ_{peak}, to the total fluence, Φ_{total}, varies between 0.4~0.5 for the 246 and 389 MeV proton beams. Therefore, the corrections required to derive the response can be considerable. They can be significantly reduced if, in addition to the measurement at $0°$ neutron emission angle, the response is measured at a larger angle as well. This is because only the transitions to the ground state and the first excited state in ^{7}Be are strongly peaked forward.

Figure 6 shows angular distribution of neutron energy spectra for 246 and 389 MeV ^{nat}Li(p,xn) reactions at angles of $0°$, $2.5°$, $5°$, $10°$, $15°$, $20°$ and $30°$. All neutron energy spectra in the energy region below 50 MeV are comparable, but the shape of the continuum above 100 MeV changes considerably with angle. The high-energy neutron peak is significantly reduced at larger angles. The peak neutron cross-section of the ^{7}Li(p,n) reaction has frequently been measured [18] and Taddeucci [13] offered a good fitting formula for the angular cross-sections in the CM energy system between 80 and 800 MeV. The formula is expressed in terms of a zero order Bessel function:

$$\sigma(q) = \sum_{j=1}^{N} a_{0j} J_0 \left(\frac{z_{0j} q}{q_{lim}} \right) (mb\,sr^{-1})$$

where $J_0(z_{0j}) = 0$, q is the momentum (three-dimensional) transfer in the CM system, q_{lim} is the momentum transfer limit selected as 2.6 fm^{-1}, and a_{0j} is the coefficient for the Fourier-Bessel expansions listed in Ref. [19] where the zeros, z_{0j}, are also shown. Finally, the cross-section in CM was converted to the cross-section in the LAB system to compare with our data. Figure 7 shows the angular distribution of the peak cross-section of 246 and 389 MeV ^{7}Li(p,n) reactions using $\sigma(^7\text{Li})/\sigma(^{nat}\text{Li})$. Our peak cross-sections agree well with the results of Taddeucci formula.

As mentioned earlier, in order to reduce contributions from the continuum, we have considered the corrections required to derive the response using the neutron spectra at larger angles. According to Nolte [7], the shape of the continuum resulting from break-up reactions does not change considerably for 100 MeV ^{7}Li(p,n) reactions and a synthetic difference spectrum was made for which the $16°$-spectrum was multiplied by 0.77 in order to help the flux avoid a negative value. For the high-energy protons incident above 246 MeV, the $0°$ continuum spectrum has many quasi free scattering neutrons at the peak energy down to 10-50 MeV. Therefore, it is difficult to consider the corrections using one large-angle spectrum. In Figure 8, synthetic difference spectra are shown for which the $10°$ and $30°$ spectra were multiplied by 0.3-0.4 in order to avoid negative flux values. For these spectra, $\Phi_{continuum}/\Phi_{total}$ is reduced from 0.51 to 0.21 for 246 MeV protons and from 0.67 to 0.33 for 389 MeV protons. This procedure enables the uncertainty in the response in calibrations to be reduced.

Figure 6: Angular distribution of neutron energy spectra
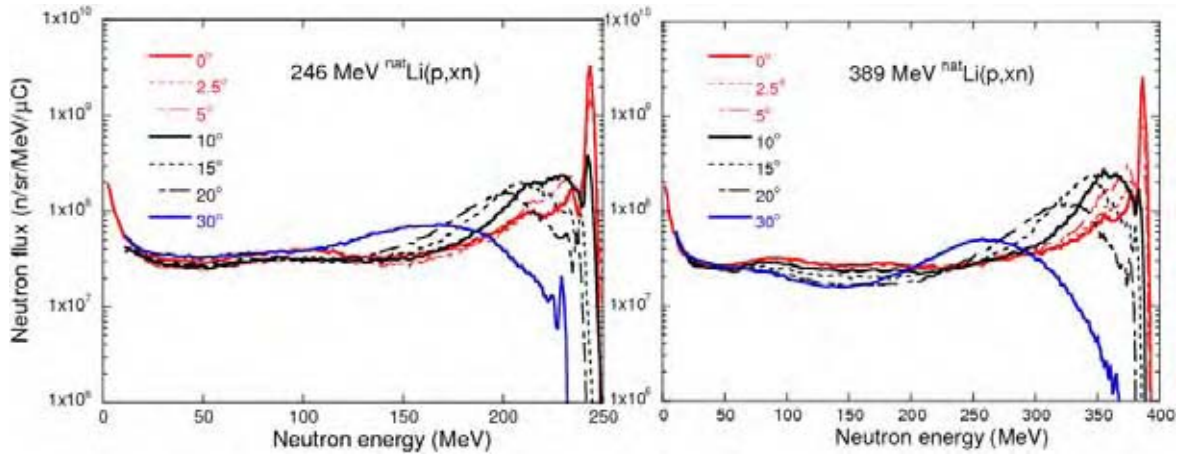
Figure 7: Angular distribution of the peak cross-sections
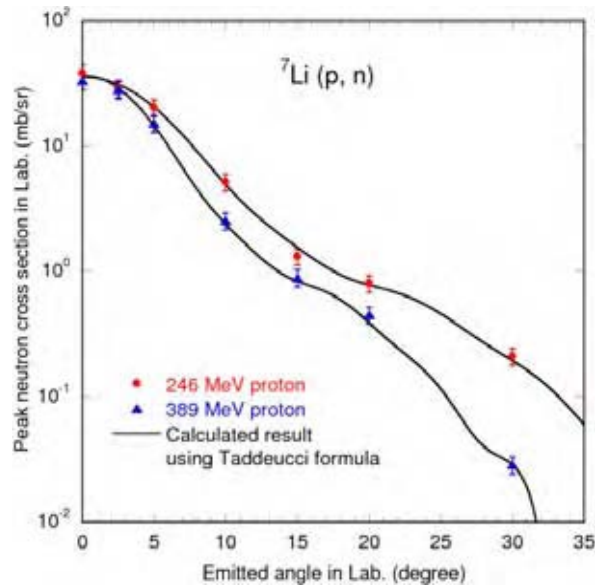
Figure 8: 0°, 10° and 30° spectra and synthetic difference spectrum
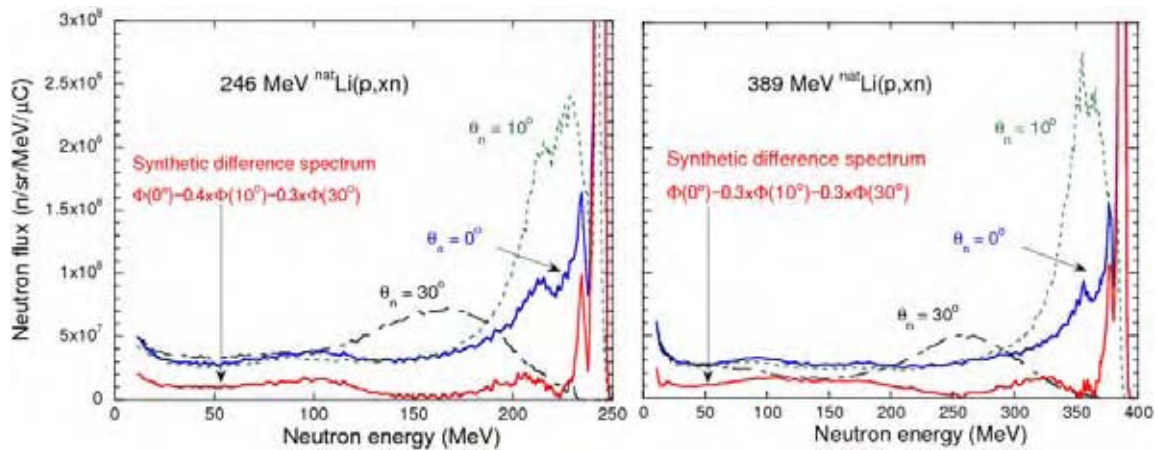
Summary

We measured neutron energy spectra using ^{7}Li(p,n) reaction with 246 and 389 MeV protons at seven angles (0°, 2.5°, 5°, 10°, 15°, 20° and 30°). Our peak cross-sections at 0° are on the 35~40 mb line of other experimental data, and our neutron angular distribution agrees well with the Taddeucci formula. Neutron energy spectra below 50 MeV at all angles are comparable, but the shape of the continuum above 100 MeV changes considerably with angle. In order to consider the correction required to derive the response in the peak region from the measured total response, we proposed a synthetic energy spectrum using the 10° and 30° spectra. The proposed method enables the uncertainty in the response in calibrations using 246 and 389 MeV ^{7}Li(p,n) reactions to be reduced.

References

[1] Blackmore, E.W., P.E. Dodd, M.R. Shaneyfelt, "Improved Capabilities for Proton and Neutron Irradiations at TRIUMF", *Radiation Effects Data Workshop*, 21-25 July 2003, pp. 149-155.

[2] Schumacher, H., *et al.*, "Neutron Fluence Measurements with a Recoil Proton Telescope", *Nucl. Instr. and Meth.*, A 421, 284 (1999).

[3] McMurray, W.R., *et al.*, "The Faure Cyclotron Neutron Source and a Particle Spectrometer for Neutron Induced Emission of Charged Particles at Energies Between 60 and 200 MeV", *Nucl. Instr. and Meth.*, A 329, 217 (1993).

[4] Nakao, N., *et al.*, "Development of a Quasi-monoenergetic Neutron Field Using ^{7}Li(p,n)^{7}Be Reaction in the 70-210 MeV Energy Range at RIKEN", *Nucl. Instr. and Meth.*, A 420, 218 (1999).

[5] Taniguchi, S., *et al.*, "Development of a Quasi-monoenergetic Neutron Field Using the ^{7}Li(p,n)^{7}Be Reaction in the Energy Range from 250 to 390 MeV at RCNP", *Rad. Prot. Dosim.*, 126, 1-4, 23 (2007).

[6] Hagiwara, M., *et al.*, "Benchmark Experiment of Neutron Penetration Through Iron and Concrete Shields for Hundreds-of-MeV Quasi-monoenergetic Neutrons. II: Measurements of Neutron Spectrum by an Organic Liquid Scintillator", *Nucl. Technol.*, 168, 304 (2009).

[7] Nolte, R., *et al.*, "High-energy Neutron Reference Fields for the Calibration of Detectors used in Neutron Spectrometry", *Nucl. Instr. and Meth.*, A 476, 369 (2002).

[8] Iwamoto, Y., *et al.*, "Measurement of Thick Target Neutron Yields at 0° Bombarded with 140, 250 and 350 MeV Protons", *Nucl. Instr. and Meth.*, A 593, 298 (2008).

[9] Ziegler, J.F., J.P. Biersack, U. Littmark, *The Stopping and Range of Ions in Solids*, Pergamon Press, New York (1985), *www.srim.org/SRIM/SRIMLEGL.html*.

[10] Satoh, D., *et al.*, *SCINFUL-QMD: Monte Carlo Based Computer Code to Calculate Response Function and Detection Efficiency of a Liquid Organic Scintillator for Neutron Energies Up to 3 GeV*, JAEA-Data/Code, 2006-023.

[11] Satoh, D., *et al.*, "Measurement of Response Functions of Liquid Organic Scintillator for Neutrons Up to 800 MeV", *J. Nucl. Sci. Technol.*, 43, 714 (2006).

[12] Niita, K., *et al.*, "PHITS – A Particle and Heavy Ion Transport Code System", *Radiat. Meas.*, 41, 1080 (2006).

[13] Taddeucci, T.N., *et al.*, "Zero-degree Cross Sections for the ^{7}Li(p,n)^{7}Be(g.s.+0.43-MeV) Reaction in the Energy Range 80-795 MeV", *Phys. Rev.*, C 41, 2548 (1990).

[14] Watanabe, Y., *et al.*, "Nuclear Data Evaluations for JENDL High-Energy File", *AIP Conf. Proceedings*, 769, 326 (2005).

[15] Yonai, S., *et al.*, "Measurement of Neutrons from Thick Fe Target Bombarded by 210 MeV Protons", *Nucl. Instr. and Meth.*, A 515, 733 (2003).

[16] Yashima, H., *et al.*, "Measurement of Neutron Activation Cross-sections for Major Elements of Water, Air and Soil Between 30 and 70 MeV", *J. Nucl. Sci. Technol.*, supplement 4, 70 (2004).

[17] Taddeucci, T.N., *et al.*, "The (p,n) Reaction as a Probe of Beta Decay Strength", *Nuclear Physics*, A 469, 125 (1987).

[18] Watson, J.W., *et al.*, "^{7}Li(p,n)^{7}Be and ^{12}C(p,n)^{12}N Reactions at 200, 300, and 400 MeV", *Phys. Rev.*, C 40, 22 (1989).

[19] Uwamino, Y., *et al.*, "High-energy p-Li Neutron Field for Activation Experiment", *Nucl. Instr. and Meth.*, A 389, 463 (1997).

Bonner sphere measurements in quasi-monoenergetic p-Li neutron fields of 243 and 387 MeV*

Vladimir Mares
Helmholtz Zentrum Muenchen, Institute of Radioprotection
Neuherberg, Germany

Abstract

This paper describes the results of neutron spectrometry using the Bonner Sphere Spectrometer (BSS) at the ring cyclotron facility at the Research Centre for Nuclear Physics (RCNP), Osaka University, Japan. The BSS system consists of 15 polyethylene (PE) spheres with spherical 3He proportional counters in their centre. It also includes two PE spheres with lead shells inside, to increase their response to high-energy neutrons above 10 MeV. Quasi-monoenergetic neutron fields at RCNP were generated from a 10 mm thick Li target using the 7Li(p,n)7Be reaction, injected by 245 and 388 MeV protons. The neutrons produced at 0° and 30° were extracted into the time-of-flight (TOF) tunnel of 100 m length through the concrete collimator of 10×12 cm² aperture and 150 cm thickness. The neutron energy spectra were measured at distance of 41 m from the target in the TOF tunnel. To deduce the energy spectra of neutrons from thermal to 1 GeV, an unfolding method with MSANB code was used together with response functions obtained by neutron transport calculations using the MCNP/LAHET code. The neutron energy spectra are discussed in terms of neutron fluence rates and ambient dose equivalent H*(10). The BSS results are also compared to neutron energy spectra measured by a NE213 organic liquid scintillator using the TOF method.

---

* The full paper being unavailable at the time of publication, only the abstract is included.

Neutron energy spectrum from 120 GeV protons on a thick copper target

Nobuhiro Shigyo[1], Toshiya Sanami[2], Tsuyoshi Kajimoto[1], Yosuke Iwamoto[3],
Masayuki Hagiwara[2], Kiwamu Saito[2], Kenji Ishibashi[1], Hiroshi Nakashima[3], Yukio Sakamoto[3],
Hee-Seock Lee[4], Erik Ramberg[5], Aria A. Meyhoefer[5], Rick Coleman[5], Doug Jensen[5],
Anthony F. Leveling[5], David J. Boehnlein[5], Kamran Vaziri[5], Nikolai V. Mokhov[5]
[1]Kyushu University, Fukuoka, Japan
[2]High Energy Accelerator Research Organization, Tsukuba, Japan
[3]Japan Atomic Energy Agency, Tokai-mura, Ibaraki, Japan
[4]Pohang Accelerator Laboratory, Pohang, Kyungbuk, Korea
[5]Fermi National Accelerator Laboratory, Batavia, Illinois, USA

Abstract

Neutron energy spectrum from 120 GeV protons on a thick copper target was measured at the Meson Test Beam Facility (MTBF) at Fermi National Accelerator Laboratory. The data allows for evaluation of neutron production process implemented in theoretical simulation codes. It also helps exploring the reasons for some disagreement between calculation results and shielding benchmark data taken at high-energy accelerator facilities, since it is evaluated separately from neutron transport. The experiment was carried out using a 120 GeV proton beam of 3E5 protons/spill. Since the spill duration was 4 seconds, proton-induced events were counted pulse by pulse. The intensity was maintained using diffusers and collimators installed in the beam line to MTBF. The protons hit a copper block target the size of which is $5\,cm \times 5\,cm \times 60\,cm$ long. The neutrons produced in the target were measured using NE213 liquid scintillator detectors, placed about 5.5 m away from the target at $30°$ and 5 m $90°$ with respect to the proton beam axis. The neutron energy was determined by time-of-flight technique using timing difference between the NE213 and a plastic scintillator located just before the target. Neutron detection efficiency of NE213 was determined on basis of experimental data from the high-energy neutron beam line at Los Alamos National Laboratory. The neutron spectrum was compared with the results of multi-particle transport codes to validate the implemented theoretical models. The apparatus would be applied to future measurements to obtain a systematic data set for secondary particle production on various target materials.

Introduction

Behaviour of high-energy radiation above the several tens GeV region is of interest in the study of high-energy accelerator shielding, space technology and so on. The Japanese-American Study of Muon Interactions and Neutron Detection (JASMIN) collaboration [1] has acquired shielding data and evaluated neutron production processes implemented in theoretical simulation codes. In a recent result of the collaboration, the experimental neutron energy spectra at the transmission experiment for 120 GeV proton beam consists of components below several GeV. The MARS code [2], a multi-particle transport code, reproduces the trend of the experimental data [3]. Neutron (and proton) production mechanism though the use of high-energy radiation as a source term is essential in order to understand the behaviour of high-energy radiation in shielding materials.

Neutron production double-differential cross-sections and thick target yields have been measured below several tens GeV [4-6]. However, there is no experimental data above several tens GeV. It is important to obtain double-differential thick target neutron and proton yields experimentally to evaluate the theoretical models in the multi-particle transport codes. In this paper, a feasibility study of experiment on double-differential neutron thick target yields by 120 GeV proton incidence was described. The preliminary experimental data was compared with the calculation results.

Experiment

The experiment was carried out at the MT6-2 area of Fermilab Test Beam Facility (FTBF), Fermi National Accelerator Laboratory. The schematic view of the experimental area and the detector arrangement are illustrated in Figure 1.

Figure 1: Experimental set-up at MT6-2 area in Fermilab Test Beam Facility (FTBF)
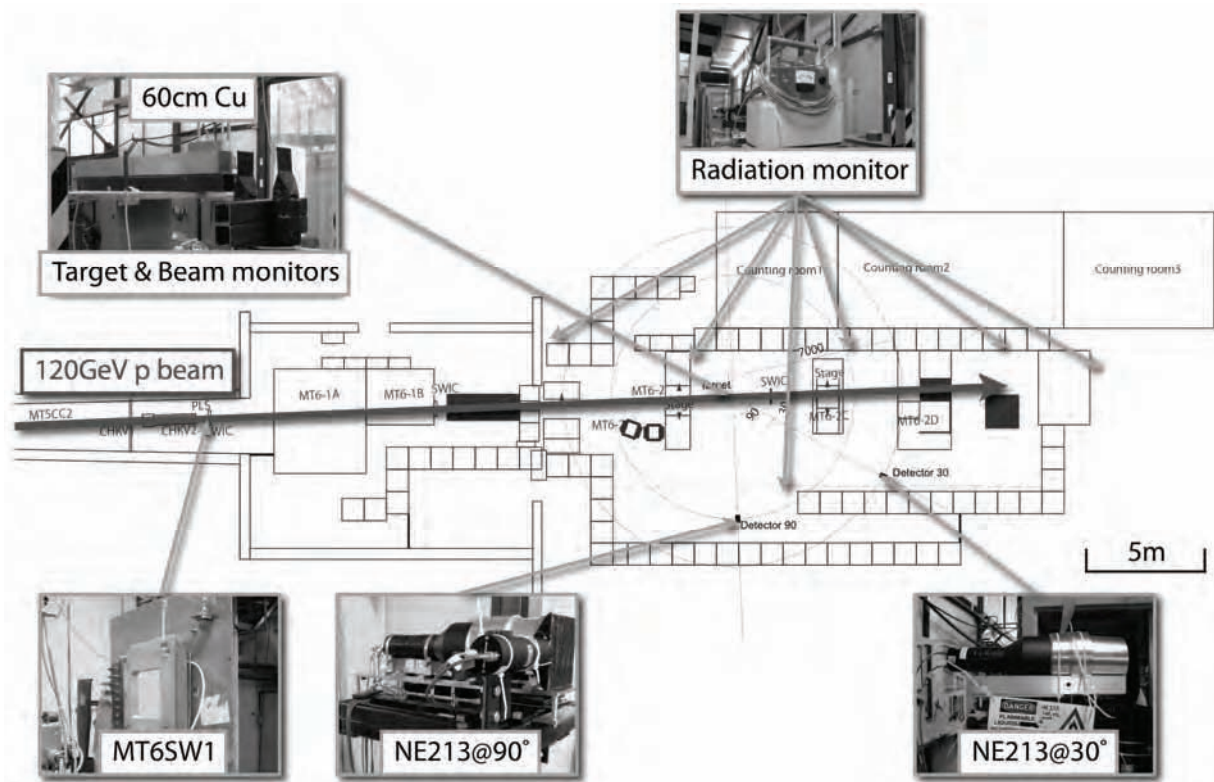
A copper block 5 cm × 5 cm × 60 cm long was chosen as a target. Measurement with target-in and target-out were performed to eliminate background neutron events.

Two NE213 liquid organic scintillators (12.7 cm thick and 12.7 cm long) were adopted as a neutron detector and placed at 30° and 90°. A plastic scintillator was set in front of each NE213 scintillator to distinguish neutron events with charged particle ones. Neutron energy was determined by the time-of-flight method. The flight paths were 5.5 m at 30° and 5 m at 90°, respectively. Some radiation monitors were installed to observe radiation level in the experimental area to keep the safety limit.

The 120 GeV incident proton beam was monitored by multiwire proportional counters (MT6SW1) on the upstream of the beam line to see the beam profile and three plastic scintillators in front of the target to count the number of incident protons. The average number of protons was limited to 3×10^5 particles/spill because of the radiation safety limitation.

Two types of data acquisition system (DAQ) were used in the measurement. One was an ordinary CAMAC DAQ to collect the integral light output from scintillator. The other was a wave form digitiser DAQ which gets wave form of light output from the scintillator as a function of time to increase the actual counting rate. Both DAQ systems acquired the neutron flight time between the target and the scintillator.

The time structure of proton beam consists of three levels as shown in Figure 2. The smallest structure was the bunch of 19 ns interval. The second one was called the "train", and included 20-36 bunches and had 11 μs intervals. The largest structure was the spill which contained trains of 4 seconds. This meant that the beam was available in just 4 seconds a minute.

Figure 2: Time structure of proton beam at MT6-2 area
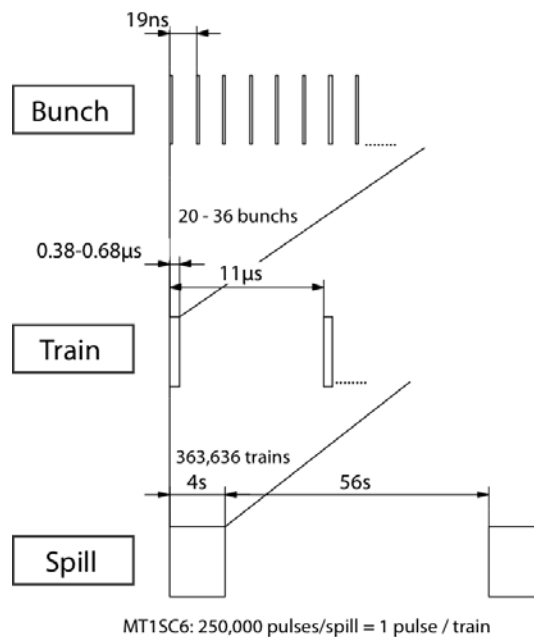
Data analysis

First of all, charged particle events were separated by the signal of a plastic scintillator in front of an NE213 scintillaor. The NE213 scintillator is sensitive to gamma-rays in addition to neutrons. The neutron and gamma-ray events were separated by the two-gate integration method. Figure 3 shows an example of neutron and gamma-ray separation. Neutron events were 5% of all events at 30° in the target-in measurement.

An example of time spectra is shown in Figure 4. One can see that several peaks with 400 ch for all charged particles, gamma-rays and neutrons. This interval shows the bunch of the beam time structure illustrated in Figure 2.

Figure 3: Neutron and gamma-ray discrimination by an NE213 scintillator
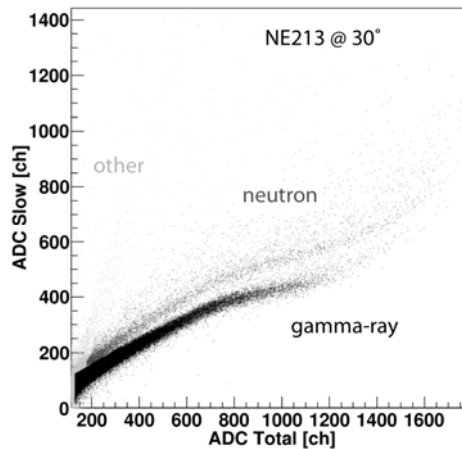
Figure 4: An example of time spectra of an NE213 scintillator
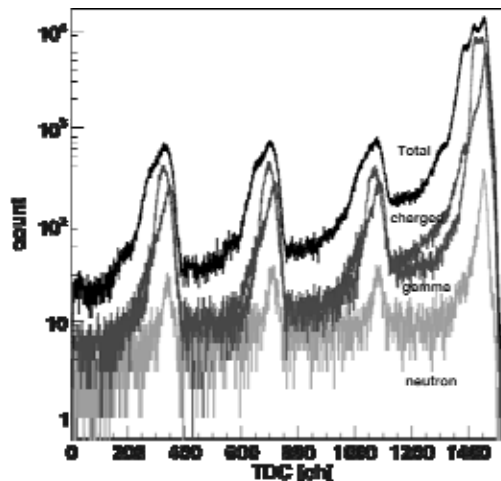
For separation of one-proton incident events from multi-proton ones, the light output spectrum of plastic scintillators in front of the copper target was used. Figure 5 indicates the light output spectrum. The one-proton incident events were distinguished from multi-proton ones. Events of 39% were one-proton incident events in the target-in measurement. Figure 6 shows the time spectra of one-proton incident events (bm = 1) after the separation process.

An example of light output spectra by one-proton incident events separated by multi-proton incident ones are seen in Figure 7. Neutron events were distinguished as seen in the figure.

Detection efficiency

The neutron detection efficiency was usually calculated by the SCINFUL-QMD code [7] above 100 MeV of neutron energy. However, the code does not consider the individual characteristics of each scintillator. In this experiment, the neutron detection efficiency for both scintillators was measured by continuous energy neutron beam at the WNR facility of Los Alamos Neutron Science Center (LANSCE) in Los Alamos National Laboratory in order to see the characteristics of both scintillators.

The WNR facility supplies pulsed neutron beam with a spallation reaction of 800 MeV proton beam and a tungsten target below 700 MeV. Each neutron energy was determined by the time-of-flight technique between the spallation target and the NE213 scintillator. The incident neutron flux was obtained by the count of a ^{238}U fission ionisation chamber and the neutron-induced fission cross-section

Figure 5: An example of ADC spectrum of the beam-monitoring scintillator
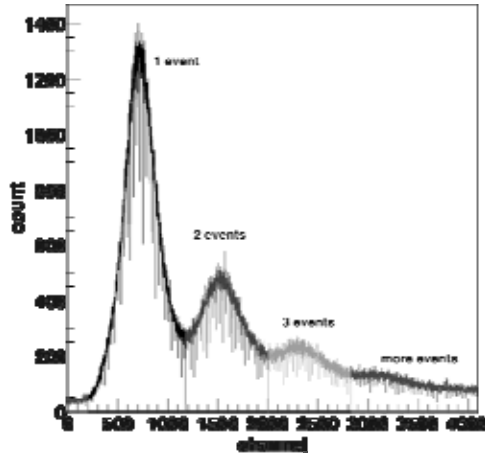
Figure 6: An example of TDC spectra of an NE213 scintillator
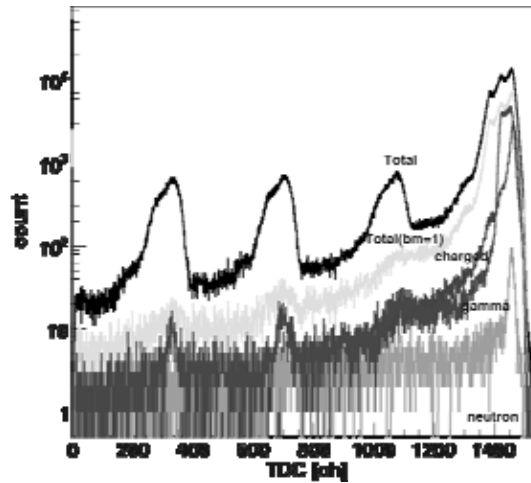
Figure 7: An example of light output spectra of an NE213 scintillator
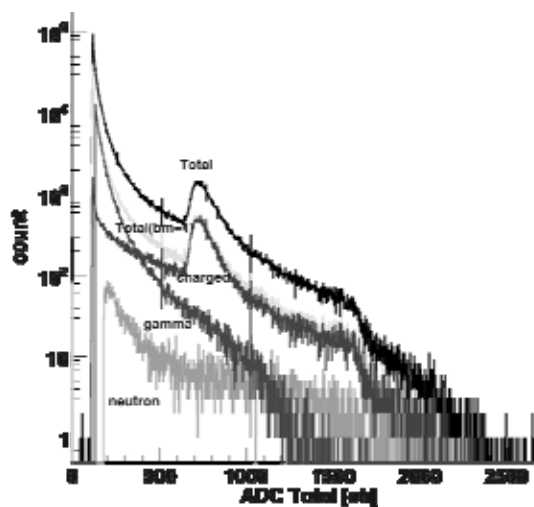
for ^{238}U. Several types of neutron-induced fission cross-sections for ^{238}U based on experimental data [8-10], calculation and evaluation [11-13] are presented in Figure 8. The neutron detection efficiency measured and derived by some neutron-induced fission cross-sections are shown in Figure 9 with calculated values by SCINFUL-QMD. The efficiency by SCINFUL-QMD overestimates the experimental ones between 60 and 200 MeV.

Figure 8: Neutron-induced fission cross-sections for ^{238}U
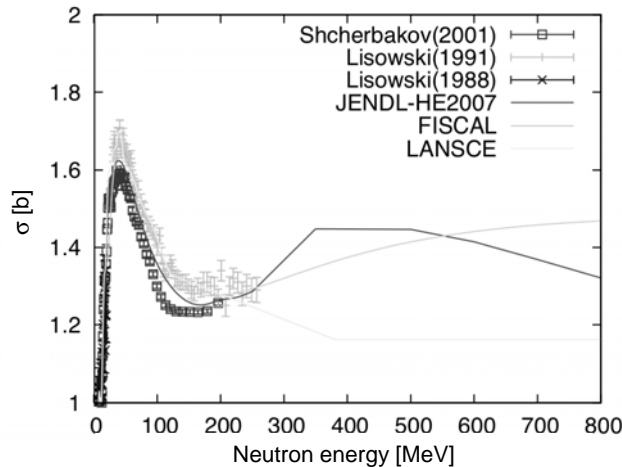
Figure 9: Neutron detection efficiency of an NE213 scintillator at LANCE
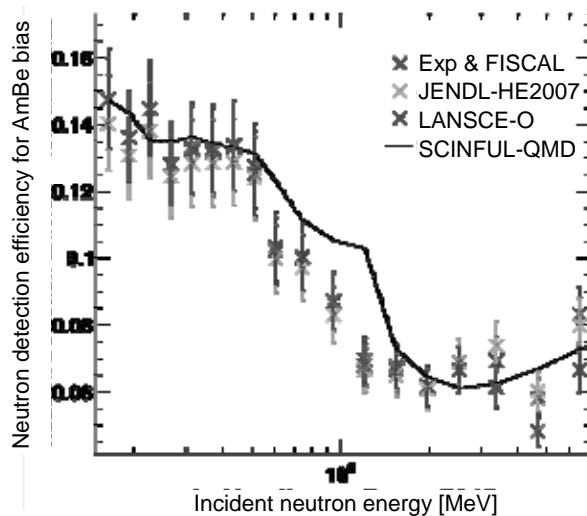
Results

The preliminary double-differential thick target neutron yields using the CAMAC DAQ system at 30° and 90° are shown in Figures 10 and 11, respectively, with the calculated values by the PHITS [14] and FULKA [15] codes. Both codes reproduce the shape of energy spectra. The experimental data at 30° were analysed by several kinds of neutron detection efficiencies. The PHITS code underestimates experimental neutron yields above 40 MeV in the direction. On the other hand, both PHITS and FULKA slightly overestimate experimental data below 300 MeV at 90°. The highest neutron energies were about 2 GeV at 30° and about 800 MeV at 90°, respectively.

Figure 10: 120 GeV proton-induced neutron thick target yield at 30° using a CAMAC DAQ system
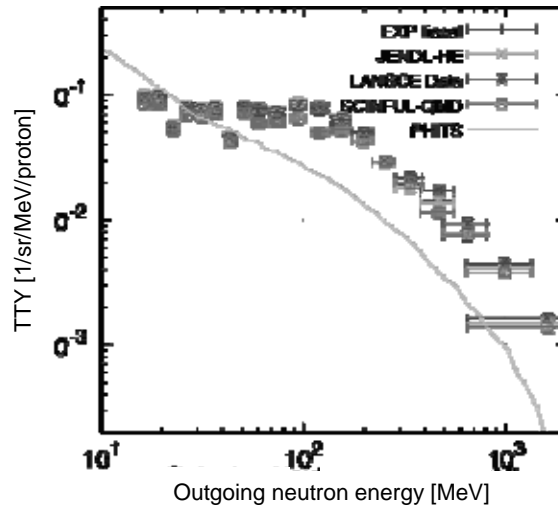
Figure 11: 120 GeV proton-induced neutron thick target yield at 90° using a CAMAC DAQ system
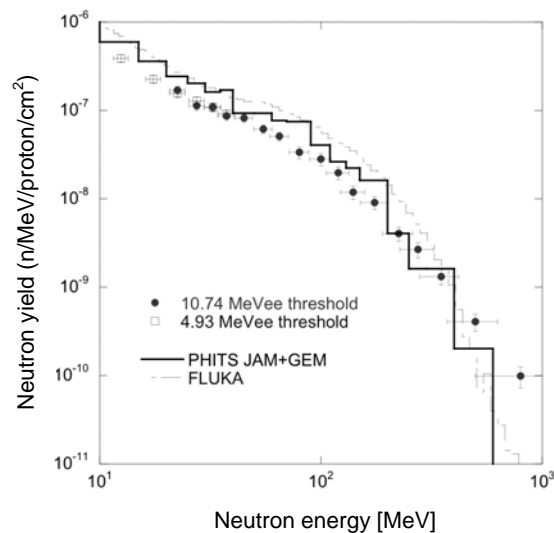
Proton and neutron energy spectra were retrieved by analysing data obtained with the wave form digitiser DAQ. Figure 12 indicates the preliminary proton and neutron energy spectra emitted from the copper target with PHITS calculation results. Experimental data of neutron energy spectra by the wave form digitiser DAQ system is consistent with that by the CAMAC DAQ system. The PHITS code generally reproduces the experimental proton up to 200 MeV and neutron data below 400 MeV, respectively.

Summary

The thick target neutron yields and proton energy spectrum on a copper target for 120 GeV proton beam as a source term of high-energy radiation behaviour were feasibly measured. The experimental procedure using the ordinary CAMAC and the wave form digitiser DAQ system was confirmed. The apparatus would be applied to future measurements to obtain a systematic data set for secondary particle production on various target materials. The multi-particle transport codes represent the shape of neutron and proton energy spectra. The calculation result by the PHITS code underestimates the experimental data of thick target neutron yield at 30°. The PHITS code generally reproduces proton and neutron energy spectrum at 90°.

**Figure 12: 120 GeV proton-induced proton and neutron
thick target yields at 90° using a wave form digitiser DAQ system**
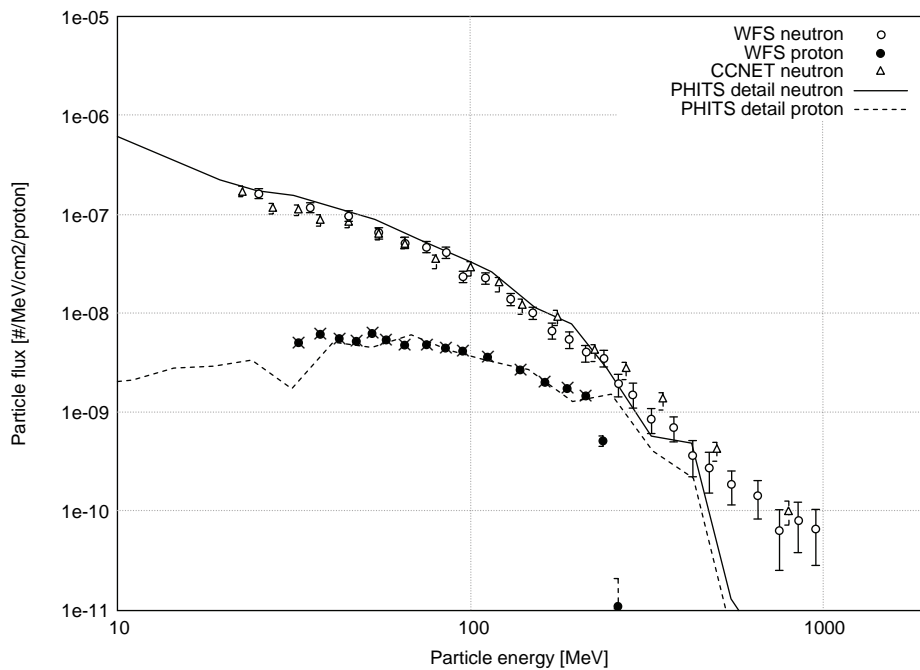
Acknowledgements

References

[1]   Nakashima, H., *et al.*, "JASMIN: Japanese-American Study of Muon Interactions and Neutron Detection", these proceedings.

[2]   Mokhov, N.V., FERMILAB-FN-628 (1995); and Mokhov, N.V., S.I. Striganov, *Hadronic Shower Simulation Workshop AIP Proceedings*, 896, Fermilab-Conf-07-008-AD (2007).

[3]   Hagiwara, M., et al., "Shielding Experiments at High Energy Accelerators of Fermilab (III): Neutron Spectrum Measurements in Intense Pulsed Neutron Fields of the 120-GeV Proton Facility Using a Current Bonner Sphere Technique", *Proc. of the 5th Int. Symp. on Rad. Safety Detec. Technol. (ISORD-5) (2010)*, forthcoming.

[4]   Ishibashi, K., et al., "Measurement of Neutron-production Double-differential Cross Sections for Nuclear Spallation Reaction Induced by 0.8, 1.5 and 3.0 GeV Protons", *J. Nucl. Sci. Technol.*, 34, 529-537 (1997).

[5]   Stamer, S., *et al.*, "Double Differential Cross Sections for Neutron Emission Induced by 256 MeV and 800 MeV Protons", *Phys. Rev.*, C47, 1647-1658 (1993).

[6]   Leray, S., *et al.*, "Spallation Neutron Production by 0.8, 1.2, and 1.6 GeV Protons on Various Targets, *Phys. Rev.*, C65, 446211-4462117 (2002).

[7]   Satoh, D., *et al.*, *SCINFUL-QMD: Monte Carlo Based Computer Code to Calculate Response Function and Detection Efficiency of a Liquid Organic Scintillator for Neutron Energies Up to 3 GeV*, JAEA-Data/Code 2006-023 (2006).

[8]   Shcherbakov, O.A., *et al.*, "Neutron-induced Fission Of ^{233}U, ^{238}U, ^{232}Th, ^{239}Pu, ^{237}Np, ^{nat}Pb and ^{209}Bi Relative to ^{235}U in the Energy Range 1-200 MeV", *J. Nucl. Sci. Technol.*, Suppl. 2, 230-233 (2002).

[9]   Lisowski, P.W., *et al.*, "Neutron Induced Fission Cross Section Ratios for ^{232}Th, ^{235,238}U, ^{237}Th and ^{239}Pu from 1 to 400 MeV", *Proc. Int. Conf. on Nucl. Data for Sci. Technol.*, 97 (1988).

[10] Lisowski, P.W., *et al.*, "Fission Cross Sections Ratios for $^{233,\ 234,236}$U Relative to ^{235}U from 0.5 to 400 MeV", *Proc. Int. Conf. Nucl. Data for Sci. and Technol.*, 732 (1991).

[11] Watanabe, Y., *et al.*, "Nuclear Data Evaluations for JENDL High-Energy File", *AIP Conf. Proc.*, 769, 326-331 (2005).

[12] Fukahori, T., *et al.*, "JENDL High Energy File", *J. Nucl. Sci. Technol.*, Suppl. 2, 25-30 (2002).

[13] Haight, R.C., N. Fotiadis, private communication.

[14] Niita, K., *et al.*, "PHITS – A Particle and Heavy Ion Transport Code System", *Radiat. Meas.*, 41, 1080-1090 (2006).

[15] Battistoni, G., *et al.*, "The FLUKA Code: Description and Benchmarking", *AIP Conf. Proc.*, 896, 31-49 (2007). Fassò, A., *et al.*, *FLUKA: A Multi-particle Transport Code*, CERN-2005-10 (2005), INFN/TC_05/11, SLAC-R-773.

Perturbation of phase space downstream by parameters upstream

Mary P.W. Chin
European Organization for Nuclear Research (CERN)
Geneva, Switzerland

Abstract

The development of a radiation history from the source particle to the end-of-life of all its progenies is of essence in Monte Carlo simulations. The progression from upstream to downstream is demonstrated here for the case of a target system of a megawatt spallation neutron source. The target system is assembled component-by-component starting with the target, followed by the moderator, the inner and outer reflectors, the decoupler and the lining. At each stage the energy and time spectra are scored, underlining the function of each component. Perturbations are then introduced to the beam energy and beam footprint to gauge the resultant changes in the escaping neutron flux, which could have major implications on the shielding design. Such a gauge is necessary as for most facilities the application for licensing takes place concurrently with the design of the target system. The study is therefore instructive in applying for a license before the full and final specification of the target system becomes available.

Motivation

The (p,xn) process offers an attractive alternative to reactor-based neutron sources. Several spallation neutron facilities are already in operation while more are underway. At high proton energies, the spallation process can produce many neutrons per reaction. The many neutrons (*e.g.* fifty) thus produced, however, are typically useless in serving neutron-as-a-probe, diffraction-based experiments. This is because the neutron energy overshoots by > 10 orders of magnitude: between the GeV range and the meV range corresponding to neutron wavelengths at the angstrom scale of interest to diffraction studies. The lone target serving the (p,xn) reaction must therefore be accompanied by energy- and time-shaping components in order to deliver useful neutrons to the experimental beamlines.

A moderator is naturally one of the first components to be added to the target system. The classical water moderator at room temperature is not able to provide low-enough neutron energies in equilibrium. Instead, cryogenic moderators are typically used. To enhance the neutron flux, surrounding reflectors are introduced into the target system. Reflectors increase the number of neutrons at the price of broadening the time pulse of emerging neutrons. Poor time resolutions are not desirable. In order to counter this effect, decoupling materials may be introduced into the target system to reduce pulse-broadening neutrons entering the wave-guide.

The selection of materials, dimensions and the relative positioning of each component in the target system is an intricate compromise of neutronics demands against heat and damage constraints. For instance, a pencil beam may be ideal for providing the maximum neutron flux emerging from the target; however, such an option would have to be discarded if it effectively drills a hole in the target or if it damages one of the components at a rate which requires unreasonably frequent change of components to which access is limited due to radiation hazards.

The design process therefore requires multiple iterations. Identifying whether a level of details is mandatory or optional for each design state is crucial. This would allow the design task to be broken down into smaller manageable parts, where a part may have dedicated experimental design and data analysis. Motivated by such needs, this work connects the episodes along the development of radiation histories from upstream to downstream. By not skipping intermediate episodes, hidden cancelling effects may be avoided. The step-by-step investigation provides a cause-and-effect gauging of the sensitivity of downstream phase space (*e.g.* particle energy and age) to upstream parameters (*e.g.* beam configurations).

Materials and methods

MCNPX 2.6.0 simulations were run to score cell-averaged neutron fluxes in the various components comprising the target system (Figure 1). The flux scored is differentiated by energy and time, where the clock starts ticking at the birth of the proton source marking the beginning of each radiation history. The weight-window generator was issued in a pre-run to generate weight window parameters for efficient scoring in the wave-guide. A 13 cm × 5 cm 2.5 GeV proton beam impinges the rectangular target (mercury). Perpendicular to the beamline, the wider faces of the target are each viewed by a cylindrical moderator (100% para hydrogen, 20 K). The target and both the moderators are surrounded by the inner reflector (beryllium), which is in turn surrounded by the outer reflector (iron). The decoupler and lining are made of AIC (68.3% Ag + 2.5% In + 29.2% Cd; 10.17 g/cm^3). The materials, dimensions and arrangement of the components in the target system are that of a *wing* geometry [1] similar to a model [2] from the Japanese Spallation Neutron Source. The model in this work incorporates two opposing moderators instead of one, in favour of symmetry.

Separate simulations, each with a different geometry, were run:

- target, prior to cutting, of dimensions 60 cm × 60 cm × 100 cm;

- target (T), after cutting, of dimensions 40 cm × 8 cm × 60 cm (the size is usually chosen after weighing neutronic considerations with heat and damage constraints);

- T and moderators (M);

- T, M and inner reflectors (Ri);

- T, M, Ri and outer reflectors (Ro);

- T, M, Ri, Ro and decoupler (D);

- T, M, Ri, Ro, D and lining (L).

Simulation of the full T-M-Ri-Ri-D-L model was then repeated with differing beam configurations:

- C1: reducing the beam footprint to 12 cm × 5 cm;

- C2: reducing the beam footprint to 13 cm × 4 cm;

- C3: introducing a 1 cm × 1 cm cavity at the centre of the beam footprint;

- C4: 1 GeV instead;

- C5: 2 GeV instead.

Simulation of the full model was also repeated with the moderator temperature at 25 K and 293.6 K.

Figure 1: The full T-M-Ri-Ro-D-L geometry: a) side view; b) top view; c) beam's eye view
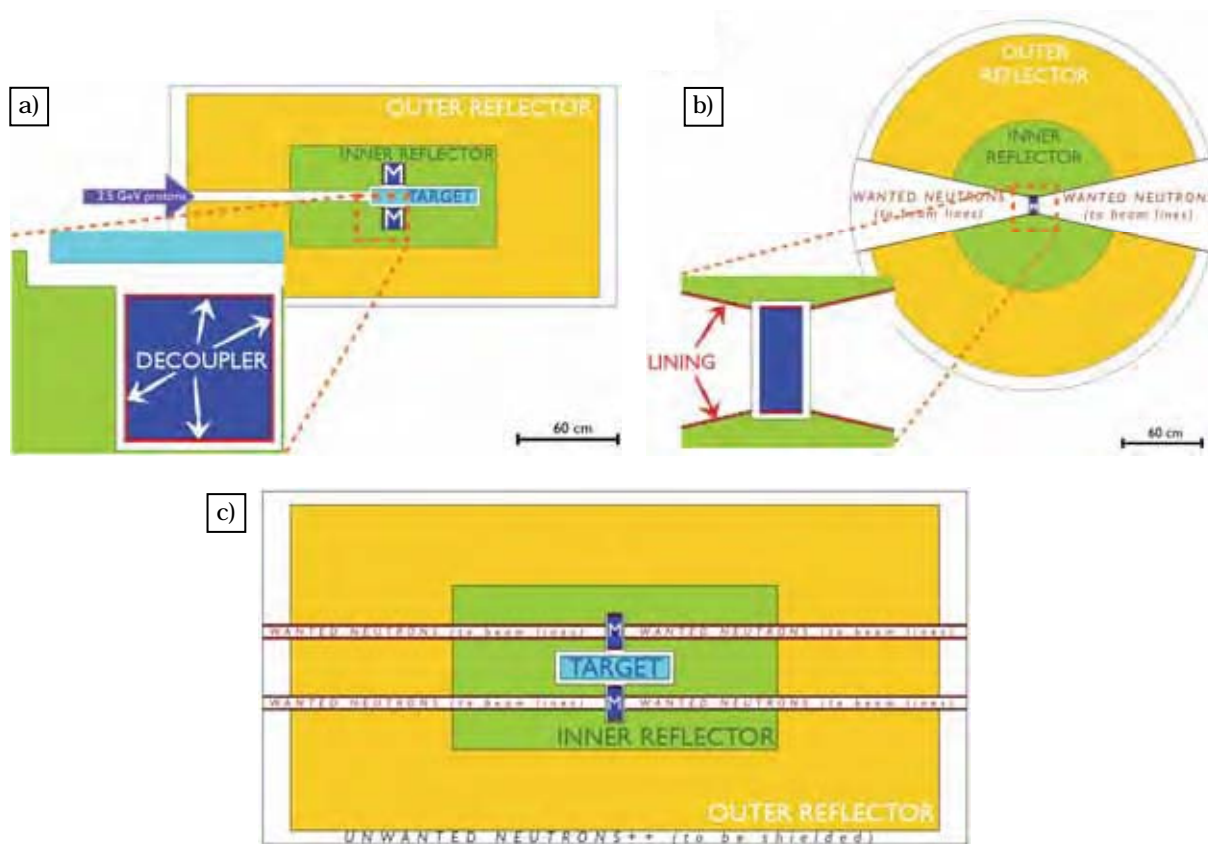
Results and discussion

The low-energy component of the neutron lethargy in the target increased as the moderator and reflectors were added to the model (Figure 2). The cutting of the target reduced the scatters due to neighbouring location of the same material. Subsequent steps in assembling the full target system in Figure 2 increased the backscatter. T-M-Ri and T-M-Ro resulted in very similar lethargy plots, as did the T-M-Ri-Ro-D and T-M-Ri-Ro-D-L pair, suggesting that this level of detail may be optional in target optimisation studies.

In the moderator (Figure 3) more dramatic changes in the neutron lethargy were observed. The introduction of the reflectors deflected the lethargy plot at a pivot point near 1 MeV, with significant

drop at high energies and a significant rise of the low-energy tail. Again, the close proximity of the plots for T-M-Ri and T-M-Ro identifies the level of detail not necessarily mandatory in moderator optimisation studies.

The neutron lethargy and time spectrum in the wave-guide [marked with "wanted neutrons" in Figure 1(b)] demonstrate best the function of the reflectors and decoupler (Figure 4). The presence of the decoupler effectively decreased the low-energy component in the neutron spectrum, apparently against the goal of maximising cold neutrons as required by the experiments at the end of the beamline. This apparent counter-effect is explained by the time spectrum: the eliminated low-energy neutrons are in fact unwanted, as they would have broadened the time resolution (at around 1 millisecond). The decoupler is thus in place to reduce the pulse broadening due to the reflectors, which were inserted to increase the count of low-energy neutrons.

Whereas the low-energy component is of greater interest in the wave-guide, the high-energy component (> 1 MeV) is of a greater concern for the escaping neutrons [to the outermost region in Figures 1(a), 1(b) and 1(c)] due to the implications on shielding (Figure 5). The decouplers provided a secondary service in terms of shielding, underlining the importance of including this detail even in estimating shielding requirements.

Reducing the beam footprint by a centimetre at each of its dimensions produced drastically different changes in the lethargy of the escaping neutrons (Figure 6). Using a 12 cm × 5 cm beam (C1) of a 13 cm × 5 cm did not change the escaping neutron lethargy very much. A 13 cm × 4 cm (C2) beam, on the other hand, produced a significantly lower high-energy component (> 100 MeV), therefore significantly decreasing the shielding requirement. Indeed the two axes perpendicular to the beamline are functionally asymmetrical especially in *wing* geometries [3].

Introducing a cavity at the centre of the beam profile (C3) also resulted in a drop in the high-energy component (> 100 MeV). Changes in the beam energy (C4 and C5) shifted the bulk of the lethargy plot down, including points in the middle-energy range which was minimally affected by changes in beam footprint (C1, C2 and C3).

No difference is visible in the lethargy in the moderator (Figure 7) whether it is at 20 K or 25 K despite the fact that the S(α,β) inelastic cross-sections obviously differ between the two temperatures (Figure 8); also despite the fact that MCNP/MCNPX offers a collection of hydrogen cross-section libraries in steps of 1 K in this region. Between 20 K and 293.6 K, as expected the lethargy is notably different at energies below 1 eV. Therefore, the need for using exact-temperature-specific cross-sections in neutronic calculations could sometimes be superfluous or otherwise, as demonstrated.

Conclusion

The progression of radiation histories has been followed step-by-step for a target system consisting of the target, moderator, inner and outer reflectors, decoupler and lining. The importance or otherwise of including each component in component-specific optimisation studies has been outlined. In terms of shielding the escaping neutrons, implications of a changed beam dimension drastically differ between the two axes perpendicular to the beamline. The shielding requirement appeared to be nearly independent of a 1 cm reduction in one axis but highly dependent of a 1 cm reduction in the other. The use of temperature-specific cross-section libraries for the hydrogen moderator was shown to be optional between 20 K and 25 K but mandatory between such temperatures and 293.6 K.

Figure 2: Neutron lethargy in the target
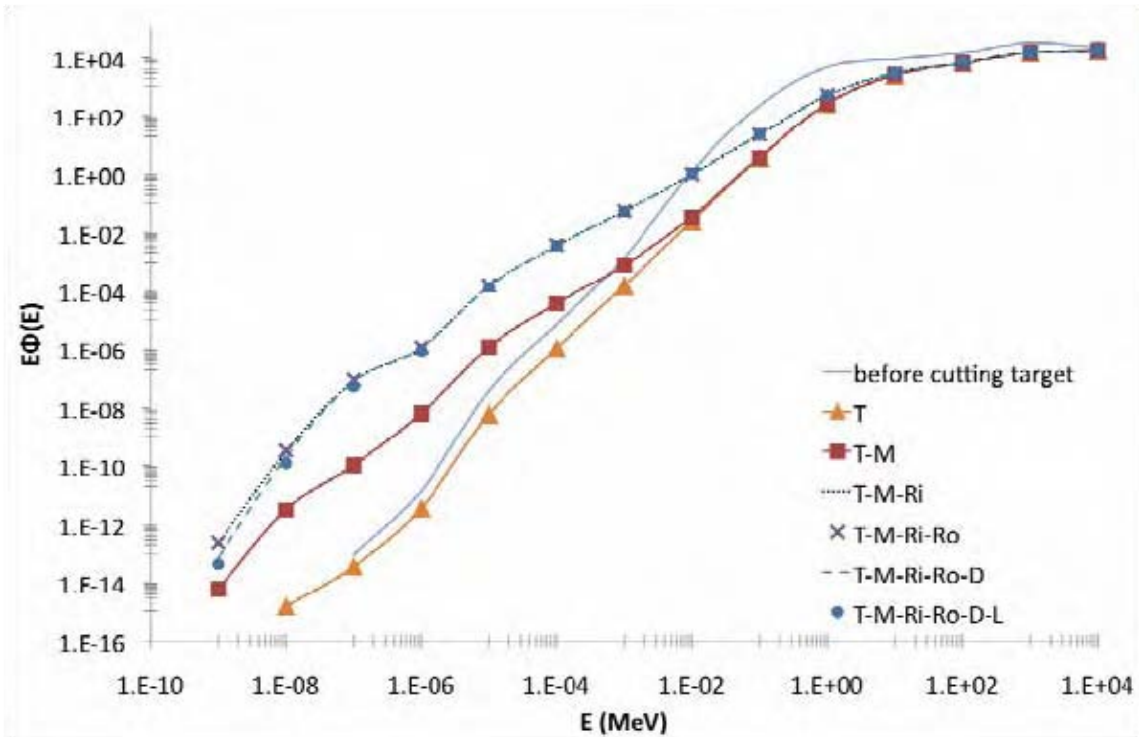
Figure 3: Neutron lethargy in the moderator
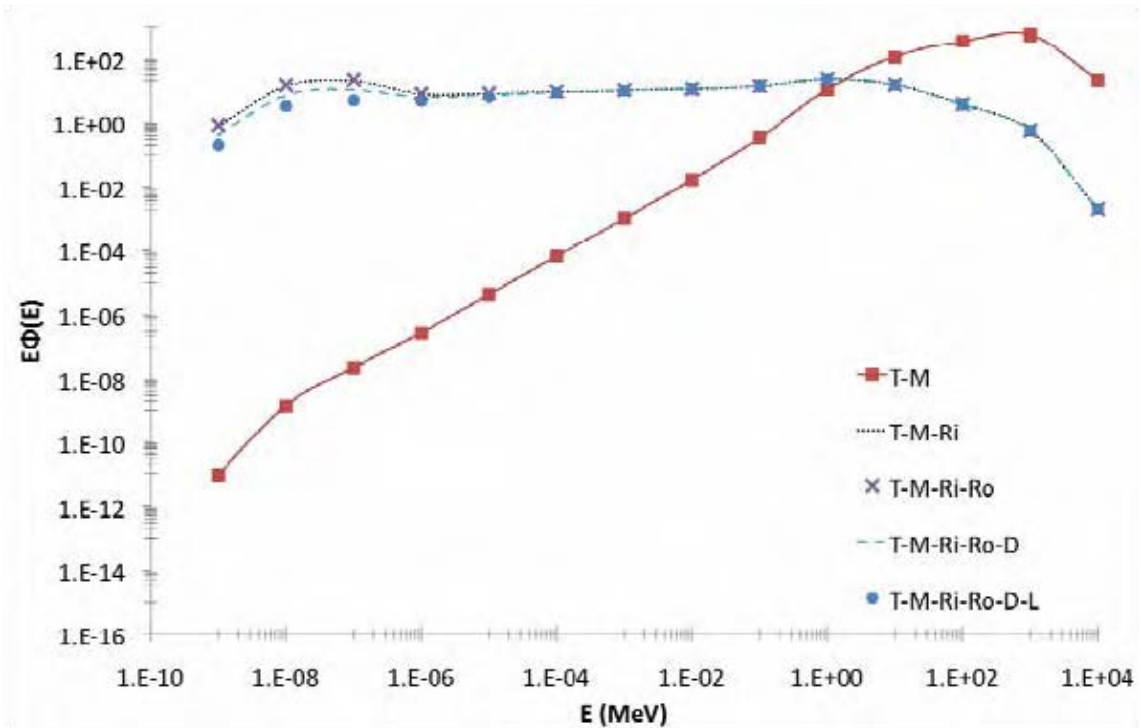
Figure 4: Neutron lethargy and time spectrum in the wave-guide
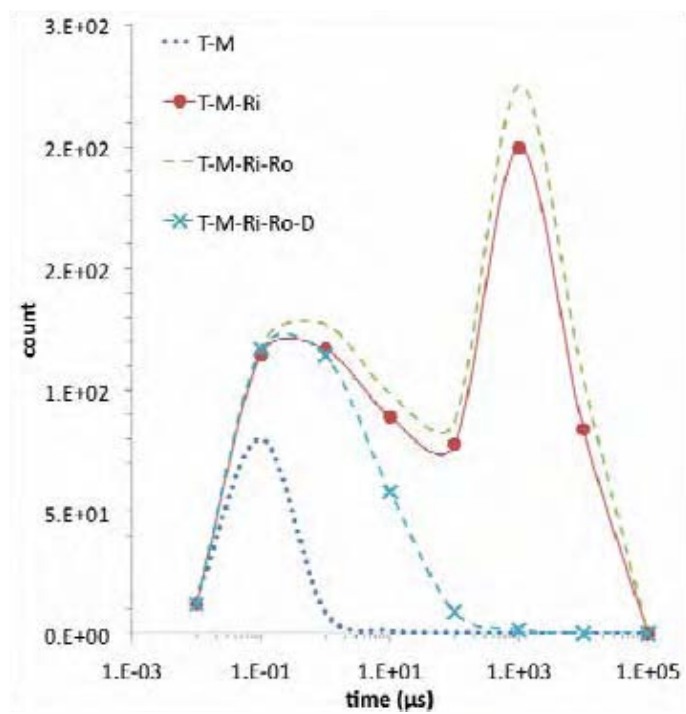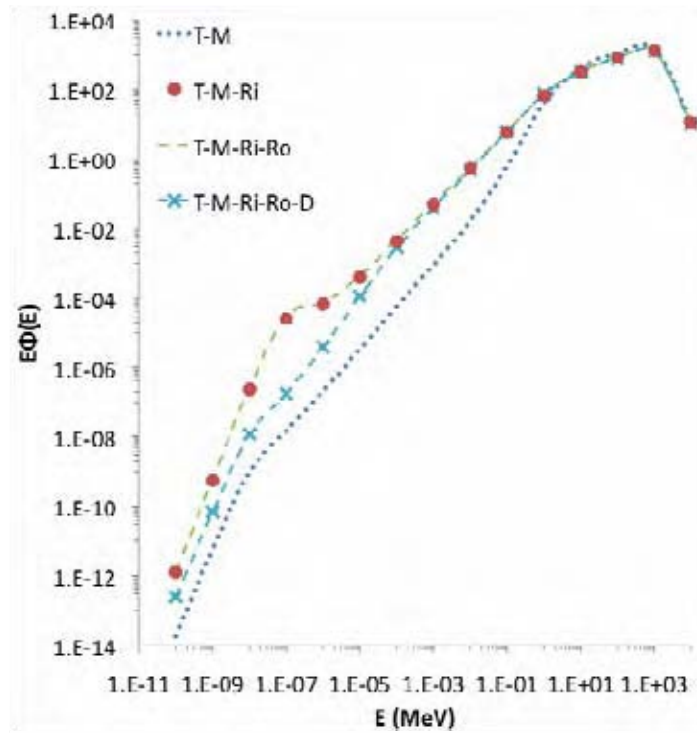
Figure 5: Neutron lethargy escaping the target system
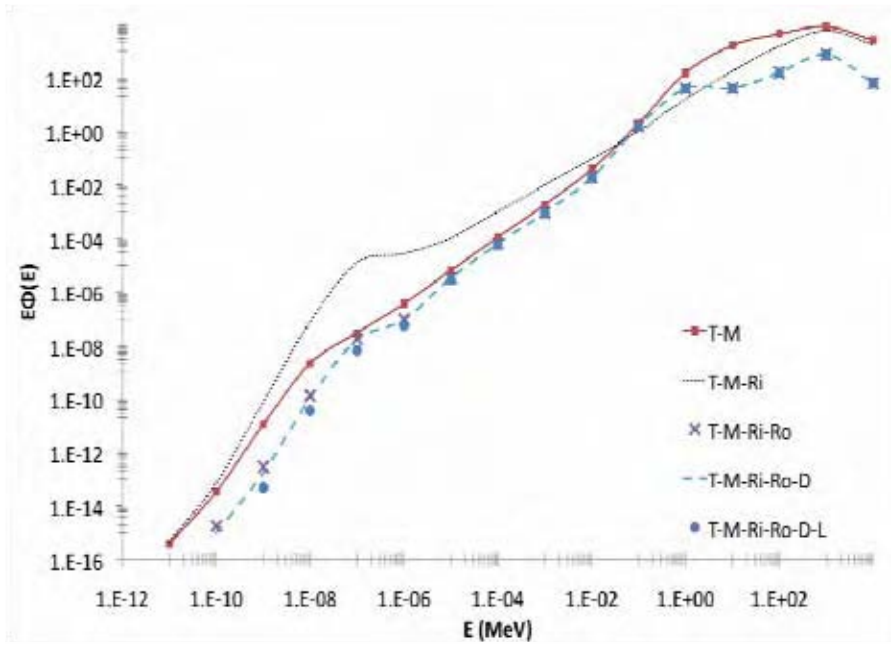
Figure 6: Fractional change in neutron lethargy escaping the target system
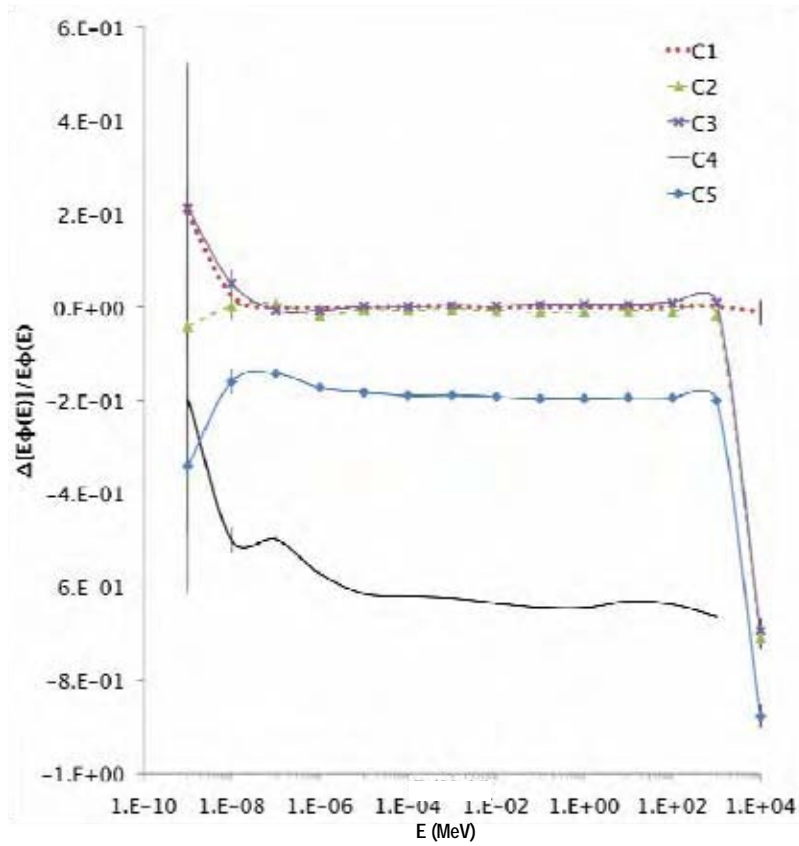
Figure 7: Neutron lethargy in moderators of different temperatures
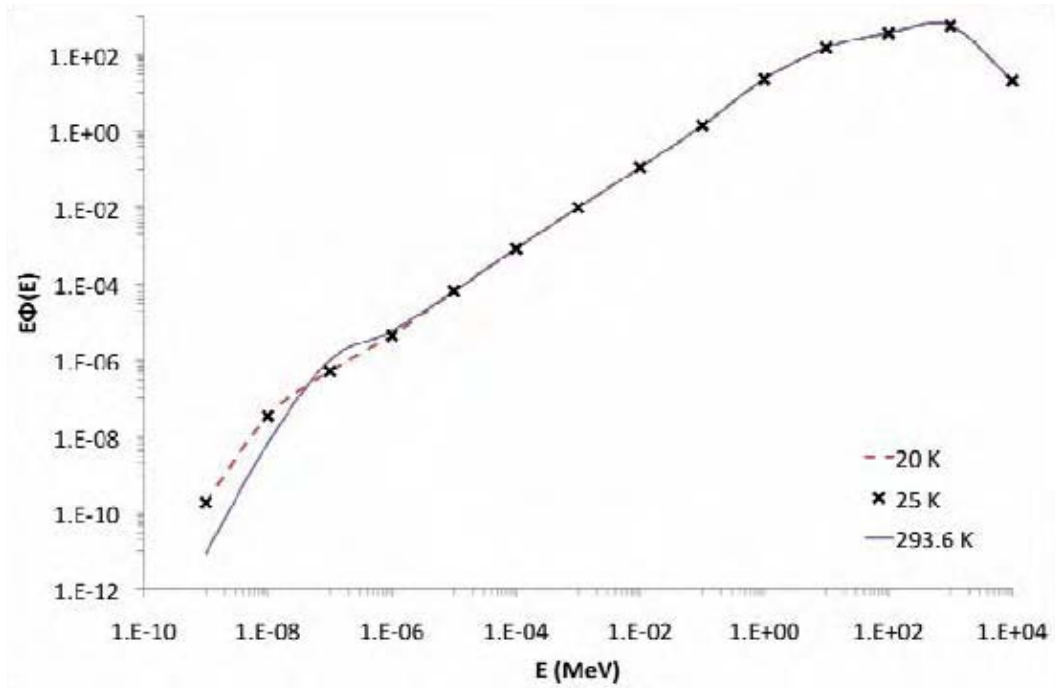
Figure 8: S(α,β) inelastic cross-sections of hydrogen at different temperatures
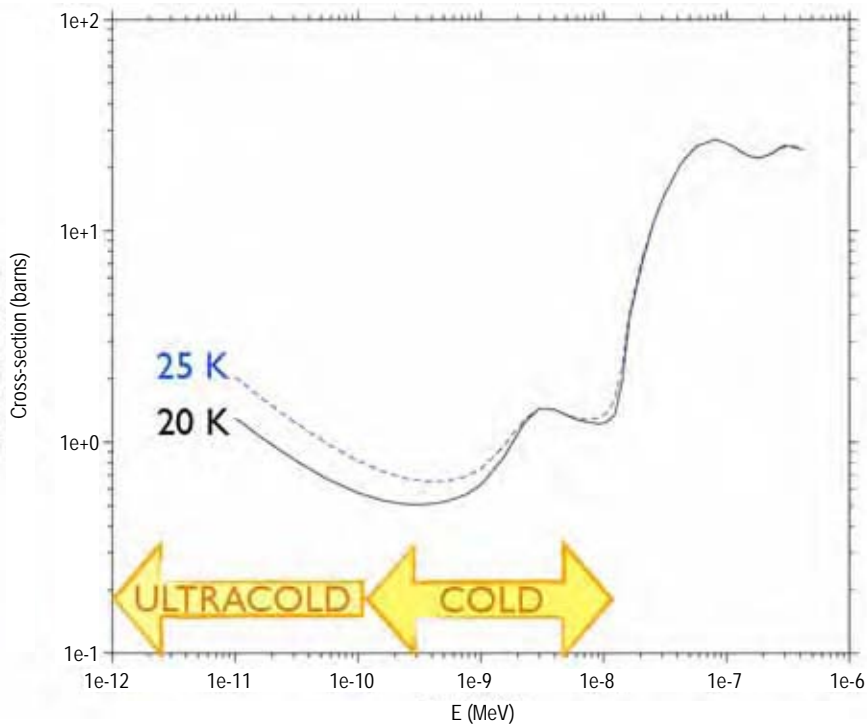
References

[1]   Watanabe, N., "Neutronics of Pulsed Spallation Neutron Sources", *Rep. Prog. Phys.*, 66, 339-381 (2003).

[2]   Harada, M., *et al.*, "Neutronic Studies on Decoupled Hydrogen Moderator for a Short-pulse Spallation Source", *NIM*, A 53, 9, 345-362 (2005).

[3]   Chin, M.P.W., *et al.*, "Proton and Neutron Penetration in Candidate Target Materials for the European Spallation Source", *19th Meeting International Collaboration of Advanced Neutron Sources*, PSI Report (2010), Grindelwald.

Shielding assessment for the ELI high-intensity laser beamline facility in the Czech Republic

A. Ferrari[1,2]**, T. Cowan**[2]**, D. Margarone**[3]**, J. Prokupek**[3]**, B. Rus**[3,4]
[1]Institut für Sichereitsforschung, Forschungszentrum Dresden-Rossendorf, Dresden, Germany
[2]Institut für Strahlenphysik, Forschungszentrum Dresden-Rossendorf, Dresden, Germany
[3]Institute of Physics of the Czech Academy of Science, Prague, Czech Republic
[4]PALS Centre, Prague, Czech Republic

Abstract

The production of laser-accelerated, high-energy and high-current particle beams requires a proper shielding assessment, especially when high-intensity laser systems operate in repetition rate. The future Extreme Light Infrastructure (ELI) European facility in the Czech Republic, where different optional laser beamlines are foreseen, will offer versatile electron and proton/ion sources, emitting in an unprecedented energy range (up to about 40 GeV for the electron case). For this facility a first extensive study that includes shielding and activation calculations for the 300 J laser beamline, which is the most critical for electron acceleration experiments, has been performed. Starting from analytical calculations, as well as from dedicated simulations, the main radiation fields produced in the laser/ matter interaction have been defined. These fields have been then characterised as "source terms" in a full simulation with the Monte Carlo code FLUKA, where the produced secondary radiation has been studied to assess a proper shielding. The first results for the ELI shielding for the electron case, together with the activation calculations that drove several material solutions, are presented and discussed here.

Introduction

In recent years the dramatic rise in attainable laser intensity has triggered a strong evolution of the research field that is associated with the non-linear laser/matter interaction. The production and acceleration of electrons up to 1 GeV over accelerating distances of a few millimetres (to be compared with the hundreds of meters that are typical for conventional accelerators) are a visible result of this evolution [1]. Moreover, at the existing laser facilities in the 100 TW range, low-emittance protons are accelerated up to energies of 20-30 MeV from thin (few tens of micrometers) solid metallic targets [2]. The present limit in terms of kinetic energy has recently been set at the LANL 200 TW Trident laser facility, where protons with energies in excess of around 67.5 MeV have been accelerated from micro-cone targets [3].

The achieved goals in terms of laser-accelerated particle beam energy and brightness require a proper shielding assessment for the primary and secondary ionising radiation, especially when high-intensity laser systems operate in repetition rate (typically in the range 0.1-10 Hz).

The Extreme Light Infrastructure (ELI) beamline facility in the Czech Republic is one of the four European pillars that is foreseen in this ambitious project: different optional laser beamlines will offer several versatile electron and proton/ion sources, emitting in an unprecedented energy range. Moreover, the source compactness, as well as the spectacular increase in the particle beam brightness and decrease in particle bunch duration, will have direct implications in biology, chemistry, nuclear medicine and solid-state physics [4].

In the following a first study about the shielding for the electron acceleration area is presented. As first step the radiation beams that are produced in laser/matter interactions have been characterised both for the electron and the proton case. Then these "source terms" have been inserted in a full simulation with the FLUKA Monte Carlo code [5,6]: a key point for this choice has been the possibility to calculate in the same simulation the development of the electromagnetic and hadronic showers in the whole energy range of interest and the neutron production and transport until the thermal energies, as well as the ambient dose equivalent, that is due to all the radiation field components.

The characterisation of the source terms

Unlike a standard accelerator facility, the definition of a source term case for the ELI laser acceleration beamline facility is a tangled issue. In fact, this facility will allow laser/matter interaction experiments in a new regime of laser intensity, the so-called ultra-relativistic regime ($I_L > 10^{23}$ W/cm^2), and will use an ultra-short pulse (a few tens of femto seconds). Hence, there are no experimental data in literature reporting the spectral range of the produced ionising radiation in those conditions, as well as the correspondent ambient dose equivalent. The only way to define a source term is to use analytical estimations, numerical simulations and sometimes scaling laws. In addition, various configurations for the future experiments have been proposed by several scientists: our general criterion has been, therefore, to set the laser/target interaction conditions by considering the "worst" scenario in terms of radiation protection issues.

Even if the ELI pillar in the Czech Republic will provide several beamlines at different laser energy/power and repetition rates, we will take into account two general cases: experiments with the highest energy/power laser beamline at 0.1 Hz and experiments at 10 Hz with the highest, but relatively low energy/power laser beamline that is compatible with this repetition rate. The former can be considered a "hazard" because of the ultra-high energy range of the associated emitted radiation, while the latter can provide higher secondary particle fluences at a comparable working time. Moreover, we classified the possible experiments that are planned at the *Particle Accelerator Target* Area into two main classes: *Electron Acceleration* and *Particle Acceleration* experiments, which will occur in different experimental rooms, as reported in the sketch of Figure 1.

Electron acceleration

In this target area only experiments where the laser beam interacts with gas targets will take place. The non-linear interactions will accelerate electron beams with different energies and charge, depending on the scheme studied.

Figure 1: Sketch of the experimental areas at the ELI beamline facility in the Czech Republic

The electron acceleration area and the proton acceleration area are in evidence. The R1/R2/R3 classification is related to the radiation protection requirements in these areas: < 7.5 μSv/h in R1, < 25 μSv/h in R2 and > 25 μSv/h in R3.
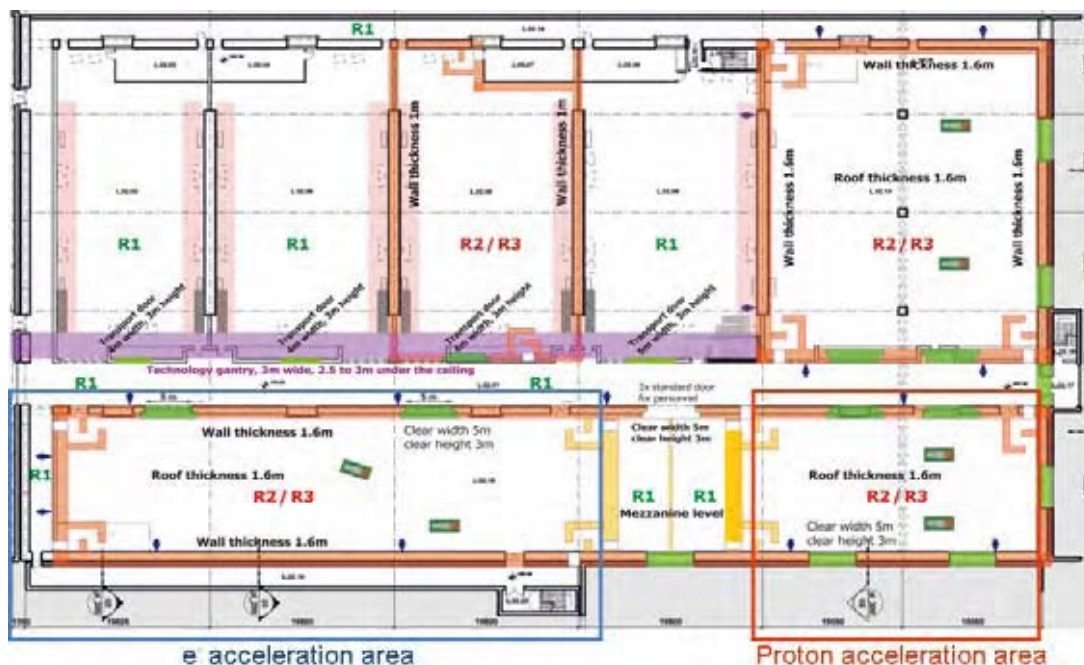
The most hazardous scheme in terms of maximum electron beam energy seems to be the blowout regime (external injection) where the 300 J, 0.1 Hz laser beamline will be focused and channelled through many Rayleigh lengths of tenuous plasma (plasma density, laser pulse length and spot size have to be chosen properly) creating a plasma wave wake on which electrons can surf and reach a very high energy. Analytical formulae [7] allowed us to estimate that the electron beam can be accelerated with a mean energy of about 50 GeV and a total charge of about 1.5 nC (nominally 41 GeV and 1.3 nC, respectively) within a distance of about 5 m. The electron beam used as input for the FLUKA simulations was supposed to have a Gaussian energy distribution with a spread of 10% and a divergence of 1°.

The second electron acceleration configuration which has been considered is the one where the 50 J, 10 Hz laser beamline will be used in the blowout regime (self-injection), in order to accelerate electrons at 5 GeV (nominally 4 GeV) with a total charge of about 1 nC within several centimeters. Also in this case the electron beam was supposed to have a Gaussian energy distribution with a spread of 10% and a divergence of 1°.

Proton acceleration

In the target area dedicated to proton/ion acceleration various experiments where different laser beamlines focused onto thin solid targets at very high intensities will be performed. In this case the main literature data, which report scaling laws and numerical simulations at similar laser irradiation conditions, have been used to define the source term [8-10].

To reduce the degree of freedom in our estimations of the maximum proton energy and the total proton current, which depend on many parameters (laser intensity, pulse duration, target thickness, target material and so on), we set some experimental configurations. Thus we considered numerical simulations with "ideal" 1 μm thick hydrogen targets [9,10] or scaling laws based on experimental results where proton beams were accelerated from hydrogen impurities on the target surface [8].

The highest energy ionising radiation is again generated at the 300 J, 0.1 Hz laser beamline which in principle could reach a maximum intensity on the target surface of about 5×10^{23} W/cm² if a future upgrading of the system at 50 PW (five beamlines at 300 J, 10 PW) is assumed. For this source term we

considered a proton beam with a mean energy of 3 GeV and a total yield of 6×10^{11}/pulse (conversion efficiency of about 20%), in agreement with literature data [9]. For simplicity the proton beam is supposed to have a rectangular energy distribution with a spread of 10% and a divergence of 40°.

The source term at 50 J, 10 Hz (2.5 PW, 10^{22} W/cm²) laser beamline was estimated to be able to generate proton beams with the following specifications: 200 MeV, 10^{12}/pulse, 50% efficiency, 5% energy spread, 4° divergence. Those estimations are in agreement with literature data in the hypothesis of a very thin target (few hundreds of nm) and circularly polarised laser pulses, the so-called *radiation pressure acceleration* regime [10].

Moreover, another ionising radiation source, intrinsically associated with the proton one, has to be considered: a part of the electrons in the target material are accelerated at high energies, as confirmed by particle-in-cell simulations. Specifications of associated electron beams for the two cases considered are: 1.5 GeV, 2×10^{11}/pulse, 40° divergence (3% efficiency) at 50 PW, 0.1 Hz, and 100 MeV, 2×10^{11}/pulse, 40° divergence (8% efficiency) at 2.5 PW, 10 Hz laser beamline.

Table 1: Main properties of the source term in the electron beam case

Laser properties				Accel. regime	Electron beam properties					
					Nominal		Used in FLUKA simulations			
Energy (J)	Width (fs)	R. rate (Hz)	Pow. (PW)		e-Energy (GeV)	Charge (nC)	Sim. e-Energy (GeV)	Sim. charge (nC)	ΔE/E (FWHM)	Beam divergence
300	280	0.1	~1	Blowout ext. inj.	41	1.3	50	1.5	10%	1°
50	80	10	~0.6	Blowout self inj.	3.7	1	5	1	10%	1°

Table 2: Main properties of the source term in the proton beam case

Laser properties					Proton beam properties				
					Nominal	Assumptions for FLUKA simulations			
Energy (J)	Width (fs)	R. rate (Hz)	Power (PW)	Intensity (W/cm²)	Energy cut-off (GeV)	Simulated energy, rectangular (GeV)	Sim. p/pulse	ΔE/E (GeV)	Beam divergence
1 500 (5 × 300)	30	0.1	~ 50	$5 \cdot 10^{23}$	3.7	3	$6 \cdot 10^{11}$	0.3	40°
50	20	10	~ 2.5	$10^{21} \div 10^{22}$	$0.2 \div 0.3$	0.2	10^{12}	0.01	4°

Shielding optimisation in the electron case

To have a realistic description of the irradiation in the electron case, the source has been considered inside a typical chamber, to take into account the secondary radiation that is generated through the interaction of the accelerated electron beam with the materials around. A standard chamber model for the ASTRA-GEMINI [11] project at RAL has been considered: a rectangular chamber in aluminium, 6 cm thick, with external dimensions 150 cm × 200 cm × 185 cm. A pipe in stainless steel (composition of the AISI-316L has been assumed), 2 cm thick, comes out from the chamber for a length of 2 m, and is closed at the end by 1 cm of stainless steel.

As a first step we have studied the longitudinal shielding by using a simple high-Z one-material dump. Four different materials have been studied: lead, stainless steel AISI-316L, iron and copper. Several meters of shielding are expected due to the fact that the most penetrating radiation is given by high-energy muons that are generated both by direct pair production and by pion and kaon decay, together with high-energy spallation neutrons and a less critical fast neutron spectrum coming from photoproduction processes on the high-Z material. Figures 2 and 3 show the ambient dose equivalent

integrated over a day of operation for the two most critical cases, in energy and in beam intensity, according with the operation times reported in Table 3. The two two-dimensional vertical projections (plane z-y) are calculated averaging along the horizontal direction, x, perpendicular to the beam direction, over a symmetric volume 20 cm deep around the beamline, and using a step of 5 cm in z and 2.5 in y (see [12] for the FLUKA graphical interface). Very similar results, in terms of shielding capability, have been obtained for the four materials used. Figure 2 shows that for the 50 GeV electron beam a high-Z dump 4 m long, associated with a final heavy concrete wall 2.5 m thick, guarantees an optimal residual radiation level of around 10 nSv/day beyond the shielding wall. Figure 3 shows, on the other hand, that the higher intensity/lower energy beamline is not at all a critical case: the high-energy muons reach the end of their range in the first 50 cm of the final shielding wall and the secondary neutron radiation is fully absorbed in the very first part of the concrete as well. We can conclude, therefore, that a good solution for the 50 GeV beamline will automatically satisfy the shielding requirement for the 5 GeV/10 Hz beamline.

Table 3: Operation times for the two most critical electron beamlines

Repetition rate (Hz)	Shots/day	Daily operation time (min/day)
0.1	100	~15
10	6 000	10

Figure 2: H*(10) rate (in μSv/day) in the case of the 50 GeV electron beam, 0.1 Hz, impinging on a mono-material dump in AISI-316L

From the left to the right are visible the electron source inside the vacuum chamber, the beam pipe that comes out from the chamber, the beam dump and the final heavy concrete wall
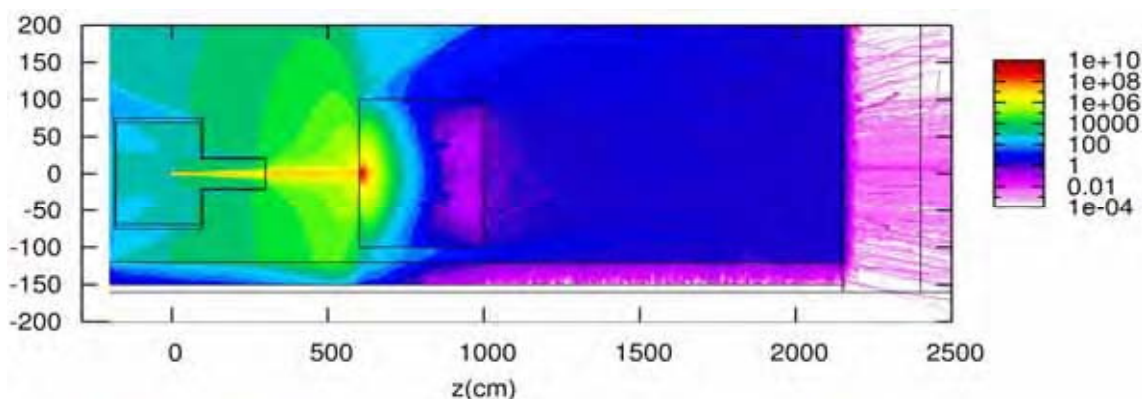
Figure 3: H*(10) rate (in μSv/day) in the case of the 5 GeV electron beam, 10 Hz, impinging on a mono-material dump in copper
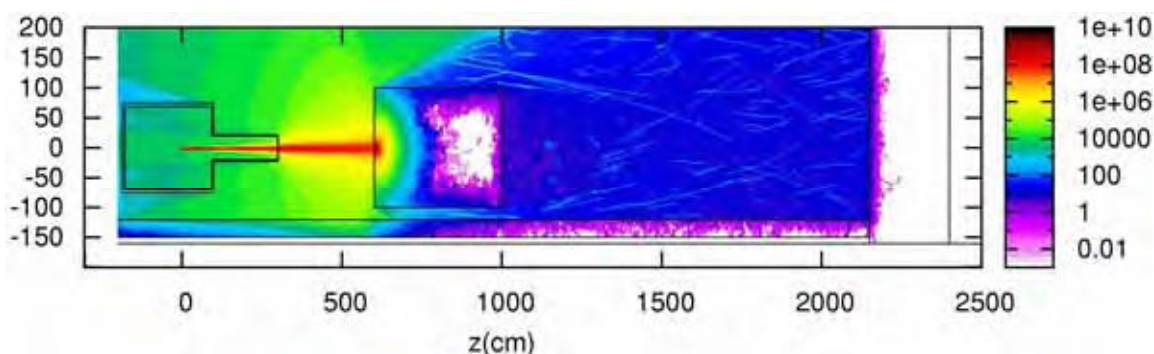
A one-material dump solution appears, however, to be less than optimal for two main reasons, both related to the neutron secondary radiation. The first reason is the huge amount of backscattered radiation due to the fact that in this case the maximum intensity of both the electromagnetic and the hadronic cascades are located in the very first part of the high-Z material dump. As a consequence, a huge amount of radiation, which is mainly due to neutrons coming from spallation processes and from evaporation of nuclei in inelastic interactions, is travelling in air in a backward direction, being potentially dangerous both for the lateral/backward containment of the radiation and as source of background in the experimental area inside the vacuum chamber. This can be observed in Figure 4, where the neutron fluence for the higher energy case is drawn (the vertical projection is the same as in the previous pictures). The second reason appears evident looking at the same picture: the longitudinal containment of neutrons, even if fully satisfactory in terms of doses beyond the final heavy concrete wall, is not total, the main reason being the fact that the secondary neutrons are not moderated with a suitable material. A solution to this problem will be the choice of a multi-material structure and will be discussed in the last section.

Figure 4: Neutron fluence rate (neutrons cm^2 s^{-1}) in the case of the 50 GeV electron beam, 0.1 Hz, with a mono-material dump in AISI-316L
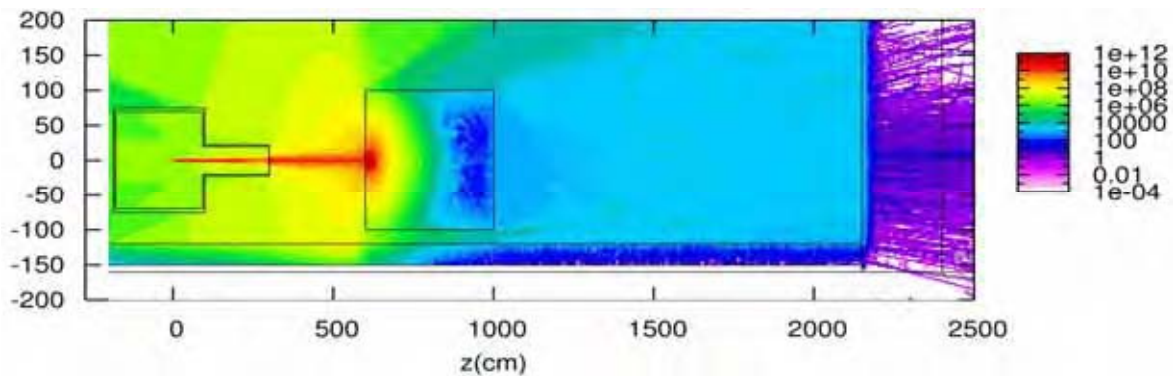
The choice of the high-Z material as main absorber

The choice of the high-Z material to be used as main absorber in the dump structure has been done via a study of the induced radioactivity. Different samples of the four candidate materials have been simulated with a simple geometry: a cylinder 50 cm long and with a radius of 20 cm. With the aim to evaluate both the short-time effects, very important for the protection of the workers, and the effect of long irradiation periods, which are mostly related with decommissioning problems, two irradiation patterns with the 50 GeV electron beam were considered: a one-day irradiation period (100 shots/day considered as continuous), followed by an analysis of the residual radiation at cooling times that go from few minutes to several hours, and a one-year irradiation period, followed by an analysis at longer cooling times. In Figure 5 the results for the residual H*(10) distribution due to the induced radioactivity 10 minutes after the end of a daily irradiation is shown for the most and the least activated samples: the copper sample, which shows a specific activity of 2 830 Bq/g, gives a dose rate at the level of 10 µSv/h at 1 m, while the sample in stainless steel, which shows the considerably lower specific activity of 134 Bq/g, gives a dose rate well below 1 µSv/h. The behaviour of the stainless steel after the one-year irradiation has been found satisfactory as well, especially in comparison with the lead: the specific activity after one day of cooling for the AISI-316L has been estimated 364 Bq/g, to be compared with the value of 3 925 Bq/g found for the lead. In Figure 6 the distribution of the specific activity for the stainless steel sample after the long-term irradiation is presented in the A-Z plane. These results have moved the choice of the absorber on the stainless steel.

The three-material dump structure

An optimal solution to the problem of the backscattered radiation which also allows for a better general shielding is given by the insertion, in the first part of the dump, of a "soft" core in a low-Z material with moderation properties. Due to the softness of the material, the electromagnetic and the

Figure 5: Residual ambient dose equivalent (μSv/h) due to the induced radioactivity in two different high-Z samples (left: copper; right: AISI-316L) irradiated by the 50 GeV electron beam for one day of operation, 10 minutes after the end of the irradiation
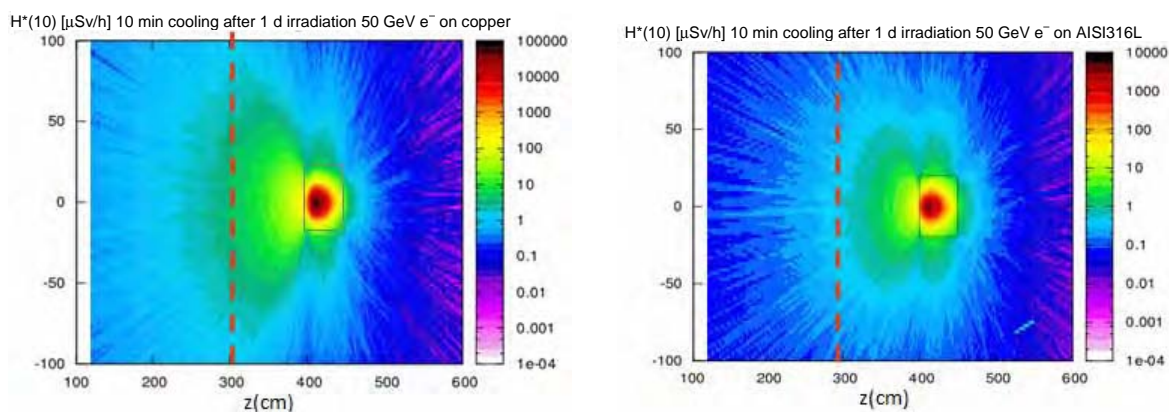
Figure 6: Distribution of the specific activity in the A-Z plane for the AISI-316L sample, after an irradiation of one year with the 50 GeV electron beam and a cooling time of 24 hours
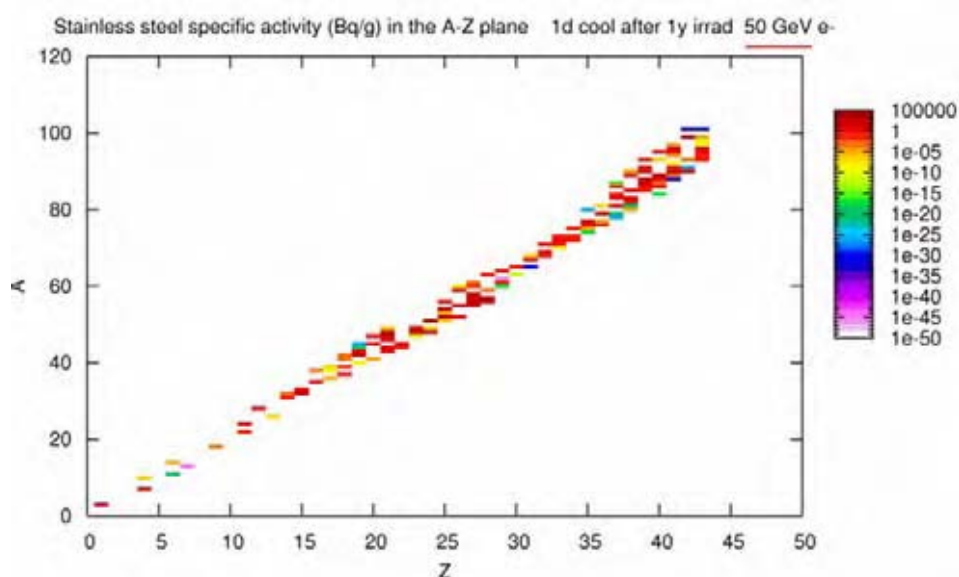
hadronic cascades develop more deeply in the dump, with the effect that the first part of the dump can properly shield against the backward radiation. If the low-Z material is a good moderator (a very effective choice is given by high-density carbon fibres, with typical densities of 1.9 g/cm³) the secondary neutrons produced will be slowed down along the moderator, increasing the shielding properties of the part of the dump in stainless steel. Finally, the addition of a first layer made of absorber material for low-energy neutrons will significantly increase the containment of the backscattered neutron radiation. Figure 7 shows an example of this three-material dump: 60 cm of borated polyethylene are followed by a cylinder, 2 m long, in high-density carbon fibres, surrounded and followed by the AISI-316L material, which acts as main absorber. An optimal longitudinal behaviour of the neutron fluence is guaranteed by 3 m of stainless steel after the carbon cylinder. In Figure 8 the behaviour of the ambient dose equivalent rate, integrated over a day of operation time, is shown: the residual prompt radiation after the final shielding wall, basically due to the survived attenuated muons, is at the very satisfactory level of 10 nSv/day, as can be observed in the longitudinal profile of Figure 9. Even imaging to increase in the future the number of shots per day by a factor 10, reaching a value of 1 000 shots/day, the radiation beyond the shielding would remain at the absolutely safe level of 100 nSv/day.

Figure 7: Neutron fluence rate (neutrons cm^{-2} s^{-1}) in the case of the 50 GeV electron beam, 0.1 Hz, with a three-material dump structure in borated polyethylene, high-density carbon fibres and AISI-316L
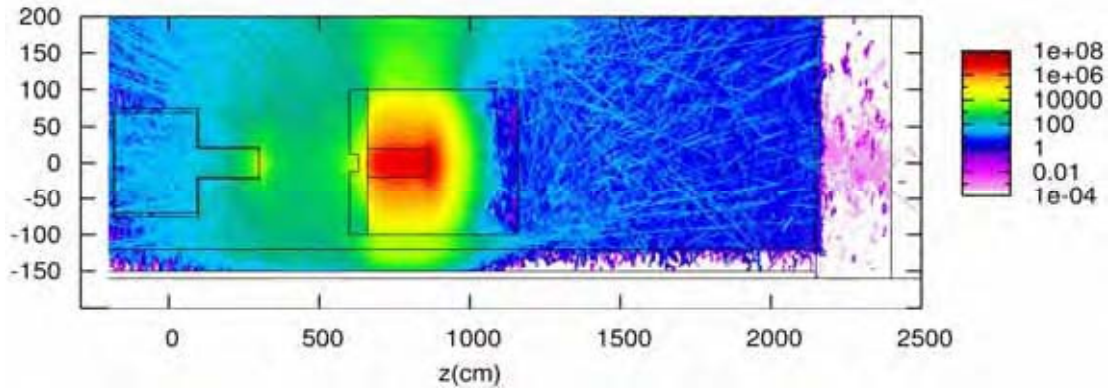
Figure 8: H*(10) rate (μSv/day) in the case of the 50 GeV electron beam, 0.1 Hz, impinging on the three-material dump structure
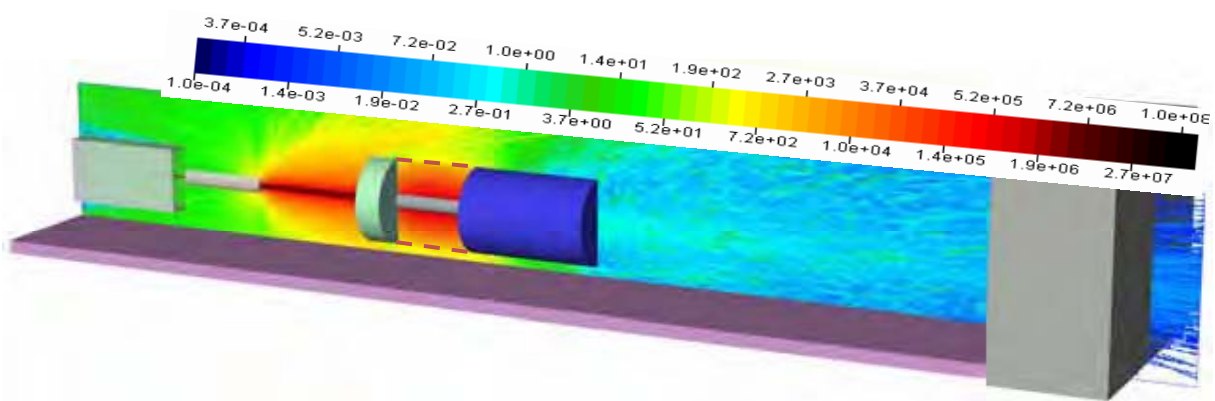
Figure 9: Longitudinal profile of the ambient dose equivalent rate shown in Figure 8, obtained by averaging the H*(10) rate in the vertical co-ordinate *y* in a small volume 20 cm large around the beamline
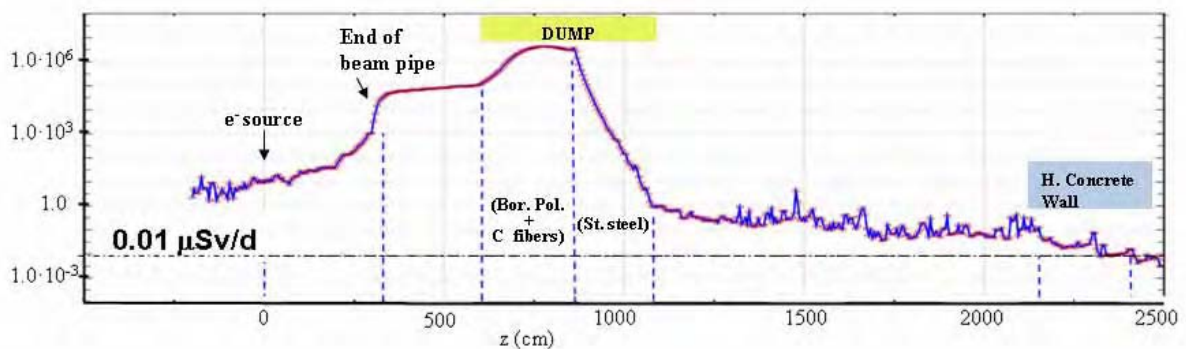
Conclusions

In this paper has been presented the first extensive study about the shielding assessment at the ELI laser-acceleration beamline facility in the Czech Republic. The source terms have been defined both for the electron and the proton case. The shielding study is at present almost complete for the electron acceleration area in the worst scenarios, in energy and in beam intensity: a key point has been the choice of a three-material dump with a structure low-Z neutron absorber/low-Z moderator/high-Z absorber and energy degrader, opportunely dimensioned to guarantee both the longitudinal and the lateral containment of the radiation.

In the future the planning of the experimental activities that are foreseen at the ELI beamline facility will trigger more detailed simulations, completing the present evaluations.

References

[1] Leemans, W.P. *et al.*, "Progress on Laser Plasma Accelerator Development Using Transversely and Longitudinally Shaped Plasmas", *C. R. Physique*, 10, 130-139 (2009).

[2] Allen, M., *et al.*, "Proton Spectra from Ultraintense Laser-plasma Interaction with Thin Foils: Experiments, Theory, and Simulation", *Physics of Plasmas*, 10, 3283 (2003).

[3] Cowan, T., *et al.*, "Theoretical Understanding of Record Proton Energies from Laser Acceleration with Cone Targets and Future Prospects", *Proceeding of the 2010 Advanced Accelerator Concepts Workshop*, Annapolis, MD, USA, 13-19 June 2010.

[4] *www.eli-beams.eu*.

[5] Battistoni, G., *et al.*, "The FLUKA Code: Description and Benchmarking", *Proceedings of the Hadronic Shower Simulation Workshop 2006*, Fermilab, 6-8 September 2006, M. Albrow, R. Raja (Eds.), AIP Conference Proceedings, 896, 31-49 (2007).

[6] Fassò, A., *et al.*, *FLUKA: A Multi-particle Transport Code*, CERN-2005-10 (2005), INFN/TC_05/11, SLAC-R-773.

[7] Lu, W., *et al.*, "Generating Multi-GeV Electron Bunches Using Single Stage Laser Wakefield Acceleration in a 3D Nonlinear Regime", *Phys. Rev. ST Accel. and Beams*, 10, 061301 (2007).

[8] Fuchs, J., *et al.*, "Laser Acceleration of Low Emittance, High Energy Ions and Applications", *C. R. Physique*, 10, 176 (2009).

[9] Davis, J., G.M. Petrov, "Generation of GeV Ion Bunches from High-intensity Laser-target Interactions", *Physics of Plasmas*, 16, 023105 (2009).

[10] Qiao, B., *et al.*, "Stable GeV Ion-beam Acceleration from Thin Foils by Circularly Polarized Laser Pulses", *Phys. Rev. Lett.*, 102, 145002 (2009).

[11] Hooker, C.J., *et al.*, "The Astra Gemini Project – A Dual-beam Petawatt Ti:Sapphire Laser System", *J. Phys. IV France*, 133, 673-677 (2006).

[12] Vlachoudis, V., "FLAIR: A Powerful but User Friendly Graphical Interface for FLUKA", *Proceedings of the International Conference on Mathematics, Computational Methods & Reactor Physics (M&C 2009)*, Saratoga Springs, New York (2009).

Shielding aspects of the new nELBE photo-neutron source

A. Ferrari[1,2]**, R. Beyer , E. Birgersson , J. Claussner , E. Grosse**[2,3]**,**
R. Hannaske , A. Junghans , T. Kögler , I. Kösterke , R. Massarczyk , A. Matič ,
K-D. Schilling , G. Schramm , R. Schwengner , A. Wagner , F.P. Weiss
[1]Institut für Sichereitsforschung, Forschungszentrum Dresden-Rossendorf, Dresden, Germany
[2]Institut für Strahlenphysik, Forschungszentrum Dresden-Rossendorf, Dresden, Germany
[3]Institut für Kern- und Teilchenphysik, Technische Universität Dresden, Dresden, Germany

Abstract

The nELBE beamline at Forschungszentrum Dresden-Rossendorf (FZD) provides intense neutron beams by stopping a primary electron beam in a liquid lead radiator and then producing neutrons by bremsstrahlung photons through (γ,n) reactions. To increase the neutron yield through the electron energy enhancement (from the current 40 MeV limit up to 50 MeV), to optimise the neutron/photon ratio and to minimise several sources of background at the present time, a new neutron beamline with a new, larger experimental room has been designed. Extensive simulations with the particle interaction and transport code FLUKA have been performed to assess all the shielding aspects of the design. Starting from the primary electron beam, both the photon and neutron secondary radiation fields have been fully characterised. To have a cross-check of the results, the calculated values of the neutron yields at different energies of the primary beam have been compared with an independent simulation with the MCNP code, obtaining a very satisfactory agreement at the level of few per cent. The photo-production area has been studied in a mixed field condition, while, for statistical reasons, the penetration of the beam through the collimator and then in the neutron experimental room has been studied by writing a separate source term for the photon and the neutron radiation component. The results for the nELBE shielding, together with some aspects of the optimisation of the photo-neutron beamline, are here presented and discussed.

Introduction

At the radiation source ELBE (Electron Linear Accelerator with High Brilliance and Low Emittance) at FZD [1] a superconducting linac produces high brilliance electron beams that can be delivered with energies up to 40 MeV, intensities up to 1 mA and within a pulse width of less than 10 ps. With these parameters the electron beam is used also to provide high-intensity neutron beams, by stopping the electrons in a liquid lead target, which is 1.22 cm long (two radiation lengths) and enclosed by a thin (0.05 cm) molybdenum channel: on such radiator bremsstrahlung photons produce neutrons through (γ,n) reactions. Behind the radiator, a dump in aluminium surrounded with a lead shield acts as absorber of the electron beam and of a large fraction of the bremsstrahlung produced on the lead target. A view of the photo-neutron source close to the target is shown in Figure 2. Since the photo-produced neutrons have an isotropic spatial distribution, a high suppression of the electrons and photons is obtained by selecting neutrons far from the forward peak of the bremsstrahlung: the neutron beam is then actually defined at 95.5° with respect to the electron beamline, through a collimator with a borated polyethylene/lead structure inserted in a concrete wall, 2.4 m deep. After the collimator the neutron beamline enters the experimental room, where after several meters available for time-of-flight measurements is stopped by a final dump, which is positioned close to the final wall and is made in borated polyethylene, enveloped by a thin layer of cadmium and lead. A sketch of the present neutron beamline in the ELBE accelerator complex is visible in Figure 1, and detailed references can be found in Refs. [2,3].

The primary physics objective of the nELBE neutron beamline is to measure fast neutron cross-sections relevant for the nuclear transmutation of long-lived radioactive nuclides and of interest for Gen. IV reactors. The measurement programme is based on the NEA high-priority list of target accuracies for fast reactors (see Table 32 in [4]). The list includes requests for neutron cross-sections between about 25 keV and 20 MeV, which is the relevant energy range at nELBE.

Figure 1: Sketch of the ELBE accelerator complex

The present neutron hall with the photo-neutron source and the collimator
channel toward the neutron TOF experimental room are visible on the right

1: Diagnostic station, IR-imaging and biological IR experiment
2: Femtosecond laser, THz-spectroscopy, IR pump-probe experiment
3: Time-resolved semiconductor spectroscopy, THz-spectroscopy
4: FTIR, biological IR experiment
5: Near-field and pump-probe IR experiment
6: Radiochemistry and sum frequency generation experiment, photothermal deflection spectroscopy

Figure 2: A detailed view of the target area

The radiator channel containing the liquid lead, the steel shell confining a
vacuum volume close to the target and the aluminium-lead dump are visible
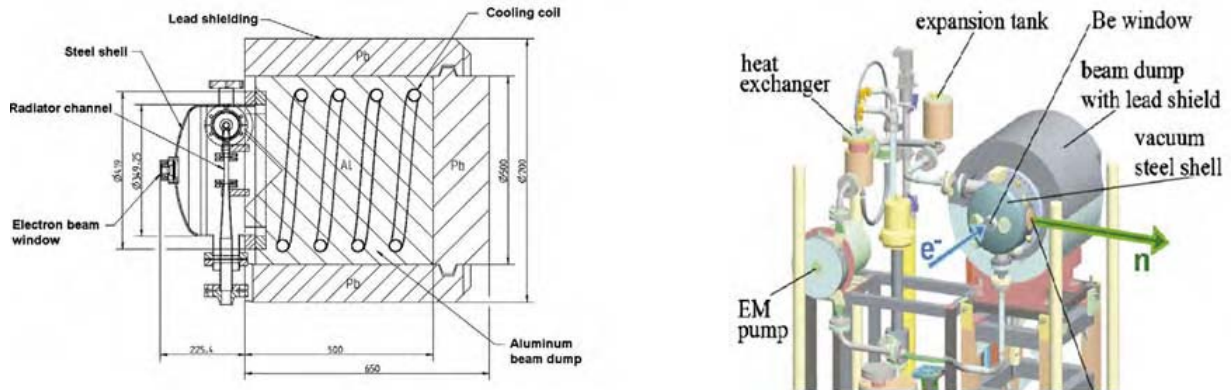
The new nELBE photo-neutron beamline

A new neutron experimental room dedicated to the measurements of fast neutron cross-sections for transmutation studies will be built at FZD in the next years, as a part of the expansion project of the ELBE facility. The goal is the creation of a national centre for high-power radiation sources, the X-ray source using laser-Compton backscattering and the high-power petawatt laser for ion acceleration being the other two key research areas.

A sketch of the new neutron beamline is shown in Figure 3. The electron beam will have an enhanced energy up to 50 MeV and will hit the photo-neutron source travelling along a line at 1.8 m from the floor (40 cm higher with respect to the normal electron line). After 1 m flight the selected neutron beam will enter the collimator inserted in a heavy concrete wall (52% Fe, density 3.6 g/cm³), which will be 2.5 m long. The beam will then enter the experimental room, which will be considerably larger than the actual one and therefore less affected from the background due to the neutron scattering in the room. Moreover, a longer length (the room is about 9.5 m long) will be available for TOF measurements. The walls of the experimental room, as well as the roof, will be in normal concrete (density 2.6 g/cm³) while all the walls around the photo-neutron source will be in heavy concrete and 2.5 m long, as the one containing the collimator.

Figure 3: Sketch of the new neutron beamline

(a) The newly designed electron line toward the liquid lead target is visible, together with the new
experimental room; (b) a lateral view. The dose limits required out of the shielding are reported.
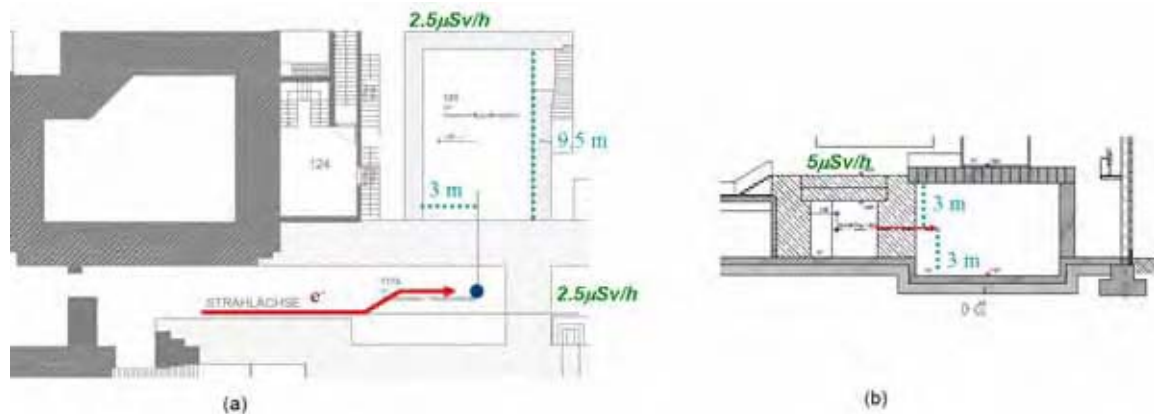
In order to satisfy all the radiation protection requirements (the dose limits for the different areas of interest are reported in Figure 3), a complete simulation of the photo-neutron beamline has been performed with the FLUKA Monte Carlo code, version 2008.3c [5,6]. Starting from the photo-production process, we included an accurate description of the photo-neutron source, the shielding walls (lateral walls, floor and roof), the collimator, the experimental room and the final dump at the end of the beamline. For the electron beam the most critical operation conditions (1 mA current, 50 MeV energy) have been assumed.

Radiation field characterisation

As a first step, the radiation fields due to the neutron and photon components coming from the liquid lead radiator have been fully characterised. Figure 4 shows the neutron and photon spectra that are calculated by integrating over all the solid angle the particle current exiting from the radiator. They are obtained by considering only the photoproduction target, at this level without the dump simulation: their integral gives, therefore, the total neutron and photon yield of the source. We have obtained n_{yield}(tot) = 5.67 10^{-3} n/e$^-$, γ_{yield}(tot) = 6.68 γ/e$^-$. At the entrance of the collimator (*i.e.* at 1 m from the source) we estimate n_{yield} = 4.34 10^{-8} n per cm^2 per primary e$^-$.

Figure 4: Neutron and photon spectra from the liquid lead radiator, integrated over the whole solid angle. An ideal source is considered here, without the beam dump beyond the target.
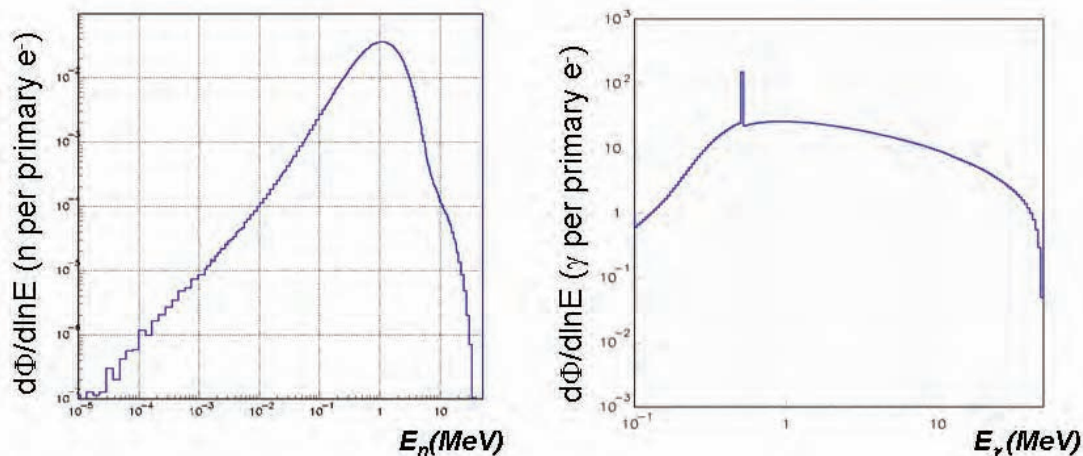
Strength of the improved source and FLUKA/MCNP comparison

Since the treatment of the photo-production is quite a delicate issue, and with the aim to cross-check the results, a comparison with the nELBE published results [2] obtained with the MCNP code has been done, at energies ranging between 20 and 40 MeV. Table 1 shows the comparison, which exhibits a very satisfactory agreement at the level of few per cent. The data obtained with the FLUKA code have a statistical accuracy ≤ 1%.

Table 1: FLUKA/MCNP comparison of the source strength at different energies of the primary electrons

Electron energy (MeV)	Neutron yield (n/e$^-$)	Neutron source strength at the radiator (n/s)	
	FLUKA	**MCNP [2]**	**FLUKA**
20	1.205 10^{-3}	7.9 10^{12}	7.52 10^{12}
30	3.108 10^{-3}	1.9 10^{13}	1.94 10^{13}
40	4.51 10^{-3}	2.7 10^{13}	2.81 10^{13}
50	5.67 10^{-3}		3.54 10^{13}

Cross-check with the Swanson semi-empirical formula

An additional cross-check can be done through the Swanson work [7]. In this paper neutron yields of semi-infinite slabs of different materials were calculated by folding the photo-neutron cross-sections available at that time with a numerical integration of the photon track length distributions derived from the analytical theory of the showers. The semi-empirical formula:

$$n_{yield} = 9.3 \cdot 10^{10} \, Z^{(0.73 \pm 0.05)} \, neutrons \, s^{-1} \, kW^{-1}$$

expresses the neutron yield as a function of the atomic number of the target material and the incident beam power, and is valid at high energy and for semi-infinite targets. For the asymptote of the lead curve we find: $2.32 \cdot 10^{12}$ n s^{-1} kW^{-1}. By using the Swanson curves that can be found in [7] to correct the energy effect, and a dedicated simulation to find the correction factor for the finite dimensions of the slab (two radiation lengths in our case), we estimate a neutron yield: $1.92 \, 10^{13}$ n s^{-1} at 30 MeV and with 1 mA, in a very good agreement both with MCNP and FLUKA.

Shielding calculations

The dose rates in the photo-neutron source hall have been studied starting from the photo-production process, to have in each point the mixed field given by the neutron isotropic beam and the bremsstrahlung spectrum. On the contrary, for statistical reasons, the penetration of the beam through the collimator and then its behaviour in the neutron experimental room has been studied by writing two separate source terms for the photon and the neutron radiation components.

Radiation fields are calculated in terms of particle fluences and then the ambient dose equivalent H*(10) is evaluated. A precious advantage of the FLUKA code is the possibility to evaluate, in the same simulation, the particle fluences that contribute to a mixed field and the ambient dose equivalent that is due to the sum of all the contributors, each one weighted with its proper set of conversion coefficients. For the H*(10), the proper set is based on the ICRP74 values [8] and on the Pelliccioni conversion coefficients [9].

The photo-neutron hall

In the photo-neutron hall the containment of the radiation through the lateral walls and through the roof was studied. To verify the lateral shielding, the ambient dose equivalent rate was calculated in a horizontal projection (plane z-x), averaging along the vertical direction, y, over a symmetric volume of ±50 cm around the beam level and using a step of 5 cm in z and in x. The H*(10) rate behaviour is shown in the left side of Figure 5 (where the FLUKA graphical interface FLAIR was used [10]). On the right side of Figure 5 the H*(10) rate profile, obtained by averaging the same data over a column which is parallel to the z axis and contains the "hot" beam dump section, is also shown. In the dose rate profile are well in evidence the photo-neutron source peak at the radiator position, the different dose attenuation behaviours in the aluminium and in the lead part of the dump, the path in air and then the attenuation in heavy concrete. This one is especially effective: the very satisfactory level of 1 µSv/h is reached as soon as about 150 cm inside the wall.

A special study has been dedicated to the optimisation of the roof material and thickness. The roof level over the source begins at about 180 cm from the beamline and is therefore one of the most irradiated surfaces in the neutron hall. Since the original solution in normal concrete was not able to lower the residual dose rate at the required level of 5 µSv/h at the exit of the roof, a solution in heavy concrete (160 cm) was adopted. As is visible in Figure 6, the ambient dose equivalent at the exit of the roof is at the very satisfactory level of about 1 µSv/h.

The neutron experimental room

In the neutron experimental room the behaviour of the ambient dose equivalent was studied starting from the photon and neutron source terms at the target and then adding the results. Both the longitudinal and the lateral containment of the radiation were analysed.

Figure 5: Dose containment in the heavy concrete lateral walls (left) and H*(10) rate profile from the photo-neutron source to the wall behind the beam dump (right)
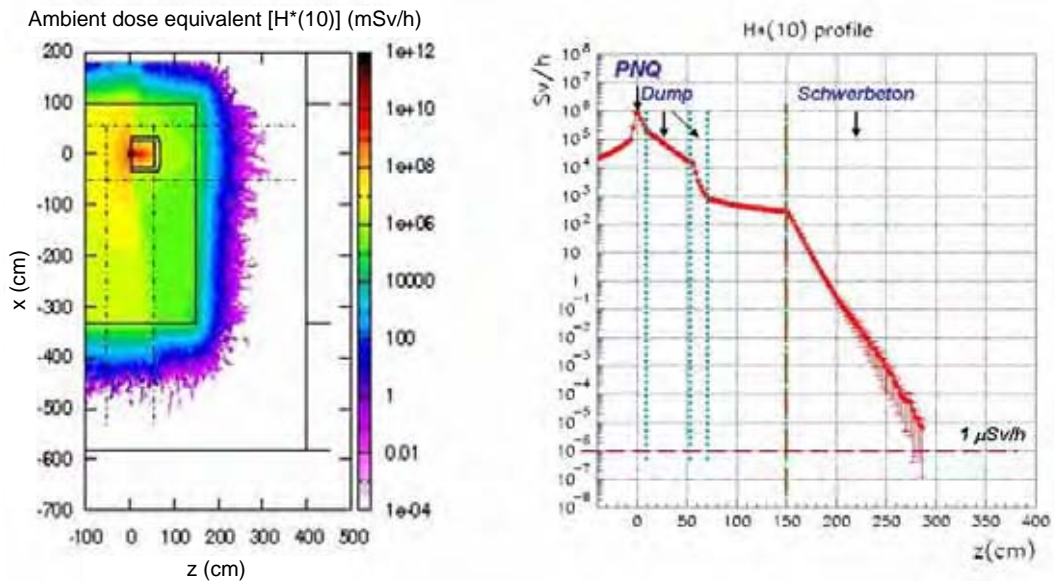
Figure 6: Ambient dose equivalent rate distribution in a vertical projection containing the source and crossing the roof in heavy concrete (left). On the right side the H*(10) rate profile calculated along a narrow column that contains the source is also shown.
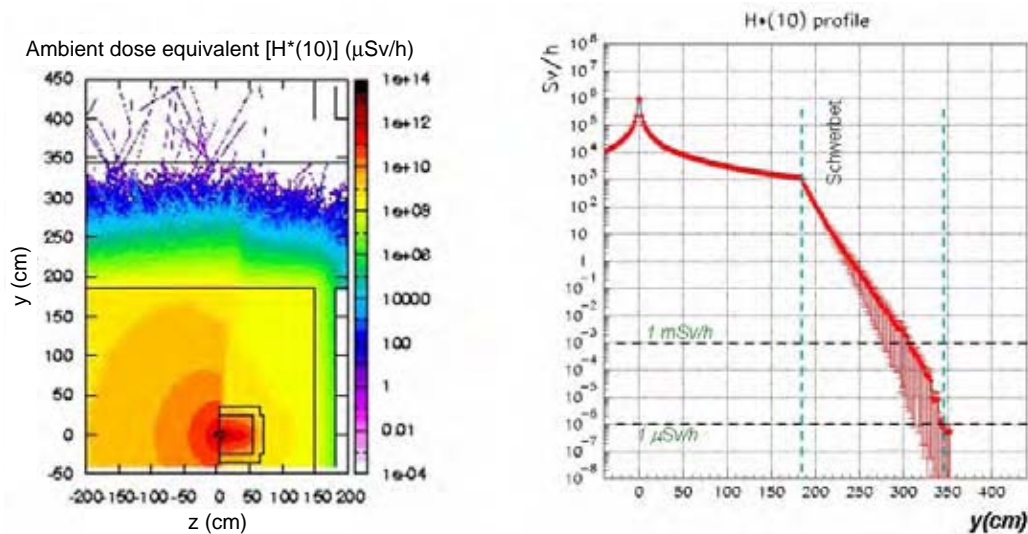
The longitudinal shielding was studied by considering photon and neutron beams that reach the final dump and then the final wall in normal concrete without interacting with any target in the experimental room. On the left side of Figure 7 the two two-dimensional projections of the H*(10) rate in a vertical plane crossing the beamline are shown for the photon and neutron source terms. The average in the horizontal direction, perpendicular to the neutron beamline, was done on a narrow volume, 20 cm thick. On the right side of the same picture the radiation profile shows that around 48 cm of borated polyethylene, 15 cm of lead and 1 m of normal concrete guarantee an ambient dose equivalent dose rate of 1 µSv/h at the exit of the wall.

Figure 7: Ambient dose equivalent rate distributions inside the experimental neutron room, due to the photon and neutron beams from the radiator (left); H*(10) rate profile obtained by averaging the same data in a volume 20 cm large and centred along the beamline (right)
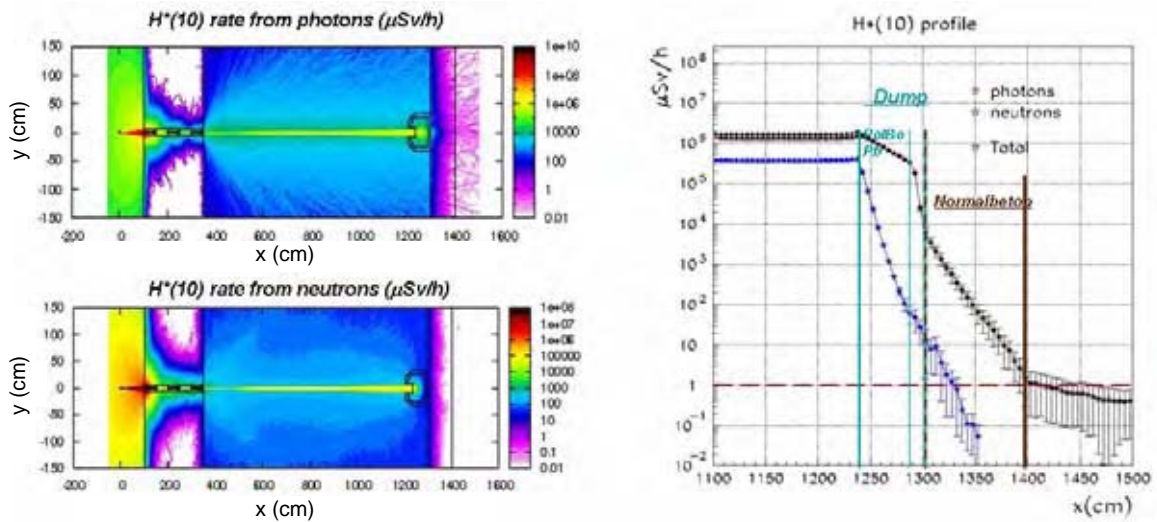
The lateral radiation containment was studied by considering the penetration of the radiation both in the lateral walls and in the roof. On the left side of Figure 8 the H*(10) rate profile through one of the lateral walls is reported, showing that both the neutron and the photon radiation fields are rapidly attenuated in the wall: the residual dose rate value of 1 µSv/h is reached after a few tens of centimetres. The results for the radiation penetration in the roof are comparable, as well as the results that were obtained by repeating the simulations with a typical target along the beamline (a simulation with a Pb target, 4 cm thick, was done). It can be concluded therefore that the shielding of the lateral walls and of the roof is not at all a critical issue in the experimental room.

Figure 8: H*(10) rate profile through a lateral wall (left), obtained by averaging the FLUKA data on a volume that crosses the horizontal plane containing the beamline and is narrow in *y* (20 cm) and several meters long in x; photon energy spectra calculated on different scoring surfaces, as illustrated in the text (right)
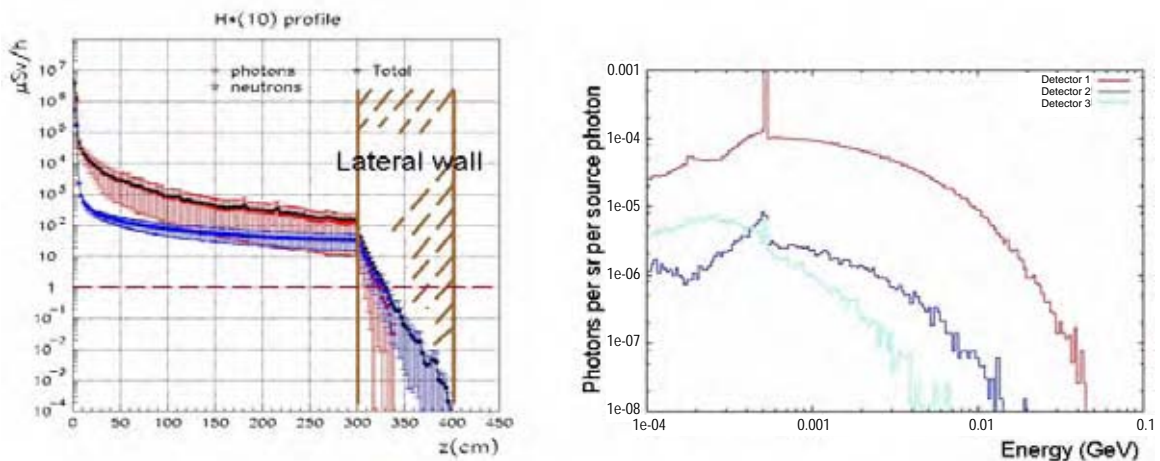
From the comparison of the profiles of Figures 7 and 8 we can observe that in the longitudinal direction the photon component of the radiation is dominant, while in the lateral profile through the shielding wall neutrons become more important in the dose contribution. This behaviour can be clarified by looking at the photon spectra of the right side of Figure 8, where the energy distributions

of photons are calculated on the external surface of the dump (red), on the final wall outside the dump (dark blue) and on the surface of the lateral walls and of the roof (light blue). The whole high-energy component of the photon spectrum hits the dump, while the photon component reaching the lateral walls and the roof presents a lower-energy spectrum that ends at 6-7 MeV, and is therefore rapidly absorbed.

From shielding to physics: The optimisation of the neutron beamline direction

A key point of the design of the new photo-neutron source is the optimisation of the neutron beamline direction: taking into account the isotropy of the neutron production and the typical shape of the bremsstrahlung, the ratio n_{yield}/γ_{yield} can be maximised. The optimised direction will be implemented in the new neutron beamline by rotating the whole photo-neutron source (the liquid lead target and the dump). With this goal a dedicated simulation was done (see Figure 9), by looking at the neutron/ photon ratio at the exit of several collimators, oriented at different angles in the range [90°, 115°]. Since only the collimator channel has been described, considering the materials around as infinite absorbers, all the analysed directions have been studied in the same simulation. Moreover, since in the real experimental arrangement we have to avoid a possible contamination coming from the neutrons that are scattered on the beam dump or photo-produced in the dump material, two simulations were done: one with the ideal case of the radiator without dump and a second one with the liquid lead target and the dump. The results are shown in Table 2: we increase the neutron/photon ratio of about 40% by moving the angle from 90° to 115°. The contamination starts to be visible only at 110° (around 1%) and at 115° is still at an acceptable level of 3%.

Figure 9: Neutron and proton fluences (part cm^{-2} per primary e$^-$) around the photo-neutron source, with the selection of different collimation lines
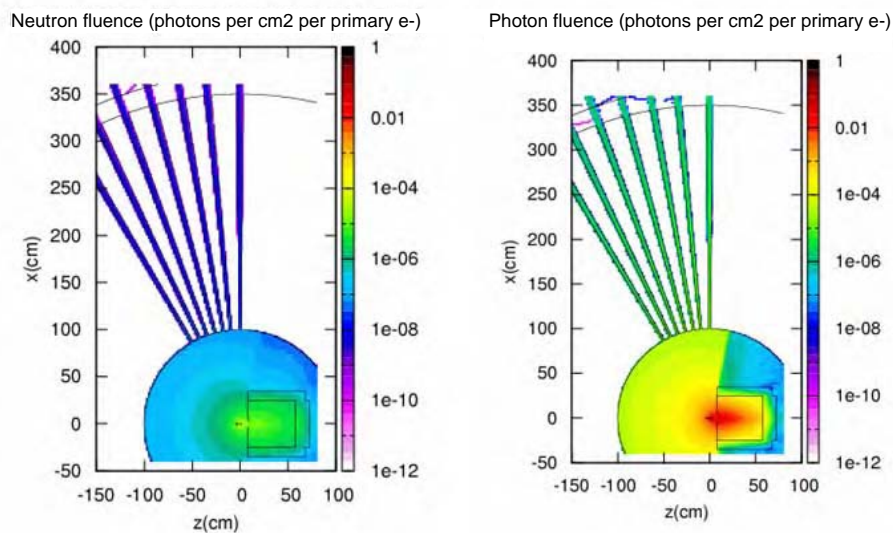
Table 2: Neutron/photon ratio at the exit of the collimator, for different choices of the collimator orientation with respect to the electron beamline

	90°	95.5°	100°	105°	110°	115°
Ideal source n_{yield}/γ_{yield}	2.20 10^{-3}	2.38 10^{-3}	2.52 10^{-3}	2.77 10^{-3}	2.88 10^{-3}	3.05 10^{-3}
Real source n_{yield}/γ_{yield}	2.17 10^{-3}	2.39 10^{-3}	2.53 10^{-3}	2.78 10^{-3}	2.92 10^{-3}	3.14 10^{-3}

Conclusions

In this paper the extensive study undertaken to assess the shielding problems at the new nELBE neutron beamline that will be realised at Forschungszentrum Dresden-Rossendorf in the next years has been presented. All the shielding calculations needed have been completed. The large dimensions of the experimental room, the very satisfactory shielding conditions and an optimised orientation of the neutron beamline will allow us to perform measurements less affected by background and with an enhanced neutron/photon ratio.

References

[1]   Teichert, J., *et al.*, "Results of Beam Parameter Measurement of the ELBE Electron Accelerator after Commissioning", *NIM*, A 507, 354-356 (2003).

[2]   Altstadt, E., *et al.*, "A Photo-neutron Source for Time-of-flight Measurements at the Radiation Source ELBE", *Ann. of Nucl. En.*, 34, 36-50 (2007).

[3]   Klug, J., *et al.*, "Development of a Neutron Time-of-flight Source at the ELBE Accelerator", *NIM*, A 577, 641-653 (2007).

[4]   Nuclear Energy Agency, "Uncertainty and Target Accuracy Assessment for Innovative System Using Recent Covariance Data Evaluations", *International Evaluation Co-operation*, Vol. 26, NEA-WPEC-26, OECD/NEA, Paris (2008), *www.nea.fr/html/science/wpec/volume26/volume26.pdf*.

[5]   Battistoni, G., *et al.*, "The FLUKA Code: Description and Benchmarking", *Proceedings of the Hadronic Shower Simulation Workshop 2006*, Fermilab, 6-8 September 2006, M. Albrow, R. Raja (Eds.), AIP Conference Proceedings, 896, 31-49 (2007).

[6]   Fassò, A., *et al.*, *FLUKA: A Multi-particle Transport Code*, CERN-2005-10 (2005), INFN/TC_05/11, SLAC-R-773.

[7]   Swanson, W.P., *Calculation of Neutron Yields Released by Electrons Incident on Selected Materials*, SLAC-PUB-2042 (1978).

[8]   International Commission on Radiological Protection, *Conversion Coefficients for Use in Radiological Protection Against External Radiation*, ICRP Publication 74, Annals of ICRP, 26, 3-4 (1996).

[9]   Ferrari, A., M. Pelliccioni, "On the Conversion Coefficients from Fluence to Ambient Dose Equivalent", *Rad. Prot. Dosim.*, 51 (4), 251-255 (1994).

[10]   Vlachoudis, V., "FLAIR: A Powerful but User Friendly Graphical Interface for FLUKA", *Proceedings of the International Conference on Mathematics, Computational Methods & Reactor Physics (M&C 2009)*, Saratoga Springs, New York (2009).

Dealing with MegaWatt beams

Nikolai V. Mokhov
Fermi National Accelerator Laboratory
Batavia, Illinois, USA

Abstract

The next generation of accelerators for MegaWatt proton, electron and heavy-ion beams places unprecedented requirements on the accuracy of particle production predictions, the capability and reliability of the codes used in planning new accelerator facilities and experiments, the design of machine, target and collimation systems, detectors and radiation shielding and minimisation of their impact on environment. Recent advances in code developments are described for the critical modules related to these challenges. Examples are given for the most demanding areas: targets, collimators, beam absorbers, radiation shielding, induced radioactivity and radiation damage.

Introduction

The next generation of accelerators for MegaWatt proton, electron and heavy-ion beams moves us into a completely new domain of extreme specific energies of ~0.1 MJ/g and specific power up to 1 TW/g in beam interactions with matter. Challenges arise also from the increasing complexity of accelerators and experimental set-ups, as well as design, engineering and performance constraints. All these place unprecedented requirements on the accuracy of particle production predictions, the capability and reliability of the codes used in planning new accelerator facilities and experiments, the design of machine, target and collimation systems, detectors, radiation shielding and minimisation of their impact on environment. This has led to research activities involving new materials and technologies, and also code developments whose predictive power and reliability are absolutely crucial.

A list of high-power proton and heavy-ion accelerators include those under:

- *operation*: ISIS, PSI, J-PARC and SNS with 0.2 to 1 MW beam power and upgrade plans up to 1-3 MW;

- *construction*: CSNS, 0.1-0.2 MW;

- *design*: FAIR and FRIB with proton to uranium beams up to 0.4 MW, ESS with a few MW beams, and Project-X with proton beams up to 4 MW;

- *consideration*: subcritical accelerator-driven systems with proton beams up to 10 MW.

Another category is high-energy colliders, operating: proton/antiproton 2 MJ beams of the Tevatro and up to 350 MJ proton beams of the LHC, and planned: e^+e^- (ILC and CLIC, up to 20 MW) and $\mu^+\mu^-$ with a 4-MW proton source.

Critical areas

Components of the three critical systems of the accelerators listed are especially vulnerable to the impact of the high-power beams: target stations, beam absorbers and collimators.

Targets

The principal issues include: production and collection of maximum numbers of particles of interest; suppression of background particles in the beamline; target and beam window operational survival and lifetime (compatibility, fatigue, stress limits, erosion, remote handling and radiation damage); protection of focusing systems including provision for superconducting coil quench stability; heat loads, radiation damage and activation of components; thick shielding and spent beam handling; prompt radiation and groundwater activation. The most challenging issue is a choice of a target technology. Fundamentally, it depends on a peak power density and power dissipation in the target material as illustrated in Figure 1 generated for the FRIB project [1]. It is clear how severe this problem is for intense heavy-ion beams (up to uranium) of a small spot size impinging on a target or beam window material. As an example of this extreme, the uranium ion beam power at SIS-100 of the FAIR project [2] will be up to 0.1 TW, ion energy range 0.4 to 27 GeV/u, peak specific energy and power in a lead target 0.1 MJ/g and 1 TW/g, respectively. Rotating multi-slice carbon disks, liquid lithium or lead targets for heavy ions and open mercury jets for proton beams at neutrino factories, no-material windows are just one of several technologies considered in such projects. Radiation damage to solid targets, downstream magnets and auxiliary equipment is identified as one of the key issues in these systems along with reliability and cost of complex remote handling equipment.

Beam absorbers

Absorbers for misbehaved beams along the beamlines, abort beam dumps and those downstream of the production targets and interaction regions (at linear colliders) are another challenging systems in the MegaWatt accelerators. These should be able to withstand an impact of beams of up to full power, say, 0.2 to 20 MW, without destruction over a designed lifetime (at least a few years), fully contain the beam energy, and execute the initial shielding functions. The absorber technologies for high-intensity beams include:

- A laminated graphite core in a cooled aluminium shell. It is proven in more than 20 years of operational experience at the Tevatron, with the peak instantaneous temperature rise of ΔT ~1 000°C per pulse. The core is contained in steel shielding surrounded by concrete. A similar design is used at the LHC with the beam swept in a spiral during the abort pulse.

- A stationary beryllium, aluminium or nickel wall liquid-cooled dump. Thin two-layer walls are arranged in a V-shape, with a liquid flowing between the layers and a beam hitting the walls at a small grazing angle. It is successfully used in several high-power proton machines, but is not feasible for intense heavy-ion beams: estimated lifetime due to radiation damage is only three months for 0.4 MW uranium beam at FRIB [1].

- A water-cooled aluminium-shell rotating drum considered for the FRIB project, with a lifetime estimated at five years.

- A water-vortex beam absorber considered for an 18-MW electron beam at ILC. The beam is rastered with dipole coils to avoid water boiling. The entrance beam window and catalytic recombination are of a serious concern in this design.

Figure 1: Choice of target technology
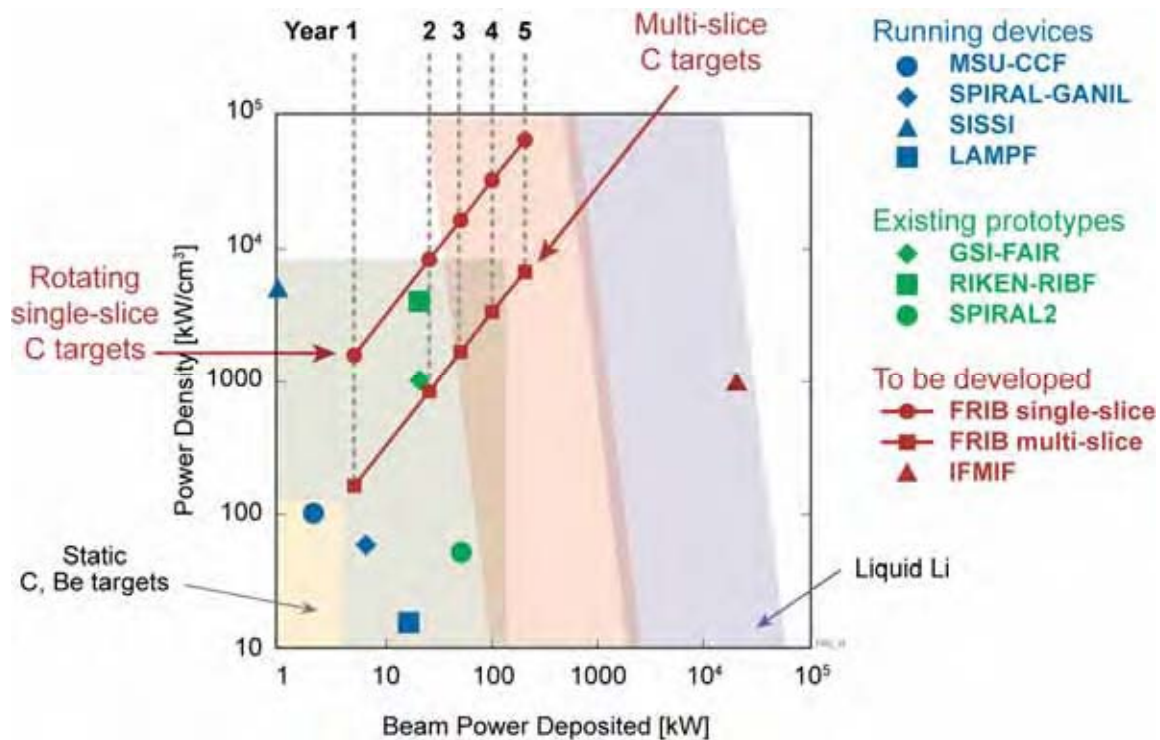
Courtesy of W. Mittig.

Collimators

Only with a very efficient beam collimation system can one reduce uncontrolled beam losses in the machine to an allowable level, thus protect personnel and components, maintain operational reliability over the life of the machine, provide acceptable hands-on maintenance conditions, and reduce the impact of radiation on environment, both at normal operation and accidental conditions. Collimators – as the last line of defence in high-power accelerators – must withstand a predefined fraction of the beam hitting their jaws and – at normal operation – survive for a time long enough to avoid very costly replacements. Design of the collimation systems is especially challenging at the high-energy colliders. At the LHC, the overall collimation efficiency should be better than 99.9% (this value is typical of the Tevatron collider). The system should manage substantial beam losses of 0.5 MW

at normal (slow) operation, 20 MW in a transient regime of ~1 ms, and up to 5 TW at a beam accident (1 MJ in 0.2 μs into 0.2 mm² area). Novel collimation techniques include crystal channelling and multiple volume reflection, hollow electron beam scraper, volume reflection radiation, rotatable/consumable collimators, and marble shells to mitigate hands-on maintenance problems.

Modelling challenges

Particle transport simulation tools and the physics models and calculations required in developing relevant codes are all driven by these demanding applications. This puts unprecedented requirements on the accuracy of particle production predictions, the capability and reliability of the codes used. The challenge is detailed and accurate (to a % level) modelling of all particle interactions with 3-D system components (up to tens of kilometres of the lattice in some cases) in energy region spanning up to 15 decades as a basis of accelerator, detector and shielding designs and their performance evaluation, for both short-term and long-term effects.

Five general-purpose, all-particle codes are capable of this – FLUKA, GEANT, MARS, MCNPX and PHITS – and they are used extensively world wide for accelerator applications. A substantial amount of effort (up to several hundreds of man-years) has been put into development of these codes over the last few decades. The user communities for the codes reach several thousands of people world wide. All five codes can handle very complex geometry, have powerful user-friendly built-in GUI interfaces with magnetic field and tally viewers, and variance reduction capabilities. Tallies include volume and surface distributions (1-D to 3-D) of particle flux, energy, reaction rate, energy deposition, residual nuclide inventory, prompt and residual dose equivalent, displacement per atom (DPA) for radiation damage, event logs, intermediate source terms, etc.

As an example, the advanced features in the MARS15 code [3] – instigated by accelerator developmental needs – include: reliable description of cross-sections and particle yields from a fraction of eV to many TeV for hadron, photon and heavy-ion projectiles (event generators); precise modelling of leading particle production and low-momentum transfer processes (elastic, diffractive and inelastic), crucial for beam-loss and collimation studies; reliable modelling of π^0-production (electromagnetic showers), K^0-production (neutrino and kaon rare decay experiments), proton-antiproton annihilation, and stopped hadrons and muons; nuclide inventory, residual dose, DPA, hydrogen and helium production; precise modelling of multiple Coulomb scattering with projectile and target form-factors included; reliable and CPU-efficient modelling of hadron, lepton and heavy-ion electromagnetic processes with knock-on electron treatment and – at high energies – bremsstrahlung, direct pair production; hadron/muon photo- and electro-production; accurate particle transport in arbitrary geometry in presence of magnetic fields with objects ranging in size from microns to kilometres; variance reduction techniques; enhanced tagging of origin of a given signal/tally – geometry, process and phase-space – invaluable for source term and sensitivity analyses; user-friendly geometry description and visual editing; interfaces to MAD, ANSYS and hydrodynamics codes.

An example of a state-of-the-art particle production module in MARS15 [3] is a Quark-Gluon String Model event generator LAQGSM [4] combined with the Fermi break-up model, the coalescence model, and the generalised evaporation-fission model. The module is used for photon, hadron and heavy-ion projectiles with energies ~1 MeV/A to 1 TeV/A. This provides a powerful fully theoretically-consistent modelling of exclusive and inclusive distributions of secondary particles, spallation, fission and fragmentation products needed for numerous applications.

Opportunities and benchmarking for high-power beam applications

All new developments in the codes are always a subject for thorough benchmarking [5], which is crucial for applications in the MegaWatt domain. Two areas relevant to the SATIF mission are of special importance here: beam impact on materials and thick shielding applications.

As stated above, the short- and long-term effects in materials impacted by high-intensity beams have the potential to be a showstopper in many instances, with a choice of target, beam window, collimator and beam absorber technologies being the most challenging. Corresponding R&D is launched in all the projects listed in the introduction. The analysis performed at the dedicated materials workshop [6] revealed that despite the difference in energy and other beam parameters, all the high-intensity beam facilities have common issues in this area: choice of the most promising

materials, the most suitable configurations of target, collimator and absorber assemblies, materials and technological limits, the critical properties of materials for a specific system, and – in many cases – a lack of reliable experimental data matching the needs of the new generation of accelerators.

The needs for measurements on materials include: mechanical properties for different doses and different strain rates; electrical and thermal properties for different radiation doses; damage thresholds and extent; radiation resistance; desorption and vacuum properties versus temperature. The following measurements are needed for the mock-up assemblies: robustness against beam shock impact; cooling efficiency; pressure increase in cooling water pipes; geometrical stability (flatness, deformations, etc.); impedance, RF trapped modes and vibrations. The facilities to perform these tests are available around the world; the issue is to match their capabilities to the conditions required.

Analysis of displacements per target atom (DPA) is the most universal means to describe deterioration of material critical properties under irradiation. Predictions of the MARS15 DPA model have recently been compared to other calculations [7]. The first case is a 1-GeV proton beam of 1-cm² area on a 3-mm thick iron target. SRIM, PHITS and MCNPX results are courtesy of Susana Reyes. As one can see in Table 1, there is a quite substantial difference between the predictions, with SRIM giving a very small value and the MARS15 result being a factor of 2.6 to 2.9 above those by PHITS and MCNPX. Calculated with MARS15 contributions to DPA of physics processes are as follows: 75.5% nuclear inelastic, 16% nuclear elastic, 2.75% electromagnetic elastic, 5.5% low-energy neutrons and 0.25% electrons. The dominance of nuclear interactions in this case explains the above differences.

Table 1: DPA for 1-GeV protons on 3-mm iron

Code	SRIM	PHITS	MCNPX	MARS15
DPA/pot	1.18e-22	2.96e-21	3.35e-21	8.73e-21

The second case is a 0.32-GeV/u uranium beam of 9-cm² area on a 1-mm thick beryllium target. SRIM and PHITS results are again a courtesy of Susana Reyes. Table 2 shows that SRIM and MARS15 results are now very close to each other, while those calculated with PHITS are a factor of 70 lower. Calculated with MARS15 contributions to DPA of physics processes are as follows: 0.3% nuclear inelastic, 99.06% electromagnetic elastic, 0.02% low-energy neutrons and 0.62% electrons. The dominant role of Coulomb scattering in this case explains the similarity of the SRIM and MARS15 predictions.

Table 2: DPA for 0.32-GeV/u uranium on 1-mm beryllium target

Code	SRIM	PHITS	MARS15
DPA/pot	2.97e-20	5.02e-22	2.13e-20

The third case is a 0.13-GeV/u germanium beam of 0.004-cm² area on a 1.2-mm thick tungsten target. TRIM and PHITS results are courtesy of Yosuke Iwamoto. Table 3 gives calculated DPA values in the first hundred microns of the target. The difference between TRIM and MARS15 needs to be understood.

Table 3: Entrance DPA for 0.13-GeV/u germanium on 1.2-mm tungsten target

Code	TRIM	PHITS	MARS15
DPA/pot	8.04e-16	1.25e-17	1.43e-16

A majority of data on radiation damage is available for reactor neutrons. Studies with hundred MeV protons [8] have revealed that a threshold of about 0.2 DPA exists for carbon composites and graphite. MARS15 studies helped realise that the BLIP beam tests with 0.16-0.18 GeV protons can emulate the 2.3-MW LBNE neutrino target situation for a 120-GeV proton beam (Table 4). It turns out that despite a substantial difference in the beam energies in these cases, nuclear interactions and Coulomb scattering contribute about the same way (45-50% each) to the peak DPA in thick graphite targets irradiated at these two facilities. A corresponding experiment at BLIP with 0.18-GeV proton beam of 96-mA current on a set of carbon-based materials was launched earlier this year with post-irradiation tests starting in late summer 2010.

Table 4: Peak DPA in POCO graphite targets at BLIP and LBNE

Target	E_p (GeV)	Beam σ (mm)	N_p (1/yr)	DPA (1/yr)
LBNE	120	1.1	4.0e20	0.45
BLIP	0.165	4.23	1.12e22	1.5

A Japan-USA collaboration (JASMIN) conducts – since 2007 – joint studies at Fermilab facilities focusing on issues related to high-intensity accelerators [9]: measurements and code benchmarking in deep-penetration shielding conditions; studying effects of shielding composition and imperfections; thick target particle yields; nuclide production; residual activation; characterisation of radiation fields for studies of radiation effects in materials and electronics components. One of the unique components of this all-encompassing programme is measurements of material activation directly due to muon-induced photo-spallation and to hadrons produced by muon interactions in shielding that can become quite important at high beam power hadron and lepton colliders and neutrino factories.

Summary

At new generation of accelerators, extremely high peak specific energy (up to ~0.1 MJ/g) and specific power (up to ~1 TW/g) in beam interactions with matter make design of such critical systems as targets, absorbers and collimators very challenging, requiring novel approaches. This also puts unprecedented requirements on the accuracy, capability and reliability of the simulation codes used in the designs. Particle production, DPA, nuclide inventory, deep penetration, energy deposition and hydrodynamics coupling are the modules of special importance. Benchmarking in these areas is absolutely crucial. Justified emulation of extreme conditions at existing lower-energy and beam power facilities is the way to go. JASMIN (Fermilab/Japan), BLIP (BNL) and HiRadMat (CERN) activities are excellent examples. Joint efforts with material experts are needed.

Acknowledgements

References

[1]   FRIB: Facility for Rare Isotope Beams, *www.frib.msu.edu*.

[2]   FAIR: Facility for Antiproton and Ion Research, *www.gsi.de/fair/index_e.html*.

[3]   Mokhov, N.V., *The MARS Code System User's Guide*, Fermilab-FN-628 (1995); and Mokhov, N.V., S.I. Striganov, "MARS15 Overview", *Proc. of Hadronic Shower Simulation Workshop*, Fermilab, September 2006, AIP Conf. Proc., 896, pp. 50-60 (2007); *www-ap.fnal.gov/MARS*.

[4]   Mashnik, S.G., *et al.*, *CEM03.03 and LAQGSM03.03 Event Generators for the MCNP6, MCNPX and MARS15 Transport Codes*, LANL report LA-UR-08-2931 (2008); arXiv:0805.0751v1 [nucl-th] 6 May 2008.

[5]   *Proc. of Hadronic Shower Simulation Workshop*, Fermilab, September 2006, AIP Conf. Proc. 896 (2007).

[6]   Schmidt, R., *et al.*, *Summary of the CERN Workshop on Materials for Collimators and Beam Absorbers*, LHC Project Report 1164 (2008).

[7]   Mokhov, N.V., I.L. Rakhno, S.I. Striganov, *Simulation and Verification of DPA in Materials*, Fermilab-Conf-09-645-APC (2009).

[8]   Simos, N., *et al.*, "MOPC093", *Proc. of EPAC08*, Genoa, Italy, June 2008.

[9]   Nakashima, H., N.V. Mokhov, *et al.*, "JASMIN: Japanese-American Study of Muon Interactions and Neutron Detection", these proceedings.

Session II

Induced radioactivity

Chair: Stefan Roesler

Activation calculations in accelerator environments – an overview*

Franz Gallmeier
Oak Ridge National Laboratory
Oak Ridge, Tennessee, USA

Abstract

Accelerator activation analyses involve radionuclide production terms from two different branches of analyses, directly from event generators, indirectly by folding fluxes with activation cross-sections, for particle types and energy ranges where activation cross-sections exist. Advances have been made in the predictive power of event generators, and also in activation cross-section databases.

Nowadays two approaches of performing activation analyses exist, firstly, the traditional way of sampling fluxes and radionuclides in transport analyses and feeding this information into external activation codes; and secondly, plugging in activation modules into transport codes solving for the radionuclide build-up and decay online and a per-event basis. Both methodologies will be discussed. All the tools and databases require verification. Benchmarking is an instrumental process for verification. An overview of benchmarking efforts will be given and the need of further benchmark experiments discussed.

---

* The full paper being unavailable at the time of publication, only the abstract is included.

Studies for a H^0/H$^-$ dump for the CERN Linac4: Energy deposition, induced radioactivity and BLM signal

R. Versaci, A. Mereghetti, M. Silari, R. Chamizo
European Organization for Nuclear Research (CERN)
Geneva, Switzerland

Abstract

This paper presents an estimate of the energy deposition and activation for the H^0/H$^-$ dump for Linac4, the new CERN 160 MeV injector linac. Residual dose rates at different cooling times were calculated as well. The aim of the first part of this study was to compare the behaviour of three different materials (graphite, boron nitride and aluminium nitride), in order to identify the most suitable for the dump. For the second part, a dedicated study has been done in order to test whether it could be feasible to insert beam loss monitors to check the status of the beam. All calculations were performed with the Monte Carlo particle transport code FLUKA.

Introduction

Linac4 is the 160 MeV H⁻ linear accelerator presently under construction at CERN, intended to replace the existing 50 MeV Linac2 as injector for the Proton Synchrotron Booster (PSB). The beam from Linac4 will be split into four separated beams and injected into the four PSB rings through four graphite stripping foils converting H⁻ into protons. The conversion efficiency during normal operation is expected to be ~0.98 [1,2]. Unstripped and partially stripped ions must be intercepted by a beam dump. This dump also has to stop the whole beam in case of failure of the stripping procedure. Monte Carlo simulations with the FLUKA [3,4] code were performed to evaluate the energy deposition in the dump and in the surrounding components as well as the induced radioactivity, simulating only one PSB ring. The main purpose of this study was the selection of the best possible material for the dump core. Estimations of beam loss monitors (BLM) signal were performed in order to check whether they could be used to keep under control the efficiency of the stripping foil. For a more realistic simulation, each of the four PSB rings was separately simulated, so that the results could be summed up in a suitable linear combination. This paper provides a summary of the results of these studies.

Simulation set-up

Geometry

The geometry used for the simulations is shown in Figure 1. The origin of the Cartesian reference system is taken along the axis of the beam pipe on the plane of the upstream face of the dump. The *x* axis is parallel to the ground and directed toward the centre of the PSB; the *y* axis is orthogonal to the ground and directed opposite to *g* (gravity); the axis of the beam pipe has been taken as the *z* axis, having the same direction as the beam.

The dump is a parallelepiped having dimensions 8 cm × 4 cm × 20 cm (see Figure 1). It is placed inside a C-shaped magnet (magnetic length 37 cm) used in the injection bump into the PSB. The magnet (both the yoke and the coils) and the beam pipe were modelled. All the components, with the exception of the dump, are 40 cm long. The walls of the PSB are included in the geometry for ±10 m around z = 0 cm. A detailed description of the geometry used can be found in Ref. [5].

Figure 1: Left: transverse section of the dump at z = 0 (front view);
right: horizontal section of the dump at y = 0 (top view)
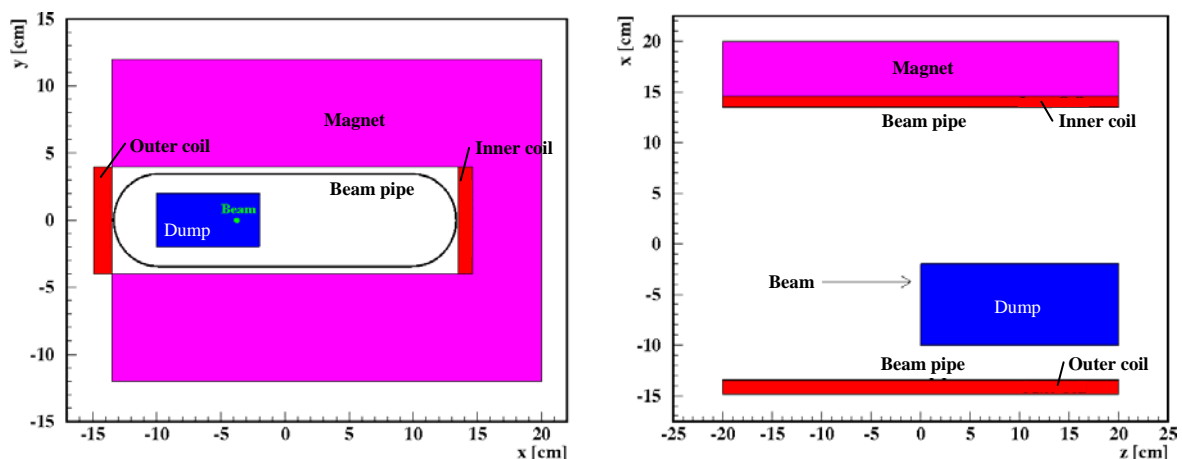
Materials

Whenever possible, a detailed description of the materials composition was used. Three sets of simulation were performed with three possible materials for the dump: graphite, boron nitride, aluminium nitride. The detailed composition of each material is given in Ref. [5].

Beam description

The Linac4 beam parameters [1,2] are summarised in Table 1. The 160 MeV H⁻ beam pulse from Linac4 contains $N_{bp} = 10^{14}$ H⁻ ions divided into four bunches, each about 100 μs long ($T_{bp} = 4 \times 100$ μs = 400 μs) and separated by 1 μs particle-free gap. The peak and average currents for a Linac4 pulse can be calculated with the equations:

$$I_{peak} = Q/\Delta t = N_{bp} \times 1.602 \cdot 10^{-19}\ C/T_{bp} = 0.04\ A$$

$$I_{average} = Q \times \nu_{bp} = N_{bp} \times 1.602 \cdot 10^{-19}\ C \times 1.11\ Hz = 18 \cdot 10^{-6}\ A$$

where ν_{bp} is the beam pulse frequency. The four bunches are injected one per each PSB ring. Each bunch crosses a graphite stripping foil that removes the two electrons from the H⁻ ion. The H⁻ to H⁺ conversion efficiency is expected to be $\varepsilon_s \approx 0.98$ and the H⁰/H⁻ ratio should be ≈10 [1,2], so that only the H⁰ beam was simulated for the energy deposition and activation studies. Both the H⁻ and H⁰ beam were instead simulated for the BLM study. The number of ions impinging on each dump per second, N_i, is (Table 1):

$$N_i = N_{bp} \cdot \nu_{bp} \cdot (1 - \varepsilon_s)/N_{dump} = 5.55 \cdot 10^{11}\ s^{-1}$$

The profile of both the H⁰ and H⁻ beams is assumed Gaussian with $\sigma_H = 0.2$ cm and $\sigma_V = 0.3$ cm. A continuous operation of 200 days was considered.

Table 1: Linac4 beam parameters

Number of particles per beam pulse	N_{bp}	10^{14}
Beam pulse frequency	ν_{bp}	1.11 Hz
Pulse length	T_{bp}	$4 \cdot 10^{-4}$ s
Peak current	I_{peak}	0.04 A
Average current	$I_{average}$	$18 \cdot 10^{-6}$ A
Stripping efficiency	ε_s	0.98
Number of dumps	N_{dump}	4
Number of particles impinging each dump per second	N_i	$5.55 \cdot 10^{11}$

Results

Energy deposition

The energy deposition was evaluated in the dump and in the two coils of the magnet using a Cartesian mesh. The size of the bin is 0.1 cm except along the *z* axis of the dump where it is 0.05 cm*.

The peak energy deposition and the peak absorbed radiation dose in the dump are shown in Figure 2. The corresponding plots for the coils can be found in Ref. [5]. Figures 3 and 4 show the energy deposition profile in the dump for each of the three materials (see Ref. [5] for further plots). The neutron fluence was also studied for a qualitative cross-check of the different components of the neutron spectrum exiting the dump and their attenuation in the surrounding magnet; two representative plots are shown in Figure 5 (see Ref. [5] for more complete information).

---

*   The FLUKA results are given in GeV cm⁻³ per primary, and were converted into J cm⁻³ per pulse and Gy year⁻¹ using the following equations:

$$E[J\ cm^{-3}\ per\ pulse] = E'[GeV\ cm^{-3}\ per\ primary] \cdot C_{GeV2J} \cdot N_{bp} \cdot (1 - \varepsilon_s)/N_{dump}$$

$$D[Gy/y] = E[J\ cm^{-3}\ per\ primary] \cdot N_{py} \cdot 10^3/\rho$$

where E′ is the energy value provided by FLUKA, $C_{GeV2J} = 1.602 \cdot 10^{-10}$ is the coefficient for the conversion from GeV to Joule, ρ is the density of the dump material in g/cm³ and N_{py} is the number of pulses per year given by the beam pulse frequency, ν_{bp} times the seconds in 200 days.

Figure 2: Peak energy deposition (left) and peak absorbed radiation dose (right) in the dump, for the three materials considered. The beam comes from the left.
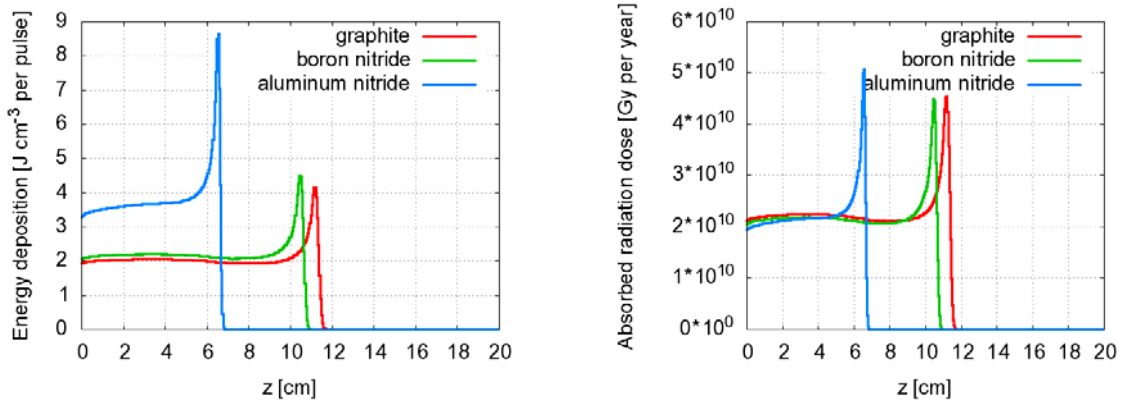
Figure 3: Profile (left: front view; right: top view) of the average energy deposition inside the graphite dump. Units are J cm⁻³ per pulse.
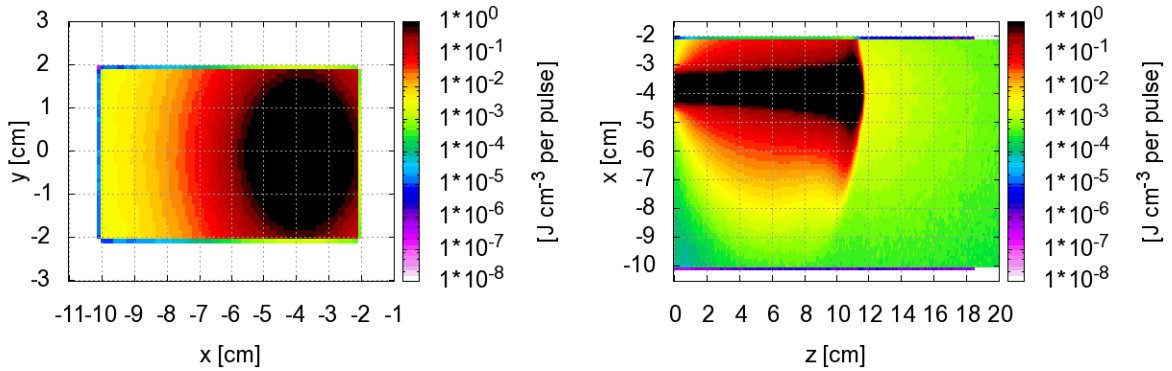
Figure 4: Profile (top view) of the average energy deposition inside the boron nitride dump (left) and the aluminium nitride dump (right). Units are J cm⁻³ per pulse.
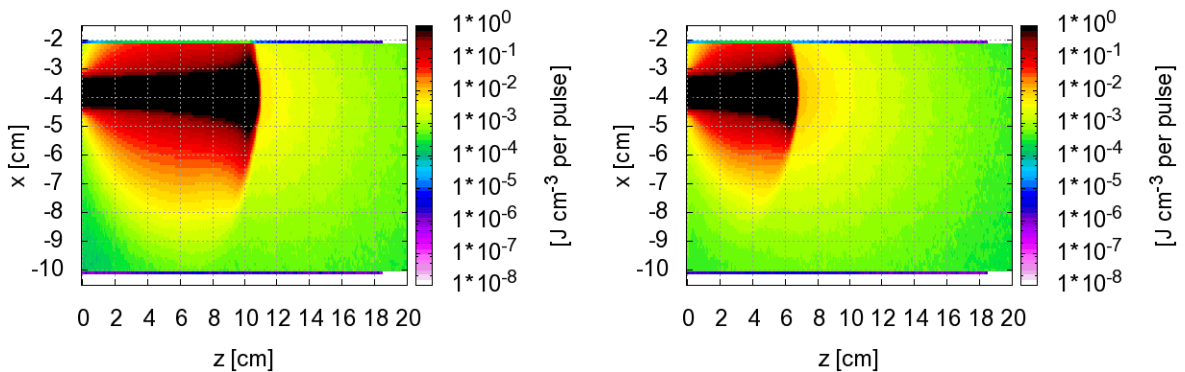
**Figure 5: Neutron fluence. Left: from dump to downstream
vacuum. Right: from dump to the dump shield region.**
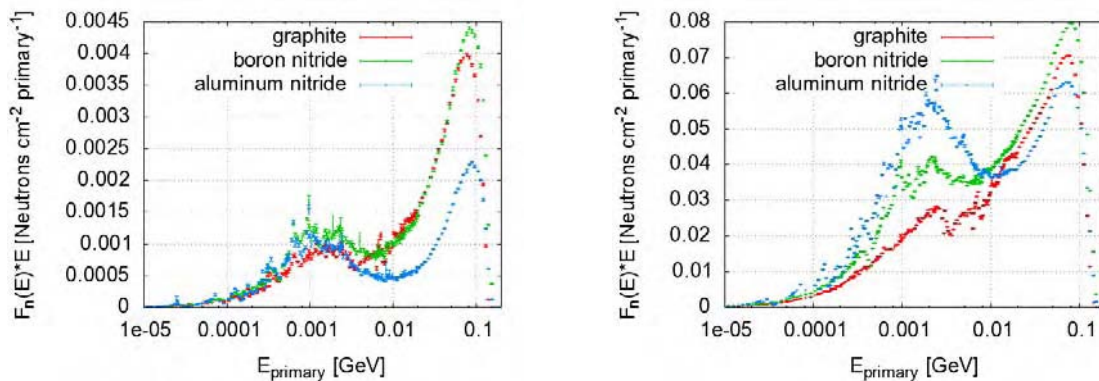
Residual dose rates

The residual dose rates were scored by means of a track length density (fluence) detector (USRBIN card) with a Cartesian binning covering the whole simulated volume. Bins of $100 \times 50 \times 200$, each of 10 cm size were used. Seven cooling times were considered: T = 0 s, 1 hour, 1 day, 1 week, 1 month, 3 months and 1 year. Tables and plots of the ambient dose equivalent values at some locations around the dump, for the seven cooling times and for each dump material were made. As an example, Figures 6 and 7 show the plots of the ambient dose equivalent rates, H*(10), around the graphite dump, for one week cooling time. A complete set of plots of residual ambient dose rates and induced radioactivity for the different materials and different cooling time can be found in Ref. [5], which also provides the plots showing the contribution from the various radionuclides in the elements of the dump. The total induced radioactivity (in Bq) in the dump (for the three materials) and in the surrounding materials at the seven cooling times is shown in Figures 8 and 9.

Feasibility of BLM usage

A dedicated set of simulations was performed to study the possibility of monitoring the ageing of the stripping foils by measuring, by means of BLM, the flux of particles emerging from the dump. Instead of inserting various BLM in the simulation, a dedicated routine to simulate the BLM response was used. This routine allows inserting a 3-D grid in the geometry, simulating the presence of a BLM centred in each cell. The estimate of the energy deposited is expected to have a maximum uncertainty of about 5 to 10%. This has been verified inserting four BLM in the geometry (these are visible in Figure 10, left), obtaining differences smaller than 1%.

**Figure 6: Average ambient dose equivalent rate H*(10) (in μS/h) around the graphite dump after
1 week (for each plot the average was performed over the whole range of the missing co-ordinate,
-10 m < x < 10 m). x-y (front) view. Left: the whole geometry; right: zoom around the dump.**
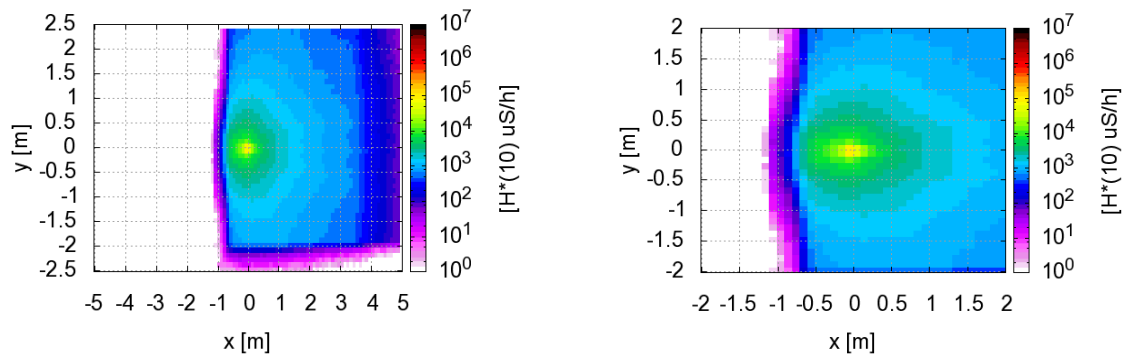
Figure 7: Average ambient dose equivalent rate H*(10) (in µS/h) around the graphite dump after 1 week (for each plot the average was performed over the whole range of the missing co-ordinate, -5 m < x < 5 m, -2.5 m < y < 2.5 m). Top: z-x (top) view, bottom: z-y (lateral) view. Left: the whole geometry; right: zoom around the dump.
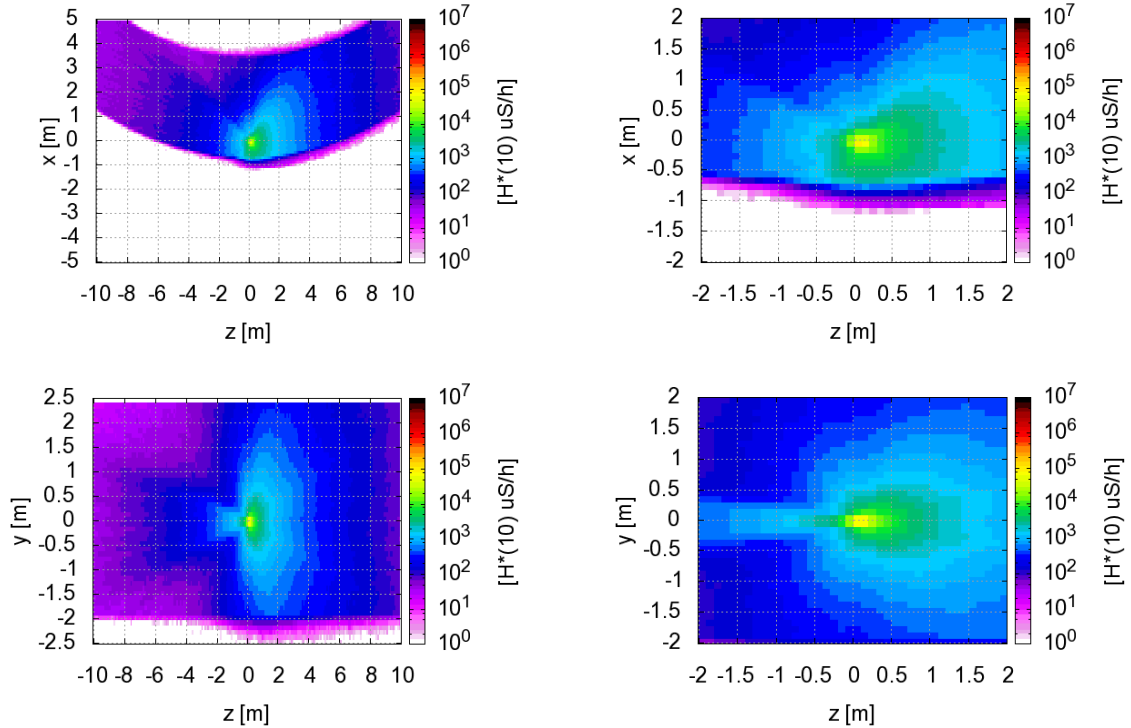
Figure 8: Total induced radioactivity (in Bq) in the dump (for graphite and boron nitride dump) and in the surrounding materials at the seven cooling times
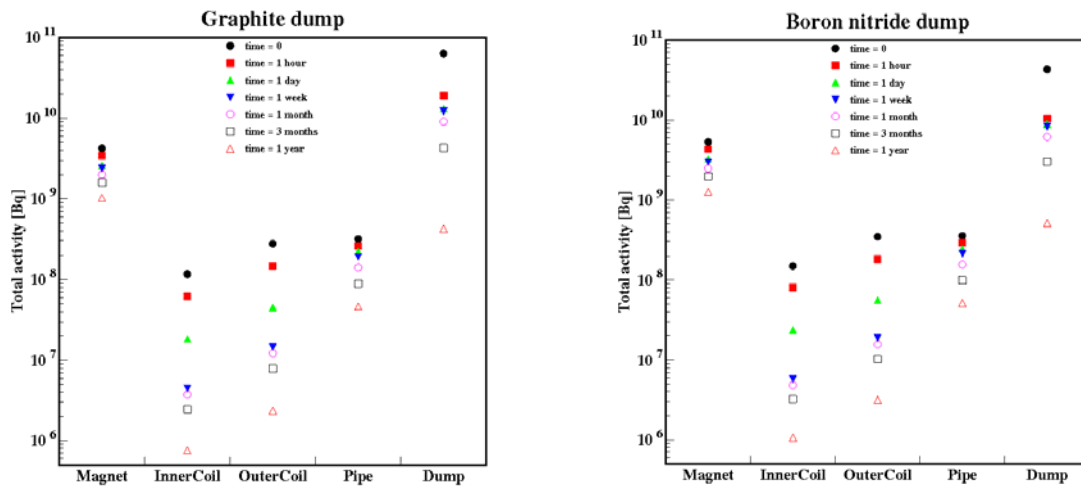
Figure 9: Total induced radioactivity (in Bq) in the dump (for aluminium nitride dump) and in the surrounding materials at the seven cooling times
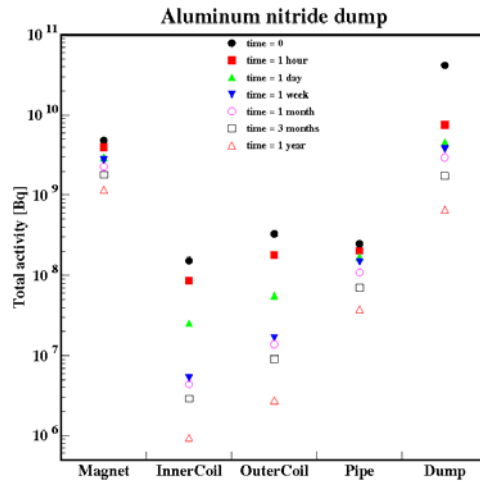
For the case of a graphite dump, eight different simulations were performed, one for each of the four rings and one for each of the two beams (H⁻ and H⁰). The outcomes of these simulations are eight 3-D matrices that can be used as a basis for the evaluation of the charge deposited in the BLM. The result of one of the BLM simulations is shown in Figure 10 as an example.

Looking at the result of the simulations, we expect to collect ~10^{-8} pC cm^{-3} per primary in a BLM placed on the sides of the dump. This value corresponds to a charge deposition within the whole BLM of the order of 10^{-6} C s^{-1}, which is three orders of magnitude below the saturation threshold for a BLM. Therefore, the possible use and position of the BLM seem feasible.

Figure 10: Plot of the charge deposited into a hypothetical BLM centred on the corresponding co-ordinates for a H⁰ beam in the third PSB ring

Left: horizontal view for y = 0 cm, right: vertical view for x = -50 cm
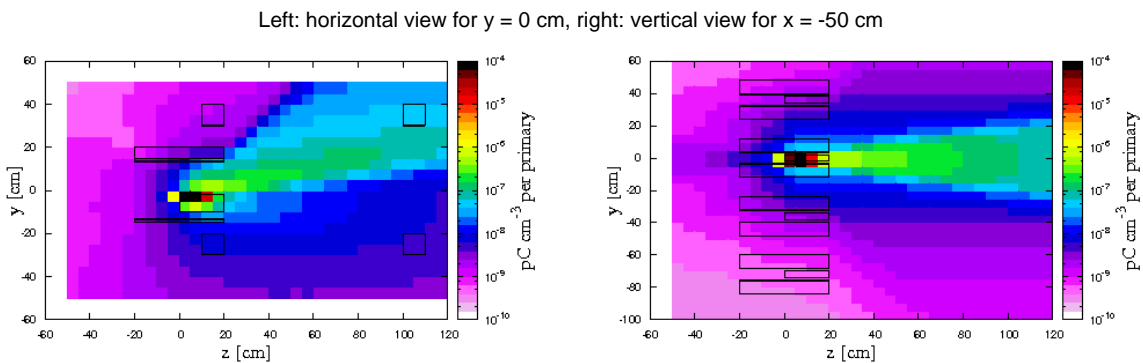
Conclusions

Comparing the results of the simulations, it is important to remember the differences in the description of the three materials used for the dump. The chemical composition of the graphite dump does not account for possible impurities, and the density used for it is lower than that of pure graphite, but similar to that of the actual graphite used for beam dumps at CERN.

The description of the boron nitride is extremely precise and based on the specifications of the supplier. The aluminium nitride dump is described without any impurity and probably overestimating its density.

For the energy deposition, the most important factor is the density of the dump. The aluminium nitride dump has a much higher stopping power and can stop the H^0 beam in about 2/3 of the longitudinal space needed by the other two dumps (Figure 2).

The graphite dump, being the one with the lowest density, shows the highest fraction of escaping energy, both vertically and horizontally (Figures 3 and 4). It could be interesting to consider the possibility of a denser shield surrounding the dump to reduce the fraction of escaping energy, especially vertically. Concerning horizontal losses, it is not possible to make the dump larger without interfering with the beam circulating in the PSB.

Nevertheless, it would be desirable to study the possibility of increasing the dump width (along x) with z, profiting from the curvature of the circulating beam. This solution could be useful regardless of the material chosen for the dump.

Comparing the results for the ambient dose equivalent rates, it is possible to see a difference between the three materials considered. While downstream (z > 0, Figure 11) there are small differences, upstream (z < 0, Figure 12) the ambient dose equivalent rates are higher in case of the aluminium nitride dump. This can be understood remembering that, first, a larger amount of neutrons is produced in aluminium, and second, because of the shorter penetration of the proton beam into the aluminium nitride dump, the induced radioactivity is generated in a smaller volume and is less self-absorbed toward the entry face of the dump than toward the downstream face. Differences between the graphite and the boron nitride dump are negligible for cooling times longer than 1 hour, and after a few days of cooling time the dose rates are of the order of 10-100 μS/h, according to the location around the dump. The dose rates are a factor of 3-4 times higher for aluminium nitride.

The neutron spectra (Figure 5) at the various locations are similar for the three materials, with the evaporation component being the largest for the aluminium nitride, the lowest for the graphite and boron nitride in between.

Figure 11: Comparison between the ambient dose equivalent rates, H*(10) in μS/h, for the three dumps. Left column: z = 50 cm, right column: z = 100 cm. The four rows, from top to bottom are for x = -50, 0, 50, 100 cm respectively. The point at T = 0 s has actually been moved to T = 1 s because of the logarithmic scale on the x axis.
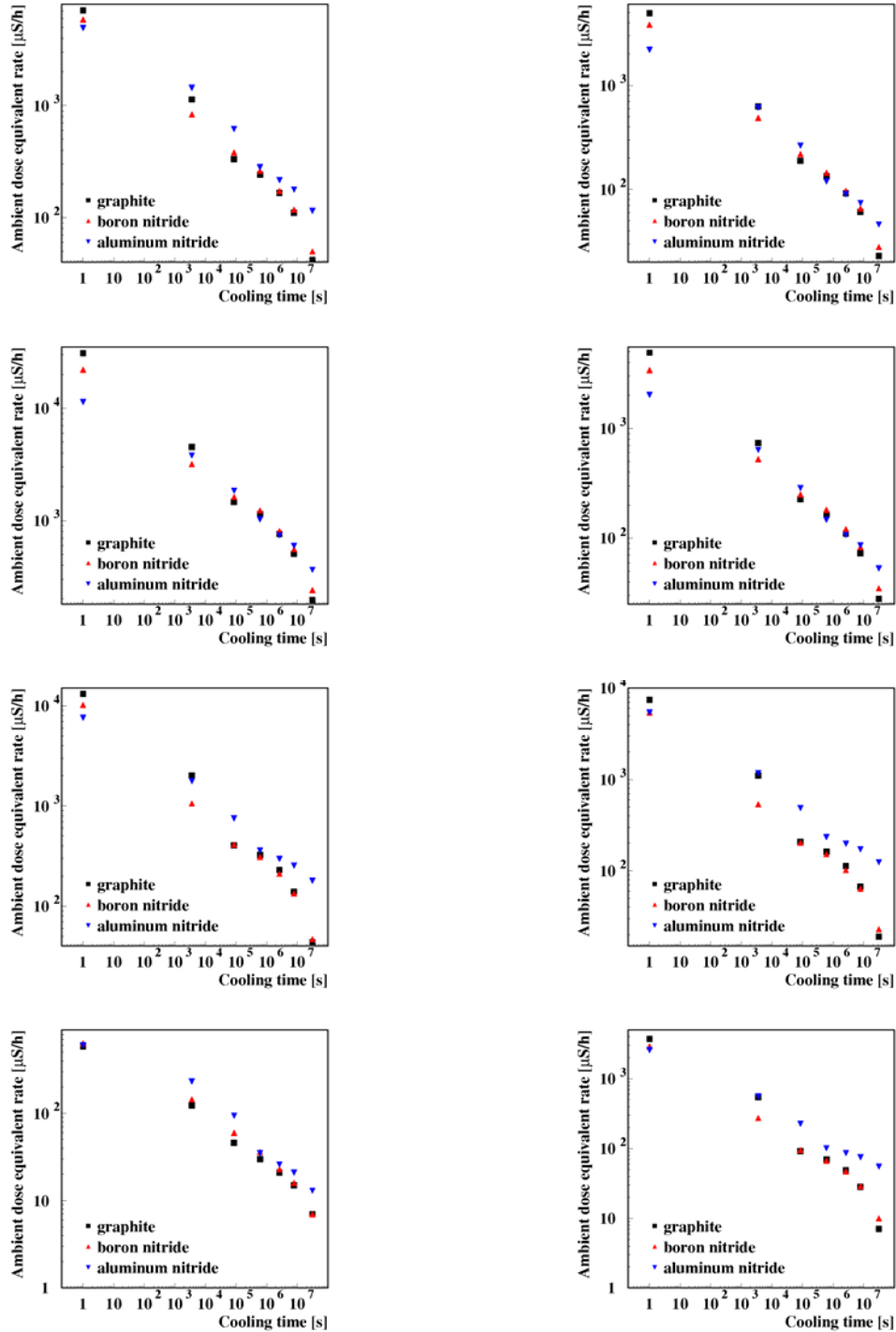
Figure 12: Comparison between the ambient dose equivalent rates, H*(10) in μS/h, for the three dumps. Left column: z = -50 cm, right column: z = 0 cm. The four rows, from top to bottom are for x = -50, 0, 50, 100 cm respectively. The point at T = 0 s has actually been moved to T = 1 s because of the logarithmic scale on the x axis.
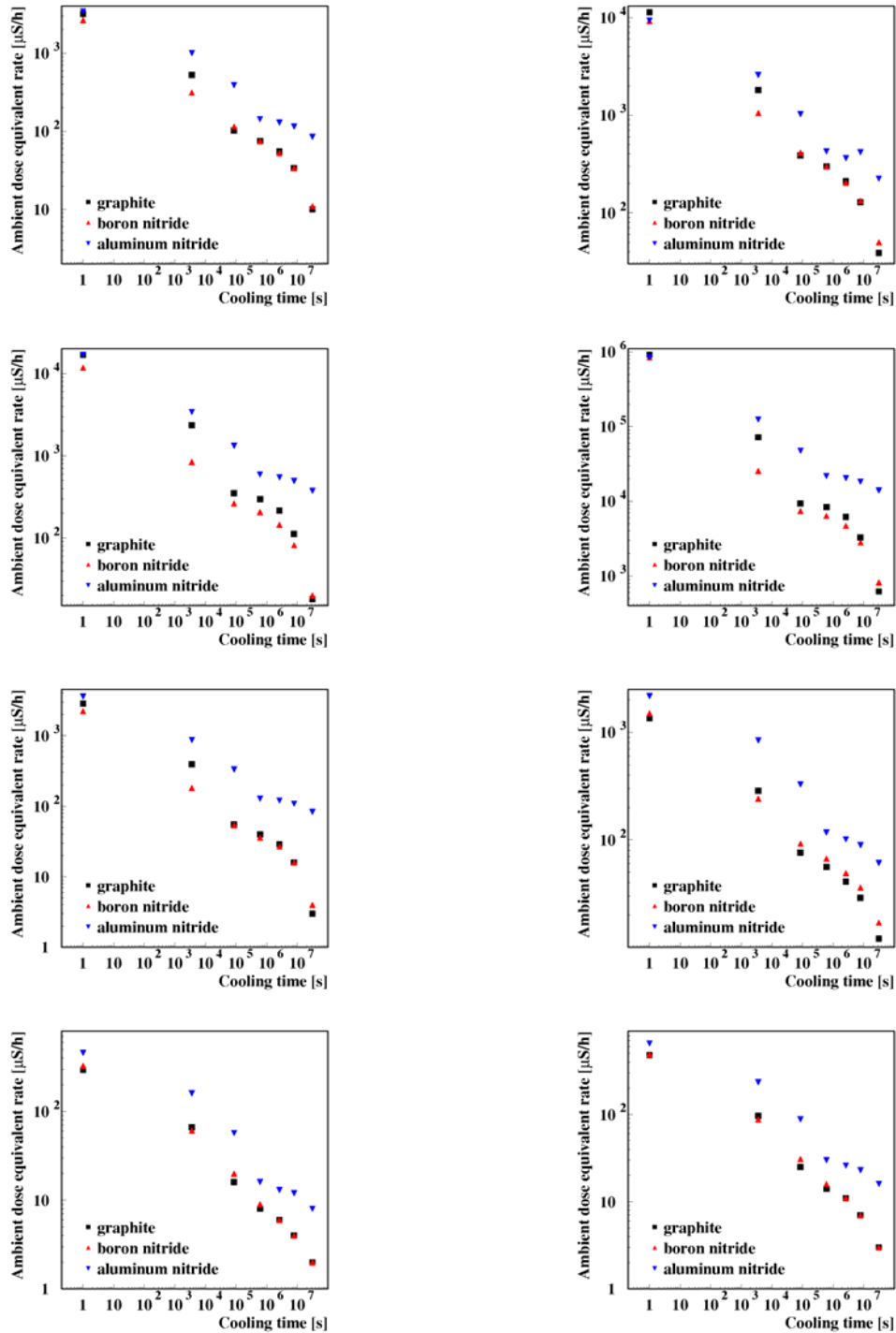
References

[1]   Weterings, W., B. Goddard, *Loading Assumption for Beam Dumps of Linac4 PS Booster Injection*, L4-T-EP-0001, EDMS Id 963395 (2008).

[2]   Weterings, W., *et al.*, "160-MeV H⁻ Injection into the CERN PSB", *Proceedings of Particle Accelerator Conference (PAC 07)*, Albuquerque, New Mexico, 25-29 June 2007, pp. 1628.

[3]   Battistoni, G., *et al.*, "The FLUKA Code: Description and Benchmarking", *Proc. of the Hadronic Shower Simulation Workshop 2006*, Fermilab 6-8 September 2006, M. Albrow, R. Raja (Eds.), AIP Conference Proceedings, 896, 31-49 (2007).

[4]   Fassò, A., *et al.*, *FLUKA: A Multi-particle Transport Code*, CERN-2005-10 (2005), INFN/TC_05/11, SLAC-R-773.

[5]   Versaci, R., *et al.*, *Studies for the H⁰/H Dump for Linac4: Energy Deposition, Induced Radioactivity and BLM Signal*, CERN Internal Report EDMS Id 1073028 (2010).

Activation and beam-loss criteria for "hands-on" maintenance on heavy ion accelerators

Ivan Strašík[1,2]**, Edil Mustafin**[1]**, Nikolai Sobolevsky**[3]**, Márius Pavlovič**[4]**, Vera Chetvertkova**[1,2]
[1]GSI Helmholtzzentrum für Schwerionenforschung, Darmstadt, Germany
[2]Johann Wolfgang Goethe Universität, Frankfurt am Main, Germany
[3]Institute for Nuclear Research of the Russian Academy of Sciences, Moscow, Russia
[4]Slovak University of Technology, Bratislava, Slovak Republic

Abstract

In the frame of the Facility for Antiprotons and Ion Research (FAIR) project, residual activity induced by heavy ions was studied both experimentally and numerically using Monte Carlo particle-transport codes. In the present work we report on the validation of the transport codes FLUKA and SHIELD based on the measurements of the residual activity of copper and stainless steel targets irradiated with uranium and argon beams at different energies. After the validation, the codes were used for simulations of the residual activity in two beam-loss scenarios representing: i) losses in a beam pipe of an accelerator; ii) losses in a bulky accelerator structure like a magnet yoke or a coil. The main task of the study was establishing a scaling law that expands the existing beam-loss criterion of 1 W/m for "hands-on" maintenance on proton machines to heavy ion accelerators. This scaling law enables specifying hands-on maintenance criteria for all projectile species from proton up to uranium at energies from 200 MeV/u up to 1 GeV/u.

Introduction

Quantification of the residual activity of accelerator components induced by beam losses is necessary to evaluate radiation hazard to personnel during "hands-on" maintenance [1-4]. It provides fundamental information that can be used in several ways: *i)* to specify the tolerable beam losses in the machine; *ii)* to optimise the choice of construction materials; *iii)* to estimate the necessary cooling time after turning off the beam and to optimise the whole regime of machine operation. All these measures are important with respect to the reduction of personnel exposure, which is required by important radiation-safety principle "As Low As Reasonably Achievable" (ALARA). Activation level induced by the beam losses below 1 W/m is accepted for hands-on maintenance on proton accelerators [4]. Tolerances for heavy ion accelerators were specified by scaling the existing criterion for proton machines [5-7].

As a part of the FAIR project [8,9], extensive experimental studies [10-12] and Monte Carlo simulations [5,6,13] of the residual activity induced by high-energy heavy ions in stainless steel, copper and aluminium were performed at GSI Helmholtzzentrum für Schwerionenforschung in Darmstadt. Experiments and simulations showed that the activation of the heavy ion accelerators is in general lower than the activation of the proton machines [5-7] and induced activity significantly depends on the energy and mass of the projectiles as well as on the target material [5-7,10-12]. The results of the simulations by FLUKA [14,15] and SHIELD [16,17] presented in this paper follow the previous residual activation studies and give more elaborated beam-loss criteria for hands-on maintenance on heavy ion accelerators.

Experimental studies and validation of the simulation codes

The beams from SIS-18 synchrotron at GSI were used for experiments. Stainless steel, copper and aluminium targets were irradiated by high-energy uranium and argon beams. The main task of the study was: *i)* to identify the isotopes with dominating contribution to the residual activity; *ii)* to calculate the residual activity of the identified isotopes; *iii)* to measure depth profiles of residual activity of induced isotopes. Gamma-ray spectroscopy was used as the main analytical technique. The results of the experiments are presented in Refs. [10-12]. The data collected in these experiments can be used to verify, improve and complete the physical models and data libraries of pertinent simulation codes.

Monte Carlo codes FLUKA and SHIELD were used to simulate the experiments and to investigate consistency of the results. Comparison of the experimental and the calculated data is reported in Refs. [5,6,12,13]. As an example, comparison of the measured and simulated total activities (all isotopes together) in stainless steel and copper targets irradiated by uranium ions with energy of 500 MeV/u and 950 MeV/u is presented in Figure 1. The activities of each target were compared at the time points when the gamma spectra of the pertinent targets were acquired. It can be seen that the discrepancies between measured (A_E) and simulated (A_S) values expressed as a ratio A_E/A_S vary from a factor of 0.66 to 1.51. In general, FLUKA tends to underestimate and SHIELD tends to overestimate the activities. Nevertheless, this result can be interpreted as a reasonably good agreement for both codes keeping in mind the enormous complexity of the activation process.

Beam-loss criterion for hands-on maintenance on proton accelerators of 1 W/m

The well known available information is that activation caused by uncontrolled beam losses uniformly distributed along the beam line on the level of 1 W/m can be accepted for high-energy proton accelerators as a threshold for the hands-on maintenance [4]. In order to quantify the activation caused by 1 W/m of proton-beam losses, the FLUKA code was used to calculate the effective dose rate in the vicinity of a beam pipe irradiated by 1 GeV protons. The beam particles were distributed uniformly along the beam line as shown in Figure 2.

The assumed beam pipe geometry was a 10 m long tube made of stainless steel, 10 cm inner diameter, 2 mm wall thickness. The glancing angle between the incident beam particles and the inner surface of the beam pipe was 1 mrad. The irradiation time was 100 days. The effective dose rate was calculated 4 hours after the end of irradiation. These conditions were agreed upon in the accelerator community as representing a typical operating period of an accelerator followed by a reasonable

Figure 1: Ratio A_E/A_S for the total residual activities of all isotopes induced in stainless steel and copper targets irradiated by 500 MeV/u and 950 MeV/u uranium ions

A_E is the experimentally measured total activity and A_S is the total activity calculated by FLUKA and SHIELD
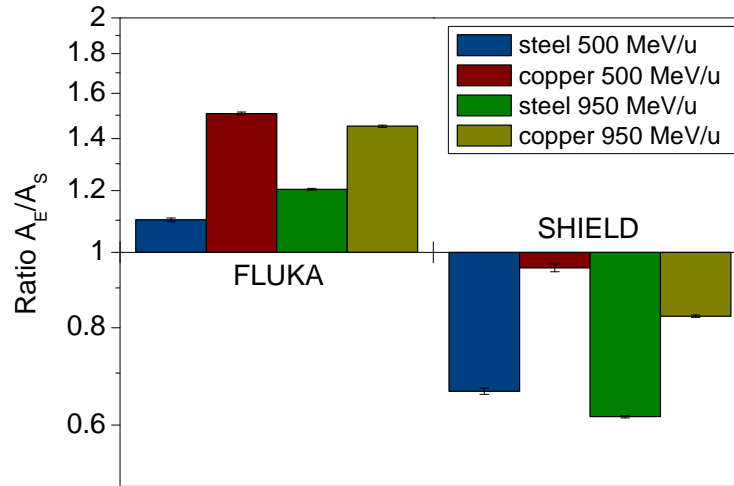
Figure 2: A model of the beam pipe irradiation
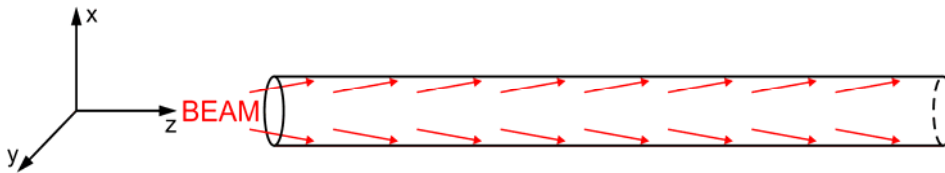
cooling-down time before the hands-on maintenance [18]. The effective dose rate at the distance of 30 cm from the surface of the tube is about 1 mSv/h, which is well consistent with previous activation studies using other simulation codes [18-22].

Beam-loss criteria for hands-on maintenance on heavy ion accelerators

Inventory of the isotopes induced in the beam pipe of an accelerator

The FLUKA and SHIELD codes were used for simulation of the residual activity induced by various projectiles in the stainless steel beam pipe in order to compare heavy ions with protons. The simulations were performed for ^{1}H, [4]He, ^{12}C, [20]Ne, [40]Ar, [84]Kr, [132]Xe, [197]Au and [238]U at energies from 200 MeV/u up to 1 GeV/u. The simulated irradiation time was 100 days. The residual activity and the effective dose rate at the distance of 30 cm from the beam pipe outer surface were calculated at different time points during and after irradiation.

It was found that the inventory of isotopes with dominating contribution to the total activity as well as their relative activities (relative with respect to the total activity of all isotopes) do not depend on the projectile species (see Figure 3). This can be explained by the fact that the isotopes are produced mostly by secondary particles rather than by the primary projectiles, as was also confirmed experimentally [10-12].

Time evolution of the activity

Since the inventory of the isotopes and their relative activities are very similar for all projectiles, the time evolution of the activity can be described by means of a generic curve that can be made independent from the projectile mass. In order to do so, the activities must be first normalised to the activity at a certain specific time point, most conveniently at the end of irradiation. The generic curve

Figure 3: Relative activities of the isotopes induced by 1 GeV/u projectiles from proton up to uranium in the stainless steel beam pipe one day after the end of irradiation calculated by FLUKA
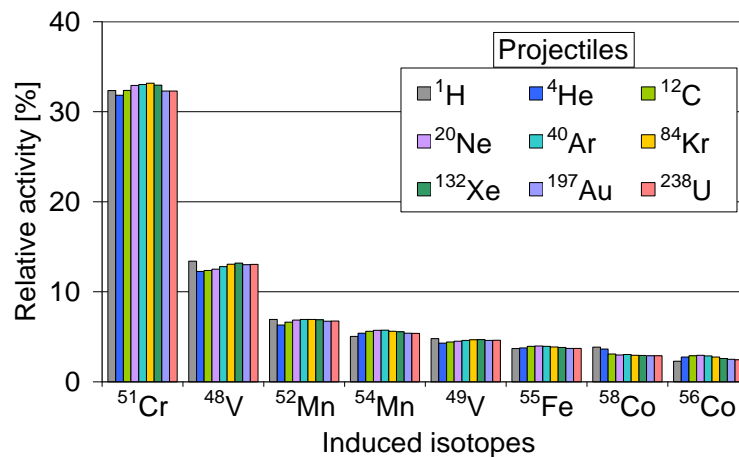
Figure 4: Time evolution of the relative activity induced in the beam pipe by different projectiles at 500 MeV/u calculated by FLUKA
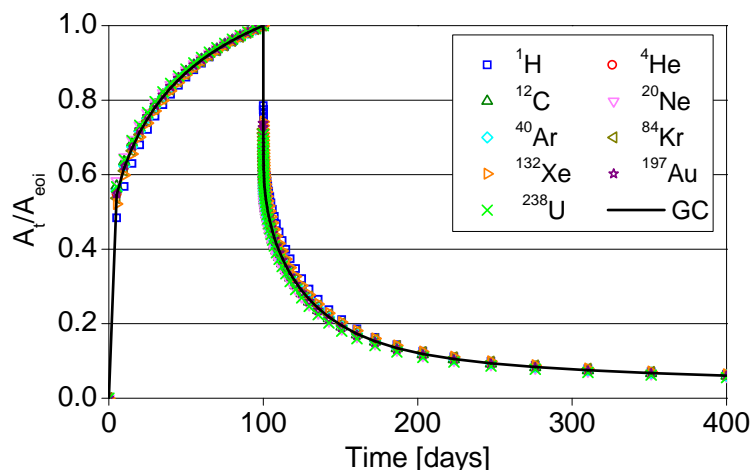
is then obtained by averaging the data points of the individual curves corresponding to different primary ions. As an example, the time evolution curves for projectiles at 500 MeV/u calculated for 100 days of continuous irradiation and followed-up during 400 days after the end of irradiation is shown in Figure 4 together with the corresponding generic curve.

Dependence of the residual activity on selected beam parameters

Dependence of the residual activity induced in the beam pipe by 1 W/m of primary beam loss on ion mass is shown in Figure 5 for 1 GeV/u and 200 MeV/u beams. The residual activity was calculated at several time points after the end of irradiation: immediately, 1 day, 1 week, 2 months, 1 year and 10 years. It can be seen that the induced activity decreases with increasing ion mass. It also decreases with decreasing energy. The same trend was observed for the effective dose rate.

The decrease of activity with increasing ion mass as well as with decreasing ion energy can be explained by the fact that the primary ions at lower energies and with higher mass number are stopped mostly by Coulomb interaction with the target electrons and only a minor part of them interacts with the target nuclei. In other words, the Coulomb stopping range of these particles is shorter compared to their mean free-path for nuclear interaction. In contrary, protons and light ions have their ranges longer than the mean free path [6,7].

Figure 5: Activity of the stainless steel beam pipe induced by 1 W/m of primary beam loss at 1 GeV/u (left) and 200 MeV/u (right) calculated by FLUKA
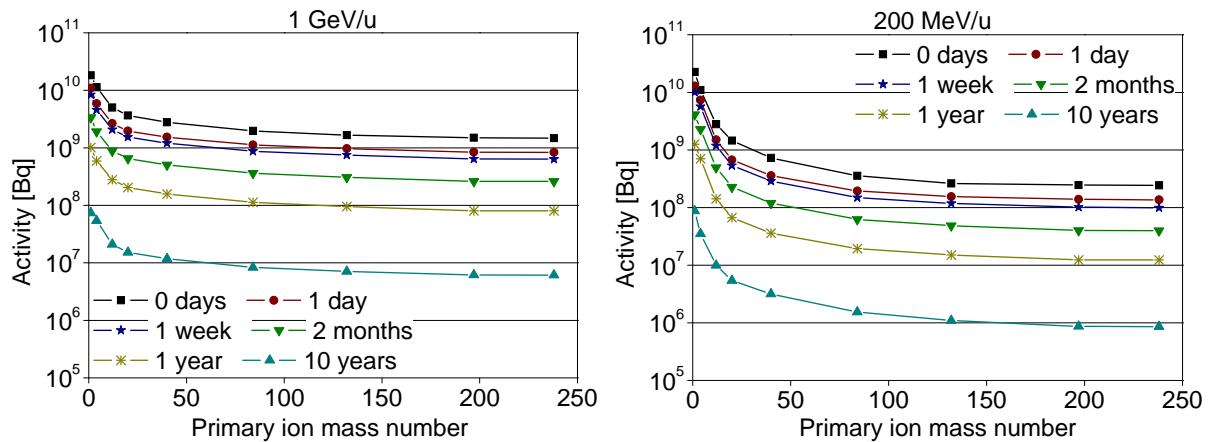
Scaling law for beam loss criteria

So far, it was found out that: *i)* inventory of the isotopes induced in the stainless steel beam pipe does not depend strongly on the projectile species; *ii)* time evolution of the induced activity correlates to the generic curve; *iii)* the activity induced by 1 W/m of beam losses decreases with increasing ion mass and with decreasing energy. These facts allow us to introduce a scaling law for heavy ion beam loss tolerances based on the accepted criterion of 1 W/m for protons. For this purpose, we define the normalised activity as the activity induced by unit beam power of 1 W representing the lost beam particles hitting the accelerator structures. In case of the beam pipe geometry, these lost beam particles are assumed to be distributed uniformly along the beam pipe. The scaling factor is then obtained as the ratio of the normalised activity induced by the 1 GeV proton (reference) beam to the normalised activity induced by the beam of interest. Although the normalised activity induced by 1 GeV protons is slightly different from the normalised activity induced by protons at lower energy, 1 GeV protons were taken as a reference in order to get a universal criterion.

FLUKA simulations of the beam pipe activation showed that normalised activity induced by uranium ions is about 12 times lower at 1 GeV/u, 23 times lower at 500 MeV/u and almost 75 times lower at 200 MeV/u compared to 1 GeV protons. Therefore the tolerable beam losses for uranium beam could be 12 W/m at 1 GeV/u, 23 W/m at 500 MeV/u and 75 W/m at 200 MeV/u. Other particles were treated in the same manner and results are plotted in Figure 6 (left panel). The same results were obtained from calculated effective dose rates.

The FLUKA simulations were compared with simulations performed by the independent Monte Carlo particle transport code SHIELD. The DCHAIN-SP 2001 code [23] was used for calculation of the time evolution of the activity obtained from the SHIELD code. The main purposes of this comparison were code/code benchmarking and investigation of a possible influence of the 100 MeV/u threshold for heavy ion inelastic interactions in the FLUKA code. The heavy ions below this value are excluded from the simulation of the activation process. The results of the simulations are presented in Figure 6. It can be seen that except for the beam energy of 200 MeV/u, the results are very similar. In case of the 200 MeV/u beam energy, the beam loss criterion calculated by FLUKA is less strict than those calculated by SHIELD. The beam loss criterion for 200 MeV/u ^{238}U ions calculated by FLUKA is 75 W/m, whereas it is 60 W/m when calculated by SHIELD. This discrepancy (25%) is very likely caused by the 100 MeV/u threshold for heavy ion interactions in FLUKA, since the discrepancy at higher beam energies is smaller.

Activation of bulky accelerator structures

Simulation model

In addition to the beam pipe, accelerators also contain bulky structures like a magnet yoke, a coil or a collimator. For this reason, FLUKA and SHIELD simulations of the activity induced by various projectiles

**Figure 6: Scaling factor for the hands-on maintenance
criteria in the beam pipe as a function of primary ion mass**

The scaling factor is represented by the ratio of the normalised activity induced by 1 GeV
proton beam, A_P(1 GeV), to the normalised activity induced by the beam of interest at given energy,
A_i(E). The activities were calculated by FLUKA (left) and SHIELD (right) at the end of irradiation.
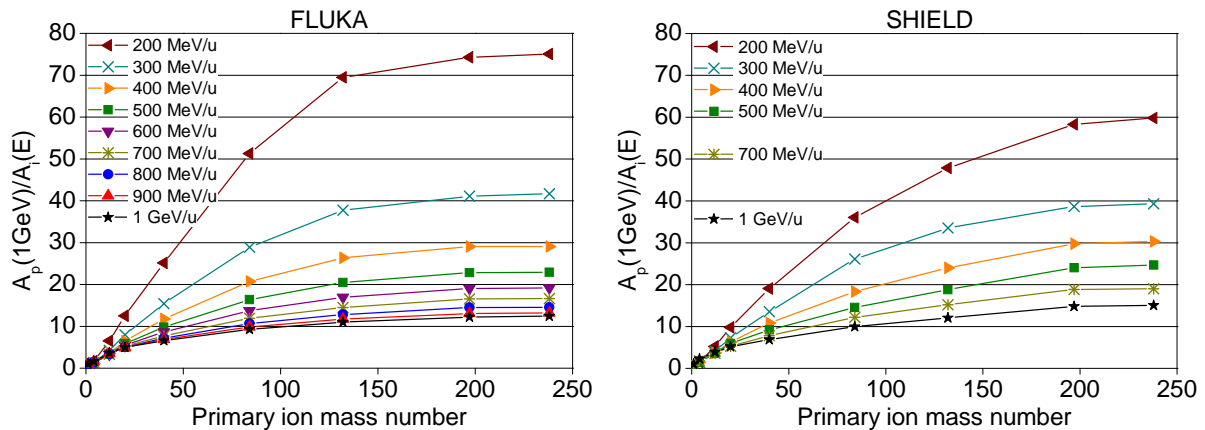
Figure 7: Geometrical model of the bulky target irradiation

were also performed for a bulky target. The assumed geometry of the bulky target was a full material cylinder of 20 cm in diameter, 60 cm long. In this case the beam particles were not distributed uniformly along the target, rather than they impacted to the basement of the cylinder perpendicularly to its surface (see Figure 7).

The simulations were performed for the same projectiles as for the beam pipe: ^{1}H, ^{4}He, ^{12}C, ^{20}Ne, ^{40}Ar, ^{84}Kr, ^{132}Xe, ^{197}Au and ^{238}U at energies from 200 MeV/u up to 1 GeV/u. The calculated induced activities were normalised to the unit beam power of 1 W delivered continuously to the target during 3 months. The activity was calculated again at several time points after irradiation: at the end of irradiation, 1 day, 1 week, 2 months, 1 year and 10 years after the end of irradiation.

Scaling law for beam loss tolerance

Similarly to the beam pipe, the inventory of the isotopes induced in the bulky target and their relative activities do not depend strongly on the projectile species, especially for the stainless steel. However, a well-pronounced dependence on the target material was observed (see Figure 8).

The normalised activity induced in the bulky target again decreases with increasing ion mass. For uranium ions, it is about 5 times lower at 1 GeV/u, about 12 times lower at 500 MeV/u and almost 60 times lower at 200 MeV/u compared to 1 GeV protons. Therefore the tolerable beam losses for uranium beam could be 5 W/m at 1 GeV/u, 12 W/m at 500 MeV/u and 60 W/m at 200 MeV/u. Other particles were treated in the same manner; results are plotted in Figure 9 for both materials. Although the inventory of induced isotopes and their relative activities in stainless steel and copper are different, the ratio of the normalised activity induced by protons to the normalised activity induced by heavy ions is almost the same in both materials. This is due to the fact that normalised activities change similarly with the change of the target material, hence keeping the ratio almost constant.

Contrary to the beam pipe, there is no such discrepancy between FLUKA and SHIELD at 200 MeV/u in the bulky target. Results of the SHIELD simulations are plotted in Figure 10. The reason

**Figure 8: Isotope inventory and their relative activities 1 day after the
end of irradiation induced by 1 GeV/u projectiles from proton up to uranium
in stainless steel (left) and copper (right) bulky target calculated by FLUKA**
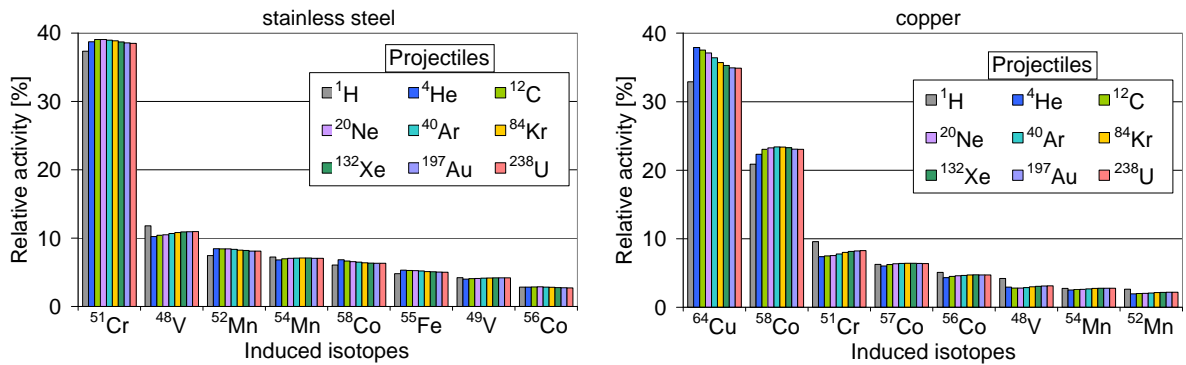
**Figure 9: Scaling factor for the hands-on maintenance
criteria as a function of ion mass for the bulky target**

The scaling factor is represented by the ratio of the normalised activity induced by 1 GeV proton beam, A_P(1 GeV), to the normalised activity induced by the beam of interest at given energy, A_i(E). The activities were calculated by FLUKA in the stainless steel (left) and copper (right) at the end of irradiation.
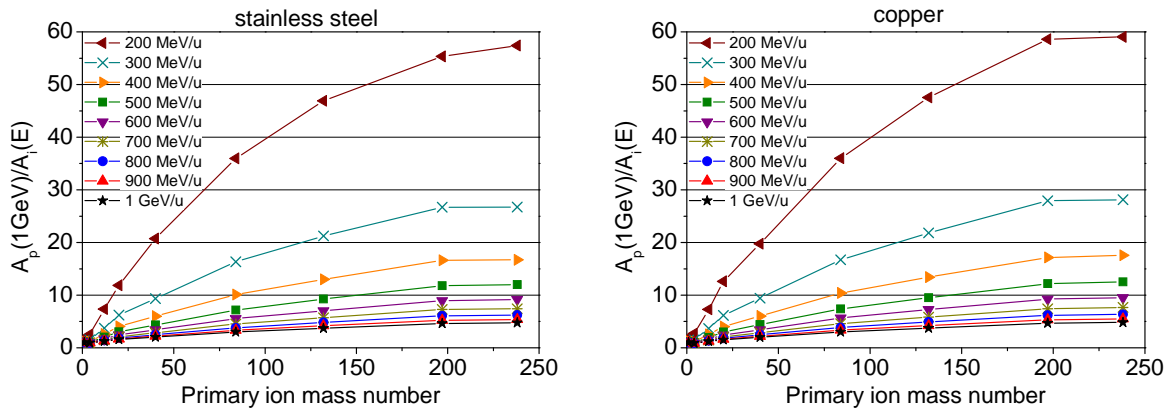
**Figure 10: Scaling factor for the hands-on maintenance
criteria as a function of ion mass for the bulky target**

The scaling factor is represented by the ratio of the normalised activity induced by 1 GeV proton beam, A_P(1 GeV), to the normalised activity induced by the beam of interest at given energy, A_i(E). The activities were calculated by SHIELD in the stainless steel (left) and copper (right) at the end of irradiation.
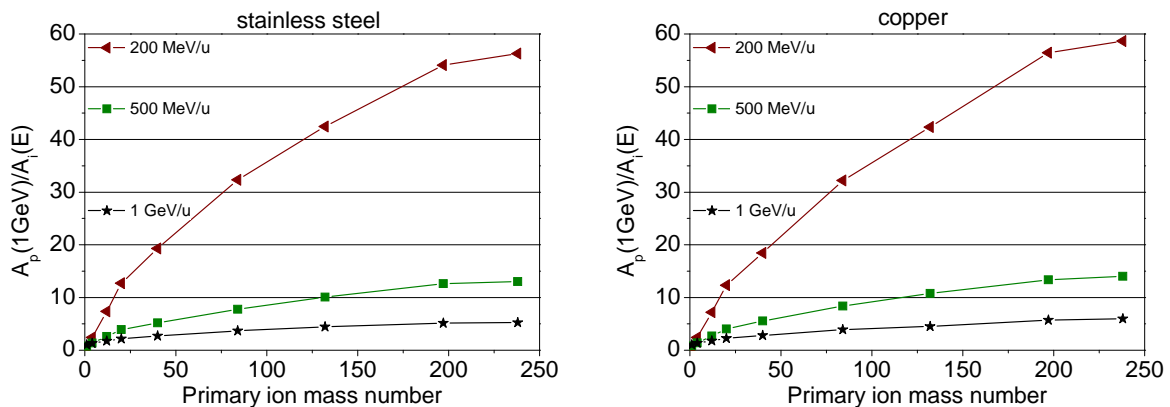
can be that the activity induced by primary particles compared with the activity induced by secondary particles is higher in case of the beam pipe than in case of the bulky target. The leakage of the secondary particles such as neutrons and protons from the target is more probable for the beam pipe than for the bulky target. Consequently, the impact of the 100 MeV/u threshold on the total induced activity is more pronounced in the beam pipe simulations.

Comparison of the hands-on maintenance criteria for the bulky target and for the beam pipe

It can be seen by comparing Figure 6 with Figures 9 and 10 that the hands-on maintenance criteria for heavy ions are less strict in case of the beam pipe than in case of the bulky target. In general, the scaling factor for the hands-on maintenance criteria depends on the target thickness as shown in Figure 11. The tolerable beam losses for heavy ions decrease with increasing wall thickness.

Figure 11: Scaling factor for the hands-on maintenance criteria for the stainless steel beam pipe with different wall thickness and for the bulky target

The scaling factor is represented by the ratio of the normalised activity induced by 1 GeV proton beam, $A_P(1\ GeV)$, to the normalised activity induced by 1 GeV/u ion beam of interest, $A_i(1\ GeV/u)$. The activities were calculated by FLUKA at the end of irradiation.
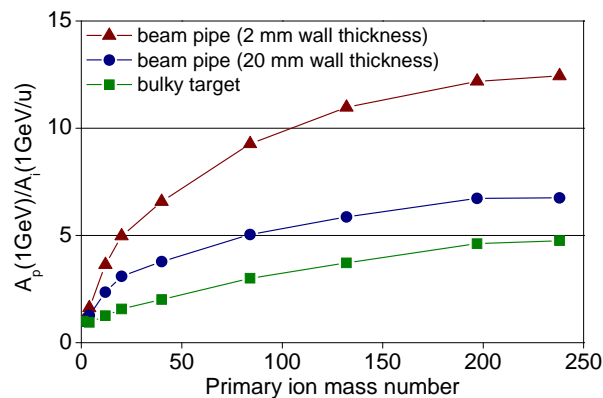
The interpretation of Figure 11 is based on the knowledge that the major role in the activation process is played by secondary particles, mainly neutrons and protons [10-12]. However, a large number of these nucleons escape from the target in case of a thin-wall beam pipe, which lowers the induced activity. The heavy ion reactions involve projectile break-up and emission of secondary nucleons from the projectile [24,25]. The break-up nucleons with high energies do not undergo much interaction with the target nuclei and fly away at very forward angles [26]. This allows them to escape from the thin-wall beam pipe. Their contribution to the beam pipe activation is missing and the induced activity is lower than in the case of the bulky target.

The angular distribution of the nucleons that had escaped from the beam pipe was calculated by FLUKA for two different wall thicknesses. Figure 12 shows the nucleon yield per watt as a function of output angle for the beam pipe wall thickness of 2 mm and 20 mm. It can be seen that in the case of the 2 mm thick wall, there is much higher yield of nucleons leaving the beam pipe at small angles (up to 10 degrees) than in case of the 20 mm wall. These nucleons must come from the projectiles heavier than protons since they are not observed in the case of proton irradiation. They escape from the thin beam pipe wall, which lowers the induced activity. It can also be seen that the leakage of the nucleons is significantly reduced in case of the thicker beam pipe wall.

Results

The beam loss criteria for hands-on maintenance on heavy ion accelerators were specified for the beam pipe geometry and the bulky target geometry using the Monte Carlo codes FLUKA and SHIELD. Simulations showed that in the materials of interest (stainless steel and copper), the inventory of the induced isotopes and their relative activities do not depend strongly on the projectile species and

**Figure 12: Angular distribution of nucleons escaping
from the beam pipe for wall thickness of 2 mm and 20 mm**

The angles are given with respect to the beam pipe longitudinal central axis
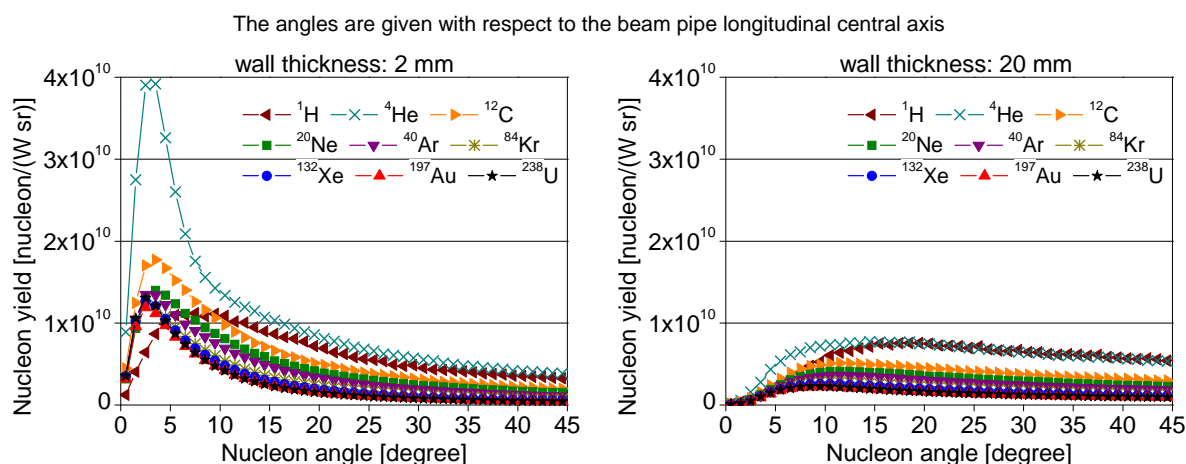
energy in the investigated energy interval from 200 MeV/u up to 1 GeV/u. They depend mainly on the target material. Since the isotopes and their relative activities are very similar for all projectiles, the time evolution of the induced activity correlates to a generic curve. The induced activity normalised per unit beam power decreases with increasing primary ion mass and with decreasing energy.

The tolerable beam losses for heavy ions were specified by scaling the existing value of 1 W/m for protons. The scaling yields the beam loss tolerances for uranium beam of 12 W/m at 1 GeV/u in case of the beam pipe geometry. The beam loss tolerances for the bulky accelerator structures are stricter. They are 5 W/m for 1 GeV/u uranium beam. The thin wall beam pipe exhibits significant leakage of the projectiles' break-up nucleons, which decreases the induced activity by heavy ions and consequently the strictness of the hands-on maintenance criteria.

Comparison of the FLUKA and SHIELD simulations showed that the 100 MeV/u threshold for heavy ion inelastic interactions in the FLUKA code has only modest impact on the hands-on maintenance criteria. The largest discrepancy of about 25% was observed for low-energy (200 MeV/u) beams and beam pipe geometry. In the cases of the higher energies as well as the bulky targets, the hands-on maintenance criteria calculated by FLUKA and SHIELD are similar.

References

[1]   Sullivan, A.H., A *Guide to Radiation and Radioactivity Levels Near High Energy Particle Accelerators*, Nuclear Technology Publishing, Ashford, Kent, United Kingdom (1992), Chap. 4, p. 93.

[2]   Ulrici, L, *et al.*, "Radionuclide Characterization Studies of Radioactive Waste Produced at High-energy Accelerators", *NIM*, A 562, 596 (2006).

[3]   Mauro, E., M. Silari, "Radiation Protection Studies for a High-power 160 MeV Proton Linac", *NIM*, A 605, 249 (2009).

[4]   Mokhov, N.V., W. Chou (Eds.), "Beam Halo and Scraping", *Proceedings of the 7th ICFA Mini-Workshop on High Intensity High Brightness Hadron Beams*, Wisconsin, USA (1999), p. 3.

[5]   Strašík, I., *et al.*, "Simulation of the Residual Activity Induced by High-energy Heavy Ions", *Nucl. Tech.*, 168, 643 (2009).

[6]   Strašík, I., *et al.*, "Residual Activity Induced by High-energy Heavy Ions in Stainless Steel and Copper", *Proceedings of the 11th European Particle Accelerator Conference EPAC08*, Genoa, Italy (2008), p. 3551.

[7]   Mustafin, E., I. Hofmann, H. Weick, "Influence of Electronic Stopping Power on the Total Neutron Yield of Energetic Heavy Ions", *NIM*, A 501, 553 (2003).

[8]   Henning, W.F., "FAIR – Recent Developments and Status", *Nucl. Phys.*, A 805, 502c (2008).

[9]   Spiller, P., G. Franchetti, "The FAIR Accelerator Project at GSI", *NIM*, A 561, 305 (2006).

[10]   Fertman, A., *et al.*, "First Results of an Experimental Study of the Residual Activity Induced by High-energy Uranium Ions in Steel and Copper", *NIM*, B 260, 579 (2007).

[11]   Strašík, I., *et al.*, "Experimental Study of the Residual Activity Induced by 950 MeV/u Uranium Ions in Stainless Steel and Copper", *NIM*, B 266, 3443 (2008).

[12]   Strašík, I., *et al.*, "Experimental Study and Simulation of the Residual Activity Induced by High-energy Argon Ions in Copper", *NIM*, B 268, 573 (2009).

[13]   Kozlova, E., *et al.*, "Benchmark Test of the FLUKA Monte Carlo Code for Residual Production with 500 MeV/u and 950 MeV/u Uranium Beam on Copper and Stainless Steel Target", *Nucl. Tech.*, 168, 747 (2009).

[14]   Battistoni, G., *et al.*, "The FLUKA Code: Description and Benchmarking", *Proceedings of the Hadronic Shower Simulation Workshop 2006*, Fermilab, USA (2007), p. 31.

[15]   Fassò, A., *et al.*, *FLUKA: A Multi-particle Transport Code*, CERN-2005-10, INFN/TC_05/11, SLAC-R-773 (2005), *www.fluka.org*.

[16]   Dementyev, A.V., N.M. Sobolevsky, "SHIELD – Universal Monte Carlo Hadron Transport Code: Scope and Applications", *Rad. Meas.*, 30, 553 (1999).

[17]   *www.inr.ru/shield*.

[18]   Alonso, J., "Beam Loss Working Group Report", *Proceedings of the 7th ICFA Mini-Workshop on High Intensity High Brightness Hadron Beams*, Wisconsin, USA (1999), p. 51.

[19]   Santoro, R.T., *et al.*, "Spallation Neutron Source Radiation Shielding Issues", *Proceedings of the 3rd International American Nuclear Society Topical Meeting on Nuclear Applications of Accelerator Technology (AccApp'99)*, Long Beach, USA (1999), p. 417.

[20]   Fikani, M.M., E.J. Pitcher, "Expected Dose Rates from Component Activation in the APT Accelerator", *Trans. of the Am. Nucl. Soc. Journ.*, 79, 384 (1998).

[21]   Krivosheev, O.E., N.V. Mokhov, "Tolerable Beam Loss at High-intensity Proton Machines", *Proceedings of the 7th ICFA Mini-Workshop on High Intensity High Brightness Hadron Beams*, Wisconsin, USA (1999), p. 85.

[22]   Ronningen, R.M., G. Bollen, I. Remec, "Estimated Limits on Uncontrolled Beam Losses of Heavy Ions for Allowing Hands-on Maintenance at an Exotic Beam Facility Linac", *Nucl. Tech.*, 168, 670 (2009).

[23]   Kai, T., *et al.*, *DCHAIN-SP 2001: High Energy Particle Induced Radioactivity Calculation Code*, JAERI-Data/Code 2001-016 (2001).

[24]   Maiti, M., *et al.*, "Angular Distribution of Neutrons from Heavy Ion Induced Reactions in Thick Targets", *NIM*, A 556, 577 (2006).

[25]   Brosa, U., W. Krone, "Fast Neutrons in a Wide Angular Range", *Phys. Lett.*, B 105, 22 (1981).

[26]   Bonaccorso, A., D.M. Brink, "Neutron Angular Distribution from Halo Breakup", *Phys. Rev.*, C 57, 22 (1998).

Neutron double differential distributions, dose rates and specific activities from accelerator components irradiated by 50-400 MeV protons

F. Cerutti[1], N. Charitonidis[1,2] M. Silari
[1]European Organization for Nuclear Research (CERN), Geneva, Switzerland
[2]Department of Physics, National Technical University of Athens, Athens, Greece

Abstract

Systematic Monte Carlo simulations with the FLUKA code were performed to estimate the induced radioactivity in five materials commonly used in particle accelerator structures: boron nitride and carbon (dumps and collimators), copper (RF cavities, coils and vacuum chambers), iron and stainless steel (magnets and vacuum chambers). Using a simplified geometry set-up, the five materials were bombarded with protons in the energy range from 50 to 400 MeV. This energy range is typical of intermediate-energy proton accelerators used as injectors to higher-energy machines, as research accelerators for nuclear physics, and in hadron therapy. Ambient dose equivalent rates were calculated at distances up to one meter around the target, for seven cooling times up to six months. A complete inventory of the radionuclides present in the target was calculated for all combinations of target, beam energy and cooling time. The influence of the target size and of self-absorption was investigated. The energy and angular distributions of neutrons escaping from the target were also scored for all materials and beam energies. The influence on the neutron spectra of the presence of concrete walls (the accelerator tunnel) around the target was also estimated. The results of the present study provide a simple database to be used for a first, approximate estimate of the radiological risk to be expected when intervening on activated accelerator components.

Introduction

Proton accelerators in the intermediate-energy range (from a few tens to a few hundreds of MeV), being continuously used for nuclear physics research, over the past several years are increasingly applied for cancer radiation therapy [1]. Machines in this energy range are also commonly used as injectors for high-energy accelerators (which work in the GeV region or above). An example is the 160-MeV linac presently being built at CERN to replace the existing 50 MeV proton injector [2]. Beam-machine interaction during the operation of these accelerators has to be carefully investigated, due to the large beam intensities required for injectors on the one hand, and because medical installations are usually inside highly populated areas on the other.

The main radiation affecting the surrounding area is the neutron field produced by the interaction of the proton beam with the components of the accelerator, of the beam transfer lines and (in the case of medical machines) of the beam delivery system used to irradiate the patient (such as collimators and field-shaping devices), and with the patient himself. Related measurements for this intermediate energy range are not abundant in the literature and are usually limited to specific conditions, geometries and incident energies.

To overcome this lack of information, a systematic simulation study of proton beams impinging on different accelerator materials has been performed. The study was done using a simplified reference geometry, over the proton energy range from 50 MeV to 400 MeV, in steps of 50 MeV. Three quantities were calculated via two separate sets of simulations: *i)* the double differential spectra of neutrons escaping the target; *ii)* the type and amount of radionuclides generated by the irradiation of the given material; *iii)* the ambient dose equivalent rates around the irradiated material, which is the relevant quantity for the assessment of the radiological risk (personnel exposure). Finally, a special case was investigated, that of an iron target enclosed in a concrete tunnel, in order to evaluate the differences in both neutron spectra and activation with and without the presence of a surrounding concrete shield.

Simulation set-up

Materials

Boron nitride, carbon, copper, iron and stainless steel were selected as reference materials for the present study. These are common materials which make up main accelerator components. Iron constitutes magnet yokes, copper is the main component of RF cavities and magnet coils, stainless steel is found in vacuum chambers, boron nitride and carbon graphite are used in collimators, dumps and beam stoppers.

The exact composition of the materials used in this study is given in Table 1. The compounds BN, SiO_2, B_2O_3 present in BN, are detailed in Table 2. The listed values reflect the specifications usually adopted at CERN.

Geometry

A simplified geometry was considered consisting of a solid cylinder with diameter equal to its height (right cylinder) and the centre of the upstream face located at the origin of a Cartesian co-ordinate system. The dimensions of the cylinder thus varied as a function of material and beam energy (Table 3). More specifically, the height of the cylinder was chosen to slightly exceed (by a factor of 1.2) the corresponding proton range [3]. The cylinder was surrounded by air.

Beam and irradiation profile

Simulations were performed with a monoenergetic pencil proton beam impinging on the centre of the upstream face of the cylinder, towards the positive direction of the z-axis. For activation calculation purposes, we assumed an intensity of 6×10^{12} protons/s and a constant irradiation lasting nine months. Results can obviously be scaled to a different beam current.

Table 1: Material composition used in the simulations

Boron nitride (ρ = 1.92 g/cm^3)		Carbon (graphite) ρ = 2.00 g/cm^3		Copper (ρ = 8.98 g/cm^3)		Iron (ρ = 7.86 g/cm^3)	
Component	Mass content (%)	Element	Mass content (%)	Element	Mass content (%)	Element	Mass content (%)
BN	92.90	C	100.00	Cu	99.9596	Fe	99.91
SiO$_2$	0.20			O	0.0004	Mn	0.06
O	4.00			Ag	0.0100	C	0.01
B$_2$O$_3$	0.40			Mo	0.0100	P	0.01
Ca	2.50			Si	0.0200	S	0.01

Stainless steel (ρ = 7.90 g/cm^3)			
Element	Mass content (%)	Element	Mass content (%)
Fe	69.19	Cu	0.393
Cr	18.62	Al	0.277
Ni	8.32	Co	0.172
Si	0.648	V	0.070
Mn	1.520	W	0.040
P	0.030	Ca	0.036
S	0.037	Na	0.033
Mo	0.567	Mg	0.016
Sn	0.020	Nb	0.008
As	0.003		

Table 2: Composition of compounds of BN material

Compound	Element	Atom content (%)
BN	B	50
	N	50
SiO$_2$	Si	33.3
	O	66.7
B$_2$O$_3$	B	40
	O	60

Table 3: Target sizes used in the simulations

Boron nitride								
Beam energy [MeV]	50	100	150	200	250	300	350	400
Radius [cm]	0.67	2.34	4.80	7.86	11.52	15.66	20.16	25.02
Height [cm]	1.34	4.69	9.60	15.72	23.04	31.32	40.32	50.04
Carbon (graphite)								
Beam energy	50	100	150	200	250	300	350	400
Radius	0.65	2.25	5.00	7.50	11.00	15.00	20.00	25.00
Height	1.30	4.50	10.0	15.0	22.00	30.00	40.00	50.00
Copper								
Beam energy	50	100	150	200	250	300	350	400
Radius	0.23	0.78	1.58	2.58	3.75	5.06	6.50	8.00
Height	0.46	1.57	3.16	5.16	7.50	10.12	13.00	16.00
Iron								
Beam energy	50	100	150	200	250	300	350	400
Radius	0.25	0.85	1.72	2.81	4.09	5.53	7.10	8.79
Height	0.50	1.70	3.44	5.62	8.18	11.06	14.20	17.59
Stainless steel								
Beam energy	50	100	150	200	250	300	350	400
Radius	0.25	0.85	1.71	2.80	4.08	5.50	7.02	8.70
Height	0.50	1.70	3.43	5.60	8.16	11.01	14.04	17.40

Scored quantities

Two sets of simulations were performed, with the development version of the FLUKA Monte Carlo code [4,5] implementing the most updated physics models, in order to score prompt neutron fluence and activation levels, respectively. Transport thresholds were set at 100 keV for protons and 10^{-5} eV for neutrons. The prompt electromagnetic radiation was neglected, whereas a cut off of 10 keV (100 keV) was applied to photons (electrons/positrons) emitted in the decay of the produced radioisotopes. In the first set of simulations, the residual nuclei distribution in the target was scored after seven cooling times. The ambient dose equivalent [H*(10)] (as defined in Ref. [6]) was also scored in a cylindrical grid, up to a distance of 1 m from the target boundaries.

In the second set of simulations, the double differential yield of the escaping prompt neutrons was scored. Importance biasing was applied to increase statistics by compensating the fluence attenuation inside the target. For this purpose, the latter was divided into three cylindrical regions of increasing importance from the inner to the outer one, as shown in Figure 1.

**Figure 1: The importance biasing applied to the target in order
to compensate for the attenuation of the neutron fluence**
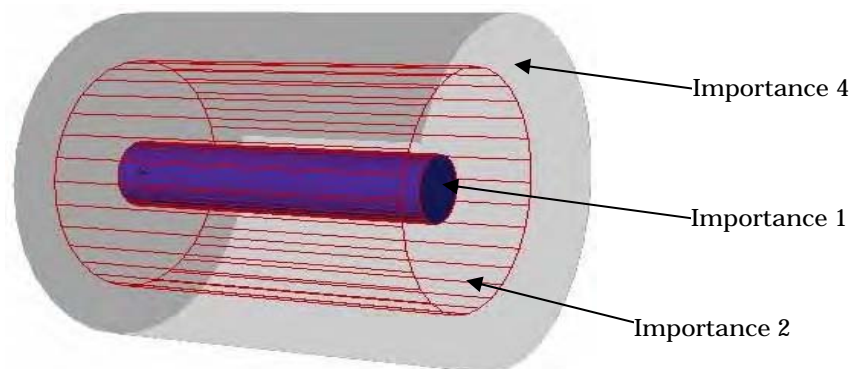
Results

Dose rates

The ambient dose equivalent rates, in µSv/h*, are visualised in the plots of Figures 2-4, referring to one day after the end of bombardment and to beam energies of 50 MeV, 100 MeV, 200 MeV and 400 MeV. The x-axis is along the axis of the cylinder, while the y-axis gives the radial position. Boron nitride and iron display similar dose rate patterns with respect to carbon and stainless steel, respectively, so they are omitted here.

The plots of Figure 2 show that the dose rate at a distance of 20 cm laterally from the target is of the order of 1 mSv/h for 50 MeV and 5 mSv/h for the case of 400 MeV. At 1 m distance the values reduce to about 50 µSv/h and 500 µSv/h, respectively. The different gradient and the non-uniform distribution in Figure 2(d) are due to the large size of the target (in this case the target thickness is 50 cm) which causes significant absorption of the photons in the target itself. Indeed lower values are found near the corners, corresponding to longer paths for the decay photons.

In copper (Figure 3), the overall ambient dose equivalent rate is higher than in carbon, due to the significantly higher number of radionuclides produced (both short-lived and long-lived). Note that the colour scale is different from that of Figure 2. As above, there is a significant difference between the values of the ambient dose equivalent near the target, which are of the order of 50 mSv/h for 50 MeV and 500 mSv/h for 400 MeV, versus values of 5 mSv/h and 10 mSv/h, respectively, at 1 m distance from the target. Values for stainless steel (Figure 4) are not significantly different from those for copper.

---

*   The ambient dose equivalent H*(10) is calculated by folding the particle fluence with the appropriate set of particle and energy-dependent conversion coefficients available in FLUKA. When referring to a given cooling time, ambient dose equivalent rate is given by the code in pSv/s.

Figures 5-9 show the evolution of the ambient dose equivalent rate, at a 50 cm lateral distance from the target and at the longitudinal position corresponding to the target centre, as a function of cooling time for all materials. For the sake of clarity, only the curves for four out of the eight energies are presented, for 50, 100, 200 and 400 MeV (the end of bombardment (EOB) is shown for visualisation purposes at 10^{-1} hours). The curves which are not shown lie in between, scaling with energy. The shape of the curves reflects the contribution of the short-lived isotopes decaying rapidly, and of the long-lived ones dominating at longer cooling times (after one day). The order of the curves does not strictly follow the order of the energies. This is due to the combination of two factors: the different production yields of short-lived and long-lived isotopes as a function of proton beam energy, and the self-absorption of the photons inside the target, which depends on the target size.

For carbon (Figure 6) the 50 MeV curve has a different slope for cooling times shorter than one day with respect to the curves for higher energies. For relatively short cooling times (of the order of one day), the ambient dose equivalent rate is dominated by short-lived isotopes. The ratios of the total activities at the EOB and at one day are 6.5 and 4.7 for 50 MeV and 100 MeV, respectively, indicating a comparatively larger fraction of short-lived isotopes for the lower energy. From the residual activity distribution, Be-7 and and He-3 are the dominant radionuclides after one day from the end of the irradiation.

For iron (Figure 8) the cross-over between the dose rate curves for different energies is more evident than with, *e.g.* boron nitride and copper. This can be explained again by the ratio between short- and long-lived isotope yields, which at 50 MeV is lower than at the other energies. As an example, the ratios of the total activities at the EOB and at one day are 1.26 and 1.59 for 50 MeV and 400 MeV, respectively. On the other hand, the target size does not play any role on the slope of the curves, as shown in Figure 10: the self-absorption provided by the target only attenuates the gamma emission but does not modify the shape of the decay curve.

Residual nuclei

For all materials, the total and specific activities of all produced radionuclides were calculated for all cooling times. As an example, Table 4 gives the most abundant radionuclides (*i.e.* the radionuclides accounting for about 90% to 95% of the total activity) for carbon and copper targets irradiated by 400 MeV protons, at the EOB and after one month. The specific activity (activity per unit mass) was calculated according to the mass of each individual target. The complete list of activities and specific activities of all produced radionuclides, for all materials, proton energies and cooling times, can be found in Ref. [7].

Double differential neutron yields

The double differential yields of neutrons escaping from the target were calculated in six angular bins (0°-15°, 15°-45°, 45°-75°, 75°-105°, 105°-135° and 135°-180°) in respect to the beam axis. Figures 11-13 show the neutron spectra for the carbon, copper and iron targets. The neutron spectra from the boron nitride and carbon targets are similar, and the same is valid for iron and stainless steel. The curves are normalised per incident proton. For better visualisation the plots display a lower limit of 10 keV.

In copper (Figure 12) the total yield is significantly higher than the yield in carbon, and the evaporation peak in the 1 MeV region is clearly observed at all angles for the higher beam energies. Because of the large size of the target for the 400 MeV beam, the peak is slightly shifted towards lower energies, due to neutron energy degradation in the target. Moreover, the forward peak just below the beam energy is well distinguished in all frames. The plots for iron, in particular for 200 and 400 MeV [Figures 13(c) and 13(d)] clearly show the resonance structure.

Effect of a concrete tunnel around the target

Finally, the effect of a concrete shielding around the target, simulating a tunnel-like structure in which an accelerator is usually located, was investigated. The ambient dose equivalent rate and the neutron spectra were scored inside the tunnel with a dedicated set of simulations. The results are compared with the corresponding case without the tunnel. The tunnel was very simply modelled as a

sphere centred on the target and with a radius of 2 m. The thickness of the tunnel wall was 1 m. The space between the target and the concrete sphere was filled with air. Figure 14 shows, as a function of cooling time, the ambient dose equivalent rate at distances of 50 cm and 1 m from the lateral surface of the iron target for a proton beam of 400 MeV.

Figure 14 clearly shows that the ambient dose equivalent rate increases when the target is located inside a tunnel. This effect is clearer near the tunnel walls. This increase is mainly due to thermal neutrons that enhance the ambient dose equivalent rate by activating both the concrete and the target. Figure 15 shows the impressive increase in the thermal neutrons population looking at the neutron spectrum in the air region, due to the thermalisation induced by the presence of concrete walls.

Conclusions

The aim of the present study was to provide generic estimates of the radiological risk encountered in proximity of irradiated accelerator components. Real situations differ from each other in terms of target material and dimension, irradiation geometry, irradiation conditions and cooling times, proton beam energy, etc. It is obviously impossible to provide activation data that can be directly applied to many different experimental situations. A precise estimate of the expected dose rate from an irradiated target can only be made by a detailed (and time consuming, in terms of setting up the input file, actual computing time and time needed for the data analysis) Monte Carlo simulation. In addition, if the composition of the irradiated material is not exactly known (and "exactly" can mean down to the ppm level), a Monte Carlo prediction can easily be off by an order of magnitude or more from what can be encountered in reality. Therefore generic activation data like those presented in this work, calculated for a set of specific accelerator materials in use at CERN (the composition of which is well known) can be useful to obtain at least order-of-magnitude (and probably better) predictions. For example, they can be used to estimate the ambient dose equivalent rate in an area where a maintenance intervention has to take place, and make a first guess of the expected individual exposures.

This paper has provided decay curves for the five materials up to six months of cooling time, and some examples of total activities and specific activities for a low-Z (carbon) and medium-Z (copper) target. The general trend is towards increased activation and dose rates with increasing Z. The role of self absorption in the cases of thick targets has briefly been evaluated. Tables listing total activities and specific activities of all residual nuclei produced in the five materials investigated, for the eight proton energies and the seven cooling times, are given in Ref. [7]. The energy distributions of neutron emitted from the target have been shown, and the influence on the neutron spectra of the presence of concrete walls (the accelerator tunnel) around the target has been briefly addressed. The present work is now being extended with more calculations to include the presence of shielding surrounding the target.

Figure 2: Ambient dose equivalent rates for a carbon target [μSv/h], impacted by a proton beam of: (a) 50 MeV, (b) 100 MeV, (c) 200 MeV and (d) 400 MeV after a cooling time of one day
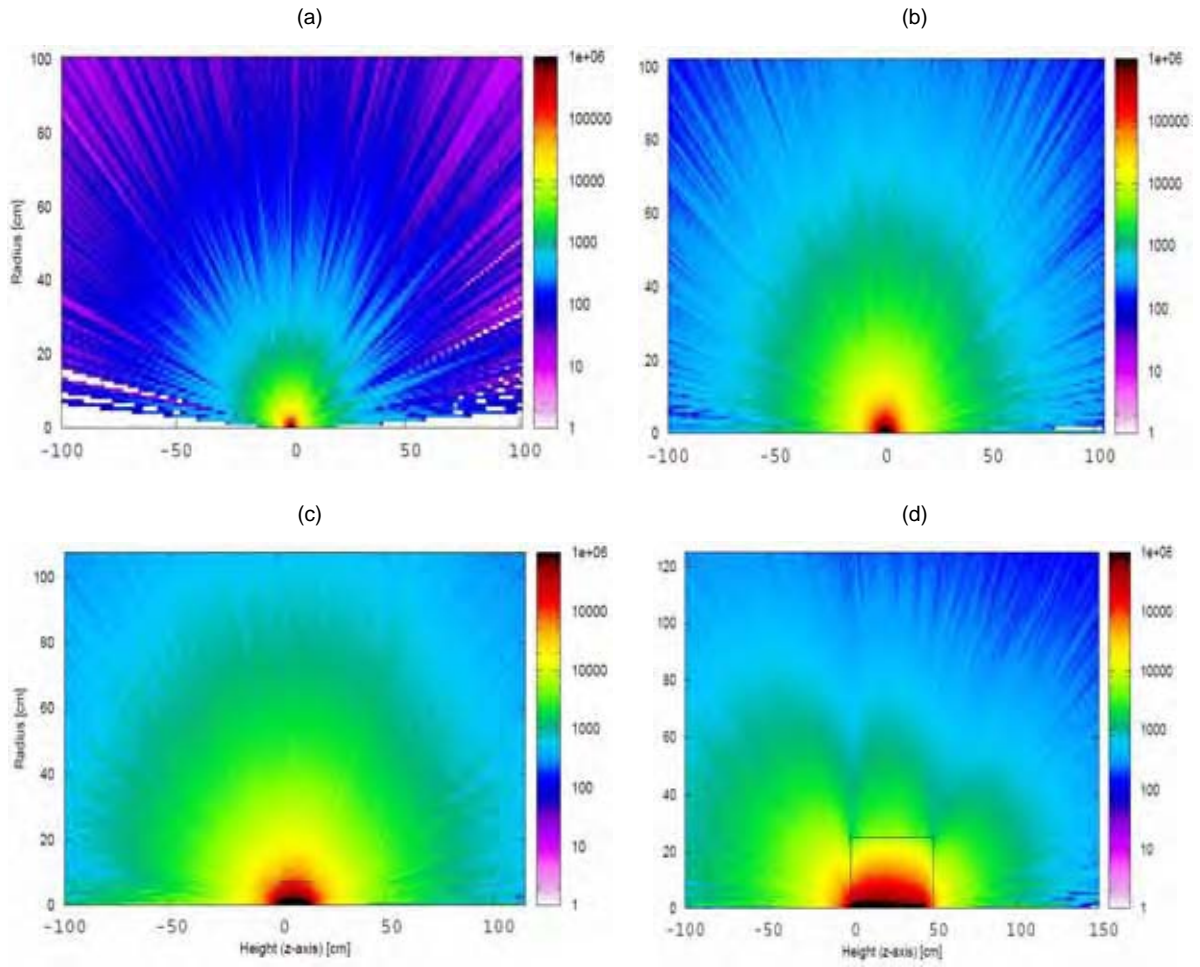
Figure 3: Ambient dose equivalent rates for a copper target [μSv/h], impacted by a proton beam of: (a) 50 MeV, (b) 100 MeV, (c) 200 MeV and (d) 400 MeV after a cooling time of one day
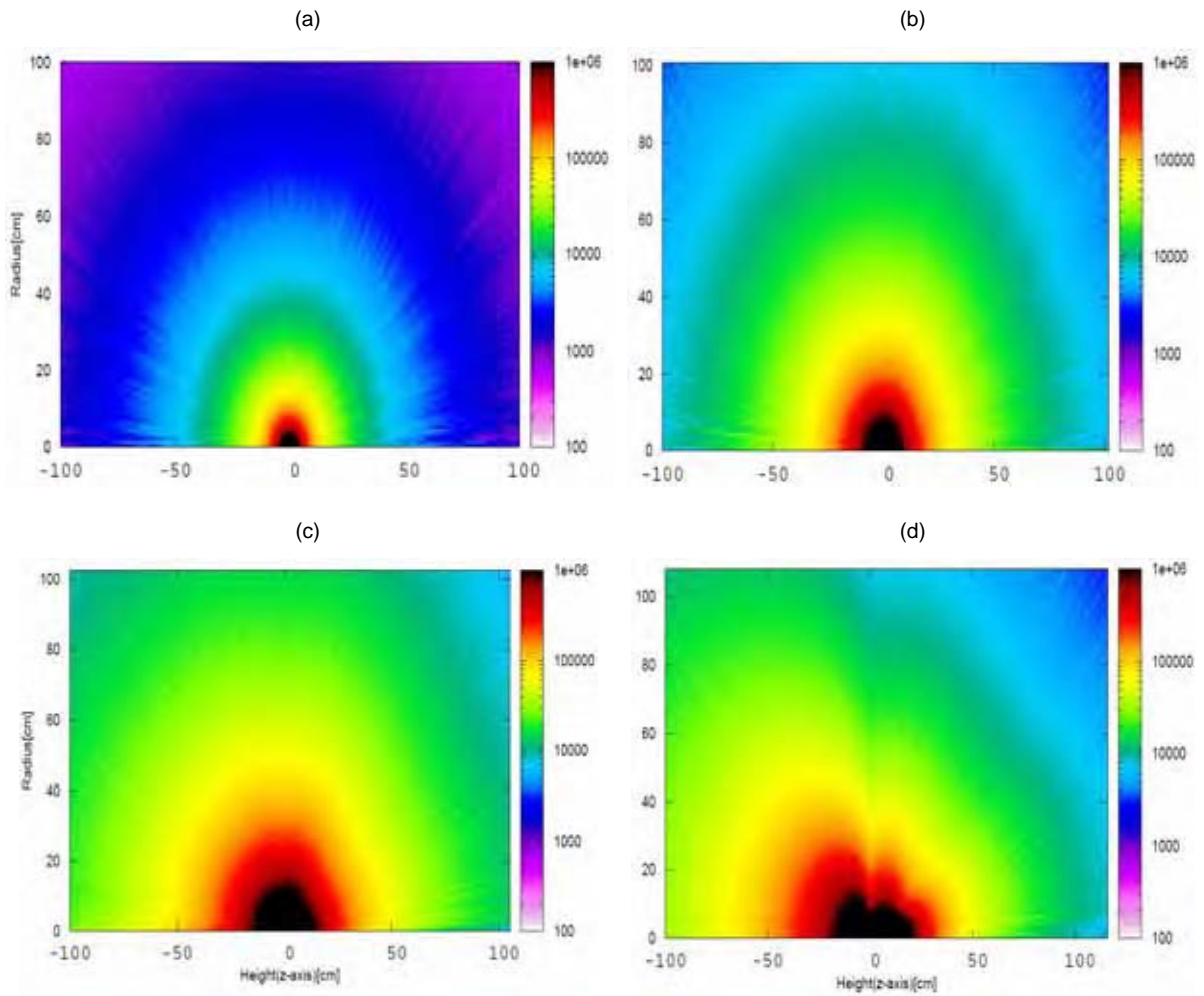
Figure 4: Ambient dose equivalent rates for a stainless steel target [µSv/h], impacted by a proton beam of: (a) 50 MeV, (b) 100 MeV, (c) 200 MeV and (d) 400 MeV after a cooling time of one day
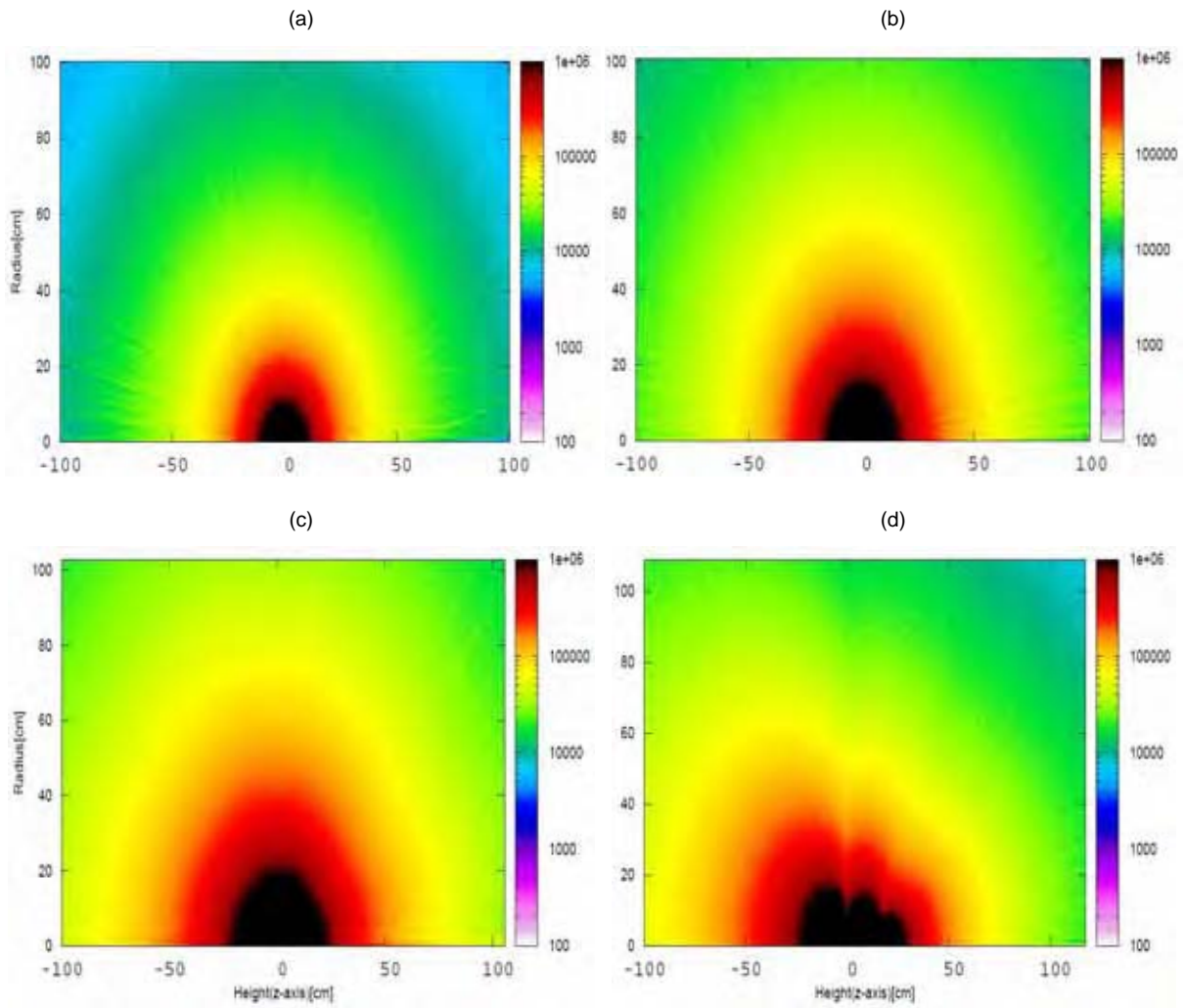
**Figure 5: Ambient dose equivalent rate, as a function of cooling time, from
a boron nitride target impacted by a proton beam of the indicated energies**

EOB values refer to the end of the bombardment. The dose rate is evaluated at 50 cm lateral distance.
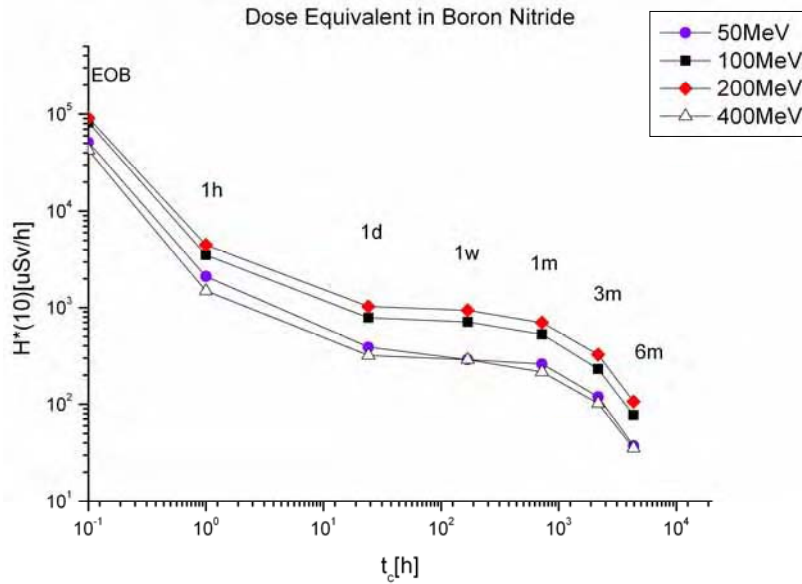
**Figure 6: Ambient dose equivalent rate, as a function of cooling time,
from a carbon target impacted by a proton beam of the indicated energies**

EOB values refer to the end of the bombardment. The dose rate is evaluated at 50 cm lateral distance.
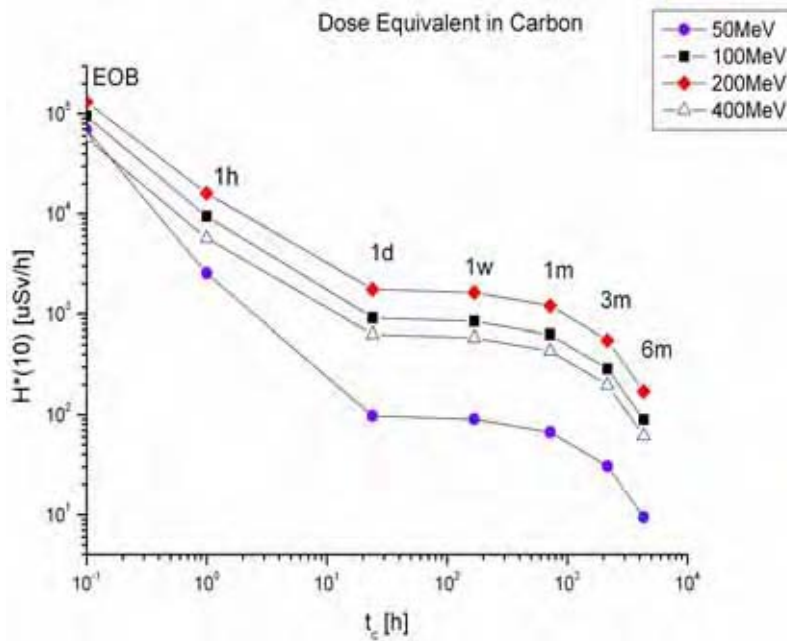
Figure 7: Ambient dose equivalent rate, as a function of cooling time, from a copper target impacted by a proton beam of the indicated energies

EOB values refer to the end of the bombardment. The dose rate is evaluated at 50 cm lateral distance.
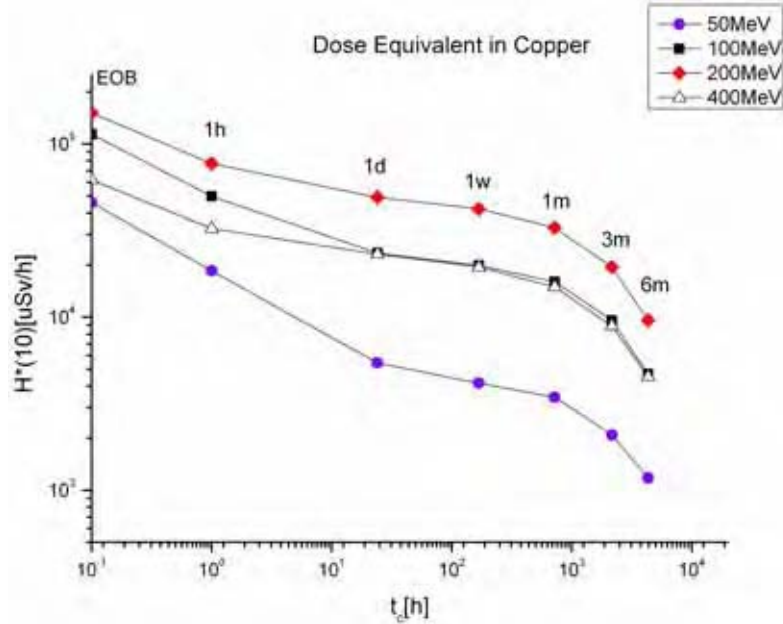
Figure 8: Ambient dose equivalent rate, as a function of cooling time, from an iron target impacted by a proton beam of the indicated energies

EOB values refer to the end of the bombardment. The dose rate is evaluated at 50 cm lateral distance.
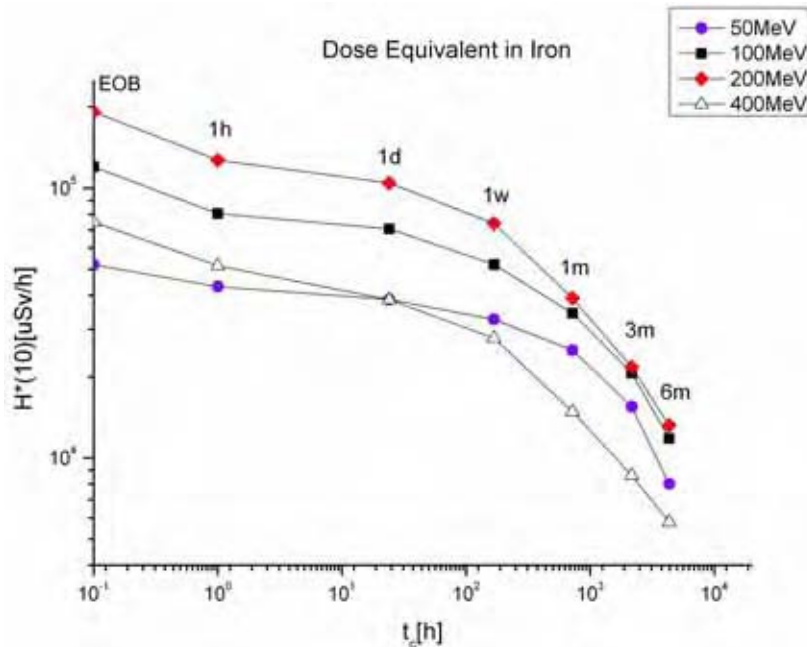
**Figure 9: Ambient dose equivalent rate, as a function of cooling time, from
a stainless steel target impacted by a proton beam of the indicated energies**

EOB values refer to the end of the bombardment. The dose rate is evaluated at 50 cm lateral distance.
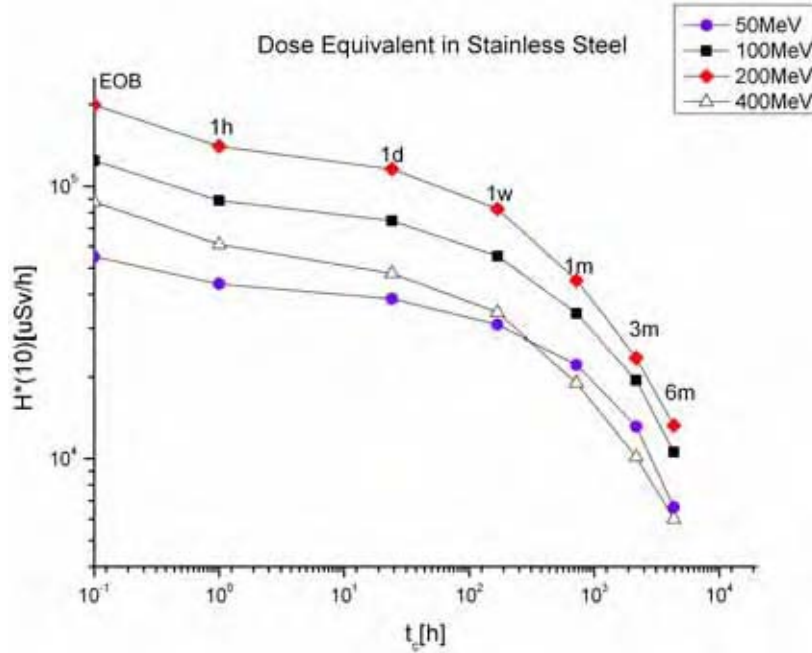
**Figure 10: Ambient dose equivalent rate around an iron target, after irradiation
with a 400 MeV beam, as a function of cooling time for different target radii**
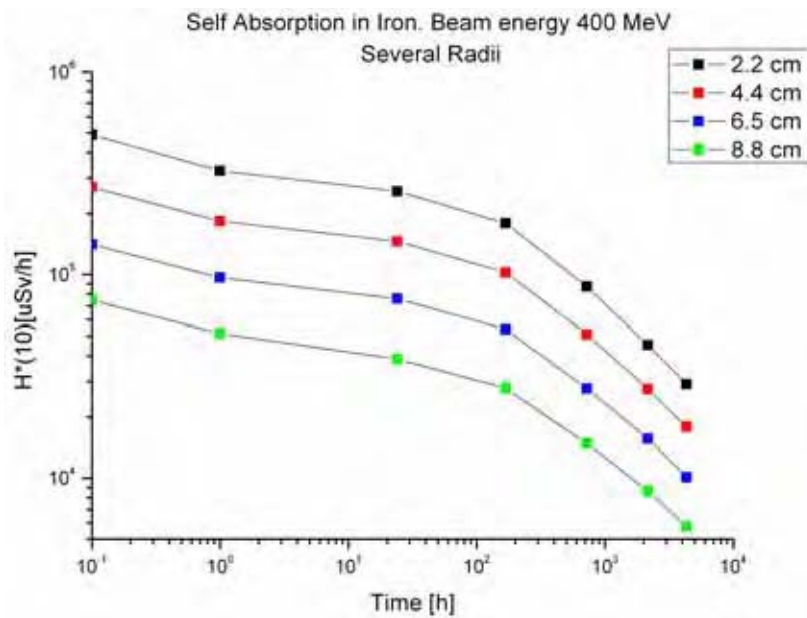
**Table 4: Most abundant radionuclides in carbon and copper at
the EOB and after one month of cooling (400 MeV beam energy)**

Carbon					
EOB			1 month		
Radionuclide	Specific activity [Bq/g]	Total activity [Bq]	Radionuclide	Specific activity [Bq/g]	Total activity [Bq]
C-11	5.40E+06	1.06E+12	Be-7	1.12E+06	2.19E+11
Be-7	1.65E+06	3.24E+11	H-3	9.42E+04	1.85E+10
Be-8	3.12E+05	6.12E+10	Be-10	1.08E-01	2.13E+04
C-10	2.40E+05	4.72E+10	C-14	3.17E-03	6.23E+02
B-12	1.73E+05	3.40E+10			
Li-8	1.72E+05	3.37E+10			
B-8	1.18E+05	2.31E+10			
Copper					
EOB			1 month		
Radionuclide	Specific activity [Bq/g]	Total activity [Bq]	Radionuclide	Specific activity [Bq/g]	Total activity [Bq]
Cu-62	2.26E+07	6.52E+11	Co-58	5.75E+06	1.66E+11
Cu-64	1.52E+07	4.40E+11	Co-57	3.98E+06	1.15E+11
Cu-61	8.72E+06	2.52E+11	Co-56	1.99E+06	5.76E+10
Co-58	7.68E+06	2.22E+11	Mn-54	1.22E+06	3.51E+10
Co-57	4.29E+06	1.24E+11	Fe-55	9.90E+05	2.86E+10
Co-58m	4.12E+06	1.19E+11	Cr-51	9.14E+05	2.64E+10
Co-56	2.60E+06	7.52E+10	V-49	4.88E+05	1.41E+10
Cr-51	1.94E+06	5.60E+10	Co-60	2.28E+05	6.60E+09
Cu-60	1.56E+06	4.52E+10	H-3	2.04E+05	5.88E+09
Cu-66	1.38E+06	3.98E+10	Zn-65	1.85E+05	5.33E+09
Mn-54	1.30E+06	3.76E+10			
Co-60m	1.23E+06	3.55E+10			
Zn-63	1.15E+06	3.32E+10			

**Figure 11: Neutron double differential yield on the carbon (graphite) target boundary.
Impinging beam energy: (a) 50 MeV (b) 100 MeV (c) 200 MeV (d) 400 MeV.**

The relatively high statistical uncertainty for the 50 MeV case is attributable
to the lower neutron production as compared to the higher energies

(a)   (b)

(c)   (d)
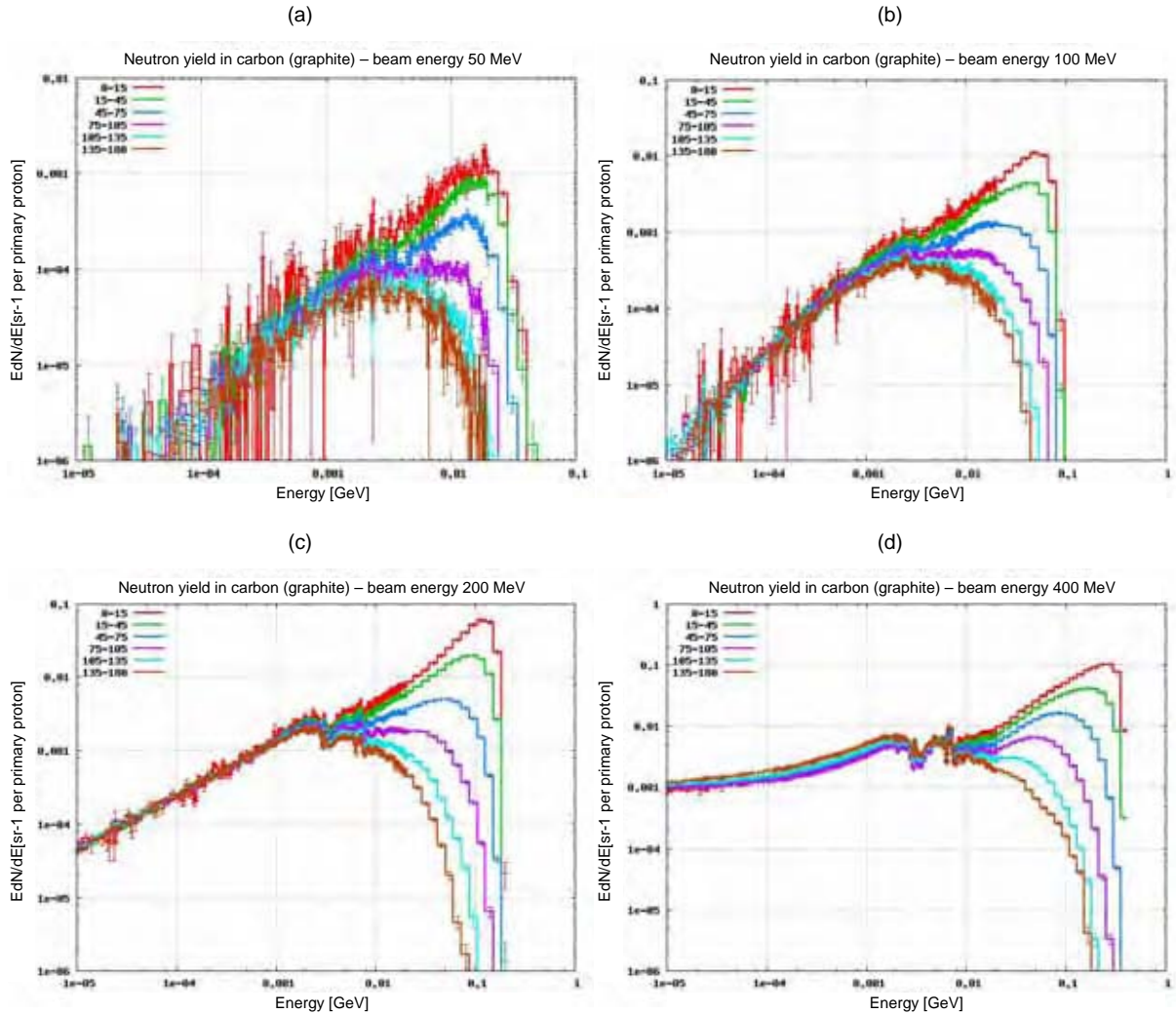
**Figure 12: Neutron double differential yield on the copper target boundary.
Impinging beam energy: (a) 50 MeV (b) 100 MeV (c) 200 MeV (d) 400 MeV.**

(a)   (b)

(c)   (d)
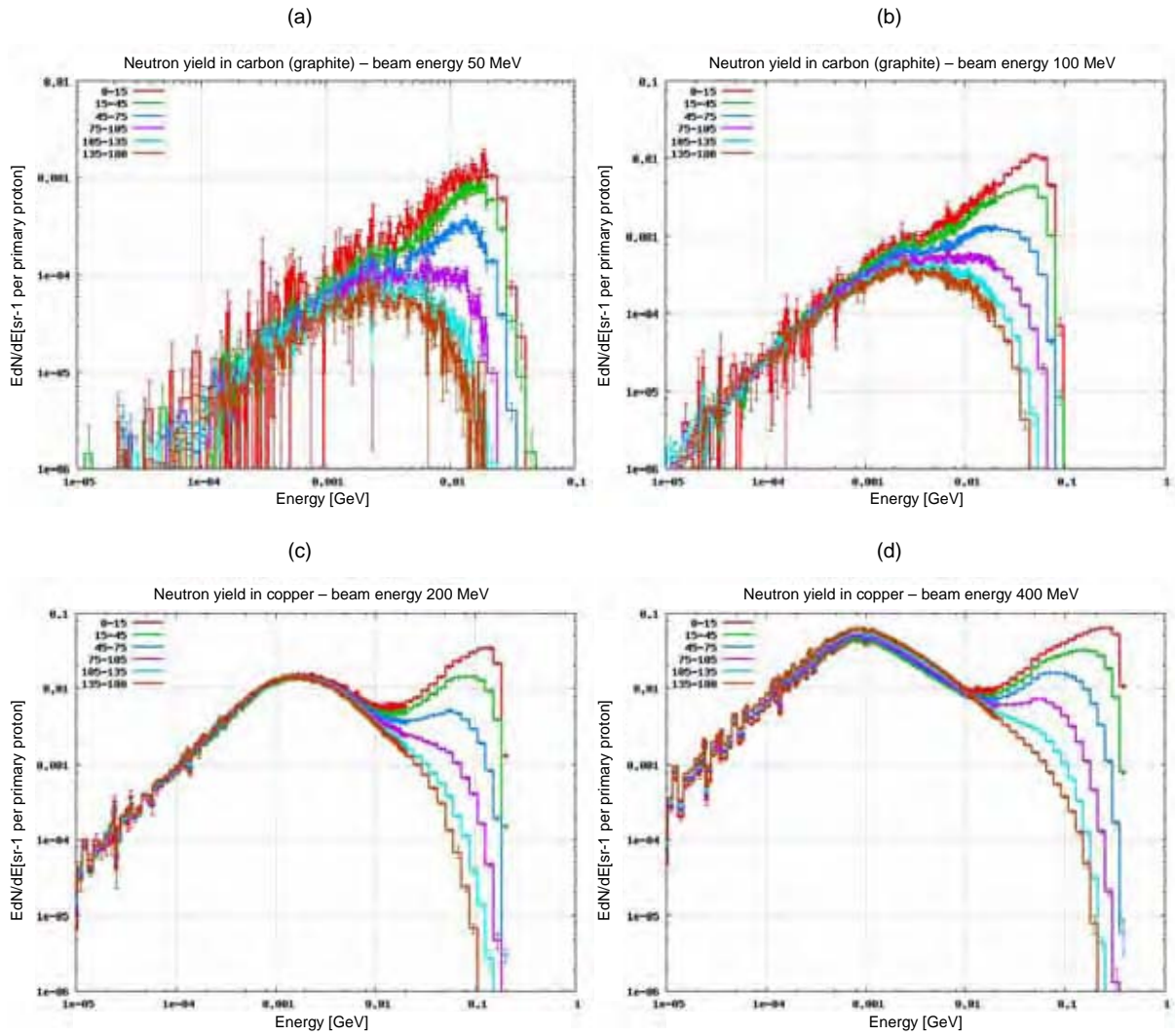
**Figure 13: Neutron double differential yield on the iron target boundary.
Impinging beam energy: (a) 50 MeV (b) 100 MeV (c) 200 MeV (d) 400 MeV**

(a)

(b)

(c)

(d)
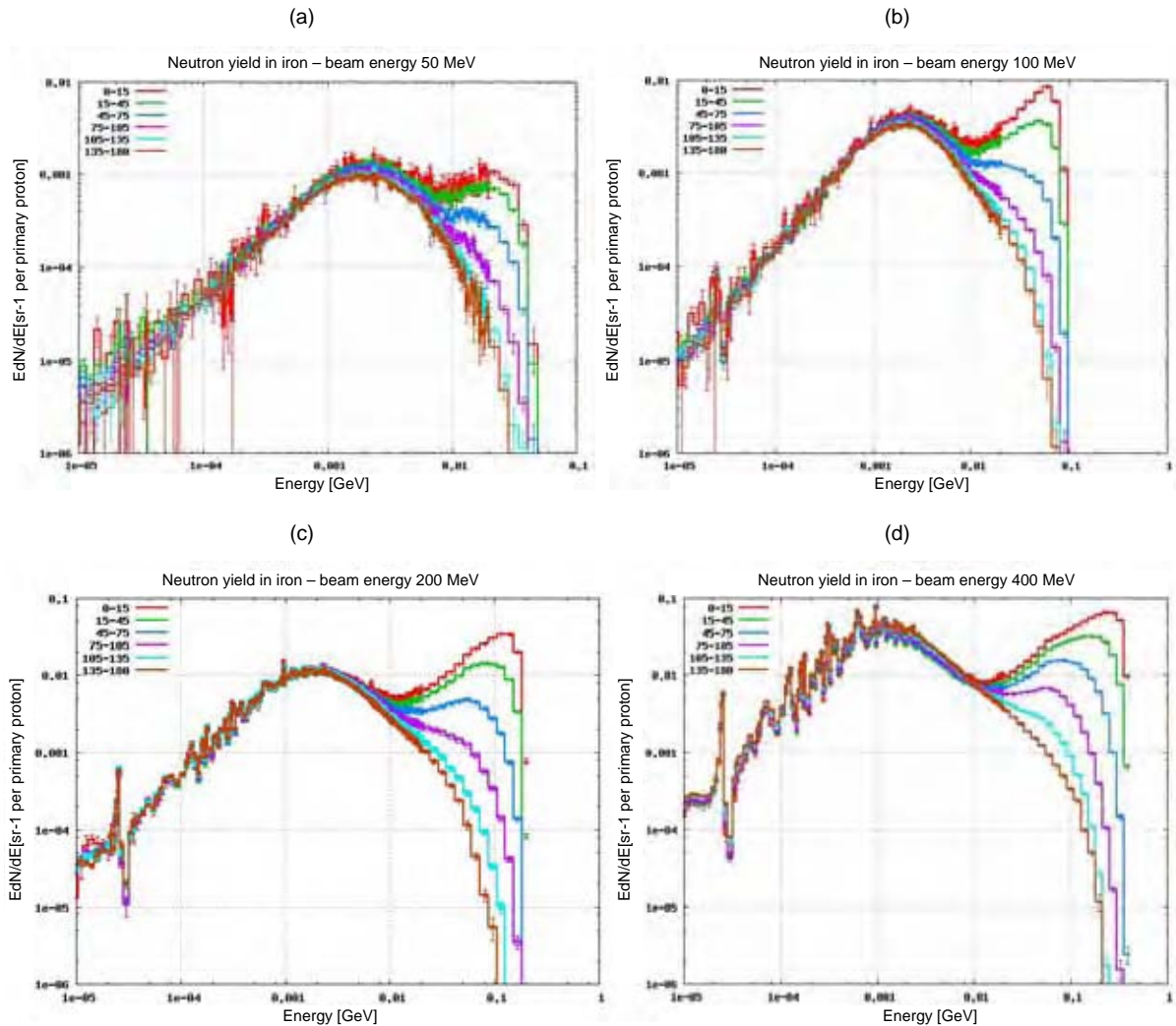
**Figure 14: Effect of the presence of a concrete tunnel around the target
on the ambient dose equivalent. (a) Scoring distance 50 cm laterally
from the target (b) Scoring distance 1 m laterally from the target.**
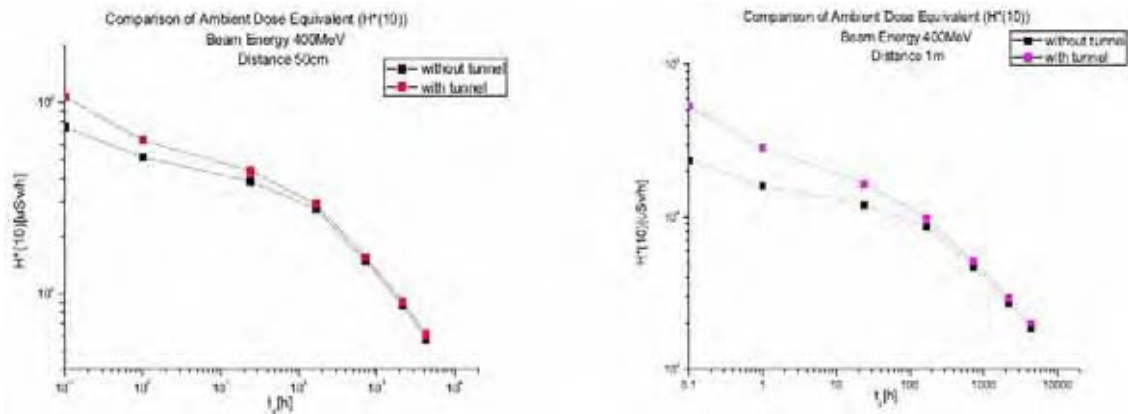
**Figure 15: Comparison of the neutron track-length spectra in air with
and without the concrete tunnel, for an impinging beam energy of 400 MeV**
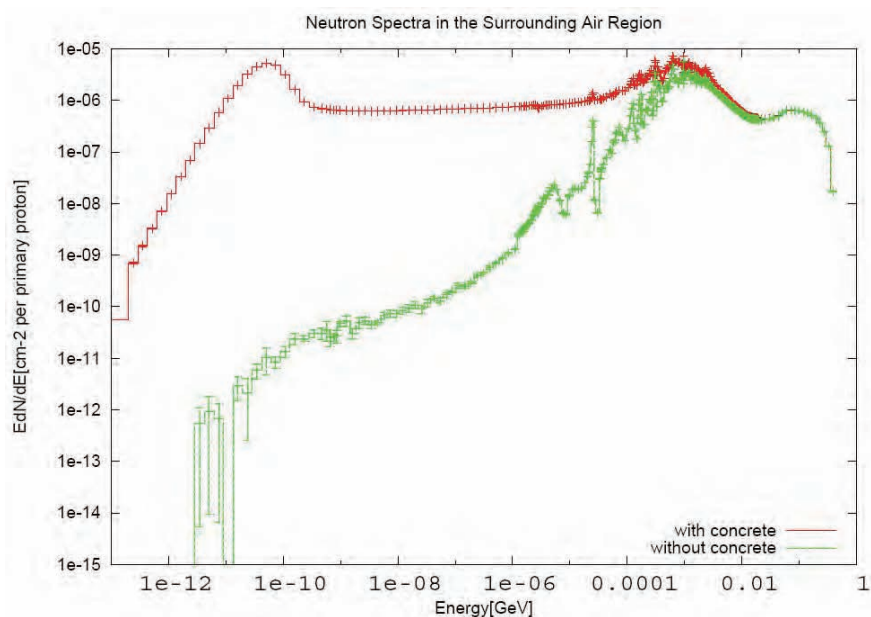
Acknowledgements

We would like to thank Markus Brugger for providing the compositions of the CERN materials and Alfredo Ferrari for useful discussions on the results of the simulations.

References

[1]   Silari, M., "Applications of Particle Accelerators in Medicine", *Radiation Protection Dosimetry*, submitted.

[2]   Arnaudon, L., *et al.*, *Linac4 Technical Design Report*, Report CERN-AB-2006-084-ABP/RF (2006).

[3]   Joseph F. Janni, "Proton Range Energy Tables, 1 keV-10 GeV", *Atomic Data and Nuclear Data Tables*, 27, 147-339 (1982).

[4]   A. Fassò, *et al.*, *FLUKA: A Multi-particle Transport Code*, CERN-2005-10 (2005), INFN/TC_05/11, SLAC-R-773.

[5]   G. Battistoni, *et al.*, *Proceedings of the Hadronic Shower Simulation Workshop 2006*, Fermilab, 6-8 September 2006, M. Albrow, R. Raja (Eds.), AIP Conference Proceedings, 896, 31-49 (2007).

[6]   International Commission on Radiation Units and Measurements (ICRU), *Fundamental Quantities and Units for Ionizing Radiation*, ICRU Report 60 (1998).

[7]   Cerutti, F., N. Charitonidis, M. Silari, *Neutron Double Differential Distributions, Dose Rates and Specific Activities from Accelerator Components Irradiated by 50-400 MeV Protons*, CERN Technical Note CERN-SC-2010-014-RP-TN (2010).

Activation studies on benefit of the selection of the ESS target concept*

Dana Ene
European Spallation Source (ESS)
Scandinavia Secretariat
Lund University, Lund, Sweden

Abstract

Presently, the ESS project is in the update phase of the conceptual design that was preliminarily defined in 2003 through the joint efforts of several European countries.

According with the baseline of the ESS update design, the linac will deliver 5 MW of 2.5 GeV protons to a single target, in 2 ms long pulses with a 20 Hz repetition rate.

The material activation in such a facility is an important aspect that has to be taken into account in the early design phase. In particular the choice of the target material and the design of the target have to consider the following radiation protection issues: i) radiation level received by personnel during maintenance; ii) accident scenarios; iii) the production, handling and disposal of the radioactive wastes.

The aim of this work is to assess the radioactive inventory, decay heat and resulting gamma-ray spectra determining the radiation levels expected during maintenance work and to evaluate the amount of the residual radioactivity to be disposed of after the facility will shut down for various target concepts under analysis.

In this respect a comparison of the two code systems: i) MCNPX2.6.0 (particle transport) and CINDER'90 (activation); and ii) PHITS (particle transport) and DCHAINSP 2001 (activation) was initially done in order to investigate their predictions and to determine the appropriate simulation tool for the problem.

Results of a sensitivity analysis accounting for various proton beam conditions (energy and profile) are also discussed.

---

* The full paper being unavailable at the time of publication, only the abstract is included.

Nuclide inventory in proton-irradiated lead: Comparison of simulation and measurement

D. Kiselev[1], Y. Dai[1], S. Lüthi[1], J. Neuhausen[1],
D. Schumann[1], P.W. Kubik[2], H-A. Synal[2], V. Alfimov[2]
[1]Paul Scherrer Institut, Villigen, Switzerland
[2]Swiss Federal Institute of Technology (ETH), Zurich, Switzerland

Abstract

The ring cyclotron at the Paul Scherrer Institut's (PSI) accelerator facility produces protons of 590 MeV with a current of up to 2.3 mA at present. After penetrating two graphite targets with an effective thickness of 0.5 cm and 4 cm, the beam is dumped into the target of the spallation neutron source SINQ. This target consists of several tens of rows of steel tubes (currently Zircaloy) filled with lead. After two years in operation, the target has become highly activated and needs to be replaced due to radiation damage of the material. After a cooling period, the used SINQ targets are treated as radioactive waste which needs to be disposed of. For this procedure, the nuclide inventory is required by the authorities. For components directly activated by the proton beam, it is calculated using MCNPX coupled to build-up and decay codes like SP-FISPACT07 and CINDER'90. For the calculation, three physical models available in MCNPX were applied: BERTINI-DRESNER-RAL, ISABEL-ABLA and CEM3.02.

The calculated nuclide inventory is compared to measured activities of several isotopes extracted from a central lead rod of SINQ Target 4, which was irradiated with 10 Ah. The rod was cut into several pieces. Two pieces from different positions along the lead rod were analysed employing radiochemical separation where necessary. The gamma measurements were made with a high-purity germanium detector (HPGe). For long-lived radionuclides such as ^{26}Al and ^{36}Cl, accelerator mass spectrometry (AMS) was used. Due to the position of the two samples, they have seen different compositions of proton and neutron flux spectra, which leads to a different nuclide inventory. Since the sizes of the samples are quite small, more effort was needed to achieve a reasonable statistical error in the Monte Carlo simulation.

The need for activation calculations

In the environment of a proton accelerator facility like PSI, the surroundings get activated due to the interaction of primary protons with material, in particular in the vicinity of loss points like targets, collimators and beam dumps. Further away from the loss points, neutrons produced by nuclear reactions of the primary protons cover large distances, which leads to a larger volume of radioactive material. If components close to the beam line have to be replaced due to malfunctioning or upgrading they become radioactive waste, which must eventually be stored in a final repository if the nuclide inventory is far above the exemption limits. In this case, the Swiss authorities require the declaration of the nuclide inventory. Since the measurement of the complete nuclide vector is not feasible, the use of calculational methods, which have to be validated, is accepted by the authorities. Therefore, validation by periodical comparisons with experimental data is required. Activation calculations are also needed for the planning of safe dismantling procedures of installations and facilities at the end of their lifetime. In addition, they are used to estimate the amount of material which needs to be disposed as radioactive waste or which can be temporarily stored for free release after a sufficient cooling time. Nowadays, to obtain approval for the operation of a new installation or facility, an estimation of the amount of waste after the final shutdown of the facility is required.

At PSI, the high-intensity proton accelerator (HIPA) [1] generates a beam of 590 MeV at a current of 2.3 mA at present. The accelerator facility consists of a Cockroft-Walton pre-accelerator, an injector cyclotron (Injector II) and the ring cyclotron. Injector II is used to pre-accelerate the protons to 72 MeV. The high-intensity proton beam is used for miscellaneous experimental research and applied physics with mesons and neutrons. Pions are produced by the interaction of the protons with two graphite wheels of 5 mm and 40 mm thickness. Polarised muons are obtained via the decay of the pions. Due to multiple scattering, the beam is broadened and needs to be shaped by a collimator system with an elliptical aperture, which leads to 18% beam loss. The two targets as well as the collimators are locations where a considerable fraction of primary protons activates the surrounding material. After passing the collimator, the beam is bent down and hits the spallation target of the SINQ facility vertically from below. The spallation target consists of several tens of rows of Zircaloy tubes filled with lead. An older version of the target, from which activated samples were taken, will be described in more detail below. The neutrons are moderated in large volumes of heavy water (D_2O) around the target as well as in cold deuterium at 25 K and are then transported to the 13 instruments installed at SINQ. By the end of 2010, a pulsed spallation source producing ultracold neutrons (UCN) will be brought into operation.

Lead samples from one of the older SINQ targets (Target 4) were analysed on their nuclide content as part of the validation programme for the activation calculations at PSI.

Method for obtaining the nuclide inventory and dose rates

The first step for obtaining a nuclide inventory is the calculation of isotope production cross-sections as well as neutron fluxes, which later get folded with neutron reaction cross-sections. Since the proton can induce many nuclear reactions besides the continuous slowing down, producing several secondary particles like neutrons, pions and alphas, the calculation is done by a Monte Carlo program. At PSI, the particle transport program MCNPX [2,3] is used to calculate the activation induced mainly by direct irradiation. It can handle several types of particles like neutrons, protons, pions, photons but also light to heavy ions in the newer versions from 2.6.f on. Since the neutrons are an important contributor to the induced activity and due to their ability to travel large distances, not only the geometry of the sample is needed but also that of its surroundings. The material composition of the regions of interest has to be known as close as possible to the actual one, since small additions of isotopes on the ppm level can significantly contribute to the nuclide vector if the size of the production cross-section is large. The difficulty in the Monte Carlo simulation is to get good statistics for the small fractions in the material composition. This problem was overcome by the *active* card [4], implemented by F.X. Gallmeier in MNCPX2.5.0, which allows all elements of the material composition, including impurities, to undergo a nuclear reaction at each collision (subsequently, the appropriate weight is applied). This is of advantage when good statistics have to be collected to achieve an acceptable uncertainty.

The reaction cross-sections can be obtained via tables from evaluated libraries or by physical models. For neutrons of energies E less than 20 MeV, no appropriate models are available due to the importance of the shell structure of the nuclide. On the other hand, the cross-section library ENDF/B

offers an almost complete coverage of all reactions involving neutrons with E < 20 MeV on almost all relevant isotopes of the nuclide chart. In this calculation, the ENDF/B-VI library for neutrons with E < 20 MeV was used. For all other reactions, the following models were applied: BERTINI-DRESNER-RAL, ISABEL-ABLA and CEM3.02. These models rely on the assumption that the nuclear reaction takes place essentially in three stages: the Intra-nuclear Cascade (INC), the pre-equilibrium and the equilibrium evaporation/fission stage. The energy introduced by the primary particle is dissipated to several nucleons by nucleon-nucleon collisions. The INC proceeds until the dissipated energy falls below a specified value, related to the depth of the nuclear potential well. The typical duration of the intra-nuclear cascade is 10^{-22} seconds. During the INC, high energetic particles might be emitted in the forward direction. Sometimes, particularly in older models, the second stage can be switched off or is omitted. Nowadays, it is known that light particles can already be emitted before the equilibrium is reached. These particles have higher energies than the ones from the evaporation stage and they are emitted preferably in the forward direction. The versions of BERTINI [5,6] and ISABEL [7] used in MCNPX2.5.0 contain the pre-equilibrium stage. The nucleus loses its energy (de-excitation) by evaporating particles or by fission. Mainly low-energetic neutrons of 1-2 MeV are emitted, but larger clusters can also be emitted. The evaporation is covered by the DRESNER [8] code whereas RAL [9] provides the fission. In the models mentioned above, only CEM3.02 [10], the Cascade Exciton Model, is able to create light fragments up to ^{28}Mg. CEM3.02 contains all three stages and no other codes need to be linked. The third stage in CEM3.02 is processed by GEM2 [11], which contains RAL but with modified fit parameters. With the newest version of ABLA [12], not yet implemented into MCNPX, it is also possible to release clusters up to a mass number of 8 including ^{4}He during the evaporation/fission stage. For this, the code was extended by a coalescence model. The version ABLAV3p [13], available in MCNPX2.5.0, can only emit neutrons, protons and ^{4}He. Therefore the tritium content is always underestimated using ABLAV3p.

To obtain the nuclide production rates for neutrons of E < 20 MeV, the corresponding fluxes have to be folded with production cross-sections. The production rates from models are directly written to the output of MCNPX using the *active* or *histp* card. Decay and build-up of the nuclide inventory needs to be taken into account by providing the irradiation history to external programs made for such purpose. To simplify the coupling between the results of MCNPX and decay and build-up codes, a PERL script ("activation script" [14]) was used. It provides the information needed by CINDER'90 version 7.4.2 [15], SP-FISPACT07 [16], Orihet3 [17] via an input mask. CINDER'90 includes its own cross-section library, whereas for FISPACT07, the EAF2007 [18] library is used. The nuclide inventory is extracted from the output files by a user-written FORTRAN code. The output also contains photon emission data from the decaying nuclides. They can be used as photon source in MCNPX to calculate dose rates. The source definition appropriate for the use with MCNPX is automatically prepared via a Perl script ("gamma script" [19]). If the dose rates one wants to compare with were measured in another environment as the component was irradiated in, the geometry input must be modified accordingly.

Activation calculation for Pb samples from SINQ Target 4

A sketch of the lower part of the SINQ Target 4 insert is shown in the left part of Figure 1. The target consists of steel 316L tubes, which are filled with Pb (90% filling factor), except for the ones later used for testing their mechanical properties after irradiation (so called STIP probes). In addition, the first row of tubes is intentionally left empty to achieve a better distribution of the cooling medium, D_2O. The target holder is made out of Zircaloy and has a rectangular cross-section. The AlMg (3%) container consists of two shells and serves safety purposes (safety hull). The right part of Figure 1 shows the central part of the model for the SINQ target station. The tubes appear to have an oval shape, since the model is not cut orthogonally through the tubes. On the far left side, a part of the cold moderator is shown. Both target and moderator are surrounded by D_2O. Behind the target, several meters of steel blocks shield the secondary particle production.

The proton beam hits the target from below and has an elliptical profile which just fits the rectangular shape of the target, if tilted by 45°. The intensity distribution of the beam is taken as Gaussian with standard deviations of σ_x = 2.1 cm and σ_y = 3.0 cm. In fact, the beam profile was measured using the intensity distribution of the gamma radiation at the front of the irradiated safety hull [20]. It turns out that the profile is close to an ideal Gaussian. Differences in calculated fluxes in the target, due to the small deviation from a Gaussian shape, are negligible (see below).

Figure 1: Left: Sketch of the SINQ target insert No. 4. The tubes are from steel 316L and filled with lead. Right: Cut through the geometrical model built in MCNPX. Due to the oblique cut, the cross-section of the rods looks oval shaped.
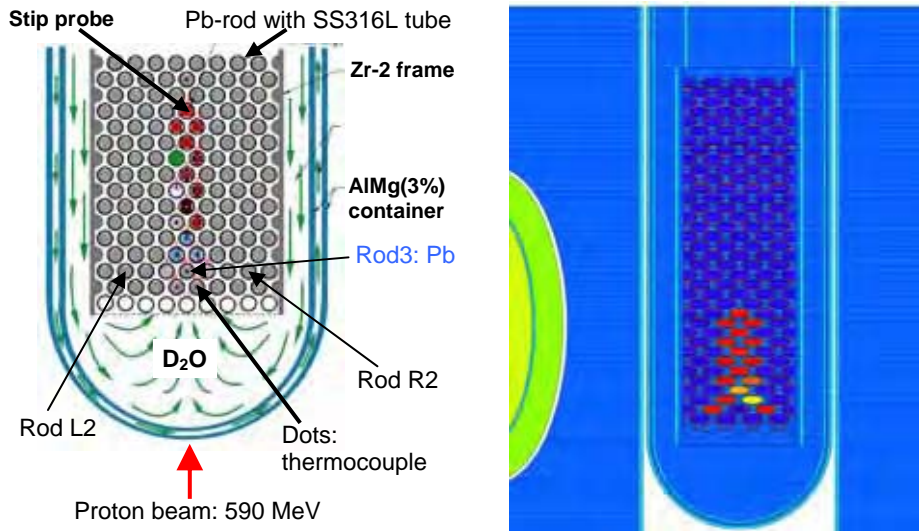
SINQ Target 4 was in operation from March 2000 to December 2001. The total charge sums up to 10.03 Ah. The two Pb samples taken are from Rod 3. It is the central rod in the second (filled) row. Its position is marked in Figure 1. The rod itself is shown in Figure 2 with the locations of the samples D9 and D14 indicated. D9 is 2.5 cm away from the beam centre; D14 is located on the same side but at 5 cm distance from the centre. The diameter of the samples is about 10 mm and their thickness 1.5 mm. The small size of the samples has the advantage that their positions are well localised.

Figure 2: Rod 3 from SINQ Target 4 and its dimension.
The locations of the samples D9 and D14 are indicated.
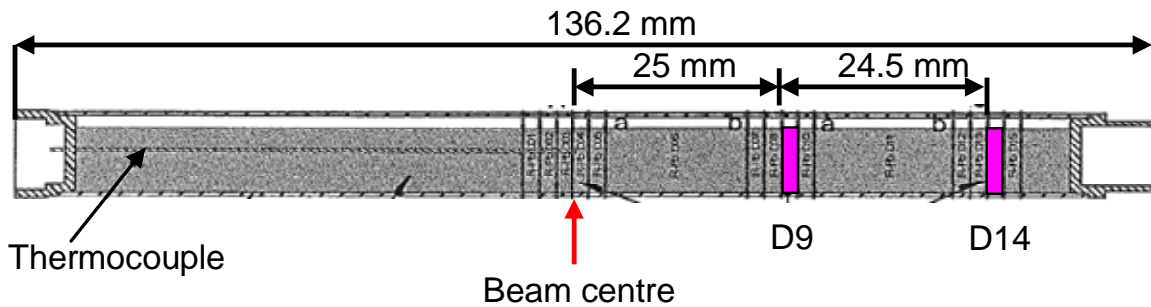
The material composition used for the lead filling in the steel tubes of the target is shown in Table 1. The main elements beside Pb are antimony (Sb), copper (Cu) and bismuth (Bi). The material analysis [21] was performed specifically for the lead to be used in Target 4, employing the method of Induced Coupled Plasma-Optical Emission Spectroscopy (ICP-OES). Two material samples were analysed. The values shown in Table 1 are averages from the two analyses. In fact, only half of the analysed elements are listed, since the others were below the detection limit. To estimate a possible error in the activity calculation due to the material composition used, a second material vector was built, which includes elements below the detection limit; their abundance was set to the detection limit. The additional elements in the second material composition are listed in the last two rows of Table 1. The effect on the nuclide inventory will be discussed below.

Table 1: Material composition of lead used in the MCNPX calculation. On the right, additional elements below the detection limits of the material analysis are shown.

Element	Pb (w-ppm)	Element	Pb (w-ppm)	Element	Pb (w-ppm)	Element	Pb (w-ppm)
Na	28	Zn	5.8	Ce	2.0	Ir	2.0
Mg	0.4	Ge	24.1	Nd	3.0	Os	10.0
Al	1.5	Mo	2.5	P	2.0	In	10.0
P	17.5	Ag	45.4	Sn	3.0	Ru	3.0
S	16.5	Sn	130	Hg	5.0	Ga	2.0
Ca	2.6	Sb	1 039.5	K	6.0	Pt	20.0
Ti	0.4	Ba	0.3	Cs	2.0	Pd	3.0
Cr	1.8	Tl	4	Se	5.0	Rh	2.0
Fe	9.2	Pb	998 000	W	10.0	U	5.0
Ni	6	Bi	220.5	Te	5.0	Th	2.0
Cu	467			Re	2.0		

Evaluation of the proton and neutron fluxes

The left-hand graph in Figure 3 shows the proton and neutron fluxes along Rod3, simulated with MCNPX. The centre of the rod is located at zero and the positions of both samples are indicated as well. The calculation was performed with and without the STIP samples. The effect can be clearly seen in the reduction of the neutron flux by about 20%. This is due to the higher neutron absorption cross-section of the materials filled in the STIP tubes compared to lead. For these calculations, a Gaussian beam profile was used, as mentioned above. The lines represent Gaussian fits to the data. The blue points were obtained using a pointwise source definition in MCNPX, derived from the gamma radiation distribution in front of the safety hull. The difference from the one in red, which uses the Gaussian beam, is small: the neutron and proton fluxes for D9 are reduced by a few per cent. In general, the neutron distribution is much broader compared to protons, because the neutrons are secondary particles from nuclear reactions with a broader angular distribution.

Figure 3: Left: Proton and neutron flux distribution in Rod3. The positions of the samples D9 and D14 are indicated. Right: Neutron and proton fluxes in the D14 sample and rod L2. The fluxes are normalised to one primary proton.
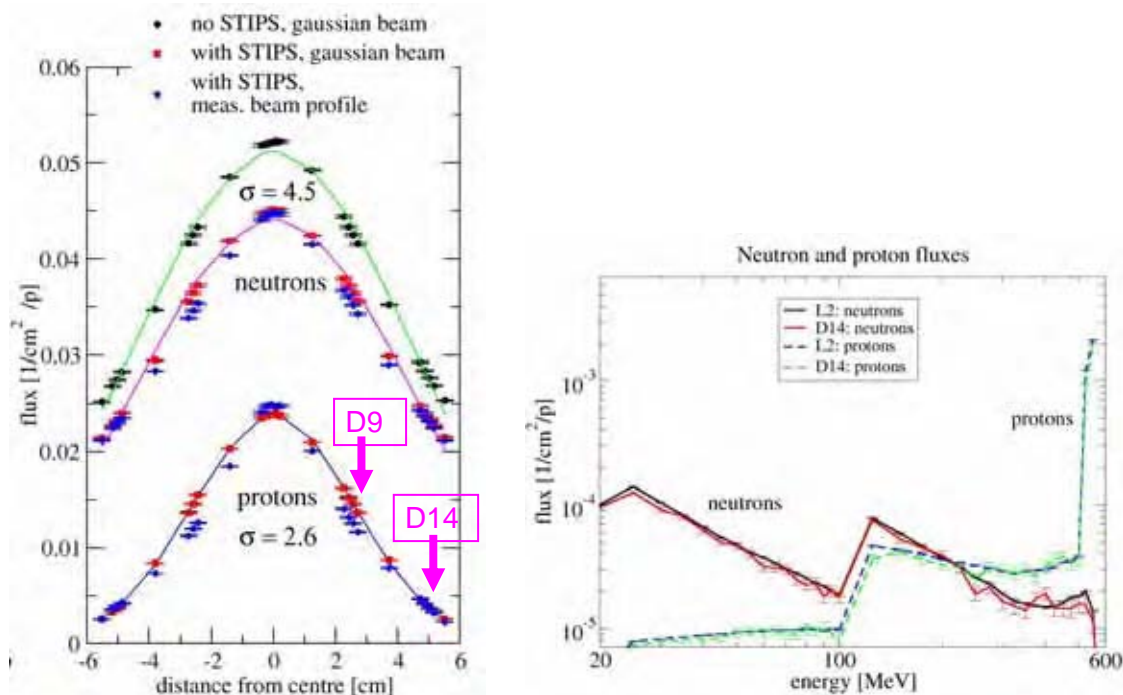
It was found that the neutron and proton fluxes of the D14 sample are almost identical to the corresponding fluxes averaged over rod L2 (see Figure 3, right), which is the second outer one in the row (see Figure 1, left). Due to the symmetric beam profile, the flux in L2 is the same as in rod R2. Similarly, the fluxes in D9 are just the ones averaged over Rod3. This fact was exploited to sample much larger regions than the size of D9 and D14. This is needed to get sufficient statistics for the isotope production rates in D9 and D14.

Experimental results for the activity

A detailed γ–analysis was carried out at the end of September 2006, using a high-purity germanium detector. After a chemical separation [22], ^{26}Al and ^{36}Cl was measured by accelerator mass spectrometry (AMS) at ETH Zurich. The results are shown in Table 2. The sensitivity of both detection methods is reflected in the small sample size (in fact, a few milligrams of material are sufficient) and in the small activity measured with AMS. This is beneficial for the personnel measuring and preparing the samples with respect to the accumulated dose.

**Table 2: Specific activity of selected radionuclides in D9 and
D14 of Rod 3 (measuring dates: γ – 09/2006, LSC – 11/2006)**

	D9 [Bq/g]	D14 [Bq/g]		D9 [Bq/g]	D14 [Bq/g]
^{207}Bi	$3.00 \cdot 10^7$	$1.01 \cdot 10^7$	^{106}Ru	$4.83 \cdot 10^6$	$3.91 \cdot 10^6$
^{172}Lu/^{172}Hf	$2.00 \cdot 10^7$	$5.41 \cdot 10^7$	^{110m}Ag	$1.29 \cdot 10^6$	$3.93 \cdot 10^5$
^{173}Lu	$2.76 \cdot 10^7$	$4.30 \cdot 10^7$	^{125}Sb	$1.32 \cdot 10^6$	–
^{194}Au/^{194}Hg	$1.86 \cdot 10^7$	$3.13 \cdot 10^6$	^{133}Ba	$2.8 \cdot 10^6$	$7.94 \cdot 10^5$
^{102m}Rh	$5.53 \cdot 10^6$	$1.44 \cdot 10^5$	^{44}Sc/^{44}Ti	$8.00 \cdot 10^4$	$2.84 \cdot 10^4$
^{202}Tl/^{202}Pb	$4.80 \cdot 10^5$	$1.87 \cdot 10^5$	^{108m}Ag	$3.75 \cdot 10^5$	$1.56 \cdot 10^4$
^{60}Co	$3.67 \cdot 10^6$	$1.40 \cdot 10^6$	^{194m}Ir	$2.61 \cdot 10^4$	–
^{54}Mn	$2.29 \cdot 10^5$	$7.01 \cdot 10^4$	^{26}Al	0.5	0.2
^{58}Co	$1.55 \cdot 10^6$	$9.47 \cdot 10^5$	^{36}Cl	$9.5 \cdot 10^1$	$4.8 \cdot 10^1$

Comparison to the calculations

In the following figures, the activities in the D9 and D14 samples are compared to the calculations. The efficiency of the calculation was improved by using a larger sampling region, as mentioned above. For neutron fluxes of E < 20 MeV, statistics is not an issue. Therefore, two separate runs were made. For the calculation of the production rates the neutron energy was restricted to E > 20 MeV. This accelerates the calculation time significantly. Depending on the model, up to $5 \cdot 10^8$ primary protons could be processed in 17 h on 512 CPU on the Horizon Cluster of CSCS in Manno.

Figure 4 shows the results for the BERTINI-DRESNER-RAL model, Figure 5 for ISABEL-ABLA and Figure 6 for CEM3.02. For the latter calculation, MCNPX2.7.c was used, which is the newest available version. The other simulations were performed with MCNPX2.5.0, since the applied models have not been changed in the newer versions. For all calculations, CINDER'90 version 7.4.2 was used in conjunction with MCNPX.

In all calculations and in both samples, ^{36}Cl is significantly underestimated by a factor of about 10. The reason is probably that chloride is missing in the material composition. Therefore, the main production of ^{36}Cl via neutron capture on ^{35}Cl cannot take place. Since the method used for the material analysis, ICP-OES, cannot detect gaseous elements like chloride, it might be present in the material. Another prominent deviation is observed on ^{194m}Ir. It was only detected in the D9 sample and no ^{194}Ir has been measured. Using the measured ^{194m}Ir activity as ^{194}Ir activity, the ratio for ^{194}Ir has also been plotted. It is interesting to note that a good agreement would be achieved, if the definition of the metastable and ground state were exchanged in the simulation. Iridium itself is not present in the material composition but has a detection limit of 2 ppm. Using the material composition including the impurities below the detection limit, an increase of only 30% more ^{194m}Ir is obtained.

Figure 4: Ratio of the measured to calculated activity, on the right for the D9 sample, on the left for the D14 sample. The BERTINI-DRESNER-RAL model was used. Note that ^{194}Ir was not measured.
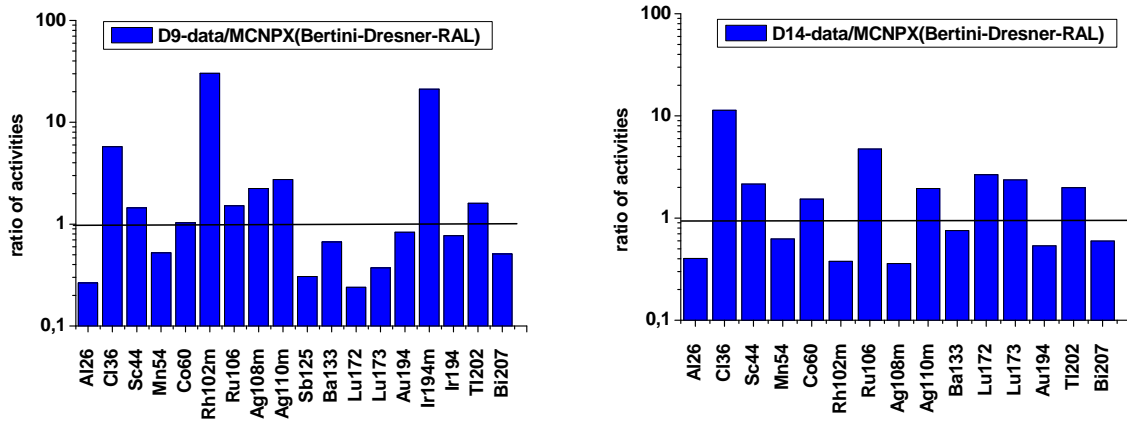
Figure 5: Same as Figure 4 but for the ISABEL-ABLA model. Note that ^{194}Ir was not measured.
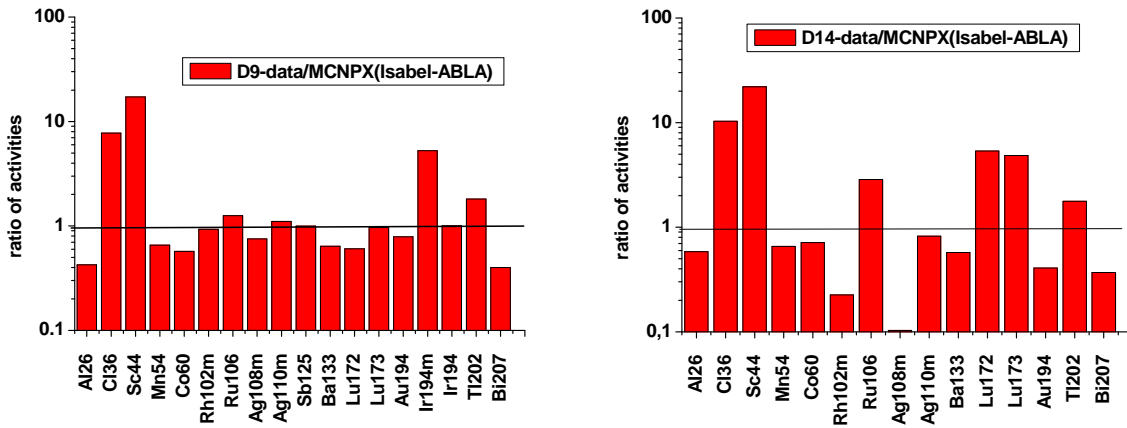
Figure 6: Same as Figure 4 but for the CEM3.02 model. Note that ^{194}Ir was not measured.
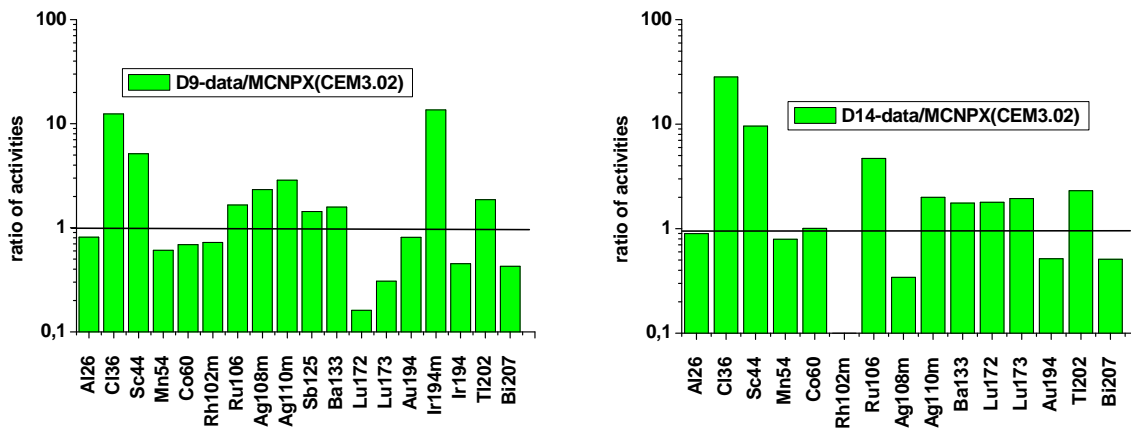
For the D9 sample, the model BERTINI-DRESNER-RAL over-predicts [26]Al as well as the deep spallation region. This deficiency is overcome by ISABEL-ABLA. CEM3.02 gives too-large values for the Lu isotopes. Compared to BERTINI-DRESNER-RAL, the other two models show a significant underestimation for [44]Sc in both samples.

The D14 sample shows similar characteristics when compared to the predictions. Most striking is the large overestimation of [108m]Ag with ISABEL-ABLA and [102m]Rh with CEM3.02. However, the other two models also show these tendencies for both isotopes. These deficiencies were not observed for the D9 sample. However, since the compositions of neutron and proton fluxes are different for the two samples, this discrepancy cannot be interpreted as an uncertainty in the measured activities. In D14, the intensity of protons and neutrons of E > 20 MeV is five times less than of neutrons with E < 20 MeV, whereas for D9 it is only two times less. Thus, their contribution to the induced activity is different.

Activities were also calculated using the combination MCNPX and FISPACT07 for comparison. The main differences are: No [194m]Ir at all would be obtained after five years of cooling time. In addition, the activities for both Lu-isotopes would be reduced by a factor of 2-3 using CEM3.02, which would even worsen the agreement.

It should be mentioned that the requirement to have almost identical flux distribution is not very strict. Almost the same nuclide inventory is obtained when all rods of the second row of the SINQ target are used for sampling. The two rods with STIP samples have to be excluded. The reason is that the cross-sections are almost flat for energies larger than 200 MeV. Only for residual nuclides close to the target nuclei up to 20% deviations are observed. These radioisotopes are mainly produced by direct reactions whose cross-sections depend on the energy of the projectile.

Comparison of measured and calculated dose rates

Ten months after the end of beam, the target insert was transported to the hot cell. Before dismantling, dose rates were measured along the target and the first shielding section in a distance of 3 cm, 30 cm and 100 cm at the positions shown in Figure 7. At this time, the D_2O used for cooling and moderating, was already drained, which is taken into account in the simulations. These calculations were performed with MCNPX2.5.0 using the BERTINI-DRESNER-RAL model and CINDER'90.

Figure 7: Layout of the Target 4 insert. The labelled dots indicate the locations of the measured dose rate.
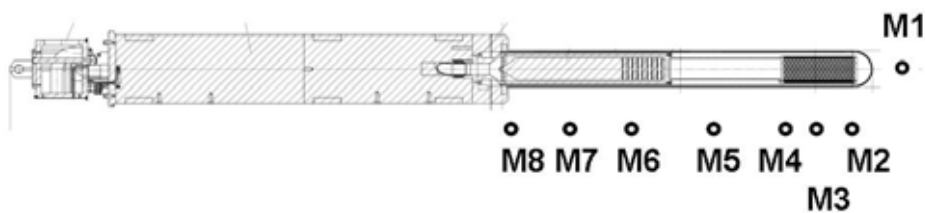
The measured and calculated dose rates at 100 cm are shown in Figure 8. The deviations are within a factor of 2, which is the usual predictive power of the applied technique. However, for the dose rates at 3 cm, much worse agreement is achieved along the steel shielding. Some investigations show that more precise predictions require the division into finer regions (cells) along the first steel shielding. The target was already subdivided into small regions, each corresponding to one row of lead tubes.

Summary

Several radioisotopes were measured in two samples of a central Pb-rod in the SINQ Target 4 using accelerator mass spectrometry and an HPGe gamma-ray detector. These samples were chosen because they were activated by different compositions of neutron and proton fluxes. The activities were calculated using MCNPX coupled to the decay and build-up code CINDER'90v7.4.2. The statistical

Figure 8: Dose rates in Sv/h at 100 cm distance along Target 4 (see Figure 7). The measured values are indicated by the squares, the calculated dose rates by the blue dots.
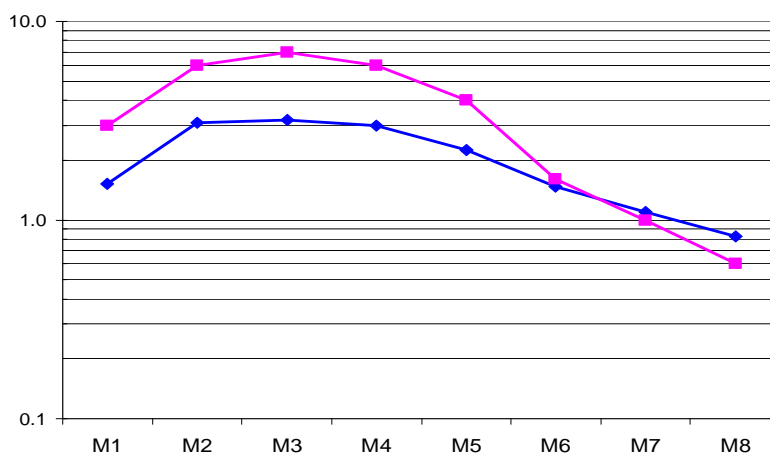
uncertainty was improved by using larger sampling regions with essential the same neutron and proton fluxes as for the two samples. Other regions with different flux distributions were used and confirmed that the calculated activities depend little on the specific choice, since most cross-sections are almost constant above 200 MeV nucleon energy.

The experimentally determined activities were compared to the calculated ones using three different physical models: BERTINI-DRESNER-RAL, ISABEL-ABLA, CEM3.02. The overall agreement is good (within a factor of 3) with larger discrepancies for individual nuclides, depending on the model. Even though the first model is the default in MCNPX, it lacks predictive power particularly in the deep spallation zone. On the other hand, a significant underestimation of ^{44}Sc was observed in both samples for the two other models. Using ISABEL-ABLA or CEM3.02 leads to a much better agreement in the case of ^{26}Al. The disagreement for the ^{194m}Ir activity could be resolved if the metastable and ground state were exchanged in the calculation. The results obtained with FISPACT07 instead of CINDER'90 are similar for most of the isotopes measured.

Finally, the dose rates along the target and the first shielding section were measured in the hot cell before dismantling. At a distance of 100 cm from the safety hull, they agree with the calculated ones within a factor of 2. Closer to the hull the deviations get large in the shielding region. The reason is that the shielding was not subdivided into smaller regions. Therefore, the inhomogeneous activation is not taken into account. In the target model, each row of rods is represented by one region (cell).

Acknowledgements

References

[1]   Adam, A., M. Seidel, *et al.*, "Production of a 1.3 MW Proton Beam at PSI", *Proc. of the 1st. Int. Part. Acc. Conf. (IPAC10)*, Kyoto, Japan (2010), forthcoming.

[2]   Pelowitz, D.B. (Ed.), *MCNPX Users Manual, Version 2.5.0*, Los Alamos National Laboratory, LA-CP-05-0369, Los Alamos (2005).

[3]   Pelowitz, D.B., *et al.*, *MCNPX 2.7.C Extensions*, Los Alamos National Laboratory, LA-UR-10-00481, Los Alamos (2010).

[4]   Wohlmuther, M., *et al.*, "Activation of Trace Elements and Impurities – A New Ansatz for Monte Carlo Calculation", *Proc. of the 11th Int. Conf. on Radiation Shielding and 15th Topical Meeting of the Radiation Protection and Shielding Division of ANS*, Georgia, USA (2008).

[5]   Bertini, H.W., *Phys. Rev.*, 131, 1801 (1963).

[6]   Bertini, H.W., *Phys. Rev.*, 188, 1711 (1969).

[7]   Yariv, Y., Z. Fraenkel, *Phys. Rev.*, C20, 2227 (1979); *Phys. Rev.*, C24, 488 (1981).

[8]   Dresner, L., *EVAP-A Fortran Program for Calculating the Evaporation of Various Particles from Excited Compound Nuclei*, Oak Ridge National Laboratory, ORNL-TM-7882 (1981).

[9]   Atchison, F., *Nucl. Instr. Meth.*, B, 259, 909 (2007).

[10]   Mashnik, S.G., *et al.*, *CEM03.03 and LAQGSM03.03 Event Generators for the MCNP6, MCNPX, and MARS15 Transport Codes*, Los Alamos National Laboratory, LA-UR-08-2931 (2008); E-print: arXiv:0805.0751v2 [nucl-th].

[11]   Furihata, S., *Nucl. Instr. Meth.*, B 171, 252 (2000).

[12]   Leray, S., *et al.*, *Instr. Meth.*, B 268, 581 (2010).

[13]   Junghans, A.R., *et al.*, *Nucl. Phys.*, A 629, 635 (1998).

[14]   Gallmeier, F.X., *et al.*, "An Environment using Nuclear Inventory Codes in Combination with the Radiation Transport Code MCNPX for Accelerator Activation Problem", *Proc. of the 8th Int. Topical Meeting on Nuclear Applications and Utilization of Accelerators*, Pocatello, USA (2007), 207.

[15]   Wilson, W.B., *et al.*, "Recent Developments of the CINDER'90 Transmutation Code and Data Library for Actinide Transmutation Study", *Proc. GLOBAL'95 Int. Conf. on Evaluation of Emerging Nuclear Fuel Cycle Systems*, Versailles, France (1995).

[16]   Forrest, R., *FISPACT-2007: User Manual*, UKAEA, UKAEA FUS 534 (2007).

[17]   Atchison, F., H. Schaal, *ORIHET3-Version 1.12, A Guide for Users* (2001).

[18]   Forrest, R., J. Kopecky, J-C. Sublet, *The European Activation File: EAF-2007 Neutron-induced Cross Section Library*, UKAEA FUS 535 (2007).

[19]   Wohlmuther, M., *et al.*, "Calculation of Remanent Dose Distribution with MCNPX", *Proc. of the 8th Int. Topical Meeting on Nuclear Applications and Utilization of Accelerators*, Pocatello, USA (2007), 226.

[20]   Dai, Y., *et al.*, "The Second SINQ Target Irradiation Program, STIP-II", *J. Nucl. Mater.*, 343, 33 (2005).

[21]   Keil, R., *Chemical Analysis of Lead from SINQ Target 4*, PSI, No. 7129 (1999).

[22]   Schumann, D., *et al.*, *Nucl. Instr. Meth.* B 264, 83 (2007).

Activation studies for a beta-beam decay ring: Residual dose rates during maintenance and airborne activity

Stefania Trovati, Matteo Magistris
European Organization for Nuclear Research (CERN)
Geneva, Switzerland

Abstract

In a future beta-beam facility radioactive ions (^{6}He and ^{18}Ne) are produced, accelerated and then stored in a large decay ring, where they eventually produce anti-neutrino and neutrino beams through $\beta^\pm$ decay. CERN is one of the candidate sites for the beta-beam facility, as existing machines like the Proton Synchrotron and the Super Proton Synchrotron could be used for the acceleration.

This work focuses on some radiation protection aspects related to the operation of the DR, namely the induced radioactivity and the air activation generated by collimation and decay losses. All the calculations are performed with the Monte Carlo transport code FLUKA and are based on a continuous three-month operation. The induced radioactivity in the machine components and the expected residual dose rates inside the tunnel during maintenance are calculated for three different waiting times. Airborne activity is evaluated through the convolution of predicted particle spectra in the tunnel with isotope-production cross-sections. Using activity-to-dose coefficients, previously calculated for the ISOLDE facility at CERN, and a laminar flow model for the air diffusion, the airborne activity is converted into effective dose to the reference population group.

Introduction

In a future beta-beam facility at CERN, after the acceleration in the Proton Synchrotron (PS) and the Super Proton Synchrotron (SPS), radioactive beams (^{6}He and ^{18}Ne) are injected at nearly 92 GeV per nucleon into the decay ring (DR), a high-energy superconducting machine, in which they are stored in order to decay into neutrino and anti-neutrino beams. It is composed of two long straight sections (SS), of which one is directed towards the detector situated in the Frejus tunnel, and two arcs, for a total length of 6 911.5 m (same as the SPS length) [1]. The injection system is hosted in one of the two arcs, whilst one of the SS houses the collimation and two bumps. A sketch of the DR is given in Figure 1. Magnets in the arcs are based on the same superconducting technology used for the design of the Large Hadron Collider (LHC), with niobium-titanium cables and copper wedges, whilst in the collimation and bump sections there are warm magnets only.

Figure 1: The decay ring (DR)
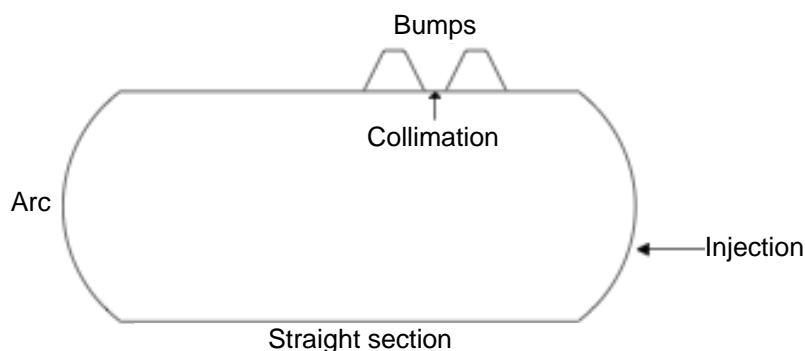
The decay of the stored ions causes a continuous power loss of, on average, 10.8 W m^{-1} for ^{6}He and of 11.8 W m^{-1} for ^{18}Ne. At the end of the SS the total deposited power in the first dipole of the arcs would be of several tens of kilowatts. Beam collimation also produces losses distributed in the collimator area. In order to prevent energy deposition and magnet quenching, two dedicated extraction sections are needed at the entrances of the arcs.

Magnet protection systems must also be foreseen all along the arcs: two solutions have been considered, of which one is to insert absorbers between the magnets and one is to use open mid-plane magnets. In the latter layout, aluminium absorbers replace the mid-plane coils.

In the present work, all activation calculations are performed for the collimation and bump sections, and for the arcs (both the layouts). The loss maps are calculated with the particle tracking code ACCSIM [2] coupled to the Monte Carlo code FLUKA [3,4], whilst the induced activity and the consequent residual ambient dose equivalent H*(10) rates are estimated with FLUKA and an analytical model for the air diffusion [5].

Residual ambient dose equivalent rates in the collimation and bump sections

Bumps

The injection is located in a dispersive area, the stored beam is deviated towards the septum blade by four kickers while the entering beam is injected "off momentum" on its chromatic orbit. This is obtained through dispersion bumps created by warm dipoles of 1.6 T. The lattice of a bump, shown in Figure 2, is composed of nine quadrupoles (Q) and four dipoles (BN2, BN3); most of the losses occur at the entrance of the bumps. The cross-sections of magnets used in the simulations are based on SESAME models [6]. Dipoles are C-shaped magnets, 12 m long with flat parallel ends and a magnetic aperture of 8 cm, quadrupoles are 2 m long and have an aperture radius of 8 cm (Figure 3). The coils are in copper, the yokes are made of a low-carbon iron; details on material compositions for yokes are given in Table 1. The beam pipe has an elliptical cross-section and a thickness of 3 mm, and is made of stainless steel.

Figure 2: Sketched layout of a bump
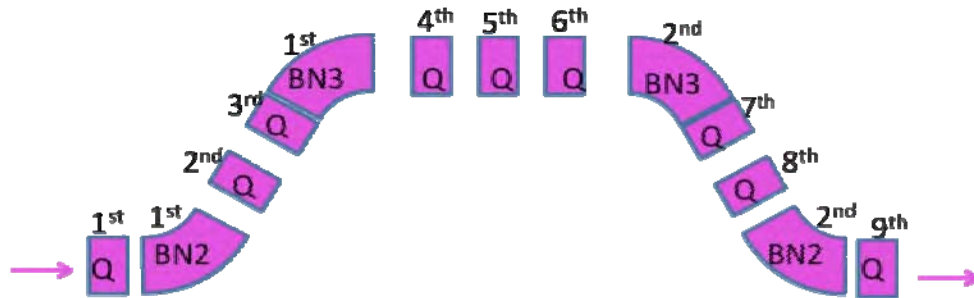
Figure 3: Layouts of warm magnets
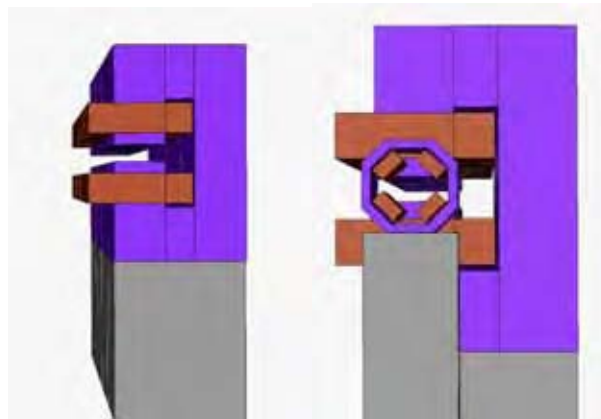
Table 1: Yoke composition in warm magnets

	Iron	Carbon	Silicon	Manganese	Phosphorus	Sulphur	Aluminium
Yoke composition in warm magnets (%)	98	0.001	1.5	0.2	0.05	0.0005	0.2

The results for both the bumps, in the worst cases and for different waiting times, are summarised in Table 2. ^{6}He is the worst case. In the third dipole area, most of the losses are concentrated in the next quadrupole and the residual dose rate at 1 m from the beam line is nearly 30 mSv h^{-1} after one week. According to the CERN Safety Code [7] this value corresponds to a high-radiation area. At the entrance, losses are concentrated at a distance of nearly 10 m from the dipole. The residual dose rate at 1 m from the beam line in this area is around 3.6 mSv h^{-1} after one week in the first set of bumps and 7.5 mSv h^{-1} in the second one; this dose rate corresponds to a high-radiation area. The same classification applies for the second quadrupole area in which the dose rate after one week is of 5.4 mSv h^{-1}. These values are valid without considering the possible installation of dumps before the dipoles in the two bump areas. In the case dumps are present the critical points are those close to the quadrupoles, where there would be a maximum of 5.44 mSv h^{-1} after 1 week. In Figure 4 the residual dose rates after one week for ^{6}He and ^{18}Ne are shown for the case of the second quadrupole.

Table 2: Residual ambient dose equivalent rates (mSv h^{-1})
for several waiting times in the worst cases

Waiting time	First bump		Second bump	
	^{6}He	^{18}Ne	^{6}He	^{18}Ne
1 hour	90	8	90	27
1 day	50	3	60	11
1 week	30	2	33	5

Figure 4: On the left ⁶He, on the right ¹⁸Ne – residual H*(10) after 1 week near a quadrupole
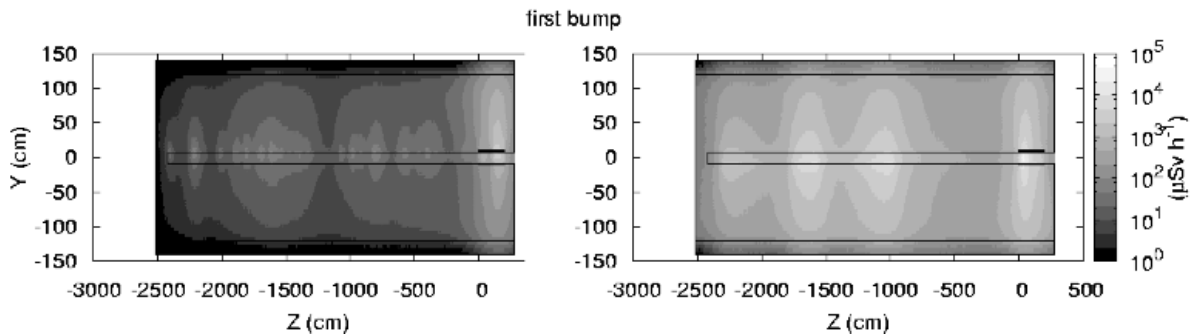
Collimators

The collimation section stays in between the two bumps and foresees the combination of a primary and two secondary collimators, all made of carbon. In Figure 5 the dose rate maps after 1 week is presented for the ¹⁸Ne case, *i.e.* the worst case between the two ions: the area around the primary collimator has the highest dose rate (the peak dose rate is above 100 mSv h⁻¹). The dose rate decreases with the increasing distance from the primary collimator reaching the value of 1 mSv h⁻¹ at 200 m from it. In order to protect the quadrupoles in the straight section, several carbon absorbers are placed between the magnets: their activation contributes to the residual dose rates in the tunnel. Therefore a dedicated material study is necessary to find the best compromise between absorption (including heat dissipation) and activation.

Figure 5: Residual H*(10) in the collimation section for ¹⁸Ne after 1 week
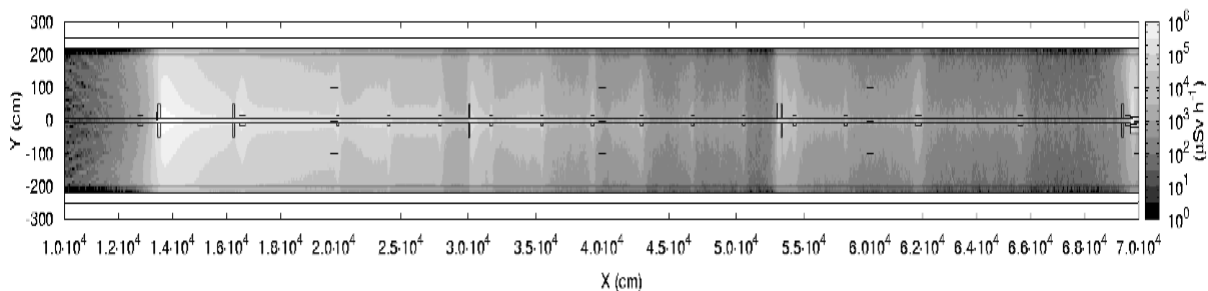
Residual ambient dose equivalent rates in the arcs

One of the main issues related to magnets in the DR is the considerable amount of power lost in the horizontal plane due to ion decay. In the present phase of design two solutions to avoid quenching are considered: steel absorbers in between each couple of magnets and open mid-plane dipoles without the use of absorbers. Losses have a repetitive pattern along the lattice in the arcs and the characteristic cell is composed of two dipoles, one quadrupole, two dipoles and one quadrupole. The calculations are made for one of this cell in the arcs. Two critical positions in terms of losses are represented by the entrances of both the arcs: all the decay products coming from the straight sections reach the entrance of the arcs. Two dumps have been considered to drive these losses away.

Dipoles and quadrupoles in the arcs are cold magnets, cooled by liquid helium. Figure 6 shows magnet cross-sections used for calculations. A more detailed representation is given for dipoles: Cu wedges alternate with NbTi cables, while for quadrupoles a unique compound material is used to describe both copper wedges and cables. Whilst liquid helium is represented in quadrupoles, it is added in the cable compound material for dipoles. The compositions of the materials are summarised in Table 3. In the open mid-plane layout, aluminium absorbers replace the mid-plane layers of cables.

Figure 6: Left: dipole cross-section. Right: quadrupole cross-section.

Ni-Ti cables have different compositions, according to the position (see Table 3)
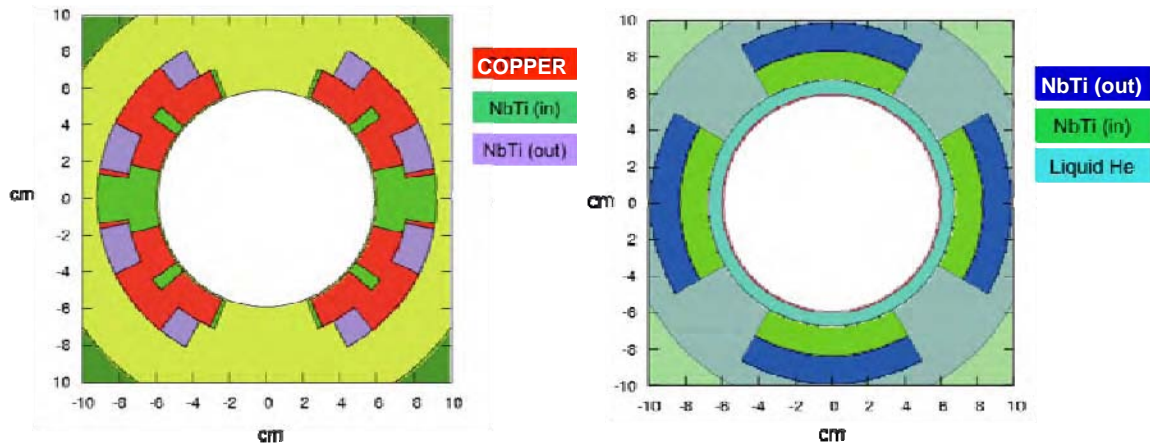
Table 3: Compositions of materials for dipole and quadrupole cables

		ρ g cm³	Cu vol. fraction (%)	Nb vol. fraction (%)	Liq. He vol. fraction (%)	Kapton vol. fraction (%)	Ti vol. fraction (%)
Dipole	NbTi(in)	6.1	48	10	12	13	17
	NbTi(out)	7.6	47	9	11	17	16
Quadrupole	NbTi(in)	7.0	63	7	10	9	11
	NbTi(out)	6.3	53	8	10	15	14

In Table 4 the residual dose rates at 1 m from the beam pipe are shown for the two settings, with steel absorbers and with open mid-plane dipoles. The values show the range from the minimum to the maximum dose rate. There is not a noticeable difference between the two layouts for the ^{6}He case whilst it is more evident in the ^{18}Ne case, especially after one day and one week.

Table 4: Residual dose rates in mSv h^{-1} in the arcs with absorbers or with open mid-plane dipoles

	^{6}He			^{18}Ne		
	1 hour	1 day	1 week	1 hour	1 day	1 week
With absorbers	0.12-1.2	0.05-0.5	0.015-0.3	0.1-6	0.06-3	0.02-1.5
Open mid-plane dipoles	0.03-1	0.01-0.4	0.001-0.2	0.02-6	0.001-1.2	0.001-0.8

In Figure 7, the dose rate maps on the left show the case with absorbers and those on the right the case without absorbers. The hot spots are in different locations, namely between the first and second dipole when absorbers are present and between the second and the third dipole without absorbers.

The dose rates are lower, on average, all along the beam pipe when the absorbers are not present, even if the specific activities of the residual nuclides in the dipole yokes are slightly higher for the open mid-plane dipoles setting, as shown in Figure 8, but the difference is within the calculation uncertainties. In the steel absorbers, several radionuclides are produced, such as ^{57}Ni, ^{5}Ni, ^{44}Sc, ^{47}Ca, ^{82}Rb, ^{83}Rb, and these are responsible of the higher doses nearby.

Air activation

For the airborne activity released in the environment, both the decay and the collimation losses are considered. Information about the dimensions of the DR tunnel, about the ventilation parameters

**Figure 7: Residual dose rates in the arc for both ions.
Left: with absorbers, right: with open mid-plane dipoles.**
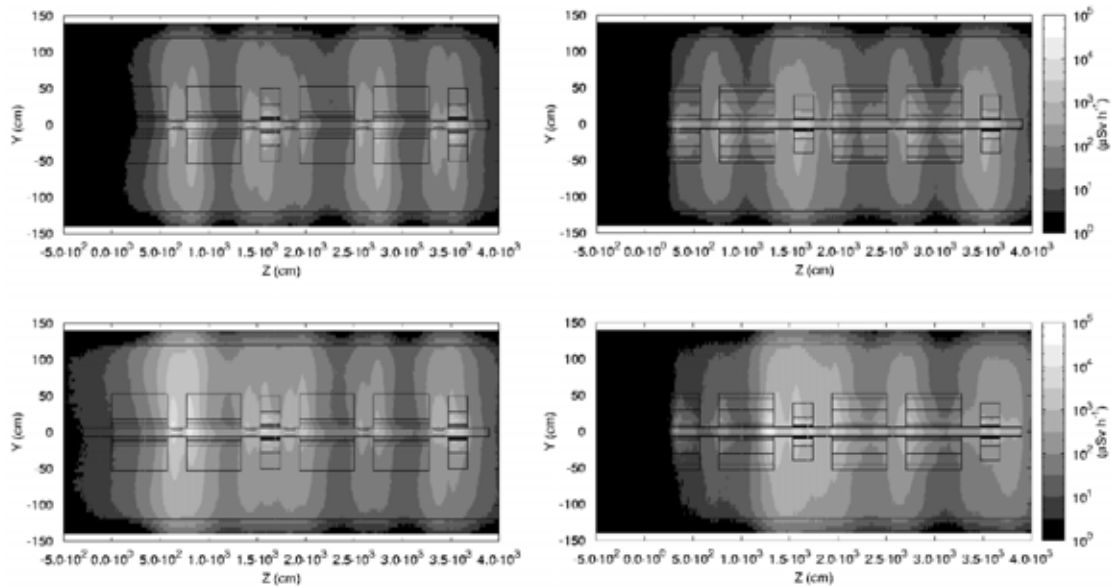
**Figure 8: Comparison between the specific activities in the two
configurations, *i.e.* with absorbers and with open mid-plane dipoles**
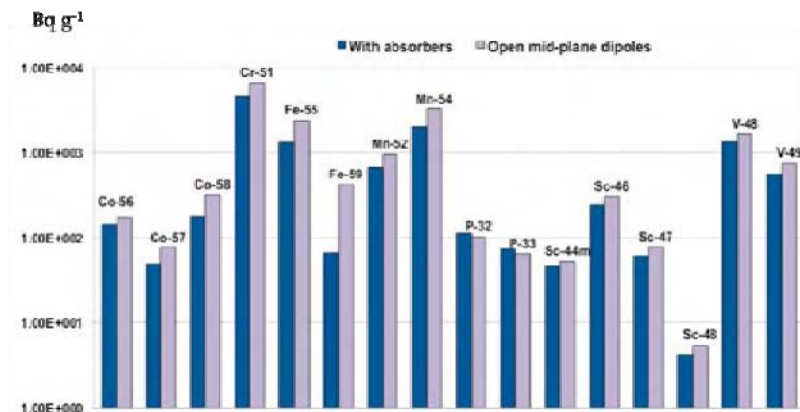
(*i.e.* number and size of ventilation outlets, ventilation rate, etc.) are not yet known. Therefore the parameters used for the calculations are not definitive and can be changed in the design phase in order to minimise the released airborne activity.

The same approach as in previous calculations is used [8]: the one-year activity of the radionuclides produced in the DR ring and transported to the release stack is calculated through the convolution of predicted particle spectra with isotope-production cross-sections, a laminar flow model for the air diffusion and the activity-to-dose conversion coefficients for the ISOLDE facility [9] are used. Table 5 displays the results.

The most contributing radionuclides are the short-lived ones, except for ^{7}Be. They are produced in spallation (^{11}C, ^{13}N, ^{15}O) and low-energy neutron capture (^{41}Ar) reactions. The total annual effective dose given to the reference population is below the CERN limit for all annual releases (10 μSv) but above the reference value used for a single installation (1 μSv). As the assessment of the released activity is highly dependent on the tunnel-ventilation parameters, a detailed calculation is not possible at the moment. Furthermore, *ad hoc* solutions can be found to reduce the emissions, such as different ventilation rates in different segments of the tunnel or balloons for the air storage.

Table 5: List of the main radionuclides produced in the air and their contributions to the total annual effective dose for both the ^{6}He and ^{18}Ne operations

Radionuclide	Half-life	Annual dose (mSv)	
		^{6}He	^{18}Ne
^{41}Ar	Hours	6.94E-03	1.50E+00
^{13}N	Minutes	1.26E-03	1.43E+00
^{11}C	Minutes	1.60E+00	1.36E+00
^{7}Be	Months	3.88E-01	5.89E-01
^{15}O	Minutes	9.27E-01	2.52E-01
^{39}Cl	Minutes	3.54E-03	1.86E-01
^{38}Cl	Minutes	6.16E-02	8.12E-02
^{32}P	Days	1.38E-01	7.71E-02
^{24}Na	Hours	3.47E-03	5.63E-02

Conclusions

The results show that residual ambient dose equivalent rates during maintenance significantly decrease in a week after the shutdown of the machine, reaching values that correspond, according to CERN area classification, to a limited stay area. The effective dose given to the reference population in one year of operation is below the reference value for all CERN emissions into the environment.

References

[1]   Autin, B., *et al.*, "The Acceleration and Storage of Radioactive Ions for a Neutrino Factory", Nufact Note 121, *J. Phys. G 29*, 1785-1796 (2003).

[2]   Jones, F.W., "Development of the ACCSIM Tracking and Simulation Code", *Proc. 1997 Particle Accelerator Conference*, Vancouver, May 1997.

[3]   Fassò, A., *et al.*, *FLUKA: A Multi-particle Transport Code*, CERN-2005-10 (2005).

[4]   Fassò, A., *et al.*, "The Physics Models of FLUKA: Status and Recent Developments", *Proc. Computing in High Energy and Nuclear Physics 2003*, La Jolla, 24-28 March, pp. 25-30 (2003).

[5]   Brugger, M., *et al.*, *Effective Dose to the Public from Air Releases at LHC Point 7*, CERN-SC-2004-064-RP-TN.

[6]   SESAME, *The White Book*, Chapter 6, July 2002.

[7]   CERN Safety Code, Radiation Protection (2006).

[8]   Trovati, S., M. Magistris, M. Silari, *Radiation Protection Issues for the Beta-beam Rapid Cycling Synchrotron*, CERN-SC-2008-070-RP-TN.

[9]   Vojtyla, P., *Dose Conversion Coefficients for Exposure of the Reference Population Group to Radionuclides in Air Released from the ISOLDE Facility*, CERN-SC-2008-001-IE-TN (2008).

Radiation protection aspects of the SPES project at LNL

L. Sarchiapone, D. Zafiropoulos
Laboratori Nazionali di Legnaro
Legnaro, Italy

Abstract

The Selective Production of Exotic Species (SPES) project will be built at the National Laboratories in Legnaro (Italy) of the National Institute of Nuclear Physics (INFN). Its goal will be the development of radioactive ion beams and the consequent re-acceleration with the already existing linac, to perform forefront research in the frame of nuclear physics. Radiation protection aspects play along with every stage of the project, e.g. civil construction planning, control system design and special technological plants. These aspects have been studied with the Monte Carlo transport code FLUKA, and are presented in this work.

Introduction

For the production of the primary proton beam, a proton cyclotron will be used, providing a beam of energy in the range 40 to 70 MeV and a current up to 750 μA. The proton beam will induce fission on a uranium carbide target; the expected rate is 10^{13} fissions per second [1].

All the shielding aspects of the facility have been investigated, with particular care for the target hall. The study includes some preliminary considerations concerning the decommissioning of the facility and the dismantling of the shielding walls.

The activation of the materials interacting with the primary beam, as well as the dose rates in closed volumes, have been studied in order to plan maintenance intervention and emergency access.

Some evaluations concerning release of activated air to the environment have been made, taking into account the recommendations of Italian legislation. All the calculations have been performed with the Monte Carlo code FLUKA [2].

Figure 1: SPES layout. The ALPI linac already exists, while the cyclotron vault and the target halls have yet to be built.
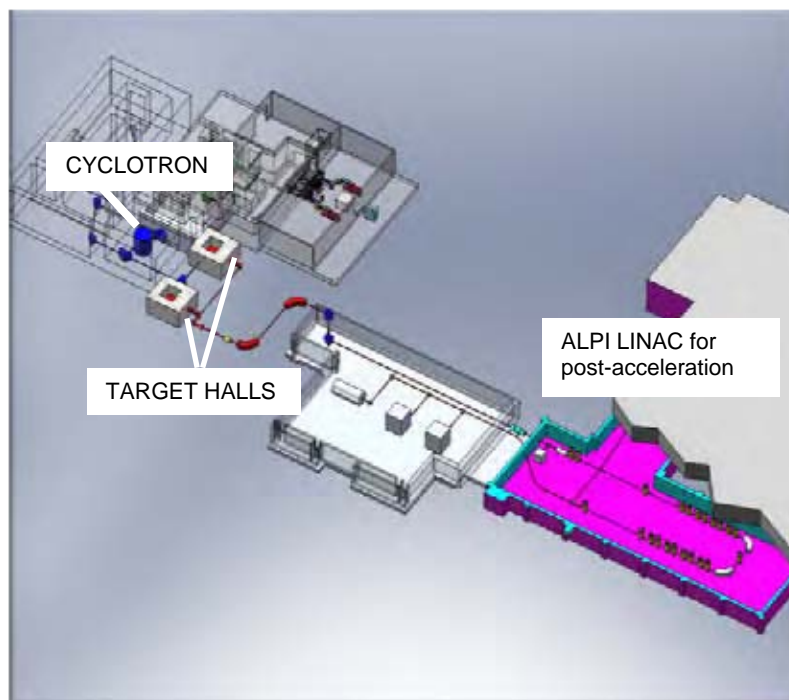
Shielding of the target hall

For the shielding studies two project dose constraints have been settled on: 5 μSv/h for controlled classified areas and 0.3 μSv /h for non-classified areas. The source term for the shielding simulation is a proton beam of energy 70 MeV and current 300 μA impinging on 30 g of uranium carbide, the irradiation period is two weeks (nominal shift time). The neutrons generated in the interaction of the beam with the target have an energetic spectrum ranging from thermal energies up to 60 MeV, peaked at 1-2 MeV. Thermal neutrons are obtained after the interaction with the air molecules in the target hall.

The neutron spectrum is attenuated in concrete, as shown in Figure 2. Fast neutrons are slowed down more rapidly in the first 50 cm, with the consequence that the thermal group is enriched in the same layer. In layers deeper than 50 cm the fast spectrum and the thermal one decrease exponentially with the same slope, as shown on the right in Figure 2.

Figure 2: Left: energetic spectrum of neutrons as function of the depth in concrete (n/cm^2/proton on target). Right: thermal (E < 1 eV) and high-energy neutrons (E > 20 MeV) as function of depth in concrete.
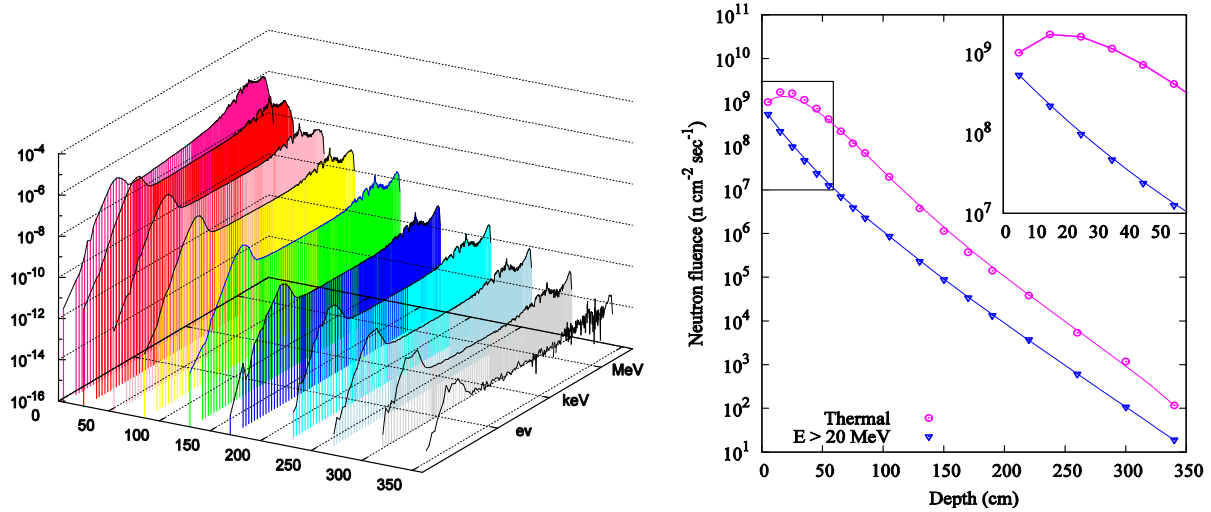
The ambient dose equivalent due to neutrons during the irradiation at the distance of 1 m from the target is 10^{10} μSv/h. The attenuation that can be achieved with a 360 cm thick wall in the forward direction is a factor 10^8. Considering that the target is 2 meters far from the wall the ambient dose equivalent at 0° angle outside of the shielding is 10 μSv/h. In the halls adjacent to the target room the access is prohibited during the irradiation.

Figure 3: Ambient dose equivalent rate (μSv/h) due to neutrons in the target hall and in the adjacent rooms
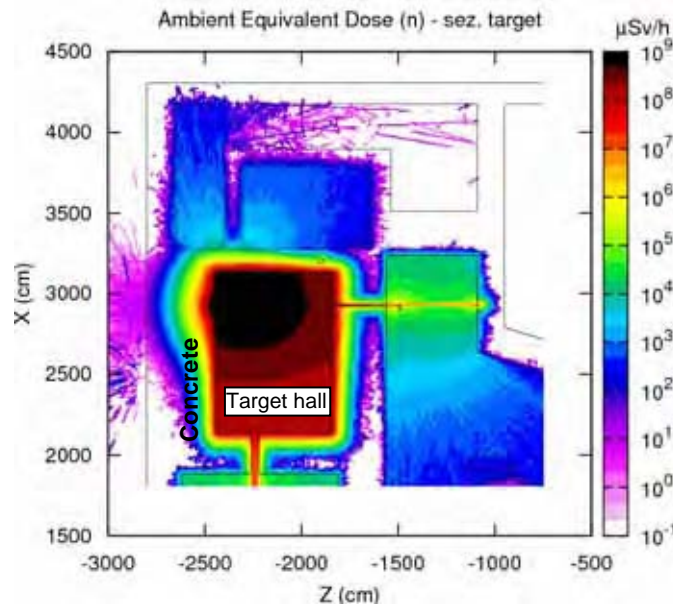
The roof and the floor of the target room are 300 cm thick, and they guarantee that the ambient dose equivalent rate is less than 5 μSv /h both outside of the roof, where personnel access is prohibited during target irradiation, and in the ground below the floor, as shown in Figure 4.

**Figure 4: Ambient dose equivalent rate (μSv/h) due to neutrons
in the vertical direction (roof and floor areas are highlighted)**
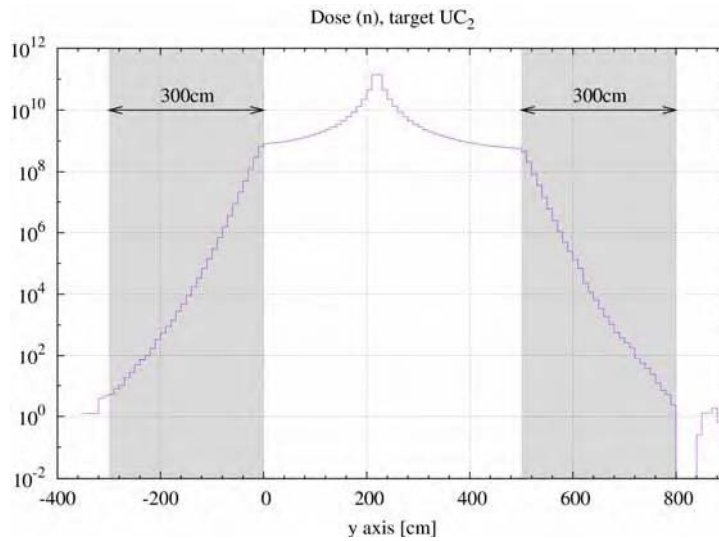
Since a first phase of the SPES project will be held using conventional, non-fissionable targets, some evaluations for the shielding in these configurations have been done. In addition to the standard concrete wall, the shielding capability of other materials has been checked.

One particular focus of study is a sandwich-like composition with concrete as container and gypsum (hydrated calcium sulphate, no impurities included) as content. This structure has proven to be very effective in terms of neutron attenuation, thanks to the high hydrogen content in the gypsum composition; another advantage concerns the low activation after long irradiation periods. Nevertheless its use is quite impractical in view of the dismantling; being very dry and dusty it could be easily spread and dispersed during the demolition. The other option was a ferrous content (composition specified in Table 1), available as blast furnace waste. This content has a lower shielding efficiency and it activates more with respect to concrete alone because of the metallic filling components.

**Figure 5: Comparison of the attenuation efficiency of concrete and sandwich-like
structure with gypsum or blast furnace waste as filling. The target irradiated is made of SiC.**
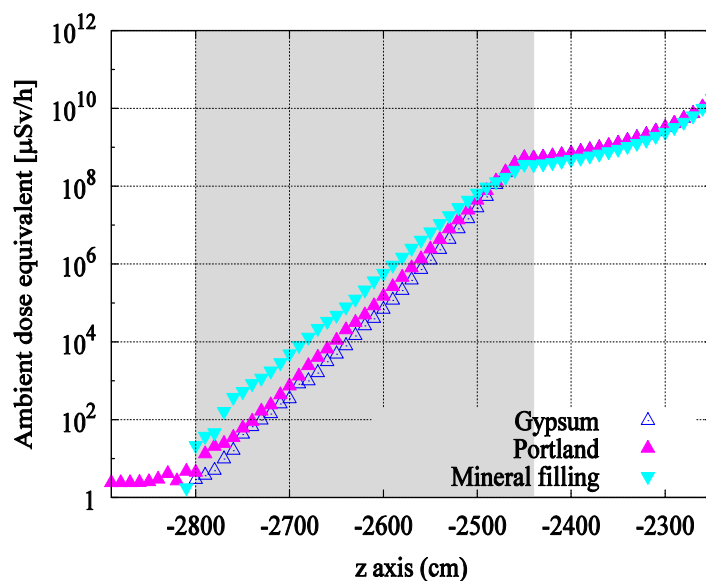
**Table 1: Sample composition of the blast furnace waste
used to fill the sandwich-like shielding structure**

Compound	Partial density
CaO	26%
Fe	26%
Na_2O	45%
SiO_2	13%
Al_2O_3	6%
MgO	5%
Cr_2O_3	2%
MnO_2	0.6%
As, Cd, Co, Cu, Hg, Mb, Ni, Pb, V, Zn	<0.1%

Activation sources and related doses

Target

The irradiation of the UC_2 target with the proton beam of energy 40 MeV and current 200 µA will be done in cycles of two weeks. The activity built up in the target at the end of one irradiation cycle will be 10^{14} Bq, with only 0.4% of the total activity due to nuclides with half-life longer than one month.

The ambient dose equivalent at 1 m distance from the target at the end of the irradiation cycle is 9.8 Sv m²/h, after one year of cooling time it is still higher than 1 mSv m²/h. These numbers serve just as an indication of the high activation of the target, and suggest the need for remote handling of the exhaust target from the irradiation hall to the dedicated repository outside. In case of maintenance intervention, it has to be considered the exposure of personnel to the residual dose rate due to the target front end equipment, which is a fixed structure made of aluminium. At the end of the irradiation cycle the dose at 1 m is 0.7 Sv m²/h, and after 10 days of cooling time is 2.7 mSv m²/h.

Cyclotron

The activation of the cyclotron structure has been evaluated; the protons lost during acceleration and extraction of the beam constitute the source term of the simulation, with energy and current distribution specified in Table 2.

**Table 2: Energy and current of the protons lost
during acceleration and extraction in the cyclotron**

Energy [MeV]	Current
30	22.5 µA
40	22.5 µA
50	11.25 µA
60	11.25 µA
70	45 µA

At the end of an irradiation cycle (two weeks) after 10 days of cooling time, the residual dose in the cyclotron vault is less than 10 µSv/h at the distance of approximately 5 meters. However, in the vicinity of the extraction point, that is the considered point of impact of the proton beam with the cyclotron aluminium case, the dose rate is 1 mSv/h. Long maintenance intervention must be previously authorised, planned and clocked in order to avoid excessive exposure of the operators.

Considering an irradiation period as long as one year, thus taking build-up of residuals into account, and 10 days of cooling time it has been seen that the dose rate in the cyclotron vault at distances up to 5 meters is the order of 100 µSv/h, and close to the extraction point it can reach 10 mSv/h.

These doses are mainly due to the activation of the aluminium-intercepting protons and the activation of aluminium and copper by secondary neutrons. The important residuals are indicated in Table 3 along with their half-life.

Table 3: Residual nuclei in the cyclotron components

Residuals from protons on Al	
^{26}Al	$7.4 \cdot 10^5$ y
^{24}Na	14.96 h
^{22}Na	2.6 y
^{7}Be	53.29 d
Residuals from neutrons on Cu	
^{65}Zn	244.26 d
^{64}Cu	12.7 h
^{60}Co	1 925.1 d
^{59}Fe	44.5 d
^{58}Co	70.82 d
^{57}Co	271.79 d
^{56}Co	77.27 d
^{54}Mn	312.12 d

Airborne activity

The airborne activity has been evaluated in a two-step approach; the particle fluence has been scored with FLUKA simulations and then folded with the cross-sections for the production of the main radioactive nuclides in air [4,5].

Through the equation for the calculation of activation in presence of a ventilation system, the radioactivity exhausted for the operations with both fissionable (UC$_2$) and conventional (SiC) targets has been evaluated. According to Italian law [7], the release of radioactive substances with certain characteristics to the environment must be authorised. In particular for those radioisotopes whose half-life is shorter than 75 days, it must be guaranteed that the activity concentration is below 1 Bq/g in order to release it freely to the environment. For radioisotopes with a half-life longer than 75 days, if the total effective dose equivalent to the public (TEDE) is below 10 μSv/year, it is not necessary to take them into account because there is no concern from a radiological point of view.

Figure 6: Realistic map of the SPES installation and release point

The contour curves give the dose received annually by the public: internal contour level (red, up to 600 m from the stack) more than 0.04 μSv, with a maximum at 30 m from the stack of 4.0 μSv; middle (green, up to 1 km from the stack) between 0.04 and 0.01 μSv, external (blue, up to 1.5 km) between 0.01 and $2.5 \cdot 10^{-3}$ μSv.

The equation used to calculate the activity exhausted in the presence of ventilation is:

$$RA(t) = \frac{PR\lambda}{R + \lambda} \cdot \left(1 - e^{-(\lambda+R)t}\right)$$

where P is the production rate (atoms/cm^3/sec), λ is the decay constant (sec^{-1}), R is the ventilation rate (sec^{-1}) and t is the irradiation period (sec). The ventilation rate is 50 m^3 per hour (the volume of the target room is 300 m^3) and it is supposed to compensate for the leaks in the depression system.

These data have been used to give an estimate of the dose to the public due to inhalation of the radioactive gases and submersion in the exhausted plume (Total Effective Dose Equivalent). The TEDE has been calculated using the Hotspot code and the recent ICRP coefficients for dose-activity conversion [6].

The annual activity released irradiating a fissionable target is $7 \cdot 10^{14}$ Bq. More than 99% is due to nuclides with half life shorter than 75 days (^{7}Be, ^{11}C, ^{13}N, ^{15}O, ^{41}Ar). A cooling time of about two hours is sufficient to reduce the activity concentration to 1 Bq per gram, and thus release the air to the environment without further authorisation. In order to cool the continuous air flow pumped out of the irradiation room a forced path with a dilution system to the stack is foreseen.

For long half-life nuclides (^{3}H, ^{14}C, ^{35}S) the TEDE to the population under the worst atmospheric conditions has been calculated. This value being less than 10 µSv/y, the practice is not relevant from a radiological point of view.

Using a non-fissionable target (SiC) the radioactivity produced in air is $5 \cdot 10^{12}$ Bq per year. The concentration of short-lived nuclides is less than 1 Bq/g at the exhaust and in principle there would be no need for a dilution system to reduce the concentration further on. For long-lived nuclides the TEDE is less than 1 µSv per year; as mentioned above, this is not relevant from a radiological point of view.

Table 4: Annual activity released and TEDE to the public due to the long-lived radionuclides

Nuclide	$T_{1/2}$	Activity release rate Bq/y		TEDE Sv/y	
		UC_2	SiC	UC_2	SiC
^{3}H	12.33 y	$1.8 \cdot 10^9$	$1.1 \cdot 10^8$	$3.0 \cdot 10^{-6}$	$3.0 \cdot 10^{-7}$
^{14}C	5 730 y	$2.7 \cdot 10^8$	$4.3 \cdot 10^7$		
^{35}S	87.51 d	$7.7 \cdot 10^8$	$6.8 \cdot 10^6$		

Conclusions

The radiation protection aspects of the SPES project have been studied using the FLUKA code. Simulations have been run using nominal irradiation conditions in order to classify the areas close to the target irradiation room and to the cyclotron vault during and after the irradiation of the target.

In particular, inside the irradiation hall and in the cyclotron vault, an indication of the remnant dose rate after some days of cooling after the beam stop has been given in order to plan interventions on the equipments.

The airborne activity has been calculated taking into account the ventilation system of the target room; the residual nuclei and their activity at the stack have been estimated in order to give, at any time, a non-relevant dose to the population.

References

[1]   Prete, G., A. Covello, *SPES Technical Design Report.*

[2]   Battistoni, G., *et al.*, "The FLUKA Code: Description and Benchmarking", *Proceedings of the Hadronic Shower Simulation Workshop 2006*, Fermilab 6-8 September 2006, M. Albrow, R. Raja (Eds.), AIP Conference Proceedings, 896, 31-49 (2007).

[3]   Fassò, A., *et al.*, *FLUKA: A Multi-particle Transport Code*, CERN-2005-10 (2005), INFN/TC_05/11, SLAC-R-773.

[4]   Huhtinen, M., *Determination of Cross Sections for Assessment of Air Activation at LHC*, Technical Memorandum CERN/TIS-RP/TM/96-29 (1997).

[5]   Brugger, M., *et al.*, *Effective Dose to the Public from Air Releases at LHC Point 7*, Technical Note, CERN-SC-2004-064-RP-TN (2004).

[6]   Homan, S.G., *Hotspot: Health Physics Codes Version 2.07.1 User's Guide*, National Atmospheric Release Advisory Center Lawrence Livermore National Laboratory, Livermore, CA (2010).

[7]   Legislative Decree 17 March 1995, n. 230 and successive integration and corrections (241/00 and 257/01).

Estimates of radiation levels in the main linac tunnel and drive beam dump caverns for the CLIC design study

Sophie Mallows[1]**, Thomas Otto**[2]
[1]University of Manchester, Manchester, UK
[2]European Organization for Nuclear Research (CERN), Geneva, Switzerland

Abstract

The Monte Carlo particle transport code FLUKA was used to simulate beam losses in the CLIC tunnel at four different energies. This paper presents estimates of the resulting residual ambient dose equivalent rates, the absorbed doses from prompt radiation, the fluence of hadrons with energies higher than 20 MeV and the 1 MeV neutron equivalent fluence inside the tunnel. In addition, FLUKA was used to simulate a beam dumped inside the drive beam dump cavern. Preliminary estimates of the residual ambient dose equivalent rates inside the cavern are presented.

Introduction

The Compact Linear Collider (CLIC) study [1] investigates the feasibility of a high-energy electron-positron linear collider optimised for a centre of mass energy of 3 TeV. The total tunnel length will be about 48 km, requiring CLIC to operate at very high accelerating gradients of 100 MV/m. The RF power will be produced by a two-beam acceleration method [2], in which a drive beam supplies energy to the main accelerating beam. To transfer the energy to the main beam, the drive beam passes through power extraction and transfer structures (PET), where it excites strong electromagnetic oscillations. This RF energy is extracted from the PET and sent via waveguides to the accelerating structures in the main beam. The main beam will be accelerated from 9 to 1 500 GeV over approximately 20 km and each drive beam decelerated from 2.37 to 0.237 GeV in 24 decelerating units per main beam linac, each 625 m long. The main beam parameters are summarised in Table 1.

Table 1: CLIC beam parameters

	Max energy (GeV)	Min energy (GeV)	Particles per bunch train	Repetition rate (Hz)
Main beam	1 500	9	1.16E+12	50
Drive beam	2.4	0.24	1.53E+14	50

The CLIC tunnel will contain elements for both the main and drive beams running parallel to each other at 65 cm apart. The beam lines consist of repeated modules, each approximately 200 cm long with two drive beam quadrupoles per module. The modular type and sequence are dependent on the energy of the main beam [3]. The low-energy drive beam will be dumped at the end of every drive beam decelerating unit. Each drive beam dump will be required to absorb 0.3 MW.

Calculating the potential radiation levels in the tunnel is an important part of the CLIC design study; ionising radiation can cause damage to materials, lead to errors in semiconductor devices and have long-term health effects on exposed personnel. This paper presents estimates of residual ambient dose equivalent rates inside the main linac tunnel and inside the drive beam dump caverns.

FLUKA simulations – main linac tunnel

Simulations of electron beam losses at four energies corresponding to the maximum and minimum energy of each beam line were made using version 2008.3 of the FLUKA code [4,5]. For each of the four loss energies, the build-up and decay of radiation over an 11½ year period with cycles of 180 days continuous running followed by 185 days shutdown was simulated. The residual ambient dose equivalent rates at various waiting times within the shutdown periods were calculated. Quantities related to the potential damage to electronic devices were also calculated: the prompt absorbed dose, the 1 MeV neutron equivalent fluence on silicon and the fluence of hadrons with energies higher than 20 MeV.

Geometry and materials

The FLUKA geometry includes an air-filled concrete tunnel 4.5 m in diameter, tunnel floor, silicon carbide girders and beam line components. The FLUKA representation of the beam line components including quadrupole magnets, PET, acceleration structures and beam position monitors (BPM) is shown in Figure 1. The quadrupoles consist of iron poles and yokes with copper blocks surrounding the poles. The type and sequence of the modules used in main beam simulations were consistent with design specifications [3]. In the model used for simulations at 1 500 GeV, the main beam quadrupoles are 193.5 cm in length and in the model for simulations at 9 GeV, they are 42 cm in length. The drive beam quadrupoles are 27 cm in length. The span of the main beam quadrupole is 25 cm and the drive beam quadrupole, 31 cm. The PET are modelled as solid copper cylinders, of outer radii 6.5 cm with a vacuum chamber of radius 1.15 cm running through the centre. The accelerating structures are modelled as copper cylinders with outer radii 4 cm with a vacuum chamber of radius 0.5 cm running through the centre. The accelerating structures are modelled with central "cross" of reduced density (4.5 gcm^{-3}) to represent void regions along the accelerating structure. The drive beam BPM are modelled as cylinders 1.2 cm in diameter and 6.5 cm in length of a half iron and half copper

**Figure 1: FLUKA representation of main and drive beam line components
for 1.5 TeV main beam simulations, visualised using SimpleGeo [6]**

Two modules are shown. Drive beam PET (modelled as copper cylinders) are parallel to
accelerating structures in the main beam. There are no PET parallel to the main beam quadrupoles.
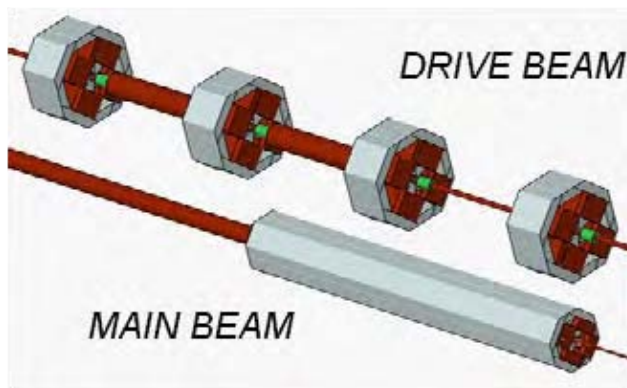
mix with reduced density (4.0 gcm^{-3}) to represent void regions. All concrete shielding components
have a density of 2.3 gcm^{-3} with the following chemical composition: oxygen (52.9%), silicon (33.7%),
calcium (4.4%), aluminium (3.4%), iron (1.4%), hydrogen (1.0%), carbon (0.1%), magnesium (0.2%),
sodium (1.6%) and potassium (1.3%).

Beam loss

The beam losses, which are expected to have a very small impact angle, were represented by electrons
travelling parallel to the beam generated in a circular distribution just inside the copper beam pipe.
The drive beam losses were sampled over 40 m at four loss points per module, corresponding to the
aperture restrictions at the end of every PET structure. The main beam losses were represented as a
continuous distribution over 60 m, an approximation of the eight aperture restrictions per module at
the end of every accelerating structure.

FLUKA thresholds, biasing and settings

In all simulations, the transport cut-offs for charged and uncharged hadrons were set at 10 keV,
except for neutrons, which were tracked to thermal energies. The electromagnetic cut-off energies are
summarised in Table 2.

Table 2: Electromagnetic cut-off energies used in FLUKA simulations for various beam energies

	e+/e- production (MeV)	Photon production (MeV)	e+/e- transport (MeV)	Photon transport (MeV)
Main beam – 1.5 TeV	10	10	10	10
Main beam – 9 GeV	10	10	10	5
Drive beam – 2.4 GeV	10	10	10	5
Drive beam – 0.24 GeV	5	5	1	1

The evaporation model was activated to account for the evaporation of heavy fragments and the
peanut model was activated for all electron energies. The ambient dose equivalent was calculated using
the deq99c package [7]. Full leading particle biasing was activated in the electromagnetic processes.
Photo-neutron production was biased by a reduction factor of 0.02 for the inelastic interaction length
of photons. The magnetic fields in the quadrupole magnets were not taken into account.

Results – main linac tunnel

Whilst an estimate of the losses along the aperture of the main beam is not yet known, the losses should be controlled to less than 0.1% in nominal operation, over the whole main beam linac and each drive beam accelerating unit, to avoid beam loading variations [8]. Assuming uniform losses along the beam line, this corresponds to maximum permitted losses of 5×10^{-8} m^{-1} of the main beam intensity and 1.6×10^{-6} m^{-1} of the drive beam intensity. Whilst in reality the losses will not be uniform along the linac, the average loss per metre serves as an adequate scaling approximation for conservative estimates under nominal operation.

Figure 2 shows the ambient dose equivalent rates after 180 days continuous running and 4 h waiting time for losses from each beam at maximum energy. The dose rates are averaged over the two tunnel modules (4 m) situated at the centre of the loss pattern. The results are scaled to losses of 5×10^{-8} m^{-1} and 1.6×10^{-6} m^{-1} in the main and drive beams respectively, where it was assumed that they were running at full intensity (Table 1). It can be expected that the residual dose rates in most areas of the tunnel will be less than 100 μSvh^{-1} after 4 h waiting with the exception of areas close to the beam line. Simulations for the same losses but at minimum beam energies in the main and drive beam result in dose rates of less than 1 μSvh^{-1} and 10 μSvh^{-1} respectively in the tunnel after 4 h waiting. In each case, the dominant nuclide contributing to the residual activity in the beam line components at the start of the shutdown period is ^{29}Cu, with a half-life of 12.7 h. After one week waiting, the dose rates in most areas of the tunnel fall to below 1 μSvh^{-1}, with the exception of areas near the drive beam for losses at 2.4 GeV. There were little differences in the dose rates during different shutdown periods at the same waiting times.

Figure 2: Residual ambient dose equivalent rates in the CLIC tunnel after 180 d running and 4 h waiting time, from losses at 1.5 TeV main beam (left) and 2.4 GeV drive beam (right), assuming maximum beam losses permitted by beam dynamics considerations
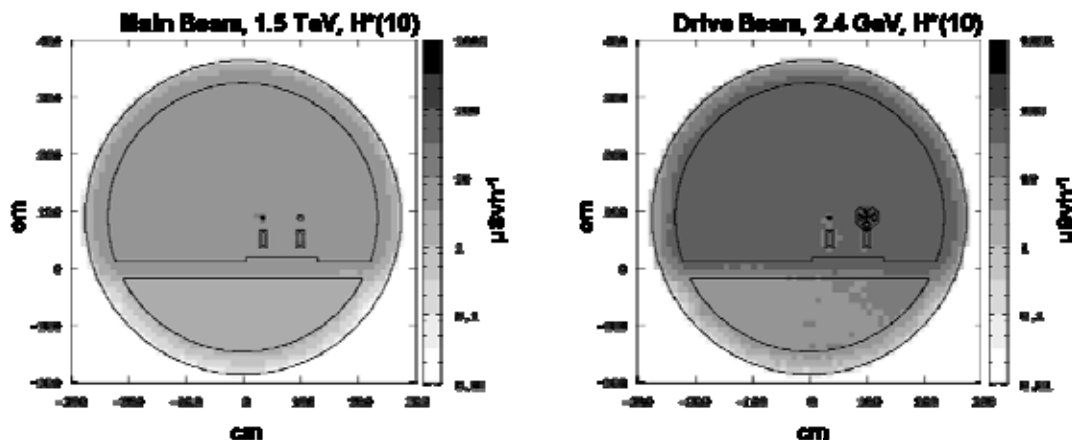
Figure 3 shows the annual 1 MeV neutron equivalent fluence on silicon, the fluence of hadrons with energies higher than 20 MeV and absorbed doses in the tunnel resulting from losses of the 2.4 GeV drive beam at 1.6×10^{-6} m^{-1}, assuming 180 days running per year at full intensity. The fluences and doses are averaged over two modules. The annual 1 MeV neutron equivalent fluences are between 10^{12} cm^{-2} and 10^{13} cm^{-2}. The annual fluence of hadrons with energies higher than 20 MeV is found to be between 10^{10} cm^{-2} and 10^{11} cm^{-2} and the absorbed doses do not exceed 1 MGy. Losses of the 1 500 GeV main beam at 5×10^{-8} m^{-1} result in the same magnitude of fluence of hadrons with energies higher than 20 MeV, whereas the 1 MeV neutron equivalent fluences and absorbed doses are approximately a factor of ten less.

A more detailed study of the maximum dose absorbed in the copper coils and in the regions surrounding the quadrupole magnets indicates that in nominal operation, the maximum absorbed doses are unlikely to exceed 1 MGy per year for any loss energy. However, in most parts of the quadrupole region, the absorbed doses in nominal operation would not exceed 0.1 MGy per year for all loss energies.

Figure 3: Annual fluences and absorbed doses in the CLIC tunnel from drive beam losses at 2.4 GeV assuming maximum beam losses permitted by beam dynamics considerations
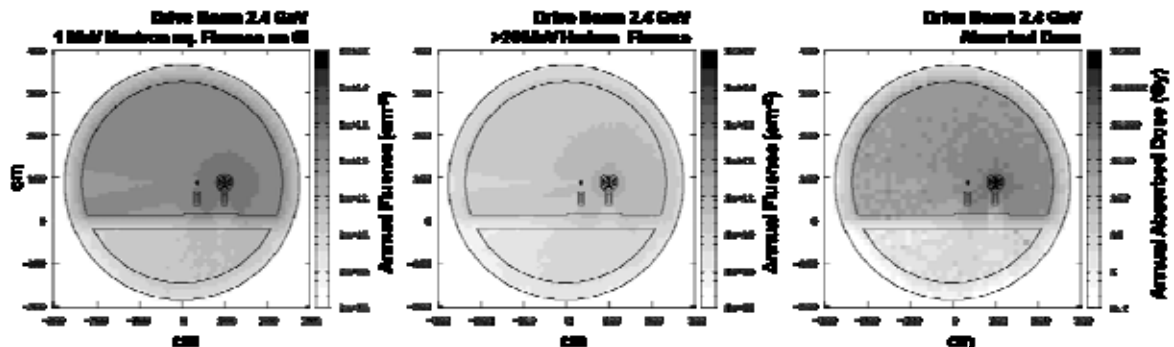
FLUKA simulations – drive beam dump caverns

A 0.24 GeV electron beam with a Gaussian profile of standard deviation, σ, equal to 2.4 cm in the vertical and horizontal planes, intercepted by a composite graphite and iron beam dump was simulated using version 2008.3 of the FLUKA code [4,5]. The build-up and decay of radiation over 180 days continuous running was included in simulations and the residual ambient dose equivalent rates inside the dump cavern at various waiting times were calculated. An estimate of the spatial distribution of the deposited energy from prompt radiation inside the dump was made to determine the feasibility of the dump design.

FLUKA geometry and materials

The FLUKA geometry used in simulations includes the composite graphite and iron dump, a concrete cavern, a concrete "dump tunnel" leading from the dump cavern to the main tunnel, and a section of the main tunnel, as shown in Figure 4. The composition of the concrete is the same as that listed in the "simulations – main linac tunnel" section. The graphite block has faces of side 40×40 cm perpendicular to, and centred on the beam line. The side parallel to the beam line is 100 cm in length, approximately five irradiation lengths in graphite. The graphite block is surrounded by iron as shown in Figure 4.

Figure 4: FLUKA representation of drive beam dump and cavern
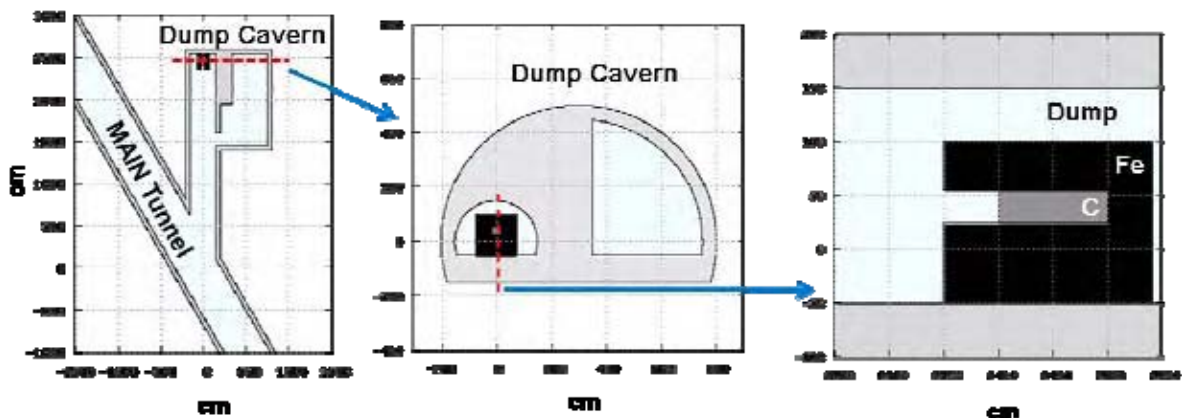
FLUKA settings

For prompt radiation, the production and transport cut-offs were set at 1 MeV and 500 keV respectively for electrons, positrons and photons. For decay radiation they were reduced by a factor of ten. All other FLUKA settings were identical to those listed for the CLIC main linac tunnel simulations of the drive beam at 0.24 GeV.

Results – drive beam dump caverns

Figure 5 shows the ambient dose equivalent rates inside the cavern averaged over a depth of 50 cm, centred on the beam line. The results show the dose rates after 180 d continuous irradiation at full intensity and at waiting times of 1 h and 1 week. After 1 h waiting time the dose rates do not exceed 10^6 µSvh⁻¹ with the exception of the graphite block region, where they do not exceed 10^7 µSvh⁻¹. With no shielding between the beam dump and the main tunnel, the activated dump and surrounding concrete contribute significantly to the dose rates in the main tunnel. The dose rates at 1 h waiting are up to 100 µSvh⁻¹ in the main tunnel region near the entrance of the dump tunnel. The dose rates exceed 100 µSvh⁻¹ in the dump tunnel, which in this design serves as the access route to the shielded part of the cavern.

**Figure 5: Residual ambient dose equivalent rates in a drive beam cavern after
180 days irradiation and 1 h waiting time (left) and 7 days waiting time (right)**
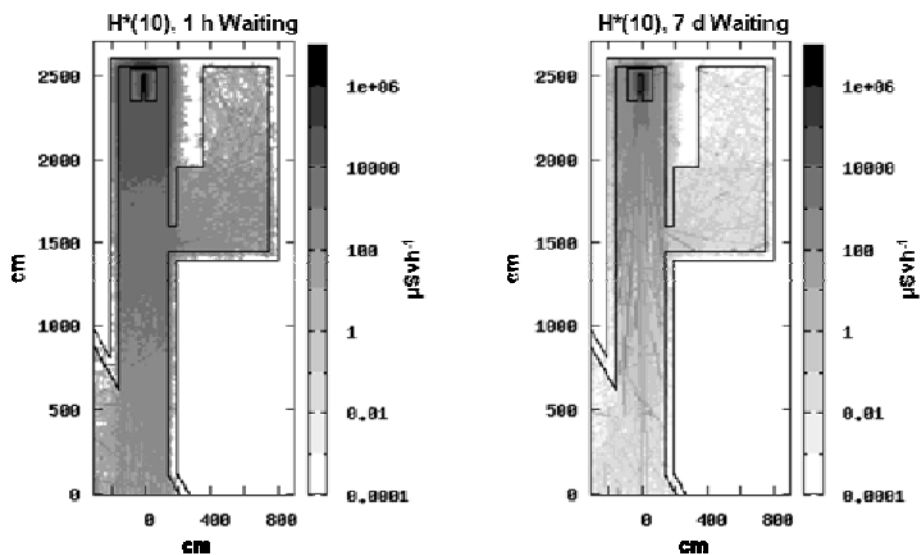
The highest energy deposition inside the dump, averaged in cubic bins of side 0.5 cm, was found to be 150 J in one second, meaning that the composite dump design will not be adequate due to the insufficient heat diffusion in graphite.

Conclusions

The simulations of radiation levels in the CLIC tunnel indicate that the ambient dose equivalent rates resulting from standard beam losses in nominal operation inside the tunnel after 4 h shutdown will require standard intervention practices but little or no remote handling of gear.

Assuming 1 MGy per year is a conservative limit for the conservation of the quadrupole copper coils over the lifetime of the accelerator [9]; damage to the quadrupoles is unlikely to be the limiting factor in terms of the maximum permitted beam loss in standard operation. Damage to the insulating cables, depending on their location in the quadrupole region, may be a limiting factor for the maximum permitted beam loss in standard operation [10].

Estimates of the fluences and absorbed doses indicate that placement of non-radiation hard electronic devices in the tunnel may require careful consideration [11]. It should be noted, however, that all estimates were based on maximum losses permitted from beam dynamics considerations. An estimate of the expected losses along the linac will better indicate the feasibility of type and placement of electronic devices inside the tunnel. Alternatively, their damage thresholds would place a lower limit on the maximum permitted beam loss.

Initial simulations indicate that the composite dump will be inadequate. Whilst future simulations are likely to be based on a water dump, it is clear that high residual dose rates in the beam dump region might necessitate strict control times for interventions. Simulations will therefore be performed to investigate shielding options in the cavern region. For example, shielding immediately after the dump would prevent contribution of the activated dump material to residual dose rates in the access route from the main tunnel to the shielded part of the cavern and would reduce the doses from the prompt radiation interfering with the beam loss monitors in the main tunnel.

References

[1]   Guignard, G., *et al.*, *A 3 TeV e+ e- Linear Collider Based on CLIC Technology*, CERN-2000-008.

[2]   Sessler, A.M., "The FEL as a Power Source for a High Gradient Accelerating Structure", *AIP Conf. Proc.*, 91, P.J. Channel (Ed.), p. 154 (1982).

[3]   Riddone, G., *et al.*, "Technical Specifications for the CLIC Two-beam Module", *EPAC08*, Genoa, Italy.

[4]   Fassò, A., *et al.*, *The FLUKA Code: Description and Benchmarking*, CERN-2005-10, INFN/TC_05/11, SLAC-R-773, NIM Z 265(1938) 581-598 (2005).

[5]   Battistoni, G., *et al.*, "FLUKA: A Multi-particle Transport Code", *Proceedings of the Hadronic Shower Simulation Workshop 2006*, Fermilab, 6-8 September 2006, M. Albrow, R. Raja (Eds.), AIP Conference Proceedings, 896, 31-49 (2007).

[6]   Theis, C., *et al.*, "Interactive Three Dimensional Visualization and Creation of Geometries for Monte Carlo Calculations", *Nuclear Instruments and Methods in Physics Research*, A 562, pp. 827-829 (2006).

[7]   Roesler, S., R. Stevenson, *deq99.f – A FLUKA User-routine Converting Fluence into Effective and Ambient Dose Equivalent*, EDMS 809389 (2006).

[8]   Schulte, D., private communication.

[9]   Tsumaki, K., *et al.*, Radiation Damage of Magnet Coils Due to Synchrotron Radiation, *Proceedings of EPAC 2004*, Lucerne, Switzerland.

[10]   Schoenbacher, H., A. Stolarz-Izycka, *Compilation of Radiation Damage Test Data, Part 1: Cable Insulating Materials*, CERN-79-04, CERN, Geneva, p. 221 (1979).

[11]   Brugger, M., for the R2E Study Group, "LHC Radiation Environment and Future Electronics Policy for the Accelerator Sector", *1st R2E Radiation School and Workshop*, Divonne, 2-3 June 2009.

The EURISOL Multi-MW Target Unit:
Radiological protection and radiation safety issues

Yuriy Romanets[1], Raul Luís[1], Oleg Alyakrinskiy[2], Marina Barbui[2], Judilka Bermudez[2],
Jean-Christophe David[3], Daniela Ene[3], Isabel Gonçalves[1], Yacine Kadi[4],
Cyril Kharoua[4], Florin Negoita[5], Roberto Rocca[4], Luigi Tecchio[2], Pedro Vaz[1]
[1]Instituto Tecnológico e Nuclear (ITN), Sacavém, Portugal
[2]Instituto Nazionale de Fisica Nucleare (INFN)-Laboratori Nazionale di Legnaro (LNL), Legnaro, Italy
[3]Commissariat à l'énergie atomique (CEA-Saclay), DSM/IRFU/SPHN, Gif-sur-Yvette, France
[4]European Organization for Nuclear Research (CERN), Geneva, Switzerland
[5]National Institute for Physics and Nuclear Engineering (NIPNE), Bucharest, Romania

Abstract

Research with radioactive beams has strengthened the link between technical developments and physics output. The study of radioactive beams allows following the evolution of nuclear structure over extended regions in the nuclear chart. Two different ways of producing radioactive beams, in-flight separation and the ISOL approach, can be combined with different post-processing of the radioactive nuclei. In Europe, the preference is to construct separate facilities built on these two complementary production schemes. Immediate priority is given to the in-flight project FAIR, for which the first experiments are planned for 2012. Highest priority for further projects is given to the next-generation ISOL facility EURISOL, which can be constructed in the next decade. An intense R&D programme is being carried out to bridge the technological gap between present-day facilities and EURISOL. It is recognised that progression needs to occur via several intermediate-stage projects, one of them being HIE-ISOLDE and others, including SPIRAL2 at GANIL. Outside Europe several projects also exist. Funding is already secured for the upgrade of the RI Beam Science Laboratory at RIKEN and for ISAC2 at TRIUMF, and in the USA a large community around the FRIB project is working towards construction of a new facility.

The Eupeuropean Isotope Separation On-line Radioactive Ion Beam (EURISOL) facility, the detailed design of which was achieved in 2009, aims at producing high-intensity (100-1000 times higher than currently operating facilities) radioactive ion beams with energies up to 150 MeV/u. Such characteristics will be achieved due to the high power (multi Megawatt) delivered by a proton beam of energies in the 1-2 GeV range and intensities up to 4 mA in a high-density spallation target (liquid mercury, commonly referred to as the neutron converter). As a result of the spallation reactions induced by the proton beams in the converter, very high neutron fluxes (in excess of 10^{15} n cm^{-2} s^{-1}) are produced to induce fission in surrounding targets containing fissile materials (uranium). The produced fission fragments are then extracted, accelerated and mass-separated and delivered to the experimental areas where measurements are to be performed.

As a result of the high-intensity proton beam, of the high-power delivered to the converter (spallation target) and of the very high neutron fluxes generated by spallation reactions, the Target Unit of the EURISOL facility is a critical component of the facility. The associated radiation safety and radiological protection aspects are extremely important and very complex. In this paper, the Monte Carlo simulations of the neutronics, dose rate and activation of the several components of the EURISOL facility are detailed in its MAFF configuration, which allows an easier manipulation, repair and maintenance of the fission targets. The extremely high levels of the material activation (up to 10^{12} Bq g^{-1} in some cases) and dose rates (dose equivalent ~10^6 Sv h^{-1}) could be a show stopper for the operation of the facility. Appropriate radiation shielding needs to be designed and implemented in order to assure the safe confinement of the radiation inside the facility during operation.

The results reported in this study were obtained using the state-of-the-art Monte Carlo codes MCNPX and FLUKA. Analysis of the activation of the structural materials is performed and discussed.

Introduction

In EURISOL, a proton beam of energy 1 GeV and intensity up to 4 mA impinges and delivers a power of 4 MW power on a heavy metal (liquid mercury) target (the converter). High neutron fluxes, in excess of 10^{14} neutrons cm^{-2} s^{-1} per mA of the proton beam current, must be obtained in order to achieve the aimed rate of 10^{15} fissions s^{-1} in the fissile targets. Such high neutron fluxes are generated by spallation reactions triggered by the high-energy protons hitting the converter [1-3].

The choice of liquid mercury as the best candidate material for the converter is based on studies that show its superior neutronics, thermal and radiological-related (no alpha-emitters of sizable lifetime and no long-lived radioactive isotopes are produced) performances, also taking into account the fact that it is liquid at room temperature [4].

In the previous studied configuration for the Multi-MW target station of the EURISOL facility, UC_x fission targets were considered. This led to significant amounts (several kg) of UC_x in the fission targets; due to the build-up of fissile materials, namely ^{239}Pu, proliferation and safety aspects acquired a significant relevance and called for alternative materials and configurations for the fissile targets of the system.

The fact that the facility is operated under intense and high-energy particle (proton, neutron, photon, etc.) fluxes makes such issues as shielding, radiation protection, radiation safety and material activation extremely important. Therefore the need to improve the access to the targets in terms of inspection, loading and unloading, maintenance and repair operations dictates the need to seek for an alternative and much more efficient systems and components for the facility. That was achieved by implementing a new geometry for the EURISOL Multi-MW Target Station inspired in the Munich Accelerator for Fission Fragments (MAFF) concept, in which a fission target is exposed to the thermal neutron flux in the core of the research reactor FRM-II, in Munich [5]. This is achieved by means of a remote-controlled positioning device that can be moved inside a through-going tube in the reactor core.

The objective of this study was to analyse the radiation protection and safety issues as well as to identify the parts of the facility, spaces in use and construction materials which can be highly influenced by the required conditions/parameters of operation.

The state-of-the-art Monte Carlo programs MCNPX [6,7] and FLUKA [8] were used for the implementation of the detailed geometry and materials of the system, as well as for the detailed description of the source term (the proton beam) and the physics processes, namely the modelling of the spallation reactions in the converter and the neutron-induced reactions in the fissile targets.

The EURISOL Multi-MW target station geometry

The implemented geometry and respective material of each element of the system are displayed in Figure 1, and it includes six fission target elements which are oriented perpendicularly to the liquid mercury converter tube. The fission target placement was determined allowing for the homogeneity of the neutron flux distribution around the spallation target, in order to obtain the maximum fission rate. The fission target geometry was chosen in order to make possible individual handling of each fission target, making the facility more flexible and safer during operation and maintenance.

The facility layout (FLUKA geometry model) of the EURISOL Multi-MW Target Station is shown in Figure 2. The plane perpendicular to the beam (z = 0) shows the fission target handling room, radioactive ion beam (RIB) extraction elements, fission targets and spallation target area. It also shows plane x = 0, where the impact point of the proton beam is located. The main areas of interest for this study, presented in Figure 2, include the fission target handling room, mercury loop handling room, beam dump (mercury loop trolley), fission targets and spallation target (liquid mercury) elements, fission product extraction tubes and concrete shielding of the spallation area (active area). The large size of the facility can be explained by the high intensity of the particle fluxes during operation. Therefore proper bulky concrete shielding must be considered. In this study 6 m thick concrete shielding was used as a separation between the spallation target area and the fission target handling room. Due to the high levels of radiation and for safety reasons the spallation target area should be placed underground. Various support areas, such as a new fission target storage room, unloaded/processed fission target cooling space and a remote control room for spallation target handling during maintenance must be added and considered.

Figure 1: General view of the spallation target and fission target geometry (FLUKA modelling)
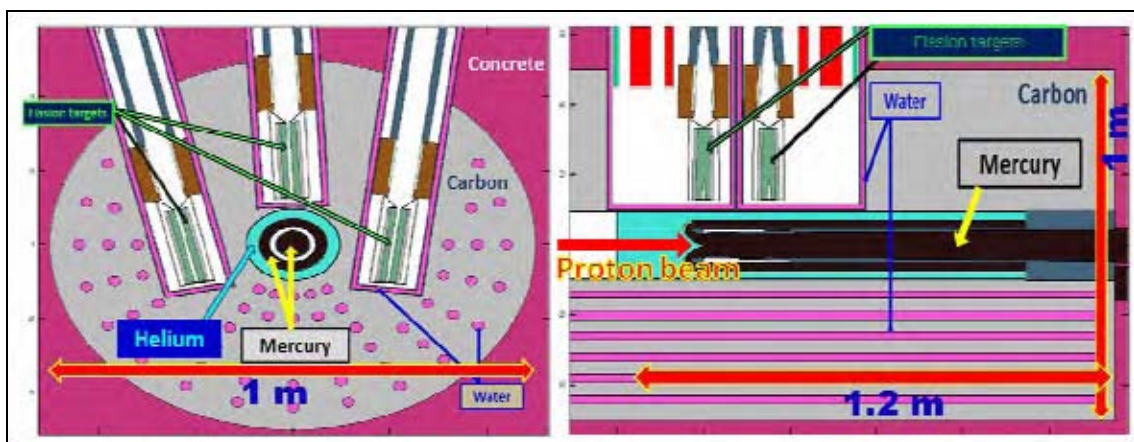
Figure 2: General view of the facility (FLUKA geometry)
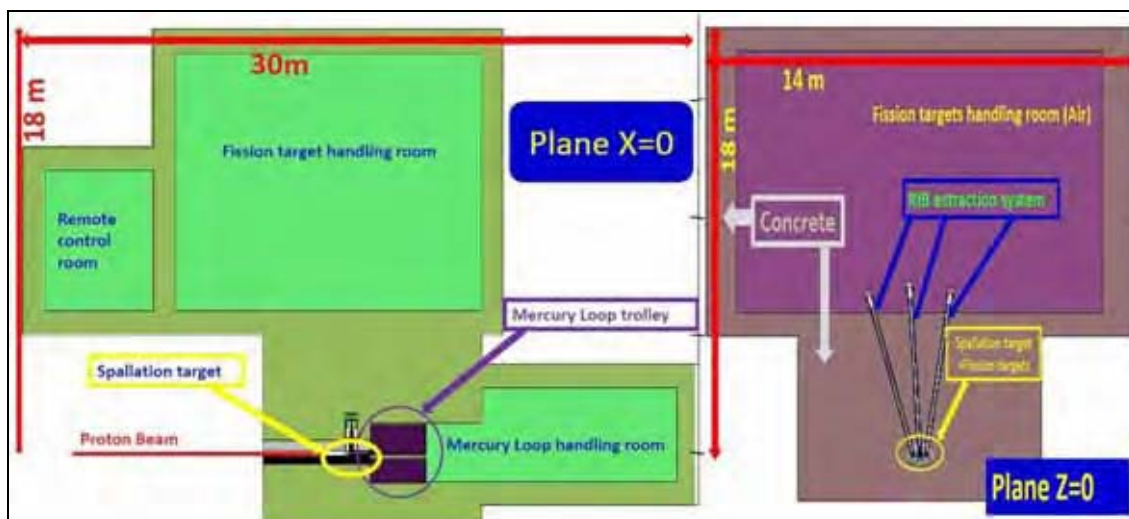
Results

Figure 3 shows the neutron flux distribution in the facility. As displayed in the figure, 4 m thick shielding behind the spallation target and 6 m thick shielding on top of the spallation area seem to be sufficient to confine the radiation inside the facility. However, a huge leak of particles through the fission targets' extraction tubes is observed.

Material activation is one of the major issues to solve for the facilities and installations with such energies and intensities as the ones expected for the EURISOL Multi-MW Target Station. Figure 4 represents the activity in the spallation target area for different cooling times after shutdown. The activity of the spallation target area remains significant even after 1 year of cooling time. The most activated elements, as expected, are the fission targets and the spallation target. These targets have to be removed (fission targets) and discharged (spallation target) after shutdown, during the maintenance of the facility.

Dose rates which in the fission target and spallation target to choose of the access type for these elements during maintenance. It can be done by remote or by staff access. Figure 5 represents dose equivalent and respective evolution with time after shutdown for the spallation target, fission target and spallation target's carbon reflector.

Figure 3: Spallation target and fission targets areas.
Neutron flux (n cm^{-2} mA^{-2}), FLUKA performed calculations.
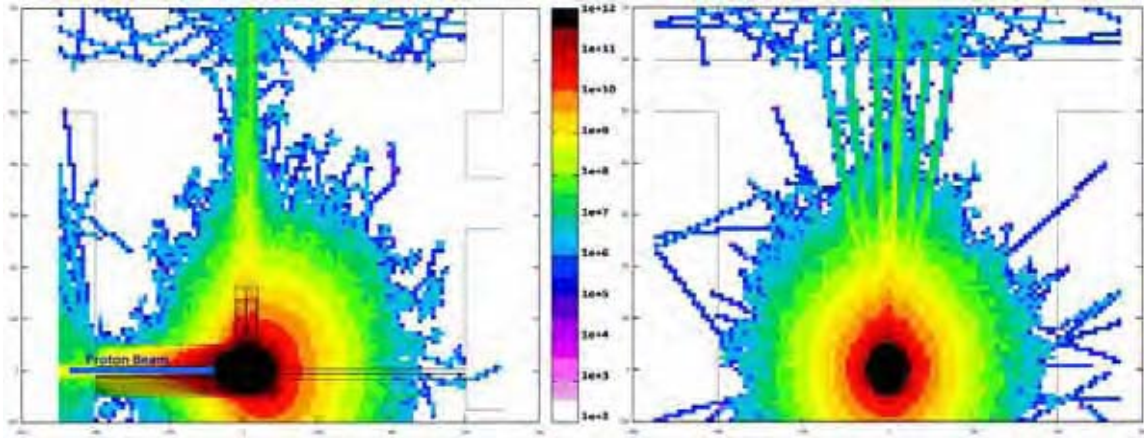
Figure 4: Activities (Ci*g^{-1}) after shutdown. Decay contribution
after 200 days of irradiation (4 MW power proton beam).
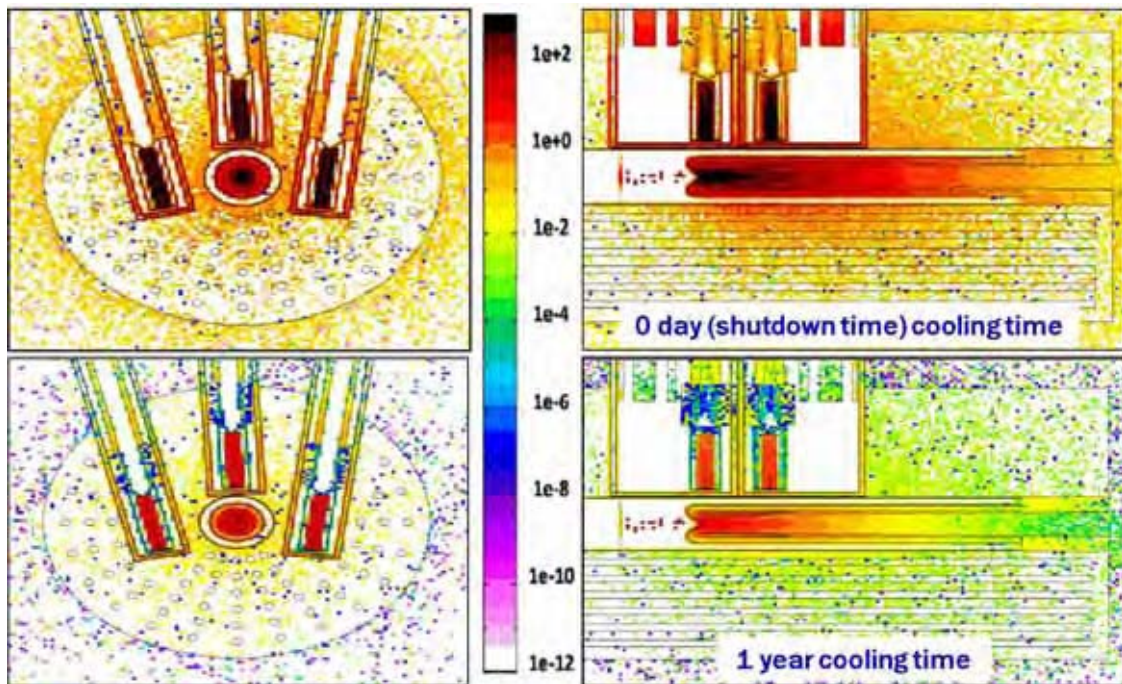
Figure 5: Dose equivalent after shutdown
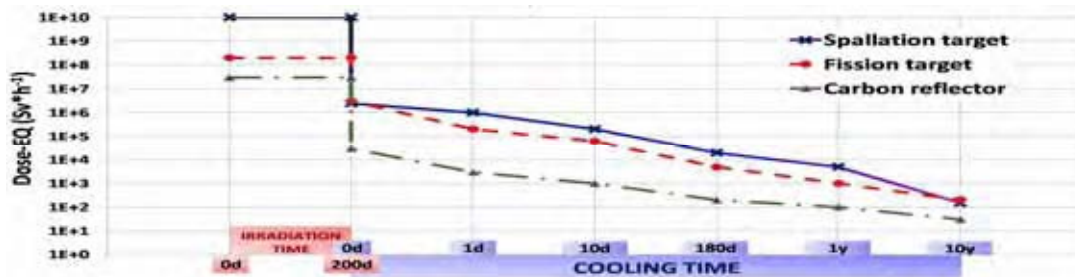
Conclusions

The Multi-MW Target Station of the EURISOL facility will be a very complex system from the radioprotection and waste management points of view. This work is intended to contribute to a better knowledge of the system and to provide important information for future decisions regarding material choices, cooling times needed before accessing the different regions and access type to these regions.

Very high doses were registered during operation, especially near the impact point of the proton beam, where the proton and neutron fluxes are the highest. The doses are still high after the stoppage of the beam, due to the decay on the radioactive nuclides that are formed in the different materials by activation. For this reason, the access to the Multi-MW target station will have to be made by remote control when maintenance is required. The most activated regions are the spallation target and the fission targets.

Acknowledgements

References

[1] *EURISOL DS: European Isotope Separation On-line Radioactive Ion Beam Facility Design Study*, EC − FP6 Research Infrastructure Action – Structuring the European Research Area, Project Contract no. 515768 RIDS, *www.eurisol.org.*

[2] Herrera-Martínez, A., Y. Kadi, *EURISOL-DS Multi-MW Target Neutronic Calculations for the Baseline Configuration of the Multi-MW Target*, AB Dept. ATB/EET European Organization for Nuclear Research (CERN) CH-1211 Geneva, Switzerland (2006).

[3] Cornell, J. (Ed.), "Neutronic Calculations for the Baseline Multi-MW Target, EURISOL Multi-MW Target", *The EURISOL Report: A Feasibility Study for a European Isotope-Separation On-line Radioactive Ion Beam Facility*, GANIL, France (2003).

[4] Herrera-Matínez, A., Y. Kadi, *Preliminary Study of the Liquid Metal Proton-to-neutron Converter*, EURISOL DS/TASK2/TN-05-01 and CERN-AB-06-013 ATB (2006).

[5] Maier, H.J., *et al.*, "Target Development for the Munich Fission Fragment Accelerator", *Nuclear Instruments and Methods in Physics Research*, A 480, 1 (2002).

[6] *MCNPX User's Manual*, LA-CP-02-408 (and later) (2002).

[7] Briesmeister, J.F., *et al.* (Eds.), *MCNP – Version 4B* (and later), LA-12625-M, LANL (1997).

[8] Ferrari, A., *et al.*, *FLUKA: A Multi-particle Transport Code*, CERN, 2005-10, INFN/TC-05/11, SLAC-R-773 (2005).

Activation and neutronics studies for the CERN n_TOF facility with the FLUKA Monte Carlo code

E. Lebbos, M. Brugger, M. Calviani, P. Carbonez,
P. Cennini, A. Ferrari, R. Losito, M. Pangallo, V. Vlachoudis,
the n_TOF Collaboration (www.cern.ch/ntof)
European Organization for Nuclear Research (CERN)
Geneva, Switzerland

Abstract

The n_TOF facility, a spallation white neutron source, uses a pure lead target for production of neutrons by means of a 20 GeV/c proton beam extracted from the CERN Proton Synchrotron (PS). After four years of operation and three years of cooling, from 2001 to 2007, the target assembly has been successfully removed. After a detailed analysis of the target status, the decision to substitute it with a new target has been taken. Within only a few months, a strong effort was made toward the development of a new target and a new cooling system, both ready for a restart of the facility at the end of 2008. This study presents the first detailed results for the produced nuclide vector in the respective installation and target components, as well as a three-dimensional residual dose rate fields for different geometrical configurations. These calculations formed an important input to prepare and plan intervention scenarios, foresee proper waste disposal and help in the analysis of the target status. For the design of the new target, numerous aspects were taken into account, including neutronics and activation calculations compared with the ones performed for the old target. A respective comparison of the activation of several possible target configurations is presented in a second part, as well as the comparison of the expected fluence – in the experimental area – between the new and the old spallation target, together with the results of the simulation using borated water in the moderator circuit, a recent upgrade of the facility. In 2009 a new target cooling station with improved performances was installed. It includes a de-gassing system, which is used to maintain the oxygen level in the cooling water down to an average value of 40 ppb and two ion-exchanger cartridges to retain spallation products. In addition, the primary area is also now being ventilated and maintained with an under pressure of 40 Pa with respect to the surrounding environment. In this context, the impact of an unforeseen release of short-lived isotopes from the exhaust stack is shown, as well as the actions taken to mitigate this issue.

Introduction

In 1998, plans were made for a spallation neutron source at the CERN Proton Synchrotron (PS). A proton beam with a momentum of 20 GeV/c impinges on a production target made of lead and generates neutrons by spallation (see Figure 1). The nominal proton intensity is 7×10^{12} per pulse, and the facility operates with four pulses per supercycle of 16.8 s duration, *i.e.* an average intensity of 1.6×10^{12} s^{-1} [1]. In 2004, the last operation period of n_TOF, CERN's Research Board authorised a total of 1.6×10^{19} protons/year for n_TOF, the highest intensity run as of yet. The spallation neutrons emerging from the lead target are moderated by the cooling water which is in contact with the target and then enters the evacuated time-of-flight tube (~200 m long) at an angle of 10° to the proton beam direction.

**Figure 1: Schematic overview of the n_TOF installation
in the context of the CERN accelerator complex**
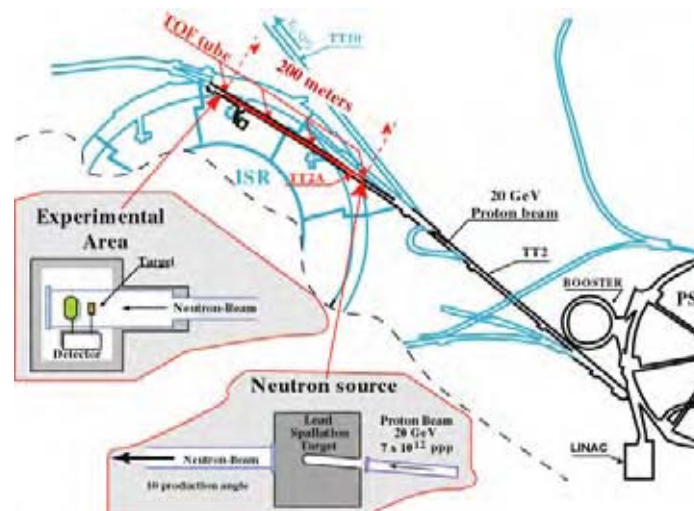
After four years of operation and three years of cooling, from 2001 to 2007, the decision to remove the n_TOF lead target has been taken, using the crane available in the access gallery above the TT2A tunnel (where the facility is located). The removal was mainly motivated by a previously encountered activity increase of the cooling water due to dilution of lead spallation products. In order to study the status of the target after four years of radiation, and to limit risks of contamination during the removal of the target and also for its planned long-term storage at PSI, detailed isotope production and residual dose rate simulations were performed using the FLUKA Monte Carlo code [2,3]. All the interventions were successfully finished, minimising the individual and collective received dose. Technical design drawings as well as pictures taken from the TT2A tunnel and during the intervention were used to verify and update the existing geometrical implementation in the simulation as detailed as possible, with the FLUKA model containing the full facility from the target station to the experimental area (*e.g.* see Figure 2 for a comparison between the old target and the corresponding FLUKA implementation).

Based on the important influence of the cobalt content within stainless steel around the lead target, and also to detailed ambient residual dose rate measurements, a very good agreement was obtained between the simulations and the measurements, as will be presented here.

After the target inspection, the decision to set up a new target has been taken and a huge effort was made within a few months in order to have a target ready for the restart of the facility at the end of 2008. Numerous critical aspects were taken into account for the design of the new target and FLUKA calculations were performed with several target configurations to evaluate the neutronics and activation effects. Furthermore, prompt dose calculations were performed with the finally chosen target design, which is based on a detailed geometrical implementation in FLUKA, and the comparison with the measurements performed during the commissioning in 2008 is shown in a second part. A section is devoted to the neutron beam characteristics measured in 2009 in the experimental area and compared with the FLUKA results.

Figure 2: First n_TOF lead target (left) compared to the geometrical FLUKA implementation (right) [4]

The n_TOF facility now features a new lead spallation target with a more efficient cooling circuit and with a ventilation system in the target area. Some characteristics of the present status of the target area are described in the last part.

Target removal: residual dose rate benchmark and waste disposal

After three years of cooling, the decision to remove the n_TOF lead target from the installation pit has been made. Before constructing a new replacement target and, one of the main motivations being to determine the status of the existing target after four years of operation, several interventions were scheduled. The latter were based on detailed dose planning using the FLUKA simulation results. A careful optimisation of procedures was performed using the calculated three-dimensional residual dose rate maps (see Figures 3 and 4) and led to only minor total collective doses of the order of several hundred µSv – a very low level given the complexity of the intervention carried out.

With the standard method to calculate residual dose rates in FLUKA it is not possible to determine the residual dose rate when a part of the shielding is removed or the target is put elsewhere. To perform such a calculation a two-step method can be used [5]. In the first part of the calculation, the information concerning the production of excited residual nuclei is stored in a dedicated file after taking into account the irradiation pattern and for a given cooling time. In the second part of the calculation, the information concerning the radionuclides is used to sample decay particles (photons, electrons and positrons) using detailed data on branching ratios, gamma energies and positron energy spectra. A pure electromagnetic transport calculation is then performed and the ambient dose equivalent maps can be calculated using fluence-to-dose conversion factors [6,7]. For the second step, it is eventually possible to sample decay particles originating from a reduced number of regions as well as to modify the geometry allowing for a calculation of the residual dose rate when the shielding blocks are removed.

Pit survey

When compared with the first measurement taken inside the pit, the first FLUKA predictions showed an important disagreement. To understand this difference and estimate possible shortcomings in both measurements and simulations, a second set of detailed measurements were performed using a laser attached to the crane continuously controlling the position of the remote detector (attached to the hook). This way, the real depth of the pit could be measured, and several precise positions inside the pit were chosen. The detector, especially designed for the CERN CNGS facility, allows for a continuous readout and can be fully controlled from a distance using wireless communication. At the same time, using the latest pictures from the target and the pit inspection, the FLUKA geometry was further updated. This included the exact depth of the pit and adding important parts around the container at the bottom of the pit, *e.g.* a thick aluminium plate below the container and another one against the wall of the pit, as well as numerous steel screws around the tube close to the neutron window. For the second pit survey, the comparison between the updated FLUKA simulations and the second set of measurements is presented in Figure 3 and are in very good agreement with a maximum difference of only 30%.

Figure 3: Comparison of residual dose rate measurements and FLUKA simulations inside the n_TOF installation pit down to the target position (without the target being installed)
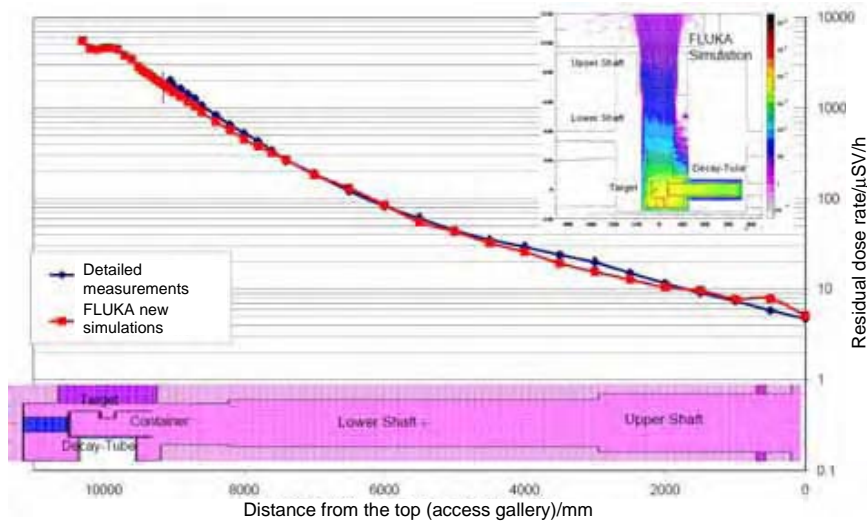
Target survey

The same method was used to perform the second measurements around the lead target. The FLUKA geometry was further updated to include all details of the stainless steel support structure (see Figure 2). In addition, to study the dominant contribution of ^{60}Co, several calculations were performed by ranging the cobalt content within stainless steel (^{59}Co) from 0.01% to 0.1%. Missing a detailed chemical analysis of the used stainless steel, a content equal to 0.1% is justified by several standard stainless steels used at CERN and showing similar ^{59}Co concentrations. The residual dose rate measurements around the target and the FLUKA comparison for different cobalt contents are presented in Figure 4; measurements start at 3 meters distance from the target and go towards the target exit surface. The comparison between the FLUKA simulation, using a cobalt content equal to 0.1%, and the measurements are in very good agreement, with a maximum difference again of the order of 30%.

Figure 4: Comparison of residual dose rate measurements (dark blue) and FLUKA simulations for the target exit face and for different cobalt contents (brown, blue, green and red)
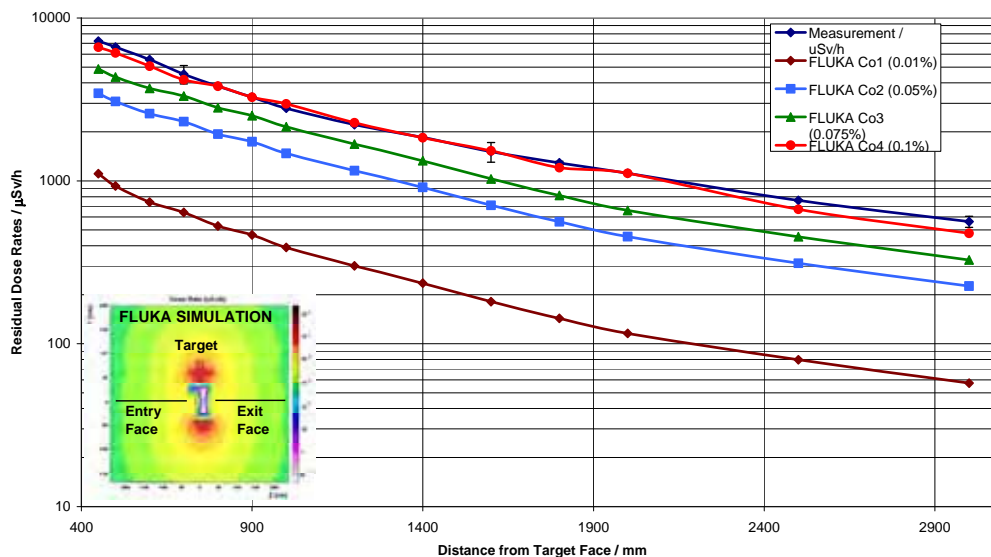
Radioactive waste and nuclide vector

For the storage and transport of the n_TOF target, waste calculations were performed with FLUKA. This section lists the nuclide vector for the lead target, *i.e.* the specific activities of the isotopes being produced after four years of operation and three years of cooling, thus corresponding to the target intervention in September 2007. In addition, the results are also given in terms of the respective exemption limit (L_E) according to Swiss legislation [8,9]. Components are considered as radioactive waste if the activity concentration (specific activity) a of an isotope exceeds the exemption limit L_E and the total activity A of that isotope exceeds 100 L_E.

The values of L_E are defined isotope-specifically [8,9]. In case of components containing a multitude of isotopes, they must furthermore fulfil the following conditions:

$$\sum_i \frac{a_i}{LE_i} > 1 \tag{1}$$

where a_i is the specific activity of nuclides *i*: 1, 2,..., *n* in Bq/g and LE_i is the exemption limits of nuclides *i*: 1, 2,..., *n* in Bq/g [8,9].

$$\sum_i \frac{A_i}{LE_i} > 100 \tag{2}$$

where A_i is the total activities of nuclides *i*: 1, 2,..., *n* in Bg.

Table 1 compares the specific activity a and total activity A of (non-alpha emitting) isotopes within the lead of the n_TOF target assembly, three years after the last radiation corresponding to September 2007. Because of the important number of isotopes produced, the table only lists isotopes with a specific activity being superior to five L_E equivalents.

Table 1: List of (non-alpha emitting) radioactive isotopes within lead three years (September 2007) after the last radiation

Isotope	T 1/2 (s)	Specific activity a (Bq/g)	Error statistic (%)	Exemption limit L_E (Bq/g)	Multiple of L_E	Total activity A (Bq) in 4 000 kg	Multiple of 100 L_E
^{204}Tl	1.19E+08	2.27E+04	0.14	8.00	2 841.17	9.05E+10	1.13E+08
^{194}Hg	1.40E+10	3.02E+02	0.10	0.20	1 509.07	1.20E+09	6.01E+07
^{60}Co	1.66E+08	3.21E+02	0.54	1.00	320.53	1.28E+09	1.28E+07
^{3}H	3.89E+08	5.48E+04	0.06	200.00	274.25	2.18E+11	1.09E+07
^{207}Bi	1.04E+09	1.82E+03	0.14	8.00	227.32	7.24E+09	9.05E+06
^{172}Lu	5.79E+05	1.29E+03	0.44	8.00	160.86	5.12E+09	6.40E+06
^{172}Hf	5.90E+07	1.27E+03	0.44	10.00	127.42	5.07E+09	5.07E+06
^{90}Sr	9.12E+08	1.91E+01	1.72	0.40	47.66	7.59E+07	1.90E+06
^{195}Au	1.61E+07	1.56E+03	0.12	40.00	39.07	6.22E+09	1.56E+06
^{109}Cd	3.99E+07	1.54E+02	0.65	5.00	30.79	6.13E+08	1.23E+06
^{173}Lu	4.32E+07	1.01E+03	0.27	40.00	25.22	4.02E+09	1.00E+06
^{65}Zn	2.11E+07	6.28E+01	0.76	3.00	20.93	2.50E+08	8.33E+05
^{202}Pb	1.66E+12	1.58E+01	0.06	1.00	15.84	6.31E+07	6.31E+05
^{194}Au	1.37E+05	3.02E+02	0.10	20.00	15.09	1.20E+09	6.01E+05
^{101}Rh	1.04E+08	2.72E+02	0.81	20.00	13.60	1.08E+09	5.42E+05
^{54}Mn	2.70E+07	1.27E+02	0.57	10.00	12.75	5.08E+08	5.08E+05
^{193}Pt	1.58E+09	3.48E+03	0.07	300.00	11.60	1.39E+10	4.62E+05
^{179}Ta	5.74E+07	2.02E+03	0.29	200.00	10.08	8.03E+09	4.01E+05
^{55}Fe	8.64E+07	2.76E+02	0.91	30.00	9.20	1.10E+09	3.66E+05
^{106}Ru	3.23E+07	9.19E+00	2.98	1.00	9.19	3.66E+07	3.66E+05
^{106}Rh	2.98E+01	9.19E+00	2.98	1.00	9.19	3.66E+07	3.66E+05
^{133}Ba	3.32E+08	6.11E+01	1.14	10.00	6.11	2.43E+08	2.43E+05
^{134}Cs	6.52E+07	2.97E+00	6.62	0.50	5.94	1.18E+07	2.37E+05
TOTAL		9.19E+04				3.70E+11	

For the same cooling time, Table 2 lists all alpha-emitting radionuclides within lead classified by multiple of L_E. In Switzerland everything which is not spent fuel and alphatoxic waste (ATA) is defined as "low and intermediate radioactive waste". In this context, waste is considered as ATA when the alpha inventory exceeds 20.000 Bq/g. A lower activation level is clearly shown in Table 2 (1.06×10^2 Bq/g in total), thus confirming the fact that the n_TOF target does not fall into the ATA category.

Table 2: List of all alpha-emitting radionuclides within lead three years (September 2007) after the last radiation

Isotope	T 1/2 (s)	Specific activity a (Bq/g)	Error statistic (%)	Exemption limit L_E (Bq/g)	Multiple of L_E	Total activity A (Bq) in 4 000 kg	Multiple of 100 L_E
^{148}Gd	2.24E+09	2.95E+01	1.06	0.20	147.42	1.17E+08	5.87E+06
^{208}Po	9.15E+07	6.97E-02	1.31	0.01	6.97	2.77E+05	2.77E+05
^{210}Po	1.20E+07	8.10E-02	0.07	0.04	2.02	3.22E+05	8.06E+04
^{145}Pm	5.59E+08	7.32E+01	0.82	90.00	0.81	2.92E+08	3.24E+04
^{209}Po	3.22E+09	1.04E-03	2.95	0.01	0.10	4.16E+03	4.16E+03
^{151}Gd	1.07E+07	3.13E+00	0.41	50.00	0.06	1.25E+07	2.49E+03
^{146}Sm	3.25E+15	1.99E-05	0.83	0.20	0.00	7.92E+01	3.96E+00
^{148}Eu	4.71E+06	2.97E-05	6.04	8.00	0.00	1.18E+02	1.48E-01
^{190}Pt	2.05E+19	1.35E-07	0.09	1.00	0.00	5.36E-01	5.36E-03
^{147}Sm	3.35E+18	1.75E-08	0.80	0.20	0.00	6.98E-02	3.49E-03
^{152}Gd	3.41E+21	1.87E-11	0.76	0.20	0.00	7.46E-05	3.73E-06
^{147}Eu	2.08E+06	1.54E-11	0.68	20.00	0.00	6.15E-05	3.07E-08
^{188}Pt	8.81E+05	5.57E-29	0.17	10.00	0.00	2.22E-22	2.22E-25
^{149}Gd	8.02E+05	2.56E-33	0.83	20.00	0.00	1.02E-26	5.11E-30
^{206}Po	7.60E+05	4.86E-39	1.57	0.08	0.00	1.94E-32	2.42E-33
^{154}Dy	9.47E+13	8.92E-04	0.49	0.00	0.00	3.55E+03	0.00E+00
^{150}Gd	5.65E+13	1.04E-03	0.86	0.00	0.00	4.15E+03	0.00E+00
TOTAL		1.06E+02				4.22E+08	

New target design

After the target removal, several analyses were done in order to evaluate whether the target could be reused. As shown in Figure 5, the inspection of the target led to several conclusions, such as an insufficient cooling especially at the entrance of the proton beam, an oxidation due to the contact with hot air, a mechanical instability due to the block structure. Therefore, the decision to design and construct a new target was made. Critical aspects were considered during the design of the new target, and numerous FLUKA calculations were performed with different target configurations to evaluate both the neutronics and respective activation effects as well as auxiliary radiation protection aspects (future waste disposal, air activation, etc.). For the residual dose rate calculations, two scenarios were considered: a short operation of six months followed by five months of cooling, and a long operation of 10 years followed by one year of cooling (see Figures 6, 7 and 8 for an example).

Figure 5: n_TOF lead target during the inspection after four years of radiation

Activation studies

For safety, thermal and mechanical reasons, and to allow for an unclad construction solution, the lead material solution has been maintained. To reduce the mass of the target, the new overall shape is now cylindrical instead of rectangular.

FLUKA calculations were performed comparing different lead chemical compositions to evaluate the consequences in terms of activation. Indeed, mechanical studies showed that adding scandium (^{45}Sc), silver (^{107}Ag) and antimony (^{123}Sb) in the lead impurities allows for a more solid lead structure. Therefore a high-purity 99.99% lead target was compared with a lead containing 3% of Sb, 0.05% of Sc and 0.01% of Ag, and FLUKA results are presented in Figure 6. As shown in Figure 6, the lead solution containing impurities leads to a higher activation by a factor of 5 after six months of operation and five months of cooling, the main dominant isotope being ^{124}Sb with a half-life time of 5.19×10^6 s.

Figure 6: Residual dose equivalent rates (in μSv/h) shown for a transverse section through the new target after six months of operation and five months of cooling

Results are given for two design options for the lead target, pure lead (left) and lead with impurities (right)
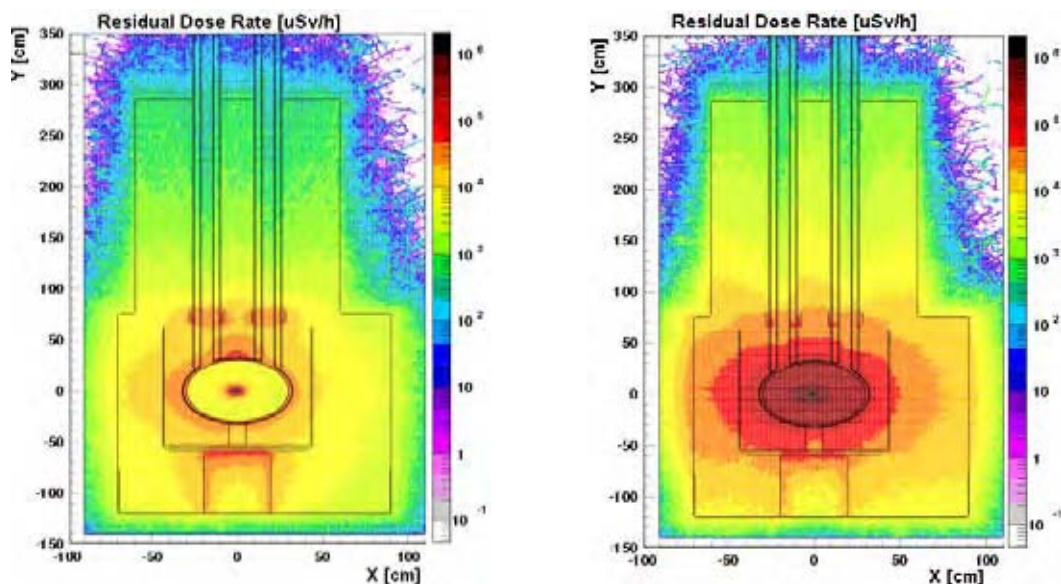
To reduce the residual dose rate coming from the stainless steel container, a proposed solution was to add additional shielding around the target laterally and upstream, particularly borated polyethylene blocks of 10 cm thickness with 6% of natural boron, in order to reduce the thermal neutrons' contribution (similarly boron-carbide could be used in praxis). The absorption of thermal neutrons will be in competition with the ^{60}Co production, thus reducing the expected effective residual dose rate. The FLUKA results are presented in Figure 7 and show a reduction by almost a factor 2 when this shielding is added.

However this reduction factor is significantly less comparing with an aluminium solution instead of stainless steel as material for the container. As shown in Figure 8, the FLUKA simulations put in evidence a significant difference in residual dose rate around the container for the two materials, especially for long cooling times. The dose rate around the target after 10 years of operation and one year of cooling is lower by about a factor of 5 for the aluminium container. While this difference might be irrelevant during operation (it is not foreseen to remove the target assembly from the pit) it will be important for the decommissioning phase. Therefore, among other reasons, aluminium was adopted for the final design.

After few months of co-ordinated effort, the new target was built and ready for the restart of the facility. The new n_TOF spallation target is now a cylindrical high-purity 99.99% monolithic lead block of 60 cm diameter and 40 cm length cooled by demineralised water (without cladding). The lead core is enclosed in a new pressurised vessel made of an AW5083 H111 aluminium alloy, and the new target

Figure 7: Residual dose equivalent rates (in µSv/h) shown for a transverse section through the new target after 10 years of operation and one year of cooling

Results are given for two design options for the target, without borated polyethylene shielding (left), with borated polyethylene shielding (right)
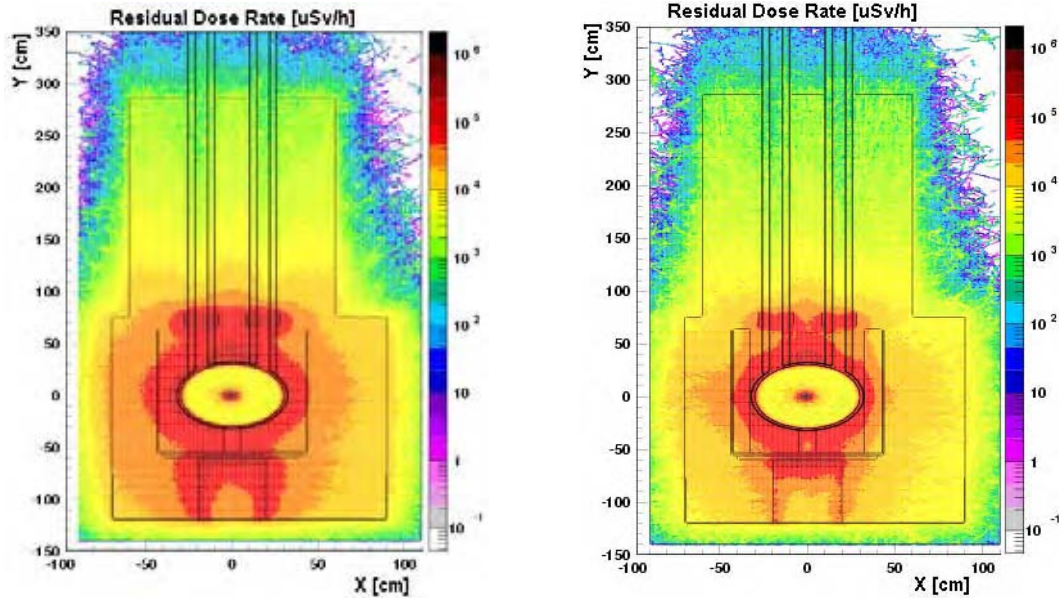
Figure 8: Residual dose equivalent rates (in µSv/h) shown for a transverse section through the new target after 10 years of operation and one year of cooling

Results are given for two design options for the target container, aluminium (left) and stainless steel (right)
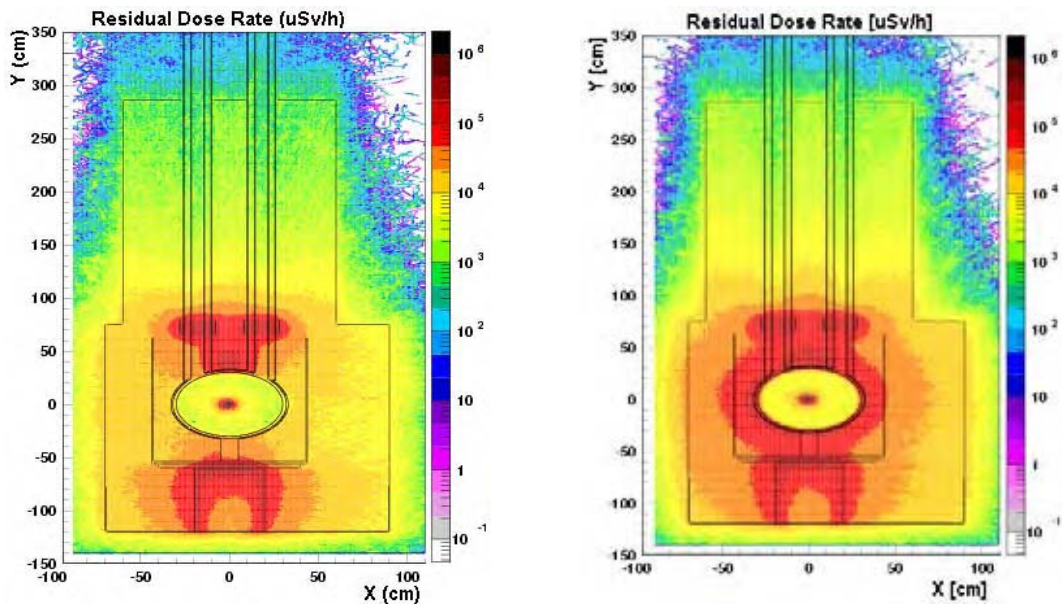
assembly is placed in the same aluminium alloy vessel used for the containment of the cooling water of the first spallation target (see Figures 9 and 13 for an illustration). Figure 9 shows the new target assembly being lowered in the n_TOF pit in October 2008. The FLUKA geometrical implementation is well detailed as shown in Figure 9.

Figure 9: n_TOF new spallation target assembly being lowered in the pit (left); geometrical FLUKA implementation of the new target assembly inside the old container (right) [4]

The commissioning of November 2008 allowed for a prompt dose rate benchmark as illustrated in Figure 10. Few pulses were taken into account when the beam was stable with a nominal intensity of 1.7×10^{11} pr/s. During this period the averaged prompt dose rate given by the PMITOF02 RadioProtection detector, located 10 meters downstream from the target behind the marble and concrete shielding, was equal to 4.35×10^5 µSv/h (see Figure 10). The FLUKA results at the monitor location and for the same beam intensity present a value around 5×10^5 µSv/h, thus in good agreement with the measurements within a maximum discrepancy of about 20% and very well within the given uncertainties due to the complexity of the geometry, the exact position, as well as the calibration of the detector (mixed field versus pure gamma calibration).

Figure 10: Prompt dose rate (in µSv/h) measured by PMITOF02 during few pulses on 11/11/2008 (left); FLUKA simulation of the prompt dose (in µSv/h) in the target area (right)
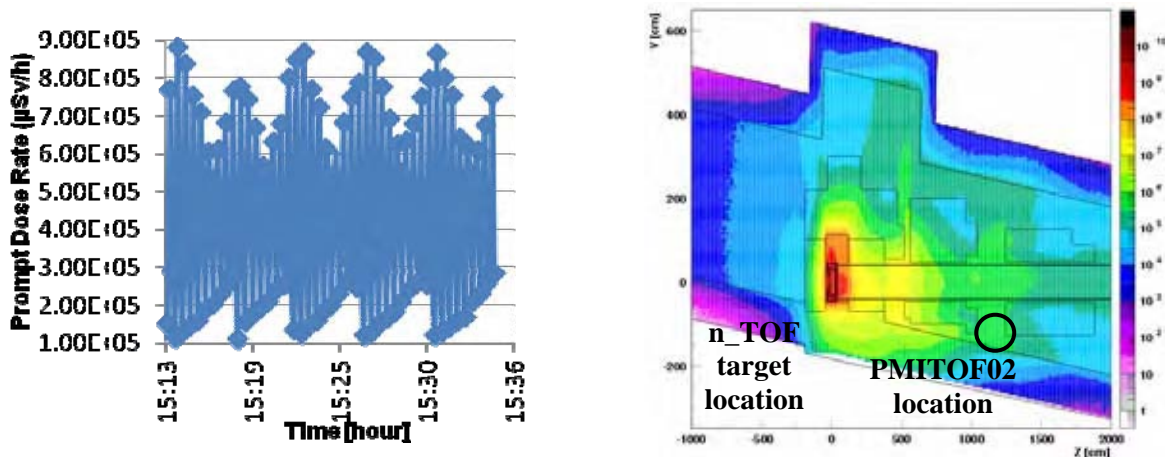
Neutronics calculations

One of the most important aspects taken into account during the design of the new target was the intensity and quality of the neutron fluence exiting the lead target. Indeed, the n_TOF facility produces a wide energy neutron beam characterised by a high instantaneous neutron flux which is employed for neutron-induced cross-section measurements 200 meters from the spallation target. Therefore FLUKA calculations were performed to compare the characteristics of the neutron beam

between the old and the new target, and results are shown in Figure 11. The thermal neutron peak value is lower by roughly 20% with the new target because of the thickness of the new water moderator which is equal to 5 cm instead of 5.8 cm in the past. Furthermore, more pronounced absorption resonances can be observed in the keV neutron energy region, due to the new aluminium target vessel structure. However, the new n_TOF target does not present an overall loss of neutron fluence in comparison with the old target.

During the 2009 run (the first complete physics run with the new spallation target), the experimental neutron fluence was measured and compared with the simulations and results are presented in Figure 12; a very good agreement is observed [10].

**Figure 11: Simulated neutron fluence in the experimental
area for the old target (in blue) and the new target (in red)**
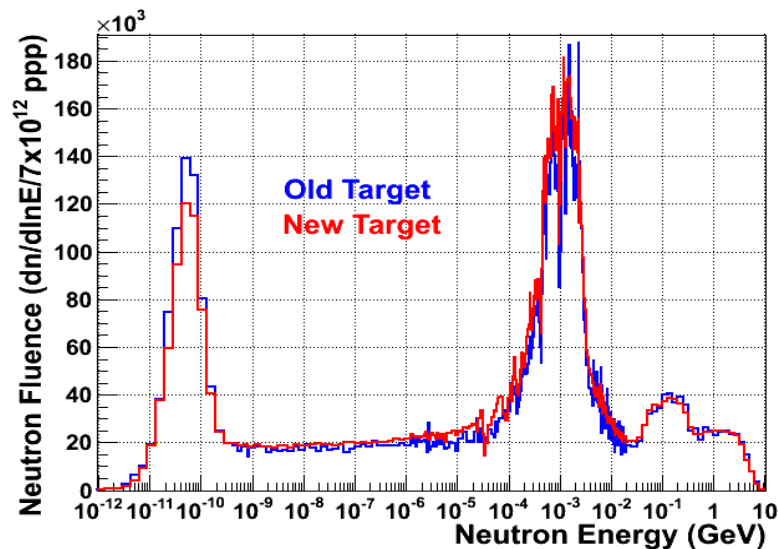
Figure 12: Experimental neutron fluence per a standard pulse of 7×10^{12} protons

The MicroMegas ^{10}B(n,α) data as well as the FLUKA simulations have been rescaled to the PTB measurement between 0.1 and 1 eV. The rescaling of the simulations is needed due to misalignment of the neutron beam collimators [10].
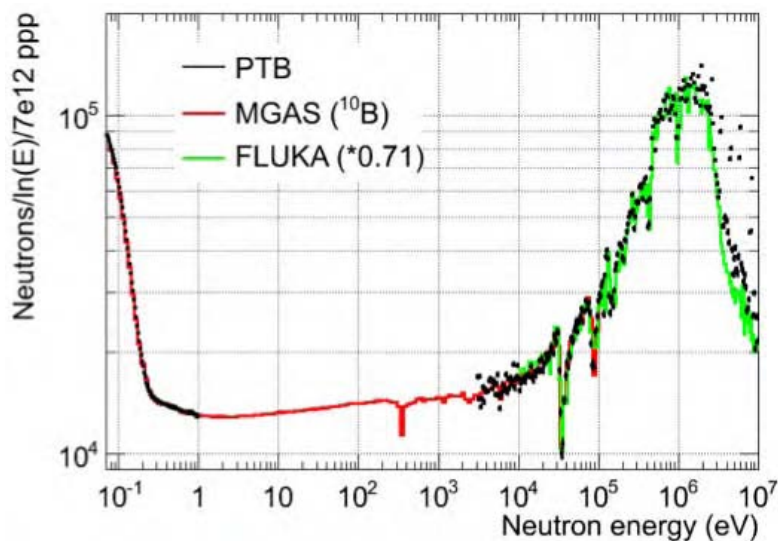
Furthermore, the new water moderator is divided into two parts. As shown in Figure 13, a layer of 1 cm of demineralised water in contact with lead is followed by an external moderator circuit of 4 cm of thickness, recently filled with borated water for the 2010 run. This will reduce the background in the experimental area due to the 2.2 MeV in-beam γ-rays generated by the neutron capture on ^{1}H, which is a significant problem for the neutron capture measurements performed with the C_6D_6 detector. Figure 14 shows the comparison between the simulated neutron fluence with 5 cm of demineralised water (black line), a situation similar to that of the 2009 run, and the one in which the borated water is introduced in the moderator circuit (red line). FLUKA simulations have shown that the reduction of the 2.2 MeV γ-rays will be of the order of a factor of 10; the neutron fluence will remain unchanged above ~10 eV, while the thermal peak, due to the presence of ^{10}B, will decrease by around 1 order of magnitude [10].

**Figure 13: Scheme of the new spallation target, with the 1 cm
thickness for the cooling liquid and the 4 cm thickness for the moderator**

The 60 cm diameter, 40 cm length cylindrical lead core is placed at the centre enclosed within a pressurised vessel

**Figure 14: FLUKA simulation of the neutron fluence in the experimental area under
the present conditions (5 cm layer of demineralised water) (black line) and the
neutron fluence expected with the borated water in the moderator loop (red line) [10]**
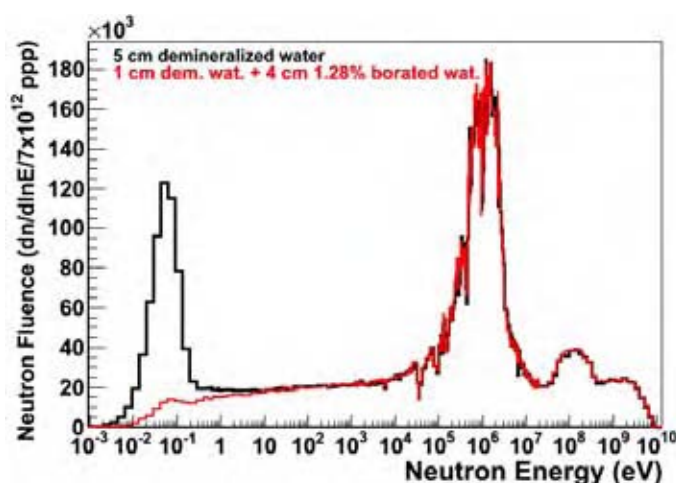
Present status of the target area

Before the 2009 campaign, several upgrades were performed in order to align the facility to the safety and operational requirements of CERN and of the respective French and Swiss safety authorities.

New cooling station

After the old target inspection, critical aspects were considered to improve the cooling of the new target, especially at the entrance of the beam where the water boiling point occurred in the past leading to a pitting corrosion, also due the O_2 content in the water circuit (see Figure 5 for an illustration of the radiated old target).

The new cooling system is constituted by a pressurised circuit ensuring a water flow inside the target vessel in order to maintain the temperature of the lead surface at a value sufficiently below the water boiling point, particularly on the proton entrance face of the target. As shown in Figure 15, secure piping now ensures the water flow between the target vessel and the cooling station located above the target in a separate area.

The system also includes a de-oxygenator to decrease the O_2 content in the water circuit, in order to reduce target corrosion. The de-gassing system uses a microporous membrane acting as a separation between the liquid and gas phases. The remote de-gassing system now allows having the O_2 level below the nominal value of 80 ppb, by applying a flow rate of N_2 gas (~4 m³/h) that flushes the accumulated oxygen [10].

Ventilation system

Following the design and operation rules of ventilation systems for nuclear installations other than nuclear reactors, the confinement of the n_TOF target area was required. The n_TOF Collaboration has therefore implemented a ventilation system which captures the aerosols containing radioactive isotopes in absolute filter and allows the monitoring of the released dose to the public. The target area is continuously flushed out with an air flow rate of 500 m³/h, in order to set a negative pressure of roughly 40 Pa between the target area and the adjacent rooms. The air is then released in the atmosphere, after having passed through two H10 and H13 HEPA (EN1822 standard) absolute filters and through an activation monitoring system connected to the CERN integrated radiation monitoring system. The dose rate to the general public outside of the CERN perimeter is estimated to be of the order or less than 1 µSv/year, in agreement with CERN's radioprotection rules [10].

Figure 15: Layout of the new n_TOF cooling circuit [11]
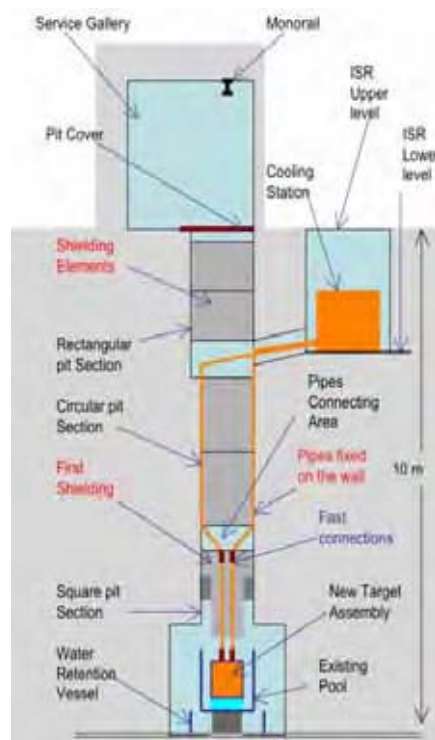
Results

Detailed FLUKA simulations for isotope production and residual dose rates were performed for the n_TOF installation at CERN. They formed not only an important input to prepare and plan intervention scenarios, foresee proper waste disposal and help in the analysis of the target status, but also built the basis for the new target design.

The removal of the n_TOF lead target, done in September 2007 after four years of operation and three years of cooling, was a success. The detailed activation measurements performed during the target removal and inspection interventions allowed for a careful benchmark of the FLUKA simulations.

Within almost one year, a huge effort involving several groups at CERN has been made to set up a new spallation target ready for the restart of the facility at the end of 2008. Critical design questions were considered and numerous FLUKA calculations were performed for neutronics and activation issues, considering different materials and target configuration. Prompt dose rates and neutron beam characteristics were measured and successfully compared with the FLUKA simulations.

The n_TOF facility now features a new lead spallation target with no loss of neutron fluence in comparison with the previous target. The new water cooling system is more efficient, allowing for a monitoring of the O_2 level in the water. It is equipped with a resin filter which stops the spallation products coming from the lead. The target has been safely operated since May 2009 with full beam condition. Furthermore, by request of the radiation protection authority, the target area is continuously flushed and the new ventilation system allows a dose to the public lower than 1 μSv per year.

The presented work not only shows the clear advantage of Monte Carlo calculations being performed for the design of facilities and for planning intervention scenarios and foreseeing proper waste disposal, but also the important need of a detailed description of all installation components, such as the complete chemical composition and the correct irradiation profile.

This study aims at defining, understanding and solving radiation protection issues in different fields such as the activation and residual dose rates, the handling issues, the radioactive waste concerns, the air activation and dose to the public.

Acknowledgments

References

[1]   Chiaveri, E., *et al.* (Eds.), *CERN n_TOF Facility: Performance Report*, CERN-INTC-O-011, INTC-2002-037, CERN-SL-2002-053-ECT, January 2003.

[2]   Fassò, A., *et al.*, *FLUKA: A Multi-particle Transport Code*, CERN- 2005-10 (2005), INFN/TC_05/11, SLAC-R-773.

[3]   Battistoni, G., *et al.*, "The FLUKA Code: Description and Benchmarking", *Proceedings of the Hadronic Shower Simulation Workshop 2006*, Fermilab, 6-8 September 2006; M. Albrow, R. Raja (Eds.), *AIP Conference Proceedings*, 896, 31-49 (2007).

[4]   Theis, C., *et al.*, "Interactive Three-dimensional Visualization and Creation of Geometries for Monte Carlo Calculations", *Nuclear Instruments and Methods in Physics Research*, A 562, pp. 827-829 (2006).

[5]   Brugger, M., S. Roesler, *et al.*, "Benchmark Studies of Induced Radioactivity Produced in LHC Materials, Part II: Remanent Dose Rates", *Radiation Protection Dosimetry*, Vol. 116, No. 1-4 (2005).

[6]   Pelliccioni, M., "Overview of Fluence-to-effective Dose and Fluence-to-ambient Dose Equivalent Conversion Coefficients for High Energy Radiation Calculated Using the FLUKA Code", *Radiation Protection Dosimetry*, 88, 279-297 (2000).

[7]   Roesler, S., G.R. Stevenson, *deq99.f – A FLUKA User-routine Converting Fluence into Effective Dose and Ambient Dose Equivalent*, CERN/SC/2006-070-RP-TN (2007).

[8]   Le Département fédéral de l'intérieur, Ordonnance du 22 juin 1994 sur la radioprotection (ORaP), RS 814.501, Switzerland, Annex 3, Column 9 (in French).

[9]   Le Département fédéral de l'intérieur, Ordonnance du 22 juin 1994 sur la radioprotection (ORaP), État le 4 avril 2000, Switzerland (in French).

[10]   Calviani, M., *et al.*, "The n_TOF Facility at CERN: Present Status and Future Upgrades", *ICANS XIX*, Grindelwald, Switzerland, 8-12 March 2010.

[11]   *n_TOF Facility Safety File*, CERN EDMS No. 934369 v.0.11 and later. *https://edms.cern.ch/document/934369/*.

Session III

Benchmarking code/code and code/experimental data

Chair: Hiroshi Nakashima

Monte Carlo benchmarking: Validation and progress*

Paola Sala
European Organization for Nuclear Research (CERN)
Geneva, Switzerland

Abstract

Calculational tools for radiation shielding at accelerators are faced with new challenges from the present and next generations of particle accelerators. All the details of particle production and transport play a role when dealing with huge power facilities, therapeutic ion beams, radioactive beams and so on. Besides the traditional calculations required for shielding, activation predictions have become an increasingly critical component.

Comparison and benchmarking with experimental data is obviously mandatory in order to build up confidence in the computing tools, and to assess their reliability and limitations. Thin target particle production data are often the best tools for understanding the predictive power of individual interaction models and improving their performances. Complex benchmarks (e.g. thick target data, deep penetration, etc.) are invaluable in assessing the overall performances of calculational tools when all ingredients are put at work together.

A review of the validation procedures of Monte Carlo tools will be presented with practical and real life examples. The interconnections among benchmarks, model development and impact on shielding calculations will be highlighted.

---

* The full paper being unavailable at the time of publication, only the abstract is included.

Intercomparison of medium-energy neutron attenuation in iron and concrete (8)

Hideo Hirayama
High Energy Accelerator Research Organization (KEK)
Ibaraki, Japan

Attenuation Length Sub-Working Group in Japan

Abstract

The same problems examined at SATIF-9 were used for intercomparison mainly to compare between AGS experiments provided by H. Nakashima with various codes. A new item has been added, and the participants were to send their results concerning "particles treated to obtain the results".

This paper presents a comparison of the neutron attenuation length of iron and concrete sent from five groups to the organiser before the end of May, including results presented at previous SATIF meetings and future themes resulting from this intercomparison.

Introduction

Neutron attenuation at high energies above a few GeVs is not supposed to depend on the energy. Its energy dependence below this energy, especially below 1 GeV, has not been well understood. It is desired to obtain common agreements concerning the behaviour of neutrons inside various materials. This is necessary in order to agree on definitions of the attenuation length, which is very important for shielding calculations involving high-energy accelerators. As one attempt, it was proposed by Japanese participants of SATIF-2 to compare the attenuation of medium-energy neutrons inside iron and concrete shields between various computer codes and data, and was cited as a suitable SATIF action. From the results for neutrons below 400 MeV presented at SATIF-3 [1], it has become clear that neutrons above 20 MeV are important for understanding that the attenuation length and the geometry, planar or spherical, do not greatly affect the results. The attenuation length of neutrons above 20 MeV was compared with the planer geometry included for secondary neutrons produced by medium-energy protons at SATIF-4 [2]. Though the attenuation lengths were different, all of the results showed the same tendency for an attenuation length to increase along with an increase in the neutron energy up to 100 GeV [3-6]. Considering results at SATIF-8, revised problems which include the comparison with the experimental results of AGS shielding experiments [7] presented by H. Nakashima, *et al.* were prepared by the Japanese Working Group and sent to the participants of this action. At SATIF-9, the results from two groups were sent to the organiser for the revised problems. From the comparison, the following results are summarised [8].

- *General tendencies are the same as those presented at SATIF-8. The differences in the attenuation length and dose become little bit smaller with the improved results of GEANT4 but are still large.*

- *The C/E values for the AGS experiments show different tendencies among the codes used.* It is desired to receive the results from other groups.

Considering these results, the same problems examined for SATIF-9 were used for intercomparison mainly to compare between AGS experiments. A new item has been added, and the participants were to send their results concerning "particles treated to obtain the results".

The results from four groups were sent to the organiser by the end of April.

Problems for an intercomparison

Problems for an intercomparison were the same as those at SATIF-9.

Summary of contributors

Five groups sent their results to Hideo Hirayama at KEK before the end of May. Table 1 lists the participants, the names of the computer codes used and the particles treated to obtain the results.

Results and discussions

Attenuation length for mono-energy neutron

The neutron attenuation lengths of iron are shown in Figure 1. Dose distributions and the neutron spectrum at 4 m for 1 GeV neutrons are shown in Figures 2 and 3, respectively. PHITS presents two results with and without transport of Λ_0 particle. The general tendency of the attenuation length is similar for all results except PHITS with Λ_0 particle even dose itself still differs, shown in Figure 3. Figure 4 shows dose difference at 4 m inside iron for 0.1 to 100 GeV neutrons between ROZ 6.6, FLUKA, MARS, GEANT4 and PHITS which present results for the whole energy region. The difference between Monte Carlo results (except PHITS) with transport Λ_0 particle is about 10.

As shown in Figure 5, the effects of Λ_0 particle in PHITS can be seen from 3 GeV and maximum at 10 GeV. The effects decrease at 50 and 100 GeV. Matsuda and Niita calculate particles emitted from 1 cm diameter and 1 cm iron and concrete by high-energy neutrons. Figure 6 shows Λ_0 particles portion within produced particles except neutrons and protons, Λ_0 portion becomes maximum at 20 GeV and decreases with increase of neutron energy.

Matsuda and Niita estimate the effect of the Λ_0 particle to the neutron attenuation length as follows:

- The Λ_0 particle is one of the stable baryons, the lifetime of which is 2.6×10^{-10} sec and which decays to nucleon and pion. If the Λ_0 particle decays very quickly after its production, as shown in Figure 5, the additional contribution of Λ_0 disappears. Therefore the additional contribution of the Λ_0 particle is realised by the collisions of lambda on the material nucleus.

- The mass of the Λ_0 particles is heavier than that of the nucleon. Thus much larger energy can be transported by the lambda particles.

- This is the reason, we suppose, that the attenuation through the lambda particle is much flatter than that that does not go through the lambda particle.

It is desired to check the contribution of the Λ_0 particle to the neutron attenuation by other codes and also to compare various particles production rates from small target.

The neutron attenuation lengths of concrete, dose distributions and the neutron spectra at 4 m for 10 GeV neutrons are shown in Figures 7, 8 and 9, respectively. The tendency that the attenuation length increases with the increase of neutron energy is the same for all codes. The differences of dose within the Monte Carlo calculation are smaller than those in the case of iron, as shown in Figure 10. The contribution of the Λ_0 particle in PHITS does not appear in the 12 m concrete.

Attenuation length for secondary neutrons

The attenuation lengths of iron and concrete for secondary neutrons from a Hg target with 3 GeV protons are shown as a function of the emission angle in Figures 11 and 12, respectively, together with the experimental results at ISIS [17] and LANSCE [18] for 800 MeV protons. The attenuation lengths of iron and concrete for secondary neutrons emitted 90° from an iron target from high-energy protons and from a Hg target from 24 GeV protons are shown in Figures 13 and 14, respectively. In these figures, the experimental results at ISIS [17] and LANSCE [18] for 800 MeV protons are also plotted for comparison.

General tendencies for secondary neutrons from a Hg target with 3 GeV protons are same as those determined at SATIF-9:

- In the case of iron, all results show similar weak dependence on the emission angle but their values are largely scattered among one other.

- In the case of concrete, all results show stronger dependence on the emission angle than in the case of iron and a different dependence between the codes used.

General tendencies for secondary neutrons emitted 90° from an iron or a Hg target are also the same as those determined at SATIF-9.

- All results show a similar tendency to reach an almost constant value above 1 GeV protons.

The differences of dose from secondary neutrons emitted to 90° by high-energy protons are relatively small compared with mono-energy neutrons as shown in Figures 15 and 16.

Comparison with experimental results at AGS

Comparison of reaction rates in the steel and concrete shields are shown in Figures 17 and 18, respectively. The dependence of reaction rate C/E values on shield thickness in the steel and the concrete shields is shown in Figures 19 and 20, respectively.

For the steel shield, the calculated results for 2.83 GeV protons agree with each other but smaller than the measured ones in general. The C/E value differences for 24 GeV protons are larger than those for 2.83 GeV. The FLUKA results agree well with the measured ones than other calculations.

For the concrete shield, the results of PHITS, GEANT4, FLUKA and MARS relatively agree well each other and with the measured results than for the steel shield.

Summary

From the comparisons given above, the following results are summarised:

- General tendencies of the attenuation length are the same as the results presented at SATIF-8 except the case of PHITS with Λ_0 transport for iron above 3 GeV neutrons.

- Dose differences deep inside iron or concrete are large especially for monoenergetic neutrons in the high-energy region.

- The C/E values for the AGS experiments show different tendencies among the codes used.

Future themes

It is necessary to discuss and perform the following activities as the next step:

- The Λ_0 effects for iron presented in PHITS must be checked by other codes.

- It is necessary to compare various produced secondary particles from small target to understand the reason for dose differences in the high-energy region.

- To determine the reason for the large differences in calculated dose deep inside iron or concrete.

- To study the reason for differences between measured results and calculated ones by various codes and the reasons for the different tendencies of C/E values among codes.

Table 1: Summary of contributors

Name of participants and organisations	Name of computer codes	Particles treated
T. Koi and D. Wright (SLAC National Accelerator Laboratory)	GEANT4 v9.3 [9,10][a] (released Dec. 2009)	All particles (including recoil nucleus)
Y. Uwamino (Riken)	HETC-3STEP [11][b]	neutron, proton, π^-
N. Matsuda (JAEA) K. Niita (RIST)	PHITS 2.24 [12][c]	All established hadronic states[d]
S. Roesler (CERN)	FLUKA 2008.3c. [13,14]	All hadrons which FLUKA can transport
N.V. Mokhov, I.L. Rakhno (Fermilab)	MARS15(2010) [15,16][e]	All elementary particles and heavy ions

[a] High-energy model switched from QGS to FTF model. Transition energy to the high-energy model is lowered.

[b] Calculation only inside concrete for secondary neutrons by 24 GeV protons toward 90° from a Hg target.

[c] Calculation only inside iron for 3-100 GeV neutrons.

[d] The PHITS code (Jet AA Microscopic Transport Model (JAM) [12]) explicitly treats all established hadronic states including resonances with explicit spin and isospin as well as their anti-particles. All hadron-hadron interactions including lambda hyperons can be simulated up to 200 GeV/u.

[e] Calculation only comparison with for the AGS experiments.

Figure 1: Comparison of the neutron attenuation length of iron
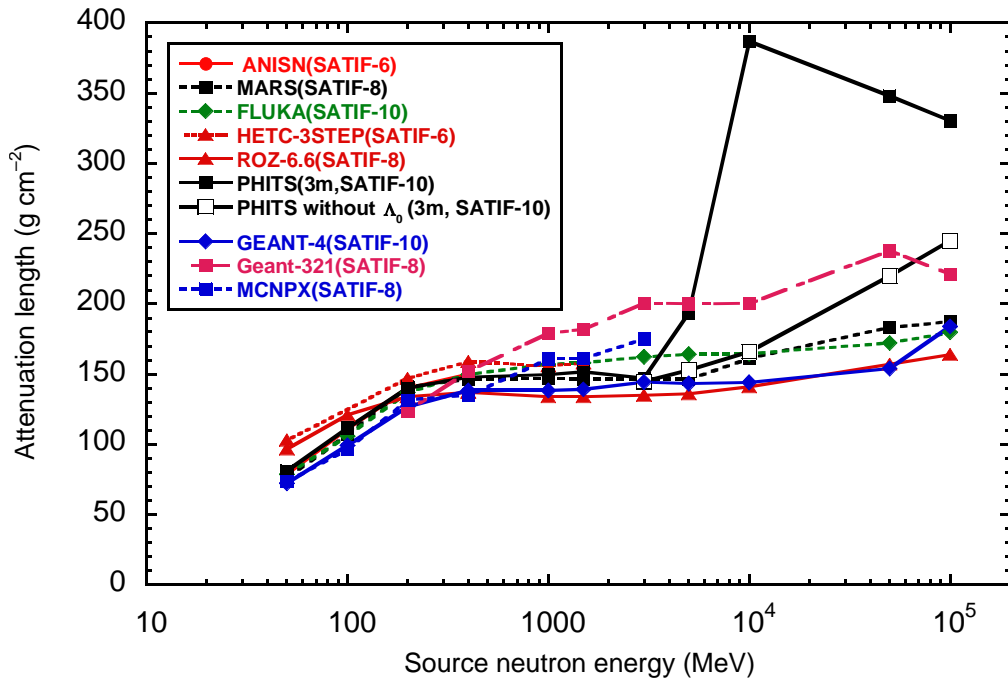
Figure 2: Dose distribution inside iron for 10 GeV protons
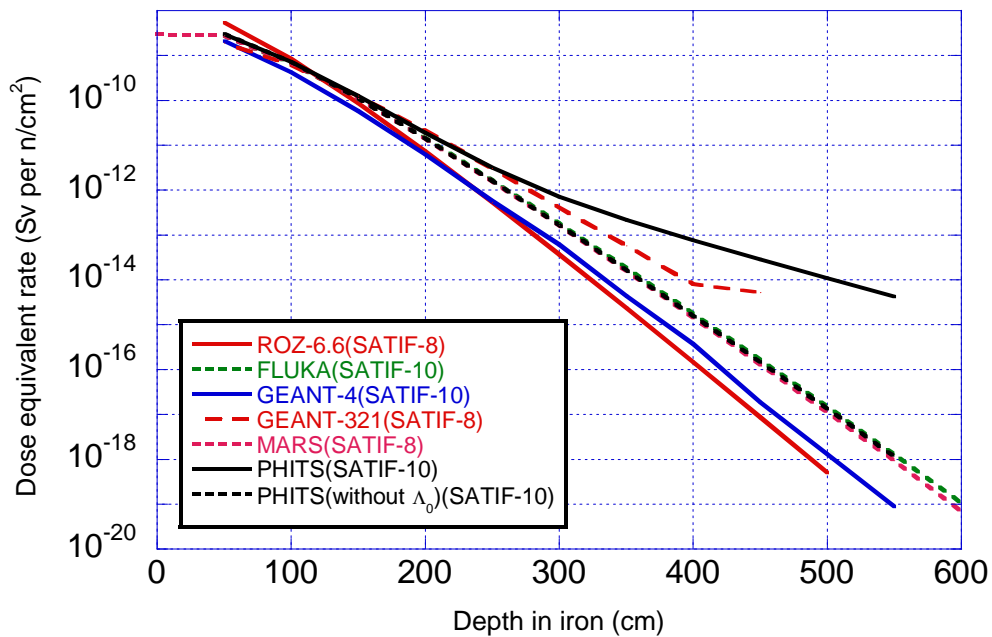
Figure 3: Neutron spectra at 4 m inside iron for 10 GeV protons
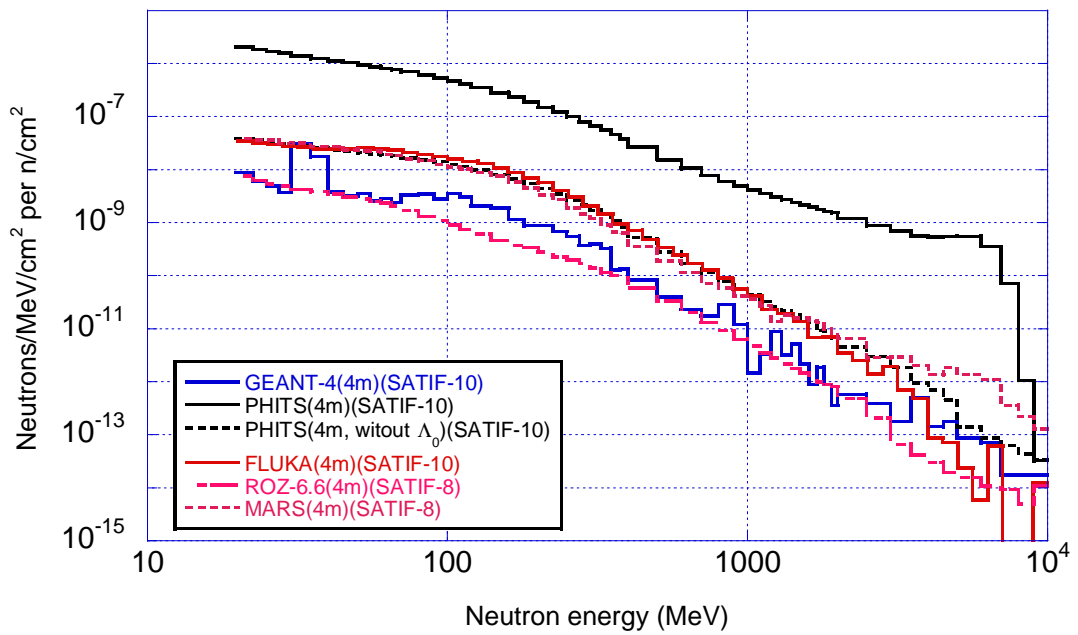
Figure 4: Neutron dose difference at 4 m inside iron between ROZ 6.6, MARS, GEANT4 and PHITS
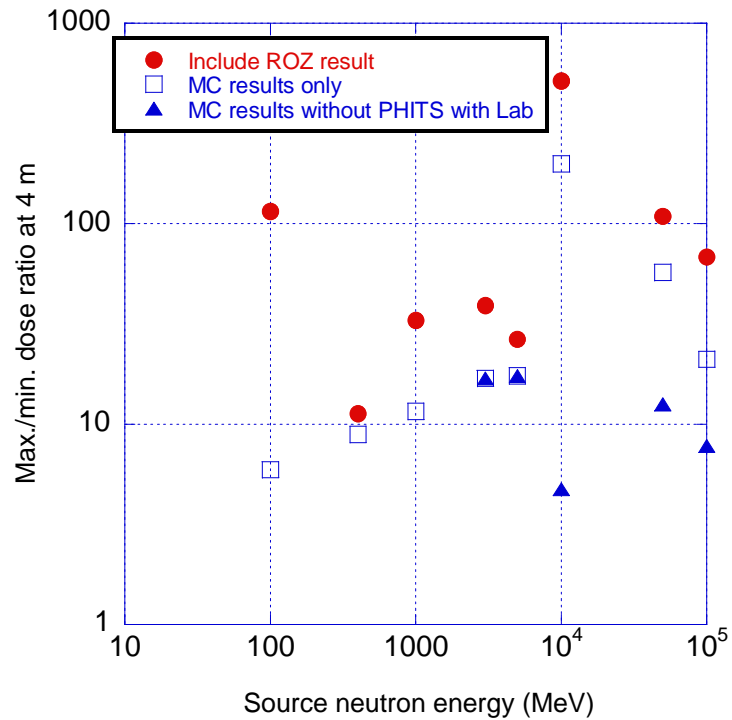
Figure 5: Dose distribution inside iron by PHITS
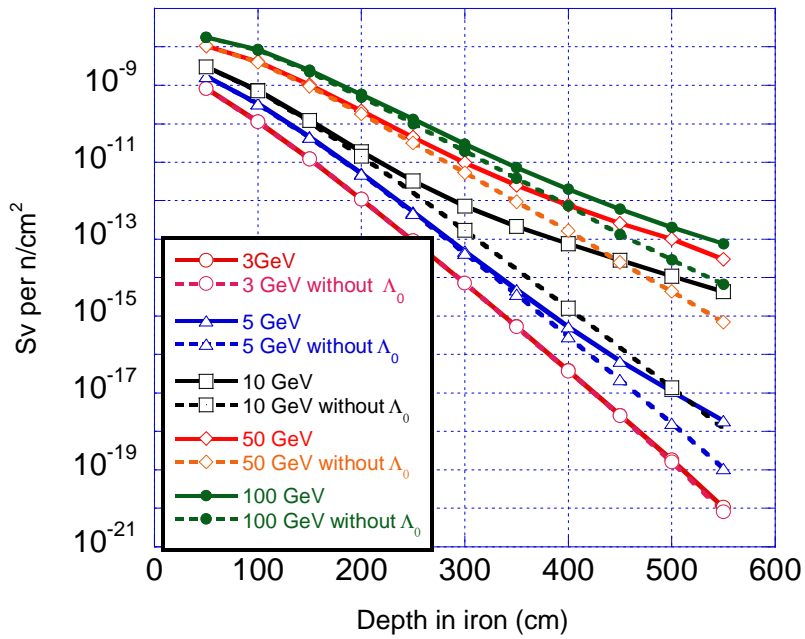
Figure 6: Λ_0 portion within produced particles except neutrons and protons from 1 cm diameter and 1 cm length of iron or concrete
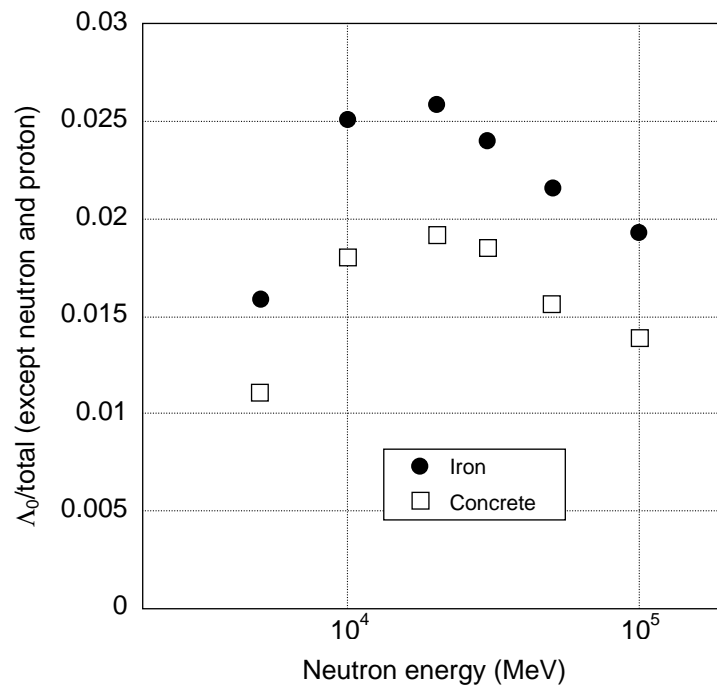
Figure 7: Comparison of the neutron attenuation length of concrete
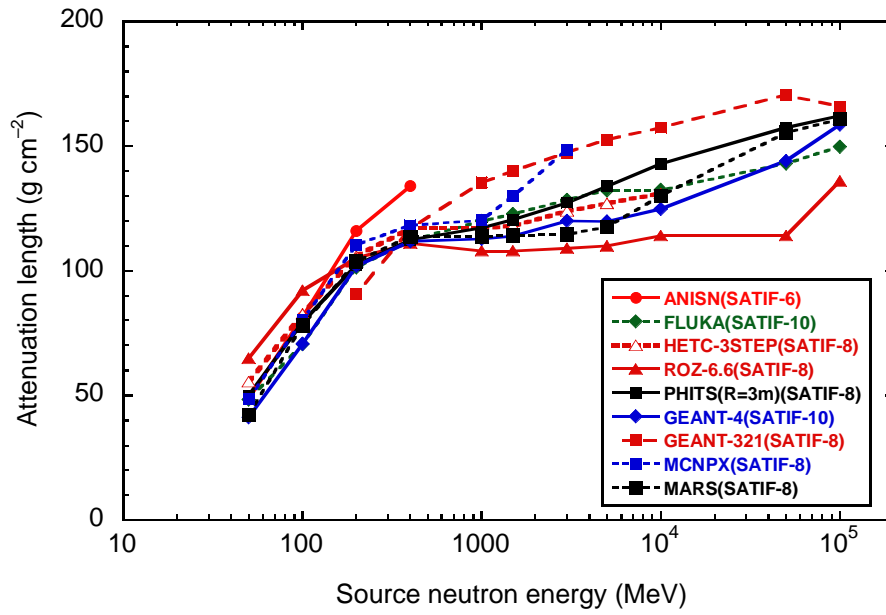
Figure 8: Dose distribution inside concrete for 10 GeV neutrons
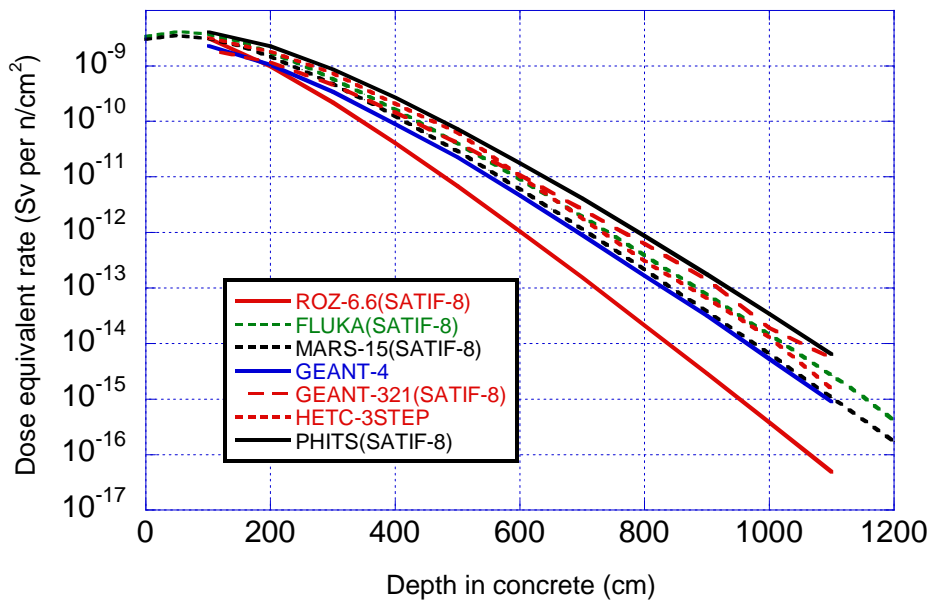
Figure 9: Neutron spectra at 4 m inside concrete for 10 GeV protons
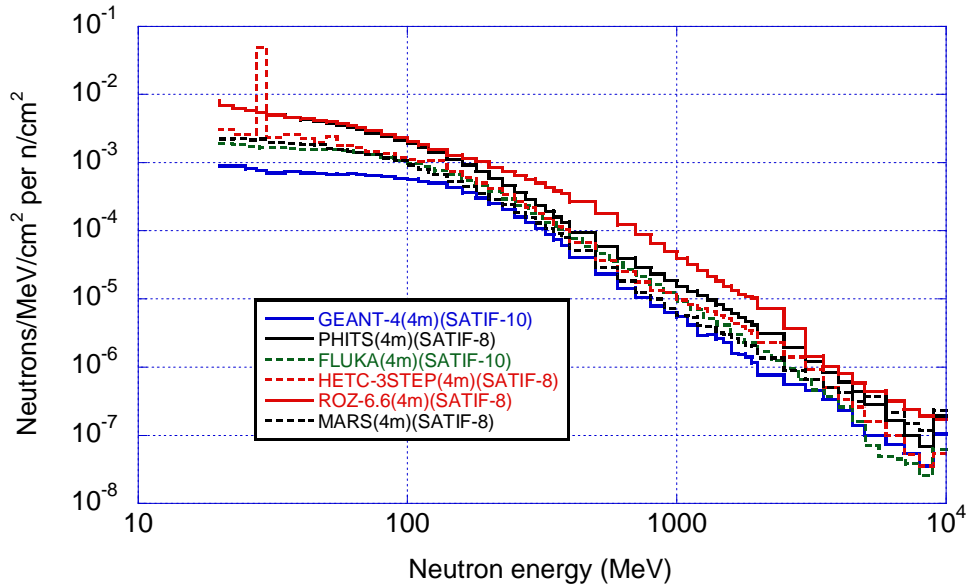
**Figure 10: Neutron dose difference at 8 m inside concrete
between ROZ 6.6, FLUKA, MARS, GEANT4 and PHITS**
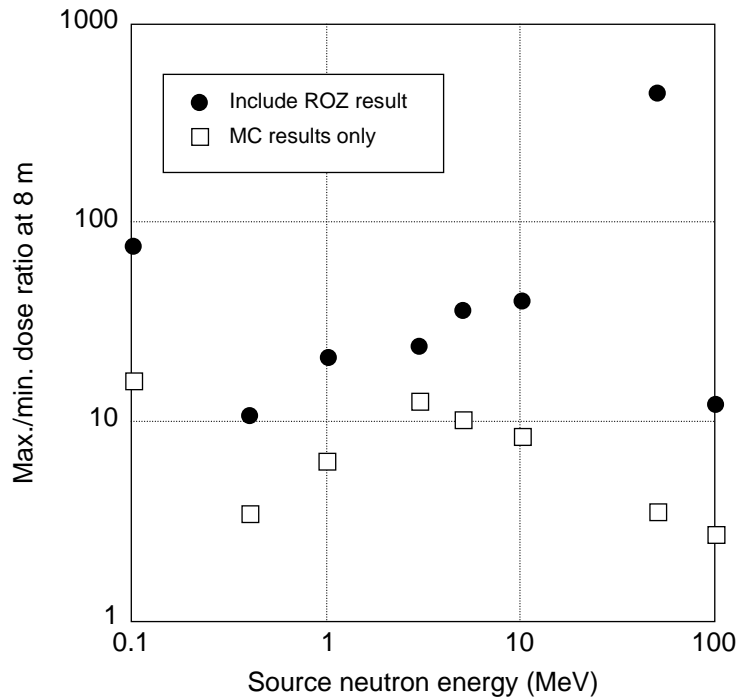
**Figure 11: Comparison of the neutron attenuation of iron for
secondary neutrons from a Hg target with 3 GeV protons**
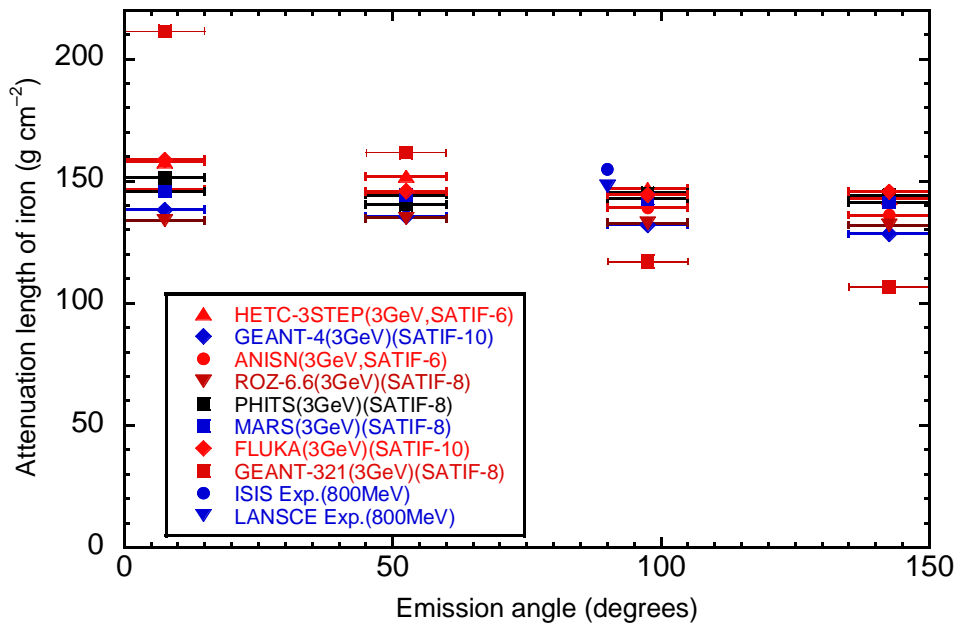
**Figure 12: Comparison of the neutron attenuation length of concrete
for secondary neutrons from a Hg target with 3 GeV protons**
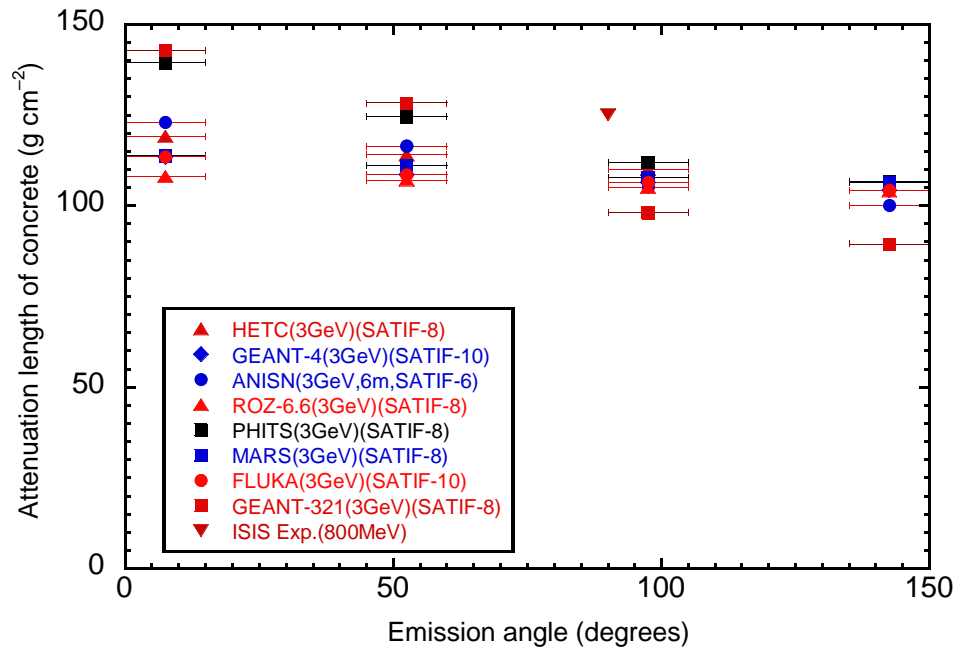
Figure 13: Comparison of the neutron attenuation length of iron for secondary neutrons emitted to 90° from Fe and Hg (24 GeV) target with protons
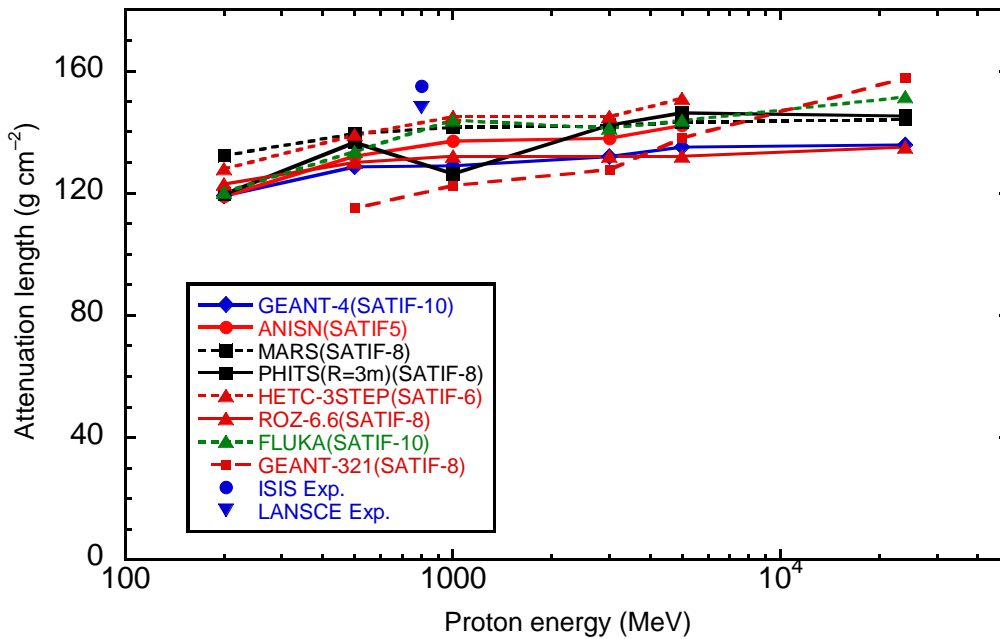
Figure 14: Comparison of the neutron attenuation length of concrete for secondary neutrons emitted to 90° from Fe and Hg (24 GeV) target with protons
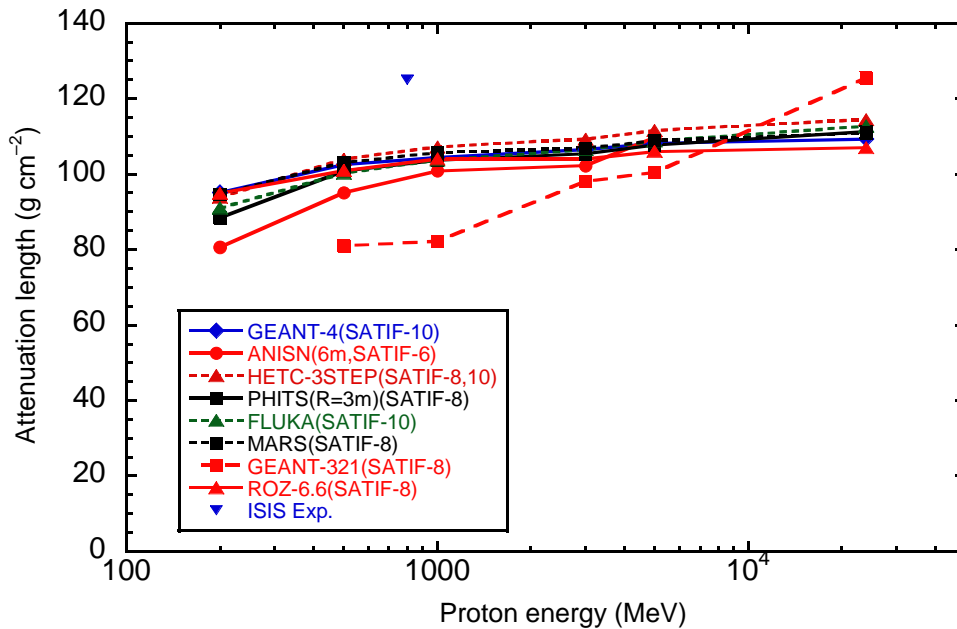
Figure 15: Neutron dose difference at 4 m inside iron from secondary neutrons emitted to 90° between ROZ 6.6, FLUKA, MARS, GEANT4 and PHITS
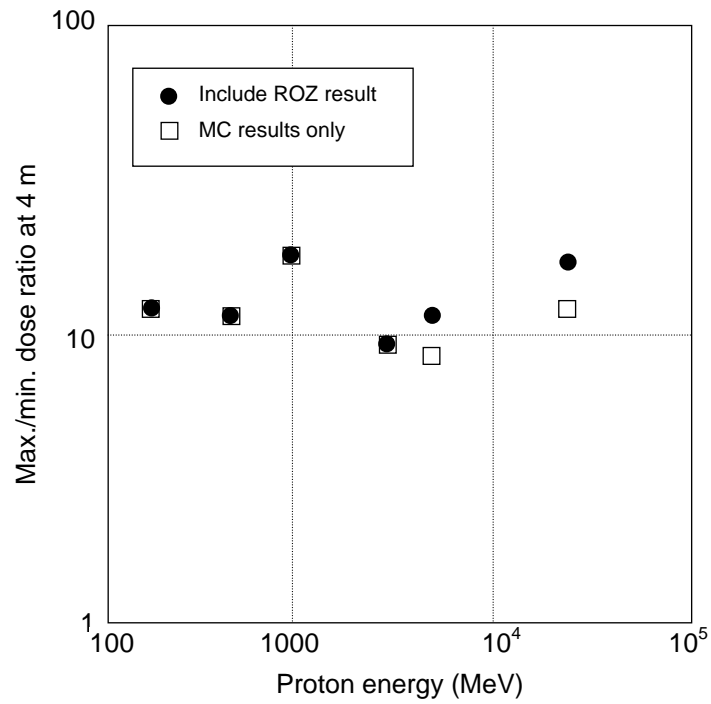
Figure 16: Neutron dose difference at 8 m inside concrete from secondary neutrons emitted to 90° ROZ 6.6, FLUKA, MARS, GEANT4 and HETC-3STEP
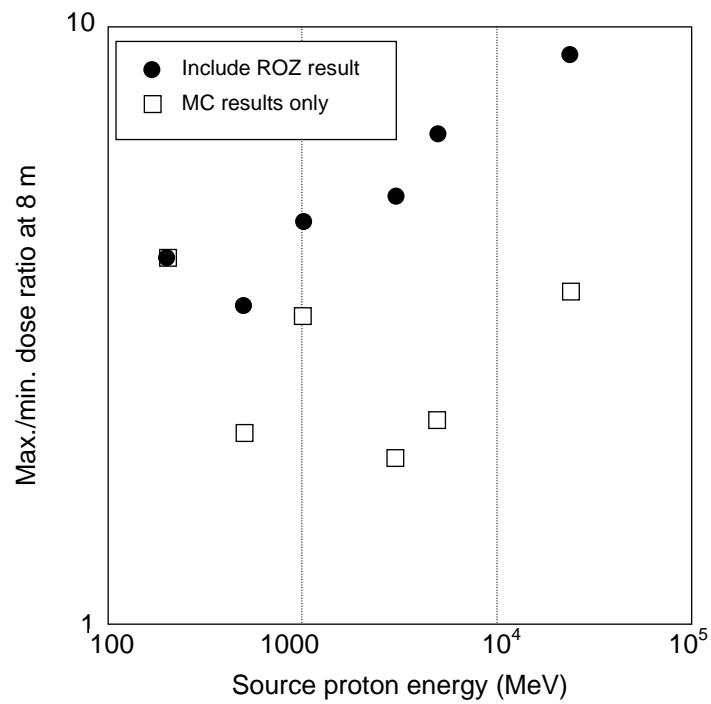
Figure 17: Comparison of calculated and measured reaction rates for the steel shield
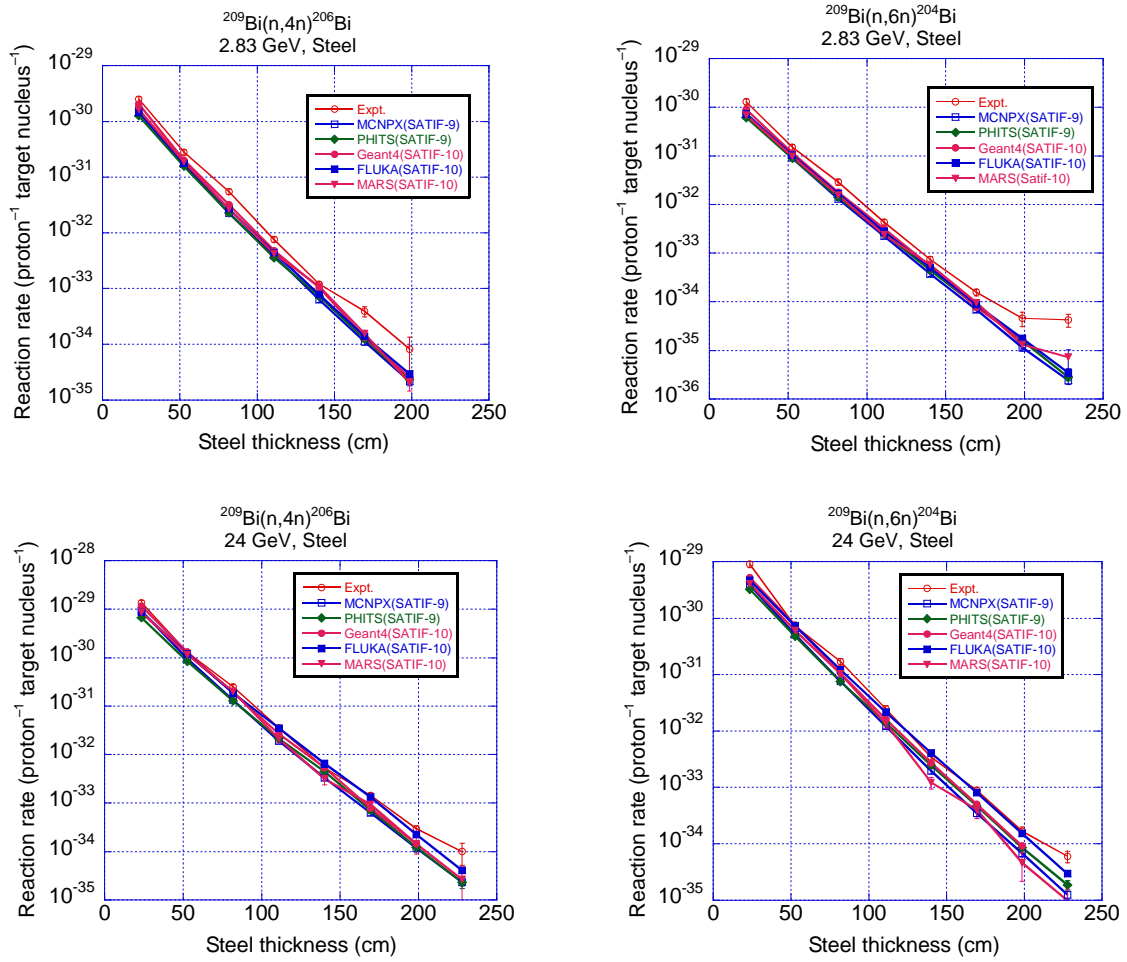
Figure 18: Comparison of calculated and measured reaction rates for the concrete shield
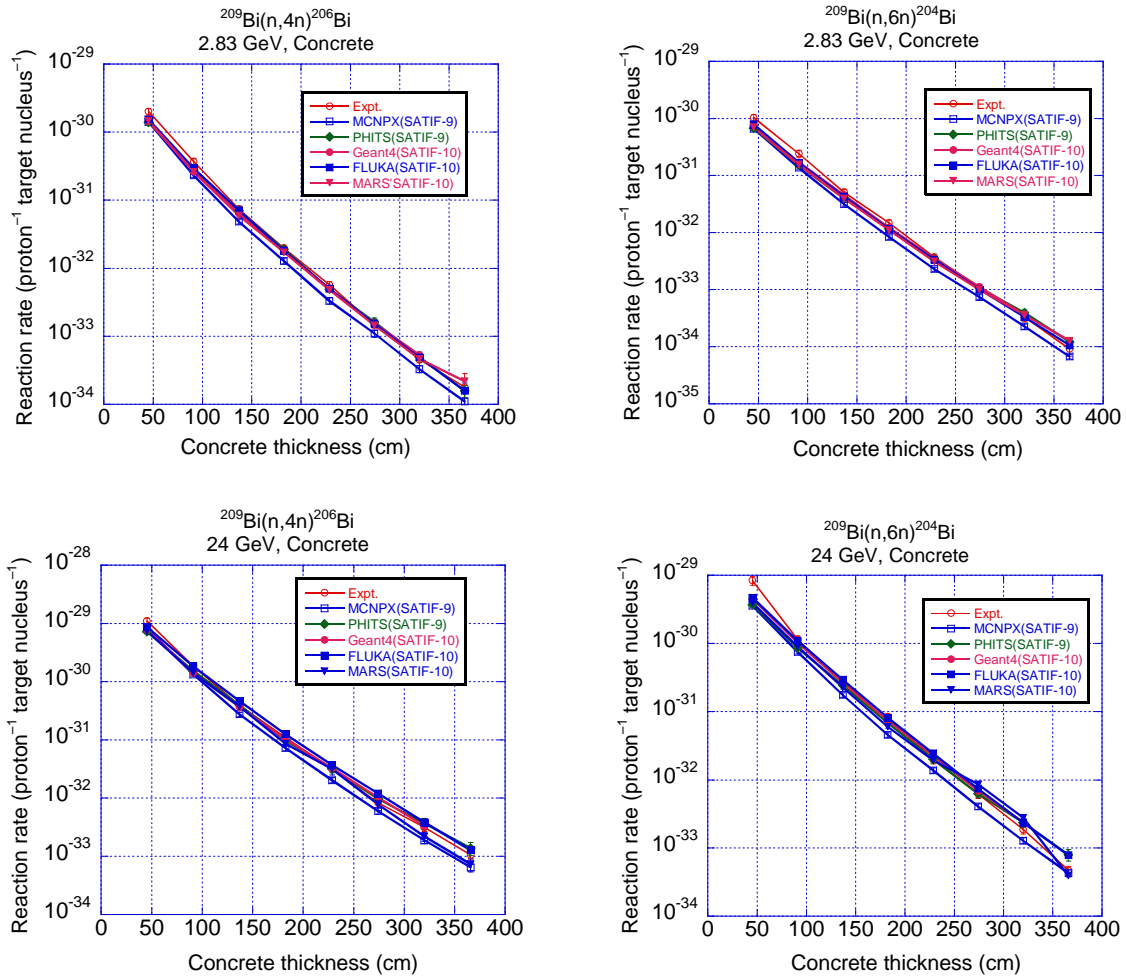
Figure 19: The C/E values of the reaction rates for the steel shield
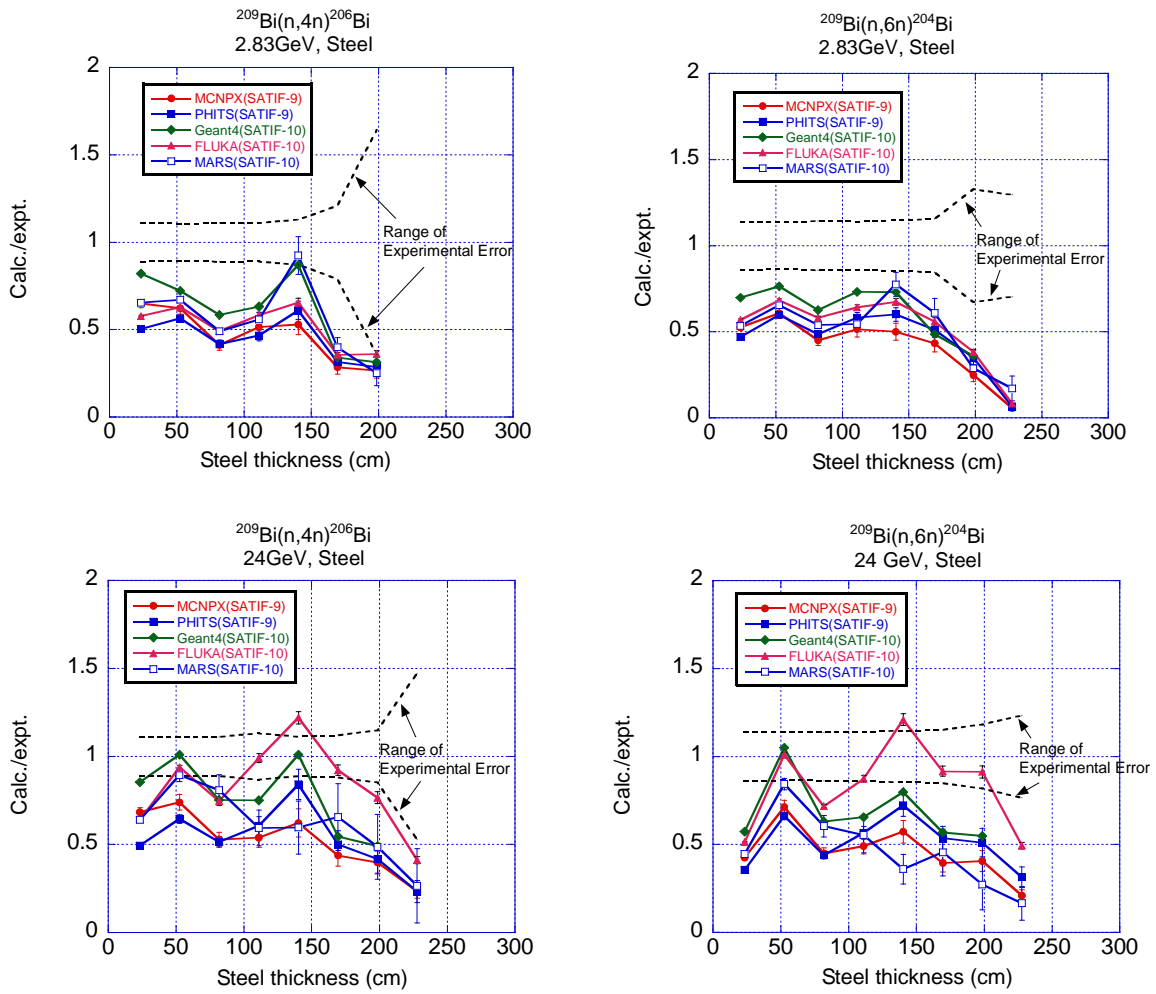
Figure 20: The C/E values of the reaction rates for the concrete shield
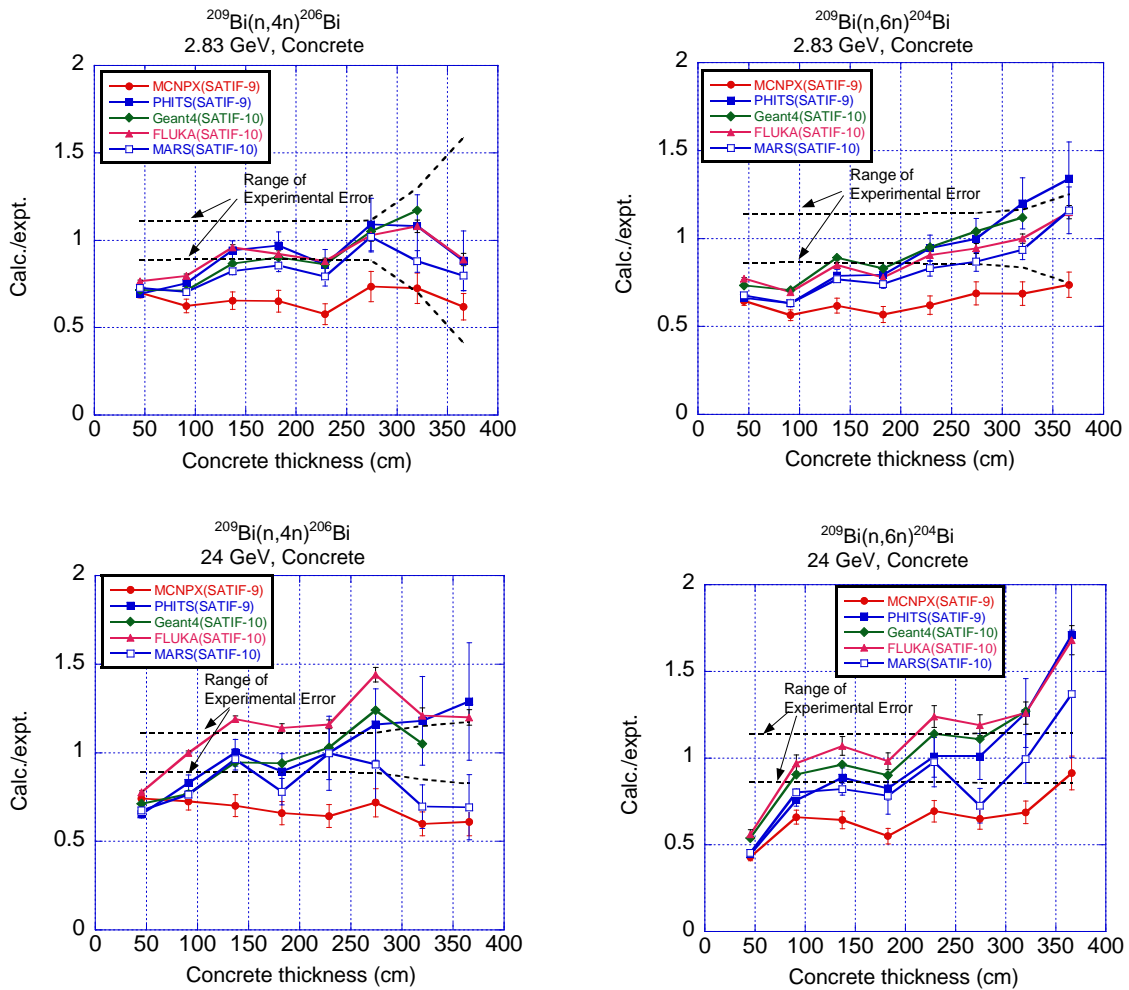
References

[1]   Hirayama, H., *et al.*, "Intercomparison of the Medium-energy Neutron Attenuation in Iron and Concrete", *Shielding Aspects of Accelerators, Targets and Irradiation Facilities (SATIF-3)*, Tohoku University, 12-13 May 1997, OECD/NEA, Paris (1998), pp. 185-195.

[2]   Hirayama, H., *et al.*, "Intercomparison of the Medium-energy Neutron Attenuation in Iron and Concrete (2)", *Shielding Aspects of Accelerators, Targets and Irradiation Facilities (SATIF-4)*, Knoxville, Tennessee, USA, 17-18 September 1998, OECD/NEA, Paris (1999), pp. 143-154.

[3]   Hirayama, H., *et al.*, "Intercomparison of the Medium-energy Neutron Attenuation in Iron and Concrete (3)", *Shielding Aspects of Accelerators, Targets and Irradiation Facilities (SATIF-5)*, Paris, France, 18-21 July 2000, OECD/NEA, Paris (2001), pp. 189-201.

[4]   Hirayama, H., *et al.*, "Intercomparison of the Medium-energy Neutron Attenuation in Iron and Concrete (4)", *Shielding Aspects of Accelerators, Targets and Irradiation Facilities (SATIF-6)*, SLAC, USA, 10-12 April 2002, OECD/NEA, Paris (2003), pp. 173-182.

[5]   Hirayama, H., *et al.*, "Intercomparison of the Medium-energy Neutron Attenuation in Iron and Concrete (5)", *Shielding Aspects of Accelerators, Targets and Irradiation Facilities (SATIF-7)*, Sacavém, Portugal, 17-18 May 2004, OECD/NEA, Paris (2005), pp. 117-126.

[6]   Hirayama, H., *et al.*, "Intercomparison of the Medium-energy Neutron Attenuation in Iron and Concrete (6)", *Shielding Aspects of Accelerators, Targets and Irradiation Facilities (SATIF-8)*, Pohang Accelerator Laboratory, Republic of Korea, 22-24 May 2006, OECD/NEA, Paris (2010), pp. 237-250.

[7]   Matsuda, N., *et al.*, *Analyses of Benchmark Problems for the Shielding Design of High Intensity Proton Accelerator Facilities*, JAEA-Technology 2008-030 (2008).

[8]   Hirayama, H., *et al.*, "Intercomparison of the Medium-energy Neutron Attenuation in Iron and Concrete (7)", *Shielding Aspects of Accelerators, Targets and Irradiation Facilities (SATIF-9)*, ORNL, Oak Ridge, Tennessee, USA, 21-28 April 2008, OECD/NEA (2010), pp. 261-274.

[9]   Allison, J., *et al.*, "Geant4 Developments and Applications", IEEE Transactions in *Nucl. Sci.*, 53, 1, 270-278 (2006).

[10]   Agostinelli, S., *et al.*, "Geant4 – A Simulation Toolkit", *Nucl. Instr. and Meth.*, A 506, 250-303 (2003).

[11]   Yoshizawa, N., *et al.*, "Development of High Energy Transport Code HETC-3STEP Applicable to the Nuclear Reaction with Incident Energies Above 20 MeV", *J. Nucl. Sci. Technol.*, 32, 601 (1995).

[12]   Niita, K., *et al.*, "PHITS – A Particle and Heavy Ion Transport Code System", *Radiat. Meas.*, 41, 1080-1090 (2006).

[13]   Ferrari, A., *et al.*, *FLUKA: A Multi-particle Transport Code*, CERN 2005-10, INFN/TC_05/11, SLAC-R-773 (2005).

[14]   Battistoni, G., *et al.*, "The FLUKA Code: Description and Benchmarking", *Proceedings of the Hadronic Shower Simulation Workshop 2006*, Fermilab, 6-8 September 2006, M. Albrow, R. Raja (Eds.), AIP Conference Proceedings, 896, 31-49 (2007).

[15]   Mokhov, N.V., *The MARS Code System User's Guide*, Fermilab-FN-628 (1995).

[16]   Mokhov, N.V., S.I. Striganov, "MARS15 Overview", *Proceedings of the Hadronic Shower Simulation Workshop 2006*, Fermilab, 6-8 September 2006, M. Albrow, R. Raja (Eds.), AIP Conference Proceedings, 896, pp. 50-60 (2007), *www-ap.fnal.gov/MARS*.

[17]   Nunomiya, T., *et al.*, "Measurement of Deep Penetration of Neutrons Produced by 800 MeV Proton Beam Through Concrete and Iron at ISIS", *Nucl. Instr. And Meth.*, B179, 89-102 (2001).

[18]   Bull, J.S., J.B. Donahue, R.L. Burman, "Measurement of Neutron Attenuation Through Thick Shields and Comparison with Calculation", *Proceedings of the 4th Workshop on Simulating Accelerator Radiation Environments (SARE4)*, Knoxville, Tennessee, 14-16 September 1998, pp. 201-208.

JASMIN: Japanese-American study of muon interactions and neutron detection

Hiroshi Nakashima[1], Nikolai V. Mokhov[2], Yoshimi Kasugai[1], Norihiro Matsuda[1], Yosuke Iwamoto[1], Yukio Sakamoto[1], Anthony F. Leveling[2], David J. Boehnlein[2], Kamran Vaziri[2], Toshiya Sanami[3], Hiroshi Matsumura[3], Masayuki Hagiwara[3], Hiroshi Iwase[3], Syuichi Ban[3], Hideo Hirayama[3], Takashi Nakamura[4], Koji Oishi[5], Nobuhiro Shigyo[6], Hiroyuki Arakawa[6], Tsuyoshi Kajimoto[6], Kenji Ishibashi[6], Hiroshi Yashima[7], Shun Sekimoto[7], Norikazu Kinoshita[8], Hee-Seock Lee[9], Koji Niita[10]

[1]Japan Atomic Energy Agency, Tokai, Ibaraki, Japan
[2]Fermi National Accelerator Laboratory, Batavia, IL, USA
[3]High Energy Accelerator Research Organization, Oho, Tsukuba, Japan
[4]Tohoku University, Aoba, Sendai, Japan
[5]Shimizu Corporation, Etchujima, Koto, Tokyo, Japan
[6]Kyushu University, Motooka, Fukuoka, Japan
[7]Kyoto University, Kumatori, Osaka Japan
[8]Tsukuba University, Tsukuba, Japan
[9]Pohang Accelerator Laboratory, POSTECH, Pohang, Kyungbuk, Korea
[10]Research Organization for Information Science & Technology, Tokai, Ibaraki, Japan

Abstract

Experimental studies of shielding and radiation effects at Fermi National Accelerator Laboratory (FNAL) have been carried out under collaboration between FNAL and Japan, aiming at benchmarking of simulation codes and study of irradiation effects for upgrade and design of new high-energy accelerator facilities. The purposes of this collaboration are: i) acquisition of shielding data in a proton beam energy domain above 100 GeV; ii) further evaluation of predictive accuracy of the PHITS and MARS codes; iii) modification of physics models and data in these codes if needed; iv) establishment of irradiation field for radiation effect tests; iv) development of a code module for improved description of radiation effects.

A series of experiments has been performed at the Pbar target station and NuMI facility, using irradiation of targets with 120 GeV protons for antiproton and neutrino production, as well as the M-test beam line (M-test) for measuring nuclear data and detector responses. Various nuclear and shielding data have been measured by activation methods with chemical separation techniques as well as by other detectors such as a Bonner ball counter. Analyses with the experimental data are in progress for benchmarking the PHITS and MARS codes. In this presentation recent activities and results are reviewed.

Background

-3, an international comparison has been carried out as one of the activities of SATIF, in order to compare the calculation results from an aspect of accelerator shielding. In the activity, neutron attenuation in iron and concrete has been compared, and it is pointed out at SATIF-7 that some discrepancies among the codes have been observed in the energy region above a few tens of GeV, especially more than 100 GeV, as shown in Figure 1 [1-2]. It is essential to compare with measurements to understand possible reasons for these discrepancies. The shielding experiment at CERF [3] gave already good information for benchmarking the codes for a 120 GeV beam comprised of protons and pions. At the same time, it became clear that further well-conditioned benchmark experiments are still needed for beam energies above 100 GeV.

Several high-intensity, high-energy accelerator facilities such as EURISOL and Project-X of FNAL are planned in the world [4-5]. It is critical to estimate radiation damage to the structural materials for such accelerator facilities, with displacement per atom (DPA) in materials being one of the key parameters for a facility design. Some codes have the capability of calculating DPA for estimating radiation effects on materials. The accuracy of the estimations of radiation effects, however, has not yet comprehensively been evaluated by experiments in realistic radiation fields.

At SATIF-7, an experiment on shielding and radiation effects using the accelerator complex at FNAL was proposed by Dr. N. Mokhov, and a budget was set aside by Japanese colleagues to this end. Thus, the Japanese-American Study of Muon Interactions and Neutron Detection (JASMIN), was started in collaboration with many Japanese and United States institutes and universities. In this paper, the present status of JASMIN on shielding experiment is reviewed [6-17].

JASMIN goals

The purposes of JASMIN are as follows:

- acquiring shielding data in a proton beam energy region above 100 GeV;

- further evaluation of predictive accuracy of the PHITS and MARS codes [18-19];

- modification of physics models and data in these codes if needed;

- characterisation of radiation fields for studies of radiation effects;

- development of a code module for an improved description of radiation effects.

This is to improve the confidence in applications of the codes to shielding design of high-energy accelerator facilities as well as for various research fields such as high-energy physics, space, biological and medical sciences, and nuclear and material engineering.

Experiments and results

In this study, the following three measurements have been carried out since the first campaign of FY 2007:

- measurement of particle fluxes and spectra as well as residual activity around shield at the Pbar station with a 120-GeV proton beam;

- measurement of particle fluxes and spectra as well a residual activity around shield at NuMI with 120-GeV protons;

- thick target yield measurements in the Meson area with 120-GeV protons.

In this paper the first two measurements are reviewed, and the last one is reported upon in detail in another contribution to these proceedings by Dr. T. Sanami [20].

Measurement of particle flux, spectra and residual activity around shield at the Pbar station with 120 GeV proton

Figure 2 shows a cross-sectional view of the Pbar target station. An antiproton production target, consisting of Inconel 600 disks covered by beryllium, is irradiated by 120-GeV protons with a 1.6 μs pulse width and a 2.2 sec repetition period. The typical number of protons in the pulse was 7×10^{12}, and the resultant beam power corresponded to about 61 kW at the first campaign. A collection lithium lens, collimator and a pulsed magnet are placed at the downstream of the target to focus, collimate and extract the produced antiprotons. The remaining proton and secondary particles are absorbed in a dump placed after the pulsed magnet. The dump consists of a graphite cylinder 20 cm in diameter and 120 cm long encapsulated in a 20 cm thick aluminium shell. Shields made of iron and concrete are placed on the upper side of the target and magnets. The thickness of iron and concrete above the target are 183 and 122 cm, respectively. A 183 cm air gap is between the iron and concrete shields [8].

In this experiment the following measurements have been planned and carried out:

- measurement of neutron flux inside and outside the iron and concrete shields;

- measurement of activities around the Pbar target;

- measurement of air and water activation in vault;

- measurement of streaming particle passing through duct from vault to outside.

In the measurements, various techniques were used: activation method, activation method with radiochemical separation, Bonner sphere counters (current mode, pulse mode), NE213 scintillation counter, phoswitch detector. Table 1 summarises the detector parameters outside the concrete shield. The sizes of the activation detectors were changed depending on the flux intensity at each position for each measurement. Because of the high intensity of the secondary particles (mainly neutrons) at the top of the target station, it was very difficult to use some counters there.

Figure 3 shows neutron reaction rate distributions of various reactions inside the iron shield in vertical direction to proton beam axis as a typical experimental data. In order to obtain the reaction rates in the wide energy region up to about 100 MeV, reactions of In, Al, Nb and Bi having various threshold energies were selected: ^{27}Al(n,α)^{24}Na (threshold energy E_{th} about 3.3 MeV), ^{93}Nb(n,2n)^{92m}Nb ($E_{th} \sim 9.1$ MeV), ^{209}Bi(n,4n)^{206}Bi ($E_{th} \sim 22.6$ MeV), ^{209}Bi(n,5n)^{205}Bi ($E_{th} \sim 29.6$ MeV), ^{209}Bi(n,6n)^{204}Bi ($E_{th} \sim 38$ MeV) and ^{209}Bi(n,7n)^{203}Bi ($E_{th} \sim 45.3$ MeV). After irradiation, radioactivity produced in each detector was measured by the HP-Ge detectors. Experimental errors range from ±5% to several tens of % depending on the activation counting statistics. A parameter of the Moyer model [21], attenuation length λ, was deduced for the measured attenuation of each reaction rate by using the least square fitting with the Moyer model, as summarised in the figure. The average attenuation length is 150 ± 5 g/cm². This is the first data for an incident proton energy above 100 GeV [14].

The deduced attenuation length is compared with the previous data measured at other accelerator facilities such as KEK and CERN, as a function of maximum source neutron energy, as shown in Figure 4 [22-27]. E_{max} defined in accordance with the following guidelines: a sharp peak neutron energy for quasi-monoenergetic neutrons such as p-Li sources;   the neutron energy with 1/100 of the neutron flux for that of the peak neutron energy in lethargy unit when the neutron spectrum has a clear broad peak;   the neutron energy with 1/100 of the neutron flux for that at 20 MeV in lethargy unit otherwise. In the present case, as no clear peak is seen in the calculated source neutron spectra for the direction of 90° with respect to the proton beam direction, the value of E_{max} was determined to be 600 MeV by applying the guideline in   . The attenuation length is consistent with the previous data and it increases linearly with the maximum source neutron energy up to about 1 GeV [14].

Figure 5 shows neutron reaction rate distributions of the ^{209}Bi(n,4n)^{206}Bi reaction ($E_{th} \sim 22.6$ MeV) along the proton beam line behind the iron and concrete shield as another typical experimental data. In this measurement, various activation detectors were set on the concrete cap (CC) and iron shield: air gap between concrete and iron (AG). After irradiation by the transmitted neutrons through the concrete and iron shields, radioactivity produced in each detector was also measured by HP-Ge detectors. A parameter of the Moyer Model, β, was also deduced from the measured reaction rate distributions by using the least square fitting in the angular region between 60 and 120° which is

applicable to the Moyer Model. The deduced β is about 4.0. It is larger than the previously obtained value $\beta = 2.3$ [24]. A possible reason for this is energy dependence of β energies above 100 GeV [14].

Transmitted neutron energy spectra through concrete and iron shields were measured by a multi-moderator spectrometer (Bonner spheres) using a pair of BF_3 proportional counters: $^{nat}BF_3$ (18% ^{10}B) and $^{10}BF_3$ (96% ^{10}B), of which gas pressure is 760 Torr. The detectors were covered by spherical moderators made of polyethylene (density of 0.928 g/cm³) with the diameter of 81, 110, 150 and 230 mm. Because of the high neutron intensity at the top of the concrete, electronics for the detectors were operated as a current readout mode, in which input charge of 1 pC was converted to 1 pulse and time-dependent pulse numbers were counted by a multi-channel scaler. A higher Q-value of the ^{10}B(n,α) reaction, 2.79 MeV, reduces the effect of contamination of the γ-rays, which was estimated to be less than 0.1% by a measurement in a low-intensity neutron field of ^{241}Am-Be with a pulse counting mode. Figure 6 shows the neutron energy spectrum obtained from the measurement by an unfolding method with the SANDII code [28] and response function calculated by the MCNPX code [29]. In the figure the neutron spectra calculated by the PHITS, MARS and MCNPX codes are compared with the measured spectrum. The calculations show an agreement with the measurement within a factor of two, although the PHITS and MARS calculations overestimate the measurement above a few MeV energy region while the MCNPX calculation underestimates the measurement overall [11].

The neutron reaction rates of In, Al, Bi and Cu measured by the activation method are compared with the reaction rates calculated by the neutron energy spectrum obtained by the Bonner sphere method, as shown in Figure 7. The threshold energy of the ^{115}In(n,n')^{115m}In reaction is about 0.6 MeV and the ^{209}Bi(n,7n)^{203}Bi reaction with threshold energy of about 45.3 MeV has the reaction probability up to about 100 MeV. It is shown that the results obtained by the Bonner sphere method are consistent with the results measured by the activation method in the energy region from 0.6 to about 100 MeV, and both experimental methods are reliable [11].

We are also performing a measurement of >100-MeV neutrons using the Au activation method coupled with a low-background γ-ray counting system. As an indicator for the neutron flux, we determined the production rates of eight spallation nuclides (^{196}Au, ^{188}Pt, ^{189}Ir, ^{185}Os, ^{175}Hf, ^{173}Lu, ^{171}Lu and ^{169}Yb) having high threshold energies in the Au activation detector. From these results, we will deduce neutron spectra at neutron energy higher than 100 MeV.

Measurement of particle flux, spectra and residual activity around shield at NuMI with 120 GeV protons

At the NuMI experimental station, a 94 cm long graphite target irradiated with 120 GeV protons generate the secondary particles [30]. The beam power during the run was 150 kW, about half of the NuMI beam capability. The secondary particles, mainly pions, are focused in the direction of a neutrino detector with two magnetic horns and led to a 675 m long decay pipe, in which pions decay into muons and neutrinos. The muons pass through a hadron absorber made of iron and concrete located downstream of the decay pipe, in which protons, neutrons and pions are removed from the beam axis. Figure 8 shows geometry of the experiment along the course of the flying muons. Behind the absorber, there are four caves at the flight distances of 0, 13.7, 33.5 and 67.1 m from the rock surface: "Alcove-1", "Alcove-2", "Alcove-3" and "Alcove-4" [9].

Activation detectors were installed in every alcove along the beam axis and were irradiated with muons and tertiary particles passing through the rock. In order to measure the radiation dose rates and reaction rates due to the muons and tertiary particles, Optical Stimulated Luminescence (OSL) dosimeters, TLD (thermo-luminescence detectors, Panasonic 813 PQ), solid state nuclear track detectors, CR39, the Bonner sphere counters and ionisation chamber (IC) for neutron and γ-ray survey were set along the beam axis, the passes to the alcove and the bypass tunnel [9].

As a typical experimental data at NuMI, mass distribution of isotope production on a copper sample irradiated at Alcove-1 is shown in Figure 9 [7]. The yields of 18 nuclides (^{64}Cu, ^{57}Ni, ^{58}Co, ^{57}Co, ^{56}Co, ^{55}Co, ^{59}Fe, ^{54}Mn, ^{52}Mn, ^{51}Cr, ^{48}V, ^{48}Sc, ^{47}Sc, ^{46}Sc, ^{44m}Sc, ^{43}K, ^{42}K and ^{24}Na) on copper samples were measured by the activation method. It is shown that the mass yield linearly increases with increasing the mass number between 40 and 60. The mass yield is larger than the linear slope in a lower-mass region and around copper. A reaction mechanism between muons and nuclei is still under detailed analysis of the mass distribution using the MARS code [7].

The average values of the yield ratios normalised to the value at Alcove-2 are plotted in Figure 10 as a function of the depth from the rock surface. A variation of these ratios for the nuclides studied is within a factor of two. The yields from Alcove -2 show a gradual an exponential decrease with the depth, while the yields decrease steeply between Alcove-1 and Alcove-2. Attenuation behaviour at Alcove-2 to Alcove-4 is consistent with the calculation by the MARS code, and the profile of the yields is similar to the calculated attenuation of muons in the rock. An additional experiment is planned to see if neutrons and other particles can contribute to the measurements in Alcove-1 [7].

Dose rate distributions along the pass to the Alcove-2 are shown as a function of lateral distance from the beam axis in Figure 11 [9]. OSL, TLD and ionisation chamber have sensitivity to muons, electrons and photons. CR39 and CR39(B) can measure fast and thermal neutrons, respectively, and TLD can also detect thermal neutrons. It is shown that the dose rate is dominated by muons, electrons and photons around the beam axis and the contribution of fast neutrons, which may be generated by high-energy muon interactions, increase with the distance.

The experimental results are compared with the dose calculated by the MARS code in absolute value in the figure. Lines named as DET, DEM, DEE, DEN and DEG show the calculated dose of total, muon, electron, neutron and photon, respectively. The calculated total dose shows an excellent agreement with the dose rates by OSL and TLD around the beam axis and the distance larger than 7 m. A slight underestimation between 4 and 7 m can be caused by the difference in the calculation geometry. The calculation reveals that the total dose is mainly driven by muons around the beam axis. The electrons and photons are generated in the interactions of muons in the rock around the axis. The dose rate due to the electrons dominates the total dose rate at the distance from 2 m in the pass of the alcove, because the electron generation has the angular distribution toward the lateral direction in the electromagnetic shower [9]. Both measurement and calculation show that contribution of fast neutrons drastically increases at distances larger than 4 m. An explanation is that neutrons are generated by photo-nuclear reactions induced by photons generated by muons (bremsstrahlung and deep-inelastic nuclear reactions), of which the angular distribution is more isotropic compared to that of the electron generation.

Summary

Experimental results on particle fluxes, spectra and mass distributions were obtained at the Pbar and NuMI set-ups of FNAL. Shielding parameters – such as neutron attenuation length – were estimated and compared with the previous values. The results were analysed by PHITS and MARS, and the accuracy behind thick shield was confirmed within a factor of two. The MARS results are in a good agreement with experiments on dose distributions due to the particles generated by the high-energy muons, with interaction mechanisms to be further analysed. As a future plan, thick target yields and cross-section measurements will soon begin at the Meson Test beam facility, based on the preliminary measurements. Finally, an irradiation field will be established for study on radiation damage.

Table 1: Size and purity of activation detectors used in activation method

Activation foil	Purity (%)	Size (mm)
Carbon (C)	99.99	$\phi\, 80 \times 10$
Indium (In)	99.99	$\phi\, 80 \times 10$
Aluminium (Al)	99.999	$\phi\, 80 \times 10$
Copper (Cu)	99.994	$\phi\, 80 \times 10$
Bismuth (Bi)	99.5	$\phi\, 80 \times 10$

Figure 1: Comparison of the neutron attenuation length of iron [1]
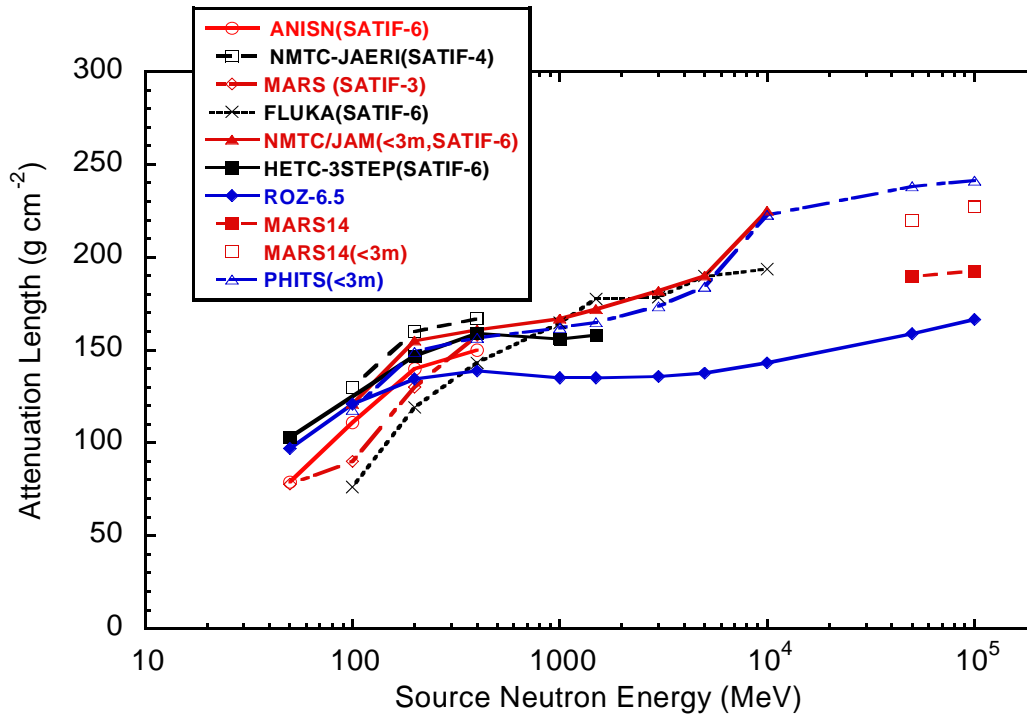
Figure 2: Cross-sectional view of the Pbar target station [8]
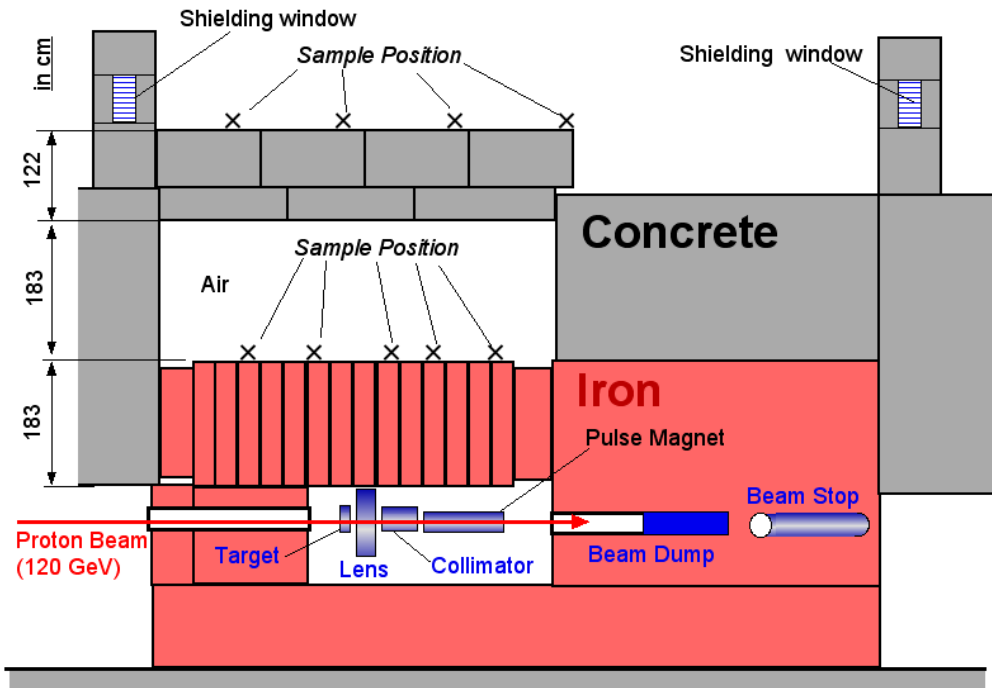
Figure 3: Reaction rate distributions in iron shield

Reaction	λ[g/cm^2]
^{27}Al(n, α)^{24}Na	152
^{93}Nb(n, 2n)^{92m}Nb	151
^{209}Bi(n, 4n)^{206}Bi	149
^{209}Bi(n, 5n)^{204}Bi	153
^{209}Bi(n, 6n)^{204}Bi	146
^{209}Bi(n, 7n)^{203}Bi	151
Average	150
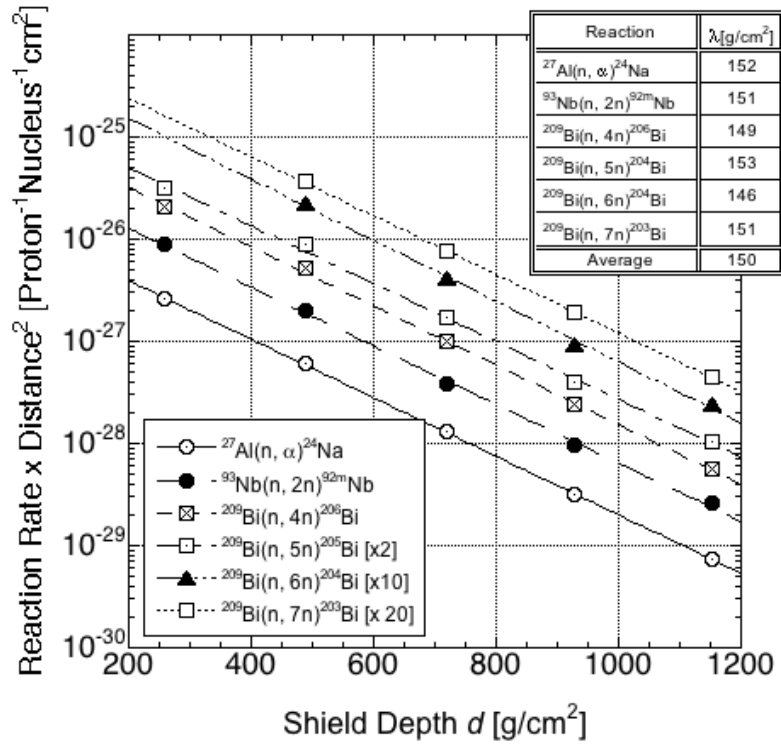
Figure 4: Comparison of attenuation length as function of maximum source neutron energy
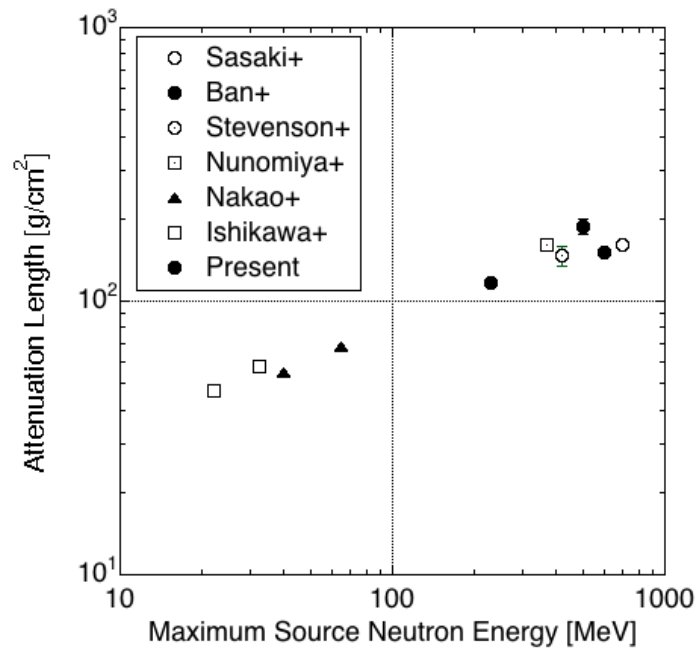
Figure 5: Reaction rate distribution of ^{209}Bi(n,4n)^{206}Bi

Open and closed circles show experimental data at the surface of iron shield (AG) and concrete (CC).
The fitting curve by the Moyer model is also shown with the solid lines [14].
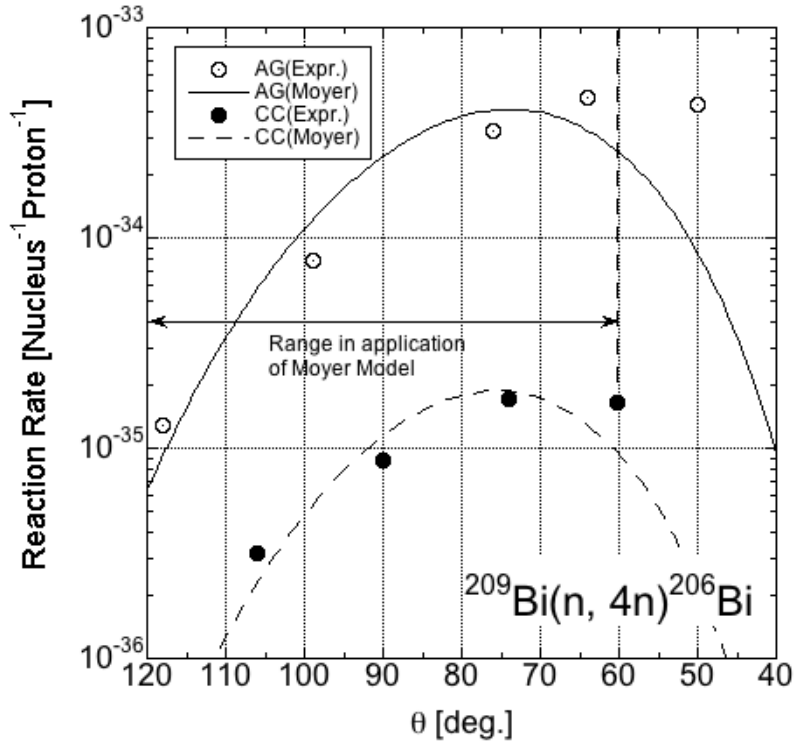
**Figure 6: Neutron energy spectra above the Pbar target station measured
by the Bonner spheres and calculated by the PHITS, MARS and MCNPX codes**
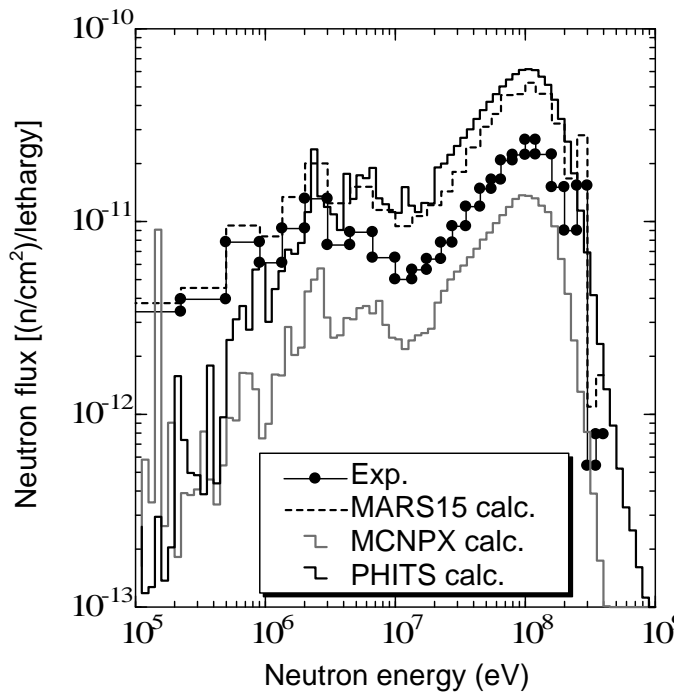
Figure 7: Comparison of reaction rates measured by the Bonner spheres and activation method [11]
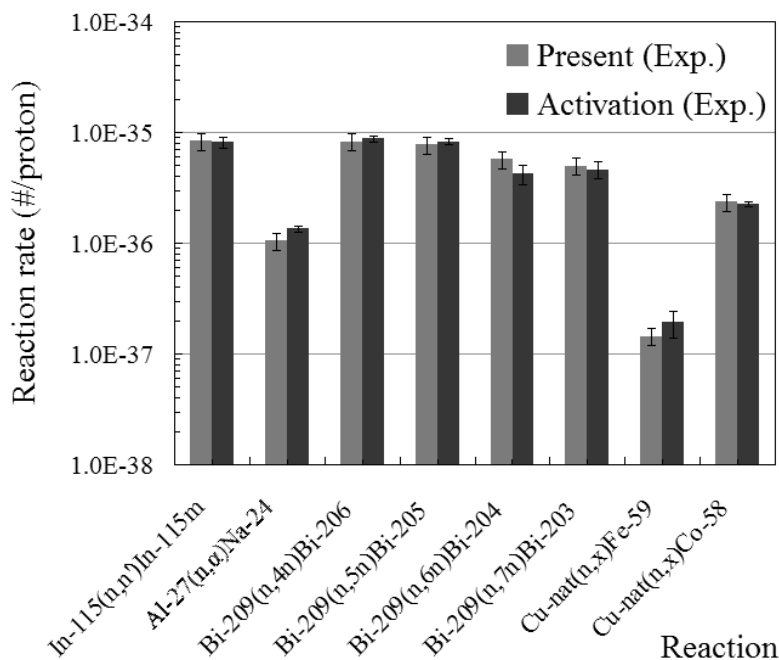
Figure 8: Schematic view of downstream of NuMI and location of dosimeters and detectors [9]
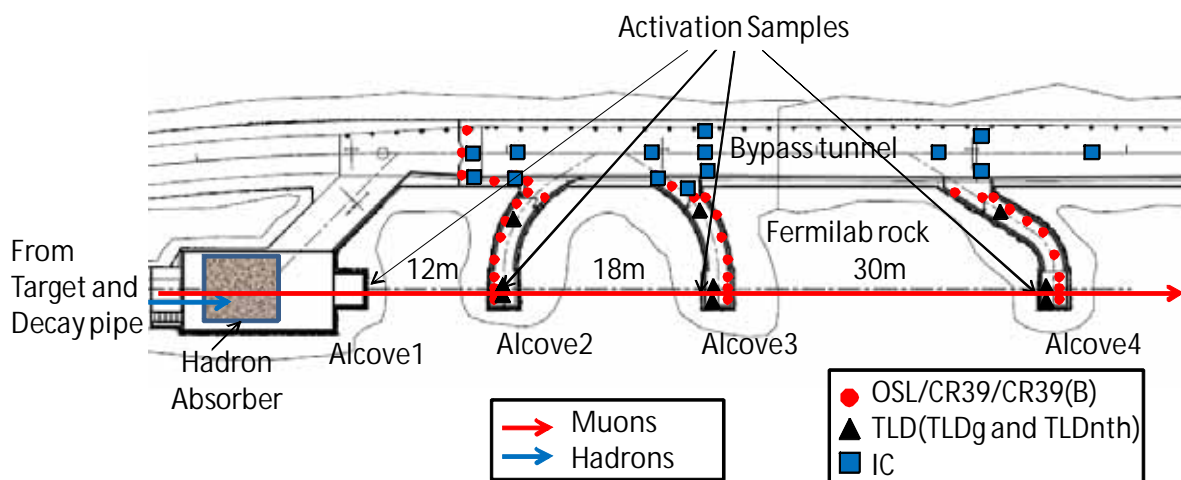
Figure 9: Mass yield distribution on Cu at Alcove-1 [7]
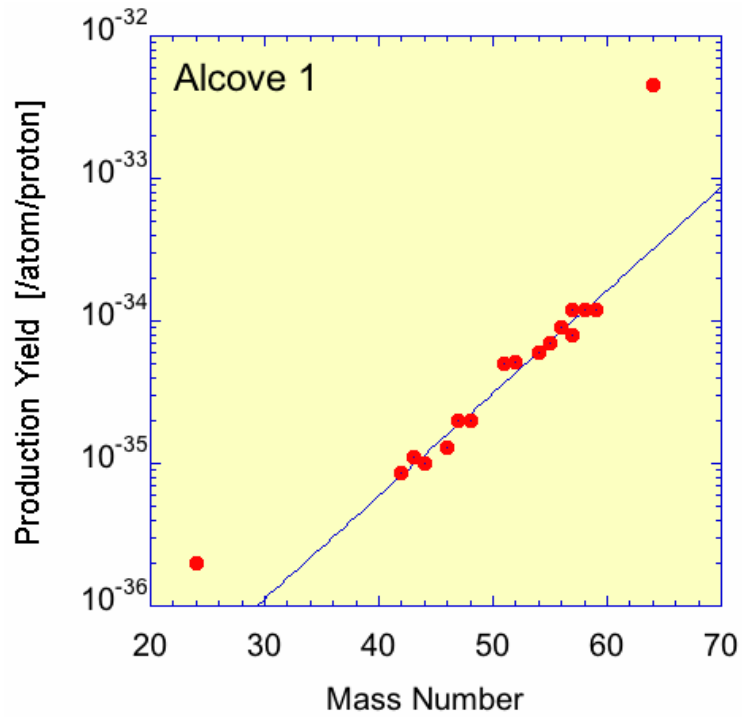
Figure 10: Attenuation profile of the mass yields in rock, which is normalised by the yield at Alcove-2. The solid line is drawn to guide the eye [7].
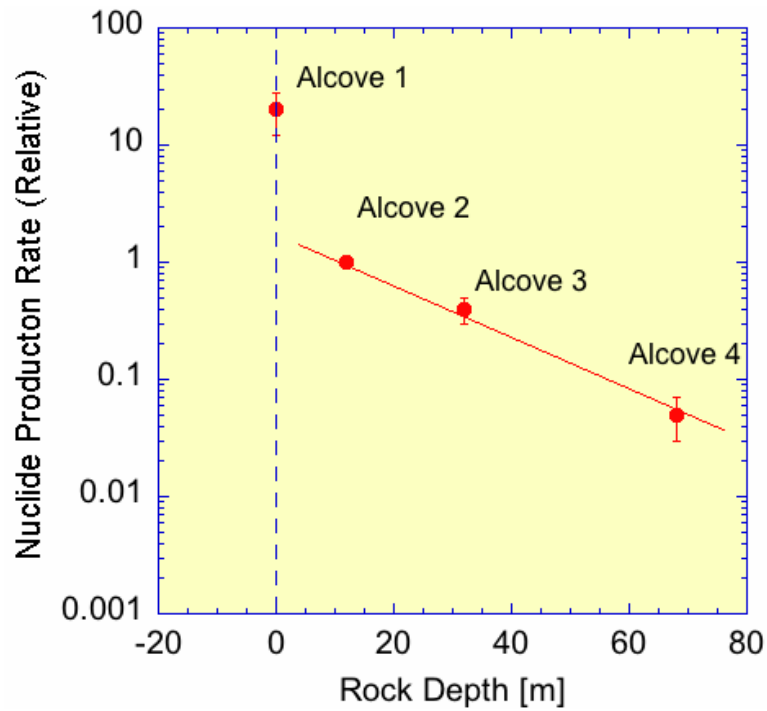
Figure 11: Dose rate distributions measured by various dosimeters along Alcove-2, which is compared with those of total, muon, photon, electron and neutron calculated by the MARS code [9]
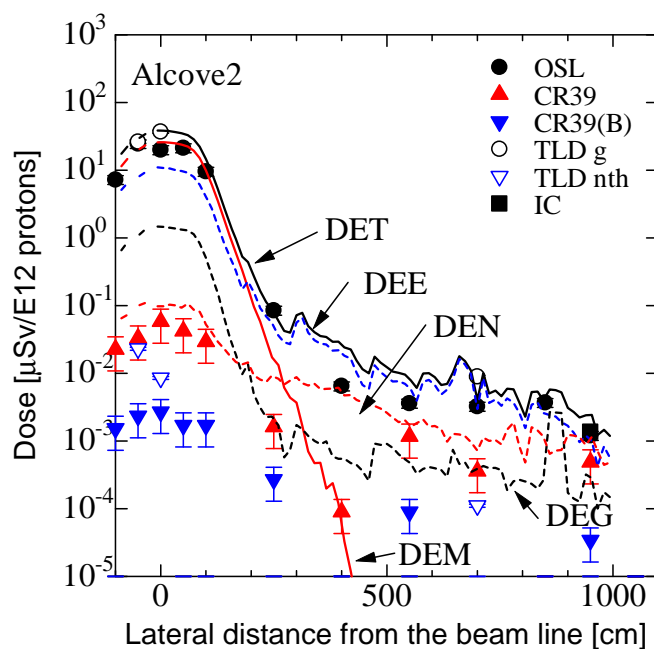
References

[1]   Hirayama, H., *et al.*, "Inter-comparison of the Medium-energy Neutron Attenuation in Iron and Concrete (5)", *Proceedings of the Workshop on Shielding Aspects of Accelerators, Targets and Irradiation Facilities (SATIF-7)*, ITN, Lisbon, 17-18 May 2004, OECD/NEA, Paris (2005), pp. 117-126.

[2]   Hirayama, H., *et al.*, "Inter-comparison of the Medium-energy Neutron Attenuation in Iron and Concrete (6)", *Proceedings of the Workshop on Shielding Aspects of Accelerators, Targets and Irradiation Facilities (SATIF-8)*, Pohang, Korea, 22-24 June 2006, NEA/NSC/DOC(2010)6, OECD/NEA, Paris, pp. 237-249.

[3]   Nakao, N., *et al.*, "Measurement of Neutron Energy Spectra Behind Shielding of a 120 GeV/c Hadron Beam Facility", *NIM* A562, 950-953 (2006).

[4]   *www.ganil.fr/eurisol.*

[5]   http://projectx.fnal.gov.

[6]   Sanami, T., *et al.*, *Proc. on Workshop on Radiation Detectors and Their Uses* (2008), forthcoming.

[7]   Matsumura, H., *et al.*, *Proc. on Workshop on Environmental Radioactivity* (2008), forthcoming.

[8]   Nakashima, H., *et al.*, "Experimental Studies of Shielding and Irradiation Effects at High Energy Accelerator Facilities", *Nuclear Technology*, 168, 482-486 (2009).

[9]   Sanami, T., *et al.*, "Shielding Experiments at High Energy Accelerators of Fermilab: (I) Dose Rate Around High Intensity Muon Beam", *Proc. of the 5th International Symposium on Radiation Safety and Detection Technology* (2009), forthcoming.

[10] Yashima, H., *et al.*, "Shielding Experiments at High Energy Accelerators of Fermilab (II): Spatial Distribution Measurement of Reaction Rate Behind the Shield and Its Application for Moyer Model", *Proc. of the 5th International Symposium on Radiation Safety and Detection Technology* (2009), forthcoming.

[11] Hagiwara, M., *et al.*, "Shielding Experiments at High Energy Accelerators of Fermilab (III): Neutron Spectrum Measurements in Intense Pulsed Neutron Fields of the 120-GeV Proton Facility Using a Current Bonner Sphere Technique", *Proc. of the 5th International Symposium on Radiation Safety and Detection Technology* (2009), forthcoming.

[12] Matsuda, N., *et al.*, "Shielding Experiments at High Energy Accelerators of Fermilab (IV): Calculation Analyses", *Proc. of the 5th International Symposium on Radiation Safety and Detection Technology* (2009), forthcoming.

[13] Boehnlein, D.J., *et al.*, "Studies of Muon-induced Radioactivity at NuMI", *Proc. of the 11th International Workshop on Neutrino Factories, Superbeams and Beta Beams*, American Institute of Physics, Chicago, Illinois, USA (2010), 344.

[14] Kasugai, Y., *et al.*, "Shielding Experiments Under JASMIN Collaboration at Fermilab: (I) Overview of the Research Activities", *Proc. of International Conference on Nuclear Data for Science and Technology* (2010), forthcoming.

[15] Yashima, H., *et al.*, "Shielding Experiments Under JASMIN Collaboration at Fermilab (II): Radioactivity Measurement Induced by Secondary Particles from the Anti-proton Target", *Proc. of International Conference on Nuclear Data for Science and Technology* (2010), forthcoming.

[16] Matsumura, H., *et al.*, "Shielding Experiments Under JASMIN Collaboration at Fermilab (III): Measurement of High-energy Neutrons Penetrating a Thick Iron Shield from the Antiproton Production Target by Au Activation Method", *Proc. of International Conference on Nuclear Data for Science and Technology* (2010), forthcoming.

[17] Matsuda, H., *et al.*, "Shielding Experiments Under JASMIN Collaboration at Fermilab (IV): Measurement and Analyses of High-energy Neutrons Spectra in the Antiproton Production Target Station", *Proc. of International Conference on Nuclear Data for Science and Technology* (2010), forthcoming.

[18] Niita, K., *et al.*, "PHITS – A Particle and Heavy Ion Transport Code System", *Radiat. Meas.*, 41, 1080-1090 (2006).

[19] Mokhov, N.V., FERMILAB-FN-628 (1995), Mokhov, N.V., S.I. Striganov, Fermilab-Conf-07-008-AD (2007), *Hadronic Shower Simulation Workshop AIP Proceedings*, 896.

[20] Sanami, T., *et al.*, "Neutron Energy Spectrum from 120 GeV Protons on a Thick Copper Target (JASMIN in M-test)", these proceedings.

[21] Moyer, B.J., "Method of Calculation of the Shielding Enclosure for the Berkeley Bevatron", *Proc. 1st Int. Conf. Shielding around High Energy Accelerators*, Presses Universitaires de France, Paris (1962), 65.

[22] Sasaki, M., *et al.*, "Measurements of High Energy Neutrons Penetrated Through Iron Shields Using Self-TOF Detector and NE213 Organic Liquid Scintillator", *NIM*, B196, 113-124 (2007).

[23] Ban, S., *et al.*, "Measurement of Transverse Attenuation Lengths for Paraffin, Heavy Concrete and Iron Around an External Target for 12 GeV Protons", *NIM*, 174, 271-276 (1980).

[24] Stevenson, G.R., *et al.*, "Determination of Transverse Shielding for Proton Accelerators Using the Moyer Model", *Health Physics*, 43, 13-29 (1982).

[25]   Nunomiya, T., *et al.*, "Measurement of Deep Penetration of Neutrons Produced by 800-MeV Proton Beam Through Concrete And Iron at ISIS", *NIM*, B 179, 89-102 (2001).

[26]   Nakao, N., *et al.*, "Transmission Through Shields of Quasi-monoenergetic Neutrons Generated by 43 and 68-MeV Protons. I: Concrete Shielding Experiment and Calculation for Practical Application", *NSE*, 124, 228-242 (1996).

[27]   Ishikawa, T., *et al.*, "Neutron Penetration Through Iron and Concrete Shields with the Use of 22.0- and 32.5-MeV Quasi-monoenergetic Sources", *NSE*, 116, 278 (1994).

[28]   McElroy, W., S. Breg, G. Gigas, "Neutron-flux Spectral Determination by Foil Activation", *NSE*, 27, 533-541 (1967).

[29]   Hendricks, J.S., *et al.*, LA-UR-08-2216 (2008), *http://mcnpx.lnal.gov.*

[30]   Anderson, K., *et al.*, *NuMI Facility Technical Design Report*, *Technical Report*, FERMILAB-AB-DESIGN-1998-01, Fermilab (1998).

Verification of Monte Carlo transport codes FLUKA, MARS and SHIELD

V. Chetvertkova[1,2]**, E. Mustafin**[1]**, I. Strasik**[1,2]**, L. Latysheva**[3]**, N. Sobolevsky**[3]**, U. Ratzinger**[2]
[1]Gesellschaft für Schwerionenforschung (GSI), Darmstadt, Germany
[2]J.W. Goethe-University Frankfurt am Main, Frankfurt am Main, Germany
[3]Institute for Nuclear Research of the Russian Academy of Sciences (INR RAS), Moscow, Russia

Abstract

The present study is a continuation of the project "Verification of Monte Carlo Transport Codes" which is running at GSI as a part of activation studies of FAIR relevant materials. It includes two parts: verification of stopping modules of FLUKA, MARS and SHIELD-A (with ATIMA stopping module) and verification of their isotope production modules. The first part is based on the measurements of energy deposition function of uranium ions in copper and stainless steel. The irradiation was done at 500 MeV/u and 950 MeV/u, the experiment was held at GSI from September 2004 until May 2005. The second part is based on gamma-activation studies of an aluminium target irradiated with an argon beam of 500 MeV/u in August 2009. Experimental depth profiling of the residual activity of the target is compared with the simulations.

Introduction

Monte Carlo transport codes like FLUKA [1,2], MARS [3-7] and SHIELD-A [8-10] are widely used in estimating the radiation hazards in hadron accelerator facilities. These codes are being constantly developed, thus the verification of new modules is of great importance. The project "Verification of Monte Carlo Transport Codes" was started in GSI Helmholtzzentrum für Schwerionenforschung in Darmstadt. A series of experiments has already been completed. Verification of stopping modules of ATIMA [10], PHITS [11], SHIELD [8,9] and SRIM [12] was done in Ref. [13] based on the measurements of energy deposition of uranium beam in stainless steel and copper targets. The isotope production module of FLUKA was validated comparing the experimental results on depth profiles of residual activity of copper irradiated by argon ions [14].

Present work is a continuation of the project. The first part, verification of electronic stopping modules of FLUKA (08.3.6), MARS (April 2009) and SHIELD-A (December 2009) is based on the experiment held in GSI from September 2004 until May 2005 and described in Ref. [13]. The second part, verification of isotope production modules, is based on recent results on argon irradiation of an aluminium target.

Verification of electronic stopping modules

Experiment

The scheme of the experiment described in Ref. [13] is shown in Figure 1. After slow extraction from the synchrotron, the uranium beam went through the secondary-electron transmission monitor (SEETRAM) for measuring the intensity. The monitor consisted of three very thin foils (10 μm each) with the diameter d = 50 mm. After passing through the vacuum window, air gap and the monitor calorimeter the beam hit the target. The energy of the uranium ^{238}U beam was 500 MeV/u and 950 MeV/u. Two different targets were irradiated: stainless steel with density ρ = 7.83 g/cm^3 (Table 1) and chemically pure natural copper with measured density ρ = 8.86 g/cm^3.

Figure 1: Scheme of the experiment
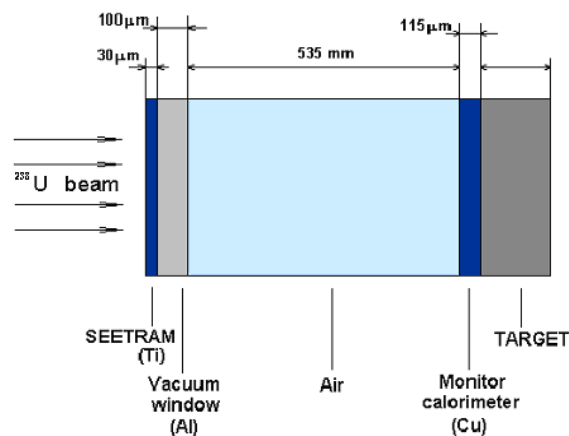
Table 1: Chemical composition of the stainless steel target

Element	Cr	Mn	Mo	V	Fe	Ni	Ti	Si
Relative content	0.179	0.0105	0.0049	0.001	0.7276	0.068	0.0042	0.0048

The "thick target" technique was used in the experiment. The concept is to change the thickness of the target to determine the energy deposition (dE/dx) dependence on thickness. Two wedges were used for that purpose; one of them was fixed and the other one could slide along the fixed one (see Ref. [13] for more details). The measurements of the deposited energy were done with a thin detector with 100 μm precision.

In Ref. [13] the simulations of the experimental set-up were done based on a simplified geometry: the target material with equivalent thickness was taken instead of the SEETRAM, vacuum window, air gap and monitor calorimeter. Namely, 235 μm of Cu was added to the Cu target and 262 μm of stainless steel was added to the stainless steel target [13].

For the convenience of the reader we reproduce the results obtained in Ref. [13] in Table 2 (there is a misprint in Table 2 and Figure 9 of Ref. [13]; the range of 950 MeV/u uranium in copper calculated by SHIELD is 14.2 mm, according to what is presented in Ref. [13], Figure 9).

Table 2: Measured and calculated ranges of U ions in Cu and stainless steel targets [13]

	Range, mm			
	E = 500 MeV/u		E = 950 MeV/u	
	St. steel	Cu	St. steel	Cu
Measurement	6.0 ± 0.2	5.5 ± 0.2	14.4 ± 0.4	13.1 ± 0.4
ATIMA	6.0	5.5	14.4	13.2
PHITS	6.1	5.6	14.6	13.3
SHIELD	5.6	5.1	15.0	14.2
SRIM	6.5	6.0	16.2	14.7

Simulations

In our study we performed simulations with actual experimental geometry. The calculations were done with 10 μm depth resolution to find the location of the Bragg-peak with good precision and after that the results were averaged over 100 μm thickness so as to represent the 100 μm thickness of the measuring detector used in the experiment.

The results are presented in Table 3 and in Figures 2 and 3. The zero point for depth was chosen to be the beginning of the target. Thus, for determining the stopping range of uranium ions in stainless steel and copper, the target material equivalent thickness should be added to the presented data.

Table 3: Measured and calculated penetration depths of U ions in Cu and stainless steel targets

	Range, mm			
	E = 500 MeV/u		E = 950 MeV/u	
	St. steel	Cu	St. steel	Cu
Measurement	5.7 ± 0.2	5.3 ± 0.2	14.1 ± 0.4	12.9 ± 0.4
FLUKA	6.11	5.65	15.46	14.31
MARS	6.00	5.43	14.63	13.31
SHIELD-A	5.83	5.34	14.34	13.10

Figure 2: Penetration depth of U ions with energy E = 500 MeV/u a) in stainless steel, b) in copper
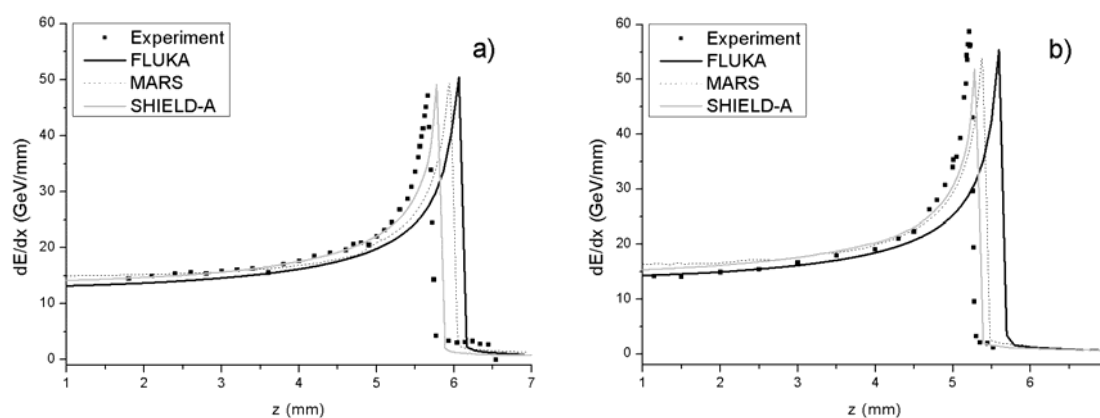
Figure 3: Penetration depth of U ions with energy E = 950 MeV/u a) in stainless steel, b) in copper
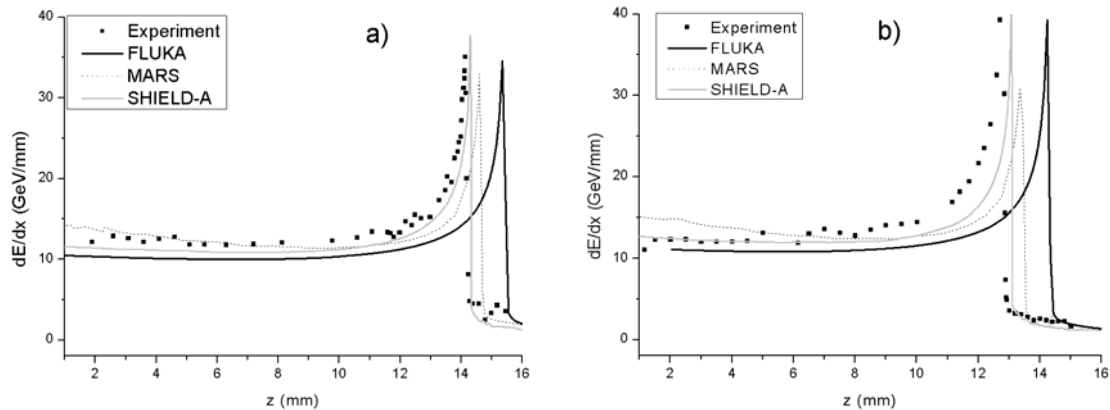
One may notice in Figures 2 and 3 the decrease of dE/dx at the beginning of Bragg curve for 950 MeV/u uranium. This slope is steeper for MARS compared to FLUKA and SHIELD-A. This could be explained by knocking out of ions from the primary beam because of nuclear interactions. Energy deposition of light secondary fragments is much lower than those of primary ions.

Comparing the experimental and simulated results for energy deposition function and the stopping range, one can see that FLUKA overestimates the range of uranium ions in stainless steel and copper by 6% for 500 MeV/u beam and 10% for 950 MeV/u beam. The ranges calculated by MARS and SHIELD-A coincide with the measured ranges within the accuracy of the measurement.

Verification of isotope production modules

Experiment

Isotope production modules were verified by comparing the experimental depth profiles of residual activity and simulated ones.

For obtaining the depth profiles experimentally the aluminium (99.2%) target was irradiated with a 500 MeV/u argon beam. The beam profile was approximately Gaussian with FWHM = 1 cm. The total number of projectiles accumulated on the target was $1.01 \cdot 10^{13}$ ions. The composition of the target is shown in Table 4. The target was assembled from thin activation foils for performing γ-analysis and thick distance-making discs. The configuration of the target is shown in Table 5.

Table 4: Chemical composition of aluminium 99.2% target

Element	Al	Si	Fe	Mn	Cu	Mg
Relative content	0.992	0.0025	0.004	0.0005	0.0005	0.0005

Table 5: Configuration of the thick target irradiated by 500 MeV/u argon beam

Foil number	[1]	[2]	[3]	[4]	[5]	[6]	[7]
Foil thickness, cm	0.1	1.402	0.1	1.401	0.1	1.389	0.1
Foil number	[8]	[9]	[10]	[11]	[12]	[13]	[14]
Foil thickness, cm	1.388	0.1	0.1	0.1	0.1	0.1	0.1
Foil number	[15]	[16]	[17]	[18]	[19]	[20]	
Foil thickness, cm	1.4	0.098	1.399	0.098	1.389	0.098	

Residual activity of the foils was measured with a germanium (HPGe) detector. First measurements were taken one month after the end of the irradiation, when all the short-lived part of γ-emitting nuclei decayed. The applied experimental method allowed registering [7]Be and [22]Na only; as a result of γ-analysis the number of isotopes at the end of irradiation per mm per incident ions was obtained. The results are shown in Figures 4 and 5.

Simulations

The results of simulations of irradiation experiment are shown in Figures 4 and 5. It can be seen from the figures that in the case of [22]Na, FLUKA gives very good agreement with the experiment. MARS and SHIELD-A describe the shape of the depth-profiles in principle correctly, but absolute values differ. MARS gives 1.3 times higher results, SHIELD-A gives at least 2 times discrepancy. This could be explained by discrepancies in simulating the number of secondary projectiles.

Figure 4: Depth profiles of ^{22}Na produced by 500 MeV/u argon beam in aluminium target. Comparison of experiment and simulations by FLUKA, MARS and SHIELD-A.
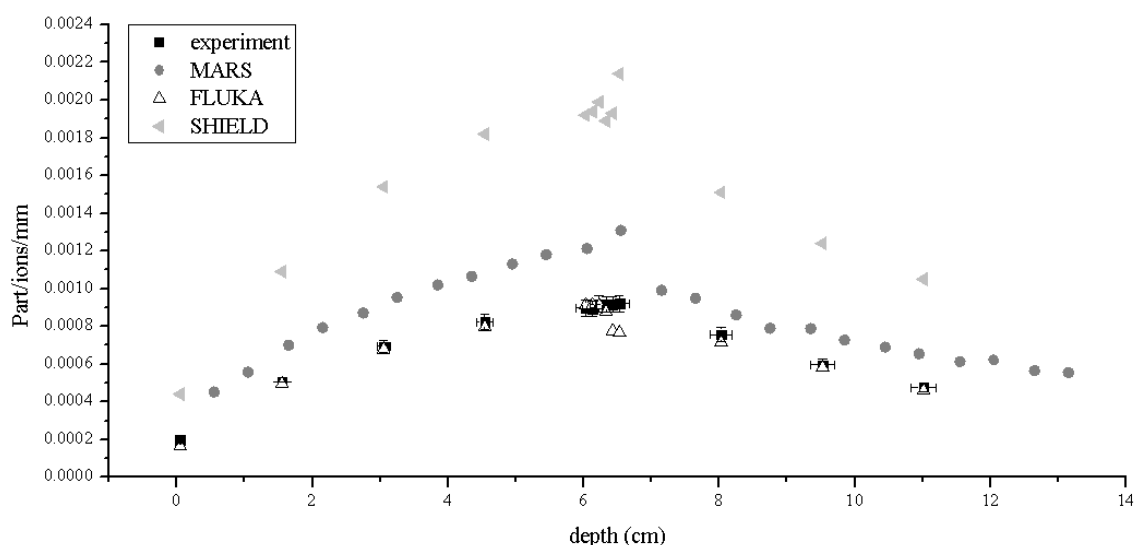
Figure 5: Depth profiles of ^{7}Be produced by 500 MeV/u argon beam in aluminium target. Comparison of experiment and simulations by FLUKA, MARS and SHIELD-A.
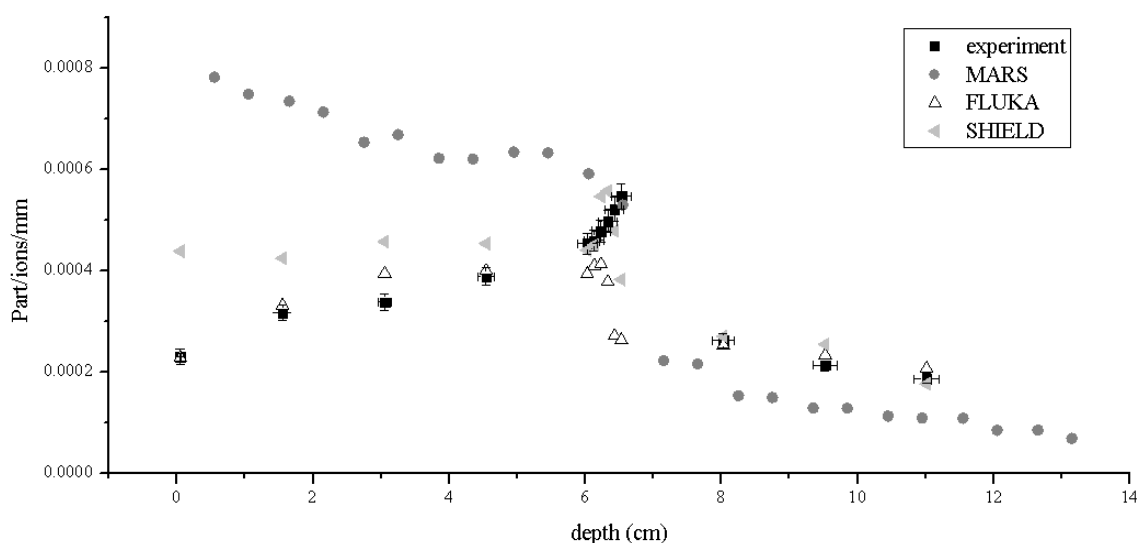
In the case of ^{7}Be, none of the codes matches the shape of the depth-profile of residual activity well in the whole target depth. FLUKA gives quite a good agreement in the regions before and after the range of primary projectiles, but it fails to describe the peak in the range area. This happens because of the cut-off of nuclear interactions for ions (A > 1) with energy below 100 MeV/u. SHIELD-A does simulate the peak and matches the profile beyond the range, but deviates from the experimental data upstream to the range. This discrepancy might be explained by differences in cross-sections and in the number of secondary projectiles produced in the target.

Conclusions

The comparison of experimentally achieved energy deposition function and the results of simulations show that FLUKA overestimates the range of uranium ions by 5% for 500 MeV/u and 10% for 950 MeV/u uranium beam. The ranges calculated by MARS and SHIELD-A give discrepancies below 5%, depending on the energy of the incident ion, which coincides with the measured ranges within the accuracy of the measurement.

Comparing the experimental and simulated depth profiles of the activated isotopes one can see that in the case of ^{22}Na all three codes show similar activation behaviour, though the discrepancies in the number of activated particles per incident ion per unit of depth are still observed. In this case FLUKA shows better agreement with the experiment in absolute values, than MARS and SHIELD-A. Let us note that the disagreement within factor of 2 is considered to be acceptable in studying the activation of thick targets. The depth profile of ^{7}Be is described satisfactorily by FLUKA and SHIELD-A in both shape and absolute value, while MARS demonstrates the shape which differs from the experiment.

References

[1]   Battistoni, G., S. Muraro, P.R. Sala, *et al.*, "The FLUKA Code: Description and Benchmarking", *Proc. of the Hadronic Shower Simulation Workshop 2006*, Fermilab, 6-8 September 2006, AIP Conference Proceedings, 896, 31 (2007).

[2]   Fassò, A., A. Ferrari, J. Ranft, *et al.*, *FLUKA: A Multi-particle Transport Code*, CERN-2005-10 (2005), INFN/TC_05/11, SLAC-R-773.

[3]   Mokhov, N.V., *The MARS Code System User's Guide*, Fermilab-FN-628 (1995).

[4]   Mokhov, N.V., K.K. Gudima, C.C. James, *et al.*, "Recent Enhancements to the MARS15 Code", *Radiation Protection and Dosimetry*, Vol. 116, Part 2, pp. 99-103 (2005), Fermilab-Conf-04/053 (2004).

[5]   Mokhov, N.V., K.K. Gudima, S.G. Mashnik, *et al.*, "Physics Models in the MARS15 Code for Accelerator and Space Applications", *Proc. Int. Conf. on Nuclear Data for Science and Technology*, Santa Fe, NM, AIP Conf. Proc., 769, Part 2, pp. 1618-1623; Fermilab-Conf-04/269-AD (2004).

[6]   Mokhov, N.V., S.I. Striganov, *MARS15 Overview*, Fermilab-Conf-07/008-AD (2007); *Proc. of Hadronic Shower Simulation Workshop*, Fermilab, September 2006, AIP Conf. Proc., 896, pp. 50-60 (2007).

[7]   *www-ap.fnal.gov/MARS*.

[8]   Dementyev, A.V., N.M. Sobolevsky, "SHIELD – Universal Monte Carlo Hadron Transport Code: Scope and Applications", *Radiation Measurements*, 30, 553 (1999).

[9]   Sobolevsky, N., *Modification of the Monte Carlo Particle Transport Code SHIELD for Needs of the FAIR Project*, GSI internal note, ACC_THEORY-note_internal-2008-001, 15 December 2008.

[10]   *www-linux.gsi.de/~weick/atima*.

[11] Niita, Koji, Tatsuhiko Sato, Hiroshi Iwase, *et al.*, "PHITS – a Particle and Heavy Ion Transport Code System", *Radiation Measurements*, 41, 1080 (2006).

[12] *www.srim.org*.

[13] Golubev, A.A., E. Mustafin, *et al.*, "Measurement of the Energy Deposition Profile for [238]U Ions with Specific Energy 500 and 950 MeV/u in Stainless Steel and Copper Targets", *Nuclear Instruments and Methods in Physics Research*, B 263, 339-344 (2007).

[14] Strasik, I., *et al.*, "Experimental Study and Simulation of the Residual Activity Induced by High-energy Argon Ions in Copper", *Nucl. Instr. and Meth. in Phys. Res.*, B 268, 573-580 (2010).

Benchmark experiment of neutron penetration through iron and concrete shields using 243 and 387 MeV quasi-monoenergetic neutrons. Part I: Measurement and calculation of neutron depth-dose distribution

H. Iwase[1], M. Hagiwara[1], Y. Iwamoto[2], D. Satoh[2], H. Yashima[3], T. Matsumoto[4],
J. Nishiyama[4], A. Masuda[4], H. Harano[4], T. Sato[2], Y. Nakane[2], T. Itoga[5], C. Theis[6], E. Feldbaumer[6],
L. Jaegerhofer[6], C. Pioch[7], V. Mares[7], Y. Sakamoto[2], H. Nakashima[2], A. Tamii[8], T. Nakamura[9]
[1]High Energy Accelerator Research Organization (KEK), Radiation Science Center, Tsukuba, Japan
[2]Japan Atomic Energy Agency (JAEA), Tokai, Japan
[3]Kyoto University, KURRI, Kumatori, Japan
[4]AIST, NMIJ Neutron Standard Group, Tsukuba, Japan
[5]RIKEN, SPring-8, Sayou, Japan
[6]European Organization for Nuclear Research (CERN), DGS-RP, Geneva, Switzerland
[7]HelmholtzZentrum München (HMGU), Neuherberg, Germany
[8]Research Center for Nuclear Physics (RCNP), Osaka University, Ibaraki, Japan
[9]Tohoku University, Sendai, Japan

Abstract

A shielding experiment using 243 and 387 MeV quasi-monoenergetic neutrons has been performed at the Research Centre for Nuclear Physics (RCNP), Osaka University, Japan. Neutron energy spectra and doses behind concrete with 25, 50, 100, 200 and 300 cm thicknesses and iron with 10, 20, 40, 70 and 100 cm thicknesses have been measured. Three different sizes of NE213 liquid scintillators of 2″, 5″ and 10″ and two types of Bonner ball neutron spectrometers were used for the neutron energy spectrum measurement.

The measured neutron energy spectra are folded with the dose conversion factor to estimate the neutron doses. Neutron doses were also directly measured by several dosimeters of Fuji wide-range REM counter, Thermo wide-range REM counter WENDI-II, Fuji REM counter, ALNOR REM counter, Chiyoda photo-luminescence personal dosimeter, Nagase Landauer Luxel personal dosimeter and the DARWIN multi-particle dosimeter. Theoretical estimation of neutron energy spectrum and dose distributions behind the concrete and iron shields were also performed by the general-purpose particle transport Monte Carlo code PHITS. A global comparison is carried out on neutron doses obtained by several methods both experimentally and theoretically as a function of the thickness of the shielding materials.

Introduction

High-energy neutron penetration through matter is a key reaction in radiation protection since energetic secondary neutrons are emitted from high-energy nucleon-nucleus or nucleus-nucleus collisions with the largest cross-sections, penetrate through matter, bring the kinetic energy to far away and finally give dose to humans or electronic devices, and also induce material damages. High-energy neutron deep penetration along the beam axis has been measured in several shielding experiments [1-4]. In this study the latest shielding experiment by an international collaboration between KEK, JAEA, AIST (Advanced Industrial Science and Technology), Kyoto University, CERN and HMGU (Helmholtz Zentrum München-Deutsches Forschungszentrum für Gesundheit und Umwelt) is reported.

Experiment

Facility

The experiment was done at RCNP Research Centre for Nuclear Physics, Osaka University, Japan. Protons accelerated by two cyclotrons are transported to the neutron TOF target room. The beam energy is 250 and 400 (246 and 389 exactly) in the experiment. The target is 1 cm thick ^{nat}Li. Neutrons are produced by the Li(p,n) reaction. The neutrons are collimated by a 10 cm × 12 cm rectangular collimator and transported to the RCNP neutron TOF tunnel. The shielding experiment was performed in the TOF tunnel.

Table 1: Proton beam energy, target and the secondary neutron energy of the experiment

Proton energy	246 MeV, 389 MeV
Target	1 cm ^{nat}Li
Neutron energy	244 MeV, 387 MeV

Detectors

Neutron energy spectra and neutron dose behind shielding materials are measured in the experiment. Neutron detectors of 2, 5 and 10 inch NE213 liquid scintillators, a set of AIST and NEMUS Bonner ball spheres, and the HMGU Bonner ball spheres are used for neutron spectroscopy. Neutron dosimeters are, JAEA wide-range dosimeter, WENDI-II wide-range dosimeter, Darwin multi-purpose dosimeter, two REM counters, and two kind of personal dosimeters.

Table 2: Detectors used in the experiment

Neutron spectrometer	2, 5, and 10 inches NE213
	AIST-NEMUS Bonner balls
	HMGU Bonner balls
Neutron dosimeter	JAEA wide range
	WENDI wide range
	Darwin multi-purpose
	Fuji REM counter
	ALNOR REM counter
	Personal dosimeters

Shielding materials

The shielding materials are iron and concrete. The densities were measured as 7.81 ± 0.04 and 2.36 ± 0.02 g/cm^3 (see Appendix at the end of this contribution). The concrete composition and density were measured by chemical sampling previously as shown in Table 3. The discrepancy in the densities of 2.33 and 2.36 (measured in the experiment by weight) for the concrete could be a result of

Table 3: Concrete composition used in the experiment

Element	Density ($\times 10^{22}$ #/cm^3)
H	1.47
C	0.836
O	4.13
Na	0.0194
Mg	0.0297
Al	0.0725
Si	0.419
S	0.018
K	0.00375
Ca	0.987
Fe	0.0192
	2.33 (g/cm^3)
+ frame, Fe	0.0323
	2.36 (g/cm^3)

the metal frames inside the concrete. The frame was assumed as iron and the amount was also estimated in Table 3. The reasoning concerning the iron fame is a guess, and can be treated as an additional systematic error in calculation. A total of 10 iron shielding blocks $100 \times 100 \times 10$ cm^3 and 12 concrete blocks $120 \times 120 \times 25$ cm^3 were prepared for the experiment. The shielding blocks have been used since the TIARA experiment [1,2].

Table 4: Shielding material and thickness for the experiment

Material	Thickness (cm)
Iron	10, 20, 40, 70, 100
Concrete	0. 25, 50, 100, 200, 250, 300
Iron + concrete	70 + 200

Figure 1: Geometry of the experiment
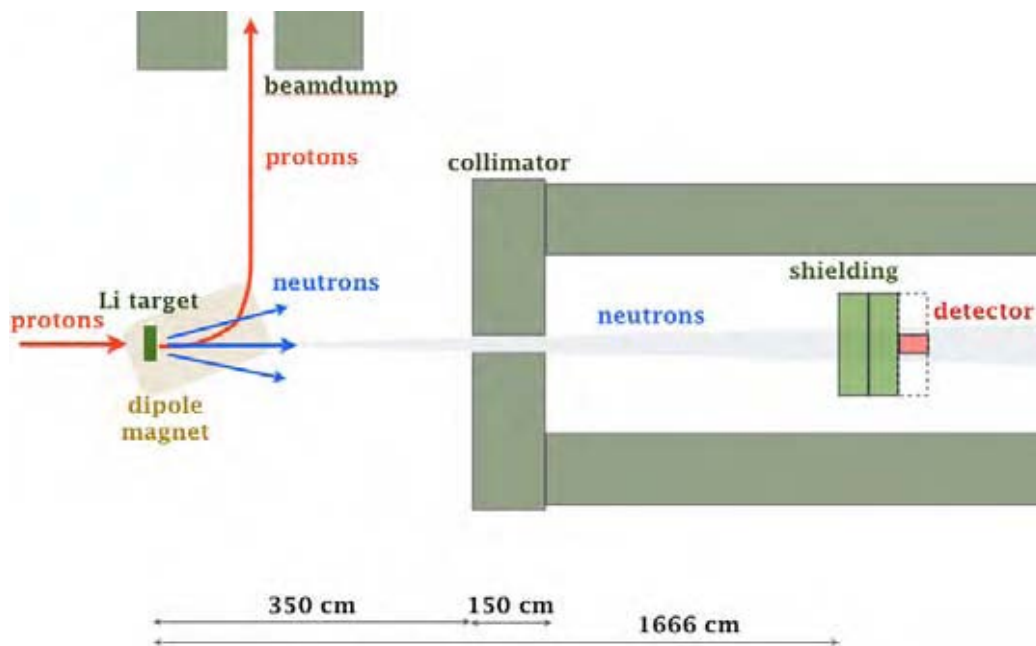
Measurement

Source measurement

Neutron energy spectra of 246 and 389 MeV Li(p,n) reaction at different angles from 0 to 30° was measured at the beginning of the experiment. NE213 scintillators of 2, 5 and 10 inchs were placed in the TOF tunnel and neutron energies were obtained by TOF measurement. The detection angles are 0, 2.5, 5, 7.5, 10, 15, 20 and 30°. Details of the source measurement were discussed by Iwamoto, *et al.* [1].

**Figure 2: Preliminary result of neutron energy spectra from
the 246 and 389 MeV proton beams on a 1 cm Li target**
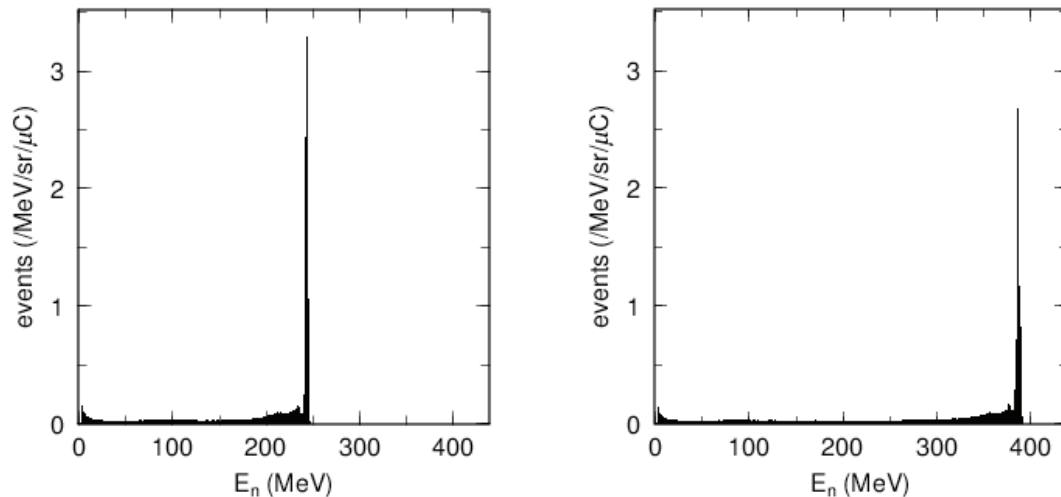
Measurement of neutron energy spectra in deep penetration

Neutron energy spectra behind different thick shielding materials were measured for the shielding thicknesses shown in Table 4. The front surface of the shielding is located 1 666 cm from the target and 1 138 cm from the collimator end (the collimator is located 350 cm from the target, is 150 cm thick, and has a 10×12 cm^2 rectangular hole). A certain distance between the collimator and detection positions was required for two reasons: keeping away from the scattering neutron at the collimator and locating the detectors in the collimated neutron beam volume (neutron beam spot size at 1 666 cm is 33×40 cm^2). Neutron energies were measured with two different methods: *i)* TOF and unfolding hybrid analysis using NE213 [4]; *ii)* unfolding data measured by a ^{3}He neutron counter with multi moderators (Bonner spheres).

NE213 hybrid neutron spectrometry

Neutron penetration through matter can be categorised into the two groups of straight penetration (no scattering) and scattered penetration. Since the former neutrons fly straight without changing the velocity, the neutron velocities, *i.e.* the kinetic energies can be measured by the time-of-flight method. On the other hand the latter neutrons energies are analysed using the unfolding method, since the flight paths of scattered neutrons are not straight and the velocities also change after each scattering and thus cannot be measured by the TOF. The measured TOF spectra have a broad distribution with one sharp peak. The peak is the straight penetration and the others are scattered neutrons. It is noted that the scattered neutrons are also measured in the peak. The amount of the scattered neutrons detected in the peak data was estimated by a PHITS calculation. The accuracy of the calculation is quite reliable since the source neutrons measured in this study were input and nuclear data of the JENDL-HE was used for neutron deep penetration calculation. The first hybrid analysis for neutron deep penetration experiment was performed by Hagiwara, *et al.* [4] and the same measurement was made in the experiment. Neutron energies above several MeV were measured.

Bonner spheres

Bonner spheres neutron spectroscopy was also applied to the shielding experiment. A set of AIST and NEMUS combination Bonner spheres of bare, 3, 5, 7, 9.5 inches poly, 457 p (4″ poly + 4-5″ Pb + 5-7″ poly), 457 c (4″ poly + 4-5″ Cu + 5-7″ poly), and 357 p (3″ poly + 3-5″ Pb + 5-7″ poly), and a set of HMGU Bonner spheres of 2.5, 3, 4, 5, 5.5, 6, 7, 8, 9, 10, 11, 12, 15 inches poly, 9.1 (0.5″ Pb), and 9.2 (1″ Pb) were used. For the whole energies of the thermal (10^{-3} eV) to the incident energy of 244 and 387 MeV, neutron energy spectra were measured. The measured neutron energy spectra were also converted to neutron doses. Bonner sphere neutron spectroscopy is also an accurate wide-range neutron dosimetry.

Measurement of neutron dose in deep penetration

Neutron doses behind different thick shielding materials were also measured using the different dosimeters listed in Table 2. The measurement was made for no shield (0 cm) and shielding thickness of 40, 70 and 100 cm iron and 100, 200 and 300 cm concrete. Neutron doses measured by the wide-range dosimeters are discussed in this study. The energy spectra measured by the AIST and HMGU Bonner spheres were also converted into neutron doses. The result is discussed in the next section.

Calculation

The neutron deep penetration is simulated by the PHITS code [6]. The target room, collimator and TOF tunnel were exactly modelled in the calculation. Since the walls, floor and roof are included, room scattering neutrons are also simulated for the purpose to estimate the amount of room scattering neutrons entering the detector and represent the measured neutron energy spectra down to thermal energies. The calculation starts from the measured Li(p,n) neutron energy spectra for 0 to 30° (0, 2.5, 5, 7.5, 10, 15, 20 and 30°). The measured data does not cover all neutrons of the reaction (above 30° neutrons are lost), however more than about 99% of the peak neutrons are included in the measured data. The measured neutron energy spectra are input into the PHITS calculation. The detail of the input data is shown in Table 5.

Table 5: Input details of the calculation

	Measured data (degrees)	Width of use (degrees)	Solid angle (sr)	Number of neutrons			
				244 MeV		387 MeV	
				#/μC	Ratio	#/μC	Ratio
1	0	0-1.5	0.002153	4.83×10^7	0.008	5.68×10^7	0.003
2	2.5	1.5-3.8	0.01166	2.12×10^8	0.035	2.99×10^8	0.018
3	5	3.8-6.9	0.03169	5.46×10^8	0.090	8.04×10^8	0.047
4	10	6.9-12.5	0.1034	1.61×10^9	0.264	2.36×10^9	0.139
5	15	12.5-17.5	0.1419	1.43×10^9	0.234	2.94×10^9	0.173
6	20	17.5-25	0.2978	1.31×10^9	0.215	4.93×10^9	0.290
7	30	25-35	0.5476	9.49×10^8	0.156	5.64×10^9	0.331
Sum	0-30			6.10×10^9		1.7×10^{10}	

Calculations were performed for each shielding thickness. Neutron deep penetrations through shielding materials were calculated using the neutron data library including high-energy reactions up to 3 GeV JENDL-HE [7] by PHITS. Neutron energy spectra behind shields were obtained. The neutron energy spectra were also converted to neutron doses by folding the effective dose conversion factors evaluated by Sakamoto, *et al.* [8].

Results

Neutron energy spectra measured and calculated at different thick shielding materials of iron and concrete were compared. The amount of the peak (non-scattered neutrons) reduces with thicker shielding materials but it still exists behind both the maximum thicknesses of the iron and concrete shields of 100 and 300 cm. The scattered neutrons lose kinetic energies and distribute down to thermal energy. Both the measured and calculated neutron energy spectra are still under analysis but

the preliminary results agree quite well. Examples are shown in Figure 3. For the energy spectra for whole neutron energy measured by the AIST Bonner spheres, discrepancies can be seen in the energy below keV, but for higher energy both agree well. For the higher energy measured by NE213 agreement is very good. The calculation was performed in principle by using measured data (source term is measured data and transport calculation is by cross-section) and the calculated results should follow the measured data. The discrepancy below the keV energy region may indicate that the calculation initial condition was slightly incorrect, perhaps the source term treatment. The discrepancy might be a result of the treatment of the collimator/room scattering neutrons.

Figure 3: Preliminary results of the measured and calculated neutron energy spectra

244 MeV neutron penetration for iron (left) and 387 MeV neutron penetration for concrete (right)
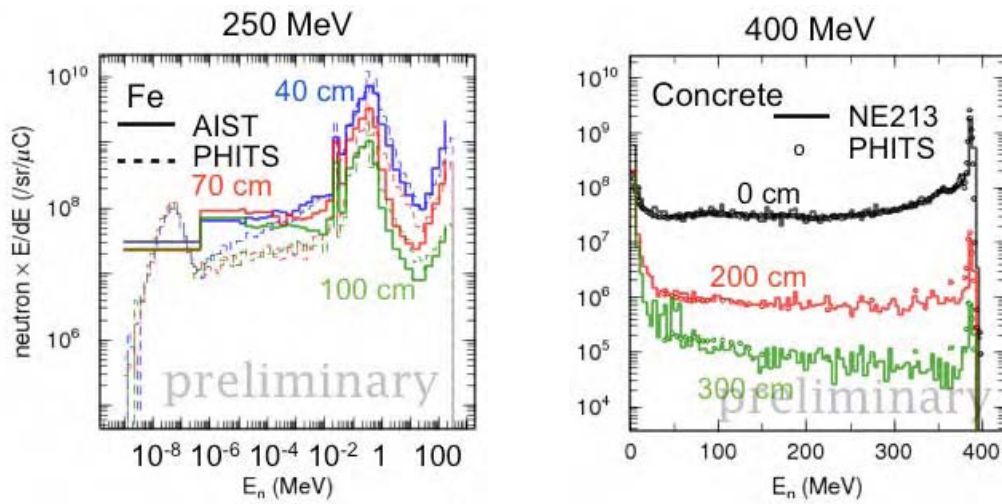
Figure 4 shows the preliminary measured and calculated neutron dose attenuation curves. All the dosimeters are of wide-range type, and measured ambient dose equivalent H*(10) per proton beam in the unit of Coulomb. The front surface of the shielding 1 666 cm from the target was set to a

Figure 4: Preliminary results of the measured and calculated neutron dose attenuation
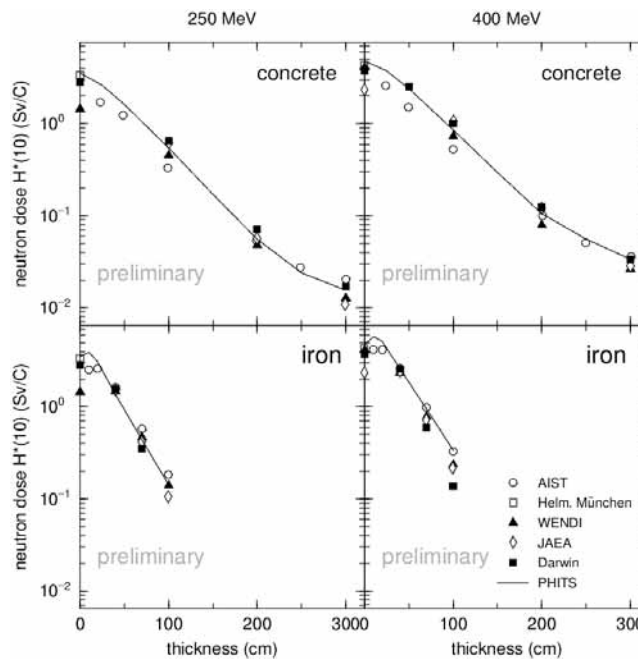
reference point and all of the data were normalised according to the measured position z by a formula $z^2/1\,666^2$ in order to compensate for the beam spreading, the so-called r^2 term. Agreements between all measured and calculated neutron doses are fairly good. Discrepancies are shown rather at the beginning of the shielding materials where high-energy neutrons are dominant. The difference of the responses of the dosimeters for the high-energy region (several hundred MeV in this study) may indicate the discrepancy.

Summary

A shielding experiment using 244 and 387 quasi-monoenergetic neutrons was performed at RCNP, Osaka University, Japan. Li(p,n) neutron energy spectra were measured for different angles up to 30° by NE213 scintillators. Neutron energy spectra and doses after deep penetration through iron and concrete materials with thicknesses of up to 100 and 300 cm were measured. The data and calculation are still under analysis, but the present data measured by different detectors and calculations agree reasonably well. After final data is prepared, four new attenuation lengths of 244 and 387 MeV neutrons for iron and concrete will be estimated. The experimental results will become an additional standard set of the benchmarking data for the radiation protection and the health physics fields.

References

[1]   Nakao, N., *et al.*, "Transmission Through Shields of Quasi-monoenergetic Neutrons Generated by 43 and 68 MeV Protons. Part I: Concrete Shielding Experiment and Calculation for Practical Application", *Nucl. Sci. Eng.*, 124, 228 (1996).

[2]   Nakashima, H., *et al.*, "Transmission Through Shields of Quasi-monoenergetic Neutrons Generated by 43 and 68 MeV Protons. Part II: Ion Shielding Experiment and Analysis for Investigating Calcualtional Method and Cross-section Data", *Nucl. Sci. Eng.*, 124, 243 (1996).

[3]   Sasaki, M., *et al.*, "Measurements of High-energy Neutron Penetrated Through Concrete Shields Using Self-TOF, NE213, and Activation Detectors", *Nucl. Sci. Eng.*, 141, 140 (2002).

[4]   Hagiwara, M., *et al.*, "Benchmark Experiment of neutron penetration through iron and Concrete Shields for Hundreds-of-MeV Quasi-monoenertic Neutrons. II: Measurements of Neutron Spectrum by an Organic Liquid Scintillator", *Nucl. Technol.*, 168, 304 (2009).

[5]   Iwamoto, Y., *et al.*, these proceedings.

[6]   Iwase, H., K. Niita, T. Nakamura, "Development of General-purpose Particle and Heavy Ion Transport Monte Carlo Code", *J. Nucl. Sci. Technol.*, 39, 1142 (2002).

[7]   Fukahori, T., *et al.*, *J. Nucl. Sci. and Technol.*, Suppl. 2, 25 (2002).

[8]   Sakamoto, Y., Y. Yamaguchi, *Dose Conversion Coefficients in the Shielding Design Calculation for High Energy Proton Accelerator Facilities*, JAERI-Tech, 2001-042 (2001).

Appendix: Measurement of densities of the shielding materials

Densities of the shielding materials of iron and concrete were estimated by weight measurement. First, a spring weight-meter was calibrated by 10, 20 and 30 lead blocks. Each lead block was measured by a precise weight-meter and the results for 10, 20 and 30 blocks were 128.86, 242.06 and 355.80 kg. The spring weight-meter gave 130, 240 and 355 kg. The uncertainty is 2-3 kg to this mass region by the weight-meter. One of the iron blocks was then measured. The volume is $100 \times 100 \times 10 = 10^5$ cm^3 and the measured weight was 781 ± 4 kg. The measured density ρ_{iron} is then 7.81 ± 0.04 g/cm^3 (only one iron block was measured since it was also assumed as a calibration for the spring weight-meter). Three concrete blocks were measured. The results were 848, 848 and 850 kg. Since the volume is $120 \times 120 \times 25 = 3.6 \times 10^5$ cm^3, the measured density is 2.36 ± 0.02 g/cm^3. The weight of hooks and ropes are measured and subtracted from both data. The reason that the measured concrete density is higher than the 2.33 g/cm^3 by a chemical sampling measurement may indicate that metal (steel) frames are included inside the concrete.

Figure A1: Calibration by lead and density measurement of iron and concrete shields

Secondary radiation measurement at BigRIPS of RIKEN RIBF

Yoshitomo Uwamino, Hiroki Mukai, Rieko Higurashi-Hirunuma, Atsuko Akashio,
Hiroyuki Fukuda, Hisao Sakamoto, Atsushi Yoshida, Koichi Yoshida
RIKEN Nishina Centre for Accelerator-based Science
Saitama, Japan

Abstract

The neutron and photon fields around BigRIPS of RIKEN RIBF were measured with activation samples of C, Al, Au and Bi, and TLD, when 345 MeV/u $^{238}U^{86+}$ and $^{48}Ca^{20+}$ beams were accelerated. The activated samples were measured with Ge detectors, and the induced radioactivity of the following reactions was observed: $^{12}C(n,2n\alpha)^{7}Be$, $^{12}C(n,2n)^{11}C$, $^{27}Al(n,\alpha)^{24}Na$, $^{27}Al(n,2n\alpha)^{22}Na$, $^{197}Au(n,\gamma)^{198}Au$, $^{197}Au(n,2n\text{-}4n)^{196}Au\text{-}^{194}Au$, $^{209}Bi(n,4n\text{-}10n)^{206}Bi\text{-}^{200}B$. The reaction rates spanned between 10^{-33} and 10^{-27} ([beam ion]$^{-1}$ [sample atom]$^{-1}$).With these reaction rates and the JENDL/HE-2007 cross-sections, neutron spectra were obtained using the SAND2 unfolding code, and the results were compared with calculated results of the PHITS heavy-ion Monte Carlo transport code. The doses obtained with TLD spanned between 10^{-21} and 10^{-16} (Sv [beam ion]$^{-1}$).

Introduction

A considerable number of intermediate-energy heavy-ion accelerators are under construction or planning for the purposes of particle therapy and nuclear research. For the latter, secondary radioisotope beam production is often the most important role of the facility, and a high-intensity beam is demanded.

For radiation safety, secondary neutron production data are important, and many data have been measured. Nakamura and Heilbronn [1] compiled these data, where thick target neutron yields (TTY) of ions up to Xe could be found. At the RIKEN Radioisotope Beam Factory (RIBF) it is available up to uranium beam and we attempted to measure the neutron and photon field around the target and the beam dump of the big RIKEN projectile-fragment separator (BigRIPS).

Accelerator facility

RIBF is a big heavy-ion accelerator complex consisting of a linac and five cyclotrons of which the last stage accelerator is a superconducting ring cyclotron (SRC). Its maximum energy is 400 MeV/u for ions lighter than Ar and 350 MeV/u for heavier ions up to uranium. The accelerated beam is transported to BigRIPS, which produces secondary radioisotope (RI) beam.

Radiation fields were measured around BigRIPS when 345 MeV/u $^{238}U^{86+}$ and $^{48}Ca^{20+}$ ions were accelerated. The primary ions were partly lost at the BigRIPS target, which produced the secondary RI beam, and totally stopped at the beam dumps in and immediately after the bending magnet. Be targets of 3 mm and 5 mm thickness and a 1 mm thick Pb target were used equally for the U beam, and a Be target of 20 mm thickness was mostly used for the Ca beam. The maximum beam intensities during the experiment were about 2×10^9 particle/s for U and 1×10^{12} particle/s for Ca.

Activation detectors

Activation samples of C, Al, Au and Bi were used; their masses are shown in Table 1. The positions where the samples were placed are shown as circled numbers in Figure 1. Position 1 and 2 are on the production-target chamber, Position 1 is at about 30° to the direction of the primary beam, and Position 2 is above the target, at 90° to the beam. Position 3 is at the entrance of the shielding tunnel, Position 4 is behind the target, Position 5 is immediately after the exit beam dump, and Position 6 is close to the side-wall beam dump. Positions 7 and 8 are along the beam line of the secondary RI beam. Position 9 is close to the beam line outside the tunnel.

Table 1: Samples and observed reactions of neutron activation measurement

Element	Weight	Reaction	Half-life	$E_{threshold}$
C	45 g	$^{12}C(n,2n\alpha)^7Be$	53.1 d	28.5 MeV
		$^{12}C(n,2n)^{11}C$	20.3 m	20.3
Al	7 g/1 g	$^{27}Al(n,\alpha)^{24}Na$	15.0 h	3.2
		$^{27}Al(n,2n\alpha)^{22}Na$	2.6 y	23.3
Au	0.8 g	$^{197}Au(n,\gamma)^{198}Au$	2.69 d	0
		$^{197}Au(n,2n)^{196}Au$	6.18 d	8.1
		$^{197}Au(n,4n)^{194}Au$	1.64 d	23.2
Bi	100 g	$^{209}Bi(n,4n)^{206}Bi$	6.24 d	22.6
		$^{209}Bi(n,5n)^{205}Bi$	15.3 d	29.6
		$^{209}Bi(n,6n)^{204}Bi$	11.2 h	38.1
		$^{209}Bi(n,7n)^{203}Bi$	11.8 h	45.4
		$^{209}Bi(n,8n)^{202}Bi$	1.72 h	54.2
		$^{209}Bi(n,9n)^{201}Bi$	1.80 h	61.7
		$^{209}Bi(n,10n)^{200}Bi$	36.4 m	70.9

Figure 1: Positions where the activation samples and TLD were placed
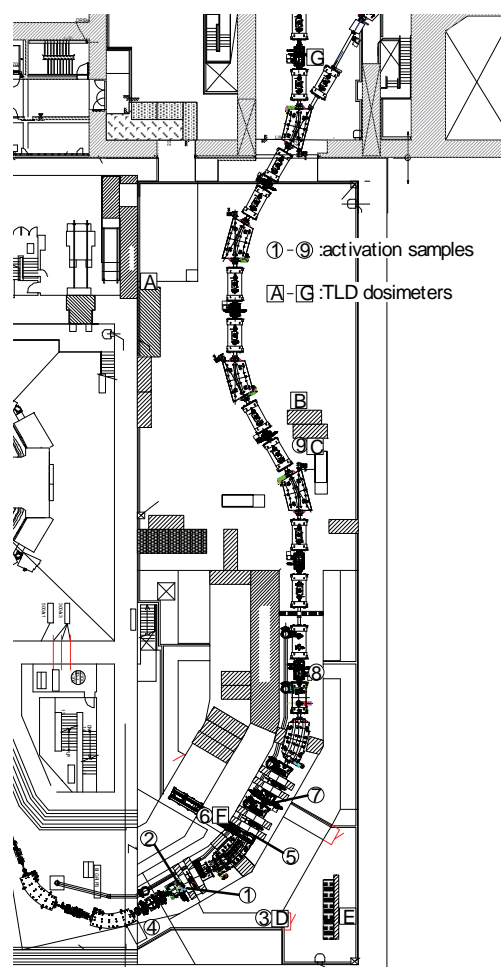
The samples were irradiated at parasite experiments during each beam time of the main experiments, whose primary purposes were the search for the undiscovered isotopes far off the line of stability. The irradiation times during U and Ca experiments were both about 12 days. The beam current was monitored by the count rate of scattered particles for the weak U beam, and by the current transformer for the intense Ca beam. The beam intensity records are shown in Figures 2(a) and 2(b) for the U and Ca beams, respectively.

The samples were taken out immediately after the beam time, and gamma rays were measured by HP-Ge detectors. The observed induced radioactive isotopes are shown in Table 1 with corresponding half-lives and threshold energies. The absolute peak efficiencies of the Ge detectors were measured with a mixed standard gamma-ray source, and the self absorption in the volume sample was estimated using the EGS4 electron photon Monte Carlo code [2].

The activation reaction rate, y ([beam ion]$^{-1}$ [sample atom]$^{-1}$), was obtained with the following formula:

$$y = N(T) \times Q \times 1.602 \times 10^{-19} \bigg/ \left(N_S \int_0^T q(t) \times e^{-\lambda(T-t)} dt \right) \tag{1}$$

where $N(T)$ is the number of radionuclides at the end of irradiation, T is the length of the irradiation, Q is the charge state of the beam, N_S is the number of atoms in the sample and $q(t)$ is the beam current in electric ampere.

Figure 2: Beam current during the irradiation. The y axis is the electric current in nA.

(a) $^{238}U^{+86}$

(b) $^{48}Ca^{+20}$
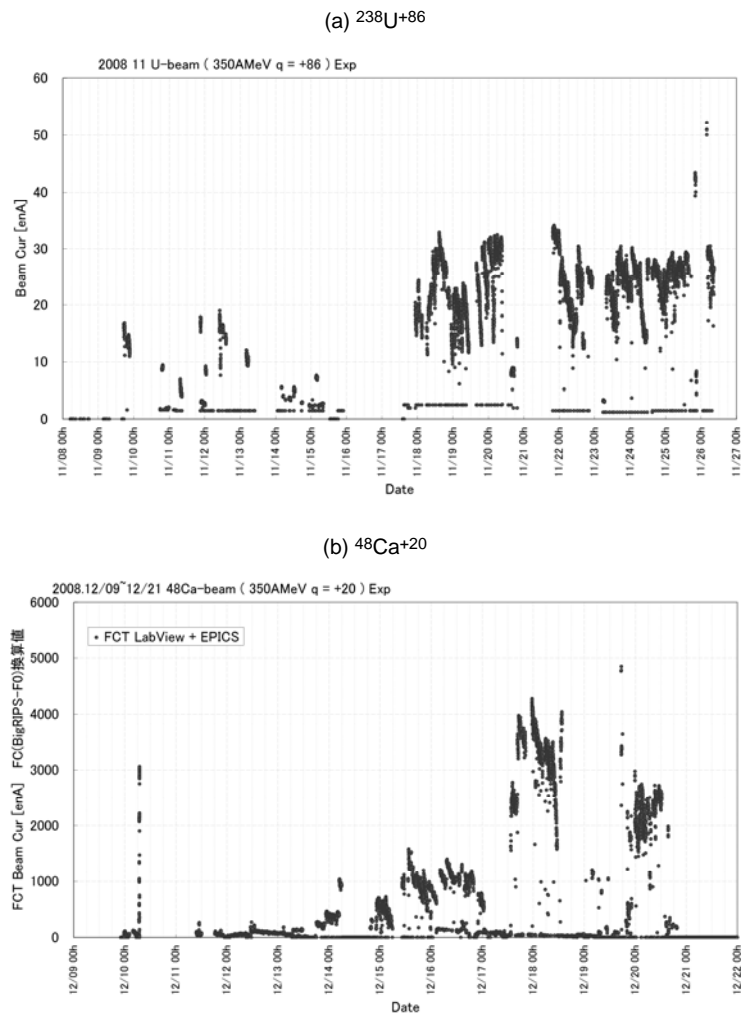
Thermoluminescence dosimeter

Neutron and photon doses were measured using thermoluminescence dosimeters (TLD). The Panasonic UD804PQ TLD, which consisted of three $CaSO_4(Tm)$ elements as shown in Figure 3(a), was put in a container for environmental photon measurement.

For neutrons, UD813PQ4 TLD was used in a specially designed polyethylene moderator [3], shown in Figure 3(b). UD813PQ4 has four elements, two elements were made of $^6Li_2{}^{10}B_4O_7(Cu)$, and the other two elements made of $^7Lia_2{}^{11}B_4O_7(Cu)$. The former was sensitive to photons and thermal neutrons, and the latter was sensitive to photons only. The difference between the responses of these elements gave the thermal neutron fluence. UD813PQ4 had the same exterior as UD804PQ, and two pieces of UD813PQ4 were put at the centre of the moderator, of which the energy response function has a similar shape to the conversion coefficients of 1 cm depth dose equivalent.

Seven pairs of photon (UD804PQ) and neutron (UD813PQ4) dosimeters were placed around BigRIPS as shown in Figure 1 with alphabets in squares. The TLD was taken out after each beam time and read.

Figure 3: Photo on the left (a) shows the Panasonic UD804PQ TLD. Photo on the right (b) shows the moderator which provides the Sv response to the UD813PQ4 thermal-neutron sensitive TLD.

(a)   (b)
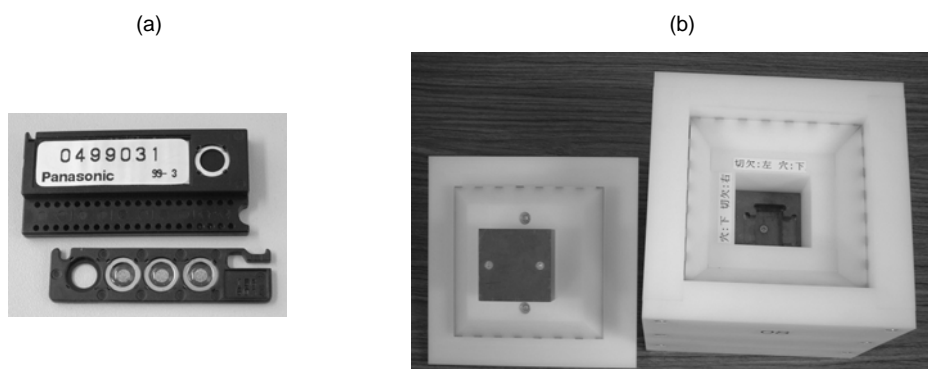
Results and discussion

The measured y values of Eq. (1) are shown in Figure 4. The results, whose statistical errors of measured gamma-ray counts are larger than 10%, are ignored and not shown. The abscissa is the produced radionuclide put in order of threshold energies of the activation reactions. The far left is the exothermic $^{197}Au(n,\gamma)^{198}Au$ reaction, and the threshold energy of the far right $^{209}Bi(n,9n)^{201}Bi$ reaction is 61.7 MeV. The data at Positions 1 and 5 of the U beam and at Position 1 of the Ca beam show flatter distributions, which mean hard neutron spectra. These positions are in the forward direction of the primary beam. The beam dump position depends on the combination of the primary beam and the extracting secondary radioactive beam, and the data at Position 5 of the Ca beam show softer spectrum than of the U bam.

Figure 4: Measured activation reaction rate, _y,_ for U and Ca beams at various Positions 1-9. The abscissa is the produced radionuclide in order of threshold energies of the production reactions.
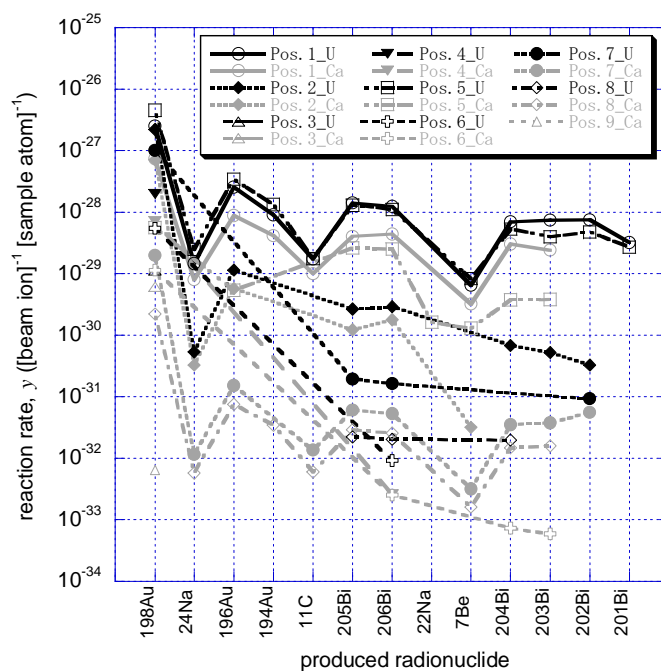
Activation cross-sections derived from JENDL/HE-2007 [4] for neutron energies higher than 20 MeV, and from JENDL-3.3 [5] for energies lower than 20 MeV are show in Figure 5. Cross-sections of C, Al and Au are shown in Figure 5(a), and those of Bi are shown in Figure 5(b). The ^{27}Al(n,α)^{24}Na and the ^{197}Au(n,2n)^{196}Au cross-sections have peaks at 13 MeV and 16 MeV, respectively. Other reactions have threshold energies higher than 10 MeV, and are effectively sensitive to neutrons higher than several tens of MeV.

Figure 5: Activation reaction cross-sections of carbon, aluminium, gold (a) and bismuth (b)
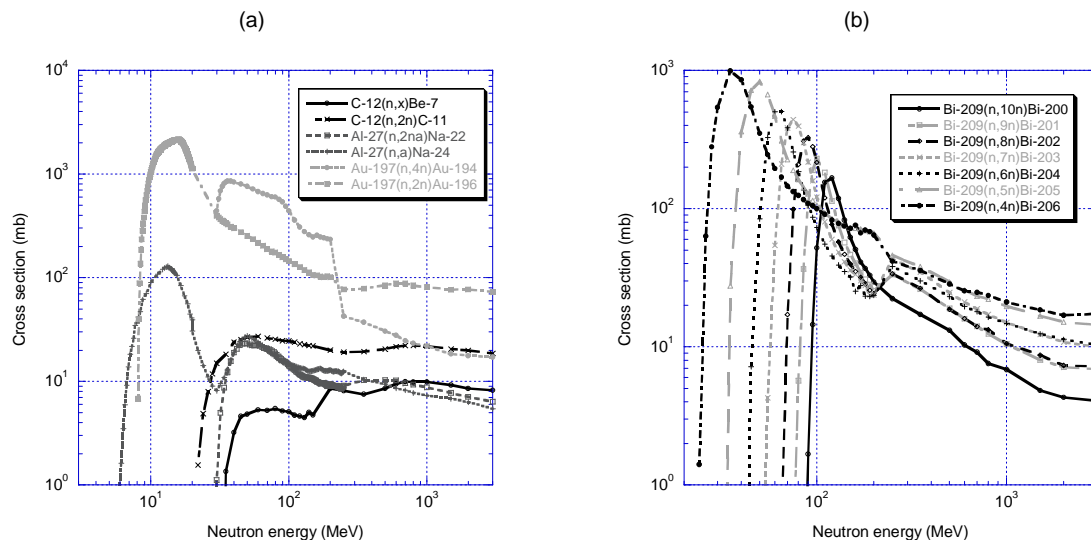
Neutrons at Positions 1 and 2 came mostly from the target. The range of Ca ions in Be is 52.3 mm [6], and the ratio of the target thickness (20 mm) to the range is 0.382. The neutron production of energy above 5 MeV in a hemisphere from 0° to 90° was calculated using the PHITS heavy-ion Monte Carlo transport code [7]. The productions in the 20 mm thick and the 52.3 mm thick Be targets were 3.58 and 8.92 neutron/ion, respectively. The production ratio, 0.401 [= 3.58/8.92], agrees well with the ratio of the target thicknesses, 0.382 [= 20/52.3]. The difference is 4.7% [= (0.401-0.382)/0.401]. In the case of the U beam, the differences are 24%, 24% and 3.4% for the 3 mm Be, 5 mm-Be and 1 mm Pb targets. Therefore, it can be roughly said that the neutron production is proportional to the target thickness. Concerning the U beam, the averaged ratio of the target thickness to the range is obtained as 0.29 (= [3/13.66 + 5/13.66 + 1/3.61]/3), where 3, 5 and 1 stand for the thickness of the Be and Pb targets and 13.66 and 3.61 represent the range of the quoted U beam inside the target.

The averaged ratios of the y values for U beam to Ca beam at Positions 1 and 2 were corrected with the ratios of the target thicknesses to the ranges. They were obtained as 2.9 (= 2.2 × 0.38/0.29) and 2.4 (= 1.8 × 0.38/0.29) for Positions 1 and 2, respectively.

Neutron spectra at Position 1 were obtained using the SAND-2 unfolding code [8] with the measured y values shown in Figure 4 and the reaction cross-sections shown in Figure 5. When all the y values were used, an unrealistic negative flux appeared at several MeV, and the y value of the ^{27}Al(n,α)^{24}Na reaction was ignored in obtaining the spectra shown in Figure 6. The beam intensity was drastically changed during the irradiation, and the target condition was not well defined. Since the half-life of the ^{27}Al(n,α)^{24}Na reaction is much shorter than the irradiation time, the y value of it is strongly affected by the ambiguity of the beam and the target conditions.

The neutron spectra calculated with the PHITS code [7] are also shown in Figure 6. A noticeable disagreement is found below several tens of MeV, and the reason may be attributed to the lack of measured information; that is, only the y values of the ^{197}Au(n,γ)^{198}Au and the ^{197}Au(n,2n)^{196}Au reactions cover this wide-energy region. On the other hand, a relatively good agreement is seen at the energy region above 100 MeV, which is most important for the thick shield of a high-energy, high-intensity facility. The calculation/experiment (C/E) values of the integrated flux above 100 MeV are 1.41 and 1.39 for the U and the Ca beam.

Figure 6: Neutron spectra near the target at 30° from beam direction. Histograms are the measured date and the marks are the PHITS results. [24]Na production data were ignored in the unfolding process.
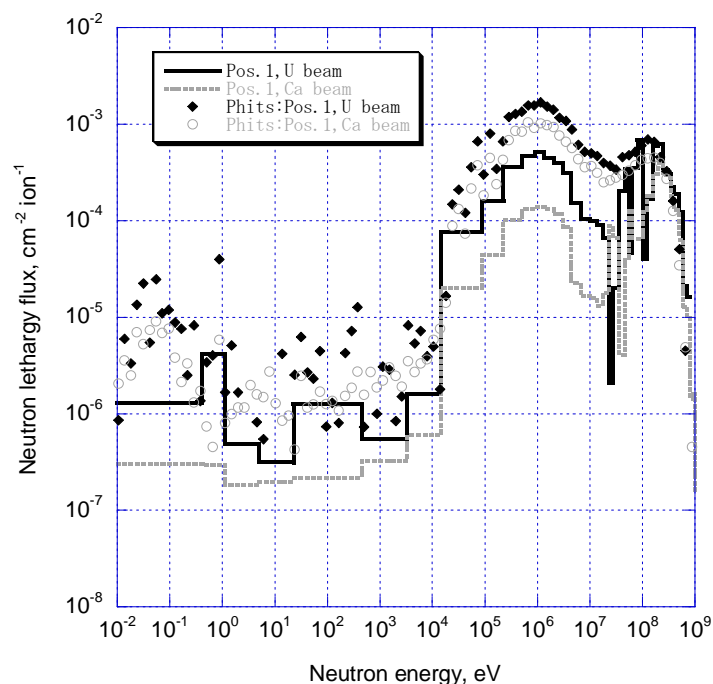
The dose equivalents measured by TLD are listed in Table 2. The values span between 10^{-23} and 10^{-16} (Sv [beam ion]$^{-1}$). Since the estimation of the error of the TLD reading is difficult, some irrational results are also shown. If the results of the U/Ca ratio larger than 5 are neglected, the average of the ratio of the total dose due to the U and Ca are 2.4.

Table 2: Measured results (Sv/ion) of TLD

Radiation	Beam	Position						
		A	**B**	**C**	**D**	**E**	**F**	**G**
Neutron	U			4.9×10^{-19}	1.2×10^{-17}	6.0×10^{-20}	1.1×10^{-16}	
	Ca	8.7×10^{-21}	2.3×10^{-21}	3.3×10^{-20}	5.0×10^{-18}	1.9×10^{-20}	5.0×10^{-17}	2.8×10^{-21}
	U/Ca	–	–	15	2.3	3.2	2.3	–
Photon	U			6.0×10^{-20}	1.3×10^{-18}		6.9×10^{-18}	
	Ca	5.8×10^{-21}	1.8×10^{-22}	4.3×10^{-20}	5.0×10^{-19}	6.5×10^{-21}	3.0×10^{-18}	7.0×10^{-23}
	U/Ca	–	–	1.4	2.7		2.3	–
Total	U			5.5×10^{-19}	1.3×10^{-17}	6.0×10^{-20}	1.2×10^{-16}	
	Ca	9.3×10^{-21}	2.5×10^{-21}	7.5×10^{-20}	5.5×10^{-18}	2.5×10^{-20}	5.3×10^{-17}	2.8×10^{-21}
	U/Ca	–	–	7.3	2.4	2.4	2.3	59

A formula that gives TTY above 5 MeV integrated over a forward hemisphere was proposed by Kurosawa [9]:

$$Y = \frac{1.5 \times 10^{-6}}{N_T^{1/3}} E_P^2 \left(A_P^{1/3} + A_T^{1/3}\right)^2 N_P \frac{A_P}{Z_P^2} \text{ (neutrons particle-1)} \tag{2}$$

where N_T is the neutron number of target, E_P is the incident particle energy (MeV/u), A_P and A_T are the mass numbers of projectile and target, N_P is the neutron number of projectile and Z_P is the atomic number of projectile. In case of a thick Be target, Y is 11.5 and 29.4 for 345 MeV/u [48]Ca and [238]U beam, respectively, and in case of a U bombardment on a thick Pb target, Y is 21.5. Since one-third of the U

beam hit the Pb target, Y can be corrected as 26.7 (= 2/3 × 29.4+1/3 × 21.5). The thus-obtained ratio of U to Ca is 2.32 (= 26.7/11.5). It can be said that our measured values of 2.9 and 2.4 support Eq. (2) even for U ions.

Conclusions

The neutron and photon fields around the target and the beam dump of 345 MeV/u ^{238}U and ^{48}Ca beams was measured with C, Al, Au and Bi activation foils, and TLD. With the activation reaction rates and the JENDL/HE-2007 cross-sections, neutron spectra near the target at 30° from the beam direction were obtained using the SAND2 unfolding code, and the results were compared with the PHITS calculation. The C/E values of the integrated fluxes above 100 MeV were 1.41 and 1.39 for U and Ca beams, respectively. These results suggest the adequacy of the PHITS code even for the U beam when it is applied to a TTY source-term calculation for a thick shield. However, further experiment with a well-defined beam and target condition is necessary to provide a benchmark data.

References

[1]   Nakamura, T., L. Heilbronn, *Handbook on Secondary Particle Production and Transport by High-energy Heavy Ions*, World Scientific Publishing Co. Pte. Ltd., Singapore (2006).

[2]   Nelson, W.R., *et al.*, *The EGS4 Code System*, SLAC-Report-265, Stanford Linear Accelerator Center (1985).

[3]   Uwamino, Y., T. Ohkubo, *Jpn. J. Health Phys.*, 33, 141-142 (1998) (in Japanese).

[4]   Takada, H., K. Kosako, T. Fukahori, *J. Nucl. Sci. Technol.*, 46, 589-598 (2009).

[5]   Shibata, K., *et al.*, *J. Nucl. Sci. Technol.*, 39, 1125-1136 (2002).

[6]   Ziegler, J.F., J.P. Biersack, U. Littmark, *The Stopping and Range of Ions in Solids*, Pergamon Press, New York, 1985 (new edition in 2009).

[7]   Iwase, H., *et al.*, *J. Nucl. Sci. Technol.*, 39, 1142-1151 (2002).

[8]   McElroy, W.N., S. Berg, T. Crocket, *A Computer-automated Iterative Method for Neutron Flux Spectra Determined by Foil Activation*, AFWL-TR-67-41, Vol. I-IV (1967).

[9]   Kurosawa, T., *et al.*, *Phys. Rev.*, C62, 044615-1 (2000).

A new benchmark of spallation models

J-C. David[1], D. Filges[2], F. Gallmeier[3], M. Khandaker[4], A. Konobeyev[5],
S. Leray[1], G. Mank[4], A. Mengoni[4], R. Michel[6], N. Otuka[4], Y. Yariv[7]
[1]Commissariat à l'énergie atomique (CEA-Saclay, Irfu-SPhN), Gif-sur-Yvette, France
[2]Forschungszentrum Jülich-Institut für Kernphysik (FZJ-IKP), Jülich, Germany
[3]Oak Ridge National Laboratory (ORNL), Oak Ridge, Tennessee, USA
[4]International Atomic Energy Agency (IAEA), Vienna, Austria
[5]Institute for Neutron Physics and Reactor Technology-Karlsruhe Institute of Technology (INR-KIT), Karlsruhe, Germany
[6]Zentrum für Strahlenschutz und Radioökologie (ZSR), Hannover University, Hannover, Germany
[7]Soreq Nuclear Research Center (Soreq NRC), Yavne, Israel

Abstract

A benchmark exercise on spallation models was performed under the auspices of the International Atomic Energy Agency (IAEA) in order to assess the prediction capabilities of the spallation models used in high-energy transport codes and support their further development for spallation source design. The selected experimental database includes nucleon-induced production cross-sections of neutrons, light-charged particles, pions and residues. Seventeen different model calculations participated in this benchmark. Necessary tools were developed to have a convenient inter-comparison of experimental data with arbitrary combinations of model calculations. Some of the final conclusions of this benchmark exercise are presented.

Introduction

Designing and operating a spallation source (neutron source, ADS, radioactive ion beam facility, etc.) require reliable high-energy transport codes. In these codes, the elementary cross-sections and characteristics of all produced particles are either obtained from nuclear data libraries (at energies below 150 MeV and mostly for neutron-induced reactions) or calculated by nuclear physics models.

For several decades spallation models have been developed aiming at reproducing the particle and residue production. The reliability of each model can only be assessed via a benchmark on experimental data. If most of the time people do their own benchmark focused on a specific use of the code, more general benchmarks are needed to clearly assess the predictive capability of the available spallation models, in order to help developers and end-users.

The idea of benchmark spallation models is not new. In 1994 a first benchmark on particle (neutron and proton) production was undertaken [1]. The goal was to test the models, with two targets, ^{90}Zr and ^{208}Pb at seven incident proton energies from 25 to 1 600 MeV. A second benchmark was organised in 1997 focused on residue production [2]. The data used were excitation functions obtained with five targets (O, Al, Fe, Zr and Au) and energies from thresholds to 5 GeV. In both benchmarks, very large discrepancies between the model participants were found, partly due to the fact that some models were more suited for low energies, *i.e.* below 200 MeV, while others were more adapted to high energies. The conclusions were that modelling calculations on a predictive basis may at best have uncertainties of the order of ±50% for neutrons and a factor of two for residues.

Since 1997 a lot of new experimental data have been measured (neutrons, light-charged particles and residues) and model developers have worked to improve existing models or propose new ones. Meanwhile, new spallation-based facilities have been proposed. If some facilities already exist (ISIS, SINQ, etc.) or have recently been built (SNS and J-PARC), developments of new targets are still in progress, and the new spallation source in Europe (ESSS) or China (CSNS), for example, should use up-to-date spallation codes or at least be aware of the quality and shortcomings of the codes they use. This is why it was decided to undertake a new spallation benchmark under the auspices of the IAEA.

Background

A first workshop was held in Trieste in 2008 in order to organise the benchmark exercise, present the physics ingredients of the models [3] that could participate in the exercise and select the set of experimental data to be calculated by the models. For the particle production (neutrons, light-charged particles from proton to alpha, and pions), the chosen observables are double differential cross-sections (DDXS), but average multiplicities and multiplicity distributions have been added for neutrons. For residue production, the selected data include isotopic cross-sections, mass and charge distributions but also excitation functions. Most of the time the projectile is proton. Different targets have been considered with a focus on Pb and Fe, as representatives of target and structure materials respectively, and the energy range goes from 20 to 3 000 MeV.

Once collected and formatted these data were uploaded on a dedicated website, as were, later, the calculation results provided by the participants (*www-nds.iaea.org/spallations*). The results of the 17 spallation models or model combinations are available and compared to the data. Tools (FORTRAN codes and Perl script) have been developed to draw all figures and calculate deviation factors. These factors were added to help the analysis.

In February 2010 a second workshop devoted to the benchmark analysis was held at CEA-Saclay. During the first part, global analyses of the results were presented and, in the second part, each model developer explained the qualities and shortcomings of its model and discussed possible improvements.

Analysis with emphasis on impact for spallation sources

Obviously, radioprotection calculations must be as reliable as possible when designing a spallation source. Then, correct predictions of neutrons, light-charged particles (LCP), in particular tritium and helium, and residues in the spallation target and surrounding materials are needed. As regards residues, β/γ or α emitters, delayed neutron progenitors that can be produced in the target, in

particular volatile elements in the case of liquid metals, are some examples of what must be properly estimated. In this section we present the global analysis of the benchmark in three sub-sections: neutrons, LCP and residues, and give some particular examples.

The global analysis of the agreement between a model and the experimental data is based on a coarse eye-guided rating of all sets of data and done independently for double differential cross-sections of neutrons and LCP and for mass, charge and isotopic residue production. R. Michel suggested the rating used for neutrons and residues, F. Gallmeier the one for LCP (Table 1).

Figures shown in the following sections aim at illustrating the main trends, but not at comparing one model to another, as this is beyond the scope of this paper. Nevertheless the full-size colour figures are available on the website, referenced above.

Table 1: Ratings used to analyse the benchmark results:
Neutron, residues (upper table) and LCP (lower table)

Quality	Points
Good	2
Moderately good, minor problems	1
Moderately bad, particular problems	-1
Unacceptably bad, systematically wrong	-2

Acceptance band [eval/x; eval*x]	Points
x = 5	1
x = 3	2
x = 2	3
x = 1.4	4

Neutron production

As mentioned previously, three observables were studied for neutrons: double differential cross-section (DDXS), average multiplicity and multiplicity distribution. The ratings described in the upper part of Table 1 were used for DDXS.

Figure 1: Rating results obtained using the method given in the upper part of Table 1 (neutron DDXS)
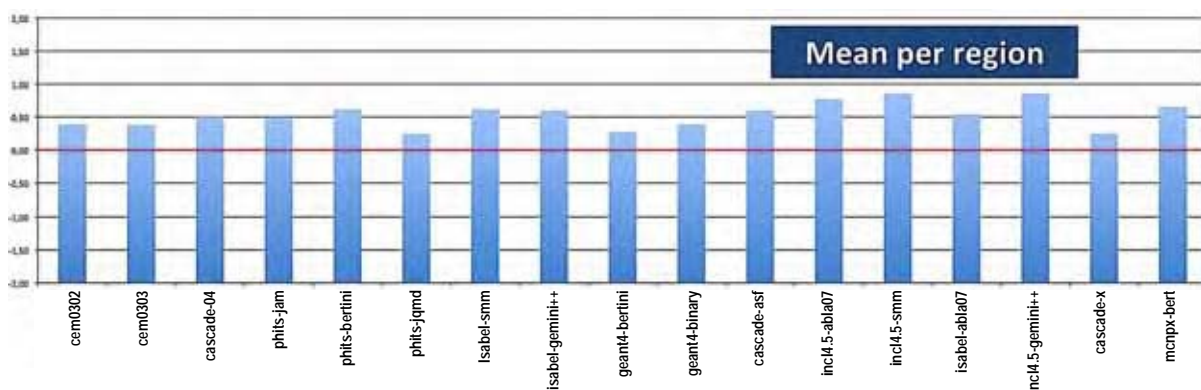
Although all models can be further improved, the results are rather good, and if some models are better than the others, the differences are not that great. Definitely, it can be said that the quality of the models has considerably improved since the 1994 benchmark (Figure 2).

The data sets can be divided according to the projectile energy in three regions: low (< 100 MeV), medium (~ 1 GeV) and high energy (> 2 GeV). Examples of results are displayed in Figure 3. At low incident energies, the models generally have difficulties to fit all the details of the experimental data, which is not surprising since, at these energies, the physics hypotheses inherent to intranuclear cascade models are not valid. However, as data libraries do not exist for all nuclei between 20 and 150 MeV,

Figure 2: Neutron DDXS, Pb (p,xn) 800 MeV. Results obtained by all models within this new benc hmark (left) and with the previous 1994 benchmark (right).
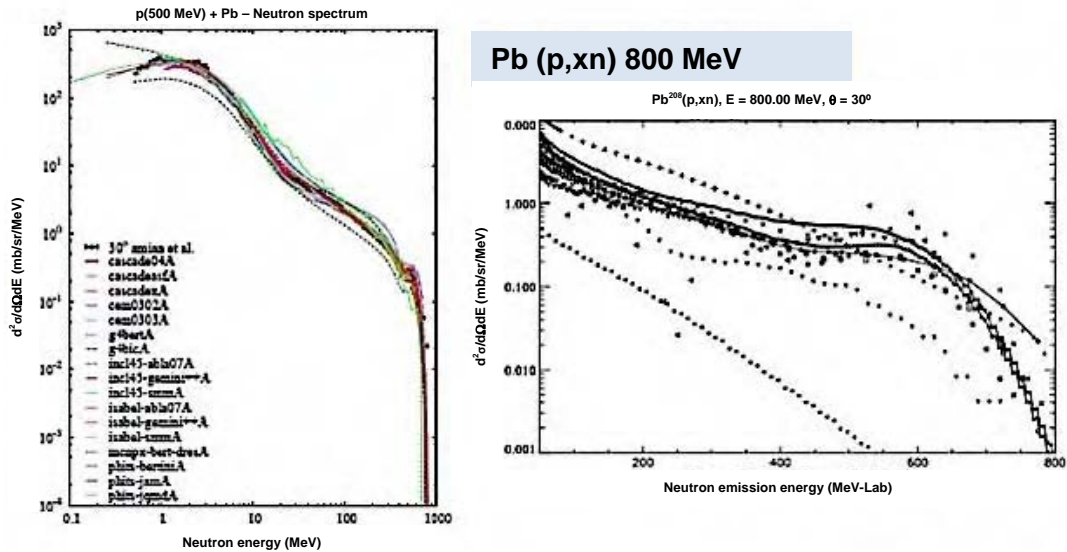
Figure 3: Neutron spectra at particular angles for three reactions. From left to right: p(63 MeV) + Pb (35°), p(1.2 GeV) + Fe (10°) and p(3 GeV) + Pb (30°). All models are plotted.
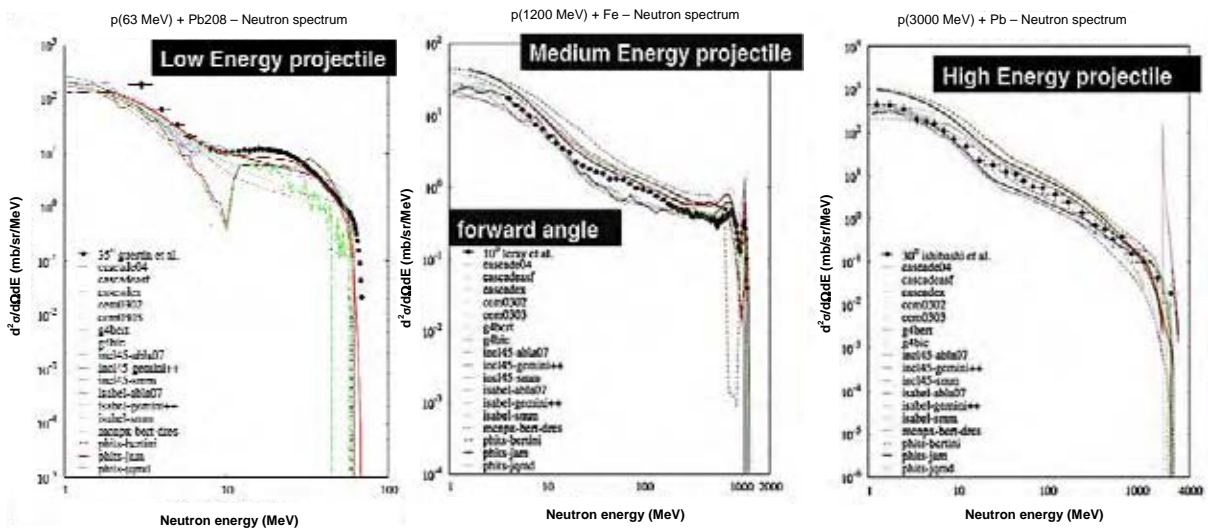
models have to be used often. Therefore it is important to check their reliability and, actually, some of them are not so bad. The medium energy is generally well described by all models, but they have still some problems for high-energy neutrons on forward direction with the quasi-elastic and quasi-inelastic peaks. Finally even at 3 GeV spallation models give good results, except one model at very high energy and a set of models in the evaporation region. It has to be mentioned that the region corresponding to neutron energies between 20 and 100 MeV, generally called the pre-equilibrium region, is sometimes less well reproduced, irrespective of the use of an explicit pre-equilibrium model in the calculation.

Average multiplicity is an observable directly related to neutron production in spallation targets. The models have been compared for two targets (Fe and Pb) and three energies (0.8, 1.2 and 1.6 GeV). The worst case is for some models with iron, but always below a factor 2, and many models fit well the data for both high- and low-energy neutrons, for iron and lead. Generally lead is better reproduced, but with more models outside the error bars. Table 2 summarises the reliability of our set of models.

Table 2: Summary of the global average multiplicity analysis (C/E: calculation/experiment)

Reliability	Fe (< 20 MeV)	Fe (> 20 MeV)	Pb (< 20 MeV)	Pb (> 20 MeV)
50% < C/E < x2	4 models			
C/E < 50%		6 models	4 models	
C/E < 30%	6 models	3 models	8 models	2 models
Close to error bars				10 models
Within error bars	5 models	6 models	3 models	3 models

Light-charged particle production

LCP (proton, deuteron, triton, helium-3 and alpha) are abundantly produced in spallation reactions and are a concern for material damage issues. For instance, helium can be responsible for swelling in the structural materials, in particular the window separating the target and the accelerator vacuum. Moreover, tritium production is often an issue from the radioprotection point of view.

The rating used is described in the lower part of Table 1 and the results averaged on all models are given in Table 3. It is clear that LCP production is much more difficult to describe well than neutron production. Figure 4 shows the rating for each model and for the different types of LCP [p(1.2 GeV) + Ta]. With regard to composite particles, it must be stressed that the high-energy tail observed in the experimental data cannot be reproduced by models which do not have a specific mechanism to emit such particles, as with coalescence in intranuclear cascade. This concerns seven of the models and explains why protons have a better rating than the others. Figure 4 shows this lack in the case of tritium production, but also gives hope, since at least two models describe well the whole spectrum.

Table 3: Rating results obtained for light-charged particle double differential cross-sections

Emitted particle	Code data averaged rating	
Protons	2.4	(*i.e.* within a factor 2-3)
Deuterons	1.2	(*i.e.* within a factor 4)
Tritons	1.2	(*i.e.* within a factor 4)
He-3	0.9	(*i.e.* within a factor 5)
Alpha	1.3	(*i.e.* within a factor 4)

Figure 4: Rating for each model for the different types of LCP [p(1.2 GeV) + Ta]. Models having no mechanism to produce high-energy composite particles have not been rated for these types of LCP.
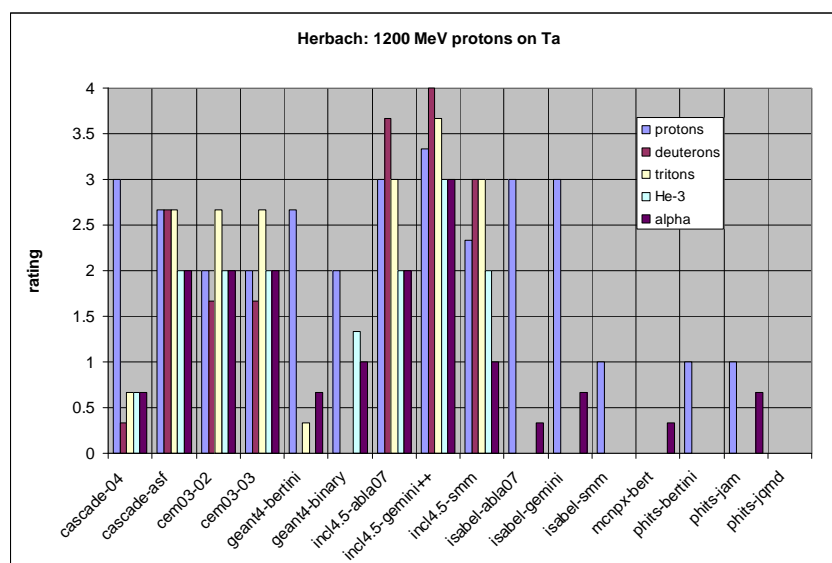
Residue production

Residue production, as LCP, is more difficult to fit to the data than neutron production. Figure 5 gives the rating obtained for isotopic production with three targets (Fe, Pb and U) and three energies (300, 500 and 1 000 MeV). It can be seen that the differences between models are quite significant in this case. However, compared to the situation in the former benchmark [2], one can state that in many reaction regimes considerable progress has been made by the modellers during the past decade. Thus, there is hope, though there is still room for improvement. In Figure 5 the maximum number of available points was 28, the minimum -28. Clearly, none of the models and codes meets all of the requirements, but there are significant differences demonstrating that some codes perform much better than others. There are also codes which generally perform badly and which need conceptual improvements.

Figure 5: Rating of the results of 16 participants for predicting the isotope distributions measured by inverse kinematics for iron, lead and uranium at all energies
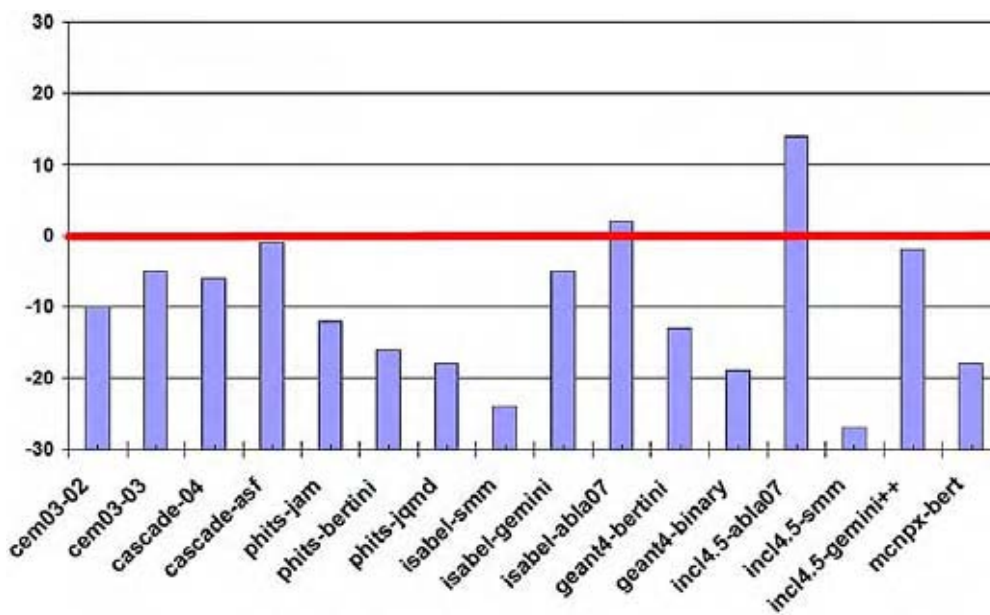
Examples of the detailed results are given in Figures 6 and 7. The charge distribution of residues produced in p + ^{56}Fe at 1 GeV shows that many models have difficulties to correctly predict intermediate mass fragments (Figure 6). The isotopic distribution of bromine produced (by fission) in the p + ^{208}Pb reaction at 1 GeV is displayed in Figure 6 (right), some isotopes being of interest for radioprotection, as the two delayed neutron precursors, ^{87}Br and ^{88}Br. This illustrates the significant discrepancies between the models, both in cross-section values and in shape of the isotopic distribution.

Finally, Figure 8 shows, as an example, the difficulty to reproduce an excitation function in shape and sometimes order of magnitude for some models, but also the danger in extrapolating results from a given projectile energy to another.

Conclusions

The new benchmark of spallation models, performed under the auspices of the IAEA, covers more than 40 reactions on 10 different targets induced by nucleons with energies ranging from 20 to 3 000 MeV. Seventeen models or model combinations participated in the exercise. Data and calculation results are available on a dedicated website (*www-nds.iaea.org/spallations*). The global analysis, presented briefly is this paper, has shown that models are generally much more reliable than they were at the time of the two previous benchmarks [1,2]. However, there is still a lot of room for improvement, in particular for the prediction of residues and composite light-charged particles. If some models seem globally better than others it must be stressed that the complexity of the spallation reactions requires great caution with any kind of extrapolation, especially concerning projectile energy.

Figure 6: Charge distribution (^{56}Fe(1 GeV.A) + ^{1}H). All models are plotted.
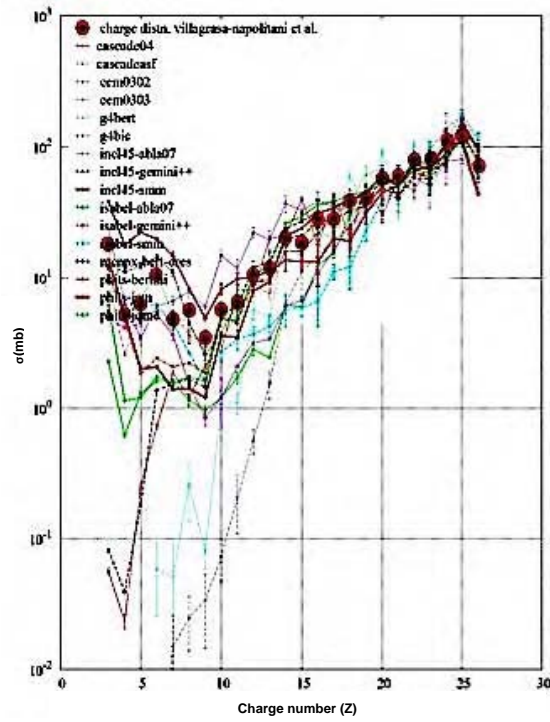
Figure 7: Br mass distribution from ^{208}Pb(1 GeV.A) + ^{1}H. All models are plotted.
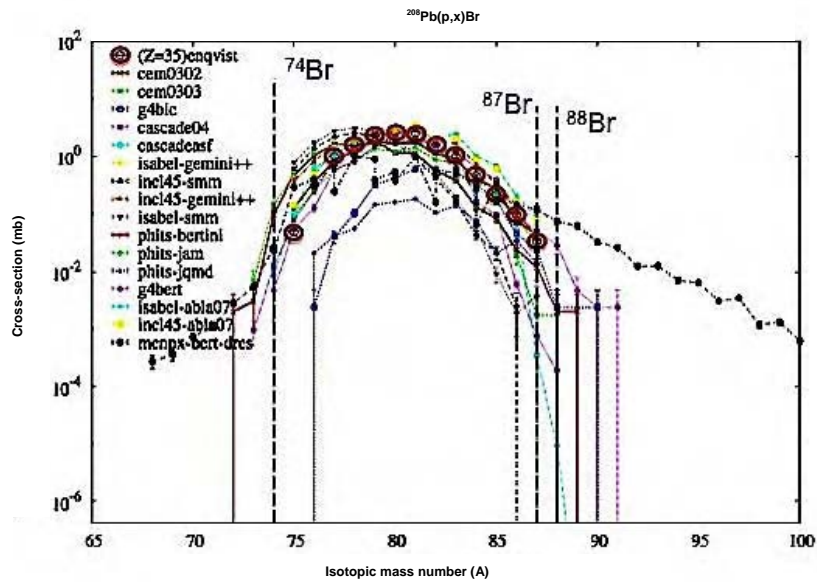
Figure 8: Excitation function of the ^{96}Nb isotope obtained with p+Pb reaction. Data (squares).
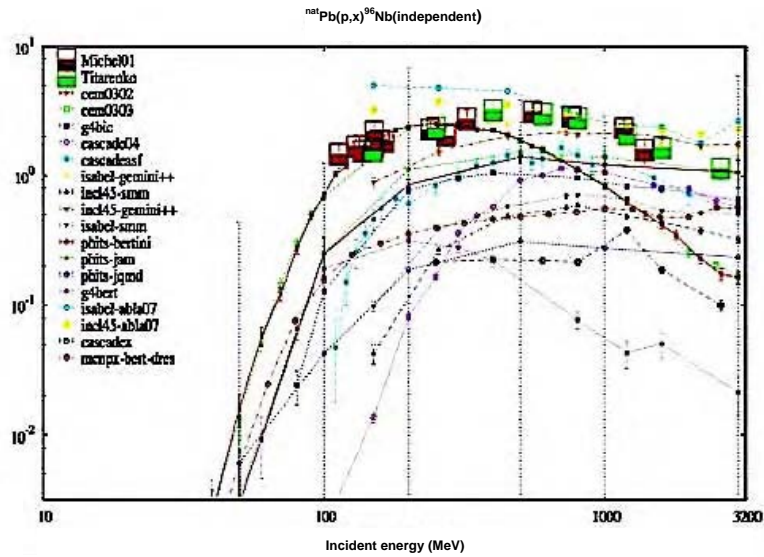
References

[1]   Blann, M., *et al.*, *International Code Comparison for Intermediate Energy Nuclear Data*, NSC/DOC(94)-2, OECD/NEA, Paris (1993).

[2]   Michel, R., P. Nagel, *International Codes and Model Intercomparison for Intermediate Energy Activation Yields*, NSC/DOC(97)-1, OECD/NEA, Paris (1997).

[3]   Filges, D., *et al.* (Eds.), *Proceedings of the Joint ICTP-IAEA Advanced Workshop on Model Codes for Spallation Reactions*, IAEA INDC(NDS)-530, ICTP, Trieste, Italy, 4-8 February 2008.

Measurement and simulation of radionuclide product yields in iron from 400 AMeV carbon ions

Tatsuhiko Ogawa[1], Mikhail N. Morev , Takeshi Iimoto[2], Toshiso Kosako[3]
[1]Dept. of Nuclear Eng. and Management, Graduate School of Eng., Univ. of Tokyo, Tokyo, Japan
[2]Division for Environment, Health and Safety, Tokyo, Japan
[3]Nuclear Professional School, Graduate School of Eng., Univ. of Tokyo, Ibaraki, Japan

Abstract

Radioactive target fragments in iron exposed to the 400 MeV/u carbon ion beam was measured as a function of depth. This irradiation was simulated using FLUKA based on its default nuclear models. In general, the simulation and experiment agree within a factor of two. Particularly simulation underestimates activity of most of the nuclides by a factor of about 10 at the end of the range of ion beam, which is probably attributed to the deficiency of the default nuclear reaction model (RQMD) to reproduce ion-induced reactions below 100 MeV/u. Furthermore, it is found that simulation tends to provide better estimates for heavier nuclides.

Introduction

Accelerators have proven to be an indispensable tool for many applications, including medical treatment, science and industry. The number of ion accelerator facilities is rapidly growing over the world. For example, a remarkable progress was achieved recently in heavy ion radiation treatment (HI-RT). With commissioning of HIMAC in 1994 at the National Institute of Radiological Sciences (NIRS) in Chiba, Japan – the first medical dedicated heavy ion synchrotron and the world's second HI-RT after Bevalac (1975-1992, Berkeley, USA) – there are four facilities currently operated and 12 planned or under construction world wide [1]. Carbon beam is the most widely used, though other ions from proton to silicon with energies of 100-800 MeV/u are also available for HI-RT.

Accurate characterisation of radionuclide inventory and residual dose rates are important for safe maintenance and decommissioning of accelerator facilities. Over the last decades a number of high-energy particle transport codes have been developed, *e.g.* FLUKA [2,3], PHITS [4], MARS [5,6], etc., implementing sophisticated hadron-nuclear and nuclear-nuclear interaction models with an inherent capability for prediction of residual radionuclide production. These codes are considered as properly validated for radiation shielding design of ion accelerators by comparison against a large pool of integral benchmarks and differential data (*e.g.* secondary particle yields, double differential cross-sections, etc.) [7]. On the other hand, accuracy of residual radioactivity prediction by the available codes is still far from being perfect. Typically, one should not expect an agreement between experiment and simulation better than a factor of 2-4 for most of individual radionuclides. In addition, the amount of experimental data on radionuclide yields is rather limited and do not cover the whole range of practical interest for energies, projectile ions and target nuclei. The data on radionuclide cross-section yields in targets by heavy ion spallation available before 2006 is summarised in Chapter 5 of Ref. [7]; among individual studies, Yashima, *et al*. [8] provides the most systematic coverage of projectiles and targets.

In this paper we report on measured depth distribution of relatively long-lived gamma-emitting radionuclides (half-life > 12 hours) in an iron target bombarded by 400 MeV/u carbon ion beam. The experimental data is compared with predictions from the FLUKA Monte Carlo code and available results from the literature [8].

Method

Experimental specifications

The experiment was set up at the general-purpose irradiation room PH-1 of Heavy Ion Medical Accelerator (HIMAC) in Chiba, Japan on 23 May 2009. A stack of thin cylindrical iron samples (hereafter coins) was exposed for 11.35 hours to a focused carbon ion beam accelerated to 400 MeV/u. The total thickness of the stack was slightly larger than the ion range. Average intensity was measured by the ionisation chamber and variation of beam intensity during the exposure period was monitored by direct current-to-current transformer (DCCT). After irradiation, the target was disassembled and γ-spectra from the irradiated samples were counted with a HPGe-spectrometer.

Target design

The target (Figure 1) is assembled of square iron plates 16 cm × 16 cm of total thickness ~68 mm. Samples are loaded into the cylindrical cavity and fixed tight. The stack is composed of thin cylindrical samples (diameter 40 mm) of various materials: 41 iron "coins" (of average thickness 1.55 ± 0.05 mm, 99.84% purity), 5 iron 0.1 mm thick foils (99.9% purity), and 6 copper 0.1 mm thick foils (99.99% purity). The order of material samples in the stack is shown in Table 1. The thickness of each coin was measured with an accuracy of 0.7%. The total thickness of the stack 50 g/cm^2 is sufficient to stop the primary ions – the range for 400 MeV/u carbon ions in iron (calculated with the SRIM code [9]) is approximately 40 g/cm^2.

Figure 1: Iron target assembly

1 – fixing ring, 2 – pushing washer, 3 – upper and middle plates, 4 – bottom plate, 5 – pin, 6 – stack of "coins"
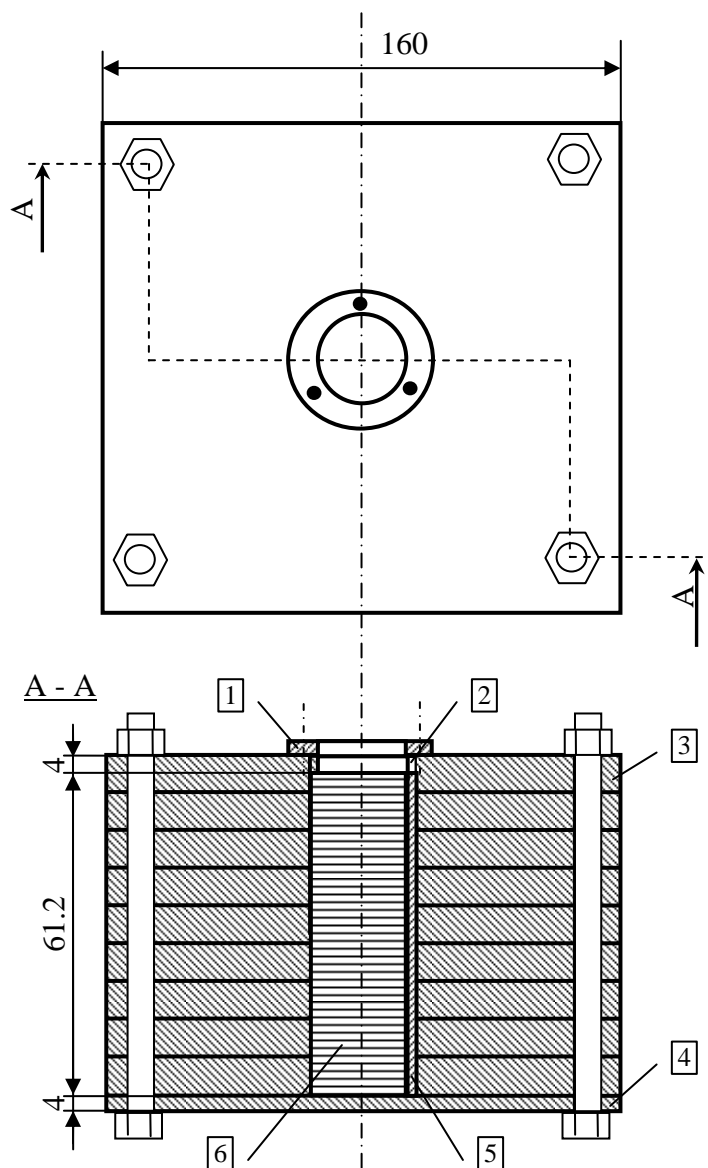
Table 1: Elemental composition of iron target

Fe-01, Fe-02	Foils 0.1 mm thick, iron 99.9% purity
C1	Coin #1, iron*
Cu-x, Cu-01, Cu-x**	Foils 0.1 mm thick, copper 99.99% purity
Fe-x	Foil 0.1 mm thick, iron 99.9% purity
C2,…C20	Coins ##2-20, iron*
Cu-x, Cu-02, Cu-x	Foils 0.1 mm thick, 99.99% purity copper
Fe-x, Fe-03	Foil 0.1 mm thick, iron 99.9% purity
C21,…C41	Coins, iron*

* Material specification: Fe 99.85%, Mn 0.05%, Si 0.04%, S 0.03%, C 0.03%.

** Cu-x and Fe-x foils are used to prevent cross-contamination between materials.

Ion beam properties

HIMAC is an ion and proton accelerator that consists of a linac and an accelerating ring (diameter approximately 42 m). The ion beam is slowly extracted from the storage ring, and delivered to the experimental area through a beam line. Approximately $4 \cdot 10^8$ particles per pulse 400-600 ms. Pulse repetition period is 3.3 s. The typical distribution of the intensity in the beam pulse is shown in Figure 2.

Figure 2: Pulse shape (as measured in synchrotron ring by HIMAC operators)

500 ms
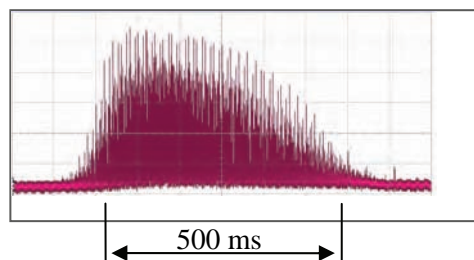
Before the start of exposure, the beam was carefully targeted onto the geometrical centre of the coin stack with the use of a luminescence plate and web camera. The beam shape in the Z-Y plane was estimated using data from a wire monitor nearest to the beam window. After irradiation the beam shape and positioning were checked by application of coins onto BAS-MS Imaging Plate.

Beam intensity variation during the accelerator run time was available from of the ring DDCT monitor records at the control panel. The DDCT voltage is proportional to the beam intensity and may be converted to particles per second (PPS) using an empirical coefficient (unknown accuracy, not used for data processing). Based on the data we accurately defined exposure time as T = 10.35 hours. The typical pulse shape of beams in HIMAC is provided in Figure 2. Absolute beam intensity integrated over the whole irradiation time was measured using an uncalibrated ionisation chamber. Absolute beam intensity I (particles) was deduced with the following equation:

$$I = \frac{cr}{\left(\frac{dE}{dx}\right)_{Air} d\left(\frac{e}{W}\right)} \tag{1}$$

where $(dE/dx)_{Air}$ is the stopping power of 400 MeV/u carbon ion in air [10], d is the thickness of the air gap inside the ionisation chamber, W is ionisation energy of air [11], c is the number of signals from the current integrator and r is the range of current integrator (signal/Coulomb).

Beam intensity fluctuation during the irradiation was monitored using a DCCT installed in the synchrotron ring and activities were corrected for this intensity fluctuation.

Spectra counting geometry, efficiency calibration

Gamma-ray spectra of irradiated samples were measured with a high-purity germanium (HPGe) detector associated with ADC, MCA, PC and the signal processing modules. HPGe (Ortec, n-type with 35% rel. eff., SN:35-TN40664A) has a crystal size 59 mm in diameter and 72.4 mm in length, Be window, additional filter to cut beta particles 4.08 mm of acryl plastic (density 1.34 g/cm^3). The HPGe detector was coupled to a spectroscopy amplifier connected to a 4 096 channel multi-channel analyser (MCA). This MCA readout was analysed by using MCAWin2000 software [12]. Long source-to-detector distance (15 cm) was used to suppress peak counts loss due to pile-up and cascade coincidence effects. The first measurement was made after ~55 hour cooling and continued for 8 hours. The measurement was repeated after a few month of cooling to improve accuracy for long-lived radionuclides.

Energy dependence of full-absorption peak efficiency for γ-rays (100÷3 000 keV) was determined by an internal calibration method with an accuracy better than ±2% and normalised to absolute efficiency measured with ^{60}Co standard source (±3%, with coverage factor k = 2). Further details of the calibration procedure are provided in Ref. [13]; the procedure is to some extent similar to the method introduced in Ref. [14].

The absolute total efficiency of the HPGe detector for cascade coincidence correction was calculated based on the detector specifications from the manufacturer. Also, the total efficiency was measured at short source-to-detector distances according to the method described in Ref. [15] using standard ^{60}Co source and was found to be in good agreement with calculated values (within 10%). The cascade coincidence loss at source-to-detector distance 15 cm was found to be insignificant for all the nuclides of interest; however, it was accounted for in data processing. When measuring samples with high activity (*e.g.* at short cooling times), a high counting rate may result in random coincidence loss (pile-up) of peak-counts. The dual source method was used to monitor pile-up effects. Spectra from coins were counted together with a ^{137}Cs source and pile-up count loss was found to be negligible (<1%) and was disregarded.

Simulation

The experimental data served as a benchmark of FLUKA, which includes an ion-induced nuclear reaction model [16,17]. The simulations were based on the accurate irradiation geometry description except for peripheral geometrical components (*e.g.* roof, floor) and nominal irradiation and cooling time. The secondary radiation was not cut off in order to take into account for the secondary particle induced reactions. For example, neutrons and protons were followed down to 10^{-5} eV and 1 MeV, respectively. Energy loss along the ion path inside the iron target was simulated using the default FLUKA routine based on the Bethe-Bloch theory [18].

Residual nuclides induced in cylindrical regions (1.5 mm in thickness and 40 mm in diameter) were scored by using the RESNUCLE option of FLUKA given the irradiation and cooling times of 11.35 hours and 1 hour, respectively. Experimental results are corrected for accurate irradiation time and cooling time in order to allow comparison with the calculation.

Results and discussion

Using the above-mentioned method, 18 nuclides (^{7}Be, ^{22}Na, ^{24}Na, ^{28}Mg, ^{42}K, ^{43}K, ^{44m}Sc, ^{46}Sc, ^{47}Sc, ^{48}Sc, ^{48}V, ^{48}Cr, ^{51}Cr, ^{52}Mn, ^{54}Mn, ^{55}Co, ^{56}Co, ^{58}Co) were identified from the surface to the depth of the target. Some typical results of the activity depth profiles are shown below.

As shown in Figure 3, production of ^{7}Be is underestimated everywhere. The underestimation from the surface to the stopping range can be attributed either to an underestimation of the ion-induced reaction cross-section or underestimation of secondary particle fluence. The underestimation beyond the stopping range is attributed either to the underestimation of secondary particle fluences or underestimation of projectile fragments, which are produced mostly at the end of the range of the primary ion.

Figure 3: Experimental and simulated ^{7}Be activity distribution inside the target
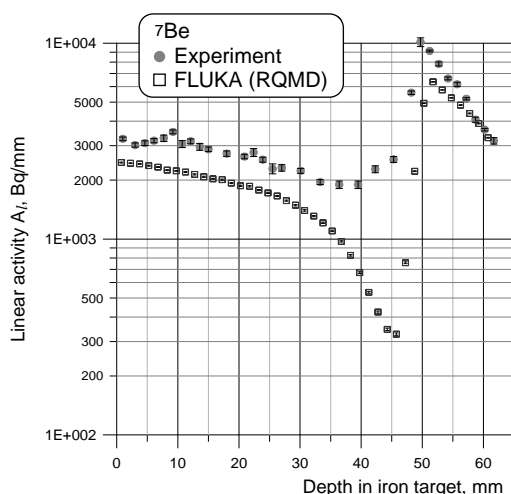
Figures 4 and 5 show production of rather light fragments (^{22}Na and ^{24}Na) that are underestimated by a factor of two from the surface to the depth. This uniformity of the discrepancy within the range independent of depth indicates underestimation of ion-induced cross-section irrespective of secondary particle yield. As neither ^{22}Na nor ^{24}Na are produced as projectile fragments, the underestimation beyond the ion stopping range may be because of the underestimation of the high-energy component of neutrons, which can induce deep fragmentation such as production of ^{22}Na. The underestimation between about 45 mm and 50 mm is due to the lower energy threshold of the RQMD model. Since the RQMD model can reproduce a nuclear reaction only above 100 MeV/u (though a nuclear reaction has actually occurred under 100 MeV/u in reality), an ion-induced reaction is not reproduced in a region between 45 mm (where the energy of primary ion beam reaches about 100 MeV/u) and 50 mm (stopping range). Implementation of a nuclear reaction model below 100 MeV/u might improve the agreement in this region.

Figure 4: Experimental and simulated ^{22}Na activity distribution inside the target
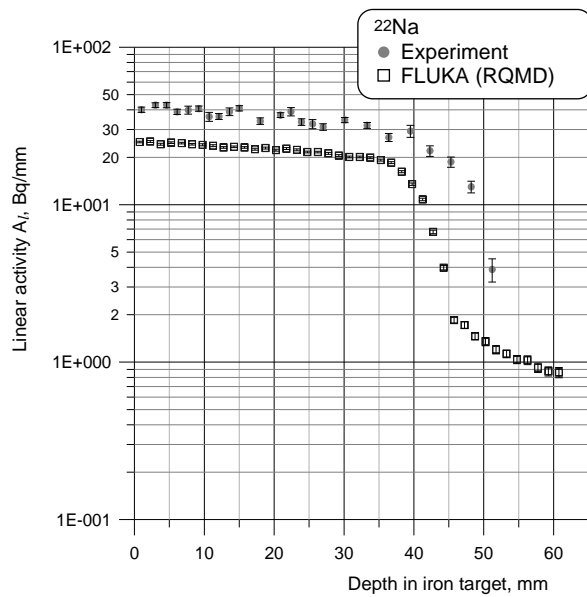
Figure 5: Experimental and simulated ^{24}Na activity distribution inside the target
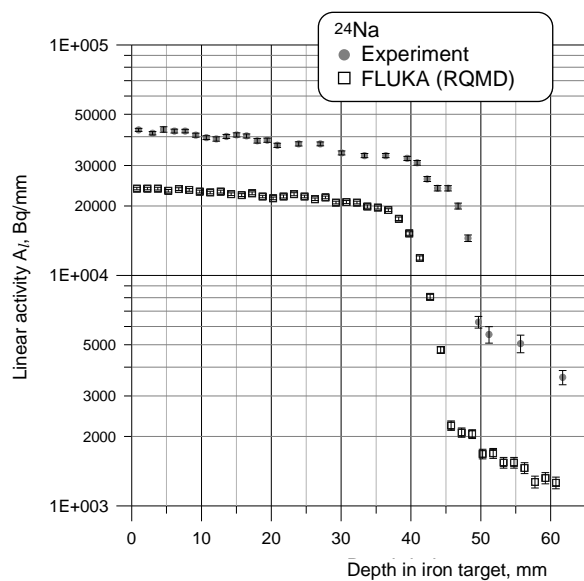
Despite the fact that a coarse assumption is adopted in FLUKA to determine the ratio of isomer to ground state nucleus for nuclides produced thorough evaporation, Figures 6 and 7 show that the current nuclear model and assumption give good agreement in isomer production between experiment and simulation. [44m]Sc is underestimated by a factor of two, which is reasonable in comparison with the results of other nuclides with close atomic numbers such as [43]K and [46]Sc. Experimental and calculated yields of [52]Mn also show good agreement as shown in Figure.7.

Figure 6: Experimental and simulated [44m]Sc activity distribution inside the target
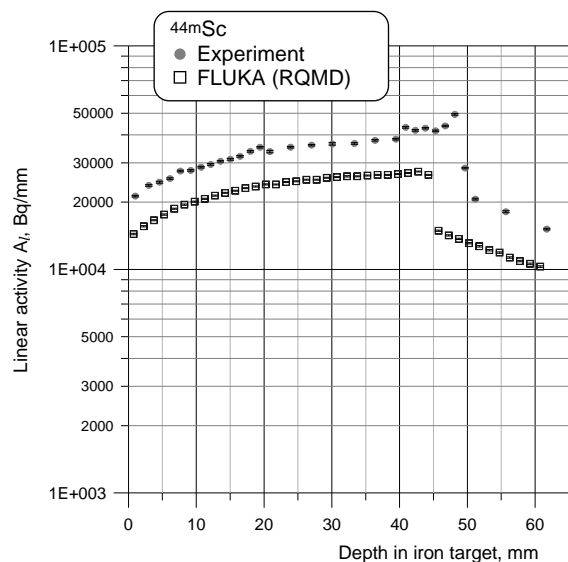
Figure 7: Experimental and simulated [52]Mn activity distribution inside the target
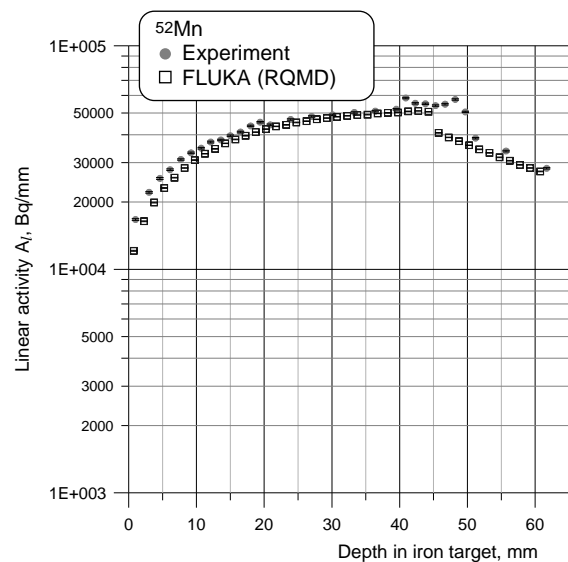
Figure 8 shows activity distribution of [58]Co, which is overestimated by at least a factor of 10. [58]Co is of particular interest in terms of the production process. Since [58]Co has higher atomic number than iron and higher mass number than most abundant isotopes in natural iron, the channels to produce [58]Co are limited, though the most effective channels are supposed to be $^{58}Fe(p,n)^{58}Co$ and $^{58-56}Fe(\alpha,X)^{58}Co$. The former reaction is simulated by PEANUT [19-22] in FLUKA, which is supposed to give good cross-section estimates. The latter reaction cannot be simulated below 100 MeV/u due to the limitation of the RQMD model in FLUKA. This underestimation can thus be attributed to the deficiency of the α particle-induced reaction model below 100 MeV/u.

Figure 8: Experimental and simulated ^{58}Co activity distribution inside the target
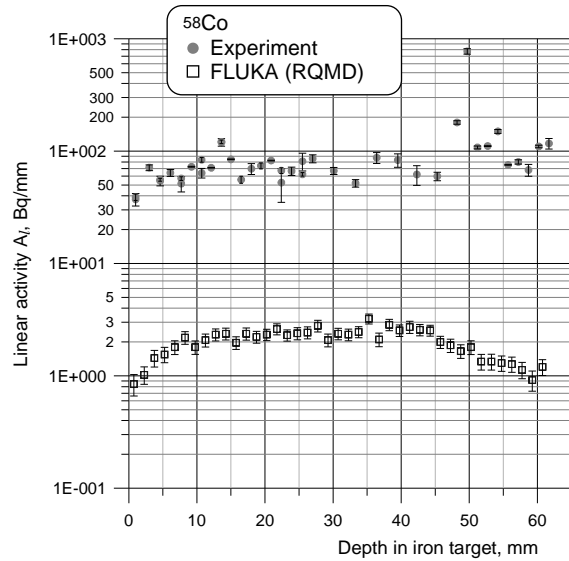
The productions of the other nuclides with rather high mass numbers are well reproduced by FLUKA. The agreement beyond the stopping range indicates good reproduction of the low-energy component (>10 MeV) of secondary particles, which are the major contributors as compared to the high-energy component (~500 MeV).

The comparison of the cross-section on the target surface in this study and that in a precedent study is shown in Table 2. The comparison between the experiment and calculation in this study shows the agreement is within a factor of two, and FLUKA underestimates cross-sections except for ^{48}Sc. The comparison of the experimental results also shows agreement within a factor of two. E/C ratio and E/E ratio seem to be little related to either gamma-ray energy, half-life, mass number, atomic number or cross-section.

Table 2: Comparison of 400 MeV/u C ion-induced reaction cross-sections (unit: mb).
Data are from the experiment in this study, calculation with FLUKA and the experiment in Ref. [8].

Nuclide	This work				Measured H. Yashima, *et al*.	
	Experiment		Calc., FLUKA		E/C	
^{7}Be	40.0	(23)	31.6	(2)	1.3	34.6	(12)
^{22}Na	9.23	(76)	5.58	(12)	1.7	4.26	(34)
^{24}Na	8.59	(24)	4.76	(9)	1.8	8.91	(52)
^{28}Mg	0.79	(8)	0.50	(3)	1.6	0.76	(4)
^{42}K	6.57	(57)	4.02	(8)	1.6	6.90	(45)
^{43}K	2.22	(14)	1.85	(6)	1.2	2.18	(7)
^{44m}Sc	12.9	(4)	8.74	(7)	1.5	13.3	(4)
^{46}Sc	15.6	(3)	10.18	(13)	1.5	11.3	(4)
^{47}Sc	5.13	(19)	4.81	(7)	1.1	5.38	(10)
^{48}Sc	0.97	(5)	1.31	(6)	0.7	1.02	(7)
^{48}V	29.3	(8)	25.72	(22)	1.1		
^{48}Cr	1.29	(5)	1.20	(4)	1.1	1.25	(3)
^{51}Cr	66.4	(53)	52.58	(35)	1.3	69.6	(21)
^{52}Mn	19.1	(60)	13.30	(14)	1.4		
^{54}Mn	88.7	(37)	72.27	(56)	1.2	94.4	(40)
^{55}Co	1.25	(29)	0.70	(6)	1.8	1.40	(5)
^{56}Co	4.69	(41)	4.18	(18)	1.2	3.38	(12)

Conclusions

An irradiation experiment with a 400 MeV/u carbon ion beam was performed and fragment distribution inside a target thicker than stopping range was obtained. It was found that FLUKA provides a reliable estimation of radionuclide production induced by heavy ions in iron for the purpose of radiation safety assessments. The comparison with data calculated using FLUKA tends to underestimate fragment yields by 50% within the range, especially in case of deep fragmentation product because of the underestimation of secondary particles' high-energy component or the underestimation of primary particle induced reaction cross-section. Discrepancy is particularly pronounced at the end of primary beam range because of the absence of nuclear reaction model applicable below 100 MeV/u. Production of nuclides with high mass number and atomic number higher than the target was remarkably underestimated. This is probably because of the underestimation of contribution from α particles. The assumption adopted in FLUKA to split produced nuclei to meta-stable state and ground state seems to be reasonable. For the other reactions, FLUKA gave reasonable estimates within ±30%.

Acknowledgements

References

[1] Kitagawa, A., *et al.*, "Review on Heavy Ion Radiotherapy Facilities and Related Ion Sources", *Rev. Sci. Instrum.*, 81, 02B909 (2010); doi:10.1063/1.3268510.

[2] Ferrari, A., *et al.*, *FLUKA: A Multi-particle Transport Code*, CERN 2005-10 (2005), INFN TC 05/11, SLAC-R-773.

[3] Battistoni, G., *et al.*, "The FLUKA Code: Description and Benchmarking", *Proceedings of the Hadronic Shower Simulation Workshop 2006*, Fermilab, 6-8 September 2006, M. Albrow, R. Raja (Eds.), AIP Conference Proceedings, 896, 31-49 (2007).

[4] Niita, K., *et al.*, *Radiation Measurements*, 41, 1080 (2006).

[5] Mokhov, N.V., *The Mars Code System User's Guide*, Fermilab-FN-628 (1995).

[6] Mokhov, N.V., K.K. Gudima, C.C. James, *et al.*, *Recent Enhancements to the MARS15 Code*, Fermilab-Conf-04/053 (2004), *www-ap.fnal.gov/MARS*.

[7] Nakamura, T., L. Heilbronn, *Handbook on Secondary Particle Production and Transport by High-energy Heavy Ions*, World Scientific Publishing Co. Pte. Ltd. (2006).

[8] Yashima, H., *et al.*, "Cross Sections for the Production of Residual Nuclides by High-energy Heavy Ions", *Nuclear Instruments and Methods in Physics Research*, B 226, 243-263 (2004).

[9] Ziegler, James F., "SRIM-2003", *Nuclear Instruments and Methods in Physics Research*, B 219-220, 1027-1036 (2004).

[10] International Commission on Radiation Units and Measurements (ICRU), "Stopping of Ions Heavier than Helium", *Journal of the ICRU, Report 73*, Vol. 5, No. 1 (2005).

[11] International Atomic Energy Agency (IAEA), *IAEA Technical Report Series*, 398, Table 43, p. 197 (2000), *www-pub.iaea.org/mtcd/publications/pdf/trs398_scr.pdf*.

[12]   Laboratory Equipment Corporation, *MCAWin2000 Manual, www.labo-eq.co.jp/support/supporte.html.*

[13]   Morev, M., T. Ogawa, T. Kosako, "An Implementation of Internal Efficiency Calibration Method For γ-ray Spectrometry Analysis of Activated Samples", *Proceedings of the 2nd Anniversary Symposium of GoNERI's Foundation* (Poster Session), pp. 157-162 (2009).

[14]   Molnar, G.L., Zs. Revay, T. Belgya, "Wide Energy Range Efficiency Calibration Method for Ge Detectors", *Nuclear Instruments and Methods in Physics Research*, A 489, 140-159 (2002).

[15]   Blaauw, Menno, "The Use of Sources Emitting Coincident γ-rays for Determination of Absolute Efficiency Curves of Highly Efficient Ge Detectors", *Nuclear Instruments and Methods in Physics Research*, A, 332 493-500 (1993).

[16]   Sorge, H., H. Stocker, W. Greiner, *Nuclear Physics*, A 498, 567c (1989).

[17]   Andersen, V., *et al.*, "The FLUKA Code for Space Applications: Recent Developments", *Advances in Space Research*, 34 1302 (2004).

[18]   Ferrari, A., *et al.*, *Nuclear Instruments and Methods in Physics Research*, B 71, 412 (1992).

[19]   Ferrari, A., P.R. Sala, *Proceedings of Workshop on Nuclear Reaction Data and Nuclear Reactors Physics, Design and Safety*, 2, 424 (1998).

[20]   Battistoni, G., F. Cerutti, A. Ferrari, *et al.*, "Recent Developments in the FLUKA Nuclear Reaction Models", *Proceedings of the 11th International Conference on Nuclear Reaction Mechanisms*, 126, Ric. Scient. Ed. Perm. Suppl. (2006), p. 483.

[21]   Fassò, A., *et al.*, "FLUKA Performances and Applications in the Intermediate Energy Range", *Proceedings of the Specialists Meeting on Shielding Aspects of Accelerators, Targets and Irradiation Facilities*, Arlington, Texas, USA, 28-29 April 1994, p. 287, OECD/NEA, Paris (1995).

[22]   Roesler, S., R. Engel, J. Ranft, *Proceedings of the Monte Carlo 2000 Conference*, Springer, Berlin, 1033 (2001).

Session IV

Dosimetry

Chair: Vladimir Mares

A review of recent studies on computational dosimetry: Calculation of dose conversion coefficients based on ICRP103

Tatsuhiko Sato, Akira Endo
Japan Atomic Energy Agency
Ibaraki, Japan

Abstract

Evaluation of the reference values of the fluence-to-effective dose conversion coefficients based on ICRP Publication 103 is urgently requested, since the calculation procedure of the effective dose was revised in the issue. Several research groups have been calculating the organ dose and effective dose conversion coefficients for various particles over wide energy ranges, following the instructions given in ICRP103 using different simulation codes. These data were compiled by the ICRP Committee 2 task groups for evaluating their reference values. This article reviews the current situation of the evaluation, together with the forthcoming impact of the introduction of ICRP103 on the radiological protection system in terms of neutron dosimetry in accelerator facilities.

Introduction

The International Commission on Radiological Protection (ICRP) recently released a new set of fundamental recommendations for a system of radiological protection in ICRP Publication 103 [1]. These recommendations replace the Commission's previous recommendations of 1990 (ICRP Publication 60 [2], and they are expected to be incorporated in radiation protection systems of many countries in the near future. In the new recommendations, the radiation and tissue weighting factors, referred to as w_R and w_T respectively, were updated based on the latest scientific information of the biology and physics of radiation exposure. The numerical values of w_R assigned to neutrons and protons were revised on the basis of the discussion given in ICRP Publication 92 [3]. In addition, the ICRP decided to introduce sex-specific voxel phantoms to represent the Reference Male and Reference Female [4] (hereafter referred to as ICRP/ICRU reference phantoms) for the forthcoming update of the organ dose coefficients for both internal and external radiation sources. Such phantoms are the result of recent efforts by the radiation protection community to adopt anatomically realistic medical images and powerful computer technologies [5].

Under these circumstances, two ICRP Committee 2 task groups, the Task Group on Dose Calculations (DOCAL) and the Task Group on Radiation Exposures of Astronauts in Space, are currently tackling the evaluation of the reference values of the fluence-to-organ dose and effective dose conversion coefficients based on ICRP103 for external exposure. The final goal of DOCAL on this task is to publish a new ICRP publication as the revision of ICRP Publication 74 [6], which includes the reference values of the dose conversion coefficients based on ICRP60. The new dataset will contain the conversion coefficients for almost all radiations that should be practically considered in radiation protection in high-energy accelerator facilities as well as conventional nuclear facilities, whereas only the data for photons, neutrons and electrons with limited energies were given in ICRP74. The reference values of the dose conversion coefficients for operational quantities such as $H^*(10)$ will also be presented in the new publication. However, the conversion coefficients for heavy ions except for He ions will not be included in the dataset prepared by DOCAL, since those data are important only for space dosimetry. Thus, the Task Group on Radiation Exposures of Astronauts in Space has the responsibility for evaluating the dose conversion coefficients for heavy ions.

Several research groups have been calculating the organ dose and effective dose conversion coefficients based on ICRP103 employing different simulation codes. Some examples of the calculated results will be presented in this paper, together with a brief explanation of its calculation procedure. The impact of the introduction of ICRP103 on the practical dose estimation will be discussed by comparing the effective doses based on ICRP60 and ICRP103 as well as $H^*(10)$ for various neutron operational fields in accelerator facilities.

Calculation of dose conversion coefficients

Calculation procedure

The fluence-to-effective dose conversion coefficients based on ICRP103 must be calculated using the ICRP/ICRU reference phantoms. The phantoms were constructed by modifying the voxel models of two individuals whose body height and weight resembled the data for the ICRP Reference Man: approximately 176 (176) and 167 (163) cm in height and 70 (73) and 59 (60) kg in weight, for the male and the female, respectively, where the values in the parentheses are the corresponding reference data. The heights and weights as well as the masses of each organ of those voxel phantoms were adjusted to the reference data without spoiling their realistic anatomy. The voxel sizes are 8 and 4.84 mm in height with in-plane resolutions of 2.137 and 1.775 mm for the male and female, respectively. One hundred forty-one (141) anatomical regions specifying organs and organ contents were segmented in the phantoms, and 52 different compositions were assigned to the segmented organs and organ contents. More detailed descriptions of the phantoms are given in ICRP110.

For calculating the organ dose conversion coefficients, simulations were performed to estimate the deposition energy in each organ of the reference phantoms using various Monte Carlo simulation codes. Table 1 summarises the irradiation conditions and simulation codes used for the calculation under the framework of the DOCAL activity. In addition, the conversion coefficients for heavy ions with atomic numbers up to 28 (Ni) and energies from 1 MeV/nucleon to 100 GeV/nucleon for the

Table 1: Irradiation conditions and simulation codes used for the calculation of the dose conversion coefficients under the framework of the DOCAL activity. Note that this information is supposed to be changed.

Particle	Energy	Irradiation geometry	Simulation code
Photons	10 keV~10 GeV	AP, PA, LLAT, RLAT, ISO, ROT	EGS, GEANT, MCNPX
Neutrons	1 meV~10 GeV	AP, PA, LLAT, RLAT, ISO, ROT	FLUKA, GEANT, MCNPX, PHITS
Electrons/ positrons	50 keV~10 GeV	AP, PA, ISO	EGS, GEANT, MCNPX
Protons	1 MeV~10 GeV	AP, PA, LLAT, RLAT, ISO, ROT	FLUKA, GEANT, MCNPX, PHITS
Charged pions	1 MeV~10 GeV	AP, PA, ISO	FLUKA, MCNPX, PHITS
Muons	1 MeV~10 GeV	AP, PA, ISO	FLUKA, GEANT, MCNPX
He ions	1 MeV/n~100 GeV/n	AP, PA, ISO	FLUKA, PHITS

isotropic (ISO) irradiation geometry have been calculated to be utilised in space dosimetry. Note that the ISO geometry is the most realistic geometry for reproducing the radiological situations in space. The organ dose conversion coefficients in most organs were simply estimated from the energies deposited in voxels assigned to each organ, divided by their masses.

The fluence-to-effective dose, E, conversion coefficients can be calculated from the organ dose conversion coefficients in each organ or tissue, D_T, with w_R and w_T updated in ICRP103, using Eq. (1):

$$E = \sum_T w_T H_T = w_R \sum_T w_T D_T \qquad (1)$$

where H_T denotes the equivalent dose in organ or tissue, T, per unit fluence, which can be simply determined from D_T multiplied with w_R for a certain monoenergetic particle irradiation.

Results of the calculation

As examples of the calculated results, Figures 1 and 2 show the conversion coefficients for the effective dose based on ICRP103 for neutrons and protons, respectively, for the anterior-to-posterior (AP) irradiation geometry calculated by PHITS [7], FLUKA [8] and MCNPX [9,10]. It is found from these graphs that the dose conversion coefficients calculated by each code agree with one another for lower energies, below 20 MeV and 1 GeV for neutrons and protons respectively, while the data above the energies vary with the codes by 50% at the maximum. The disagreements at the high-energy regimes are predominantly owing to the difference of the nuclear reaction models implemented in each code. These tendencies indicate the importance of the improvement of the nuclear reaction models not only for the shielding calculation but also for the calculation of the dose conversion coefficients, in order to improve the reliability of the shielding design of high-energy accelerators.

Figure 3 depicts the irradiation geometry dependence of the effective dose conversion coefficients for neutrons calculated by PHITS. It is evident from this graph that the values of effective dose conversion coefficients for the AP, PA and ISO irradiations are highest among all irradiation geometries for incident energies below 50 MeV, from 50 MeV to 2 GeV and above 2 GeV, respectively. This tendency is attributed to the facts that the most of the radiologically sensitive organs are located close to the front surface of human body, and their dose conversion coefficients become higher than those for other organs for such irradiation conditions, since lower and higher-energy neutrons deposit more energy close to and far from the irradiation surface, respectively, due to the attenuation and build-up effects.

Calculation of neutron doses for workers in accelerator facilities

Calculation procedure

The impact of the introduction of ICRP103 on the practical dose estimation was analysed by calculating the effective doses based on ICRP60 and ICRP103 for workers at various neutron operational fields in accelerator facilities. The neutron spectra given in the IAEA technical report 403 [11] were adopted in the calculation. Examples of the neutron spectra used in this analysis are depicted in Figure 4. In general, the neutron spectra are harder and softer at the operational fields in high- and low-energy accelerators, respectively.

Figure 1: Conversion coefficients for the effective dose based on ICRP103 for neutron AP irradiation geometry calculated by PHITS [7], FLUKA [8] and MCNPX [9]
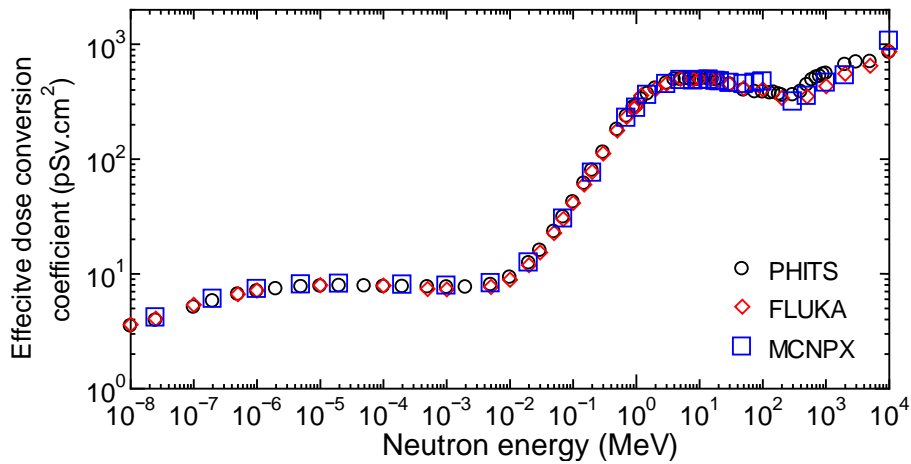
Figure 2: Conversion coefficients for the effective dose based on ICRP103 for proton AP irradiation geometry calculated by PHITS [7], FLUKA [8] and MCNPX [10]
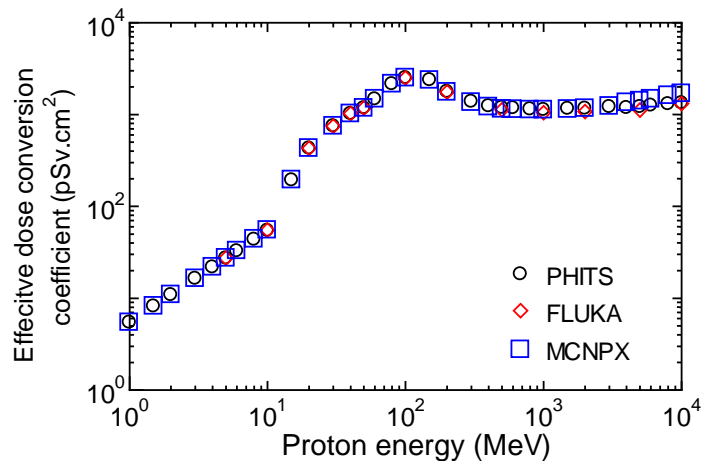
Figure 3: Irradiation-geometry dependence of the effective dose conversion coefficients for neutrons calculated by PHITS [7]
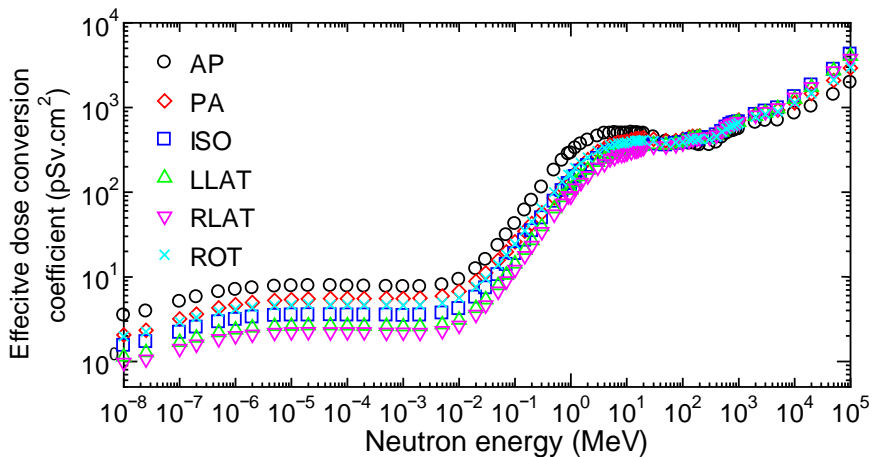
**Figure 4: Examples of the neutron spectra used in the calculation of the
effective doses and $H^*(10)$ for various operational fields. The absolute values
are arbitrarily adjusted for each spectrum in order to make each line distinctive.**
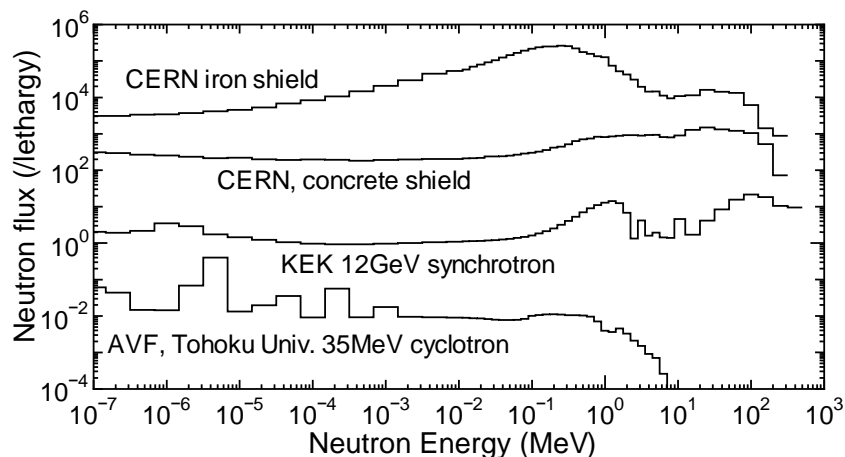
The ambient dose equivalent at 10 mm, $H^*(10)$, was also calculated for the same conditions. The adequacy of the use of $H^*(10)$ as an operational quantity in high-energy neutron fields has been under discussion for quite some time, since the ICRP60-based effective dose conversion coefficients for high-energy neutrons are larger than the corresponding values of $H^*(10)$ [12,13]. Hence, it is worthwhile to compare $H^*(10)$ in various operational fields with the respective data of the effective doses based on ICRP103 as well as ICRP60.

The conversion coefficients used in these calculations are plotted in Figure 5. The values for the AP irradiation geometry calculated by PHITS coupled to the ICRP/ICRU reference phantoms were employed in the calculation of the ICRP103-based effective doses. Note that this dataset is supposed to be different from those compiled in the forthcoming ICRP publication to be released as the revision of ICRP74, since the dose conversion coefficients calculated employing not only PHITS but also other simulation codes will be used in the evaluation of their reference values. The data given in ICRP74 were adopted as the ICRP60-based effective dose conversion coefficients for neutrons below 180 MeV, while those calculated by the PHITS code coupled to the MIRD phantom [14] were adopted above the energy [15]. For the $H^*(10)$ conversion coefficients, the data used in the cosmic-ray dose calculation program EXPACS [16] were employed.

**Figure 5: Conversion coefficients from fluence to the effective doses for
the AP irradiation geometry, E_{AP}, and the ambient dose equivalent at 10 mm,
$H^*(10)$, used in the calculation of neutron doses for various operational fields**
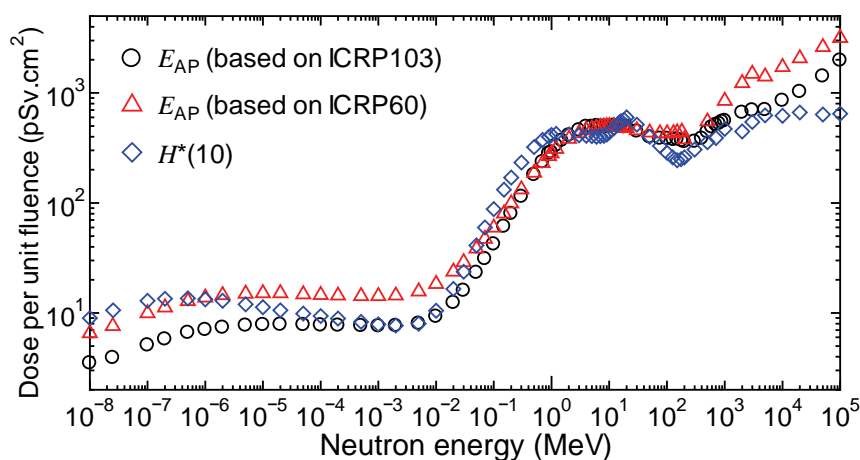
Results of the calculation

Figure 6 shows the ratios of the calculated effective doses based on ICRP103 and ICRP60 to the corresponding *(10) for various operational neutron fields. It is evident from the figure that the ICRP103-based effective doses are smaller than the respective ICRP60-based data. This tendency is attributed to the difference between the two sets of the effective-dose conversion coefficients shown in Figure 5, where the ICRP103-based values are smaller than the corresponding ICRP60-based data for neutron energies under 0.2 MeV and over 50 MeV. This difference is predominantly owing to the revision of $_R$ assigned to neutrons with those energies.

Figure 6: Ratios of the calculated effective doses based on ICRP103 and ICRP60 to the corresponding $H^*(10)$ for various operational neutron fields
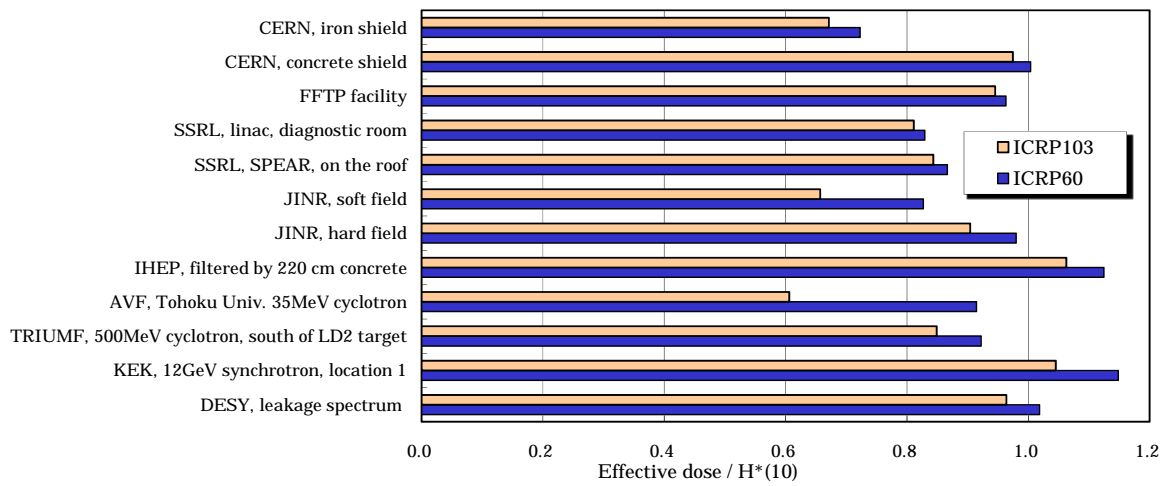
It is also found from Figure 6 that $H^*(10)$ cannot give a conservative estimation of the corresponding effective doses for some high-energy neutron fields such as "KEK, 12GeV synchrotron, location 1". This tendency is triggered by the inconsistency of the dose conversion coefficients between the operational and protection quantities at higher energies, where the values for $H^*(10)$ are smaller than those for the effective dose, as shown in Figure 5. There are two reasons considered to cause this inconsistency; one is the numerical incompatibility between the $Q(L)$ relationship and w_R defined in ICRP60, and the other is the inadequacy of the adoption of 10 mm depth for the conservative estimation of the ambient dose equivalent for high-energy neutrons, as discussed in Ref. [17]. The former reason is relevant only to the ICRP60-based data, since the numerical compatibility between $Q(L)$ and w_R is established in ICRP103 even at the high energies [7]. Thus, the magnitudes of the underestimation of the effective dose by $H^*(10)$ are reduced by the introduction of ICRP103, and approximately 6% at the maximum within the selected neutron fields. Considering the uncertainty of the dose measurement in high-energy neutron fields, this slight underestimation can be regarded as tolerable. Therefore, it can be concluded that $H^*(10)$ is able to be used as an operational quantity for the assessment of the ICRP103-based effective dose in most operational neutron fields in accelerator facilities.

Conclusions

The fluence-to-dose conversion coefficients for external exposure of various particles over wide energy ranges have been calculated using several simulation codes coupled to the ICRP/ICRU reference phantoms, following the instruction given in ICRP103. The results obtained from each code agree with one another fairly well except for higher-energy regions, where the difference of the nuclear reaction models becomes important in the calculation. The evaluation of the reference values of the dose conversion coefficients is ongoing under the supervision of the ICRP Committee 2 task groups. A new ICRP publication that contains the dataset of the reference values except for heavy ions is planned to be released in the near future, as the revision of ICRP74.

The impact of the introduction of ICRP103 on the practical dose estimation was analysed by comparing between the effective doses based on ICRP60 and ICRP103 as well as $H*(10)$ for various neutron operational fields in accelerator facilities. It is found from the comparison that the introduction of ICRP103 results in the reduction of the effective doses, and consequently, the magnitude of the underestimation of the effective dose by $H*(10)$ observed at high-energy neutron fields becomes smaller. These results suggest that the current radiological protection system can be maintained after the introduction of ICRP103, with respect to neutron dosimetry. It should be mentioned that this conclusion was derived from the analysis based on not the reference values of the dose conversion coefficients but those calculated using only the PHITS code.

Acknowledgements

References

[1] International Commission on Radiological Protection (ICRP), "The 2007 Recommendations of the International Commission on Radiological Protection", ICRP Publication 103, *Ann. ICRP*, 37 (2-4) (2007).

[2] ICRP, "1990 Recommendations of the International Commission on Radiological Protection" ICRP Publication 60, *Ann. ICRP*, 21 (1-3) (1991).

[3] ICRP, "Relative Biological Effectiveness (RBE), Quality Factor (*Q*), and Radiation Weighting Factor (w_R)", *Ann. ICRP*, 33 (4) (2003).

[4] ICRP, "Adult Reference Computational Phantoms", ICRP Publication 110, *Ann. ICRP*, 39 (2) (2007).

[5] Xu, X-G., K.F. Eckerman (Eds.), *Handbook of Anatomical Models for Radiation Dosimetry*, Boca Raton, Taylor & Francis (2009).

[6] ICRP, "Conversion Coefficients for Use in Radiological Protection", ICRP Publication 74, *Ann. ICRP*, 26 (3-4) (1996).

[7] Sato, T., *et al.*, "Fluence-to-dose Conversion Coefficients for Neutrons and Protons Calculated Using the PHITS Code and ICRP/ICRU Adult Reference Computational Phantoms", *Phys. Med. Biol.*, 54, 1997-2014 (2009).

[8] Pelliccioni, M., private communication.

[9] Xu, X-G., private communication.

[10] Endo, A., calculated for DOCAL.

[11] International Atomic Energy Agency, *Compendium of Neutron Spectra and Detector Responses for Radiation Protection Purposes*, Technical Reports Series 403, IAEA, Vienna (2001).

[12] Ferrari, A., M. Pelliccioni, M. Pillon, "Fluence to Effective Dose Conversion Coefficients for Neutrons Up to 10 TeV", *Radiat. Prot. Dosim.*, 71, 165-173 (1997).

[13] Pelliccioni, M., "Protection Quantities and Conversion Coefficients for Use in Radiation Shielding", *J. Nucl. Sci. Technol.*, Suppl. 1, 850-854 (2000).

[14] Cristy, M., K.F. Eckerman, *Specific Absorbed Fractions of Energy at Various Ages from Internal Photon Sources*, Report No. ORNL/TM-8381, Vol. 1-7, Oak Ridge National Laboratory (1987).

[15] Sato, T., *et al.*, "Analysis of Dose-LET Distribution in the Human Body Irradiated by High Energy Hadrons", *Radiat. Prot. Dosim.*, 106, 145-153 (2003).

[16] Sato, T., *et al.*, "Development of PARMA: PHITS-based Analytical Radiation Model in the Atmosphere", *Radiat. Res.*, 170, 244-259 (2008), *http://phits.jaea.go.jp/expacs*.

[17] Nabelssi, B.K., N.E. Hertel, "Ambient Dose Equivalent, Deep Dose Equivalent Index, and ICRU Sphere Depth-dose Calculations for Neutrons from 30 to 180 MeV", *Radiat. Prot. Dosim.*, 51, 169-182 (1994).

Calculations of radiation levels in the service caverns and on the surface at Point 1 of the LHC

Tatsuhiko Ogawa[1], Zuzana Zajacová[2]
[1]University of Tokyo, Tokyo, Japan
[2]European Organization for Nuclear Research (CERN), Geneva, Switzerland

Abstract

The ATLAS detector is installed at Point 1 of the Large Hadron Collider (LHC). The underground infrastructure consists of the experimental cavern UX15, which houses the detector, and two lateral service caverns, USA15 and US15. The experimental cavern is connected with the surface by two large vertical shafts, PX14 and PX16. Calculations were performed with the FLUKA code to assess the prompt radiation levels in the underground service caverns and on the surface at Point 1. The FLUKA geometry reflected the actual design of the ATLAS detector and the civil engineering infrastructure. The estimated radiation levels are given and results and methods are compared with the initial shielding design studies for Point 1.

Introduction

Several studies were carried out in the mid to late 90s addressing the radiological aspects of civil engineering infrastructure at Point 1 [1-3]. The aim of these calculations was to provide recommendations on the thickness of the wall separating the experimental cavern from the service cavern, the thickness of the plugs on the access shafts connecting the experimental cavern to the ground surface, the layout of passageways and galleries exiting from the experimental cavern, etc. The actual civil engineering works at Point 1 started in 1998 and the underground areas were completed in 2003. Afterwards began the installation of the detector in the experimental cavern. The detector was completed to its current form in 2008. The aim of the present calculations was to reassess the expected radiation levels in the areas of interest based on the as-built design.

A schematic layout of the underground areas and the surface buildings at Point 1 is shown in Figure 1. Radiation can reach the surface primarily by streaming through the two large vertical shafts, PX14 and PX16. The shafts are about 50 meters long with diameters of 18 and 12.6 meters. During LHC operation they are covered on the surface with 97 cm thick concrete beams.

Figure 1: Point 1 infrastructure: Surface and underground areas.
The lower left corner shows the position of Point 1 on the LHC ring.

The main service cavern, USA15, is separated from the experimental cavern by a 2 m thick concrete wall. Radiation can penetrate through the wall or stream through the galleries and passageways that connect the two caverns. On the opposite side, there are no such passageways leading to the US15 service cavern. However the shielding wall there is only 1.7 m thick. The position of the ATLAS detector in the experimental cavern is asymmetric. It is closer to the US15 side by 3.4 meters.

Figure 2 shows the FLUKA implementation of Point 1 infrastructure. The cavern houses a detailed model of the ATLAS detector. To simulate streaming of radiation through the galleries and passageways between the experimental cavern and the USA15 service caverns this baseline geometry was augmented to include the particular passageway under investigation.

Figure 2: The ATLAS detector inside the experimental cavern as implemented in FLUKA

Two views are given: 1) a vertical cut through the centre of the detector parallel with the
beam line; 2) a vertical cut through the centre of the PX14 shaft perpendicular to the beam line.

Calculation method

The calculations were performed with the FLUKA Monte Carlo radiation transport code [4,5] in two
steps. In the first step generation and transport of radiation inside the ATLAS detector and the
experimental cavern were simulated. Proton-proton collisions of 14 TeV were simulated with the
DPMJET-III event generator and used as the primary radiation source. Particles arriving to a selected
boundary, such as those entering the lateral cavern walls were written onto files via the FLUKA user
routine mgdraw.f. These files were then used as the particle source for the second step of the calculations
to assess radiation penetration and streaming to the location of interest. The main advantage of the
separation of the simulations into two steps was that it allowed for different transport thresholds and
settings in the two steps. The results were obtained in terms of the ambient dose equivalent.

Penetration of radiation across the lateral walls into the service caverns

The service caverns house essential electronics for the operation of the detector. Furthermore, the
USA15 service cavern is accessible to personnel while the LHC is running. It is classified as a
supervised radiation area of low occupancy for which the limit in terms of ambient dose equivalent
rate is 15 μSv/h [6]. Our initial simulations showed that radiation levels on the experimental side of the
wall reach up to about 1 mSv/h assuming design LHC luminosity (10^9 pp collisions per second). The
shielding aspects of the lateral cavern walls are therefore an essential factor of Point 1 infrastructure.

Several specific questions were addressed. The asymmetrical position of the beam line inside the
experimental cavern could result in a slightly lower radiation level on the USA15 side than on the
US15 side. Both walls contain ducts for extracting trigger cables via the shortest possible routes into

303

the service caverns. The wall on the USA15 side contains 8 such ducts, while the US15 wall contains nearly 30 of them. The effect of these holes was investigated. Finally, the horizontal and vertical dose rate distribution along the wall was studied.

Most first-step simulations, over 140 000 primaries, were performed with a 10 MeV cut-off for neutrons, photons and electrons. These were complemented with simulations transporting low-energy neutrons down to thermal energies and by simulations with lifetime biasing of charged pions and kaons in order to improve muon statistics.

In the second-step simulations neutrons were transported down to thermal energies and the cut-off for electrons and photons was set to 50 keV. The walls were split into 20 cm thick layers and region importance biasing was applied to compensate for the attenuation in the concrete. The importance of the nth layer was set to 1.3^{n-1}. The scoring of the ambient dose equivalent was performed using a Cartesian mesh.

To check the effect of the trigger cable ducts, these were implemented into the baseline geometry. The second-step calculations were repeated with the modified geometries of the walls.

Streaming of radiation into the USA15 through galleries and passageways

There are three pairs of passageways between the experimental cavern and the USA15: TE14 and TE16, UPX14 and UPX16, and ULX14 and ULX16. Each pair is symmetric with respect to the plane perpendicular to the beam line and crossing the interaction point. The TE are the main cable galleries. The UPX16 is a passageway for personnel, while UPX14 serves as the emergency exit. The ULX14 and ULX16 are technical galleries for cooling services, etc. The main passageway for personnel is ULX15. ULX15 leads to an area below the USA15 cavern. However, this area is also accessible during the accelerator operation.

In the first step of the calculations, particles arriving to a cylindrical envelope around the detector were recorded. To improve the statistics by a factor of 2, particles arriving to the half of the envelope, which faces the US15 side were translated onto the USA15 side. To gain another two-fold improvement, both galleries of the symmetric pair were implemented into the geometry but the scoring was performed in one of the galleries, using a Cartesian mesh with symmetry.

Streaming and penetration to the surface through PX14 and PX16 shafts

The surface building SX1 houses the openings of the PX14 and PX16 shafts. The openings are covered with 97 cm of concrete. The building is a non-designated area of low occupancy for which the limit in terms of dose-rate is 2.5 µSv/h*. Calculations were performed to check whether the shaft and the concrete provide sufficient attenuation to meet the limit. Possible additional shielding designs were also studied. It is worth noting that the previous design calculations led to a recommendation of 120 cm thick concrete on top of the larger shaft [2].

Results

Penetration of radiation across the lateral walls into the service caverns

Figure 3 shows the dose-depth profile, averaged over the length of the cavern, inside the wall between the UX15 and the USA15. The dose rate gets attenuated to some 2-5 µSv/h. The profile shows two peaks, one below and one above the beam height. The two peaks arise due to the modelling of the end-cap toroid in the geometry. Each individual coil of the toroid is represented as a solid rectangular block of aluminium. The space between the coils has a low average density. It consists of the end-cap toroid cryostat, which contains mainly vacuum. The local minimum at beam-height between the two peaks, which is visible across the full depth of the wall, corresponds to one of the toroid coils. This shows the strong influence of the detector geometry even on radiation levels behind the shielding.

---

* At the time of this writing, procedures are in progress to change the classification of the SX1 building for supervised radiation area.

**Figure 3: Dose-depth profile inside the wall between the experimental
cavern and the USA15 service cavern, averaged over the length of the wall**
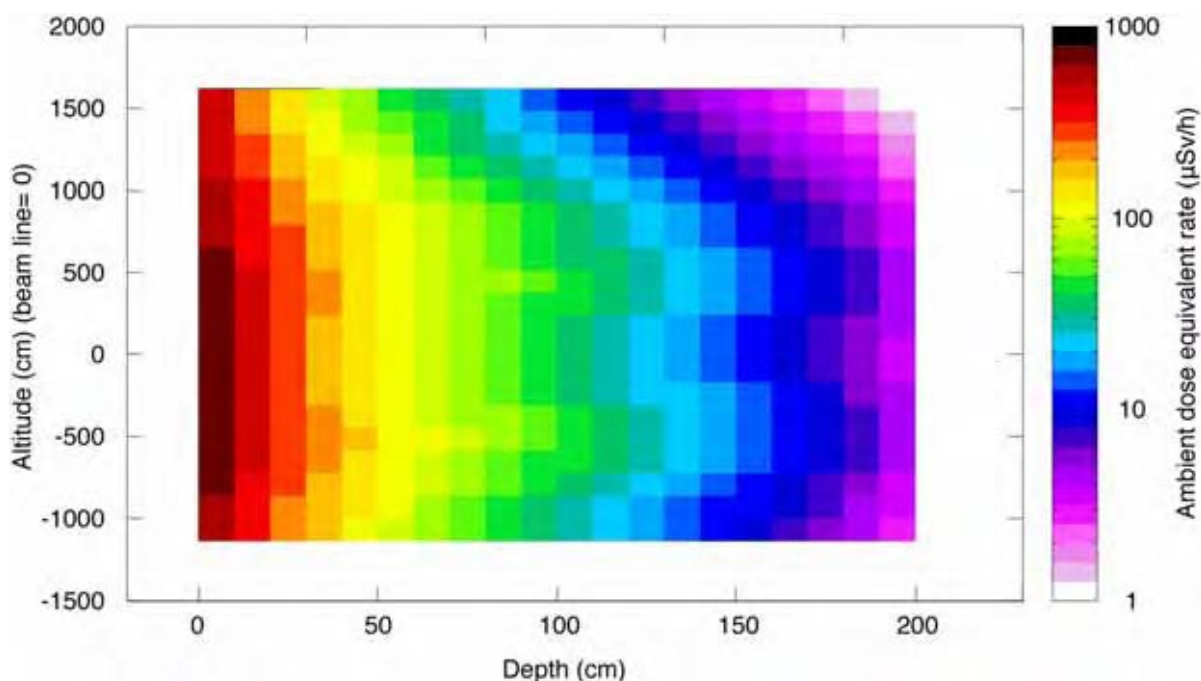
The asymmetrical position of the detector with respect to the two service caverns results in slightly higher dose rates on the US15 side. The increase is about 20%. However, because the wall between the experimental cavern and the US15 cavern is only 1.7 meters thick, the dose rate reaching the US15 is on average 10 µSv/h – about three times higher than in the USA15.

The presence of the trigger cable ducts in the shielding walls did not lead to an observable increase of average dose rate in the service caverns. However, a point-wise effect cannot be excluded by this calculation method. To monitor the dose rate directly, passive dosimeters were installed at the exits of the ducts. The average dose rate was calculated over the whole wall but also over smaller areas containing the ducts, such as the central vertical stripe of the USA15 wall.

The dose rate distribution is not homogeneous along the wall. It is interesting to relate the distribution with specific locations in the service caverns and with the positions of the galleries. Figure 4 shows the dose rate map in the last layer of the wall together with a schematic drawing of the structures of interest. The bins of the scoring mesh are 125 cm long and 137 cm high. The dose rate maximum is the result of the low self-shielding of the end-cap toroid. In the USA15 cavern, the highest dose rates are expected at its lateral edge.

Streaming of radiation into the USA15 through galleries and passageways

Figure 5 shows, as an example, the attenuation in the ULX15 passageway for personnel. The attenuation factor provided by the passageway is between 3 to 4 orders of magnitude. Assuming the design LHC luminosity, the dose rate is attenuated by the passageway to about 1 µSv/h.

The ULX15 passageway is shorter and has a larger cross-section than the UPX14 (UPX16) and the ULX14 (ULX16). Therefore, as expected, higher attenuation was seen in these galleries: a factor of 10^5 in the ULX14, and almost 10^6 in the UPX14.

The length and the cross-section of the TE14 (TE16) cable gallery are comparable to that of ULX15. However, unlike the other galleries, the TE14 is a three-legged structure. The angle between the first and the second leg is 135°, the third leg makes a 90° vertical bend. Therefore, the obtained attenuation factor was slightly higher than in ULX15.

**Figure 4: The dose rate distribution in the last 10 cm of the wall
between the experimental cavern and the USA15 service cavern**

A schematic drawing of the boundary of the USA15 cavern and of the galleries and cable ducts is given
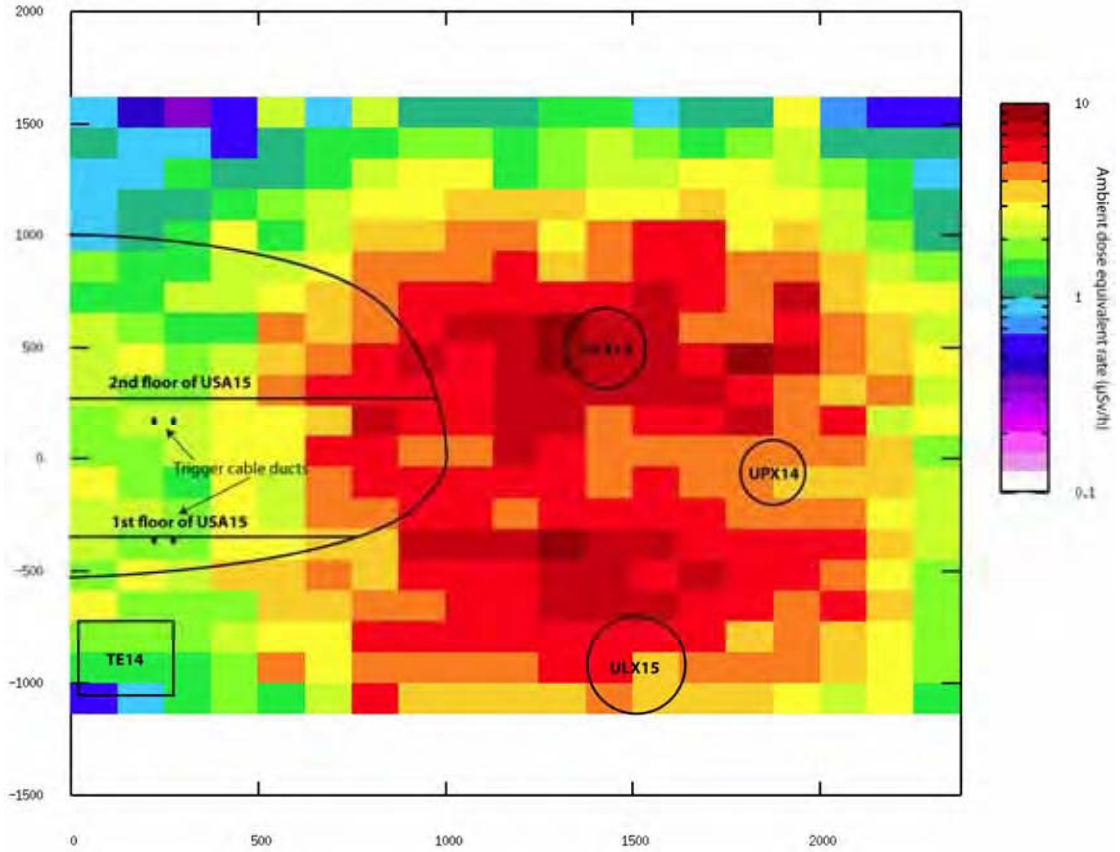
Figure 5: The dose rate distribution in the ULX15 passageway

SHIELDING ASPECTS OF ACCELERATORS, TARGETS AND IRRADIATION FACILITIES – © OECD/NEA 2010
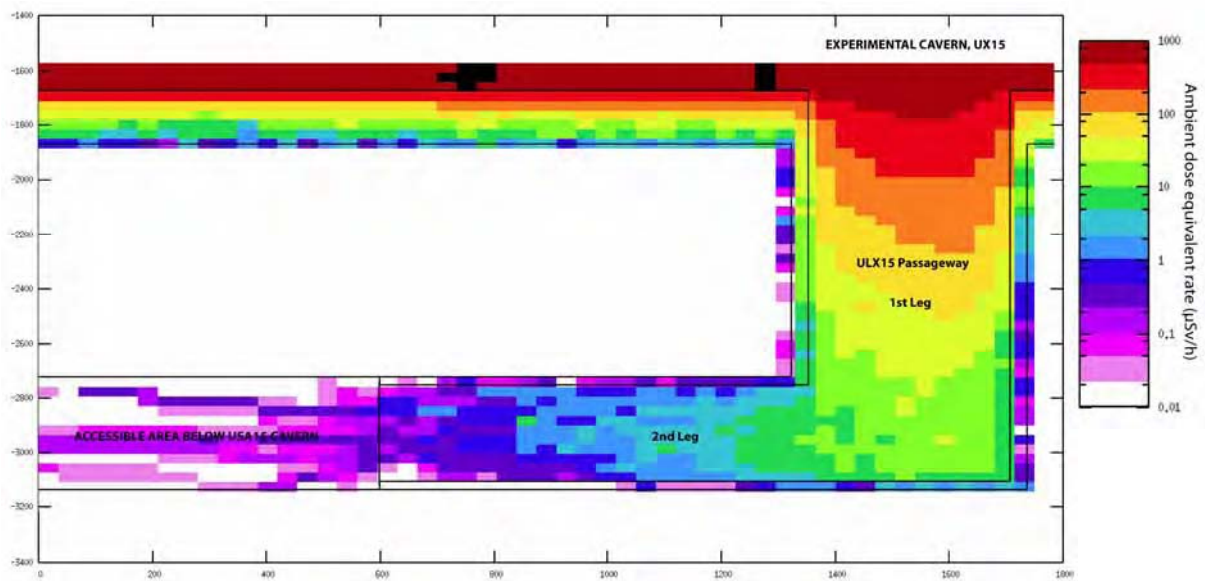
An attenuation factor and a source term define the dose rate at the end of a gallery. However, the variation between the source terms of the different galleries is comparatively smaller than the variation between the attenuation characteristics of the galleries. The dose rates at the entrances to the galleries differ within a factor of 2.

Streaming and penetration to the surface through PX14 and PX16 shafts

For the design luminosity, the predicted dose rate at the entrance to the shafts is about 500 µSv/h. It is attenuated by a factor of 10 in the larger shaft, PX14, and by a factor of 50 in the smaller shaft, PX16. It is then attenuated further in the 97 cm of concrete on top of the shafts. Finally, the dose rate reaching the SX1 building is less than 1 µSv/hour through PX16 but nearly 3 µSv/h through PX14. Additional protection measures would be necessary to ensure that the SX1 building fulfils the limits of a non-designated area. An additional 25 cm of concrete or polyethylene would be enough to reduce the dose rate below 1 µSv/h.

Conclusions

Compared to the previous design studies, the present calculations were performed with a much more accurate model of the civil engineering infrastructure at Point 1. In the past, the experimental cavern was most often represented by a coaxial cylindrical envelope around the detector. Although the results of the present calculations are slightly higher than previous estimates, generally, the agreement is very good, confirming the validity of a simplified geometrical model. In all cases, fulfilling the design recommendations on the shielding thickness would have been sufficient to fulfil the radiological requirements. However, the plug on top of the PX14 shaft is thinner than originally recommended and the dose rate on top of the plug could exceed the limit for a non-designated area. The plume of radiation from the shaft is strongly vertically collimated. To mitigate the potential radiological issue, it may be sufficient to prevent access on top of the shaft or to implement a false raised floor above the shaft. Alternatively, an additional shielding, *e.g.* 25 cm of polyethylene, could be added on top of the plug.

The main challenge in estimating attenuation through the galleries with Monte Carlo techniques is to obtain sufficient statistics. The 1999 study [3] employed a simplified set-up for the first step of the calculations. A 100 GeV proton beam hitting a copper target was used as the radiation source. The copper target was enclosed in a concrete cylindrical envelope. In this way it was possible to obtain a relative attenuation factor of a gallery but not the absolute dose rates at the entrance to the USA15. Although the present calculations give such an absolute estimate, it is clear that the dose rate at the end of the gallery is mostly dependent on the gallery's attenuation factor.

It is interesting to note that the design calculations were based on only 1 300 primary proton-proton events. An elaborate biasing scheme was implemented throughout the detector geometry to counteract strong shower attenuation inside the calorimeters and to allow enough particles to reach the shielding walls. On the contrary, very little biasing was used in the present calculations but the total amount of simulated primary p-p events was two orders of magnitude higher.

References

[1]   Ferrari, A., K. Potter, S. Rollet, *Lateral Shielding Requirements for the ATLAS Experimental Region*, CERN/AT-XA/02N/95, 8 March 1995.

[2]   Ferrari, A., K. Potter, S. Rollet, *Shielding for the ATLAS Experimental Region*, LHC Project Note 6, 11 September 1995.

[3]   Rollet, S., K.M. Potter, G.R. Stevenson, *Attenuation of Radiation in the Access Labyrinths and Service Ducts Between the ATLAS Experimental and Service Caverns*, EST-LEA/99-02, 3 November 1999.

[4]   Fassò, A., *et al.*, *FLUKA: A Multi-particle Transport Code*, CERN-2005-10 (2005).

[5]   Battistoni, G., *et al.*, "The FLUKA Code: Description and Benchmarking", *Proceedings of the Hadronic Shower Simulation Workshop 2006*, Fermilab, 6-8 September 2006, M. Albrow, R. Raja (Eds.), AIP Conference Proceedings, 896, 31-49 (2007).

[6]   Forkel-Wirth, D., T. Otto, *General Safety Instruction*, Area Classification, RGE Section 9/S3-GSI1, CERN (2006).

Estimation of entrance surface doses (ESD) for common medical X-ray diagnostic examinations in radiological departments in Mashhad-Iran

M.T. Bahreyni Toossi[1], S. Esmaili[2]
[1]Professor of Medical Physics, Mashhad University of Medical Sciences (MUMS)
[2]Academic Member in Islamic Azad University of SANANDAJ – Branch Iran

Abstract

The British National Radiological Protection Board (NRPB) introduced the use of diagnostic reference levels (DRL) as an efficient standard for optimising the radiation protection of patients. The physical parameter recommended for monitoring the DRL in conventional radiography is the entrance skin dose (ESD) and methods for measuring it are clearly described in NRPB standard protocol. The data were collected for 1 183 radiographs of adult patients. The sample of patients was chosen such that the weight of patients was between 50-80 kg. Eight conventional X-ray examinations were chosen for this study. The ESD of individual patients was directly measured by thermoluminescence dosimeter. TLD chips sealed in a plastic sachet were stuck on the skin of patient at the centre of the X-ray beam axis. In this study, third quartiles of measured ESD for patients undertaking a particular examination were selected as ESD for study sample; based on this assumption ESD for X-ray examination included in this study are as follows: chest PA – 0.37 mGy, chest LAT – 1.8 mGy, lumbar spine AP – 3.6 mGy, lumbar spine LAT – 5.6 mGy, pelvis AP – 3.5 mGy, abdomen AP – 3.7 mGy, skull PA – 2.96 and skull LAT – 1.79 mGy. The data were analysed statistically, and the minimum, median, mean, maximum, first and third quartile values of ESD are reported. Finally, our results were compared with the proposed Iranian DRL, the international reference dose values reported by the European Commission, the International Atomic Energy Agency and the National Radiological Protection Board. It is evident that ESD obtained in this work for abdomen AP, pelvis AP, lumbar AP and lumbar LAT examination do not exceed DRL values worked out by NPRB. On the contrary for chest PA, chest LAT, skull PA and skull LAT higher ESD were acquired in this study compared with the DRL suggested by NRPB. There is no single reason for dose variations, but the reasons are complex. In general, low filtration, high mAs and low tube potential are associated with higher doses arising from application of various X-ray machines.

Introduction

The radiation exposure incident on a patient during a radiological exam is entrance skin exposure, and the resultant radiation absorbed by the skin is the entrance skin dose. Skin dose is generally easy to measure or calculate, but it is a poor indicator of patient risk. Most people are aware of the use of X-rays in medical diagnostic work and may, indeed, have had practical experience of it. While it provides benefits of a unique kind in this application, it has a nuisance value when produced in situations where it is not wanted. The need to optimise the protection of patients results from the fact that medical exposure is by far the largest source of exposition of artificial origin. Radiation protection of patients is based on the application of the two major radiation protection principles, *i.e.* justification and optimisation. The third principle of dose limitation does not apply because images must meet quality criteria in order not to compromise the clinical value associated with the exposure [1]. DRL have been used effectively in the United Kingdom [British National Radiological Protection Board (NRPB)] and in Europe for more than a decade; however, establishing and implementing the use of DRL in North America has been slow. It is important to review the history of DRL to gain a perspective on current radiation protection practices. DRL are an important method of minimising radiation doses and radiation dose variations at minimal cost to radiology departments. They also increase staff awareness of radiation dose levels and radiologic technologists are better equipped to answer questions from patients [2]. The physical parameter recommended for monitoring the DRL in conventional radiography is the entrance skin dose (ESD) and methods for measuring it are clearly described in NRPB standard protocol. DRL can be used to [2]: "Improve a regional, national, or local distribution of observed results for a general medical imaging task by reducing the frequency of unjustified high or low values. Promote attainment of a narrower range of values that represent good practice for a more specific medical imaging task. Promote attainment of an optimum range of values for a specific imaging protocol."

Materials and methods

ESD is the absorbed dose (mGy) measured in air at the intersection of the axis of the X-ray beam and the patient's skin surface; ESD includes retro-scattered rays. ESD can be easily calculated or even better measured with the a thermoluminescent dosimeter (TLD) or with ionisation detectors placed on the patient's body. In the present study adult patient doses arising from five conventional X-ray examinations are examined. The following eight routine projections were studied: antero-posterior (AP) abdomen, lateral (LAT) chest, AP pelvis, postero-anterior (PA) chest, AP lumbar spine, LAT lumbar spine, PA skull, LAT skull. Dose measurements were carried out in 15 hospitals in Mashhad-Iran. Fifteen radiological departments participated in this survey, and 20 X-ray machines were operational in these departments. ESD was measured for individual patient by sticking TLD-100 chips on the patient body surface. A group of 20 TL dosimeters were used for calibration. They were exposed to 80 kVp X-rays (with 2.5 mmAl added filtration) and received a known dose (in order of mGy). The X-ray dose was measured by a 3 cm^3 ion chamber and a Radcal monitor model 323. The questionnaire for recording patient-related information (gender, age, weight), radiographic parameters (kVp, mAs, FFD, film size) and type of examination is shown in Table 1. The data were collected from 1 183 radiographies of adult patients. For each radiography one chip (in a sachet) was placed at the centre of the beam on the patient's skin. Chips were later read using a TLD reader (Harshow Model 3500).

Table 1: Questionnaire used for collecting of data in all 15 radiography departments

Gender F/M	Age (year)	Weight (m)	Projection PA/LAT	kVp	mAs	Time (s)	Film size (cm)	FFD (cm)	TLD code

Results and discussion

For each radiography department, mean values of patients' age and weight, radiographic parameters and ESD values were computed. Patient information and exposure parameters for all of the 1 183 patients are shown in Table 2. Table 3 compares mean values of kVp and mAs of this study with corresponding

values reported in Iranian references levels [7] and NRPB [1]. As DRL have been defined for Iran, in Table 4 the third quartile of patients dose distribution acquired in this work are compared with Iranian and the same studies specially recommended DRL by NRPB. It is evident that patients who were studied in this study have received higher ESD from chest radiography PA and LAT and skull PA and LAT relative to DRL reported by UK 2008, but most of the cases from the local hospitals delivered ESD values lower than the corresponding Iranian references values. Analysing Table 4, it was observed that in the case of pelvis AP, lumbar spin AP and skull PA ESD values were higher compared to Iranian DRL although the mean values of mAs in this study for these projections were lower than the Iranian DRL. The differences are related to different film screen speeds and techniques used in the radiological departments included in these two studies.

Table 2: Patient information and exposure parameters for eight X-ray projections

Examinations	Patient data		Exposure parameters	
	Age (y)	Weight (kg)	Tube potential (kVp)	mAs
Chest PA	52 (16-100)	65.3 (48-107)	72 (50-100)	13.6 (6-40)
Lat	53 (24-80)	67.2 (50-85)	80.5 (72-90)	28 (8-50)
Abdomen AP	51 (18-81)	64 (38-85)	73.8 (60-88)	46 (6.4-120)
Pelvis AP	49 (16-90)	64.5 (38-90)	67.4 (55-96)	40 (6.3-65)
Lumbar AP	40 (15-85)	67 (41-105)	71.9 (60-84)	45 (12-75)
Lat	50 (19-85)	69 (41-105)	83.4 (62-110)	57 (14-90)
Skull PA	40 (15-74)	64.6 (40-90)	68 (53-81)	37 (4-75)
Lat	40 (18-64)	67.2 (48-90)	57.6 (47-77)	23 (4-45)

The range from minimum to maximum is given in brackets.

Table 3: A comparison of the mean value of kVp, mAs between this study, Iranian DRL and NRPB

Radiograph	kVp			mAs		
	This study	Iranian DRL	NRPB	This study	Iranian DRL	NRPB
Chest PA	72	66	85	13.6	18	5
Chest LAT	80.5	72	98	28	41	15
Abdomen AP	73.8	68	74	46	54	46
Pelvis AP	67.4	66	74	40	48	35
Lumbar AP	71.9	70	77	45	50	42
Lumbar LAT	83.4	80	88	57	73	72
Skull PA	68	64	72	37	43	30
Skull LAT	57.6	59	66	23	32	19

Table 4: A comparison between third quartile ESD (mGy) in this study, Iranian third quartile and some international DRL from different countries

Adult radiograph	This study	Iranian DRL 2008 [7]	UK 2008 [8]	NRPB 2000 [1]	Switzerland 2006 [9]	Number of radiographs
Chest PA	0.37	0.41	0.15	0.2	0.3	244
Chest LAT	1.8	2.07	0.6	1	1.5	100
Abdomen AP	3.7	4.06	4	6	–	116
Pelvis AP	3.5	3.18	4	4	10	155
Lumbar AP	3.6	3.43	5	6	10	146
Lumbar LAT	5.6	8.41	11	14	30	143
Skull PA	2.96	2.83	2	3	5	144
Skull LAT	1.79	1.93	1.3	1.5	3	135

As shown in Table 4, doses at the third quartile of this study are within the limits of uncertainty with the references levels set by the UK 2008, NRPB and Switzerland 2006. In some cases, these doses are higher than the references levels, which is quite understandable as the older equipments and examination techniques could have caused this effects. TL dosimetry has been used world wide to

measure ESD in diagnostic radiology. This technique provides very accurate *in vivo* measurements of patient dose without affecting image quality. Increasing voltages allow the X-ray output values (mAs) to be reduced and produce the same film density with reduced entrance skin exposures. For given entrance skin dose, it is possible to estimate individual organ doses for many common radiological examinations. Organ doses will be substantially less than the skin dose. There is no single reason for dose variations, but the reasons are complex. In general, low filtration, high mAs and low tube potential are associated with higher doses arising from application of various X-ray machines.

Acknowledgements

References

[1]   Hart, D., M.C. Hillier, *Doses to Patients from Medical X-ray Examinations in the UK-2000 Review*, NRPB-W14.

[2]   Feritas, M.B., E.M. Yoshimura, "Dose Measurements in Chest Diagnostic X-rays: Adult and Pediatric Patients", *Radiation Protection Dosimetry*, 111, 73-76 (2004).

[3]   Burke, K., D. Sutton, "Optimization and Deconvolution of Lithium Fluoride TLD-100 in Diagnostic Radiology", *Br. J. Radiol.* 70, 261-271 (1997).

[4]   Berni, D., C. Gori, "Use of TLD in Evaluating Diagnostic Reference Levels for Some Radiological Examinations", *Radiation Protection Dosimetry*, 101, 411-413 (2002).

[5]   Compagnone, Gaetano, Laura Pagan, "Local Diagnostic Reference Levels in Standard X-ray Examinations", *Radiation Protection Dosimetry*, 113, 54-63 (2005).

[6]   Ziliukas, J., G. Morkunas, "Results of a Patient Dose Survey on Diagnostic Radiology in Lithuania", *Radiation Protection Dosimetry*, 114, 172-175 (2005).

[7]   Asadinejad, M., M.T. Bahreyni, "Doses to Patients in Some Routine Diagnostic X-ray Examinations in Iran: Proposed the First Iranian Diagnostic References Levels", *Radiation Protection Dosimetry*, 132, 4, 409-414 (2008).

[8]   Hart, D., M.C. Hillier, "National Reference Doses for Common Radiographic, Fluoroscopic and Dental X-ray Examinations in the UK", *BJR*, 82, pp. 1-12 (2009).

[9]   Federal Office of Public Health, Berne, Switzerland (2006). *Directive R-08-04. Niveaux de référence diagnostiques pour radiographies* [Diagnostic Reference Levels for Radiography], www.bag.admin.ch/themen/strahlung/02883/02885/02889/index.html?lang5fr.

Session V

Medical and industrial accelerators

Chair: Marco Silari

Radiation protection for particle therapy facilities

Georg Fehrenbacher
GSI Helmholtzzentrum für Schwerionenforschung
Darmstadt, Germany

Abstract

An increasing number of cyclotron and synchrotron facilities for medical treatments are installed world wide. Proton and light ion beams are used for tumour irradiations. In this work an overview of radiation protection topics for particle therapy facilities is given. Beam loss distributions of cyclotron and synchrotron installations in combination with passive or active beam shaping methods are quoted. Examples for neutron source distributions are presented for both proton and carbon ion beams. Methods for shielding calculations (MC, line-of-sight models) are described with an emphasis on carbon ion beams. Dose values from three different line-of-sight models (Agosteo, Ipe, GSI) are compared with the results of the international measurement campaign CONRAD conducted at GSI-Cave A. Shielding requirements for therapy rooms operated with proton and carbon ion beams are compared by reference to the example HIT facility in Heidelberg. Finally, three examples for particle therapy facilities (Loma Linda University Medical Center, HIMAC, HIT) are described.

Introduction

An increasing number of particle therapy facilities are in operation world wide. Particle therapy facilities comprise therapy installations for proton beams and beams of heavier ions, essentially carbon ions. Motivations for this trend are the encouraging results obtained at research facilities such as the Lawrence Berkeley National Laboratory (United States) [1], the Harvard Cyclotron Laboratory (United States) [2] or the Helmholtz Center for Heavy Ion Research GSI (Germany) [3]. The first dedicated facility for proton treatments in a clinical environment was the Loma Linda Medical University Center (CA, United States). A series of further proton therapy facilities was constructed mainly in the US and in Japan. In Japan, where the majority of the particle therapy centres are proton centres, therapy facilities for heavy ions – essentially carbon ions – are also in operation. These are the Heavy Ion Medical Accelerator (HIMAC) in Chiba, the Hyogo Ion Beam Medical Center and the accelerator centre at Gunma University. In Europe hospital-based therapy facilities are in operation or under construction in, *e.g.* Germany [Munich, Essen, Heidelberg (HIT), Marburg, Kiel] and Italy [Pavia (CNAO), Trento]. Further facilities are under construction in, *e.g.* France and the Czech Republic.

The planning and the operation of particle therapy facilities are highly influenced by radiation protection issues. Beam depositions in the tumour and the unwanted beam losses during the acceleration process, in the beam shaping system and during the transport to the therapy room have a particularly high implication on the shielding layout of the facility.

The scope of this work is to provide a survey on radiation protection subjects which arise during the planning phase and during the operation of particle therapy facilities. Particular emphasis is given to the protection of the personnel and the environment. The focus of the survey is the discussion of differences between cyclotron and synchrotron facilities. Criteria for the architectural shielding design are explained. The distribution of radiation sources in the facility is of particular importance. The radiation sources in particle therapy facilities are dominated by neutron radiation. Examples of measured and calculated double differential neutron source distributions (solid angle, energy) are presented for both proton and carbon ion beams. Differences of neutron source distributions for both particle types and their influence on the architectural shielding design are pointed out. The type of applied beam shaping system – passive or active – has implications on the facility layout in the area of the beam delivering system. Passive beam shaping systems such as the double scatter method require other shielding measures than active procedures like the raster scan method [4].

The definition of radiological areas according to national legal dose limits for particle therapy facilities is explained. Calculation methods, particularly the line-of-sight method for carbon ion beams, are discussed for estimation of required shielding thicknesses. Data from the Co-ordinated Network on Radiation Dosimetry (CONRAD) measurement campaign at GSI are used to examine the prediction of various line-of-sight-models for carbon ion beams.

Finally, as examples of proton and carbon ion therapy facilities, the installations at the Loma Linda University Medical Center (LLUMC), the Heavy Ion Medical Accelerator (HIMAC) and the Heidelberg Ion Therapy Center (HIT) are described.

Accelerator types, beam losses and radiological areas

Cyclotrons and synchrotrons are the accelerator types which are used for particle therapy facilities. Whereas cyclotrons are preferred for proton acceleration, synchrotrons are used for the production of beams of heavier ions like carbon ions as well as for proton beams like the facilities at the Loma Linda University Medical Center (California) or the MD Anderson Cancer Center in Houston (Texas) with a Hitachi proton synchrotron. A recent accelerator development is a superconducting cyclotron for carbon ion beams with energies of 400 MeV per nucleon by IBA [5].

The main advantage of a synchrotron is the capability for the adaptation of the ion beam energy to the actual desired beam range in the tissue of the patient. In terms of radiation protection the superiority of synchrotrons is explained by the lower beam losses during acceleration and extraction and the avoidance of the production of radiation during the beam energy degradation in a degrader. Therefore in areas with lowered beam (loss) depositions in the accelerator structure less shielding is necessary. Furthermore the levels of radioactive activation are lower too, and cause lower exposure of the personnel during maintenance work. Another benefit of a synchrotron is the opportunity to

accelerate various types of ions or to switch the accelerator operation from one ion type to the other which might be useful for those facilities which perform comparative studies in particle therapy. The weakness of a synchrotron is the need for more space for the accelerator and consequently an increased building. Due to the increased number of particle facilities for carbon ion beams in Europe and Japan more and more synchrotrons are used.

Cyclotrons are the most common accelerator types for proton therapy world wide. A large number of proton cyclotrons are installed mainly in the United States, Japan and Europe. The main advantage is the stable operation of the cyclotron for long periods without unwanted interruptions. Another big advantage is the high duty cycle (DC-Beam) compared to the spill structure of synchrotrons. Cyclotrons deliver beams with a fixed maximum energy and high currents (~0.1 μA). The actual required beam energy for the current running therapy process is obtained by the energy degradation of the beam in low-Z materials such as a carbon wheel or a plastic wedge (see below).

Cyclotrons were originally combined with passive beam-forming systems. Scanning methods are combinable with both accelerator types. In scanning a particle beam is conducted over a slice of the tumour volume by magnetic deflection in two directions and subsequently the particle energy is changed to the next slice – the Bragg peak is moved from slice to slice – and the process is repeated until the whole tumour is irradiated [4,6]. From the radiation protection point of view, active scanning prevails over passive beam-forming systems. Active systems are mainly installed in facilities which were recently built or existing facilities are converted to active systems. Due to the compactness of cyclotrons the overall essential space is lower in comparison to the necessary space for synchrotrons, although the shielding thicknesses might be larger. Cyclotrons have to use energy degrader and range shifter. This requires additional shielding structures. The energy adaptation can be performed rapidly, in contrast to a synchrotron where the ions must first run through a new cycle process to extract the ions with the desired energy. The degrader technique is advantageous when, *e.g.* moving organs are treated and a fast beam energy adaptation is necessary. Range shifters are also used for synchrotrons to enable moving organ treatments. One of the major disadvantages of cyclotrons are the high level of radioactive activations and the resulting dose rates in the vicinity of areas with high beam losses and depositions at the beam extraction area and the energy degrader. Delayed access and short time stays for maintenance are a consequence in order to ensure radiation protection. Further developments for cyclotrons include the introduction of superconductivity, which leads to another reduction of weight and space [7], or single-room synchrocyclotron systems [8].

Examples for the passive beam-shaping elements with major beam losses and production of radiation are shown in Figure 1. The left panel shows a rotating wedge. Due to the altered path length of the passing beam, the energy of the beam is adjusted to the currently required beam energy. The rotating wedge is made of graphite. Substantial production of radiation and radioactivity is observed for the wedge. In the right panel the last elements of a passive beam shaping system are shown. Here, the collimator and a compensator are present. The collimator cuts out the outer part of the beam which is not needed for the treatment. The compensator adapts the distal range distribution of the beam in the tumour of the patient. In the proximal healthy tissue of the patient higher doses can occur. Both the collimator and the compensator produce unwanted radiation and activation which is disadvantageous for the patient and causes an increased shielding effort.

Schemes for particle beam generation including beam losses and depositions by a cyclotron and a synchrotron with the different steps from the ion source, pre-acceleration, in the accelerator, extraction, high-energy beam transfer line, the passive beam forming system and the beam delivery system in the therapy room are given in Figure 2. The given numbers in % are related to the beam losses in the particular step. The values for the beam losses are taken from Noda, *et al.* [9] and from the PTCOG report [10].

Corresponding to the produced radiation levels by the particle beam, various radiological areas must be defined. In most countries four radiological areas are defined or exist in modified versions:

1. inaccessible areas without access for personnel;

2. controlled areas;

3. supervised areas;

4. public areas.

Figure 1: Beam-forming and altering elements in a facility based on passive methods

Left – a rotating wedge lowers the energy of a particle beam. Right – the last elements in front of the tissue of the patient are the collimator (high-Z material) and a compensator (low-Z material), the picture is adopted from Chu, *et al.* [11].
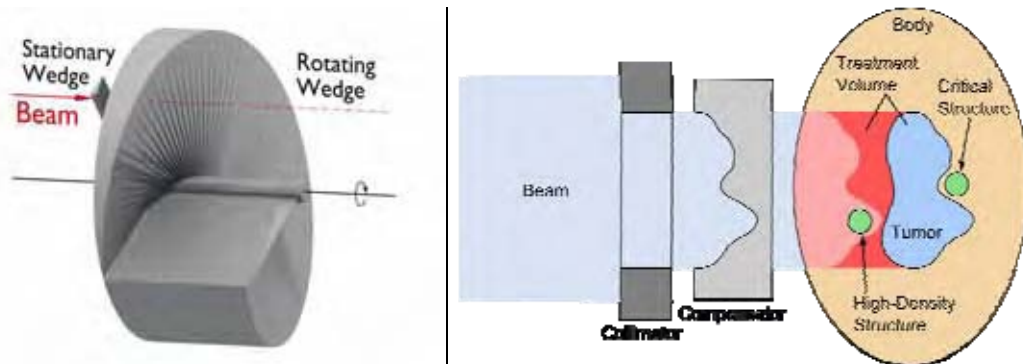
Figure 2: Schemes of accelerators used for particle therapy, synchrotrons and cyclotrons

Left – indicated beam losses and beam depositions in synchrotron facilities [9].
Right – corresponding beam losses in cyclotrons. Each example has a passive beam-forming system.
The coloured areas indicate positions with neutron production (except linac with mainly X-ray production).
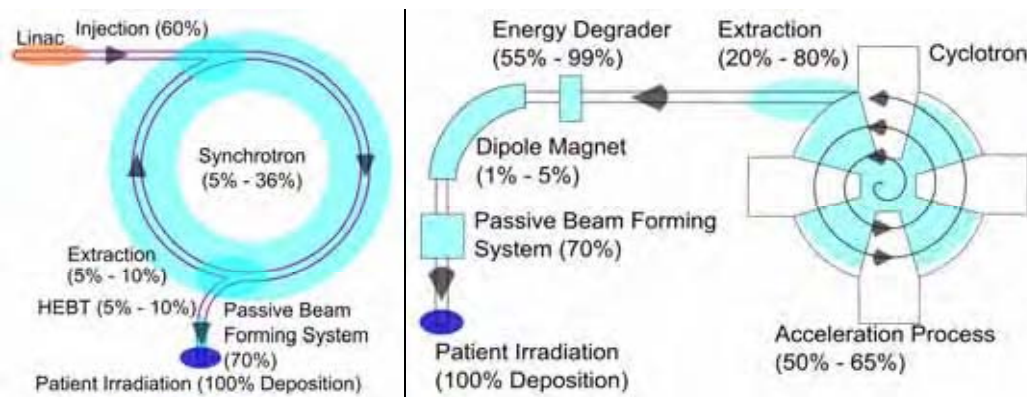
This concept projected on particle therapy facilities means that all areas where the particle beam occurs or is transported including the therapy room are inaccessible areas (see Figure 3). Zones around inaccessible areas and accelerator areas with radioactive activation are controlled areas. Supervised zones are defined around inaccessible and controlled areas. The public area is outside the facility and partially inside the facility with the lowest and most restrictive dose values. An overview of dose values and dose limits in Japan, Germany, Italy and the United States for their radiological areas is given in Table 1 [10]. Whilst the dose limits for public areas are of the same value in all countries, the corresponding value for controlled and supervised area deviates from one country to another except for those in Europe (here quoted for Germany and Italy). For the inaccessible areas there are usually no general legal regulations except for Germany.

Source distributions and methods for shielding calculations

The rate of beam losses and depositions expressed as particles per second (or other periods such as an hour or year) at a certain beam energy is a crucial quantity to determine for the architectural shielding design. The beam losses determine the magnitude and the energy distribution of the produced radiation. The neutron radiation produced is the decisive radiation component for shielding design. Therefore the investigation of the double differential distribution (energy, solid angle) of the produced neutron radiation gives an important starting point for the development of the architectural shielding layout. For this approach the thick target approximation is considered. This means that the target has at least the thickness equivalent to the range of the particle beam in the target.

**Figure 3: Various types of radiological areas and the classification of
the zones in a particle therapy facility for the accelerator, energy selection
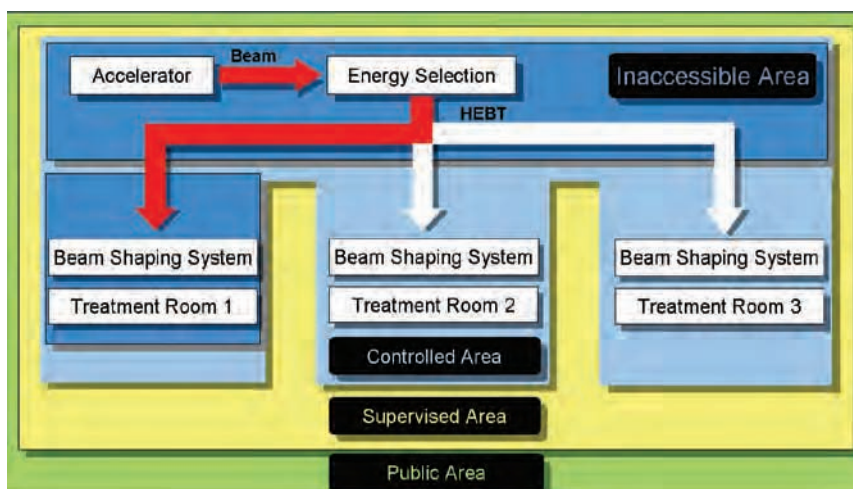system, high-energy beam transfer, therapy room and the surrounding rooms**

Table 1: Classification of radiological areas in the countries Japan, Italy and Germany

Area	Dose limit			
	Japan [12]	**Italy [13]**	**Germany [14]**	**United States [15]**
Inaccessible	Site specific	Site specific	> 3 mSv/h	Site specific
Controlled	> 1 mSv/week	> 6 mSv/y	> 6 mSv/y	≤ 5 mSv/y
Supervised	> 0.1 mSv/week - 1.3 mSv/3 months	> 1 mSv/y, < 6 mSv/y	> 1 mSv/y, < 6 mSv/y	-
Public	< 250 µSv/3 months	< 1 mSv/a	1 mSv/y	≤ 1 mSv/y, 20 µSv in 1 h

The shielding design is at first developed to achieve the compliance of the operation with the prescribed annual dose limits outside the shielding. Beside the annual dose limits which are given by the national radiation protection legislation, the dose value in a shorter period is a further criterion which is possibly applied by the authorities. In practice, this means that the dose rate, related *e.g.* to the period of one hour (µSv/h), should not exceed a certain limit if the maximum beam parameters are applied. The considerations for the annual dose can be drawn up for a mix of particle energies and the corresponding intensities depending on the medical indications. The most secure approach would be the application of the highest beam energies and intensities of the particle beam.

In the following examples there are measured and calculated neutron energy distributions presented for a carbon ion beam with the energy of 400 MeV per nucleon deposited in a thick graphite target. There are two experiments, the first experiment carried out at HIMAC in Chiba and the second one was at the GSI Helmholtz Center for Heavy Ion Research in Darmstadt. The experiments were performed on the basis of time-of-flight measurements. As neutron detectors a liquid scintillator (NE213) was used by Kurosawa, *et al.* [16] and a BaF_2 scintillator was applied by Gunzert-Marx, *et al.* [17]. A graphite block of dimensions $20 \times 10 \times 10$ cm³ was used as beam stopping target. The experimental set-up, detection efficiency, obtained energy resolution and further details are explained in detail in the experiment descriptions [16,18]. Here, a summary of the results is given. For comparisons with the experiments, FLUKA calculations were carried out [17]. The results are shown in Figure 4. In the left part the results of the BaF_2 measurements, in the right part the results of the NE213 liquid scintillator are shown. The NE213 data exceed the FLUKA results for the 0° direction by a factor of 2 at neutron energy of 0.3 GeV, whereas the BaF_2 data agree with the FLUKA data. For the 50° and 90° direction the BaF_2 data have higher values than the FLUKA data up to a factor of 10 at the neutron energy range 0.2-0.4 GeV. At 90° the NE213 data agree with the FLUKA data. All in all the agreement and deviation of the FLUKA results to both measurements are not consistent for the angular range considered here (0-90°).

Figure 4: Measured and computed neutron source spectra for carbon ion beam with energy of 400 MeV/u impinging on a graphite target (20 × 10 × 10 cm³)

The calculations are performed with the FLUKA code [17].
Left: measurements carried out with a BaF$_2$ time of flight spectrometer.
Right: measurements performed by Kurosawa, *et al.* by means of a NE213 liquid scintillator and time-of-flight technique.
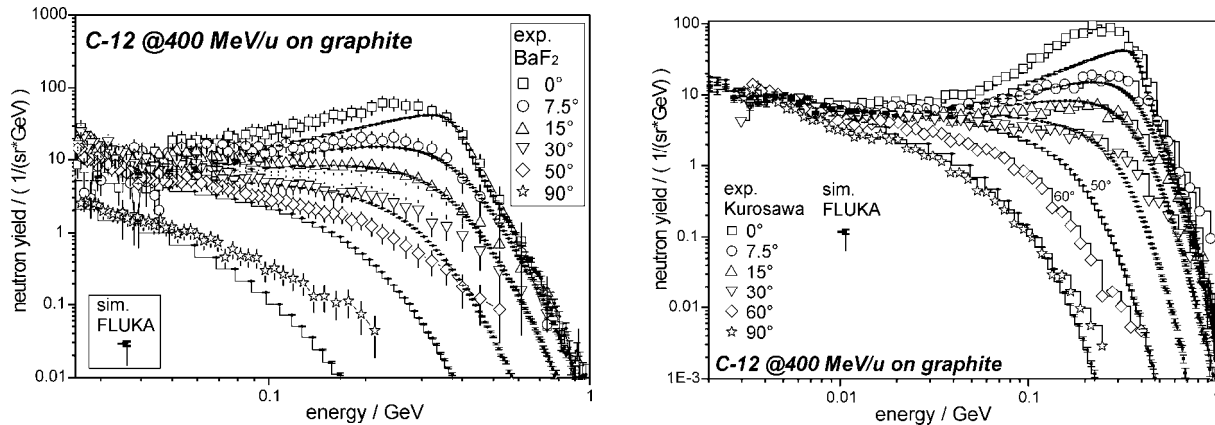
The comparison of radiation source data for both particle types, protons and carbon ions, gives important information on the design of the architectural shielding layout. Criterion for the comparison is the equivalent dose of both particle types in a certain penetration depth in tissue for a typical patient treatment. Beside the physical dose, the particle type and the tissue-specific RBE has to be taken into account. Whilst for proton beams an RBE of 1 to 1.1 is applied, the corresponding RBE for carbon ions varies largely. An RBE value of 3 is assumed for carbon ions here. For the following examination a small tumour in a depth of 26 cm in tissue is chosen. This means for proton beams an energy of 200 MeV and for carbon ion beams an energy of 400 MeV/u is considered. In order to obtain an equivalent therapy dose for both particle types, the therapy treatment program TRIP [19,20] was applied (Iancu and Krämer, 2009, pers. comm.). The calculations resulted in an intensity ratio of 33 protons to one carbon ion. In the following considerations this factor was employed. For the neutron source distributions the data of Porta, . [21] were used for the 0° and 90° direction (target material ICRU/ICRP tissue). The results are shown in Figure 5. In the left panel of Figure 5 the neutron production in forward direction (0°) is shown. The red line reflects the energy of the impinging ion beam (400 MeV/u), the black line the corresponding one for protons. A substantial part of the carbon-ion-produced neutrons have energies higher than 400 MeV up to about 1 GeV whilst the proton-generated neutrons have a sharp maximum energy of 200 MeV. At lower energies the neutron spectra agree roughly. In the right panel of Figure 5 the spectra for the lateral direction (90°) are presented. The highest energies are lower than in the 0° case. The proportion of lower-energy neutrons is higher for the proton beam than for the carbon ions. This effect is caused by the stronger lateral scattering of protons in the target as expected. From these considerations one can deduce a trend. Facilities for proton beams require a higher lateral shielding, while carbon ion beams need a reinforced shielding in the forward direction.

Line-of-sight models

For the preliminary planning of a particle therapy project simple calculational models are applied. An example is the so called line-of-sight model, which considers the angular dependent source term, the overall distance from the interaction point (target) to the reference point outside the shielding and the attenuation in the shielding with a certain thickness. Initially this method was applied for the development of the shielding structure of the Bevalac in Berkeley, United States [22]. From these models the required thickness of the shielding can be obtained rapidly, although this method is not as precise as Monte Carlo radiation transport calculations. Apart from that, for the first layout development and   rough cost estimates, this method is sufficient.

**Figure 5: Neutron source distributions for proton and
carbon ion beams with comparable ranges in tissue (~26 cm)**

The distribution of a single proton is multiplied by a factor 33 to obtain the same biologically effective therapy dose at
the prescribed depth for a small tumour volume (Iancu and Krämer, 2009, pers. comm.). Left: 0° direction, indicated is the
200 MeV value (left line) and the 400 MeV value (right line). Right: 90° direction. The data are taken from Porta, *et al.* [21].
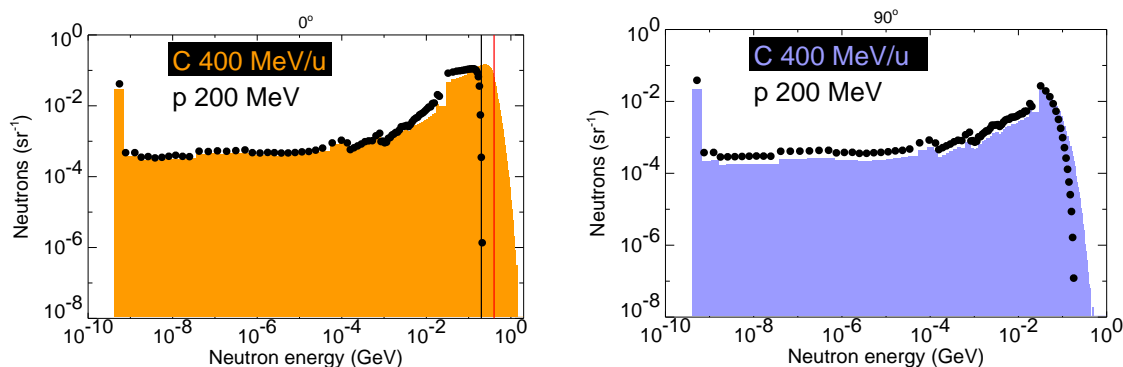
A formulation for ion beams is given in the work of Agosteo [23]:

$$H(E_P, \vartheta, d, \lambda_\vartheta) = \frac{H_0(E_P, \vartheta)}{r^2} \cdot \exp\left[-\frac{d \cdot \rho}{\lambda_\vartheta}\right] \qquad (1)$$

where H_0 is the energy and angular dependent source term (Sv·m²), r the overall distance from the interaction point to the reference point, d the thickness of the shielding (ρ density) and λ the attenuation length (g/cm²). For larger angles the source strength and the attenuation of higher-energy neutrons and lower-energy neutrons is differentiated. If a substantial proportion of evaporation neutrons contributes to the overall dose, Eq. (1) is extended by a second term which takes into account that evaporation source neutrons are differently absorbed (λ_2) than high-energy neutrons (λ_1) (see Eq. 2 [23]):

$$H(E_P, \vartheta, d, \lambda_\vartheta) = \frac{H_1(E_P, \vartheta)}{r^2} \cdot \exp\left[-\frac{d \cdot \rho}{\lambda_{1,\vartheta}}\right] + \frac{H_2(E_P, \vartheta)}{r^2} \cdot \exp\left[-\frac{d \cdot \rho}{\lambda_{2,\vartheta}}\right] \qquad (2)$$

Parameters for proton beams are comprehensively documented [24-27]. A recently published summary on shielding data is given in Report 1 of the Particle Therapy Co-operative Group (PTCOG) [10]. Here, the focus of interest is to review shielding data for carbon ion facilities. Based on measured neutron spectra at HIMAC [16], Agosteo, *et al.* developed a first set of parameters for 400 MeV/u carbon ion beams [28,29]. Ipe and Fassò [30] calculated in a full FLUKA simulation – including nucleus-nucleus collisions parameters for bare concrete and combined steel-concrete shielding for 430 MeV/u carbon beams (target ICRU sphere). On the basis of monoenergetic attenuation curves for neutron radiation [31], Fehrenbacher and Radon computed the resulting attenuation curves for neutron source distributions generated by 400 MeV/u carbon beams deposited in a graphite target in a FLUKA calculation [32]. The determined parameters related to concrete shielding are quoted in Table 2 for the angular range from 0° to 90°.

An opportunity to review shielding data for carbon ion beams is given by the measurement campaign of the working group CONRAD inside and outside Cave A of the GSI Helmholtz Center for Heavy Ion Research in Darmstadt, Germany. A carbon ion beam with an energy of 400 MeV/u is directed on a graphite target (20 × 10 × 10 cm³). A series of reference points outside the concrete shielding was defined (Z, OC-9 to OC-16, see Figure 6). Comprehensive Monte Carlo transport calculations (FLUKA, MCNPX) as well as measurements with various detectors and instruments were carried out. Further details can be found in the work of Rollet, *et al.* [33], Wiegel, *et al.* [34] and Silari, *et al.* [35]. At the reference points values for the ambient dose equivalent are provided for both the MC calculations (averaged values from several calculations from different laboratories and MC codes) and the measurements. For the measured reference values data from Bonner sphere measurements were chosen [34,35]. In Table 3 the ratio of the calculated dose values to the reference values are given for the points OC-9 to OC-14 (Figure 7). Both comparisons show the tendency to overestimate the dose at

Table 2: Parameters for carbon ion beams with the energy of 400 MeV/u and 430 MeV/u, respectively, according to Eqs. (1) and (2) for the computations of GSI, Agosteo and Ipe

The angular ranges of the GSI values are related to 5° intervals (0-5°, 10-15°,...); the values for the missing intervals (5-10°, 15-20°,...) can be derived by interpolation

Angle	GSI		Agosteo				Ipe	
	H_0 (Sv·m²)	λ (g·cm⁻²)	H_1 (Sv·m²)	λ_1 (g·cm⁻²)	H_2 (Sv·m²)	λ_2 (g·cm⁻²)	H_0 (Sv·m²)	λ (g·cm⁻²)
0-10°	2.31E-12	142.2	–	–	1.93E-12	120.98	3.02E-12	123.81
10-20°	7.56E-13	138.6	–	–	4.37E-13	120.21	4.81E-13	133.09
20-30°	3.10E-13	132.8	–	–	1.50E-13	122.15	4.81E-13	133.09
30-40°	1.50E-13	126.5	–	–	5.75E-14	122.18	–	–
40-50°	8.18E-14	119.7	–	–	2.28E-14	117.03	4.71E-14	117.64
50-60°	4.34E-14	112.8	1.03E-14	49.28	7.53E-15	111.74	4.71E-14	117.64
60-70°	2.25E-14	105.9	9.98E-15	50.07	3.19E-15	103.86	–	–
70-80°	1.16E-14	99.8	7.62E-15	48.43	1.49E-15	102.23	–	–
80-90°	6.04E-15	94.4	6.11E-15	39.88	9.54E-16	95.87	–	–
90-95°	3.36E-15	89.6	–	–	–	–	–	–

Figure 6: Scheme of the layout of GSI-Cave A, where the CONRAD measurement campaign took place in 2006

A carbon ion beam with the energy of 400 MeV/u was deposited in a graphite target. The measurement positions outside the concrete shielding are indicated as OC 9 to OC 16 and Z.
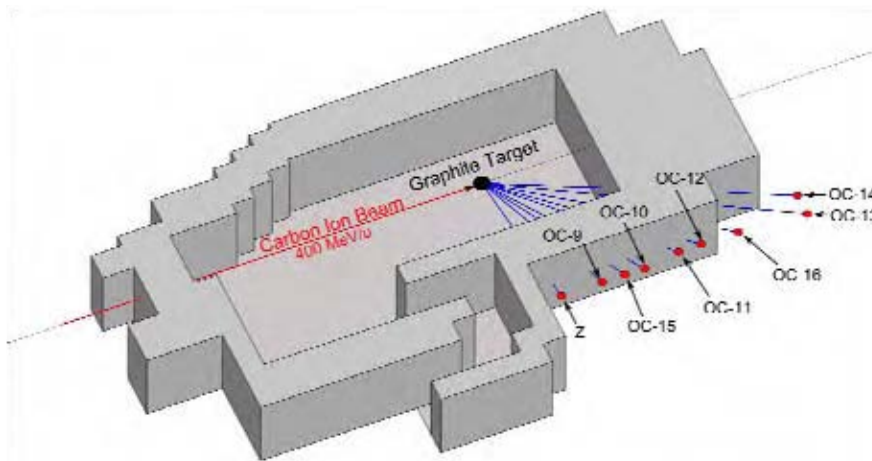
Table 3: Table of ratios of determined dose values to reference dose values from MC calculations [33] and measurements [34,35] for the GSI model [32], data from Agosteo, et al. [23] and Ipe and Fassò [30]

The values of GSI and Agosteo are correctly related to 400 MeV/u carbon beams, the values of Ipe and Fassò are related to 430 MeV/u beams, which does not exactly correspond with the beam energy 400 MeV/u of the CONRAD measurement campaign.

Position	GSI		Agosteo		Ipe	
	H/H_{MC}	H/H_{Meas}	H/H_{MC}	H/H_{Meas}	H/H_{MC}	H/H_{Meas}
OC-9	1.51	1.60	0.21	0.22	4.70	4.96
OC-10	1.20	1.57	0.20	0.26	1.56	2.04
OC-11	1.30	1.60	0.32	0.39	0.69	0.85
OC-12	1.78	1.68	0.85	0.81	0.57	0.54
OC-13	5.55	4.76	2.55	2.18	13.45	11.51
OC-14	2.40	2.45	0.62	0.63	3.78	3.87

**Figure 7: Ratio of model dose values to reference dose values
for various locations outside Cave A at GSI (see also Figure 6)**

Left – reference values from measurements, right – reference values from Monte Carlo calculations.
The values of Ipe are related to 430 MeV/u carbon ion beams.
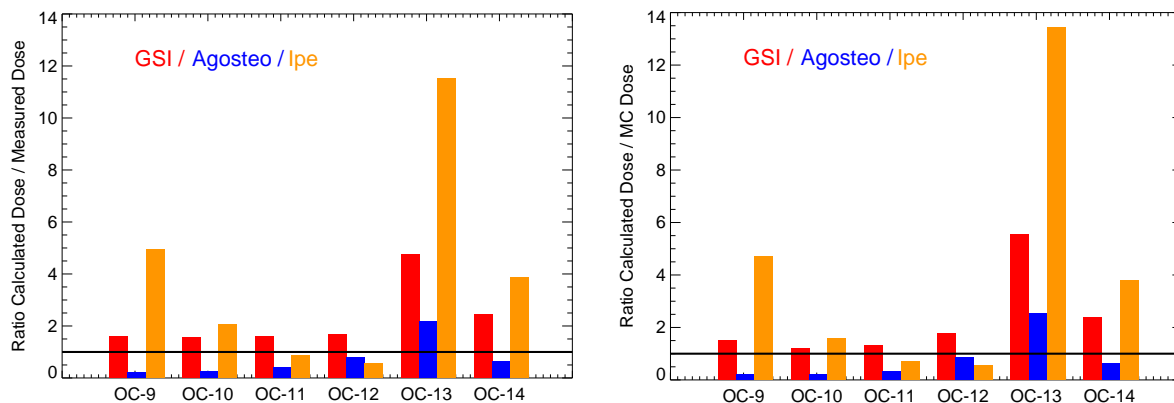
point OC-13 for all models and data (factor 2 to 13). Apart from that the model of Agosteo indicates an underestimation of the dose by a factor of 0.2 to 0.6 for the points OC-9, 10, 11, 12 and 14. The GSI model results in a general dose overestimation by a factor 1.2 to 5.6 for all positions. The Ipe data show an underestimation for OC-11 and 12 (factor 0.5, 0.8) and an overestimation for OC-9, 10, 13 and 14 (factor 1.6 to 13.5) to the reference dose values. It should be stressed that the data of Ipe and Fassò are derived for 430 MeV/u carbon ion beams and cannot be directly compared with the other values. Nevertheless these data allow an assessment of systematic effects.

MC calculations

Monte Carlo (MC) transport calculation is the superior method for the determination of radiation levels at the target or at the patient, respectively, as well as for the simulation of the radiation transport through the shielding. One important advantage is the opportunity to estimate the dose contributions of scattered radiation to the overall dose which is decisive for the development of labyrinth and duct layouts. Monte Carlo transport codes were initially available only for proton beams like the MCNPX code [36] or FLUKA [37]. Therefore for the design of heavy ion treatment facilities older MC codes were coupled with measured neutron spectra as source distributions.

In recent years MC codes were extended for transport of heavy ions including nucleus-nucleus collisions. Here, an example for a carbon ion treatment facility is presented, the Heidelberg Ion Therapy Center (HIT). The treatment rooms H_1/H_2 were considered for MC shielding calculations [38]. The shielding layout was developed on the basis of neutron source data from Kurosawa, *et al.* [16]. A carbon ion beam with 400 MeV/u and an intensity of $3 \cdot 10^8$ ions/sec was assumed for the calculations. The actual maximum energy of the accelerator is 430 MeV/u, but the average energy is lower. The dose distribution is given in Figure 8 (left) for the $H_{1/2}$ treatment rooms. The cross walls are reinforced with steel layers of 50 cm thickness. The level of dose rates outside the entrance area and outside the shielding is about ~1 μSv/h. A further FLUKA calculation was carried out for a proton beam and a comparison is drawn for the dose patterns of both particle types, protons and carbon ions.

The prescribed particle range in tissue amounts to about ~26 cm, which corresponds to 400 MeV/u for carbon ion and about 200 MeV/u for proton beams (210 MeV in the FLUKA calculations). The beam current ratio was chosen as in the example of Figure 5 (I_{Carbon}/I_{Proton} = 33). The results of the neutron dose distributions for the proton beam are given in Figure 8 (right). In this example the carbon beam produces slightly increased dose in the forward direction where as laterally a similar dose distribution is obtained for both protons and carbon ions.

**Figure 8: Neutron dose distributions in the H$_{1/2}$ treatment rooms
of the HIT facility for proton and carbon ion beams (µSv/h)**

The beam runs upwards into a target. Left: A carbon ion beam with energy of 400 MeV/u and 3·10^8 ions/sec is deposited in a graphite target. Right: A proton beam with energy of 210 MeV and 1·10^{10} p/sec is also deposited in a graphite target.
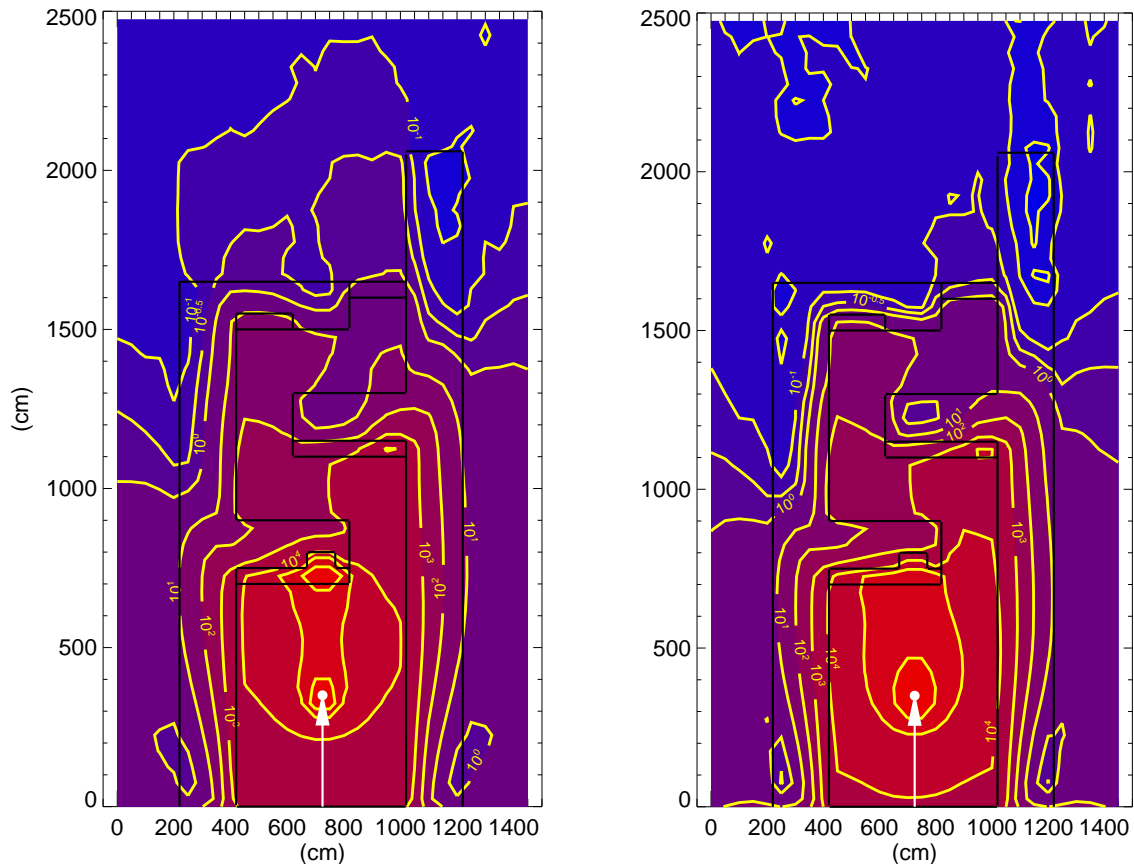
Three examples of particle therapy facilities: LLUMC, HIMAC, HIT

Loma Linda, USA

The Loma Linda University Medical Center (LLUMC) was the first hospital-based proton treatment facility world wide. The first plans for a proton therapy were established in the 1970s. The progress in X-ray diagnostics using CT and the prospect to run an accelerator facility with sufficiently high precision and adequate reliability in a hospital environment led to plans for a proton facility. In the mid-1980s Fermilab was contacted to support their plans and give advice for the technical layout of a facility in view of a certain lack of companies willing to face the challenge. In 1987 Fermilab and Loma Linda University presented the engineering design report for LLUMC and in 1988 the building of the facility began. In October 1990 the first patient was treated. The facility consists of the following installations and characteristics:

- For the accelerator a synchrotron (7 m diameter) was chosen. For the pre-acceleration a 2 MeV Radio Frequency Quadrupole (RFQ) was added to the synchrotron. The energy range of the synchrotron is 70 to 250 MeV. The design intensity is 10^{11} protons/sec. The beam extraction efficiency is higher than 95% (Ipe, *et al.*, 2010).

- There are four treatment rooms, three rooms with isocentric gantries and one room with two horizontal beam lines.

- For the beam shaping, passive systems are applied as ridge filters, scattering foils or a wobbler; active scanning was planned to be introduced [6].

- In total between 1 000 and 2 000 patients can be treated per year; in one day up to about 150 treatments can be carried out.

In the framework of preparation for the construction planning of the proton therapy facility Awschalom collected shielding data for 250 MeV proton beams. A survey of data is given in a Fermilab technical report [39]. The essential radiation safety calculations were carried out by Hagan, *et al.* [40]. In that work the radiation production, caused by protons with energies from 150 to 250 MeV, was computed by means of the MC program HETC [41] for iron and water targets. The subsequent transportation of the produced neutron radiation was calculated with the ANISN code [42] for a spherical geometry. Attenuation curves were derived for concrete thicknesses in the range up to 650 cm. At an experimental test set-up of the synchrotron facility, assembled at Fermilab, a shielding design was built around the synchrotron and the beam line. Within the concrete blocks of the shielding, holes were prepared where radiation detectors (TEPC) were positioned. Experimental attenuation curves were derived for the angular range from 0° to 90° and served as a benchmark for the theoretical attenuation curves. In that comprehensive work of Siebers, an idea was given for the accuracy of the results of analytical and computational methods of the radiation transport [24,43].

In Figure 9 the layout of the facility is shown with three gantry rooms and one room in fixed beam geometry. The whole facility is integrated in the building of the Loma Linda University Medical Center. The installations are partially underground.

Figure 9: Proton therapy facility at the Loma Linda University Medical Center

The installation consists of a synchrotron, four rooms for medical treatments, three with a gantry
and one fixed-beam branch with two beam lines (one further for calibration measurements)

HIMAC, Chiba, Japan

The Heavy Ion Medical Accelerator (HIMAC) in Chiba, Japan, is operated by the National Institute for Radiological Sciences (NIRS). At HIMAC a large variety of ions can be accelerated such as p, He, C, Ne, Si and Ar ions. For patient treatments carbon ions are mainly used. A hospital was built near the HIMAC building to attend to the patients, the first of which were treated in 1994; by 2004, the number

of patients treated annually was around 400. The accelerator installation comprises two synchrotrons, three rooms for medical treatments, a physics and general-purpose irradiation room, a medium-energy beam irradiation room and a room for biological irradiations (see Figure 10). For the patient treatments different types of rooms are available depending on the needs of the irradiation geometry. There is a room for horizontal irradiations (H), a room for vertical irradiations (V) and a room for the combination of both (H&V). The last one can be operated with two different beams from both synchrotrons (see the beam lines in Figure 10).
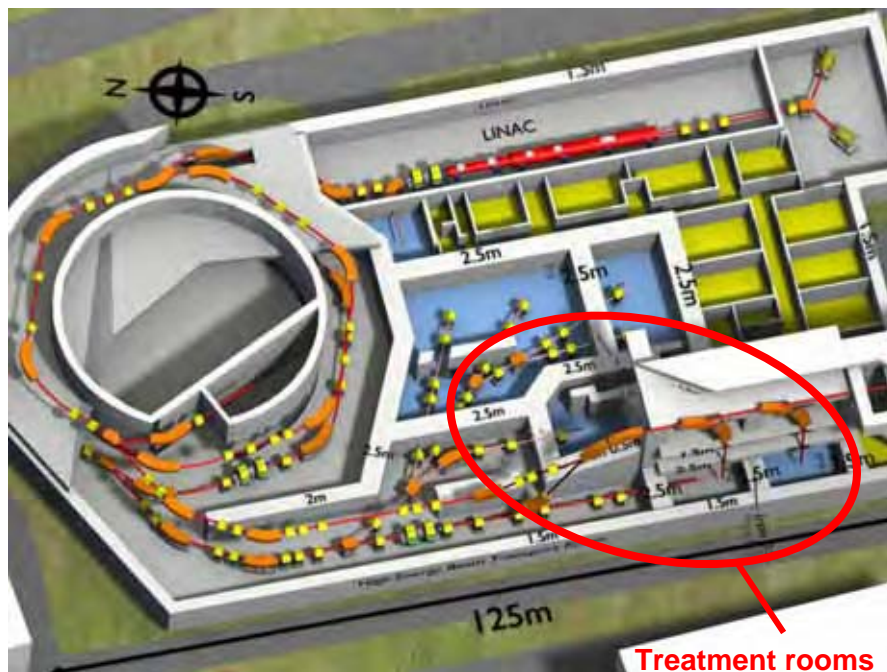
Figure 10: Schema of the Heavy Ion Medical Accelerator (HIMAC) facility in Chiba, Japan

HIMAC is operated by the National Institute for Radiological Sciences (NIRS). The facility comprises three treatment rooms (H, V, H&V) and rooms for research. In the H&V treatment room, both irradiation ports can be supplied with ion beams simultaneously (see marked area).

The beam extraction intensity for carbon ions in the synchrotrons amounts to $2 \cdot 10^8$ ions/sec. For the case of He ions (500 MeV/u, higher than is truly necessary for therapy irradiations) a detailed survey on beam loss distributions is given. It is reported that 5% beam losses occur during the extraction, 10% beam losses during the acceleration along the ring, 15% at the ring scrapers and 10% beam losses at the vertical beam transfer lines.

The beam loss data and the estimated period of operation per week (synchrotron 108 h/week, treatment rooms 11-18 h/week) served as a basis for the shielding calculations. The results of HETC-KFA calculations [41] were used for the development of an approximation formula for the calculation of the neutron fluence caused by He ions and other ion types and the possibility to compute the neutron fluence as a function of the ion energy is provided [44]. In a further step the attenuation of the neutron radiation in the bulk shield is calculated and the corresponding dose values are derived [44]. The shielding walls are partially reinforced by iron layers. The thickness of the shielding around the synchrotron amounts to 1.5 m. At the extraction area there is a 2.5 m shield in addition (Figure 10). The effective shield thicknesses for the therapy caves are 3.2 m in the forward direction. The value for the lateral one is 2.5 m.

HIT, Heidelberg, Germany

The Heidelberg Ion Therapy Center originated as a design proposal of the GSI Accelerator and Biophysics Departments, the Radiological University Clinic in Heidelberg and the Research Center Dresden-Rossendorf [45]. Based on the developments of the GSI pilot project and the encouraging

results of the carbon ion treatments [3] the planning of a hospital-based heavy ion treatment facility was initiated [46]. The facility comprises two horizontal treatment rooms (H) and a gantry suitable for carbon ion transport (*e.g.* C ions with energies of 430 MeV/u). Part of HIT is shown in Figure 11. The linac room, the synchrotron room, the therapy chambers H_1, H_2 and the gantry room are presented. Parts of the building are covered by soil layers and other bulk materials. Some parts of the building – those containing the main accelerator components – are embedded in earth.

Figure 11: Part of the HIT facility in Heidelberg

Shown are the linac, the synchrotron and the horizontal treatment chambers H_1 and H_2, each with an entrance labyrinth. The room for the gantry is also indicated. The dose distribution of the $H_{1/2}$ chambers are shown for carbon ion and proton beams in Figure 8.
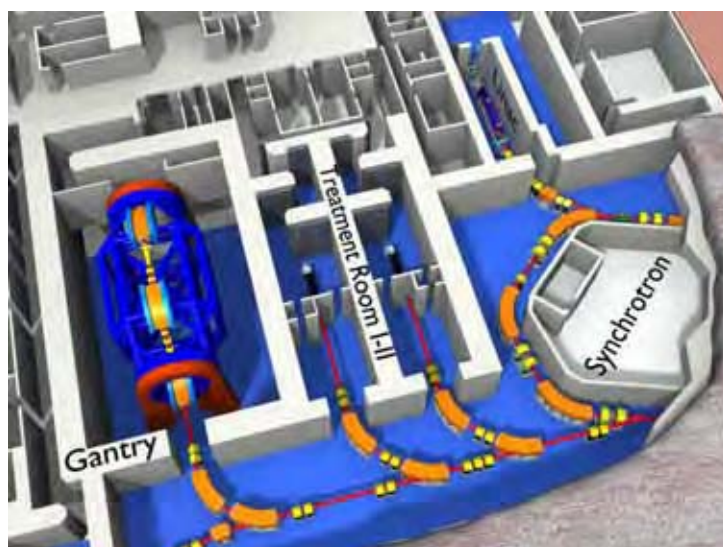
At HIT protons as well as helium ions, carbon ions and oxygen ions can be accelerated and delivered to the treatment chambers. The energies of the ions are adapted so that the maximum range in water is about 40 cm for protons and helium ions, 30 cm for carbon ions and 23 cm for oxygen ions. The beam parameters for HIT are *e.g.* $4 \cdot 10^{10}$ particles per pulse (ppp) for protons (220 MeV) or $1 \cdot 10^9$ ppp for carbon ions (430 MeV/u).

The shielding design was developed based on the Kurosawa neutron spectra for the 400 MeV/u carbon ions [16]. A line-of-sight model was developed to determine dose rates of the neutron radiation outside the shielding [47]. The model considers the angular dependence of the neutron production (0°-90°), the angular dependent neutron energy distribution ($E_n > 5$ MeV), the neutron energy dependent absorption (removal cross-section) and the build-up effect of the neutron radiation in matter. For angles greater than 90° relative to the incoming ion beam, the neutron source distribution at 90° was used. MC-based radiation transport calculations were also applied. For these computations the program FLUKA (version of the year 2000) was applied [37]. Also for the MC calculations the Kurosawa neutron spectra were used as input. FLUKA was applied for the H_1-H_2 geometry [48] as well as for the gantry geometry [49]. The results of the $H_{1/2}$ calculations are shown in Figure 8 (left) for carbon ion beams with energy 400 MeV/u and $3 \cdot 10^8$ ions/sec deposited in a graphite target [38]. For the gantry geometry calculations, the iron counterweight of 1 m thickness was taken into account, which attenuates the main neutron cone substantially in the angular range ±25° relative to the ion beam line.

In a later stage of the project the heavy ion version of FLUKA, including nucleus-nucleus collisions, was available [50]. Comparisons were performed with both calculation methods – one with the Kurosawa neutron source spectra as input for FLUKA and the other one with the complete FLUKA simulations – and results with reasonable agreement were obtained for the dose rate levels (deviations within 26%). The shield thickness in HIT was adapted to meet the annual dose limits of Germany given in Table 1. Furthermore the responsible authority for HIT gave the guideline to limit the dose rate levels outside the interlocked area particularly for 10 minute irradiation periods. The limit here is

3 µSv/h. The planning is based on assumptions on beam losses at local (specific) areas with about 10% of the beam intensity, *e.g.* at the beam extraction point and 10% beam losses in the beam deflection elements (dipoles). Due to the incomplete knowledge on the beam loss distributions in the synchrotron and the beam transfer lines, it was decided to install in cases of increased beam losses additional local shielding elements, *e.g.* a stack of concrete blocks. In HIT the radiological areas are defined as follows:

- All areas where the ion beam is transported are inaccessible.

- The adjacent therapy chambers are controlled areas.

- Other adjacent areas to the accelerator and therapy rooms are supervised areas.

- Accelerator areas with interrupted beam operation are controlled areas because of probable radioactive activation.

For the treatment rooms H_1, H_2 the crosswise shield walls (three per treatment unit) in the entrance maze have in the forward direction total thicknesses of 5.5 m, three steel layers (each 0.5 m) improve the shielding effect. The lateral shielding amounts to 2 m thickness. The building of the gantry room has a wall thickness of 2 m. The shielding effect is increased by an iron counterweight of 1 m thickness. Here the shielding calculations can take advantage of the fact that the main direction of the produced radiation varies according to the alternating irradiation position of the gantry (dose reduction factor of 10 at most, see also [51]). The roof shields (2 m) of the H_1-H_2 therapy rooms are also partially reinforced by steel layers (0.5 m). The synchrotron is shielded by a 1.5 m concrete wall and partially by soil layers on the outside area. It is expected that outside the building of the synchrotron the measurable dose rate will be negligible. Soil layers (and other bulk materials) cover the roof shield of the synchrotron and H_1, H_2 respectively as well as parts of the building for the gantry treatments. The thickness of the base plate ranges from 1.5 m to 1.8 m. The shield to the ground reduces the activation of soil and groundwater.

Conclusions

Radiation protection issues for particle therapy facilities are discussed in this work. The most important accelerator types are cyclotrons and synchrotrons, described in view of production of radiation levels during operation. Beam loss and deposition distributions determine the needs for the architectural shielding layouts. An overview for beam loss distributions is given for both accelerator types. Various kinds of beam-shaping systems (active, passive) are also discussed in terms of production of secondary radiation. The concept of radiological areas, prescribed in the radiation protection laws, is employed on particle therapy facilities. Examples for neutron source distributions are given with a particular emphasis on carbon ion beams. Comparisons are drawn for measured and calculated neutron source data. It turns out that measured sets of data are not consistent (Kurosawa, Gunzert-Marx) and also partly disagree with data of FLUKA Monte Carlo calculations (for 0° direction factor of 2 lower at 0.3 GeV for the Kurosawa data and for the 50°, 90° direction up to a factor 10 at 0.2-0.4 GeV for the data of Gunzert-Marx). On the basis of measured and computed neutron source data, shielding calculations are performed with two methods, the Monte Carlo transport calculations and the line-of-sight model with a focus on carbon ion beams. Examples for both types are given. An examination of shielding data for 400 MeV/u carbon ion beams was made for three sets of data (Agosteo, *et al.*, Ipe and GSI) for experimental and MC data obtained for the CONRAD measurement campaign. It was discovered that for the forward direction an overestimation of the dose for all three sets of data occurs (factor 13 at most), though there is a reasonable agreement for the larger angles. Improvements in the source data are especially necessary. A comparison of the shielding requirements for proton and carbon ion beams by reference to the HIT facility was drawn. The resulting dose distributions outside the shielding are similar in both cases. Finally, three examples for particle therapy facilities are described, the Loma Linda Proton Therapy Center, the HIMAC in Chiba operating with carbon ions and the Heidelberg Ion Therapy Center designed for particle beams in the range from protons to oxygen ions.

Acknowledgements

References

[1]   Castro, J., "Results of Heavy Ion Radiotherapy", *Radiat. Environ. Biophys.*, 34, 45-48 (1995).

[2]   Munzenrider, J., "Proton Therapy at Harvard", *Strahlentherapie*, 161, 756-763 (1985).

[3]   Schultz-Ertner, D., *et al.*, "Results of Carbon Ion Radiotherapy in 152 Patients", *Int. J. Radiat. Oncol. Biol. Phys.*, 58 (2), 631-640 (2004).

[4]   Haberer, Th., *et al.*, "Magnetic Scanning System for Heavy Ion Therapy", *Nucl. Instr. and Meth. in Phys. Res.*, A 330, 296-305 (1993).

[5]   Stichelbaut, F., T. Canon, Y. Jongen, "Shielding Studies for a Hadron Therapy Center", *Nucl. Tech.*, 168 (2009).

[6]   Kraft, G., "Tumor Therapy with Heavy Charged Particles", *Progr. in Part. and Nucl. Phys.* 45 (2000).

[7]   Klein, H., *et al.*, "New Superconducting Cyclotron Driven Scanning Proton Therapy Systems", *Nucl. Instr. and Meth. in Phys. Res.*, B 241, 721-726 (2005).

[8]   Still River Systems, *www.stillriversystems.com*.

[9]   Noda, K., *et al.*, "Development for New Carbon Cancer – Therapy Facility and Future Plan of HIMAC", *Proceedings of the 10th European Particle Accelerator Conference (EPAC 2006)*, Edinburgh, Scotland, 26-30 June 2006, 995-957.

[10]   Ipe, N.E., *et al.*, *Shielding Design and Radiation Safety of Charged Particle Therapy Facilities*, PTCOG Publications Report 1 (2010).

[11]   Chu, W.T., B.A. Ludewigt, T.R. Renner, "Instrumentation for Treatment of Cancer Using Proton and Light-ion Beams", *Rev. Sci. Instrum.*, 64, 2055-2122 (1993).

[12]   Japanese Radiation Protection Laws (JRPL), Law concerning prevention from radiation hazards due to radioisotopes, etc. (167), 10 June 1957 and as amended on June 2004.

[13]   Italian Radiation Protection Laws (IRPL), *Decreto legislativo del governo no. 230/1995 modificato dal 187/2000 e dal 241/2000* (in Italian).

[14]   German Radiation Protection Ordinance (GRPO), *Verordnung über den Schutz von Schäden durch ionisierende Strahlen, (Strahlenschutzverordnung – StrlSchV) vom 20. Juli 2001, zuletzt geändert durch die Artikel 2 der Gesetze vom 12 August 2005 (BGBl. I. S. 2364) und 1 September 2005 (BGBl. I. S. 2618)* (in German).

[15]   United States Nuclear Regulatory Commission (USNRC), "Standards for Protection Against Radiation 10CFR20", *Code of Federal Regulations* (2009).

[16]   Kurosawa, T., *et al.*, "Measurements of Secondary Neutrons Produced from Thick Targets Bombarded by High-energy Helium and Carbon Ions", *Nucl. Sc. and Eng.*, 132, 30-57 (1999).

[17]   Gunzert-Marx, K., *et al.*, "Double Differential Neutron Yields from Thick Targets Induced by Relativistic Carbon and Uranium Beams", *Proceedings of the International Workshop on Fast Neutron Detectors and Applications (FNDA2006)*, University of Cape Town, South Africa (2006), http://pos.sissa.it/archive/conferences/025/057/FNDA2006_057.pdf (accessed 22 September 2010).

[18]   Gunzert-Marx, K., *Nachweis leichter Fragmente aus Schwerionenreaktionen mit einem BaF$_2$-Teleskop-Detektor*, PhD Thesis, University of Darmstadt (2004).

[19]   Krämer, M., M. Scholz, "Treatment Planning for Heavy-ion Radiotherapy: Calculation and Optimization of Biologically Effective Dose", *Phys. Med. Biol.*, 45 3319-30 (2000).

[20]   Krämer, M., *et al.*, "Treatment Planning for Heavy-ion Radiotherapy: Physical Beam Model and Dose Optimization", *Phys. Med. Biol.*, 45 3299-317 (2000).

[21]   Porta, A., *et al.*, "Double-differential Spectra of Secondary Particles from Hadrons on Tissue Equivalent Targets", *Rad. Prot. Dos.*, 132 (1), 29-41 (2008).

[22]   Moyer, B.J., *University of California Radiation Laboratory Proton Synchrotron*, Rep. TID-7545, USAEC 38 (1957).

[23]   Agosteo, S., *et al.*, "Double Differential Distributions and Attenuation in Concrete for Neutrons Produced by 100-400 MeV Protons on Iron and Tissue Targets", *Nucl. Instr. and Meth. in Phys. Res.*, B 114, pp. 70-80 (1996).

[24]   Siebers, J.V., *Shielding Measurements for a 230 MeV Proton Beam*, PhD Thesis, University of Wisconsin-Madison (1990).

[25]   Tesch, K., "A Simple Estimation of the Lateral Shielding for Proton Accelerators in the Energy Range 50 to 1 000 MeV", *Rad. Prot. Dos.*, 11 (3), 165-172 (1985).

[26]   Agosteo, S., *et al.*, "Shielding Data for 100-250 MeV Proton Accelerators: Double Differential Neutron Distributions and Attenuation in Concrete", *Nucl. Instr. and Meth. in Phys. Res.*, B 265, 581-598 (2007).

[27]   Agosteo, S., *et al.*, "Shielding Data for 100-250 MeV Proton Accelerators: Attenuation of Secondary Radiation in Thick Iron and Concrete/Iron Shields", *Nucl. Instr. and Meth. in Phys. Res.*, B 266, 3406-3416 (2008).

[28]   Agosteo, S., "Radiation Protection at Medical Accelerators", *Rad. Prot. Dos.*, 96, pp. 393-406 (2001).

[29]   Agosteo, S., *et al.*, "Attenuation Curves in Concrete of Neutrons from 100 to 400 MeV Per Nucleon He, C, Ne, Ar, Fe and Xe Ions on Various Targets, *Nucl. Instr. and Meth. in Phys. Res.*, B217, 221-236 (2003).

[30]   Ipe, N.E., A. Fassò, "Preliminary Computational Models for Shielding Design of Particle Therapy Facilities", *Proceedings of the Workshop on Shielding Aspects of Accelerators, Targets and Irradiation Facilities (SATIF-8)*, 22-24 May 2006, Gyongbuk, Republic of Korea, OECD/NEA, Paris (2010).

[31]   Fehrenbacher, G., T. Radon, "Generation of Shielding Data for Neutron Radiation Produced by Heavy Ions", *Rad. Meas.*, DOI: 10.1016 (2010).

[32]   Fehrenbacher, G., T. Radon, "Shielding Data for 400 MeV/u Carbon Beams", forthcoming.

[33]   Rollet, S., *et al.*, "Intercomparison of Radiation Protection Devices in a High-energy Stray Neutron Field, Part 1: Monte Carlo Simulations", *Rad. Meas.*, 44, 649-659 (2009).

[34]   Wiegel, B., *et al.*, "Intercomparison of Radiation Protection Devices in a High-energy Stray Neutron Field, Part 2: Bonner Sphere Spectrometry", *Rad. Meas.*, 44, 660-672 (2009).

[35]   Silari, M., *et al.*, "Intercomparison of Radiation Protection Devices in a High-energy Stray Neutron Field, Part 3: Instrument Response", *Rad. Meas.*, 44, 660-672 (2009).

[36]   Waters, L.S., *MCNPX User's Manual*, Report TPO-E83-G-UG-X-00001, Los Alamos (1999).

[37]   Fassò, A., *et al.*, "FLUKA: New Developments in FLUKA, Modelling Hadronic and EM Interactions", *Proceedings of the 3rd Workshop on Simulating Accelerator Radiation Environments (SARE 3)*, KEK, Tsukuba, Japan, 7-9 May 1997, H. Hirayama (Ed.), KEK Proc. 97-5, 32-43.

[38] Fehrenbacher, G., F. Gutermuth, T. Radon, "Shielding Calculations for the Ion Therapy Facility HIT", *Annual Conference of the German-Swiss Association for Radiation Protection and 11th Workshop of Heavy Charged Particles in Biology and Medicine*, Heidelberg, 26-29 September 2007, IRPA Fachverband für Strahlenschutz, Switzerland/Germany, 33-36 (2007).

[39] Awschalom, M., *Radiation Shielding for 250 MeV Protons*, Fermi National Accelerator Laboratory, USA (1987).

[40] Hagan, W.K., *et al.*, "Radiation Shielding Calculations for a 70- to 350-MeV Proton Therapy Facility", *Nucl. Sci. and Eng.*, 98, 272-278 (1988).

[41] Cloth, P., *et al.*, *The KFA-version of the High-energy Transport Code HETC and the Generalized Evaluation Code SIMPEL*, Kernforschungsanlage Jülich Report Jul-Spez-196 (1983).

[42] Engle, W.A. Jr., *A User's Manual for ANISN, A One-dimensional discrete ordinates transport Code with Anisotropic Scattering*, USAEC report K-1963 (1967).

[43] Siebers, J.V., *et al.*, "Shielding Measurements for 230-MeV Protons", *Nucl. Sc. and Eng.*, 115, 13-23 (1993).

[44] Ban, S., *Shielding Study on High-energy Proton Synchrotron*, PhD Thesis, Faculty of Engineering, Kyoto University (1982).

[45] Debus, J., *Proposal for a Dedicated Ion Beam Facility for Cancer Therapy*, GSI, K.D. Groß, M. Pavlovic (Eds.) (1981).

[46] Heeg, P., H. Eickhoff, T. Haberer, "Die Konzeption der Heidelberger Ionentherapieanlage HICAT", *Z. Med. Phys.*, 14, 17-24 (2004).

[47] Fehrenbacher, G., F. Gutermuth, T. Radon, *Neutron Dose Assessments for the Shielding of the Planned Heavy Ion Cancer Therapy Facility in Heidelberg*, GSI Report 2001-05, GSI, Darmstadt, Germany (2001).

[48] Fehrenbacher, G., F. Gutermuth, T. Radon, *Calculation of Dose Rates Near the Horizontal Treatment Places of the Heavy Ion Therapy Clinic in Heidelberg by Means of Monte Carlo Methods*, GSI (2002), internal note (unpublished).

[49] Fehrenbacher, G., F. Gutermuth, T. Radon, *Estimation of Carbon-ion Caused Radiation Levels by Calculating the Transport of the Produced Neutrons Through Shielding Layers*, GSI Scientific Report 2001, 205 (2002).

[50] Fassò, A., *et al.*, *FLUKA: A Multi-particle Transport Code*, CERN-2005-10, INFN/TC_05/11, SLAC-R-773.

[51] Deutsches Institut für Normung e.V (DIV, German Technical Standards), *Medical Electron Accelerators – Part 2: Rules for Construction of Structural Radiation Protection*, DIN 6847-2, Berlin, September 2008.

Sandwich technology in radiation-shielded structures, Monte Carlo simulations and measurement

Reinhold Müller[1,2]**, Jan Forster**[3]**, Otto Pravida**[4]**, Jürgen Karg , Nils Achterberg**
[1]Radiation Oncology, University Hospital Erlangen, Germany
[2]Institute of Medical Physics, University Erlangen, Germany
[3]Forster Ingenieurgesellschaft, Ingolstadt, Germany
[4]Pravida Bau GmbH, Pressath, Germany

Abstract

To establish "sandwich" technology in radiation protection constructions new filling materials were fixed and their attenuation, stopping and moderation characteristics in relation to X-rays (6-25 MV), protons (150-600 MeV) and carbon ions (150-430 MeV/u) were checked by Monte Carlo simulations and even by direct measurements of transmitted dose at suitable sources.

Introduction

"Sandwich" technology for radiation protection construction has become a recognised technique for the shielding of linacs destined for medical use in Germany. The technology is vastly superior to *in situ* concrete. Use of this method reduces the time necessary for move-in readiness to less than half. The walls are immediately dry after being erected. Last, but not least, costs are significantly reduced.

Sandwich technology is suitable for all known radiation sources up to the highest energies which can be produced today. The most important component in this regard is the fluency and energy distribution of generated neutrons. Thus neutron attenuation capacity becomes the most important attribute of the radiation protecting material. In addition, long-term activation of the material must be avoided, *e.g.* no tracers such as natural Co and Cs. Measuring neutron attenuation in relation to protecting constructions makes large areas and thick layers necessary. So we decided to do this by installation of a special igloo with three windows in three directions in relation to the primary beam. The total mass which had to be installed and moved was about 240 t. The attenuation path length was up to 250 cm in different filling materials.

Figure 1: Principle of sandwich constructions with inner and outer double wall shells filled with concrete and in-between compacted filler materials of different kinds
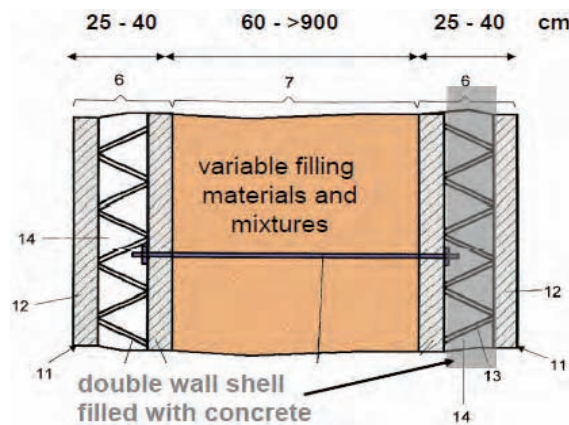
Figure 2: Isometry of the igloo for measurement of the neutron attenuation behind three windows in 0°, 45° and 90° direction in relation to the particle beam
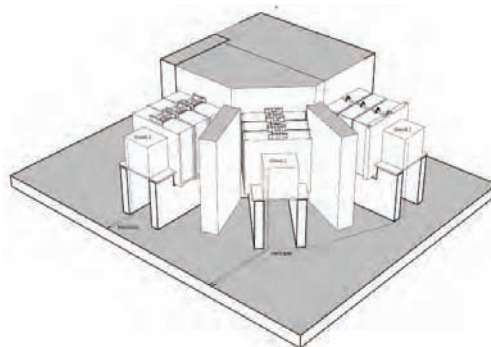
Monte Carlo simulation

Starting with linacs for medical use, MC simulation using EGS4 [8] was accomplished. For validation of the results of the MC model measurements were performed inside a treatment room of the Clinic for Radiation Oncology in Erlangen. Measured data were collected for three X-ray energies (6, 10 and 15 MV) and for about ten different materials. Measured and simulated data were identical for the

estimated errors with one exception for natural gypsum, where the measured data for the tenth value layer of area density [g/cm²], *e.g.* were about 10% worth than by simulation. Up to now no sensible reason for this discrepancy could be found besides the questionable purity and/or humidity of the material. Some results of our endeavours were introduced in the German regulations DIN 6847-2 [1]. Meanwhile more than 40 vaults were designed using our data. At that time MC simulations began for protons in use of radiation therapy up to 220 MeV. For the particle simulations we used GEANT4 [4].

Figure 3: Octagonal room design for measurement and MC simulation

Resulting neutron "volume dose" – absorbed energy per volume [J/cm³] – in arbitrary units colour coded. Left – 220 MeV protons, right – 430 MeV/u carbon ions after stopping in a graphite target. Incident point on the target plus half range at centre of the octagon. Wall construction in sandwich. Homogeneous wall for protons and 100 cm iron ore spallation layer for carbon ions.
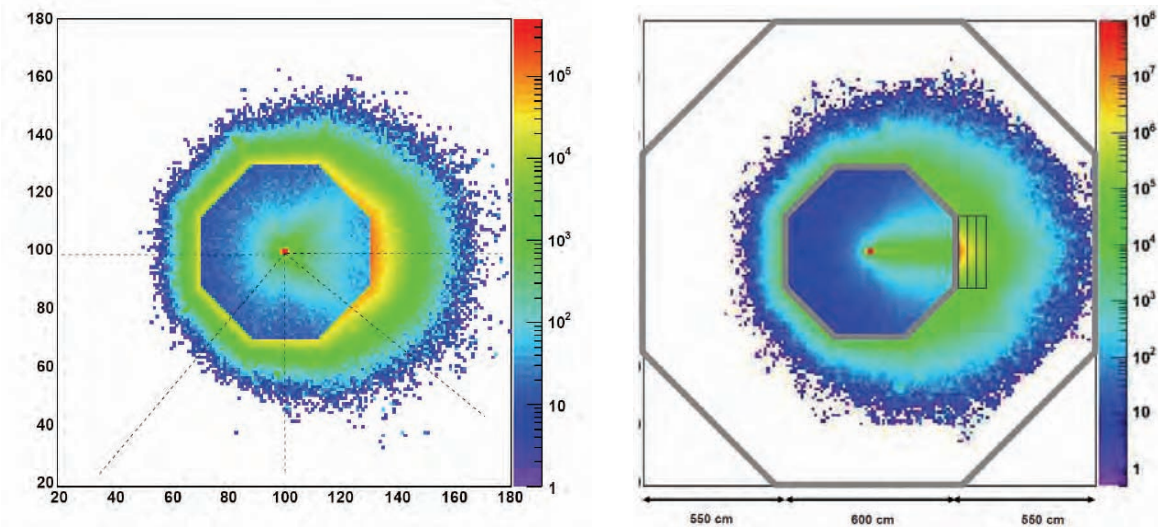
The results of simulation for protons and concrete were adopted in particular as a basis for the German regulation PAS 1078 [2]. Covering the demands of clinical use in addition, MC simulations and measurements for carbon ions became necessary. After realising the funding of the programme it could be started October 2008. In contrast to medical linacs the dose relevant component behind shielding for particle therapy is represented by secondary neutrons. Hence the effective dose becomes relevant for the purpose of radiation protection calculation. This makes a double convolution of the physical dose necessary. At first absorbed energy per volume will be calculated, than the neutron fluency and energy spectra must be calculated dependent on position inside and behind the wall. The neutron spectra will be convolved with the biological effectiveness. At the end effective dose H*(10) behind a shielding wall is resulting.

Because of the nearly logarithmic dependency of attenuation the slope of *e.g.* Figure 4 offers a good estimate for analytic radiation protection calculation passing MC simulations.

The absorbed energy per volume resulting from MC simulations can be transformed by a double convolution with the spectral distribution of the neutrons and with convenient conversion factors (see Figure 6.). There is an imperative necessity to reduce exposure of human to only one number and measure but one should always have in mind the problematic practice of doing so. The variation of measurements with different neutron dosimeter and the differences to simulated data may rise up in reality to 50% or even more.

Measurement

In contrast to the measurement with X-rays, particle measurement demands much larger operating and financial expenses. The measurement for protons and carbon ions were performed at GSI (Darmstadt, Germany). The material to be transported there was more than 240 tonnes. Fortunately we had the opportunity to get for each particle a time slot of two days minimum for measurement.

**Figure 4: Calculated effective dose H*(10) for 220 MeV
protons and a sandwich wall by double convolution**
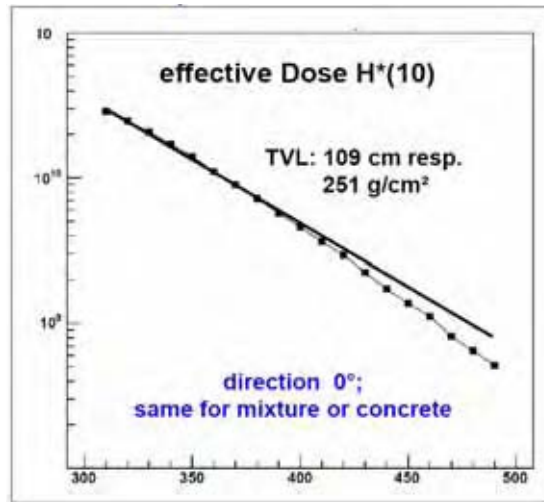
**Figure 5: Energy spectra of the neutrons generated by 430 MeV/u carbon ions
in a graphite target depending on different layers of shielding material; optimised
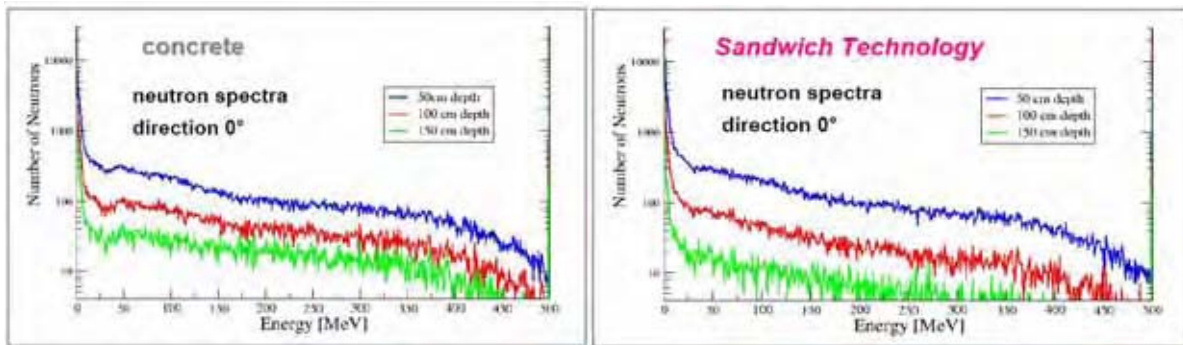mineral mixture of sandwich technology is obviously more effective than concrete**

**Figure 6: Neutron fluence-to-effective dose conversion coefficients according to ICRP 26 [5] and
ICRU 57 [6] from thermal up to 200 MeV; conversion factors above 200 MeV; see Thomas, *et al*. [7]**
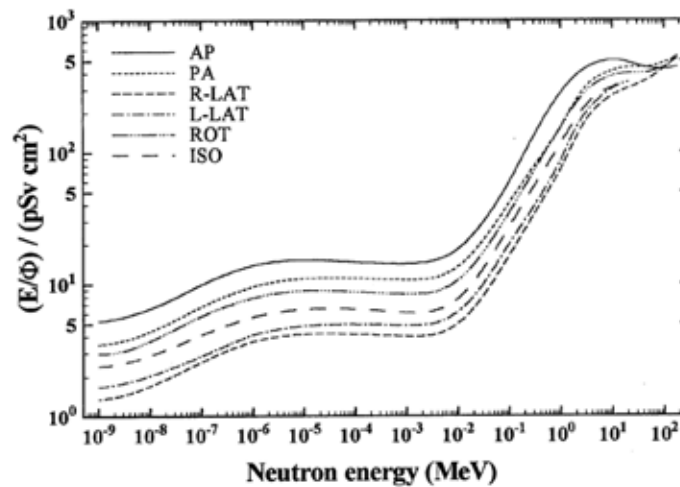
Figure 7: Sketch of the experimental setting

The igloo for measurement is a sector of the octagonal geometry. For reduction of the scattered neutrons we used concrete blocks of accurate size and thickness of 100 cm. The graphite target and particle beam were in the centre of the geometry. Depending on energy the line of neutron production could grow up to 90 cm. The material under test was placed outside the windows as blocks (concrete) or in wooden boxes (loose gravel). Dimension of the windows 160×160 cm^2.
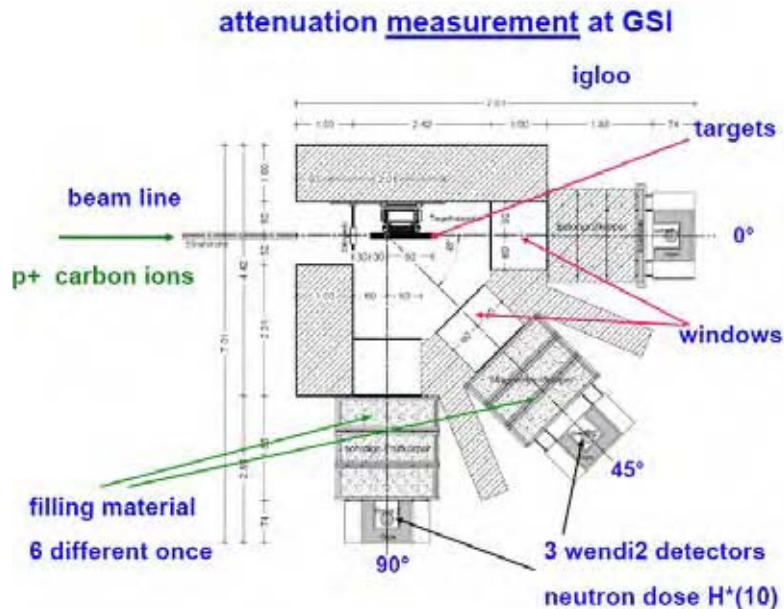
Figure 8: Real situation of the set-up in one cave at GSI (Darmstadt, Germany). The total mass which must be transported and inserted into the cave was about 240 t (igloo and testing materials).

The measuring sectors were separated with concrete side shields of 50 cm thickness. Each of the orange boxes contains a Wendi-2.

The measurement was performed in three angles (0°, 45° and 90°) at once using three Wendi-2 (ThermoFisher Scientific). Wendi-2 allows reading out one number for H*(10) for neutron spectra up to 1 GeV. For homogenising the field of scattered and back-scattered neutrons the Wendis were shielded on five sides with 20 cm gypsum and had one open window facing the target. In two runs per particle (protons and carbon ions) we measured the transmission of six different materials in five depths for four different energies (for each particle) in three directions.

Results

MC simulated and actually measured data are in good concordance. No systematic deviations exist. Figure 9 shows the excellent concordance between simulation and measurement in relation to the attenuation in concrete. Obviously the iron content of the slag EAS shows no benefit for this moderate neutron energies produced by protons. This changes using high-energy carbon ions. Then the spallation effect of high-Z material becomes obvious.

Figure 9: Transmission of neutrons generated by 220 MeV protons in a graphite target drawn for three materials: concrete (grey), electric arc slag EAS (German EOS) (green) and gypsum (beige). MC results for concrete are inserted as a light blue dashed line.

The abscissa is a real density in [g/cm^2]
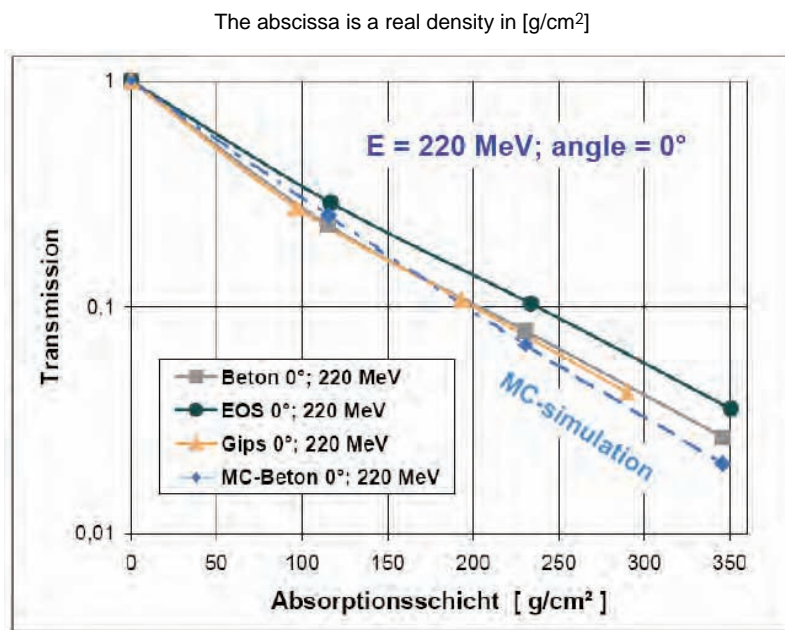
Figure 10: Measured effective dose H*(10) depending on proton energy and angle. Each energy and angle are without any absorber in the window. The MC simulation fits well to the measured normalised data.
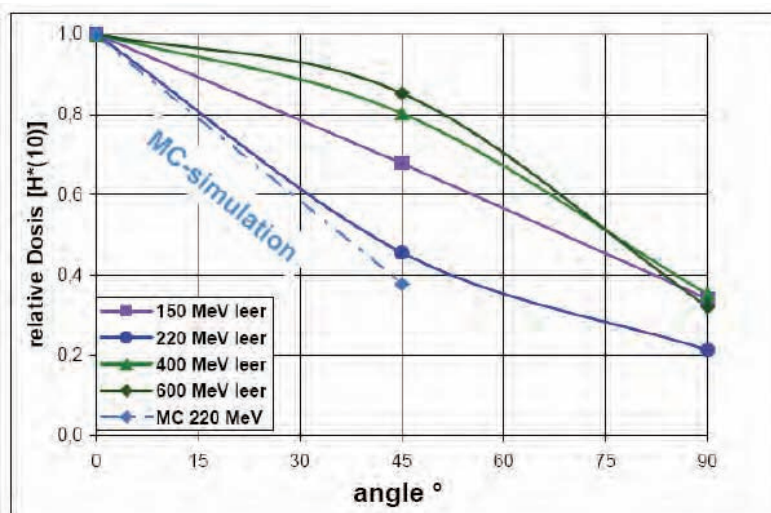
**Figure 11: Attenuation measurement for carbon ion
generated neutrons (150, 200, 300, 430 MeV) for six materials**

All data were fitted logarithmic. Evidently concrete, gypsum, limestone and asphalt are equally effective
and superior to EAS and iron ore. At the end of the wall or between the last two concrete blocks 5 cm of borax
(purple arrow and circle) reduce the neutron does by a factor of 8 independent of the primary particle energy.

Effective neutron dose H*(10) for carbon ions
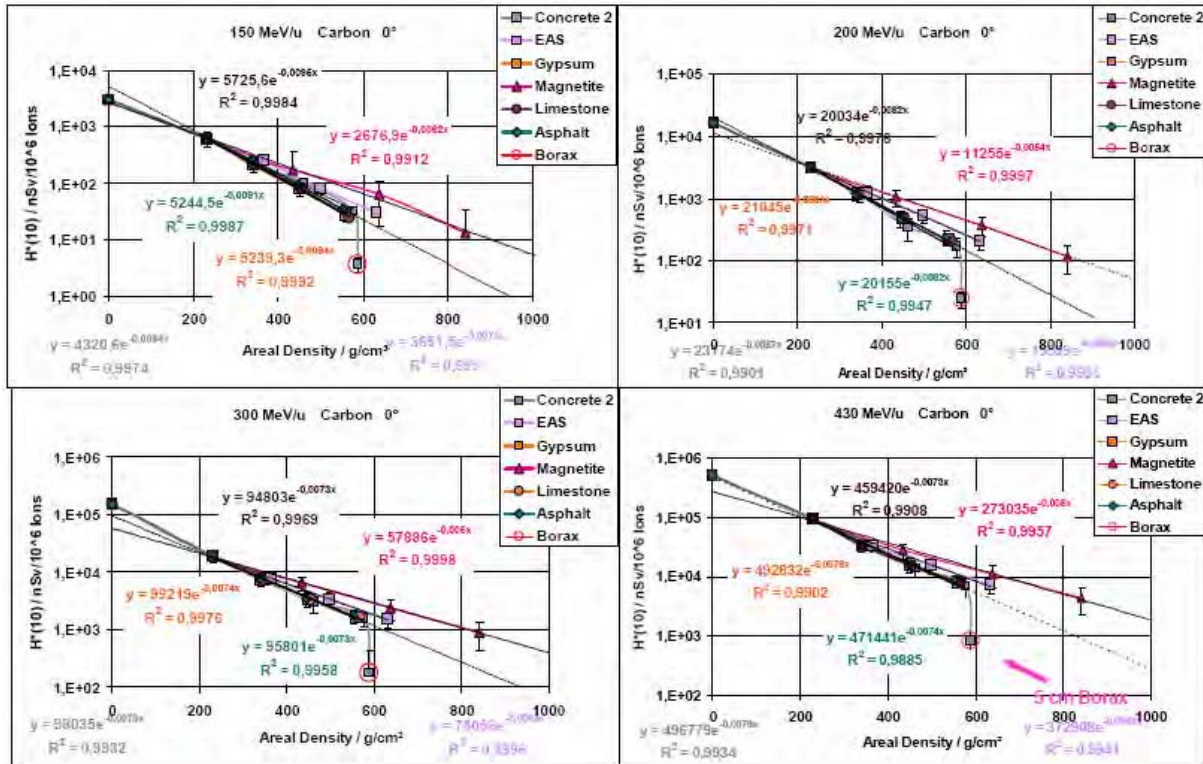
**Figure 12: Tenth value layers with respect to H*(10) for six materials for the
secondary neutron beam of carbon ion primary in the 0° forward direction**

The data are measured for four different energies. The uncertainty of the
concrete curve results from an instability of the beam diagnostic system.
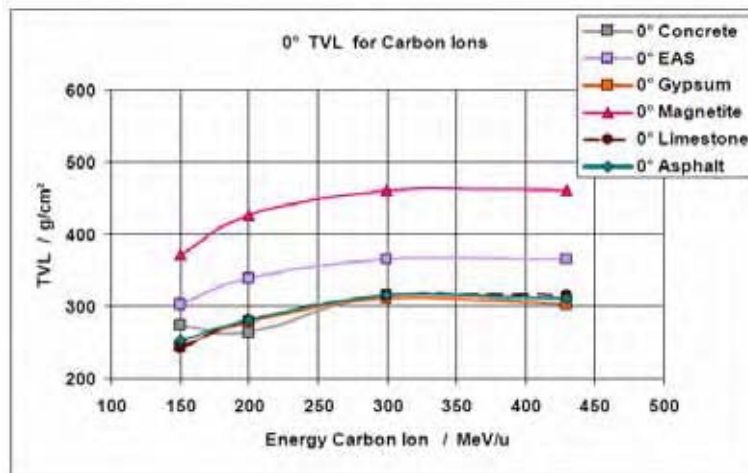
Constructive sandwich technology

This section elaborates on various solutions accomplished with sandwich technology. The material for stopping, spallation, moderation, attenuation and capturing is embedded and compacted between the constructive and static dimensioned concrete double-wall shields. Therefore there exist nearly no demands on consistency for the filling material. It would even be possible to insert tanks with liquid material. But dry gypsum for example contains more than 450 L water in one cubic meter and promises to act as ideal moderator for low- and medium-energy neutrons. The disadvantage of gypsum is the relatively low density. So in practice for the energy range of the particle therapy gypsum will be declassed by limestone, asphalt and concrete. Whilst for the attenuation of photons high-Z material and high density will be superior, low-Z hydrogen-rich material is preferable for moderation of neutrons with moderate energies. In practice we found a set of minerals which are equivalent to or better than concrete, cheap, available nearly everywhere, easy to handle and to become compacted, dry and easy to be mixed with each other. So in principle optimal materials or mixtures can be provided for each type of beams and energy distribution. For large-scale shielding of high-energy and high-intensity beam adaption with layers of different mixtures can be considered. The risk of long-term activation of the shielding materials usually exists when neutrons play a part. Activation tests must then be performed similarly to the tests of the concrete aggregates for low activation shielding.

**Figure 13: Left – erection of double wall shells for eight vaults
at once, right – closing of the bunkers and filling the walls**

**Figure 14: Basement for a huge bunker for a linac-based
material testing site, which will be completed with a linac CT**

Containers and complete cars will be tested there. The pit in the centre is necessary for the lower part of the CT-ring system.

Figure 15: Filling the walls and compacting the material. Using magnetite and EAS (electro arc slag) densities of the mixture up to 3,9 t/m^3 can be achieved.

Figure 16: Closing the house top with pre-cast concrete girders, which will also be filled with mineral aggregate

Acknowledgements

References

[1]   Deutsches Institut für Normung (DIN, German Institute for Standardization), *Medical Electron Accelerators – Rules for Construction of Structural Radiation Protection*, DIN 6847-2, DIN, Berlin (2008).

[2]   DIN, *Accelerator Systems for Proton Therapy – Rules for Construction of Structural Radiation Protection*, PAS 1078, DIN, Berlin (2008).

[3]   National Council on Radioprotection & Measurements (NCRP), Structural shielding design and evaluation for megavoltage X- and Gamma-Ray radiotherapy facilities, NCRP 151, Bethesda, Maryland, United States (2005).

[4]   Agostinelli, S., *et al.*, "GEANT4", *Nucl. Instrum. Methods*, A506, 250-303 (2003).

[5]   International Commission on Radiological Protection (ICRP), *Conversion Coefficients for Use in Radiological Protection Against External Radiation*, Publication 74, ICRP 26, Annals of ICRP, Pergamon Press (1997).

[6]   International Commission on Radiation Units and Measurements (ICRU), *Conversion Coefficients for Use in Radiological Protection Against External Radiation*, ICRU 57 (1998).

[7]   Thomas, R., *et al.*, *Fluence to Dose Equivalent Conversion Coefficients for Evaluation of Accelerator Radiation Environments*, LBNL-47423, Ernest Orlando Lawrence Berkeley National Laboratory (2001).

[8]   National Research Council Canada, *Distribution Area for egs4unix_3.0, Version 3.0 of the Unix System for EGS4* (web page), *www.irs.inms.nrc.ca/inms/irs/EGS4/get_egs4.html*.

Comparison of the German rule PAS1078 with MCNPX™ calculations

Wolfgang Dittrich
AREVA NP GmbH – PEPA-G
Erlangen, Germany

Abstract

The publicly-available German specification PAS1078 dating from January 2008 provides rules for the construction of structural radiation protection in the case of medical accelerator facilities for proton therapy. The major points of PAS1078 will be presented. Its method for the estimation of shielding thicknesses will be compared with the results of Monte Carlo calculations executed with MCNPX™. Especially, it is aimed at the comparison of the shielding curves for various energies, their angular dependency, and the proposed approximation method for scattering through mazes. The results provide suitable knowledge concerning the precision of the PAS1078.

Introduction

The publicly-available German specification PAS1078 [1] provides rules for the construction of structural radiation protection in the case of medical accelerator facilities for proton therapy which are licensed according to §11 of the German Radiation Protection Ordinance [2]. This specification was published in January 2008. Its use should enable a uniform assessment of suitable shielding thicknesses of standard construction materials following fixed equations, tables and figures. The basic content of this specification is presented here together with the results of some comparisons with MCNPX™ calculations.

The specification PAS1078 is valid for the construction of proton accelerator facilities for protons up to an energy of 300 MeV for medical irradiation treatment. The content of the PAS1078 specification follows the German norms DIN 6871-1 and 6871-2 [3,4] for shielding of PET accelerators.

The main topics are:

- Input data for the calculation:
  - legal limits;
  - requirements for proton accelerator facility rooms;
  - necessary information to be provided by the manufacturer and the future owner;
  - operational data;
  - presence factors for persons.
- Calculation:
  - neutron source strength and unshielded neutron dose rate;
  - general calculation scheme for bulk shielding;
  - transmission of neutrons through penetrations in walls;
  - transmission of neutrons through labyrinths;
  - radiation protection against radioactive substances generated due to neutron activation.

Input data for the calculation

The legal and regulatory limits for dose (or dose rate) depend on national law. They must be met and are not a point of dispute for the shielding physicist.

The requirements for rooms consist of the classification in different radiation protection areas following the mentioned regulatory limits, safety installations such as interlocks to enable a quick interruption of the proton beam in case of urgent need, warning signals and suitable control rooms with means to visually observe the dedicated irradiation room and appropriate means of communication.

The PAS1078 specification provides a listing of necessary inputs which the manufacturer and future owner of the accelerator facility shall provide for the radiation protection design like:

- maximum proton energy and current – for example 250 MeV and 500 nA;
- positions and magnitudes of beam losses;
- building drawings with indication of the radiation protection areas;
- kind and use of neighbouring rooms;
- anticipated operating modes, operating times, etc.

The specification requires the definition of a useful clinical operating model by providing details on the proton energies for shielding measures. The maximum proton current specified by the manufacturer and the possible beam directions shall be examined, as well as the net beam operating time caused by change of patients and the necessary preparation time, maintenance periods, etc.

The specification defines presence factors T for the expected presence of persons in protected areas independent of the real dwell time:

- $T = 1$ for work locations or occupationally exposed persons in controlled areas and for work locations and work places with permanent presence outside of the controlled areas (like offices, control rooms).

- $T = 0.3$ for traffic and passage ways outside the proton accelerator facility where no permanent presence of persons has to be expected (like streets, park areas).

- $T = 0.1$ outside of the controlled area but in the proton accelerator facility where a presence of less than 10% of the operation time of the accelerator is assumed (like floors, staircases, toilets).

Unshielded equivalent dose rate due to secondary neutrons

For the angle-dependent neutron flux per incident proton $\varphi(\theta)$ in $1/m^2$ at distance 1 m from the target, the specification provides the following approximation for all target materials of medium atomic number (like concrete, iron, copper):

$$\varphi(\theta) = 5000 * \frac{1 - e^{-3.6*\left(\frac{E}{E_0}\right)^{1.6}}}{\left(\frac{\theta}{\theta_0} + \frac{40}{\sqrt{\frac{E}{E_0}}}\right)^2}$$

where $\theta_0 = 1°$ and θ within $[0°;180°]$, $E_0 = 1\,000$ MeV.

Referring to ICRU-57 [5] the specification stipulates the flux-to-dose conversion factor for neutrons up to 300 MeV with the value $C = 4.0E{-}14$ Sv/(neutron/m^2) for a tissue depth of 1 cm.

Thus for an absorbed proton current I_0 in 1/s the equivalent dose rate $(dH/dt)_0$ in Sv/h at 1 m distance from the target is:

$$(dH/dt)_0 = 7.2 * 10^{-7} * I_0 * \frac{1 - e^{-3.6*\left(\frac{E}{E_0}\right)^{1.6}}}{\left(\frac{\theta}{\theta_0} + \frac{40}{\sqrt{\frac{E}{E_0}}}\right)^2}$$

For comparison with the code MCNPX™ in its version 2.5.0 [6] a very simple and relatively symmetric problem with target dimensions ensuring a total absorption of the protons was defined:

- A pencil beam of protons is vertically directed to the centre of the equator plane of a half-sphere of carbon, ordinary concrete, iron or copper.

- The radius of the half-sphere considers the proton energy meaning the Bragg peak is just inside the target.

- The secondary neutrons are counted by means of a spherical mesh tally at a distance of 1 m from the above-mentioned target point.

- Neutrons are counted only in the angle interval $[0°;90°]$.

The results for the proton energy 70 MeV are shown in Figure 1 and for the proton energy 300 MeV in Figure 2 for the four materials carbon (1.85 g/cm^3), ordinary concrete (3% water relative to dry mass acc. to DIN25413 Part 1 [7], 2.35 g/cm^3 in total), iron (7.86 g/cm^3) and copper (8.93 g/cm^3).

Figure 1: Total neutron flux produced by a 70 MeV proton beam directed onto a thick target at 1 m distance versus emission angle – comparison for various target materials with the approximation
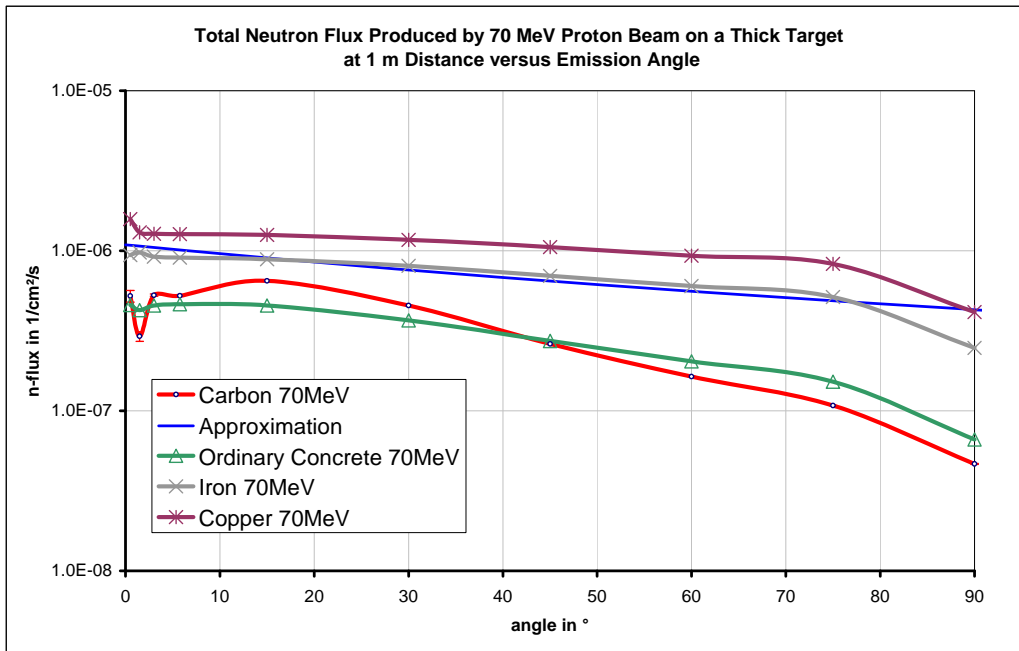
Figure 2: Total neutron flux produced by a 300 MeV proton beam directed onto a thick target at 1 m distance versus emission angle – comparison for various target materials with the approximation
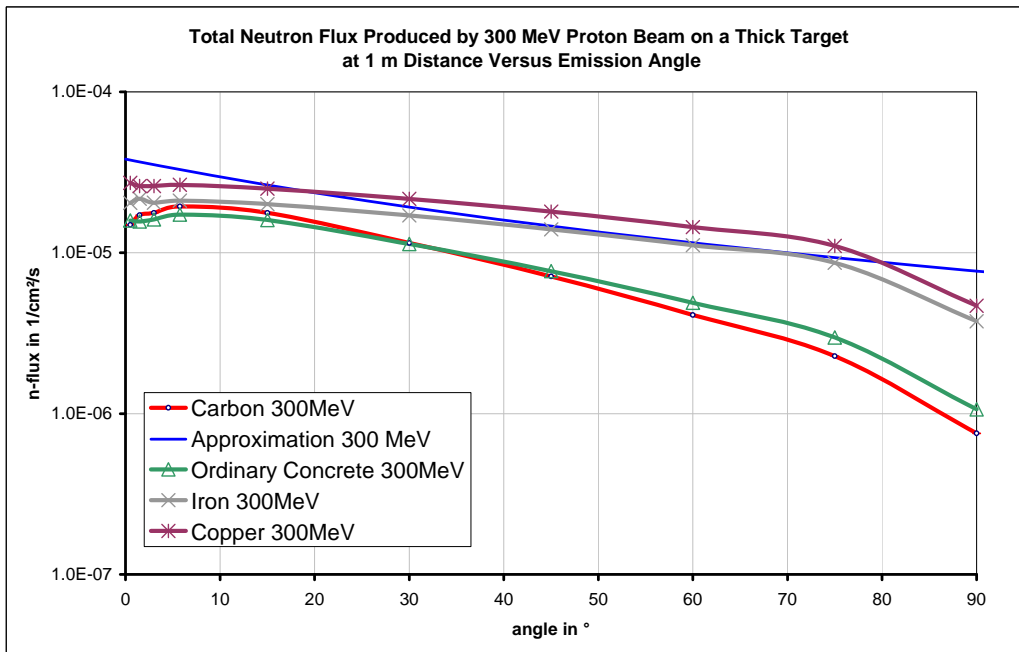
As one can see from the figures, the specification provides a fairly good approximation for the production of secondary neutrons and their angular dependency up to 90° from the forward direction in case of iron and copper with an uncertainty of about a factor 2. In case of two materials with much less density like carbon (as graphite) and ordinary concrete the deviation is larger but the specification provides a conservative result.

Bulk shielding

For the consideration of shielding walls the specification provides the following approximation for the neutron equivalent dose rate $(dH/dt)_i$ behind the shield:

$$\left(dH/dt\right)_i = \left(dH/dt\right)_0 * 10^{-\frac{x}{ZWD}} * \left(\frac{a_0}{a_i}\right)^{1.5}$$

where ZWD is a ten-fold length depending on the material, x is wall thickness, a_i is the distance from neutron source and a_0 is 1 m.

ZWD itself is approximated by considering the energy of the proton beam and the emission angle of the secondary neutrons relative to the beam direction as:

$$ZWD = ZWD_0 * \left(1 - 0.8 * e^{-4*\frac{E}{E_0}}\right) * f(\theta)$$

where ZWD_0 is ten-fold length based on protons with 1 000 MeV [ordinary concrete (2.35 g/cm³) 1.62 m, barite concrete (3.2 g/cm³) 1.39 m, iron (7.4 g/cm³) 0.82 m] and $f(\theta)$ is an angle correction term, with $f(\theta) = 1$ for θ within [0°;45°], $f(\theta) = 0.73$ for θ within [45°;90°], $f(\theta) = 0.49$ for θ within [90°;135°], $f(\theta) = 0.38$ for θ within [135°;180°].

The MCNPX™ model was generated based on that for the calculation of the angular dependency of the secondary neutron flux; a shielding shell with inner radius of 1 m around the target half-sphere was added. Carbon was used as a single target material which reflects the situation in case of a degrader in a cyclotron-driven irradiation centre; furthermore only neutrons for the forward direction and the emission angles 45° and 75° were regarded.

The comparison of calculation results with the approximation is presented in Figures 3 and 4 for ordinary concrete and in Figures 5 and 6 for barite concrete.

**Figure 3: Attenuation curve for bulk shielding made of ordinary concrete
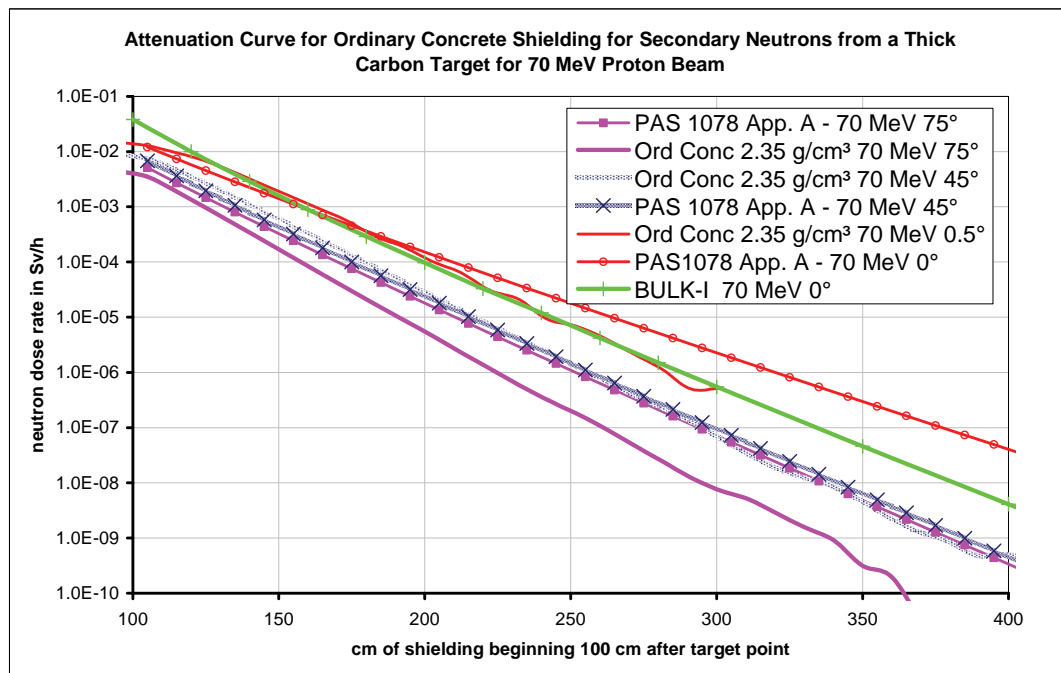for secondary neutrons from a thick carbon target hit by a 70 MeV proton beam**

Figure 4: Attenuation curve for bulk shielding made of ordinary concrete for secondary neutrons from a thick carbon target hit by a 300 MeV proton beam
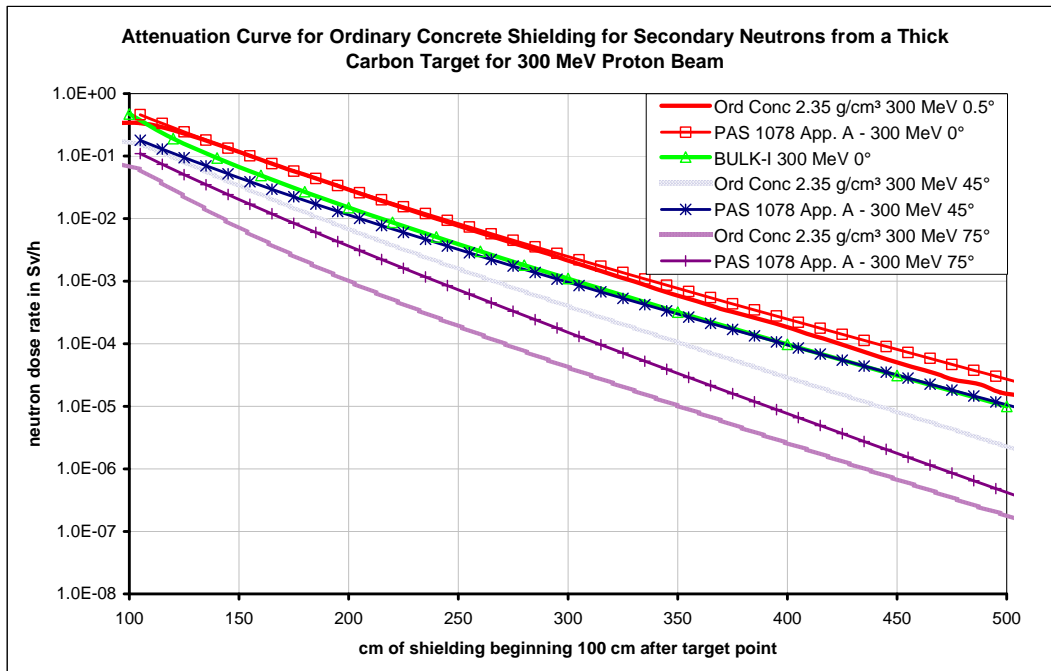

Figure 5: Attenuation curve for bulk shielding made of barite concrete for secondary neutrons from a thick carbon target hit by a 70 MeV proton beam
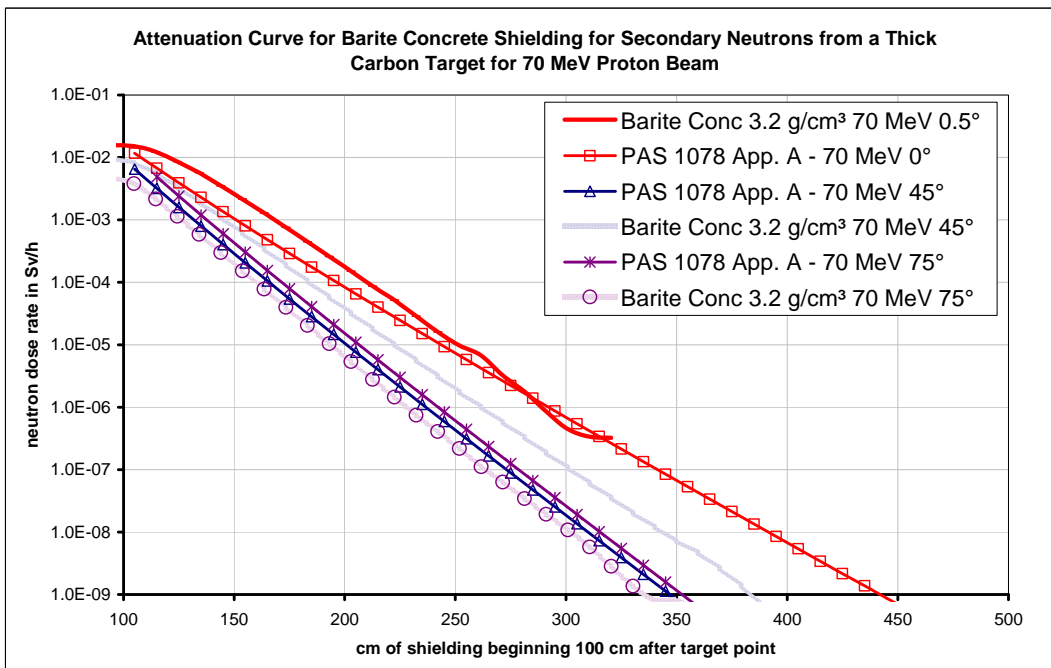
Figure 6: Attenuation curve for bulk shielding made of barite concrete for secondary neutrons from a thick carbon target hit by a 300 MeV proton beam
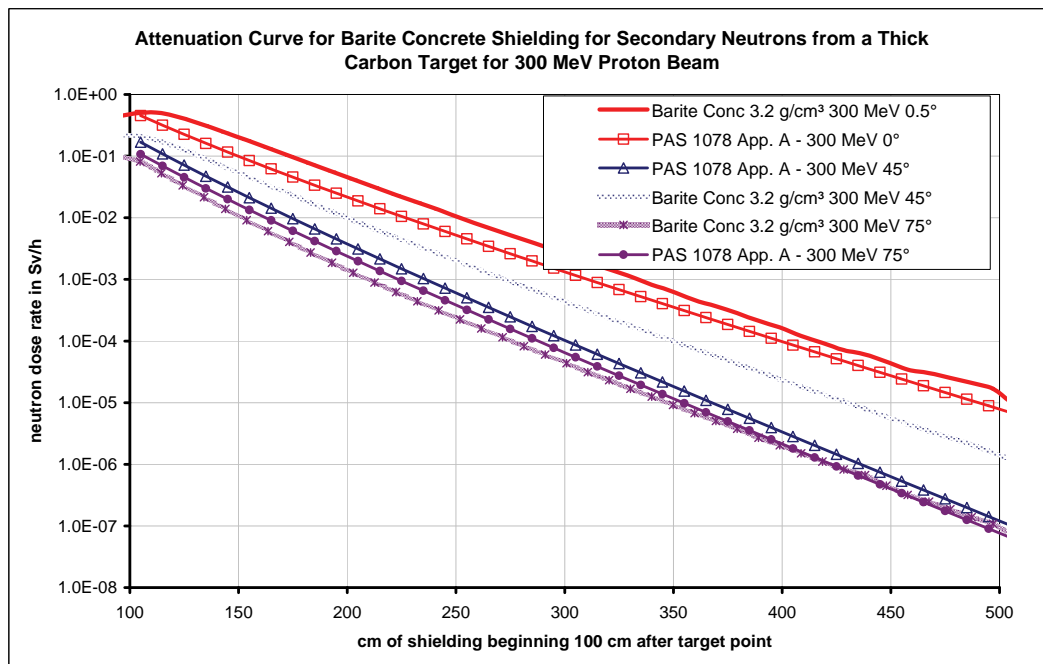
Obviously the shielding curves calculated according to the specification provide a good approximation for the shielding materials of ordinary concrete and barite concrete. Furthermore, for ordinary concrete – and the forward direction - the results of the EXCEL tool BULK-I [8] from Japanese colleagues were considered as well; the corresponding green curves are very close to our MCNPX™ results. For clarification it should be mentioned here that BULK-I is based on data originally calculated with an older version of MCNPX™.

In the case of iron, the attenuation curve according to PAS1078 cannot be confirmed: For this material the approximation deviates significantly from the MCNPX™ results as shown in Figure 7.

Because of the low value for the density of Fe given in the specification we suspected an error. Therefore we calculated an addition for a shield made of cast iron (typical data, ρ = 7.1 g/cm^3, 3.5% carbon content) getting results which are much closer to those according the specification. It is assumed that the specification means cast iron instead of steel; this assumption is supported by the material density chosen. Therefore it is recommended not to apply the specification for low carbon steel.

Penetrations and labyrinths in shielding walls

Penetrations

For the transmission of secondary neutrons through penetrations in lateral shields the specification gives the following approximation for the transmission factor TG_W (W = wall) between the dose rate before the penetration and that behind (see Figure 8):

$$TG_W = 10^{\left(\frac{\theta_m}{\theta_N}\sqrt{\frac{D}{\sqrt{A}}}\right)}$$

where θ_m is the maximum angle in degrees between the proton beam and the incident direction of the neutrons into the penetration, θ_N is an angle of 65°, D is the thickness of the bulk wall in m and A is the cross-section of the penetration in m^2.

This equation is recommended for $20° \leq \theta_m \leq 70°$, in case of $\theta_m < 20°$ it should be set equal to 20°, and for angles larger than 70° the penetration should be designed like a labyrinth.

Figure 7: Compared attenuation curves for bulk shielding made of iron (7.4 g/cm^3) and cast iron (7.1 g/cm^3, 3.5% C) for secondary neutrons from a thick carbon target hit by a proton beam
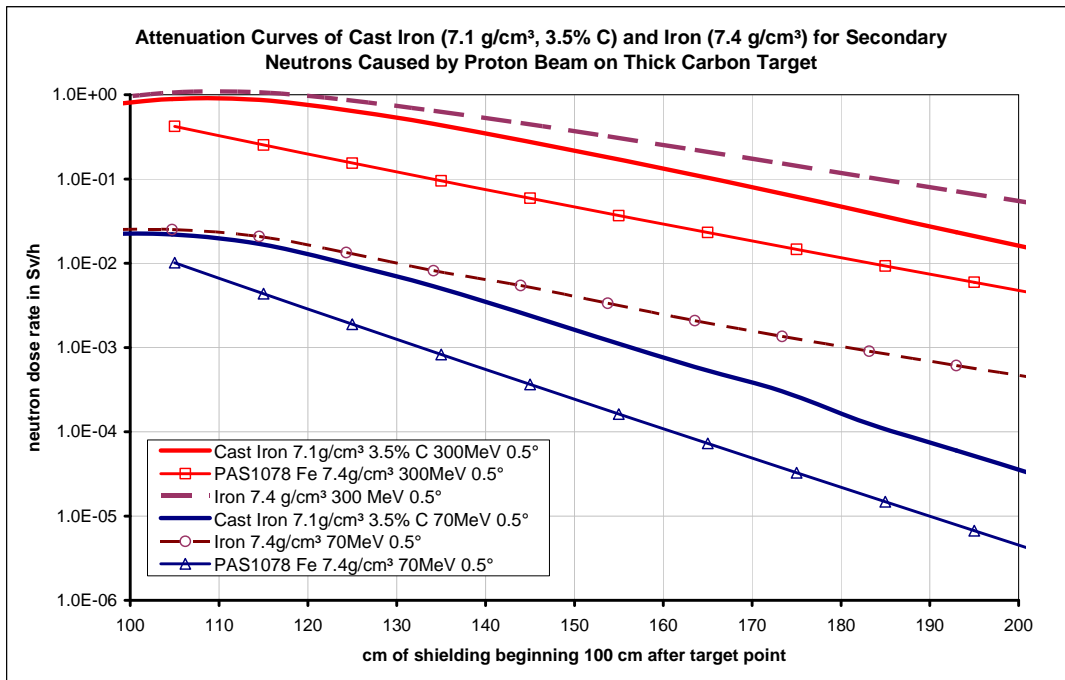
Figure 8: Sketch for the geometry model of the penetration case
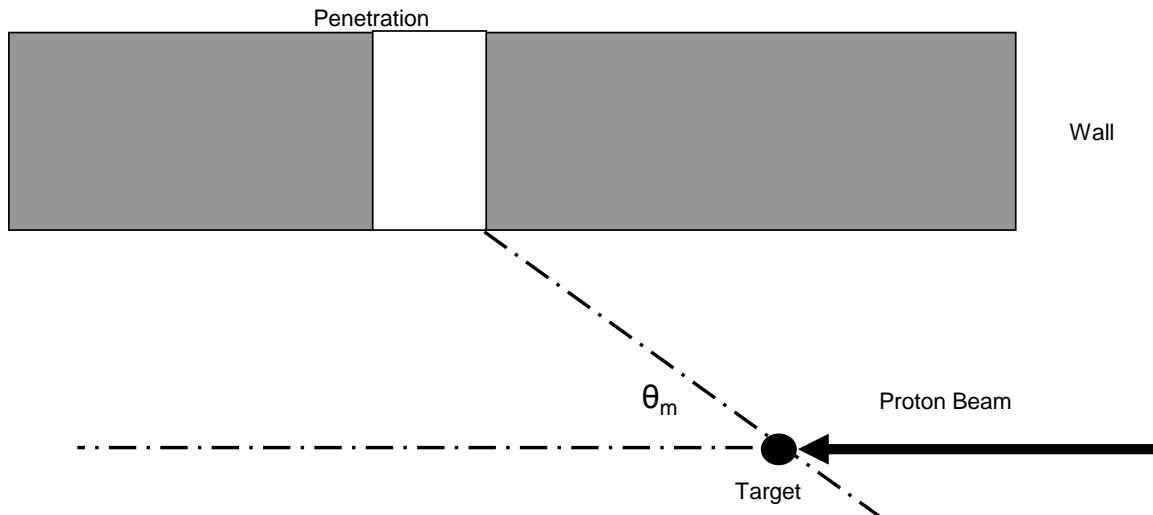
The model in Figure 8 was used to check the PAS1078 transmission approximation. The model consists of a slight modification of our geometry model for MCNPX™ described above replacing the bulk shield shaped as a half-sphere by a lateral wall (2 m thick) of ordinary concrete at 1 m distance from the proton beam. The results were evaluated by plotting a rectangular mesh tally along with the geometry; Figure 9 shows an example. Our comparison was restricted to a few cases for 300 MeV protons.

Results are plotted in Table 1 for one 30° case and three 45° cases. As can be seen the specification is generally not conservative for such problems.

Table 1

θ_m in °	$\dfrac{D}{\sqrt{A}}$	TG_W (PAS1078)	TG_W (MCNPX™)
30	10	2.0E-3	3.6E-3
45	5	2.9E-2	1.2E-2
45	10	3.4E-3	4.4E-3
45	20	1.7E-4	1.2E-3

Figure 9: Example for the mesh tally results of a penetration case

300 MeV protons, C target, 30° angle, 2 m wall, 11.3 cm radius of penetration
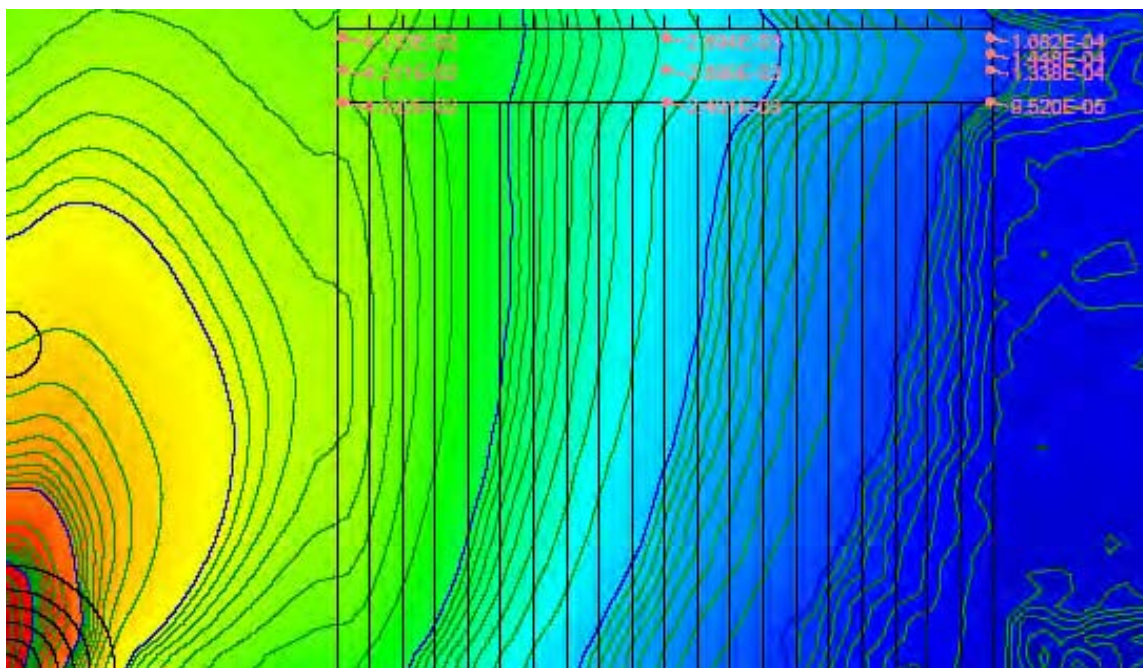
Scattering through labyrinths

In case of the scattering of radiation through a labyrinth the specification provides the following formula for the transmission factor TG_L (L = labyrinth) between the dose rate at the unshielded side of the labyrinth and that behind (see Figure 10):

$$TG_L = \frac{S^{n-1}}{L_1^2} * \frac{A_1}{A_n} * \prod_{i=2}^{n} \left(\frac{\sqrt{A_i}}{L_i} \right)^3$$

where S is 0.7 (neutron scattering albedo), A_i is a cross-section of the ith leg of the labyrinth and L_i is the length of the ith leg of the labyrinth.

For our comparison we simply applied the example in Annex C of the specification:

- $n = 3$;
- $A_1 = A_2 = A_3 = 4$ m²;
- $L_1 = 3$ m, $L_2 = L_3 = 4$ m.

Figure 10: Sketch for the geometry model of the labyrinth case
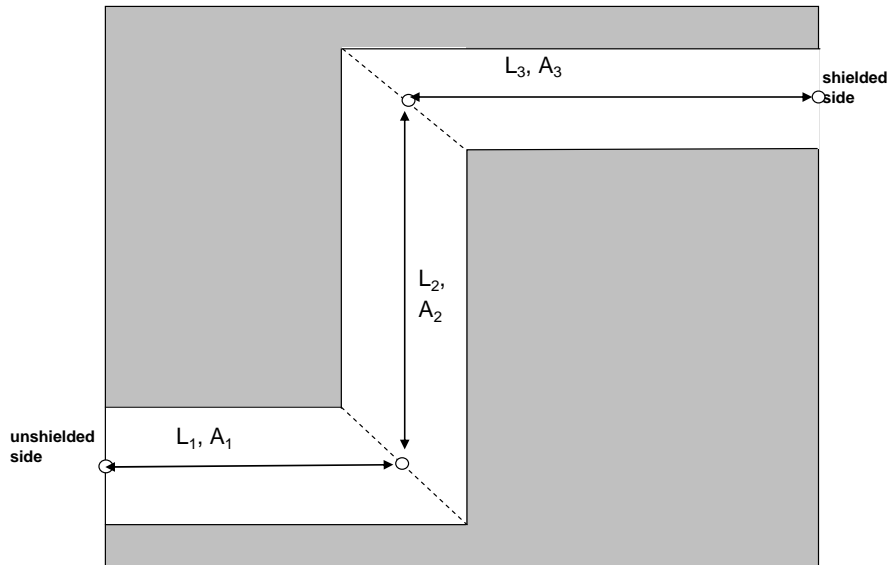
The front side of the labyrinth was put 1 m away from the point where the proton beam (300 MeV) touched the target in our half-sphere model. The thick wall of ordinary concrete was not considered in sampling the histories but a 30 cm layer on all sides of the labyrinth was inserted for the scatter process. As in the penetration case we evaluated the results by plotting a rectangular mesh tally together with the problem geometry, see Figure 11. Whereas the specification yields the value 8.5E-4 for the transmission factor TGL, the MCNPX™ calculation yields 2.2E-4.

Figure 11: Example for the mesh tally results of a labyrinth case
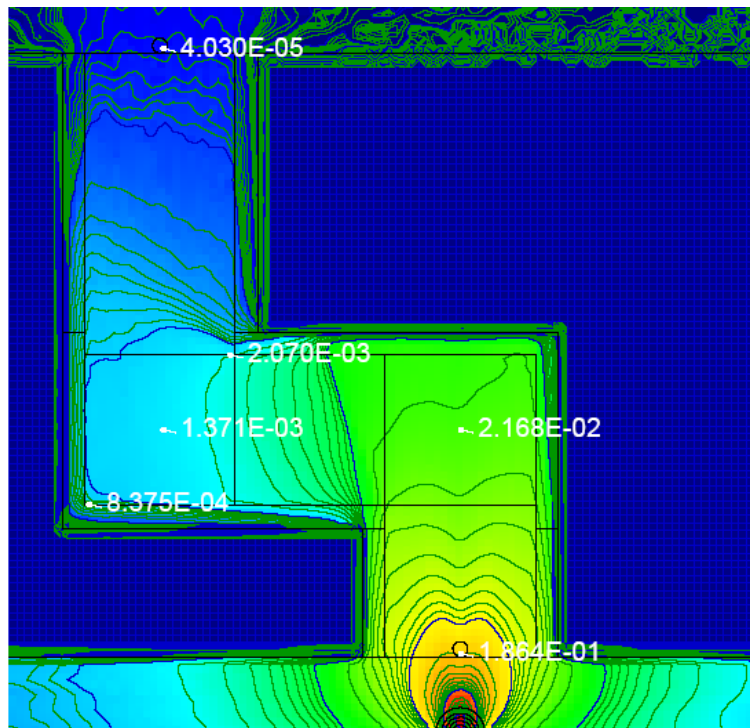
Conclusions

The German PAS1078 regulation provides suitable approximations for shielding of neutrons generated in the most common target materials and for bulk shielding in concrete and barite concrete. Its use for iron shields is not recommended. For labyrinths its approximation is sufficient for a preliminary layout, nevertheless it should be proven before design freeze. Proof by calculation seems vital for straight penetrations.

References

[1]   Deutsches Institut für Normung (DIN, German Institute for Standardization), Accelerator Systems for Proton Therapy – Rules for Construction of Structural Radiation Protection (Beschleunigeranlagen für die Protonentherapie – Regeln für die Auslegung des baulichen Strahlenschutzes), PAS1078, DIN, Germany, January 2008.

[2]   German Radiation Protection Ordinance (Strahlenschutzverordnung) from 2001-07-20 [BGBl. I S. 1714 (2002, 1459)], last change to article 2 § 3 section 31 of the law from 2005-09-01 (BGBl. I S. 2618).

[3]   DIN, Cyclotron Systems for Positron Emission Tomography, Part 1 Requirements for Constructional Radiation Protection (Zyklotron-Anlagen für die Positronen-Emissions-Tomographie, Anforderungen an den baulichen Strahlenschutz), DIN 6871, DIN, Germany, February 2003.

[4]   DIN, Cyclotron Systems for Positron Emission Tomography, Part 2 Radiation Protection Labyrinths and Wall Entrances (Zyklotron-Anlagen für die Positronen-Emissions-Tomographie, Strahlenschutzlabyrinthe und Wanddurchführungen), DIN 6871, DIN, Germany, February 2005.

[5]   International Commission on Radiation Units and Measurements (ICRU), *Conversion Coefficients for use in Radiological Protection Against External Radiation*, ICRU-Report 57, International Commission on Radiation Units and Measurements, Bethesda, MD, United States (1998).

[6]   Pelowitz, D.B. (Ed.), *MCNPX™ User's Manual Version 2.5.0*, LA-CP-05-0369, Los Alamos National Laboratory, United States., April 2005.

[7]   DIN, Classification of Shielding Concretes by Proportion of Elements, Part 1 Neutron Shielding (Klassifikation von Abschirmbetonen nach Elementanteilen, Abschirmung von Neutronen-strahlung), DIN 25413, DIN, Germany, July 1991.

[8]   Tayama, R., K. Hayashi, H. Hirayama, *BULK-I Radiation Shielding Tool for Proton Accelerator Facilities*, KEK (2004), *http://rcww.kek.jp/rc_en.html*; see also NEA Databank, Package ID NEA-1727/01, *www.nea.fr/abs/html/nea-1771.html*.

Shielding design for ETOILE hadron therapy centre

Frédéric Stichelbaut, Yves Jongen
Ion Beam Applications, S.A. (IBA)
Louvain-La-Neuve, Belgium

Abstract

The Ion Beam Applications Company is developing a compact superconducting cyclotron for hadron therapy able to deliver various ion beams with an energy of 400 MeV per nucleon and proton beams with an energy of 260 MeV. This system is being proposed to equip ETOILE hadron therapy centre in Lyon. Shielding design based on PHITS and MCNPX Monte Carlo simulation codes is presented, together with some performance figures for the energy degrader.

Introduction

The Ion Beam Applications (IBA) Company works on the development of a superconducting cyclotron called the C400 [1]. Devoted to cancer therapy, it will be able to deliver ion beams of different species with a maximal energy of 400 MeV per nucleon (MeV/u) and proton beams with an energy of 260 MeV. The beams are extracted from the cyclotron with fixed energy and energy modulation is performed by a graphite degrader located at the exit of the cyclotron.

The prototype of this machine will be installed in the Advanced Resource Centre for Hadrontherapy in Europe (ARCHADE), located on the ground of GANIL centre in Caen, France. This centre will only be equipped with fixed beam lines and will be limited to the use of ^{12}C ion and proton beams [2]. The IBA system is also proposed to equip the ETOILE centre in Lyon, France. This centre will consists of one cyclotron room and four treatment rooms, two being equipped with fixed beam lines and the other two containing a 360° rotating gantry (one for ion beams and one for proton beams exclusively). The C400 will be configured to accelerate ^{1}H, ^{4}He, ^{6}Li, ^{10}B and ^{12}C beams.

Radioprotection studies are performed to evaluate the shielding requirements around the various rooms for all possible beam usages. Interactions of the primary beams with the beam transport system and the patients are simulated using the PHITS Monte Carlo (MC) code [3]. Predictions of PHITS on the generation of secondary neutrons by ^{4}He and ^{12}C ion beams stopping in thick target are benchmarked against HIMAC measured data [4,5]. The generation of secondary charged particles due to the nuclear fragmentation of the primary ions is also evaluated with PHITS. The transport of the secondary neutrons, protons and light fragments is performed in a complete modelling of ETOILE using the MCNPX 2.5.0 code [6].

A detailed study of the performance of the Energy Selection System (ESS) is achieved using PHITS and MCNPX. The energy degrader represents the major source of radiation in the cyclotron room and the evaluation of the ESS transmission efficiency between the cyclotron and the treatment rooms is required to determine the beam intensities needed at the cyclotron exit.

The production of secondary particles by primary ions stopping in thick targets is also described, as are properties of the energy selection system. The design of the ETOILE shielding is discussed, and the presentation ends with a validation of this study though the attempt to reproduce the results obtained in the GSI Cave A experiment.

Secondary particle yields

In hadron therapy facilities, many secondary particles are created from nucleus-nucleus interactions in the various elements of the beam generation and beam transport system as well as in the final beam absorbers such as water phantom or patient. Secondary neutrons represent the major contribution to the ambient dose equivalent but secondary charged particles with larger range than the primary ions are also generated. These charged hadrons are rapidly absorbed in the shielding walls but provide an additional contribution to the neutron fluxes.

Secondary neutrons and photons

The emission of secondary neutrons and photons by high-energy ion beams stopping in thick targets is evaluated using the PHITS code [3]. The neutron angular and energy distributions obtained for ^{12}C and ^{4}He ions stopping in graphite are compared to experimental data obtained at HIMAC and published in [4,5]. Figure 1(a) shows the angular distribution of secondary neutrons produced by 400 MeV/u ^{12}C ions stopping in a graphite target. Very good agreement between measured data and PHITS predictions is obtained, except in the very forward region where the simulation underestimates the neutron yield by a factor of ~3. A similar underestimation is obtained for 180 MeV/u ^{4}He ions stopping in graphite as displayed in Figure 1(b) but extends up to 30°.

This underestimation by PHITS of the neutron yield in the forward region is also clearly visible on the neutron energy spectra obtained for specific polar angles and represented in Figure 2. For ^{12}C ions, the agreement between PHITS and the HIMAC data is excellent for all angles except for Θ = 0°. For

Figure 1: Angular distribution for: (a) 400 MeV/u ^{12}C ions and (b) 180 MeV/u ^{4}He ions stopping in graphite target. Only neutrons with energy above 5 MeV are considered.
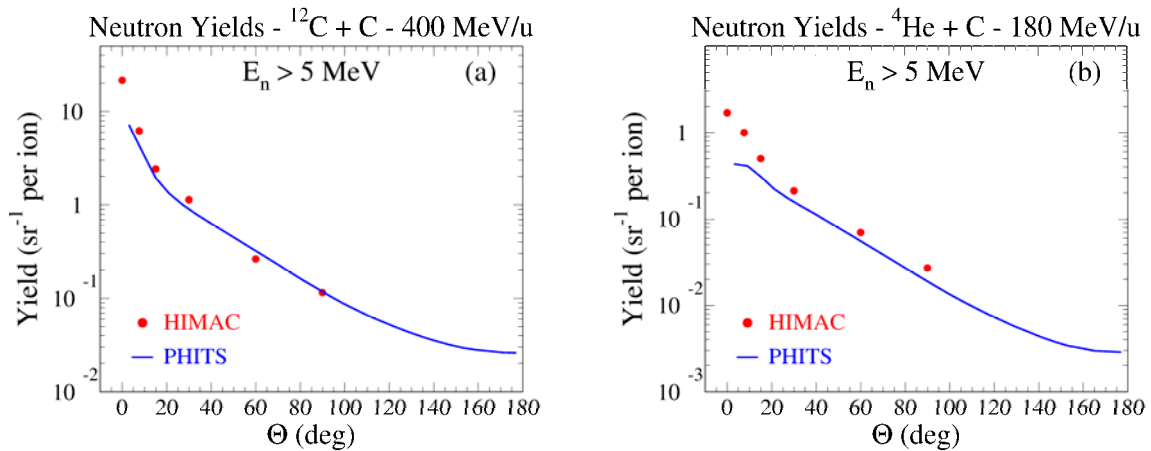
Figure 2: Comparison of the neutron doubly differential thick-target yields calculated with PHITS and the HIMAC data obtained for: (a-f) 400 MeV/u ^{12}C ions and (g-l) 180 MeV/u ^{4}He ions stopping in graphite
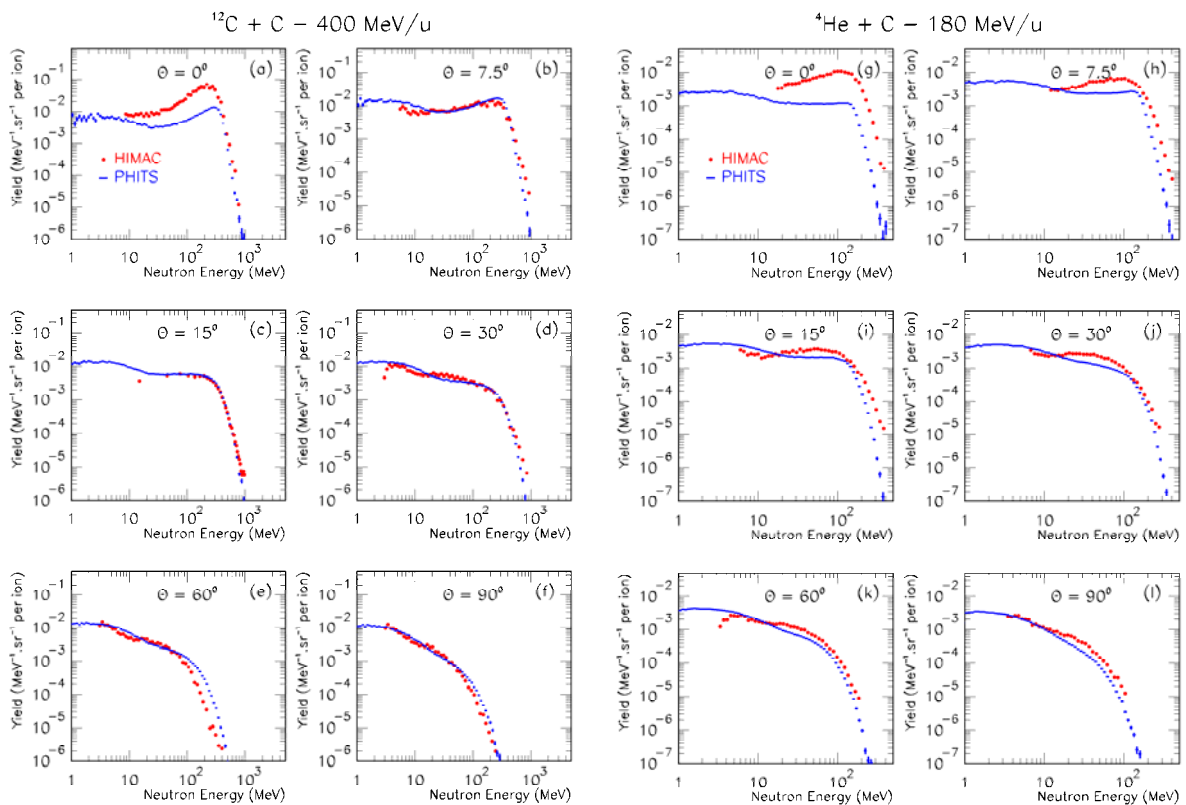
$\Theta = 60°$, PHITS predictions seem to overestimate the emission yield of neutron above 100 MeV. In the case of ^{4}He ions, PHITS underestimates the neutron high-energy tail for $\Theta = 0°$, 7.5° and 15°. A better agreement is obtained for polar angles between 30° and 90°.

Production of secondary photons is also estimated using PHITS. However, their contribution to the ambient dose equivalent obtained outside ETOILE shielding reveals to be very small, usually below 2%. This contribution to the total ambient dose equivalent can thus be neglected.

Secondary charged particles

In addition to neutral particles, the nuclear fragmentation of projectile ions leads to the emission of charged particles with substantial energy. These fragments can exhibit a larger range than the primary ion and be able to leave the thick absorber. Figure 3(a) compares the yield of secondary neutrons with the one of protons, deuteron and ^{4}He ions emitted from ^{12}C ions stopping in a 40 cm thick water absorber. For the maximal energy of 400 MeV/u, the proton yield reaches about half the value of the neutron yield. The yields for ^{2}H and ^{4}He remain about one order of magnitude smaller than the neutron yield. As can be seen in Figure 3(b), these charged fragments are strongly peaked in the forward region, the probability of finding a charged ion emitted at large angle decreasing rapidly with the ion mass.

The charged particles leaving the beam absorber will stop in the concrete walls of the treatment rooms, generating an additional contribution to the neutron flux coming directly from the absorber. We checked that this contribution remains below 10% in all cases.

Figure 3: Properties of secondary charged particles emitted by ^{12}C ions stopping in thick water absorber: (a) evolution of particle multiplicity as a function of beam energy; (b) angular distributions of charged particles for 400 MeV/u ^{12}C ions
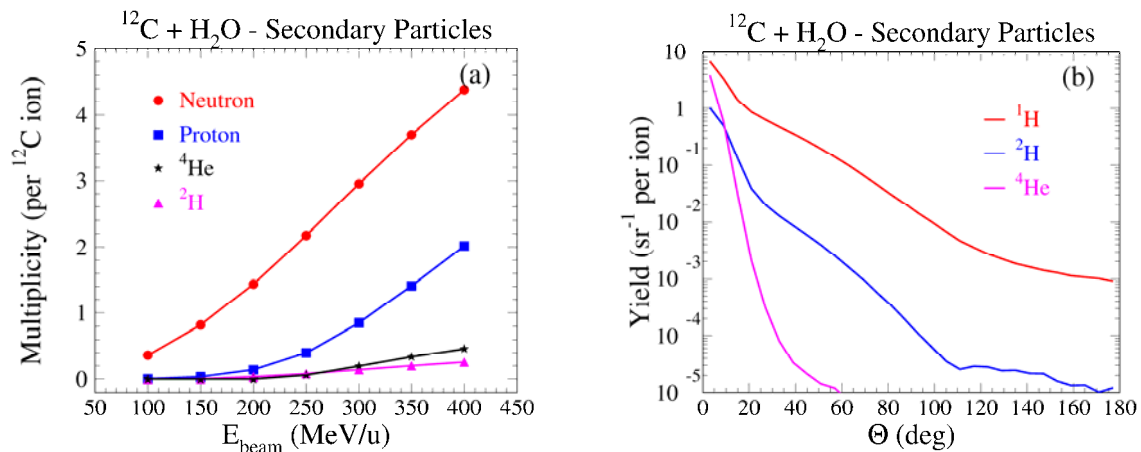
Source term determination

Angular and energy distributions of secondary neutrons, photons, protons, ^{2}H and ^{4}He ions are determined for all potential ions foreseen in ETOILE with energies ranging from 100 to 400 MeV/u and stopping in C, Cu and water. To take into account the large anisotropy of secondary particle emission during hadron-nucleus interactions, doubly differential yields are computed in 30 equal-width intervals in polar angle Θ. Comparisons of the neutron thick target yields (TTY) obtained for different ion species and different targets indicate some dependence on the atomic mass of the target, the TTY increasing significantly between water and copper targets. However, these differences vanish for neutrons with an energy above 20 MeV as these neutrons are mostly due to the fragmentation of the primary ions and not the evaporation of the target nuclei. The choice of beam absorber in the treatment room is thus irrelevant as the ambient dose equivalent obtained behind thick shielding walls is due to these high-energy neutrons and not the evaporation neutrons below 20 MeV.

The Energy Selection System

Beams are extracted from the cyclotron with a maximal energy of 400 MeV/u for the ions and 260 MeV for the protons. An Energy Selection System (ESS) is required to modulate the beam energy between 100 MeV/u and 400 MeV/u for ions, between 70 MeV and 260 MeV for protons.

The ESS is installed at the exit of the cyclotron. It comprises a graphite degrader followed by collimators used to limit the angular divergence and the energy spread of the transmitted beam. As the primary beams are always striking the energy degrader with their maximal energy, this element

represents the major source of radiation inside the cyclotron room. Figure 4 shows the variation of secondary particle yields as a function of transmitted beam energy in the case of primary ^{12}C ions. As in the case of a thick absorber, the proton yield is about one-half of the neutron yield while the ^{4}He yield represents about one-tenth of it. The production yield of ions with atomic number Z = 3 to 5 is further decreased by one order of magnitude compared to Z = 1-2 ions.

Figure 4: Yields of secondary particles emitted by 400 MeV/u ^{12}C ions traversing the graphite degrader: (a) secondary neutrons and protons; (b) secondary ions
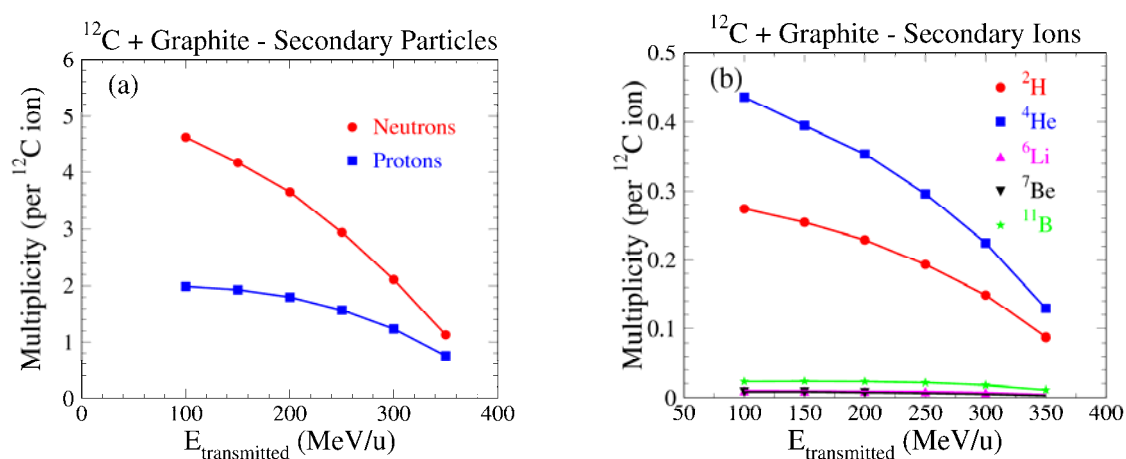
A fraction of these charged particles will be transported by the beam line together with the primary ion beam and will be able to reach the patient. However, as these particles are generated by the primary ion fragmentation, they exhibit much broader angular and energy spectra than the transmitted ions. As a consequence, the collimators disposed after the graphite degrader significantly reduce the yields of fragments transported to the end of the ESS. As shown in Figure 5, the ^{4}He yield transmitted by the ESS remains smaller than $3 \cdot 10^{-4}$ per transmitted ^{12}C ion whatever transmission energy is considered. The contribution from these parasitic ions to the dose delivered to the patient is thus totally negligible. This result demonstrates that the use of a cyclotron coupled to an energy degrader presents absolutely no drawback compared to a solution based on a synchrotron accelerator [7].

Figure 5: Evolution of the yield of secondary ions transmitted by the ESS to the patient as a function of transmitted ^{12}C beam energy
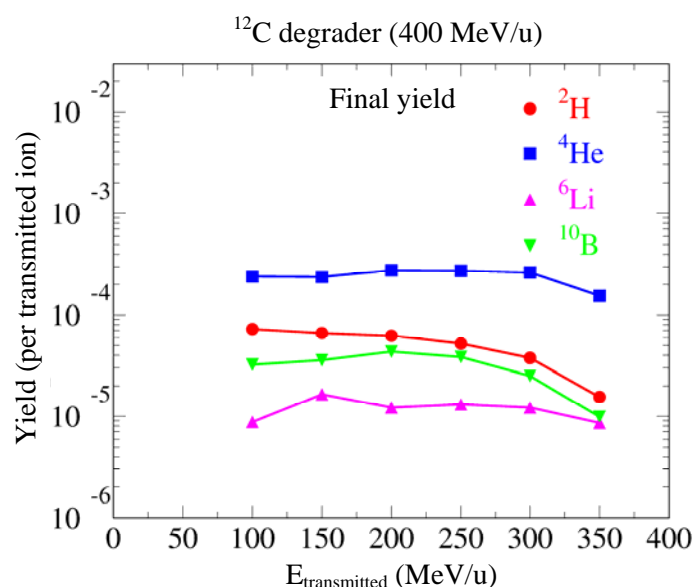
The ESS transmission efficiency is evaluated using PHITS and MCNPX. It is the product of three factors:

1) the degrader raw transmission, taking into account the beam losses due to the interactions of the primary beam with the degrader;

2) the transmission efficiency of the collimator used to limit the beam angular divergence below 12 mrad;

3) the transmission efficiency of the energy slits allowing the limitation of the beam energy spread $\Delta E/E$ below 0.6%.

The evolution of the ESS transmission efficiency as a function of the transmitted energy is shown in Figure 6 for the four ion species produced by the C400 cyclotron. For ^{12}C beams, the transmission efficiency decreases to 2.3% for the lowest transmitted energy of 100 MeV/u. The transmission efficiency becomes worse for the lighter ions, mainly because of the increase of the angular divergence. The use of MCNPX and PHITS to estimate these transmission efficiencies leads to very similar results.

Figure 6: Variation of ESS transmission efficiency as a function of beam transmitted energy for the various ions produced by the C400
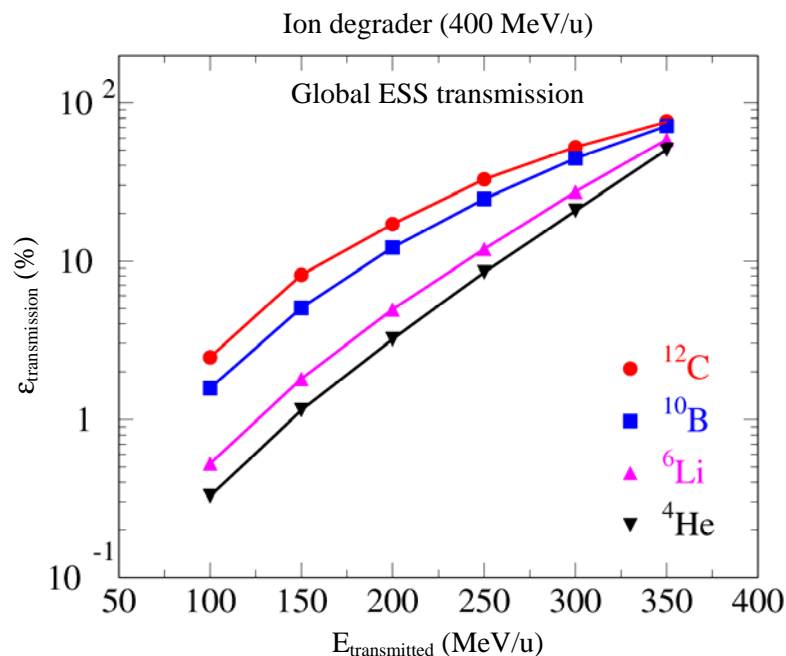
Shielding design

Full modelling of ETOILE is implemented in MCNPX. The layout of the proposed facility is illustrated in Figure 7. The left part of the facility is occupied by the C400 cyclotron and the ESS. The next rooms are devoted to therapeutic irradiations, with a carbon gantry room (GTRC), a fixed-beam room (FBR) allowing the patient irradiation with an horizontal beam and a 45° inclined beam, and a proton gantry room for paediatric treatments (GTRp). The last room at the end of the beam line is the R&D room allocated to research activities. All walls are divided into 20 cm thick layers in order to apply variance reduction techniques. They are made of standard concrete with a density of 2.3 g/cm³.

Ambient dose equivalents H*(10) are computed with ICRP74 fluence-to-dose conversion factors at low energy [8], complemented with factors from M. Pelliccioni at higher energy [9]. French regulation defines three types of area corresponding to different limits on the acceptable effective dose rate. In a public area, the monthly effective dose rate cannot exceed 80 μSv/month. In supervised and controlled

Figure 7: MCNPX modelling of the proposed ETOILE
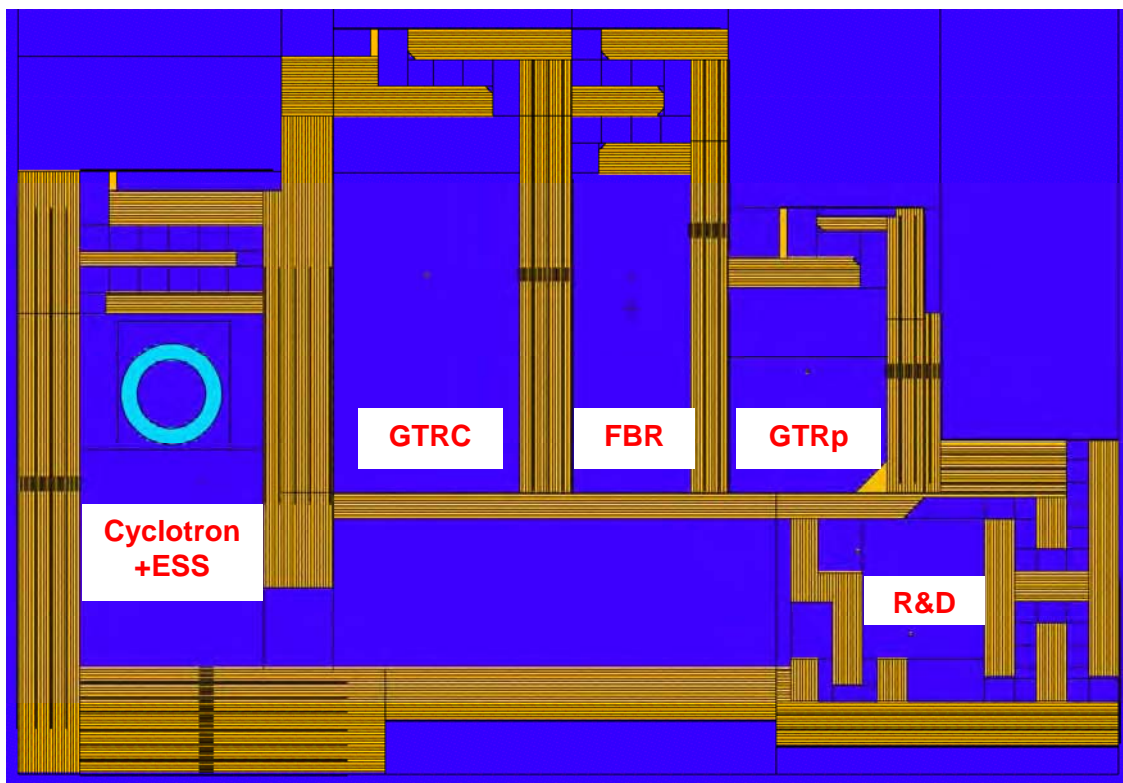
areas, the hourly dose rate cannot exceed 7.5 μSv/h and 25 μSv/h, respectively. The hour taken into account to compute the dose rate must be the worse hour for radioprotection, not an hour representing the average activity during one year. Detailed radioprotection assumptions have been determined by ETOILE to compute the hourly and monthly dose rates inside and outside the centre using proton, ^{4}He and ^{12}C beams. Irradiations with ^{6}Li and ^{10}B beams are considered as experimental studies and do not enter into the mandatory therapeutic programme.

In this paper, we present results on the hourly dose rates obtained for a continuous irradiation aiming at delivering a physical dose rate of 2 Gy/min inside a 1 litre water absorber located at the isocentre of GTRC.

Figure 8 shows the hourly dose rate obtained for different ion species behind the wall facing the energy degrader (south wall of the cyclotron room in Figure 7). The largest dose rates are obtained for the lowest beam energies transmitted through the ESS, due to the low transmission efficiency obtained for these energies. The dose rates obtained for ^{4}He and ^{6}Li ions are about one order of magnitude larger than those obtained for the heavier ions ^{10}B and ^{12}C. With a wall thickness of 7 m, the hourly dose rates always remain lower than 1 μSv/h, even for the lowest beam energy.

Dose rates obtained around the GTRC strongly depend upon the gantry orientation angle. Figure 9(a) exhibits the evolution of the dose rate as a function of concrete depth in the east wall of GTRC for 400 MeV/u ^{12}C ions stopping in a water absorber. Angle Θ = 180° corresponds to the configuration where the primary beam is directed towards the east wall while Θ = 90° and Θ = 270° correspond to a beam directed towards the roof and the floor, respectively. Because of the strong anisotropy of neutron emission, dose rates vary by several orders of magnitude between these different configurations and the case of a beam directed towards the east wall is clearly the worse case. Figure 9(b) shows that results obtained for ^{6}Li, ^{10}B and ^{12}C ions are rather similar while those obtained with α particles are about 2-3 times lower. The energy of these different ion species is selected to obtain a similar range in water.

**Figure 8: Ambient dose equivalent rate obtained behind the
south wall of the cyclotron room for various ion species**
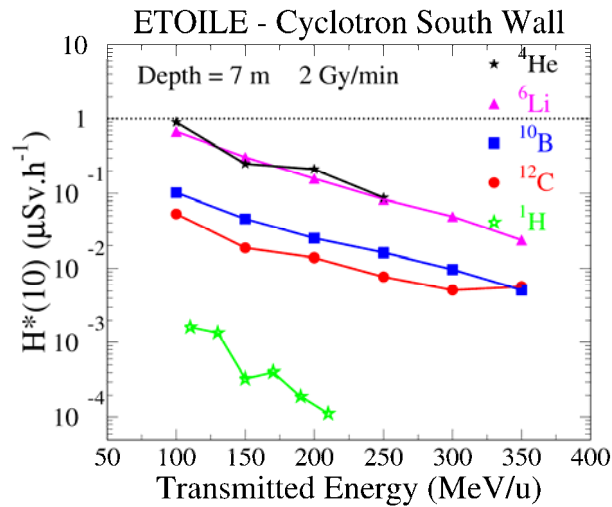
**Figure 9: Evolution of ambient dose equivalent as a function of concrete depth in
the east wall of the carbon gantry room: (a) 400 MeV/u ^{12}C ions with different gantry
rotation angles; (b) various ion species with the same gantry orientation angle of 180°**
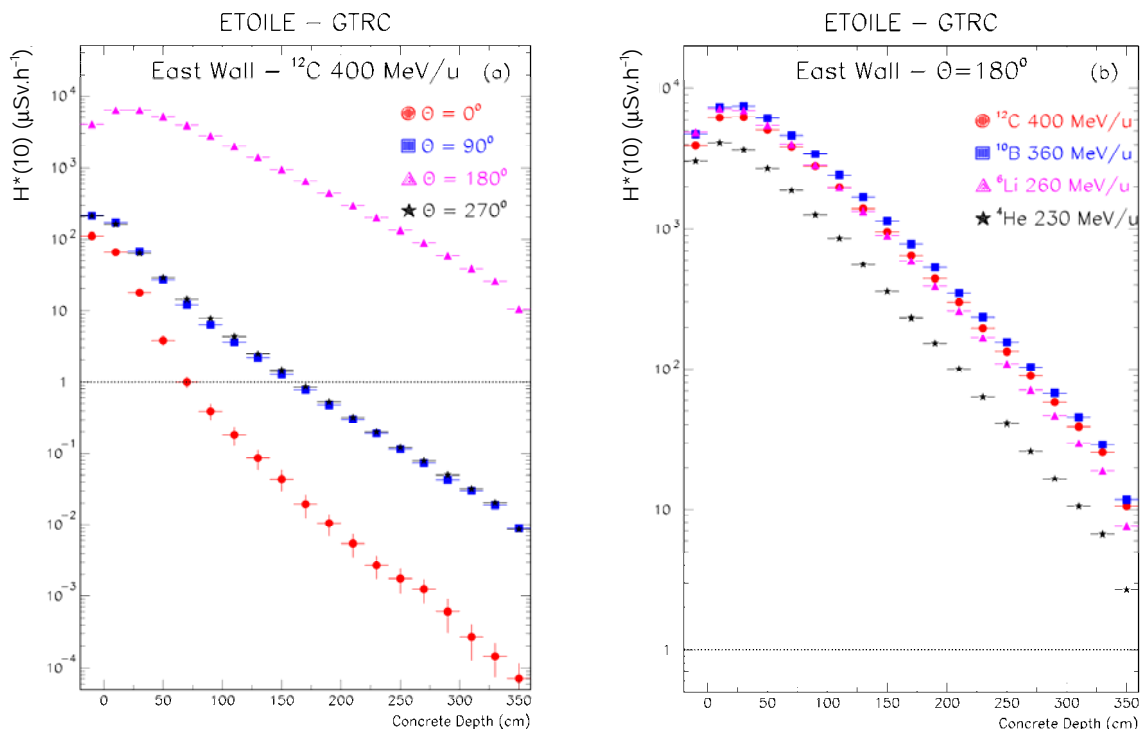
The evolution of the maximal dose rate obtained behind the GTRC east wall is presented in Figure 10 as a function of beam energy. The east wall thickness amounts to 3.5 m and the worse gantry orientation is selected. For the highest beam energies, the dose rates reach a maximal value of 11.7 μSv/h. In practice, irradiation time during a single hour shall never exceed 30 minutes, for example during QA activities. Thus, the maximal dose rate obtained in the FBR shall remain below the 7.5 μSv/h limit required for a supervised area, even in the worse conditions. Similar considerations have been applied to size the shielding walls of the different rooms.

Figure 10: Variation with beam energy of the ambient dose equivalent rates obtained in the GTRC east wall for various ion species and a gantry orientation angle of 180°
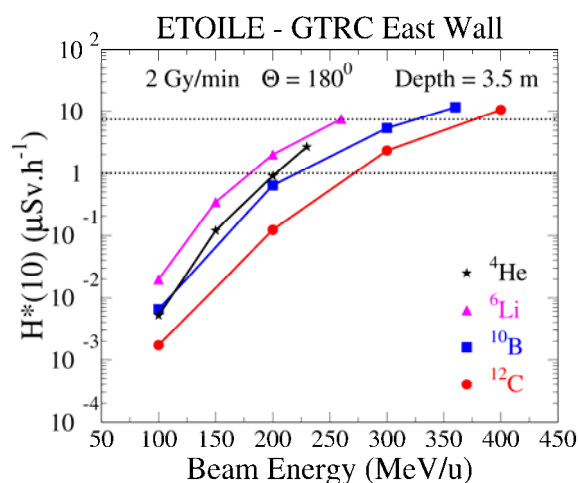
Validation of shielding calculations

The ETOILE shielding design is achieved in two steps: production of secondary particles is studied with PHITS while the transport of these particles is performed by MCNPX. As the neutron energy can reach values as high as 1 000 MeV, the neutron transport in MCNPX is mainly based on physical models. It is thus important to validate these shielding calculations by comparing MC predictions to real dose measurements.

Such measurements were recently performed in the framework of EURADOS and the results are published in [10,11]. The experiment was conducted at GSI using a 400 MeV/u ^{12}C ion beam stopping inside a $10 \times 10 \times 20$ cm^3 graphite absorber located in Cave A. Ambient dose equivalent was measured using three different Bonner sphere spectrometers (BSS) located at six positions outside the vault. MC simulations of this experiment were also performed using MCNPX and FLUKA [12] codes.

To reproduce the GSI experiment, the production of secondary particles from the graphite target is computed using PHITS. As shown in Table 1, TTY obtained for secondary neutrons and protons are very close to results obtained with FLUKA [10]. Doubly differential yields are also in excellent agreement between PHITS and FLUKA.

Table 1: TTY for 400 MeV/u ^{12}C ions stopping in a $10 \times 10 \times 20$ cm^3 graphite absorber

Secondary particle	Code	Θ = 0-90°	Θ = 90-180°	Total
Neutron	PHITS	4.487	0.659	5.146
	FLUKA	4.768	0.896	5.664
Proton	PHITS	1.758	0.017	1.775
	FLUKA	1.732	0.015	1.747

GSI Cave A is modelled in MCNPX based on information provided in [13]. Use is made of the concrete composition and density published in [10] and the scoring regions OC-9 to OC-14 are simulated by void spheres of 20 cm diameter located 75 cm below the beam level. The ambient dose equivalent H*(10) is computed using ICRP74 [8] and M. Pelliccioni's [9] fluence-to-dose conversion factors as described earlier. Separate runs are performed for each of the radiation sources computed with PHITS (n, γ, p, ^{2}H and ^{4}He).

Figure 11: Modelling of GSI Cave A in MCNPX
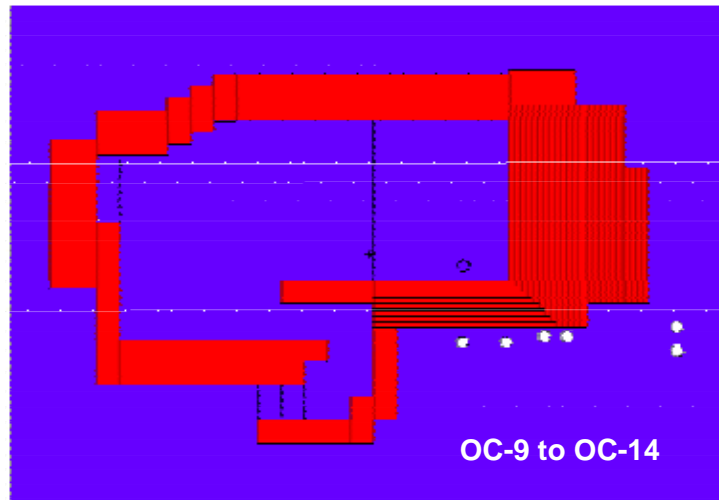
Results for the ambient dose equivalents obtained with this analysis in the various OC locations are represented in Figure 12 (labelled as PHITS). Compared to the H*(10) measurements and the values obtained with FLUKA, our predictions are in very good agreement for locations OC-11 to OC-14. PHITS results for OC-9 and OC-10 exceed the other results by about 30%. A possible explanation is that these two positions correspond to emission angles of 66.8° and 54.0° with respect to the target centre, where PHITS is known to overestimate the emission of high-energy neutrons [see Figure 2(e)]. For neutrons, the relative contribution of different energy ranges to the total ambient dose equivalent is shown in Figure 13 for our analysis and the BSS measurements. Our results are in very good agreement with the measured data and demonstrate that about 50% of the dose comes from neutrons above 20 MeV.

**Figure 12: Comparison of the ambient dose equivalents
obtained at the various OC locations with the different analyses**
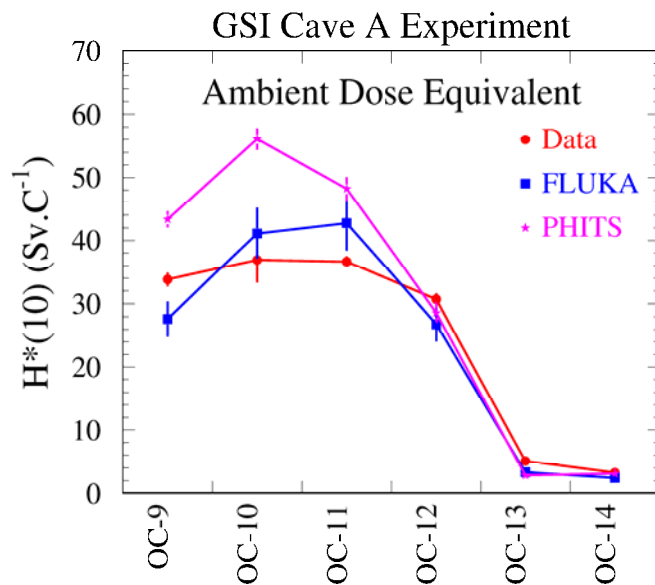
**Figure 13: Relative contribution of different energy ranges to the total ambient
dose equivalent: (a) this analysis; (b) Bonner sphere measurements [11]**
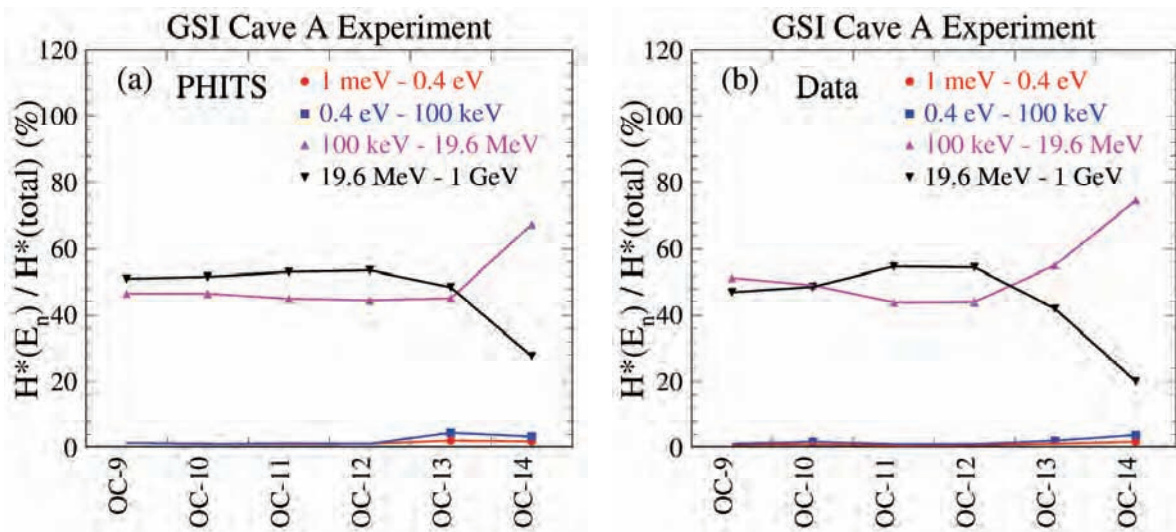
Conclusions

Shielding calculations for the proposed ETOILE hadron therapy centre are performed using PHITS to compute the secondary radiation sources and MCNPX for the transport of these radiations inside the shielding. The radiation sources are determined for beams of protons, [4]He, [6]Li, [10]B and ^{12}C ion beams. The beam energy ranges from 70 to 260 MeV for the protons and from 100 MeV/u to 400 MeV/u for the ions. Thick absorbers made of graphite, water and copper are considered.

Our calculations involving two steps and two different MC codes are validated by reproducing the results obtained in GSI Cave A experiment using Bonner sphere spectrometers and the FLUKA code.

References

[1]   Jongen, Y., *et al.*, "IBA C400 Cyclotron Project for Hadron Therapy", *Cyclotrons 2007*, Giardini Naxos, Italy (2007).

[2]   Stichelbaut, F., T. Canon T., Y. Jongen, "Shielding Studies for a Hadron Therapy Centre", *Nucl. Technol.*, 168, 477-481 (2009).

[3]   Niita, K., *et al.*, "PHITS – A Particle and Heavy Ion Transport Code System", *Radiat. Meas.*, 41, 1080-1090 (2006).

[4]   Nakamura, T., L. Heilbronn, *Handbook on Secondary Particle Production and Transport by High-energy Heavy Ions*, World Scientific Publishing Co. Pte. Ltd. (2006).

[5]   Satoh, D., *et al.*, "Reevaluation of Secondary Neutron Spectra from Thick Targets upon Heavy-ion Bombardment", *Nucl. Instr. and Meth.*, A583, 507-515 (2007).

[6]   Pelowitz, D.B., *et al.*, *MCNPX[TM] User's Manual*, LA-CP-05-0369 (2005).

[7]   Schardt, D., T. Elsässer, D. Schulz-Ertner, "Heavy-ion Tumor Therapy: Physical and Tadiobiological Benefits", *Rev. Mod. Phys.*, 82, 383-425 (2010).

[8]   International Commission on Radiological Protection (ICRP), *Conversion Coefficients for Use in Radiological Protection Against External Radiation*, ICRP 74, Ann. ICRP, 26 (1996).

[9]   Pelliccioni, M., "Overview of Fluence-to-effective Dose and Fluence-to-ambient Dose Equivalent Conversion Coefficients for High Energy Radiation Calculated Using the FLUKA Code", *Radiat. Prot. Dosimetry*, 88, 279-297 (2000).

[10]   Rollet, S., *et al.*, "Intercomparison of Radiation Protection Devices in a High-energy Stray Neutron Field, Part I: Monte Carlo Simulations", *Radiat. Meas.*, 44, 649-659 (2009).

[11]   Wiegel, B., *et al.*, "Intercomparison of Radiation Protection Devices in a High-energy Stray Neutron Field, Part II: Bonner Sphere Spectrometry", *Radiat. Meas.*, 44, 660-672 (2009).

[12]   Fassò, A., *et al.*, *FLUKA: A Multi-particle Transport Code*, CERN 2005-010, INFN/TC 05/11, SLAC-R-773 (2005).

[13]   Fehrenbacher, G., private communication.

Optimum shielding design for electron linac oncology facilities incorporating seismic base-isolation structure

Koji Oishi, Kazuaki Kosako, Takashi Nakamura
Institute of Technology, Shimizu Corporation

Abstract

We have attempted to reduce the shielding cost for the electron linac facilities incorporating seismic base-isolation structure in order to change the boundary of controlled area. The analysis of the dose rate at the new boundary was performed by using the three-dimensional calculation code MCNP5. The behaviour of photons in the pit underneath the treatment room led to the conclusions that no additional iron shielding was necessary. Measurement of dose distribution was also performed and very good agreement between measured and calculated results was obtained.

Introduction

Recently electric linac oncology facilities incorporating seismic base-isolation structure have become very popular in Japan to prevent any strong impact to the equipments due to earthquakes. When the boundary of the controlled area is set below the base-isolated foundations, as shown in Figure 1, additional iron-plate shielding is needed, which can increase costs by up to USD 1M.

Figure 1: The boundary was set blow the base-isolated foundations
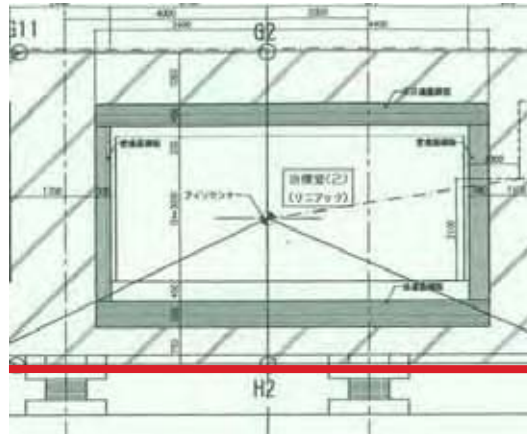
Since no one usually accesses underneath the treatment room, except short maintenance period for base-isolation structure, it is reasonable to set the boundary around the downstairs room (pit) by fence. Figure 2 shows the boundary of controlled area set outside of the downstairs room.

Figure 2: The boundary was set outside of the downstairs room
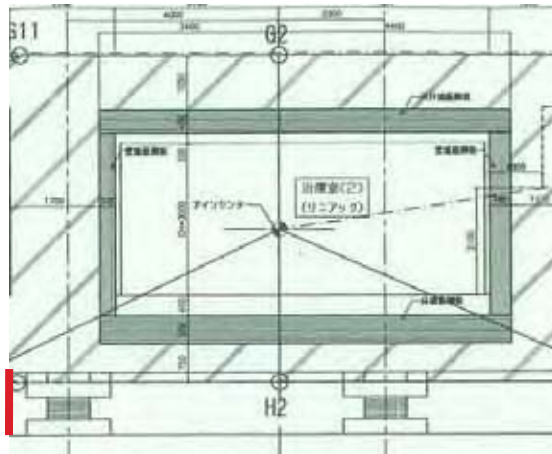
However, it is very difficult to estimate the dose rate allowed by the new boundary with a simple shielding calculation method, due to the rotating gantry head and the effect of scattering radiation in the base-isolation floor.

In this study detailed calculations using Monte Carlo calculation code MCNP5 have been performed and compared with the measured results to determine the most practical shielding design.

Objectives

The objective of this study is to investigate the complicated behaviour of photons in the "pit" employing the following analysis:

- Which angle of the gantry will most influence the dose rate at the new boundary?

- By how much can the thickness of the additional iron plate be reduced?

- Which component of the radiation is dominant at the new boundary?

The calculated results were further verified through measurement.

Calculation conditions

The calculation code applied was MCNP5 [1] along with its related cross-section libraries MCPLIB04 for photons and EL3 [2] for electrons, respectively. The source electron energy was 10 MeV, and the target to produce photons was copper whose thickness was 20 mm. The electron beam was pencil beam and the maximum beam current was 30 mA. The repetition of electron pulse was 188 pps and the pulse width was 4 micro A, that is, the average beam current was 22.4 micro A.

The tallies for photons and electrons we have used were cell tally for the lower layer in the pit and point detectors for the estimated position of the boundary of new controlled area.

Note that the criteria of the boundary dose rate is 8.3 micro Sv/h, since the operation time for three month is 156 hours (1 300 micro Sv/156 h = 8.3 micro Sv/h.) In Japan the dose rate limit criteria is 1 300 micro Sv/3 months.

Calculations

Which angle of the gantry will most influence the dose rate at the new boundary?

The geometry of the analysis is shown in Figure 3. Since the gantry head rotates in this plane, we have calculated the dose rate at the new boundary for the degree of gantry head from 0 to 73.9° in the direction perpendicular to the isolation pit. There existed a small pit to turn the table and the thickness of the concrete shield was thinner around the direction of 0°.

Figure 3: The geometry of analysis for angular distribution
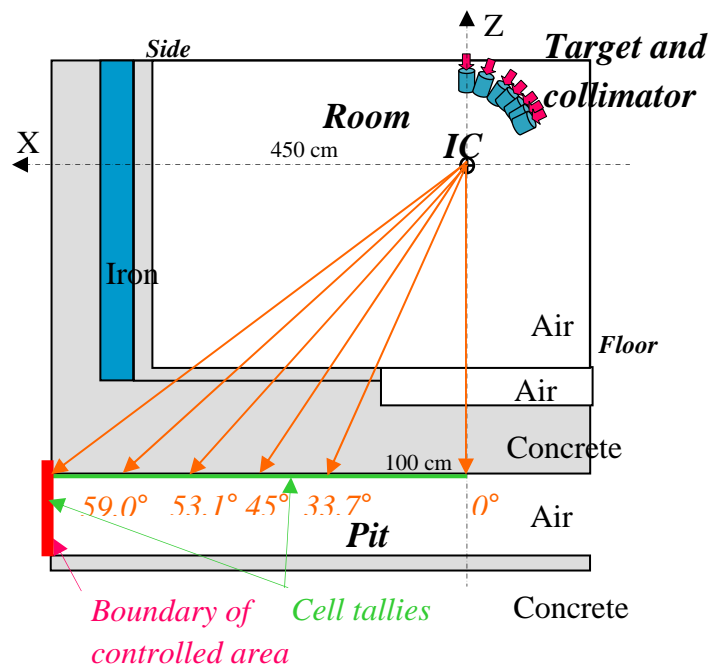
As the goal in this analysis is to determine which direction of the gantry head indicates the highest dose rate at the new boundary, the iron plate has been omitted from the calculation.

The calculated results are shown in Figure 4. The horizontal axis is the distance from the position just beneath the isocentre and the vertical axis is the dose rate distribution along the floor of the isolation pit. In the case of 0° the highest dose rate of about 3 m Sv/h underneath the isocentre was obtained. However, it decreased rapidly as the distance from the underneath of isocentre increased. It is very clear that the steep is very different between the positions within 150 cm and greater than 150 cm. The reason is that the decrease of dose rate in the positions within 150 cm is due to the attenuation of photon dose by the concrete wall. The behaviour of photons at the positions greater than 150 cm is different from that of attenuation. For other directions, the behaviours were very different from 0°. The peak of dose rate is varied around the direction of the gantry head, but the dose rate rapidly decreased when the distance from the isocentre increased. This is because the dominant dose came from the attenuation through concrete, except the 33.7° case. The highest dose at the new boundary was obtained in the direction of 0°.

Figure 4: The dose rate distribution in the pit vs. angle of gantry head
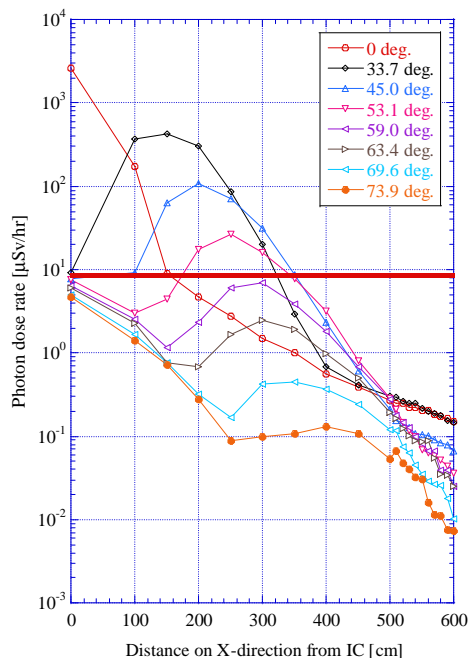
By how much can the thickness of the additional iron plate be reduced?

The dose rate of the new boundary was the highest when the degree of the gantry head was 0°. We have performed a calculation concerning how much the thickness of additional iron plate may be reduced from the safety point of view.

Figure 5 shows the geometry of the calculation. The thickness of iron was varied from 550 cm to 0 cm with every 5 cm.

The calculated results are shown in Figure 6. The horizontal axis is the distance from the underneath of the isocentre and the vertical axis is the dose rate of at the estimated positions. We can find out that the inclination of the behaviour of the dose rate distribution is almost the same for all thicknesses of the iron plate. It decreased rapidly first and from the position of about 200 cm it decreased gradually. The first part, the attenuated photons through concrete, is dominant; however from the 200 cm position the scattered photons may be dominant so that the inclination of all the results was almost the same.

Figure 5: The calculation model of estimation for iron thickness
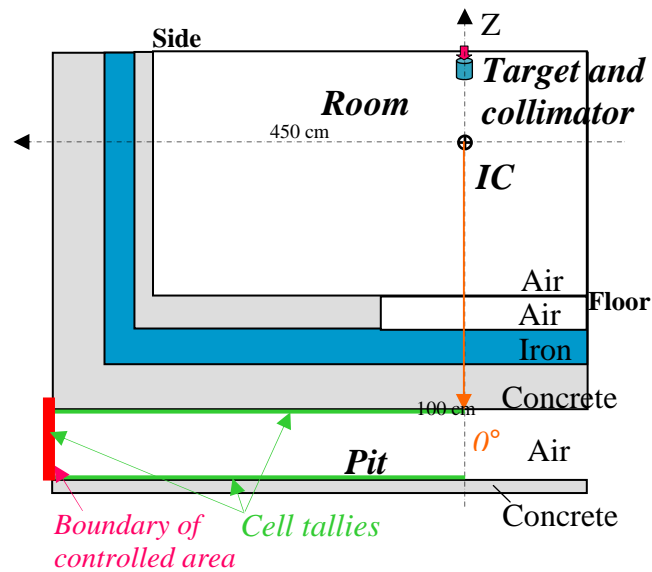
Figure 6: The calculated results of dose rate distribution in the pit for several iron thickness
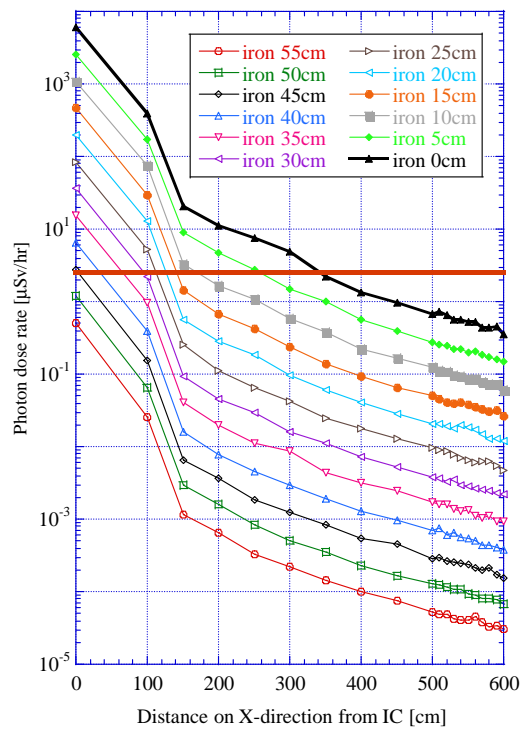
Which component of the radiation is dominant at the new boundary?

From the calculated results mentioned last chapters, it is concluded that the scattered photons strongly influence to the dose rate at the new boundary. To confirm these results we have performed analysis whether they exist on the floor of the isolation pit or not. Figure 7 shows the calculated results of dose rate distribution in the pit with and without the concrete floor.

Figure 7: Calculated results of dose rate distribution with and without concrete floor in the pit
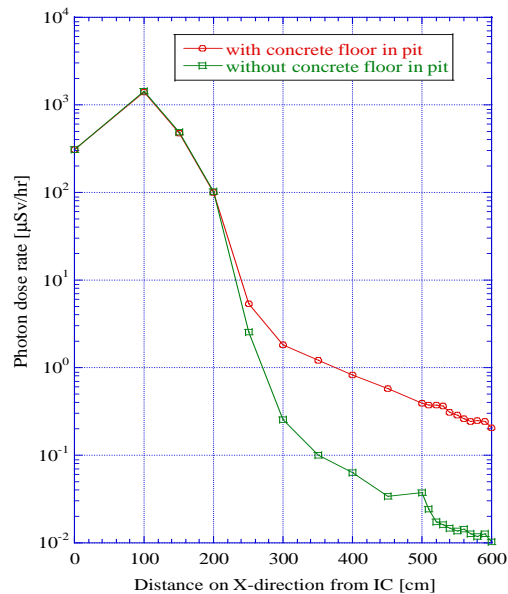
In the estimated position within 200 cm from the underneath of isocentre, the distribution of dose rate is the same for these two cases. However, the behaviour of the dose rate near the boundary is completely different between the two cases. Without the floor the dose decreased rapidly, though it decreased gradually in the case with concrete floor. We can confirm that the dominant dose for the new boundary was due to the scattering photons by the concrete floor in the pit.

Comparison between calculated and measured results

We have also performed the measurement of dose rate with an ionisation chamber along the concrete floor of the pit for the verification of the calculated results. Figure 8 shows the comparison of dose rate distribution between measured and calculated results.

Figure 8: Comparison of dose rate distribution between measurement and calculation
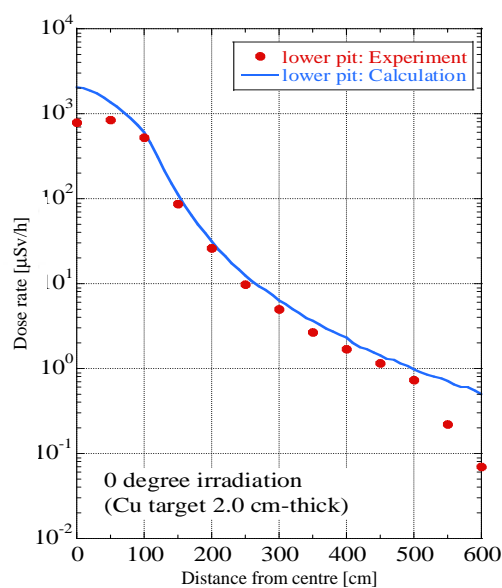
Very good agreements between measured and calculated results were obtained, except near the isocentre and new boundary. The agreement was within 20%.

The reasons why there were some discrepancies were that the base structure of the turn table near the isocentre and pipes and fences existing near the boundary were not considered by the calculation model. Figure 9 shows the pictures of the inside of the turn table and near the boundary. The structure of the base of turn table is anisotropic and the thickness of the steel base would be a shielding material. Near the new boundary some structures would also be a shield.

Figure 9: The structure of the turn table base and conditions near the boundary

Conclusions

We have performed the analysis of the behaviour of photons in the pit and found that no additional iron shielding was necessary, which can significantly reduce costs. Good agreement between calculated and measured results were obtained, and passed the examination by the regulatory authority. It is concluded that the Monte Carlo calculation code MCNP5 is very effective for the optimistic design of the electron linac oncology facilities incorporating seismic base-isolation structure.

References

[1]   X-5 Monte Carlo Team, *MCNP – A General Monte Carlo N-particle Transport Code*, Version 5, LA-UR-03-1987, Los Alamos National Laboratory (LANL) (2003).

[2]   RSICC, *Data Libraries for MCNP5*, CCC-710/MCNP, Oak Ridge National Laboratory (ORNL) (2003).

Optimised design of local shielding for the IFMIF/EVEDA beam dump

M. García[1,2]**, F. Ogando**[1,2]**, P. Ortego**[3]**, J.M. Arroyo**[4]**, B. Brañas**[4]**,**
C. Töre[3]**, D. López**[1,2]**, P. Sauvan**[1,2]**, A. Mayoral**[1,2]**, J. Sanz**[1,2]
[1]Dpto. de Ing. Energética, Escuela Técnica Superior de Ingenieros Industriales UNED, Madrid, Spain
[2]Instituto de Fusión Nuclear, UPM, Madrid, Spain
[3]SEA Empresarios Alaveses, Madrid, Spain
[4]Centro d'Investigciones Energéticas Medioambientales y Tecnológicas (CIEMAT), Madrid, Spain

Abstract

This paper describes the local shielding design process of the IFMIF/EVEDA beam dump and the most relevant results obtained from the simulations. Different geometries and materials have been considered, and the design has been optimised taking into account the origin of the doses, the effect of the walls of the accelerator vault and the space restrictions. The initial idea was to shield the beam stopper with a large water tank of easy transport and dismantling, but this was shown to be insufficient to satisfy the dose limit requirements, basically due to photon dose, and hence a denser shield combining hydrogenous and heavy materials was preferred. It will be shown that, with this new shielding, dose rate outside the accelerator vault during operation complies with the legal limits and unrestricted maintenance operations inside most of the vault are possible after a reasonable cooling time after shutdown.

Introduction

The International Fusion Materials and Irradiation Facility (IFMIF) will be an accelerator-based neutron source to test candidate materials for nuclear fusion reactors. During the Engineering Validation and Design Activities (EVEDA) phase, a prototype accelerator (125 mA, CW, 9 MeV deuterons) will be tested in Rokkasho (Japan). As no target is foreseen for the accelerated beam during this phase, a beam dump is required to stop it during commissioning and accelerator tests. The piece that stops the beam is a copper conical sheet 250 cm in length, with a 30 cm aperture diameter and a thickness of 0.5 cm.

Beam dump radioprotection concerns arise from the fact that deuterons hit the intercepting copper beam stop as well as previous deuterons implanted in it, which will result in secondary neutrons and photons as well as in deuteron-induced activation products. The generation of neutrons will induce: *i)* high neutron and prompt gamma dose rates during accelerator operation; *ii)* gamma dose rates on beam-off due to activation of all materials. The impact of the deuterons on its surface gives rise to neutron production at a rate up to $4.6 \cdot 10^{14}$ neutrons per second and the activation by this neutron source of the surrounding materials.

In the design of the beam dump (BD) the radioprotection requirements to be fulfilled are: *i)* dose rate outside the accelerator vault during accelerator operation must be below the acceptable levels for workers and/or the public; *ii)* inside the accelerator vault man-access for maintenance must be allowed during beam-off phases. The dose rate limits to be fulfilled are 12.5 µSv/h for workers and 0.5 µSv/h for the public.

Methodology

The starting point for the radioprotection analysis is the deuteron particle position and energy at the copper cone entrance provided by the TraceWin [1] code. The first step is to determine an equivalent deuteron source which could be introduced into transport codes, while retaining as close as possible the particle distribution from TraceWin.

The beam dump receives a 9 MeV deuteron beam with a maximum current of 125 mA. The radial distribution of the beam intensity at the cone entrance is shown in Figure 1.

Figure 1: Deuteron density distribution at the beam dump entrance
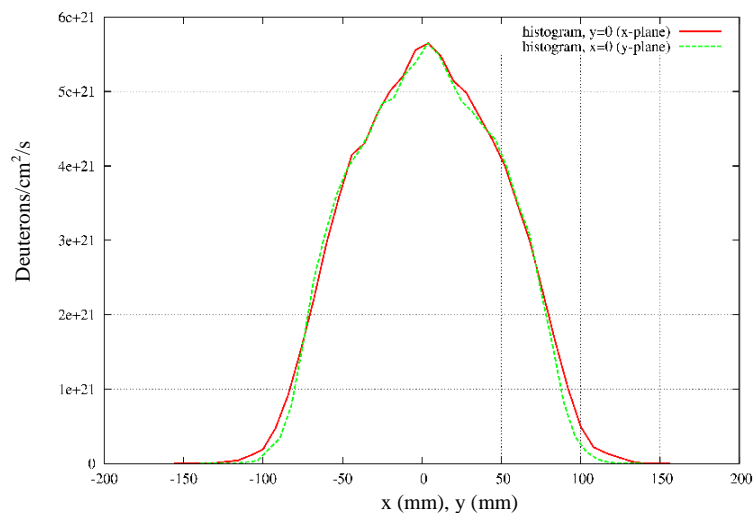
Using this information, an equivalent deuteron point source is obtained and the equivalent deuteron beam is transported by simulating with the MCNPX [2] code.

A known problem of most used transport codes when working with charged particles is their inefficient way of producing secondary particles, since for example in the deuteron-copper interaction around 10 000 deuterons are needed to produce one neutron. This problem has recently been overcome

by the MCUNED [3,4] code, which was not available at the time of this analysis. This is the reason why secondary particle transport is performed in two phases: *i)* obtaining the neutron and gamma sources from deuteron interaction once for a given beam and stopper configuration; *ii)* performing secondary particle transport calculations from these sources.

The neutron and gamma source data is obtained using the INCL4/ABLA nuclear model and is obtained from a heavy run with deuterons, the sole purpose of which is to produce as many neutrons as possible in order to study their distribution. This can be most easily done with the PTRAC option which will record the phase space parameters of secondary particles in the production moment. From these data, a suitable source distribution for MCNPX has to be devised and tested. Phase space variables are recorded by MCNPX redundantly as space (x,y,z), director cosines (u,v,w) and energy. Secondary source can in the most general case be expressed as a general function of these variables, which is not suitable for MCNPX. The following simplifications are proposed for the neutron source:

- Since 9 MeV deuteron track length inside copper is in the hundred of microns, neutrons are supposed to be produced in the internal surface of the conical beam stopper. Since the beam is supposed to be azimuthally symmetric, this leaves only one spatially independent variable.

- Particle source in every point has azimuthal symmetry around the beam axis. This is not trivially true, due to the small deuteron impact angle into the stopper material.

- The neutron spectrum in a certain direction is spatially homogeneous. That is, the spectrum, which still depends on the emission angle with respect to the beam direction, can be separated from the spatial distribution.

Under these assumptions and considering a beam following x direction, a simplified neutron source is proposed with the form:

$$S(x, y, z, u, v, E) = S_x(x) \cdot S_v(u, E)$$

which can easily be introduced into the MCNPX input. The same procedure applies not only to neutrons but to gamma prompt radiation as well.

It is worth noting that the original neutron source from the INCL4 model contains unphysical energies that violate the energy conservation principle. These particles have been taken out from the spectra for the radioprotection studies, while keeping the total neutron production.

The resulting neutron source was scaled with a 2.5 increasing factor [5] to match the cross-section at 9 MeV with experimental data giving a total neutron source of $4.57 \cdot 10^{14}$ n/s. The average number of neutrons produced per deuteron is $5.87 \cdot 10^{-4}$ and its mean energy 2.7 MeV.

The dose rates on beam-on phase are obtained using the conversion factors from ICRP74 [6] corresponding to ambient dose equivalent to convert the neutron and gammas fluxes to dose rates. In the subsequent step, with the deuteron and neutron fluxes computed previously, the radioactive inventory and the corresponding decay photon source are calculated using the ACAB [7] code with the EAF-2007 [8] nuclear data libraries. MCNPX is used to transport the emitted gamma rays and compute residual dose rates using the ICRP74 conversion factors corresponding to ambient dose equivalent.

Beam stop shielding optimisation

In Figure 2 the layout of the accelerator and the position of the BD are shown. The accelerator vault inner dimensions are the following: 41.5 m length, 8 m width and 7 m height. The walls and ceiling of the vault are made of ordinary concrete 1.5 m thick. The floor has a similar thickness and it is highly reinforced in order to support the heavy loads present in the area, including the shielding components of the beam dump.

The beam dump is located in the south east corner of the accelerator vault as shown in the figure. The accelerator axis is at 5 m distance from the south wall, and its height is 1.5 m. The dipole is situated 29.071 m from the inner part of the east wall, and turns the beam 20°. This beam turn avoids a higher activation of the accelerator devices as far as possible. The cone base of the beam dump is 4 702 m from the dipole centre.

The concrete composition of the accelerator vault walls considered for the calculations is shown in Table 1.

Figure 2: Accelerator vault layout
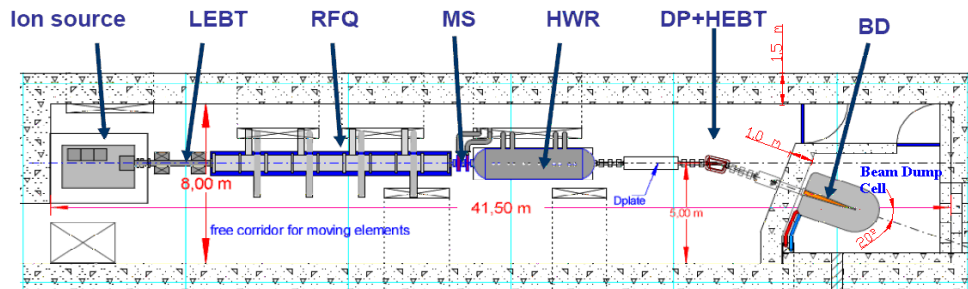
Table 1: Concrete composition of the accelerator vault walls

Element	wt.%
H	0.00555
O	0.49784
Na	0.01708
Mg	0.00256
Al	0.04691
Si	0.31471
S	0.00128
K	0.01922
Ca	0.08283
Fe	0.01238

Preliminary design

Since the beam stop behaves like a strong neutron source during operation, the preliminary design of the BD shield was based on water [9], which is typically used for neutron applications due to its high hydrogen content. A 100 cm radius water tank was used as shielding of the copper cone. Using the configuration of the beam dump shown above, Figure 3 shows a dose rate colour map where the problematic zones with regard to the beam-on phase doses are indicated as A, B, C and D.

Figure 3: Beam-on dose rates in the former water-based BD configuration (dose rates in Sv/h)
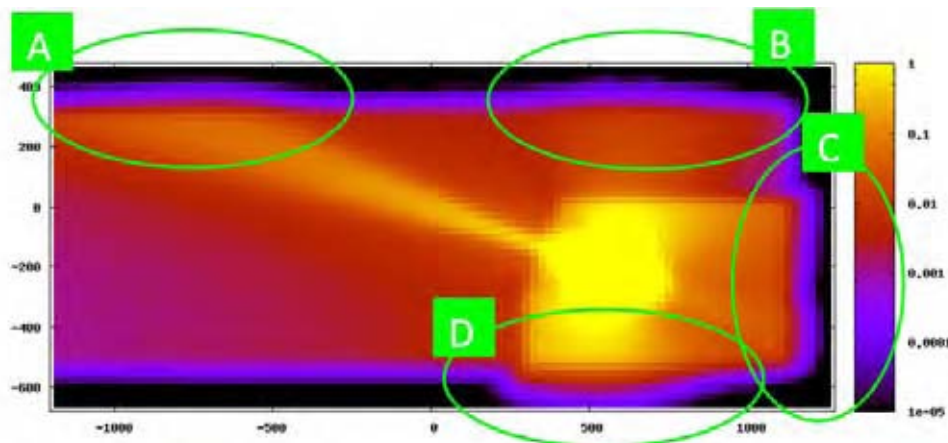
Dose rates obtained at the external surfaces of the concrete accelerator vault in areas A, C and D were higher than the limits for workers (zones A and D) and the public (zone C). The idea of shielding the beam stopper with a large water tank also arose to easy transport and dismantling the shielding

device, but it was shown to be insufficient to satisfy the dose limit requirements, basically due to photon dose generated in the water tank by neutron reactions. From the water-based model starting point, an optimised shielding has been obtained and is described as follows.

Optimised shielding design

Considering the necessity of stronger lateral shield which works on both high-energy neutrons and gamma rays, there is a need for at least two layers of different materials:

1. Internal shield the purpose of which is to absorb and/or moderate the energetic neutron flux from the beam stop.

2. External shield focused on attenuating the gamma rays originated in the internal shield from neutron reactions.

The main materials chosen are water for the inner shield and iron for the outer shield, especially as regards low cost and high mass density.

Several combinations of steel as outer shield and water as inner shield have been evaluated. The differences among these combinations are due to the different thicknesses of the layers. After optimising the thickness of the shielding layers, the configuration that shows the lowest dose rates beyond the accelerator vault fulfilling the space requirements consists of the following: *i)* 50 cm water and 25 cm steel in the lateral and rear part of the shielding; *ii)* 30 cm polyethylene and 25 cm steel in the front-lateral part of the shielding. The selection of polyethylene as inner shield in the front-lateral area is due to the necessity of easily removable materials in this location for inspection tasks, which is less difficult with this material configuration than using a water tank.

As well as the radioprotection reasons additional arguments in the selection of these materials are:

- cheap components;

- absence of iron in the high neutron flux zones, limiting the formation of cobalt 60, with its radioprotection implications;

- acceptable weight;

- beam dump diameter as originally designed fulfilling the space requirements.

The general layout of the shielding is shown in Figure 4.

Figure 4: Beam dump layout
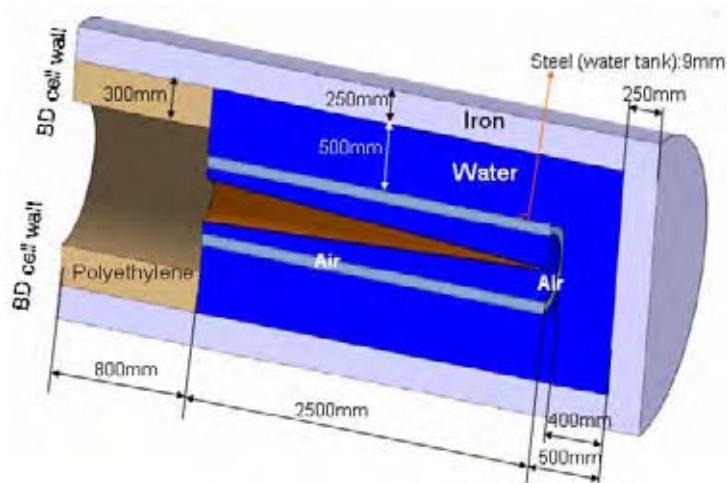
Since the entrance to the beam dump is open to the accelerator vacuum tube during accelerator operation, a wide area of the vault would be submitted to high neutron flux, thus producing in a short time such activation that hands-on maintenance would not be possible during beam-off. For the same

reason, the wide extension of uncollided neutrons reaching into the north wall still produces unacceptable dose rates outside the wall. Even with the consideration of a lead shutter, located at the copper cone entrance to allow manual maintenance in the accelerator area on beam-off phase, the dose rates are still too high. This is mainly due to the unavoidable gaps between the shutter and the concrete structure, which is a path of gamma escape that leads to too-high dose rates for hands-on maintenance.

In order to solve these problems a new design element was introduced: a dedicated room with concrete walls for the space just behind the lead shutter. This small room, which has to fit between the shielding frontal wall and the last quadrupole of the HEBT, has two main purposes:

- Its two walls perpendicular to the beam line have the main purpose of collimating the neutron current escaping the beam dump during operation

- The lateral walls will contain the radiation scattered in the frontal walls, with clear benefits for both beam-on and beam-off phases since: *i)* the region suffering high neutron flux during operation will be reduced (this will also reduce the activation of present materials); *ii)* gamma flux will be strongly reduced and restricted to the room, allowing hands-on maintenance outside it.

The dedicated room consists of 20 cm thick and 3 m tall concrete walls. They surround the space beyond THE frontal wall until the last HEBT quadrupole, which remains outside the room. The perpendicular room size has been preliminarily set to 200 cm, but may be changed when considering an unshielded entrance maze. Due to the smaller radius of the beam line at that position, it enters the room through a 14.4 cm diameter hole. Figure 5 shows the global configuration for the BD shielding with details for the diagnostics room and the lead shutter for beam-off phase.

Figure 5: Global BD layout – specific solutions
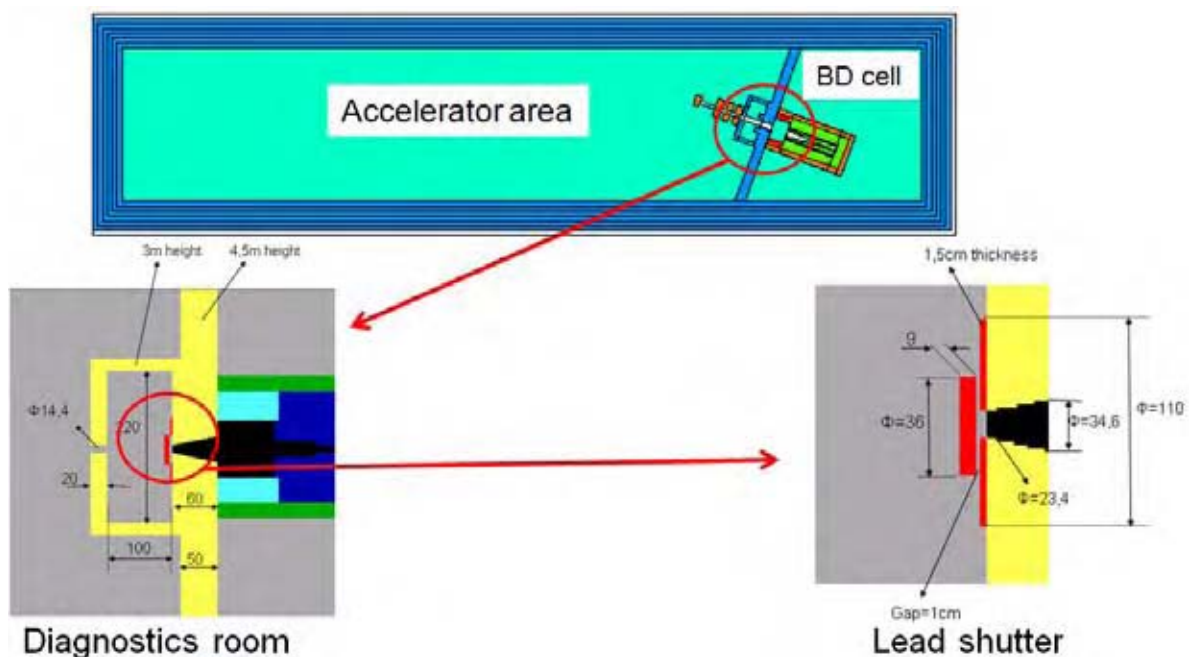
Results

This section is discusses the dose rates obtained with the optimised BD shielding for both beam-on and beam-off conditions. Dose rates on beam-on phase at the external surface of the accelerator vault are due almost totally to the neutron source and secondary gamma source (photons produced by the interaction of the neutron source with the materials). The effect of the primary gamma source, that is, photons produced by the deuteron beam interaction with the copper cone is negligible in comparison.

Beam-on dose rates

As mentioned above, the former water-based shielding configuration does not fulfil the dose rate requirements at the external surfaces of the accelerator vault in the locations A, C and D (see Figure 3). Table 2 shows the total dose rates on beam-on phase at the external surfaces of the accelerator vault for the optimised shielding design.

Table 2: Dose rates at the external surface of the accelerator vault

	A	C	D
Dose rate (μSv/h)	2	0.26	2.2
Limit (μSv/h)	12.5	0.5	12.5

Zones A and D (external surfaces of the accelerator vault) adjoin to other work rooms. In these areas, the dose rate limit is that for workers, that is 12.5 μSv/h. The external surface of the accelerator vault, C, is outside the building, and the dose rate limit to be fulfilled is that corresponding to the public, that is 0.5 μSv/h. As shown, dose rate requirements are fulfilled along the perimeter of the external surface of the accelerator vault.

Beam-off dose rates

In the evaluation of the residual dose rates around the beam dump configuration, the base case analysed is that corresponding to six months full power (125 mA) irradiation time. A reasonable cooling time of one day has been chosen.

The configuration of the beam-off phase solution to avoid high dose rates in the diagnostic cell and so allow manual maintenance in this area is shown in Figure 5 (lead shutter detail). The removable lead plug is cylindrical (36 cm diameter, 9 cm thickness) and the fixed lead sheet is also cylindrical (1.5 cm thickness, 23 cm inner diameter, 110 cm outer diameter). The gap between removable and fixed devices is 1 cm.

Figure 6 shows the locations of the dose rate detectors, and the values due to deuteron activation of the copper cone and neutron activation of the 25 cm realistic iron layer (iron plus cobalt 2 500 ppm) are shown in Table 3.

Figure 6: Location of the dose rate detectors
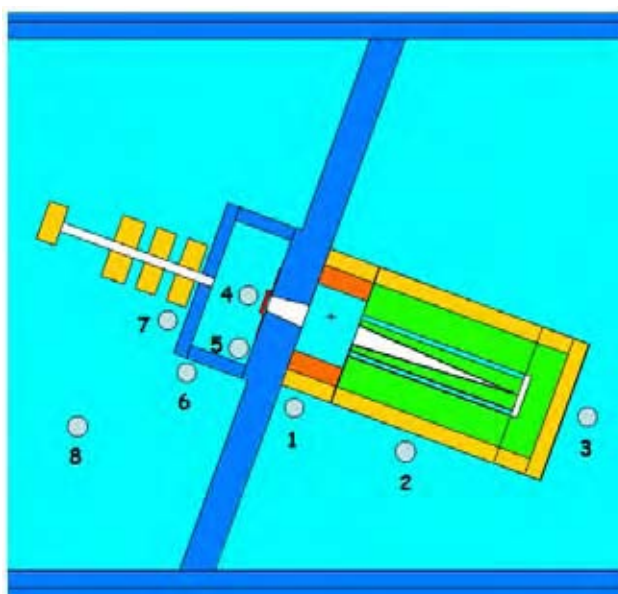
Table 3: Dose rates during beam-off phase (six months continuous irradiation, one day cooling time)

Detector	Dose rate due to deuteron activation of the copper cone (µSv/h)	Dose rate due to neutron activation of the 25 cm iron layer (iron plus Co 2 500 ppm) (µSv/h)	Total dose rate (µSv/h)
1	4.6	0.5	5.1
2	2.1	2.5	4.6
3	0.1	0.1	0.2
4	533	–	533
5	251	–	251
6	3.6	–	3.6
7	12	–	12
8	1.5	–	1.5

The contribution of the dose rates produced by neutron activation of the 25 cm iron layer to the total dose rate is negligible for all the detectors different than those located in the beam dump cell (detectors 1, 2 and 3).

As can be seen, manual maintenance is possible in the beam dump cell area without restrictions (dose rates lower than 12.5 µSv/h; limit for workers) only after one day of cooling time. The diagnostics room demonstrates its utility, as the highest dose rates are confined inside it and outside this room dose rates are lower than the limit for workers.

Conclusions

An optimised beam dump shield has been designed taking as starting point that defined in the beam dump PDR [9]. This new model makes use of an optimised combination of materials for fast neutron and photon shielding and has been achieved after successive optimisation steps from the water-based original model. The main (successful) goals of the design are:

- to limit beam-on dose rates outside the accelerator vault to the legal limits applicable in each of the contiguous rooms or areas;

- to allow for hands-on maintenance in most of the accelerator vault (both in the accelerator area and in the beam dump cell) reducing the high dose rate area to a small dedicated room;

- to keep material activation to a reasonably low level when possible, that is, apart from the beam stopper which inevitably gets highly activated.

References

[1]   Duperrier, R., N. Pichoff, D. Uriot, "CEA Saclay Codes Review", *International Conference on Computational Science (ICCS 2002)*, Amsterdam, the Netherlands, 21-24 April (2002).

[2]   Pelowitz, D.B. (Ed.), *MCNPX User's Manual, Version 2.5.0*, LA-CP-05-0369 (2005). *User's Manual, Version 2.6.0*, LA-CP-07-1473 (April 2008), Hendricks, J.S., *et al.*, *MCNPX 2.6.0 Extensions*, LA-UR-08-2216 (2008), *http://mcnpx.lanl.gov*.

[3]   Sauvan, P., J. Sanz, F. Ogando, "New Capabilities for Monte Carlo Simulation of Deuteron Transport and Secondary Products Generation", *Nucl. Instr. Meth. in Phys. Research*, A 614, 323-330 (2010).

[4]   Sanz, J., *et al.*, "Methodology to Address Radioprotection and Safety Issues in the IFMIF/EVEDA Accelerator Prototype", these proceedings.

[5]   Sanz, J., *et al.*, "First IFMIF-EVEDA Radioprotection Studies for the Preliminary Design of the Accelerator Beam Dump", *Fusion Science and Technology*, 56, 1, 273-280 (2009).

[6]   International Commission on Radiological Protection (ICRP), *Conversion Coefficients for Use in Radiological Protection against External Radiation*, ICRP Publication 74, Tarrytown, NY (1996).

[7]   Sanz, J., O. Cabellos, N. García-Herranz, *ACAB-2008: Activation Code V2008*, NEA-1839, OECD/NEA Data Bank (2008).

[8]   Forrest, R.A., J. Kopecky, J-Ch. Sublet, *The European Activation File: EAF-2007 Deuteron and Proton-induced Cross Section Libraries*, UKAEA FUS 536, March 2007; and *The European Activation File: EAF-2007 Neutron-induced Cross Section Libraries*, UKAEA FUS 535, March 2007, and *EAF-2007 Decay Data Library*, UKAEA FUS 537, March 2007.

[9]   CIEMAT and UNED teams, *Preliminary Design of IFMIF/EVEDA Beam Dump* (2009).

Session VI

Present status of data and code libraries

Chair: Hiroshi Iwase

A review of nuclear computational information

B.L. Kirk
Radiation Safety Information Computational Center (RSICC)
Oak Ridge National Laboratory (ORNL)
Oak Ridge, Tennessee, USA

Abstract

The Radiation Safety Information Computational Center (RSICC) and the Organisation for Economic Co-operation and Development (OECD) Nuclear Energy Agency Data Bank (NEADB) work together to acquire sets of computer codes, nuclear data and integral experiments relevant to shielding and dosimetry applications for fission, fusion and accelerator applications. To keep up with advances in computing technology, international researchers continue to develop nuclear software. Collection centres like RSICC and NEADB serve the community and play a role in advancing nuclear science and technology research.

Background

Since the first meeting in Arlington, Texas, in 1994, the Nuclear Energy Agency Data Bank (NEADB) and the Radiation Safety Information Computational Center (RSICC) have been working together to continue the series of meetings to stay abreast of advances in computer software technology for accelerators, targets and other radioactive environments. To date, there have been nine meetings on Shielding Aspects of Accelerators, Targets and Irradiation Facilities (SATIF):

- SATIF-1, Arlington, Texas (1994);
- SATIF-2, Geneva, Switzerland (1996);
- SATIF-3, Sendai, Japan (1997);
- SATIF-4, Knoxville, Tennessee (1998);
- SATIF-5, Paris, France (2000);
- SATIF-6, Stanford, California (2002);
- SATIF-7, Sacavém, Portugal (2004);
- SATIF-8, Pohang, South Korea (2006);
- SATIF-9, Oak Ridge, Tennessee (2008).

During the last 15 years, software developers have submitted either newly developed or updated computer codes to NEADB and RSICC. The two centres continue to work together in collecting computer codes and data for distribution to the scientific community.

New software updates since SATIF-9

The following section describes the software that has been updated or newly contributed to the centres. A more detailed listing is found in Table 1.

RSICC code package CCC 657

BETA-S 6: A code system to calculate multi-group beta-ray spectra.

Data library

ENSDF-95: Beta-decay transition data based on the Evaluated Nuclear Structure Data Files maintained by National Nuclear Data Center (NNDC) at Brookhaven National Laboratory.

Contributors

Oak Ridge National Laboratory, Oak Ridge, Tennessee

CANDU Owner Group, Toronto, Ontario, Canada

Atomic Energy of Canada Limited, Whiteshell Laboratories, Manitoba, Canada

BETA-S [1,2] calculates beta-decay source terms and energy spectra in multi-group format for time-dependent radionuclide inventories of actinides, fission products and activation products. Multi-group spectra may be calculated in any arbitrary energy group structure. The code also calculates the total beta energy release rate from the sum of the average beta-ray energies as determined from the spectral distributions. BETA-S also provides users with an option to determine principal beta-decaying radionuclides contributing to each energy group. The SCALE code system must be installed on the computer before installing BETA-S, which requires the SCALE subroutine library and nuclide-inventory generation from the ORIGEN-S code. This release is compatible with SCALE Versions 5.0, 5.1 and 6. The following enhancements were completed in this version:

- The BETA-S source code was converted to modern Fortran 90 standard.
- Dynamic memory allocation was implemented.

- The free-format input reading routines were replaced with reading modules in SCALE 5.

- The capability to obtain beta-decay branching data from either a binary or card-image format ORIGEN data library (required for compatibility with ORIGEN-ARP) was added.

- An error associated with spectral calculation in the highest energy group was corrected.

- The spectrum calculation was improved by normalising spectral energy to evaluated beta energy.

- The capability to generate plot files compatible with the PlotOPUS program was added.

RSICC code package CCC-726

CNCSN: One-, two- and three-dimensional $\underline{C}$oupled $\underline{N}$eutral and $\underline{C}$harged Particle $\underline{SN}$ code system.

Auxiliary codes included in the CNCSN package

KATRIN-2.0: Three-dimensional neutral and charged particle transport.

KASKAD-S-2.5: Two-dimensional neutral and charged particle transport.

ROZ-6.6: One-dimensional neutral and charged particle transport.

ARVES-2.5: Pre-processor for the working macroscopic cross-section FMAC-M format for transport calculations.

MIXERM: Utility for preparing mixtures based on multi-group cross-section libraries in ANISN format.

CEPXS-BFP: A version of Sandia National Laboratories' multi-group coupled electron-photon cross-section-generating code CEPXS, adapted for solving the charged particle transport in the Boltzmann-Fokker-Planck formulation with the use of discrete-ordinates method.

SADCO-2.4: Institute for High-Energy Physics modular system for generating coupled nuclear data libraries to provide high-energy particle transport calculations by the multi-group method.

KATRIF: Post-processor for KATRIN code.

KASF: Post-processor for KASKAD-S code.

ROZ6F: Post-processor for ROZ-6 code.

ConDat 1.0: Code for converting by the tracing algorithm the combinatorial geometry presentation to the bit-mapped one.

MCU Viewer: Code for combinatorial geometry visualisation.

Maplook: Script for SURFER to automate geometry visualisation on the basis of material maps given as atlas boundary (*.bna) files.

SYNTH: Utility for construction of an approximate solution of 3-D transport equation in vicinity of reactor pressure vessel by the synthesis method.

Contributor

Keldysh Institute of Applied Mathematics, Moscow, Russia

KATRIN, KASKAD-S, and ROZ-63 solve the multi-group transport equation for neutrons, photons and charged particles in 3-D (x, y, z and r, ϑ, z), 2-D (x, z, r, z and r, ϑ) and 1-D (plane, spherical and cylindrical) geometries, respectively. The transport equation for charged particles can be solved with direct treatment of the continuous slowing-down (CSD) term; for 1-D plane and spherical geometries, the Bolzmann-Fokker-Plank equation can be solved with direct treatment both CSD and continuous scattering terms. The scattering anisotropy can be treated in the P_L approximation. The adjoint solution of the problem can also be obtained (for neutral particles only). The principal application is solving of deep-penetration transport problems, typical for radiation protection and shielding calculations. Fission problems (subcritical boundary value and k_{eff}), problems with upscattering (thermalisation, etc.), electron-photon and hadron cascade problems can also be solved.

RSICC code package CCC-755

CINDER Version 1.05: Code System for Actinide Transmutation Calculations

Auxiliary codes

ACTIVATION: Script to automate the coupling between CINDER'90 and the MCNPX code (also available through RSICC), geared for accelerator-driven applications.

GAMMA_SOURCE: Script to format gamma spectral intensities from CINDER'90 into a source definition for MCNPX.

Contributors

Los Alamos National Laboratory, Los Alamos, New Mexico, USA

Oak Ridge National Laboratory, Oak Ridge, Tennessee, USA

Argonne National Laboratory, Argonne, Illinois, USA

Paul Scherrer Institut, Villigen, Switzerland

The CINDER 1.05 [4,5] package includes the CINDER'90 code Version 7.4.2, ACTIVATION 1.0, GAMMA_SOURCE 1.0. CINDER'90 is the latest in the sequence of data and code evolutions built upon the original work of T. England at Bettis Atomic Power Laboratory (BAPL) in the early 1960s. It is used to calculate the inventory of nuclides in an irradiated material. Utilising a self-contained nuclear data library, CINDER'90 calculates the atom density (atoms per unit volume) and activity density (curies per unit volume) of each and every nuclide present at a specified time. Though always providing a nuclide inventory, its functional identity depends upon the application. In nuclear reactor applications, such a code is commonly called a "burn-up code," since it follows the temporal burn-up of fissionable material and the associated production of fission products. It may also be called an "activation code" since it well describes the conversion of stable nuclides to radioactive nuclides by particle bombardment. In keeping with more recent vernacular, the code is identified as a transmutation nuclide inventory code, since the code follows all paths of nuclide transmutation – the conversion of a nuclide to a different nuclide by particle absorption and/or radioactive decay. "Nuclide evolution code" has recently become the more popular terminology, perhaps linked to R- and S-process applications in astrophysics.

The CINDER'90 library of 63-group cross-sections describes 3 400 nuclides in the range $1 \leq Z \leq 103$. The code requires a multi-group neutron flux for $E_n \leq 20$ MeV and nuclide production rates for reactions at higher neutron energies or for additional particles. Although developed for accelerator-driven problems, the code is applicable to any transmutation problem for which simulation calculations of particle reactions are available.

RSICC code package CCC-744

EASYQAD: A visualisation code system for gamma and neutron shielding calculations, Version 1.0.

Contributors

Innovative Technology Center for Radiation Safety (iTRS), Seoul, Korea

Nuclear Reactor Analysis Laboratory at Hanyang University, Seoul, Korea

EASYQAD, Version 1.0 [6], is a stand-alone Windows XP code system that facilitates gamma and neutron shielding calculations with user-friendly graphical interfaces. It is used to analyse radiation shielding problems and includes:

- eight kinds of geometry types;
- various flexible source options;
- common material library;
- various detector types.

Through intuitive windows and their interactions inside EASYQAD, the user can specify the dimensions of 3-D shapes, their material compositions, their densities, the type of radioactive sources, the locations of the sources, and the type and positions of detectors. With the ease of using these sequences, shielding problems will become simpler and more clearly understandable. Furthermore, the error-checking system can prevent users from making mistakes by automatically debugging the user inputs and giving modal dialog windows. The included Atomic Energy of Canada Limited (AECL) implementation of QAD-CGGP-A, Version 95.2 (C00645/MNYCP/00), is run from the user interface.

RSICC code package CCC-745

ERANOS 2.0: Modular code and data system for fast reactor neutronics analyses.

Contributors

DER/SPRC/LEPh, CEA-Cadarache, France, through the OECD Nuclear Energy Agency (NEA) Data Bank, Issy-les-Moulineaux, France; NEA Package ID: NEA-1683/01.

The European Reactor Analysis Optimised Calculation System, ERANOS [7], has been developed and validated with the aim of providing a suitable basis for reliable neutronic calculations of current as well as advanced fast reactor cores. It consists of data libraries, deterministic codes and calculation procedures that have been developed within the European Collaboration on Fast Reactors over the past 20 years or so, in order to answer the needs of both industrial and R&D organisations. The whole system counts roughly 250 functions and 3 000 subroutines totalling 450 000 lines of Fortran-77 and ESOPE instructions.

ERANOS is written using the ALOS software, which requires only standard Fortran compilers and includes advanced programming features. A modular structure was adopted for easier evolution and incorporation of new functionalities. Blocks of data (SET) can be created or used by the modules themselves or by the user via the LU control language. Programming and dynamic memory allocation are performed by means of the ESOPE language. External temporary storage and permanent storage capabilities are provided by the GEMAT and ARCHIVE functions, respectively. ESOPE, LU, GEMAT and ARCHIVE are all part of the ALOS software. This modular structure allows different modules to be linked together in procedures corresponding to recommended calculation routes ranging from fast-running and moderately accurate "routine" procedures to slow-running but highly accurate "reference" procedures.

RSICC code package CCC-728

GENII-LIN: Multi-purpose health physics code system with a new object-oriented interface, Release 2.1.

Contributors

Laboratorio di Montecuccolino, Bologna University, Bologna, Italy

Based on GENII-1.485 developed at Pacific Northwest Laboratory, Richland, Washington

The goal of the GENII-LIN [8] project was to develop a multi-purpose health physics code running on a Linux platform. The general features of the GENII-LIN system include:

- capabilities for calculating radiation dose both for acute and chronic releases, with options for annual dose, committed dose and accumulated dose;

- capabilities for evaluating exposure pathways, including direct exposure via water (swimming, boating, fishing), soil (buried and surface sources), air (semi-infinite cloud and finite cloud model), inhalation pathways and ingestion pathways.

The release scenarios considered are the following:

- acute release to air, from ground level or elevated sources, or to water;

- chronic release to air, from ground level or elevated sources, or to water;

- initial contamination of soil or surfaces.

GENII-LIN is the result of implementing the GENII-1.485 software package on the Linux platform. [Note that GENII-1.485 was distributed as RSICC package identifier C00601IBMPC02 and has been replaced in the RSICC collection with GENII 2.06 from Pacific Northwest National Laboratory (PNL) (C00737PC58600).] The GENII portion of the GENII-LIN package contains the program that was developed to incorporate the internal dosimetry models recommended by the International Commission on Radiological Protection (ICRP) into the environmental pathway analysis models used at Hanford. GENII is a coupled system of six programs (ENV, ENVIN, DOSE, INTDF, EXTDF, DITTY) and the associated data libraries that comprise the Hanford Dosimetry System (Generation II) to estimate potential radiation doses to individuals or populations from both routine and accidental releases of radionuclides to air or water and residual contamination from spills or decontamination operations.

GENII-LIN 2.0 came with a new set of programs (ENV13, INTDF13, EXTDF13, DOSE13) and associated data libraries. It retains all the capabilities of GENII-1.485 and incorporates into the existing environmental pathway analysis models the more recent internal dosimetry models recommended by the ICRP 72 and the radiological-risk-estimating procedures of FGR13.

GENII-LIN-2.1 is primarily a maintenance release with several bug fixes and improvements.

RSICC code package CCC-742

GES_MC: Gamma-electron Efficiency Simulator, Version 3.1

Contributor

Radiation Department, Institute of Public Health, Cluj-Napoca, Romania

GES_MC (Gamma-electron Efficiency Simulator Monte Carlo) [9] is written entirely in Java and is based on the EGSnrc (Electron Gamma Shower) source code. Although GES_MC is designed especially for the computation of the response function and peak efficiency for gamma detectors, it can also be used in various studies concerning photon or electron interactions with the matter in any cylindrical (RZ) geometry. This application is designed mainly for computation of detector peak efficiency and detector total efficiency (whole spectrum) involved in gamma spectrometry. It can also compute detector efficiency for beta radiation (electrons and positrons), absorbed dose and kerma in any cylindrical (RZ) geometry, attenuation and scatter fraction of radiation in detector walls. Furthermore, it can be used for some radiological applications such as the evaluation of scattered X radiation (secondary radiation) at a user-defined distance from the patient. GES_MC is based on the radiation transport theory and algorithms (routines taken from EGSnrc software) developed by the Stanford Linear Accelerator Center (SLAC), USA and the National Research Council (NRC), Canada. The original EGSnrc system of computer codes is a general-purpose package for the Monte Carlo simulation of the coupled transport of electrons and photons in an arbitrary geometry for particles with energies above a few keV up to several hundreds of GeV. See the GES_MC developers' website for additional information: *http://tensp.academic.ro/download/fulea*.

RSICC code package CCC-740

MCNP5/MCNPX: Monte Carlo N-particle transport code system including MCNP5 1.51 and MCNPX 2.6.0 and data libraries.

The CCC-740 package contains MCNP5 1.51, MCNPX 2.6.0 and MCNPDATA.

Auxiliary programs included in the distribution

MAKXSF: Prepares MCNP cross-section libraries, now with Doppler broadening.

ONEGXS: Creates one-group cross-sections with P0 or P1 scattering in ACE format.

VISED 22S: Visual editor for interactively constructing and visualising MCNP geometry (runs on Windows PCs only). Further VISED information can be found on-line at the Visual Consultants website *www.mcnpvised.com*.

Related data library

MCNPDATA: Standard neutron, photoatomic, photonuclear, and electron data libraries for MCNP5 and MCNPX.

Contributor

Los Alamos National Laboratory, Los Alamos, New Mexico

MCNP5 [10-12] is a general-purpose Monte Carlo N-particle code that can be used for neutron, photon, electron or coupled neutron/photon/electron transport, including the capability to calculate eigenvalues for critical systems. Some of the new features of MCNP5 1.51 include the following:

- variance reduction with pulse height tallies;
- new VAR input card added to control variance-reduction methods;
- annihilation gamma tracking;
- Doppler broadening added to the *makxsf* utility code;
- improved S(α,β) thermal scattering;
- large lattice enhancements;
- direct RSSA file reading for distributed multi-processing;
- improved Compton scattering PSC calculation for detectors and DXTRAN;
- web-based documentation.

MCNPX™ [13] is a general-purpose Monte Carlo radiation transport code that tracks virtually all particles at almost all energies. The official release date of MCNPX 2.6.0 is 30 April 2008. MCNPX began in 1994 as a code-merger project of MCNP 4B and LAHET 2.8. It was first released to the public in 1999 as version 2.1.5. In 2002, MCNPX was upgraded to MCNP 4C, converted to Fortran 90, enhanced with 12 new features, and released to the public as version 2.4.0. The release of version 2.6.0 includes many new features described in the document, "MCNPX Extensions Version 2.6.0," which is provided with the MCNPX distribution. The depletion/burn-up capability is based on CINDER'90 and MonteBurns. MCNPX depletion is a linked process involving steady-state flux calculations in MCNPX and nuclide depletion calculations in CINDER'90. The depletion/burn-up/transmutation capability is currently limited to criticality (KCODE) problems. Physics improvements include a new version of the Cascade-Exciton Model (CEM), the addition of the Los Alamos Quark-Gluon String Model (LAQGSM) event generator, and a substantial upgrade to muon physics. Current physics modules include the Bertini and ISABEL models taken from the LAHET Code System (LCS), CEM 03, and INCL4. Many new tally source and variance-reduction options have been developed. MCNPX is released with libraries for neutrons, photons, electrons, protons and photonuclear interactions. In addition, variance-reduction schemes (such as secondary particle biasing) and new tallies have been created specific to the intermediate- and high-energy physics ranges. The "mesh" and "radiography" tallies were included for 2-D and 3-D imaging purposes. Energy deposition received a substantial reworking based on the demands of charged-particle high-energy physics. An auxiliary program, GRIDCONV, converts the mesh and radiography tally as well as standard MCTAL-file results for viewing by independent graphics packages. The code may be run in parallel at all energies via PVM or MPI. Information about MCNPX development can be found on the following website: *http://mcnpx.lanl.gov*.

RSICC code package CCC-760

PARTISN 5.97: Time-dependent, parallel neutral particle transport code system.

Contributor

Los Alamos National Laboratory, Los Alamos, New Mexico

PARTISN (Uallel, <u>T</u>ime-Dependent <u>SN</u>) [14] is the evolutionary successor to CCC-547/DANTSYS. PARTISN is a modular computer program package designed to solve the time-independent or time-dependent multi-group discrete-ordinates form of the Boltzmann transport equation in several

different geometries. The modular construction of the package separates the input-processing, the transport-equation solving and the post-processing (or edit) functions into distinct code modules: the Input Module, the Solver Module and the Edit Module, respectively. PARTISN is the evolutionary successor to the DANTSYSTM code system package. The Input and Edit Modules in PARTISN are very similar to those in DANTSYS. However, unlike DANTSYS, the Solver Module in PARTISN contains one-, two- and three-dimensional solvers in a single module. In addition to the diamond-differencing method, the Solver Module also has Adaptive Weighted Diamond-Differencing (AWDD), Linear Discontinuous (LD) and Exponential Discontinuous (ED) spatial differencing methods. The spatial mesh may consist of either a standard orthogonal mesh or a block adaptive orthogonal mesh. The Solver Module may be run in parallel for two- and three-dimensional problems. One can now run one-dimensional problems in parallel using Energy Domain Decomposition (EDD, triggered by Block 5 input keyword npeg>0). EDD can also be used in two or three dimensions with or without our standard Spatial Domain Decomposition.

Both the static (fixed-source or eigenvalue) and time-dependent forms of the transport equation are solved in forward or adjoint mode. PARTISN now also has a probabilistic mode for Probability of Initiation (static) and Probability of Survival (dynamic) calculations. Vacuum, reflective, periodic, white or inhomogeneous boundary conditions are solved. General anisotropic scattering and inhomogeneous sources are permitted. PARTISN solves the transport equation on orthogonal (single-level or block-structured AMR) grids in 1-D (slab, two-angle slab, cylindrical, or spherical), 2-D (X-Y, R-Z, or R-T) and 3-D (X-Y-Z or R-Z-T) geometries.

RSICC code package CCC-756

PENELOPE2008.1: Code system for Monte Carlo simulation of electron and photon transport.

Contributors

Facultat de Fisica (ECM), Universitat de Barcelona and Universitat Politècnica de Catalunya de Barcelona, Spain, through the Nuclear Energy Agency Data Bank, Issy-les-Moulineaux, France.

PENELOPE [15] performs Monte Carlo simulation of coupled electron-photon transport in arbitrary materials and complex quadric geometries. A mixed procedure is used for the simulation of electron and positron interactions (elastic scattering, inelastic scattering and bremsstrahlung emission), in which "hard" events (*i.e.* those with deflection angle and/or energy loss larger than preselected cut-offs) are simulated in a detailed way, while "soft" interactions are calculated from multiple scattering approaches. Photon interactions (Rayleigh scattering, Compton scattering, photoelectric effect and electron-positron pair production) and positron annihilation are simulated in a detailed way. PENELOPE reads the required physical information about each material (which includes tables of physical properties, interaction cross-sections, relaxation data, etc.) from the input material data file. The material data file is created by means of the auxiliary program MATERIAL, which extracts atomic interaction data from the database of ASCII files.

PENELOPE mailing list archives and additional information about the code can be found at *www.nea.fr/lists/penelope.html*.

The following features are specific to the 2001 and later versions of the code:

- The simulation parameters (Eabs, C1, C2, Wcc, and Wcr) are defined independently for each material. This allows the user to specify regions of interest where the simulation is performed in greater detail.

- The argument DSMAX of subroutine JUMP specifies the maximum allowed path length between hard interactions of electrons and positrons. By selecting a suitably small value for this parameter, the user can control the number of hinges in thin regions (which must be larger than ten or so, to ensure accuracy). This argument is also used for simulating the transport of charged particles in the presence of static external electric and magnetic fields. DSMAX has no effect when set equal to a very large number (*e.g.* 10**35).

- The structure of the common /TRACK/ differs from previous versions. The variable ILB(5), which describes the origin of secondary particles, can be used to study partial contributions from particles originated by a given process.

RSICC computer code PSR-158

SAMMY-8.0.0: Code system for multi-level R-matrix fits to neutron and charged particle cross-section data using Bayes' equations.

Auxiliary codes

Seventeen auxiliary codes are provided along with the SAMMY code. These codes aid with such processes as preparing input, plotting results or studying statistical properties of resonance parameters. A complete list and description of the auxiliary codes is provided in Section X of the SAMMY users' manual.

ANGODF: Convert PLOT file from energy/angle to angle/energy.

CONVRT: Convert from REFIT input to SAMMY or vice versa.

SAMAMR: Add, mix, or recover variables in COVariance file.

SAMAMX: Alter the value of one non-varied parameter in the COVariance file after completion of an analysis.

SAMCPR: Compare SAMMY calculations to those from other sources.

SAMDIS: Calculate statistical distributions for resonance parameters.

SAMFTZ: Modify the experimental energies with t0 and L0.

SAMORT: Plot the ORR resolution function.

SAMPLT: Alternative form for plot files.

SAMQUA: Generate resonance quantum numbers for particle pairs.

SAMRML: Read ENDF File 2, calculate cross-sections and derivatives.

SAMRPT: Plot RPI resolution function.

SAMRST: Plot Gaussian plus exponential resolution function.

SAMSMC: Perform Monte Carlo calculation of multiple scattering corrections.

SAMSTA: Generate staircase plots of resonance widths.

SAMTHN: Thin experimental data.

SUGGEL: Estimate quantum numbers for resonances.

Contributor

Oak Ridge National Laboratory, Oak Ridge, Tennessee

The purpose of SAMMY [16] is to analyse time-of-flight cross-section data in the resolved and unresolved resonance regions, where the incident particle is either a neutron or a charged particle (p, α, d,…). Energy-differential cross-sections and angular-distribution data are treated, as are certain forms of energy-integrated data.

In the resolved resonance region (RRR), theoretical cross-sections are generated employing the Reich-Moore approximation to R-matrix theory (and extensions thereof). Sophisticated models are used to describe the experimental situation: data reduction parameters (*e.g.* normalisation, background, sample thickness) are included. Several options are available for resolution and Doppler broadening, including a crystal-lattice model for Doppler broadening. Self-shielding and multiple-scattering correction options are available for analysis of capture cross-sections. Multiple isotopes and impurities within a sample are handled accurately.

Cross-sections in the unresolved resonance region (URR) can also be analysed using SAMMY. The capability was borrowed from Froehner's FITACS code; SAMMY modifications for the URR include more exact calculation of partial derivatives, normalisation options for the experimental data, increased flexibility for input of experimental data, and introduction of user-friendly input options.

In both energy regions, values for resonance parameters and for data-related parameters (such as normalisation, sample thickness, effective temperature, resolution parameters) are determined via fits to the experimental data using Bayes' method (see below). Final results may be reported in ENDF format for inclusion in the evaluated nuclear data files. The new features added to SAMMY include the following:

- The value of ν (nu) for η (eta) calculations can now be energy-dependent.

- Extensive revisions have been made to the self-shielding multiple-scattering (ssm) module.

- Tabulated values (from Monte Carlo calculations) can be used instead of SAMMY-generated double-plus scattering corrections.

- The "simple" resolution function may include a Gaussian curve whose width is a linear function of energy.

- Input resonance parameters can now be presented as reduced-width amplitudes γ instead of partial widths $\Gamma = 2P\gamma 2$.

- For transmission measurements, the sample thickness may be non-uniform.

- SAMMY now produces a third type of output file from which plots may be made – an ASCII file (with extension "LST") is created.

RSICC code package CCC-750

SCALE 6: Standardised computer analyses for licensing evaluation modular code system for work stations and personal computers, including ORIGEN-ARP.

Contributor

Oak Ridge National Laboratory, Oak Ridge, Tennessee

The following items highlight new capabilities that are included in SCALE 6 [17]:

- Continuous energy (CE) capability in KENO V.a and KENO-VI.

- CE and 238-group ENDF/B-VI.8 and ENDF/B-VII.0 (latest ENDF release) cross-section libraries with full-range Bondarenko factors in multi-group libraries.

- MAVRIC/Monaco 3-D Monte Carlo shielding modules with automated variance reduction:

  – uses SCALE Generalised Geometry Package (same as KENO-VI);

  – flexible source description – separable spatial, energy and directional distributions;

  – tally options – region tally, point detectors and mesh tally;

  – uses CADIS methodology to perform automated 3-D variance reduction;

  – creates a biased source distribution and weight windows in space and energy;

  – uses FW-CADIS (Forward-Weighted CADIS) to optimise multiple tallies simultaneously or produce mesh tallies with more uniform relative uncertainties;

  – graphical displays of mesh tallies, weight windows, source distributions, intermediate flux files and tally convergence with Java viewer.

- ENDF/B-VII coupled neutron/gamma shielding cross-section libraries for use with MAVRIC/ Monaco (200 neutron/47 gamma groups and 27 neutron/19 gamma groups).

- Criticality accident alarm system (CAAS) analysis using CSAS6/KENO-VI criticality sequence and MAVRIC/Monaco shielding sequence.

- TRITON/NEWT enhancements:

  – depletion with doubly heterogeneous unit cells (*e.g.* pebble-bed or prismatic fuel);

- – automatic group collapse for depletion calculations;

- – extended limits for number of depletion materials and depletion steps;

- – improved treatment of depletion by flux vs. depletion by power for non-power rods;

- – full support for fixed-source calculations;

- – improved treatment for sigma-transport calculations (current weighted);

- – improved accuracy in calculations where critical buckling is supplied;

- – addition of arbitrarily high order product quadrature set;

- – new fast reactor ORIGEN-S library for fast reactor analysis with TRITON;

- – tracking of trace element nuclides in TRITON depletion calculations;

- – full support for all OPUS capabilities including stacked OPUS specifications within a single TRITON calculation.

- TSUNAMI-3D with KENO-VI (SCALE 5.1 used only KENO V.a with TSUNAMI).

- Flexible mesh grids in KENO V.a and KENO-VI for TSUNAMI or criticality accident alarm system (CAAS) analyses.

- HTML output for KENO-VI (SCALE 5.1 included HTML output for KENO V.a).

- Covariance library with data for more than 300 materials based on:

  - – Los Alamos National Laboratory (LANL) covariance data for light nuclei up to and including F-19;

  - – "integral method" in thermal and resonance range for other nuclides [Oak Ridge National Laboratory (ORNL)];

  - – nuclear model techniques in fast range for other nuclides [Brookhaven National Laboratory (BNL), LANL].

- TSURFER sensitivity/uncertainty (S/U) data adjustment tool to examine measured and calculated data and adjust integral experiment values within uncertainties to produce consistency between measured and calculated results.

- Reactivity sensitivity analysis tool, TSAR.

- New USLSTATS (Upper Subcritical Limits Statistics) entirely rewritten in Java with integrated user interface for input, output and plotting.

- VIBE (Validation, Interpretation and Bias Estimation) Java user interface to filter TSUNAMI files and sort/filter sensitivity data.

- ExSITE (Extensible SCALE Intelligent Text Editor) Java user interface for TSUNAMI-IP, TSURFER and TSAR.

- STARBUCS burn-up-credit cask-loading curve search.

- MCDancoff (Monte Carlo Dancoff) control module to calculate Dancoff factors in complicated 3-D geometries using Monte Carlo integrations in a modified version of KENO-VI called "KENO_Dancoff".

RSICC code package CCC-757

SERPENT 1.1.7: Continuous-energy Monte Carlo reactor physics burn-up calculation code.

Data libraries

Serpent 1.1.7 cross-section library based on ENDF/B-VI.8.

Serpent 1.1.7 cross-section library based on ENDF/B-VII.

Serpent 1.1.7 cross-section library based on JEF-2.2.

Serpent 1.1.7 cross-section library based on JEFF-3.1.1.

Serpent 1.1.7 thermal scattering libraries based on JEF-2.2, JEFF3.1, ENDF/B-VI.8 and ENDF/B-VII.

Contributors

VTT Technical Research Centre of Finland

SERPENT [18] is a three-dimensional continuous-energy Monte Carlo reactor physics burn-up calculation code specifically designed for lattice physics applications. The code uses built-in calculation routines for generating homogenised multi-group constants for deterministic reactor simulator calculations. The standard output includes effective and infinite multiplication factors, homogenised reaction cross-sections, scattering matrices, diffusion coefficients, assembly discontinuity factors, point-kinetic parameters, effective delayed neutron fractions and precursor group decay constants. User-defined tallies can be set up for calculating various integral reaction rates and spectral quantities.

Internal burn-up calculation capability allows SERPENT to simulate fuel depletion as a completely stand-alone application. Extensive effort has been put into optimising the calculation routines, and the code is capable of running detailed assembly burn-up calculations similar to deterministic lattice codes within a reasonable calculation time. The overall running time can be further reduced by parallelisation.

SERPENT can be used for various reactor physics calculations at pin, assembly and core levels. The continuous-energy Monte Carlo method allows the modelling of any critical reactor type, including both thermal and fast neutron systems. The suggested applications of SERPENT include group-constant generation; fuel cycle studies; validation of deterministic lattice physics codes; and educational, training and demonstration purposes.

A complete description of the project is found at the SERPENT website, *http://montecarlo.vtt.fi.*

RSICC data library DLC-237

SINBAD-2009.02: Shielding Integral Benchmark Archive and Database, Version February 2009.

Contributors

OECD Nuclear Energy Agency Data Bank, Issy-les-Moulineaux, France

Oak Ridge National Laboratory, Oak Ridge, Tennessee

Many of the organisations that contributed to this benchmark compilation are listed in the index file SINBADIS.htm.

SINBAD [19] began in 1992-93, prompted by the continued closure of experimental facilities world wide. The loss of benchmark experimental facilities jeopardises the future of new shielding data. Further, because of the loss of lab notes and/or logbook records from poor document storage and/or ageing, together with the loss of guidance from the retirement of key research staff who were conducting the experiments, complete benchmark data become a premium under today's strict quality assurance needs. The decision was made to collect, recompile and distribute benchmark information in formats acceptable to the international community in an attempt to preserve and disseminate the information. The data integrity was checked and reference sources examined for self-consistency. At times, full benchmark information was gathered from multiple sources including personal contacts and laboratory logbooks.

The guidelines developed by the Benchmark Problems Group of the American Nuclear Society Standards Committee (ANS-6) on formats for benchmark problem description have been followed. SINBAD data include benchmark information on: *i)* the experimental facility and the source; *ii)* the benchmark geometry and composition; *iii)* the detection system, measured data and an error analysis. A reference section is included with the data. Relevant graphical information, such as experimental geometry or spectral data, is included. All information that is compiled for inclusion with SINBAD has been verified for accuracy and reviewed by two scientists.

The data in the RSICC SINBAD-2009.02 package were received through the NEADB and correspond to Data Bank packages as follows:

- NEA-1517 SINBAD REACTOR (abstract last modified 11-FEB-2009);

- NEA-1552 SINBAD ACCELERATOR (abstract last modified 6-FEB-2009);

- NEA-1553 SINBAD FUSION (abstract last modified 10-FEB-2009).

RSICC code package CCC-747

TRIPOLI-4.4: Code system for coupled neutron, photon, electron, positron, 3-D, time-dependent, Monte-Carlo, transport.

Data libraries

GALILEE 0.2 processed libraries in a TRIPOLI-4 specific format based on JEFF-3.1, FENDL-2.1, JENDL-3.3, ENDFB7R0 and EPDL97. Also included are libraries produced using NJOY in a TRIPOLI-4-specific format based on JEF-2, ENDFB6R4 and ENDL.

Contributors

Commissariat à l'énergie atomique (CEA/Saclay, France), through the OECD Nuclear Energy Agency

TRIPOLI-4 [20] is a general-purpose radiation transport code. It uses the Monte Carlo method to simulate neutron and photon behaviour in three-dimensional geometries. The main areas of application include, but are not restricted to, radiation protection and shielding, nuclear criticality safety, fission and fusion reactor design, and nuclear instrumentation. In addition, it can simulate electron-photon cascade showers.

New features available in TRIPOLI-4 version 4 include the following:

- *New biasing features.* It is possible to store and reuse importance maps. Biasing with a plane or spherical surface has been added. (Cylindrical was already available.)

- *Neutron collision in multi-group homogenised mode.* Anisotropy up to the order 3 in the Legendre polynomial expansion (P3).

- *Display of the collision sites.*

- *ENDF format evaluations.* Mixed representation of the anisotropy from file 4: Legendre format used at low energy and tabulated probability distributions at high energy (*e.g.* O16 from ENDFB6R8). cf ENDF-102 Data formats and procedures for the evaluated nuclear data file ENDF-6. 07/1990, revised 04/2001.

- *Computation of the gamma source produced by neutrons.*

- *Output format for all results.* The -a execution option allows even zero results to be displayed in the output. Although the standard deviation is infinite in this case, for reason of compatibility with the rest of the code, the output file also gives a zero value for the standard deviation.

- *Verbose level for output warnings.* The code now gives only the most important information to the user. The -v option allows the warnings; the -D option gives the same verbose level as previous versions.

- *Photon reaction rates.* In the RESPONSES command, interaction code 100 (coherent scattering), 101 (incoherent scattering), 102 (photoelectric effect), 103 (pair production) and 106 (total photon) are now available.

- *XML format output.* In the SIMULATION command, the "XML_EXPORT" keyword allows the user to get an XML-format output file. Any post-processing tool that can cope with XML format may be used to process this file.

- *ENDF format evaluations*:
  - By default, evaluations produced by NJOY99 (version 81) are used.
  - It is possible to use jeff3.1, endfb7 and jendl3.3 evaluations:
    - ➢ the maximum order of Legendre polynomials is no longer limited to 21;
    - ➢ ENDF-format 2-D interpolation "unit-base" (file 6) is now supported.

- *Combinatorial geometry checks.* One can now choose the number of points for the non-overlapping tests of combinatorial volumes. The keyword is "TEST_GENERATED_POINTS n" (200 by default). The keyword may be written:
  - only once, at the beginning (after the TITLE keyword);
  - as many times as necessary in the GEOMETRY command, just before a VOLU keyword. (For each combinatorial volume, the number of generated points refers to the last TEST_GENERATED_POINTS keyword.)

- *Green's functions files.*

- *Neutronics-shielding coupling.*

- *Responses, scores, biasing names.* It is possible to give names (instead of giving a number) to responses and scores. It is necessary to give names to responses, scores and biasings for neutronics-shielding coupled simulations.

- *Units.* The -u execution option allows the code to output scores with their units.

RSICC code package CCC-759

TITAN 1.19: A three-dimensional deterministic radiation transport code system.

Auxiliary codes

PENMSHXP 2.64b: Mesh generator to build TITAN or PENTRAN input deck with the DISLIN graphic library.

PENMSHXP 2.61a: Mesh generator to build TITAN or PENTRAN input deck without the DISLIN graphic library.

Contributor

University of Florida, Gainesville, Florida

TITAN [21,22] is a time-independent deterministic radiation transport simulation code in 3-D Cartesian geometry. The hybrid approach in the TITAN code allows different transport solvers (Sn or ray racing) to be applied in different regions. TITAN solves both the k-effective and fixed-source forward/adjoint problems. It has been benchmarked on a number of OECD/NEA benchmark problems:

- 3-D radiation transport benchmarks for simple geometries with void regions (Kobayashi problem);

- benchmark on deterministic transport calculations without spatial homogenisation mixed-oxide (MOX) fuel assembly 3-D extension case (C5G7 MOX);

- benchmarks on the accuracy of solution of 3-D transport codes and methods over a range in parameter space.

The extra sweep with the fictitious quadrature technique enables TITAN to simulate the SPECT (single photon emission computed tomography) projection images that are generally produced by Monte Carlo codes. A benchmark using the TITAN code on a torso phantom has been established. In the TITAN SPECT simulation, collimators are not explicitly simulated. Instead, a technique called "circular ordinate splitting" is used to simulate the collimator blurring effects.

RSICC code package CCC-754

VIM 5.1: Continuous-energy neutron/photon transport code system.

Auxiliary codes

XSEDIT2 edits or performs binary conversion of processed physics data.

RETALLY repeats the statistical analysis of tally data, optionally collapsing energy groups and/or spatial regions or skipping early generations.

KEFCODE repeats the statistical analysis of k_{eff} tallies..

ISOVIM produces multi-group VIM material files from COMPXS or ISOTXS interface files or from CASMO ASCII output.

REBATCH regroups tally records to encompass more generations to permit assessment of serial correlation of reaction rate and flux estimates.

Slicer, a C++ program, generates colour 2-D snapshots of a specified VIM geometry.

Contributor

Argonne National Laboratory, Argonne, Illinois

VIM [23] is a continuous-energy criticality, reactor physics and shielding code. It solves the transport problem for neutrons or photons, including thermal neutron scattering effects, either in the eigenvalue mode or for photon or neutron fixed source. VIM features flexible geometry and neutron physics data carefully constructed from ENDF/B data. Special neutron physics capabilities in VIM include unresolved resonance probability tables and direct treatment of resolved resonances described with Reich-Moore parameters. VIM has been extensively benchmarked using both experiments and other accurate codes.

VIM solves the steady-state neutron or photon transport problem in any detailed three-dimensional geometry using either continuous-energy-dependent ENDF nuclear data or multi-group cross-sections. Neutron transport is carried out in a criticality mode or in a fixed-source mode (optionally incorporating subcritical multiplication). Photon transport is simulated in the fixed-source mode. The geometry options are infinite medium, combinatorial geometry and hexagonal or rectangular lattices of combinatorial geometry unit cells and rectangular lattices of cells of assembled plates. Boundary conditions include vacuum, specular and white reflection, as well as periodic boundaries for reactor cell calculations.

The VIM 5.1 (April 2009) release includes data from ENDF/B-IV, ENDF/B-V, ENDF/B-VI and ENDF/B-VII.0. ASCII data libraries and a convenient means to convert them to binary on a target machine are included.

Table 1: Software and data updates since SATIF-9

Software	Description
ACAB-2008	Activation abacus inventory code system for nuclear applications
ALICE-2008	Statistical model code system to calculate particle spectra from HMS precompound nucleus decay
ANGELO-LAMBDA	Covariance matrix interpolation and mathematical verification
BETA-S 6	Code system to calculate multi-group beta-ray spectra
BOT3P-5.3	Code system for 2D and 3D mesh generation and graphical display of geometry and results for radiation transport codes
BOXER	Fine-flux cross-section condensation, 2-D few-group diffusion and transport burn-up calculations
BULK_C-12	Code system to estimate neutron and photon effective dose rates from medium energy protons or carbon ions through concrete or concrete/iron
CINDER 1.05	Code system for actinide transmutation calculations
CNCSN	One-, two- and three-dimensional coupled neutral and charged particle SN code system
DANESS V1.0	Dynamic analysis of nuclear energy system strategies
DWBA07/DWBB07	Code system for inelastic and elastic scattering with nucleon-nucleon potential
DWUCK-CHUCK	Nuclear model code system for distorted wave born approximation and coupled channel calculations
EASY-2005.1	Inventory code system for neutron activation analysis
EASY-QAD 1.0	Visualisation code system for gamma and neutron shielding calculations
ERANOS 2.0	Modular code and data system for fast reactor neutronics analyses
GANAPOL-ABNTT	Analytical benchmarks; case studies in neutron transport theory
GENII 2.09	Environmental radiation dosimetry software system
GENII-LIN 2.1	GENII-LIN multi-purpose health physics code system with a new object-oriented interface, release 2.0
GES_MC	Gamma-electron efficiency simulator, version 3.1
IRDF-2002	The International Reactor Dosimetry File
JDL-IMPORTANCE	Adjoint function: Physical basis of variational and perturbation theory in transport and diffusion problems
JDL-REACTOR-KIN	Nuclear reactor kinetics and control
JDL-THERMODYNAM	Thermodynamics: Frontiers and foundations
LAPUR6	BWR core stability measurements
MATJEFF31.BOLIB	Fine-group cross-section library based on JEFF-3.1 for nuclear fission applications
MCNP5/MCNPX	Monte Carlo N-particle transport code system including MCNP5 1.51 and MCNPX 2.6.0 and data libraries (source and executables)
MCNP5/MCNPX-EXE	Monte Carlo N-particle transport code system including MCNP5 1.51 and MCNPX 2.6.0 and data libraries (executables – no source)
MGA8	Code system to determine Pu isotope abundances from multi-channel analyser gamma spectra
MURE	MCNP utility for reactor evolution
NRCDOSE 2.3.15	Code system for evaluating routine radioactive effluents from nuclear power plants with a windows interface
NUCHART	Nuclear properties and decay data chart of nuclides
PARTISN 5.97	Time-dependent, parallel neutral particle transport code system
PENELOPE2008.1	Code system to perform Monte Carlo simulation of electron photon showers in arbitrary materials
PHOBIA	Photon build-up factors to account for angular incidence on shield walls
PLOT-S	Plotting program with special features for windows environment
POINT2009	A temperature-dependent linearly interpolable tabulated cross-section library based on ENDF/B-VII.0
PR-EDB	Power reactor embrittlement database, version 3
PUFF-IV	Code system to generate multi-group covariance matrices from ENDF/B-VI uncertainty files, version 6.0.1
RASCAL 3.0.5	Radiological assessment for consequence analysis for windows
RSAC7	Radiological safety analysis code system

Table 1: Software and data updates since SATIF-9 (*cont.*)

Software	Description
SAMMY-8	Code system for multi-level R-matrix fits to neutron and charged-particle cross-section data using Bayes' equations
SCALE 6	Modular code system for performing criticality and shielding analyses for licensing evaluation with ORIGEN-ARP (source and executables)
SCALE 6-EXE	Modular code system for performing criticality and shielding analyses for licensing evaluation with ORIGEN-ARP (executables – no source)
SCAMPI	SCAMPI: Collection of codes for manipulating multi-group cross-section libraries in AMPX format
SELFS-3	Self-shielding correlation of foil activation neutron spectra analysis by SAND-II
SERPENT	Continuous-energy Monte Carlo reactor physics burn-up calculation code
SINBAD 2009.02	Shielding integral benchmark archive and database, version February 2009
SUSD3D	Multi-dimensional, discrete-ordinates-based cross-section sensitivity and uncertainty analysis code system
TALYS 1.0	Nuclear model code system for analysis and prediction of nuclear reactions and generation of nuclear data
TENDL-2008-ACE	TALYS-based cross-section library for use with MCNP(X)
THYDE-B1/MOD2	Computer code for the analysis of small-break loss-of-coolant accident of boiling water reactors
THYDE-P2	Computer code for PWR LOCA thermohydraulic transient analysis
TITAN 1.19	A three-dimensional deterministic transport code system
TRIPOLI 4.4	Code system for coupled neutron, photon, electron, positron, 3-D, time-dependent, Monte Carlo, transport calculations
VARSKIN 3 V3.1. 0	Code system for assessing skin dose from skin contamination, version 3.1.0
VIM 5.1	Continuous-energy neutron and photon transport code system, April 2009 release
VITENEA-J	AMPX 175-n,42-g multi-group cross-section library for nuclear fusion applications
VITJEFF31.BOLIB	A JEFF-3.1 multi-group coupled (199n + 42g) cross-section library; in AMPX format for nuclear fission applications

References

[1]   Gauld, I.C., *Upgrade of the Multigroup Beta Calculation Code BETA-S*, Oak Ridge National Laboratory, Oak Ridge, TN, December 2008.

[2]   Gauld, I.C., S.G. King, *BETA-S: A Code to Calculate Multigroup Beta Spectra*, RC-1564 (COG-93-33-I), April 1996.

[3]   Voloschenko, M., *et al.*, "The CNCSN: One-, Two- and Three-dimensional Coupled Neutral and Charged Particle Discrete Ordinates Code Package", *Int. Conf. on Mathematics and Computation, Supercomputing, Reactor Physics and Nuclear and Biological Applications*, 12-15 September 2005, Avignon, France (2005) (on CD-ROM).

[4]   Wilson, W.B., *et al.*, *A Manual for CINDER'90 Version 07.4 Codes and Data*, LA-UR-07-8412, Version 07.4.2, Los Alamos National Laboratory, Los Alamos, NM, December 2007, updated March 2008.

[5]   Gallmeier, F.X., M. Wohlmuther, *Activation Script Version 1.0 User Guide*, ORNL/TM-2008/031, Oak Ridge National Laboratory, Oak Ridge, TN, 18 August 2008.

[6]   Kim, J.K., *EASYQAD Version 1.0: A Visualization Code System for Gamma and Neutron Shielding Calculations*, iTRS at Hanyang University.

[7]   Rimpault, G., *et al.*, "The ERANOS Code and Data System for Fast Reactor Neutronic Analyses", *PHYSOR 2002*, Seoul, Rep. of Korea (2002).

[8]   Sumini, M., F. Teodori, N. Cantoro, *GENII-LIN an Object Oriented Health Physics Code for the Linux Operating System, RPSD 2006*, Carlsbad, NM (2006).

[9]   Fulea, D.C., *Java Implementation of EGSnrc* (2006).

[10]   X-5 Monte Carlo Team, *MCNP-A General Monte Carlo N-Particle Transport Code, Version 5 - Vol. I: Overview and Theory*, (file MCNP5_manual_VOL_I.pdf), LA-UR-03-1987, Los Alamos National Laboratory, Los Alamos, NM, April 2003, revised 3 October 2005, 1 February 2008.

[11]   X-5 Monte Carlo Team, *MCNP – A General Monte Carlo N-particle Transport Code, Version 5 – Vol. II: Users Guide* (file MCNP5_manual_VOL_II.pdf), LA-CP-03-0245, Los Alamos National Laboratory, Los Alamos, NM, April 2003, revised 3 October 2005, 1 February 2008.

[12]   X-5 Monte Carlo Team, *MCNP – A General Monte Carlo N-Particle Transport Code, Version 5 – Vol. III: Developers Guide* (file MCNP5_manual_VOL_III.pdf), LA-CP-03-0284, Los Alamos National Laboratory, Los Alamos, NM, April 2003, revised 3 October 2005, 1 February 2008.

[13]   Pelowitz, D.B., *MCNPX User's Manual, Version 2.6.0*, LA-CP-07-1473, Los Alamos National Laboratory, Los Alamos, NM, April 2008.

[14]   Alcouffe, R.E., *et al.*, *PARTISN: A Time-dependent, Parallel Neutral Particle Transport Code System*, LA-UR-08-07258, Los Alamos National Laboratory, Los Alamos, NM, revised November 2008.

[15]   Salvat, F., J.M. Fernández-Varea, J. Sempau, *PENELOPE-2008, A Code System for Monte Carlo Simulation of Electron and Photon Transport*, Barcelona, Spain, 30 June-3 July 2008, OECD/NEA, Paris (2009).

[16]   Larson, N.M., *Updated Users' Guide for SAMMY: Multilevel R-matrix Fits to Neutron Data Using Bayes' Equations*, ORNL/TM-9179/R8 ENDF-364/R2, Oak Ridge National Laboratory, Oak Ridge, Tennessee, October 2008.

[17]   *SCALE: A Modular Code System for Performing Standardized Computer Analyses for Licensing Evaluations*, Version 6.0, Vols. I-III, ORNL/TM-2005/39, Oak Ridge National Laboratory, Oak Ridge, Tennessee, January 2009.

[18]   Leppänen J, *PSG2/Serpent – A Continuous-energy Monte Carlo Reactor Physics Burn-up Calculation Code Methodology – User's Manual – Validation Report*, VTT Technical Research Centre of Finland, 5 September 2009.

[19]   Kodeli, I., E. Sartori, B.L. Kirk, "SINBAD – Shielding Benchmark Experiments: Status and Planned Activities", *ANS 14th Biennial Topical Meeting of Radiation Protection and Shielding Division*, Carlsbad, NM (2006).

[20]   Petit, O., *et al.*, *TRIPOLI-4 Version 4 User Guide*, CEA-R-6169 (2008) (in English).

[21]   Yi, C., *TITAN: A 3-D Deterministic Radiation Transport Code; User Manual Version 1.19*, University of Florida (2009).

[22]   Yi, C., A. Haghighat, *PENMSHXP Manual, Version 2.5b*, University of Florida (2008).

[23]   Blomquist, R.N., *VIM Monte Carlo Neutron/Photon Transport Code User's Guide Version 5.1*, accessed 28 September 2010, *www.vim.anl.gov/vimguide/vimguide.html* (2009).

Modern g,d,p,n-induced activation-transmutation systems*

Jean-Christophe Sublet
Culham Centre for Fusion Energy
Abingdon, Oxfordshire, United Kingdom

Abstract

The European Activation System (EASY) includes as the source of nuclear data the European Activation File (EAF) and as its engine the FISPACT activation-transmutation code. The latest version of the EAF, EAF-2010, contains cross-section data for gamma-, deuteron- and proton-induced reactions in addition to the traditional neutron-induced data. The main reason for the addition of these data to EAF is to enable activation-transmutation calculations to be performed for even more nuclear facilities, including "accelerator"-driven devices with incident upper energy limit of 60 or 200 MeV. EAF-2010 has benefited from the generation and maintenance of comprehensive activation files in the past and the development of the processing code SAFEPAQ-II and model code TALYS. TALYS is the source for all gamma-, proton- and deuteron-induced data and a fair share of the neutron-induced data. Cross-section validation exercises against both experimental data and systematic, which were started in 1995, enable a comprehensive assessment of the data. Although EAF-2010 is certainly the most-validated activation neutron cross-section library in the world, currently less than 3% of all the reactions can be compared with experimental information, and even then only for a very limited, and not always application-relevant, energy range. As with EAF-2010, -2003, -2005 and -2007 results of integral experiments have been used to correct, adjust and validate data. This can be done using SAFEPAQ-II by inputting the measured effective cross-sections. Validation using integral data has been performed by means of direct comparison with measurements of various materials under relevant particle spectra. A tool has recently been developed which is important now that the libraries contain so much TALYS-calculated data. Statistical analysis of cross-sections (SACS) is used to look for trends in the library data for a particular reaction type and this has proven efficient in identifying reactions with data that need correction or improvement. This method has been used with EAF-2005 and EAF-2007 and is a valuable additional validation method. However, the time has come to rethink the nuclear data generation processes alongside the transport-activation-transmutation code systems. A new approach is proposed that encompasses 25 years of research activities which can now be mobilised to fulfil the needs, using a much more systematic and automated approach. For the first time, all existing experimental data and nuclear models for all relevant materials can together be transferred to technology in a consistent manner. In this process, feedback of extensive validation and benchmark activities would automatically be taken into account.

---

* The full paper being unavailable at the time of publication, only the abstract is included.

A Geant4 physics list for shielding calculations

Tatsumi Koi
(on behalf of the Geant4 Hadronic Working Group)
SLAC National Accelerator Laboratory
Menlo Park, USA

Abstract

Geant4 is a toolkit for the simulation of the passage of particles through matter. It is widely used in many domains including high-energy physics, nuclear physics, astrophysics, space science and medical physics. Members of the Geant4 Hadronic Working Group have been involved in shielding calculations during the past four years, and have participated in the "Intercomparison of Medium-energy Neutron Attenuation in Iron and Concrete" project since SATIF-8. The toolkit approach of Geant4 allows the users to select amongst the physics models and cross-sections those which are best suited to their application domain and use case. These elements are assembled into a "physics list" class, the details of which may vary significantly among use cases. We present a physics list tailored for shielding calculations. It involves a selected set of improved physics models and cross-sections.

Introduction

The Geant4 toolkit [1] provides a complete set of class libraries for Monte Carlo simulations of particle interactions in matter. It adopts object-oriented technology, and follows an iterative-incremental software process. This technology makes it easy to add an extension or improvement of the toolkit not only for developers but also for users. Many such developments can be done without touching the existing code in the toolkit. Because it is designed as a toolkit, a distribution package of Geant4 does not include a default application, though numerous examples covering most use cases are prepared in the package. Referring to these examples, the user is usually required to code only a few classes and a main program to build a fully integrated application. A "physics list" class is one of three mandatory classes the user must prepare. The other two classes are related to detector (geometry) construction and producing the primary vertexes of the simulation. The role of the physics list will be explained in the next section.

Geant4 is used in many research fields, *e.g.* high-energy physics, nuclear physics, astrophysics, space engineering, non-destructive inspection, detector development, environmental research and medical physics. Radiation protection and shielding calculations are also areas where Geant4 may be widely used, although that is not currently the case, compared to other codes. To demonstrate its capability in this field, the Geant4 Hadronic Working Group has participated in the "Intercomparison of Medium-energy Neutron Attenuation in Iron and Concrete" project since SATIF-8 [2,3]. In this paper we will explain the physics list which we used for submitting Geant4 results to the intercomparison at SATIF-10. As already mentioned, there are three mandatory classes which the user must provide to build a Geant4 application. The shielding geometry and primary vertexes of the intercomparison are well defined by the co-ordinator of the comparison project; this paper gives information about the physics list; so that a user may easily reproduce our presented results. In the next section we explain the concept of physics list in Geant4, and then explain it in detail. The results from this physics list will be shown together with experimental data which was provided at the beginning of the comparison project. We also present a possible variation of the physics list and show how the results differ.

The Geant4 physics list

Geant4 provides abundant physics processes for particle interactions with matter, and it often offers multiple choices for a given physics process. Users must explicitly assign the chosen physics process to the particles used in his/her application. The physics list is where the user defines all the particles and sets physics processes to the particles. Cut-off parameters of user's application are also given in the physics list. Especially in the hadronic framework of Geant4, the concept of cross-section and final state generator (model) are completely separated, therefore users can choose cross-section and model independently. As already mentioned, a physics list is one of the three mandatory classes which the user must provide. This is based on the assumption that the user has a better knowledge of the requirements of his/her simulation than the developers of Geant4. This is also consistent with the toolkit approach of Geant4. However, some complete physics lists were provided in examples in early distributions of Geant4. Making a proper physics list is not a simple job, especially for a Geant4 beginner. As a result, there were many requests for the Geant4 collaboration to provide and support a default physics list. In response to these requests, "reference physics lists" were developed. These are concrete classes implementing complete physics lists and are included in the standard Geant4 library. Users can include any of them in his/her simulation by registering one of them. However, reference physics lists vary by use case and should be considered only as starting points, which users may need to modify for their application. More than 20 reference physics lists are included in the latest Geant4 distribution. Many builder classes are also in the distribution to aid the implementation of user-specific physics lists. Most examples still have their own physics lists and they also provide good bases for further implementation by users.

Physics list for the intercomparison projects

We have participated in the "Intercomparison of Medium-energy Neutron Attenuation in Iron and Concrete" project since SATIF-8. The QGSP_BERT reference physics list was used for SATIF-8. We also used QGSP_BERT for SATIF-9, but in that case the neutron cross-sections in the physics list were replaced by newly introduced cross-sections. The Geant4 versions for SATIF-8 and SATIF-9 were

8.0 and 9.1.p01, respectively, both of which were the latest version of Geant4 at the time. The results submitted for SATIF-10 used Geant4 v9.3, and the FTFP_BERT physics list which included a set of recently improved physics models and cross-sections. Hereafter we will explain the main features of this physics list. In the physics list, the FTF (FriToF string) model is used for high-energy interactions and the Precompound model is used as the nuclear de-excitation model. The FTF model is used down to 4 GeV. The Bertini model is used below that energy and is based on the classical BERTini and INUCL cascade models with many improvements related to the treatment of the nuclear medium. The Bertini model has its own low-energy model for dealing with pre-compound and nuclear de-excitations below the cascade energy. The upper limit for the usage of the Bertini model is set to 5 GeV, and in the region between 4-5 GeV the choice between FTFP or BERT models is made randomly according to the energy. A parameterisation based on the Axen and Wellisch systematic [4] is used for neutron cross-sections in the original FTFP_BERT. We replaced this cross-section by the JENDL HE 2007 cross-section [5] and Barashenkov evaluated cross-sections [6]. The former is used up to 3 GeV and the Barashenkov will be used above that energy. This is our proposed physics list for the shielding calculation.

Figures 1 and 2 show our results compared to the experimental data provided during SATIF-10. We show both the reaction rate from the unmodified reference physics list, FTFP_BERT (listed in the plot as Default XS), and the prediction from the same physics list but with the JENDL/Barashenkov cross-sections used instead of the Axen-Wellisch.

Alternative physics lists for shielding calculation

The physics list described in the previous section represents our best guess of the physics needed for shielding calculations. However in this section, three possible variations of the physics list are presented. The first variation is to change the high-energy model from FTF to the QGS (Quark Gluon String) model. In this case the basic reference physics list is QGSP_BERT. The second variation is based on FTF_BIC physics list. Here, the cascade model is changed from BERT to the BIC (BInary Cascade) model and it is also used to handle the re-scattering of secondaries from the high-energy model. Geant4 offers the neutron HP package of models and cross-sections designed specifically for precision low-energy neutron transportation. This package uses a pre-processed ENDF data library and the upper limit of neutron energies handled by this package is 20 MeV. The QGSP_BERT_HP reference physics list uses the neutron HP package, and is the third variant of physics list for shielding calculations.

Figure 1: Comparison of calculated and measured reaction rates for the steel shield
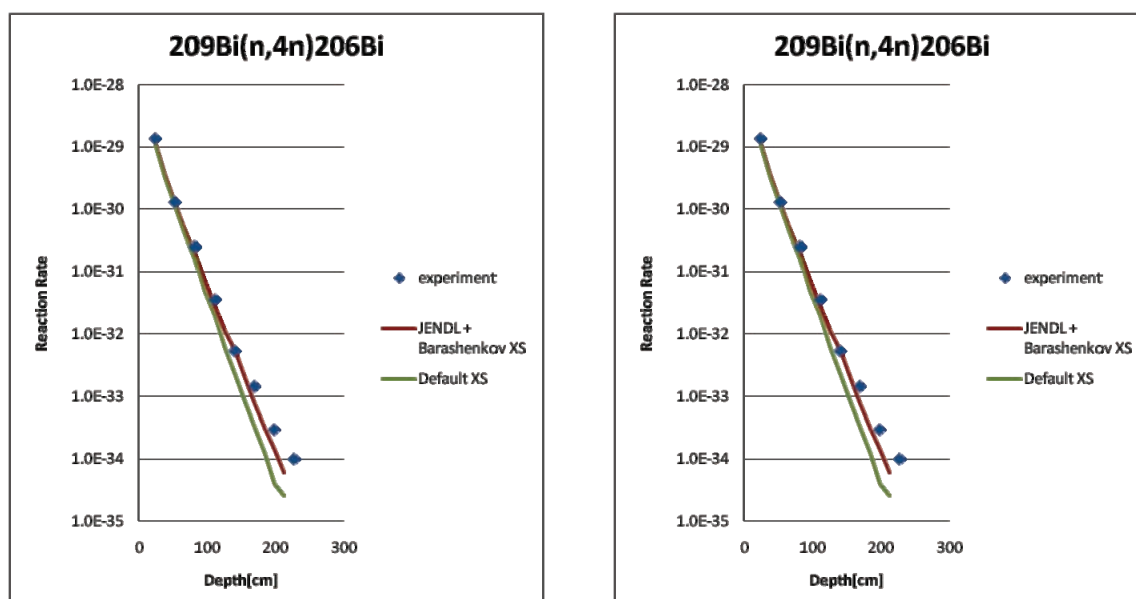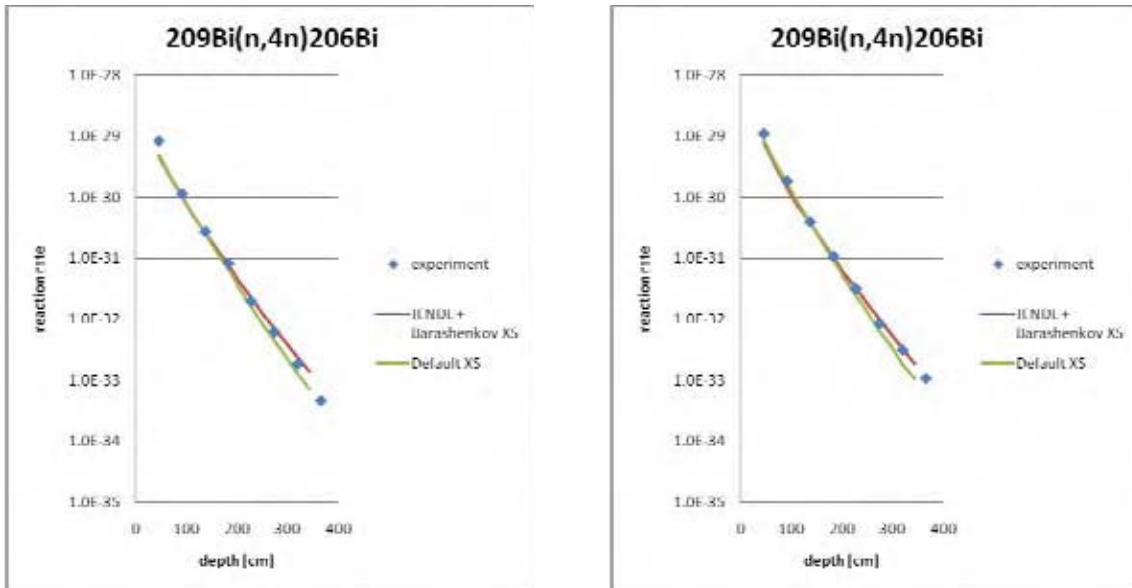
Primary beam energy is 24 GeV

Figure 2: Comparison of calculated and measured reaction rates for the concrete shield

Primary beam energy is 24 GeV

We recommend substituting the default neutron cross-section by the JENDL/Barashenkov cross-sections for shielding calculations in all energy ranges for the cases of QGSP_BERT and FTF_BIC, and above 20 MeV for the case of QGSP_BERT_HP.

Figures 3 and 4 show the results of these alternative physics lists, together with the recommended FTFP_BERT, and data. JENDL and Barashenkov cross-sections are used in all physics lists. The QGSP_BERT-based physics list gives comparable results to FTFP_BERT. The FTF_BIC-based physics list gives a more attenuated result with respect to the other physics lists and with respect to data. Because the energy threshold of ^{209}Bi(n,4n)^{206}Bi and ^{209}Bi(n,6n)^{204}Bi is above 20 MeV, we do not use the neutron HP package in this comparison.

Figure 3: Comparison of calculated and measured reaction rates for the steel shield
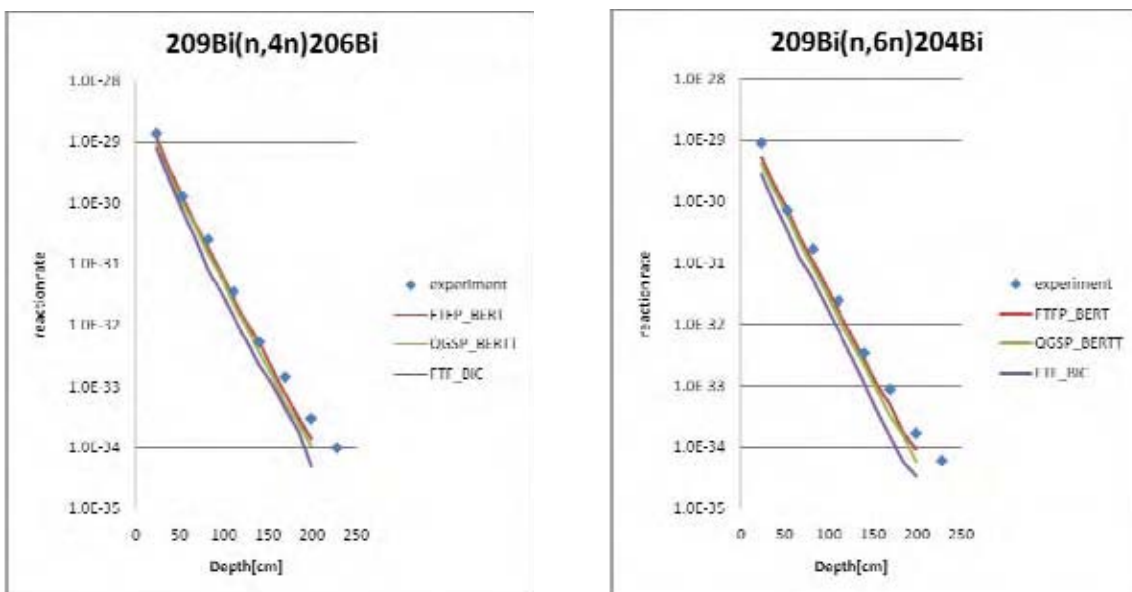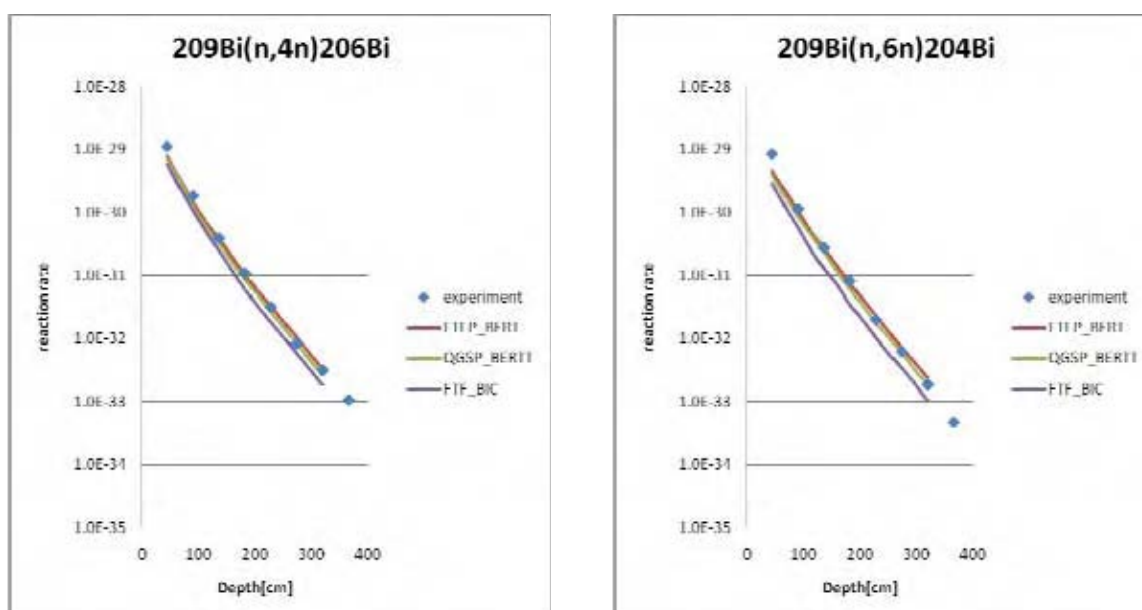
Primary beam energy is 24 GeV

Figure 4: Comparison of calculated and measured reaction rates for the concrete shield

Primary beam energy is 24 GeV

Tables 1 and 2 show the comparison of CPU performance among physics lists and test cases. At 24 GeV the QGSP_BERT-based physics list is faster than the FTFP_BERT-based list , while at 2.8 GeV they are about the same. The FTF_BIC-based physics list is much slower at both energies than the others. This is mainly due to its detailed treatment of hadronic interactions. The results in Table 2 tell us that computing time depends not only on beam energy but also the shielding material used in the test case. All calculations for this CPU performance comparison were done on the lfs batch system of a Dell Poweredge 1950 dual quad-core 2.66 GHz Xeon CPU, with 16 GB memory.

Table 1: CPU performances among physics lists

FTFP_BERT = 1, a smaller number represents better performance

	Concrete shielding		Steel shielding	
	Beam energy 2.83 GeV	Beam energy 24 GeV	Beam energy 2.83 GeV	Beam energy 24 GeV
QGSP_BERT	1.09	0.75	0.98	0.77
FTF_BIC	2.58	2.05	4.08	3.24

Table 2: CPU performances among test cases

Concrete 2.83 GeV = 1, a bigger number represents longer calculation time

	Concrete shielding		Steel shielding	
	Beam energy 2.83 GeV	Beam energy 24 GeV	Beam energy 2.83 GeV	Beam energy 24 GeV
FTFP_BERT	1.00	6.83	0.39	3.75

Conclusions

A physics list is the class where users of Geant4 define all the particles required in his/her application and assign physics processes to the particles. It is one of three mandatory classes that the user is expected to prepare. However, recent distributions of Geant4 have many concrete physics lists in the

library called reference physics lists. They can be used without modification, but they should be considered as a starting point for specific modifications by each user.

A physics list for shielding calculations is proposed in this paper. It is based on the reference physics list FTFP_BERT, and on the JENDL_HE and Barashenkov neutron cross-sections. Possible variations of the physics list are also presented. The QGSP_BERT-based physics list gives comparable results and is slightly faster. The result of the FTF_BIC based physics list is more attenuated than that of other physics lists, and it takes more CPU power. After minor modifications including employment of the neutron HP package for low-energy neutron transportation, this proposed physics list will be included in a future distribution of Geant4 as a reference physics list.

References

[1]   Agostinelli, S., *et al.*, "Geant4: A Simulation Toolkit", *Nucl. Instrum. Meth.*, A 506, 250 (2003). Allison, J., *et al.*, "Geant4 Developments and Applications", *IEEE Transactions on Nuclear Science*, 53, 1, 270-728 (2006).

[2]   Hirayama, H., *et al.*, "Intercomparison of the Medium-energy Neutron Attenuation in Iron and Concrete (6)", *Shielding Aspects of Accelerators, Targets and Irradiation Facilities (SATIF-8)*, Pohang Accelerator Laboratory, Republic of Korea, 22-24 May 2006, pp. 237-250, OECD/NEA, Paris (2010).

[3]   Hirayama, H., *et al.*, "Intercomparison of the Medium-energy Neutron Attenuation in Iron and Concrete (7)", Shielding Aspects of Accelerators, Targets and Irradiation Facilities (SATIF-9), ORNL, USA, 21-23 April 2008, pp. 261-274, OECD/NEA, Paris (2010).

[4]   Wellisch, H.P., D. Axen, "Total Reaction Cross Sections in Proton-nucleus Scattering", *Phys. Rev.*, C 54, 1329-1332 (1996).

[5]   JENDL High Energy File 2007, *http://wwndc.jaea.go.jp/ftpnd/jendl/jendl-he-2007.html*.

[6]   Barashenkov, V.S., Reprint, JINR Dubna P2-89-770 (1990).

INCL4.5 and Abla07 – Improved versions of the intranuclear cascade (INCL4) and de-excitation (Abla) models

J-C. David[1], A. Boudard[1], J. Cugnon[2], A. Kelic-Heil[3], S. Leray[1], D. Mancusi[2], M.V. Ricciardi[3]
[1]Commissariat à l'énergie atomique (CEA-Saclay, Irfu-SPhN), Gif-sur-Yvette, France
[2]University of Liège, AGO Department, Liège, Belgium
[3]Gesellschaft für Schwerionenforschung (GSI), Darmstadt, Germany

Abstract

The two codes INCL4.2 (intra-nuclear cascade) and Abla (de-excitation), combined to describe spallation reactions, have been improved in the past few years. The main points concern the light-charged particle emission and intermediate mass fragment (IMF) emission. The new versions, INCL4.5 and Abla07, now provide good results in particular on tritium and helium production. An international benchmark, where these two codes participated, shows that this spallation model combination is one of the most reliable to reproduce particle and residue production over a wide projectile energy range. These two models have been implemented recently in MCNPX2.7 (beta version).

Significant improvements in microscopic results will be shown and new calculations for the MEGAPIE target will be compared to the previous results.

Introduction

Spallation reactions exist in space and are studied for basic research (*e.g.* cosmogenic isotopes) and for application (*e.g.* activation of space-borne devices). Thanks to high-intensity proton beams such reactions can be used to produce radioactive ion beams or intense neutron fluxes, for spallation neutron sources or accelerator-driven systems. These proton accelerators and spallation targets have to be optimised to reduce the risks (cost, safety) and get the best results. This can only be achieved via reliable spallation models.

Spallation reactions are a two-step process: a first, fast stage called intra-nuclear cascade (INC) and a second and slower one called de-excitation. Several models exist to describe both steps, but this paper focuses on one model combination: The Intra-Nuclear Cascade Liège (INCL, for the INC part) followed by the Abla code from GSI (for the de-excitation phase).

Around 2000 the INCL4.2 [1] and AblaV3p [2] versions gave good results for neutrons and the residual nucleus production was really improved, especially for nuclei close to the target mass and charge and for fission fragments (case of heavy target). For these reasons they were implemented in the transport code MCNPX2.5 [3]. Nevertheless the light-charged particle and intermediate mass fragment (IMF) productions were either predicted poorly or not at all. Along with other refinements, a coalescence mechanism in INCL4.5 and a comprehensive evaporation process including IMF emission in Abla07 significantly improve the results obtained by this combination.

In the first section we will review the main results obtained by the previous versions (INCL4.2 and AblaV3p), focusing on the shortcomings. The second section will present the main new physics ingredients in both codes and the third section will be devoted to the results with thin targets (microscopic reactions), and also for the MEGAPIE target, since these new versions have been very recently implemented in a beta version of MCNPX2.7.

INCL4.2/AblaV3p

The two codes INCL4.2 [1] and AblaV3p [2] gave very good results on neutron spectra with projectile energy higher than 150 MeV, on residue yields for nuclei close to the target and on fission fragments and rather good results for proton spectra. Due to the overall quality of the obtained spallation results with this model combination the two codes had been implemented in MCNPX2.5 and used for different spallation target projects (MEGAPIE [4], Eurisol-DS [5] or ADS benchmarks [6]).

Nevertheless this combination was not able to predict all types of observables. INCL4.2 emitted nucleons and pions, but no cluster. On the Abla side nucleons and alpha were the only particles evaporated and fission was the only other means to de-excite the remnant nucleus. As a result the light-charged particles, except proton, were predicted either badly or not at all, and the IMF were produced only via fission, which is certainly not the main channel to get them especially for the light targets that do not undergo fission. Some examples are given below. Figure 1 shows that alpha production is too low within a factor 2 (left) and IMF are strongly under predicted (right).

Figure 1: Alpha excitation function with proton on Fe on the left and ^{21}Ne excitation function with proton on Ni on the right. INCL4.2-AblaV3p results are plotted in dashed line. Figures are from [7].
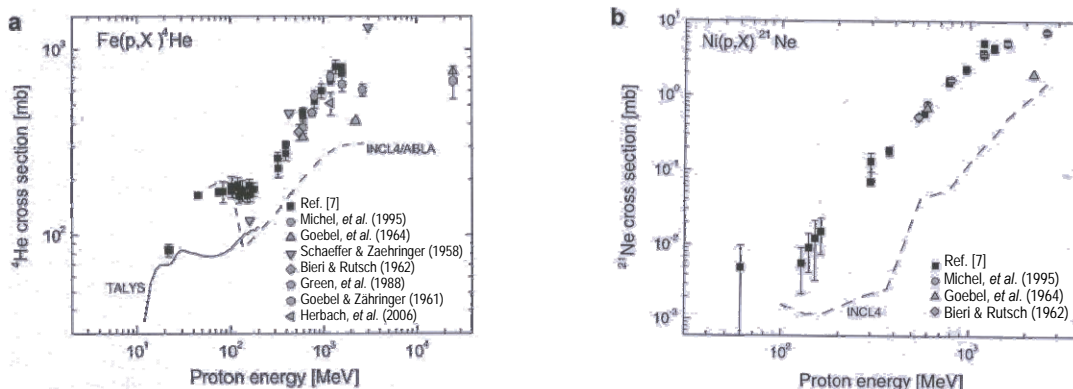
INCL4.5/ABLA07: Physics ingredients

The main new ingredients included in the last versions are presented briefly. The reader is invited to find more details in the references given in the following sections and in [8].

INCL4.5

Several improvements have been made in INCL4.2 to fix the above-mentioned problems, resulting in the version INCL4.5: composite particle emission, nucleon and pion potentials (isospin and/or energy-dependence), extension to low-energy projectile and other minor modifications.

The mechanism used to predict composite particle (or cluster) emission is based on the idea that a nucleon escaping from the nucleus can drag with it other nucleons which are sufficiently close (in phase space), and form an emitted light-charged cluster (surface coalescence). All possible clusters up to a mass 8 are considered. Going beyond this mass number would dramatically increase the calculation time since all possible clusters are built in the given phase space. The less *virtual* cluster, according to the definition given in [9], is selected and emitted if it has enough kinetic energy to penetrate the Coulomb barrier. Thus this new version is able to emit nucleons and pions, but also d, t, ^{3}He, α and all nuclei with a mass number below or equal to 8.

In comparison with other models INCL4.2 gave not too bad results concerning quasi-elastic and quasi-inelastic peaks in particle spectra. Nevertheless refinements of the nucleon potential have been performed, taken into account its dependence upon the isospin and its more or less linearly decrease when nucleon energy increases [10].

Pion production was previously not so good, so this motivated the implementation of a pion potential which was set to zero before and of a pion transmission through the barrier. The nuclear part that is described by two fitted parameters is isospin-dependent like the Coulomb part [10].

Below 150 MeV INC models are not supposed to be reliable since at that point nucleon should be sensitive to the nuclear structure. Nevertheless transport codes used them below these energies when evaluated data files for the considered nuclei do not exist. Thus, in order to be *usable* at low energies, in particular concerning the total reaction cross-section, special attention has been paid to the treatment of the first nucleon-nucleon collision and Coulomb distortion in the entrance channel has been introduced.

Finally, other minor modifications have been made. Two of them are: i) the strict Pauli blocking for the first collision (which was before statistical); *ii)* to save computing time (~25%), in addition to the stopping time criterion, when all particles are below a given energy (E_F + 10 MeV) the cascade is stopped.
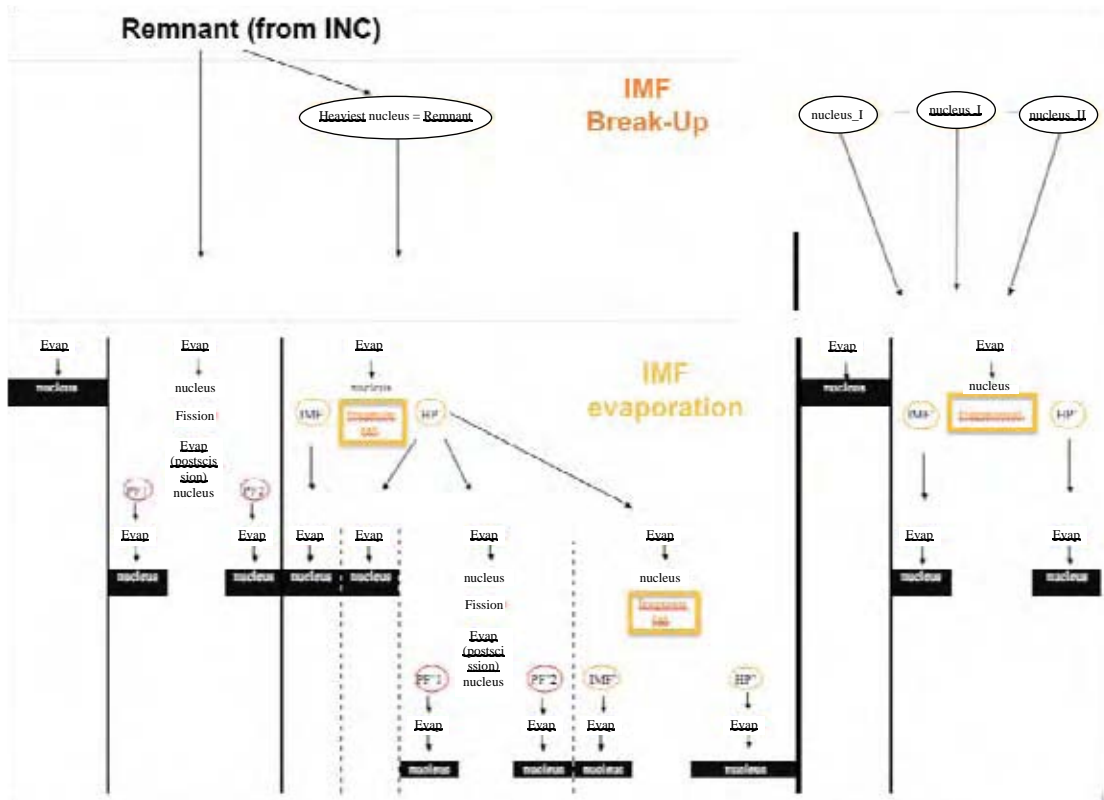
Abla07

The main improvements in Abla are the evaporation of particles from nucleons up to alpha and the emission of IMF via two processes: break-up (or multi-fragmentation), when temperature of the remnant is high enough, and evaporation (or binary fragmentation). Evaporation mechanism has been refined with much more sophisticated Coulomb barrier and inverse cross-sections. IMF evaporation is different from the particle evaporation only in the way to calculate the emission widths. They are obtained in IMF case with a power law to avoid a lengthy calculation time. This is the same type of law that is used in the break-up phase.

Fission has also been improved via for instance a dissipation based on an approximated solution of the Fokker-Planck equation, replacing the previous step function, and a possible evaporation step between saddle and scission points.

Figure 2 gives a schematic view of the different de-excitation channels in Abla07.

Figure 2: Schematic view of all possible ways to de-excite a remnant nucleus in Abla07

INCL4.5/Abla07: Results

Thin targets (no transport)

Some results on tritium, helium and IMF production with the new versions are presented below.

Figure 3 deals with two tritium excitation functions: an iron target (left) and a lead target (right). Two models other than INCL4.5/Abla07 are also plotted (CEM03 [11] and Bertini-Dresner [12,13]). For iron the production is slightly overestimated, but with values within a factor lower than 2, results obtained with lead are very good.

The same type of comparison has been made for helium production on iron (Figure 4). The alpha production is still underestimated, but significantly improved compared to Figure 1 and [3]He is now produced and very well estimated, which gives a much better confidence in helium production. With a lead target (not shown here but in [14]) the previous good results for alpha have not been changed and [3]He production is rather well described.

IMF production is now taken into account, both in INCL4.5 and Abla07. Figure 5 clearly shows the great improvement in IMF prediction: On the right (left) part the new (previous) version is plotted. Isotopes with a charge around 10 were missing before and now are produced with a rather good rate compared to data.

MEGAPIE

INCL4.5-Abla07 being strongly improved especially in tritium, helium and IMF production, they have been implemented very recently in a beta version of MCNPX2.7. This implementation allows then new predictions for the MEGAPIE target. This spallation target was a demonstrator for a liquid lead-bismuth target. It was operated 123 days in 2006 at PSI (Switzerland). Figure 6 shows the main parts with a

Figure 3: Tritium excitation functions: Fe(p,xt) on left, and Pb(p,xt) on right

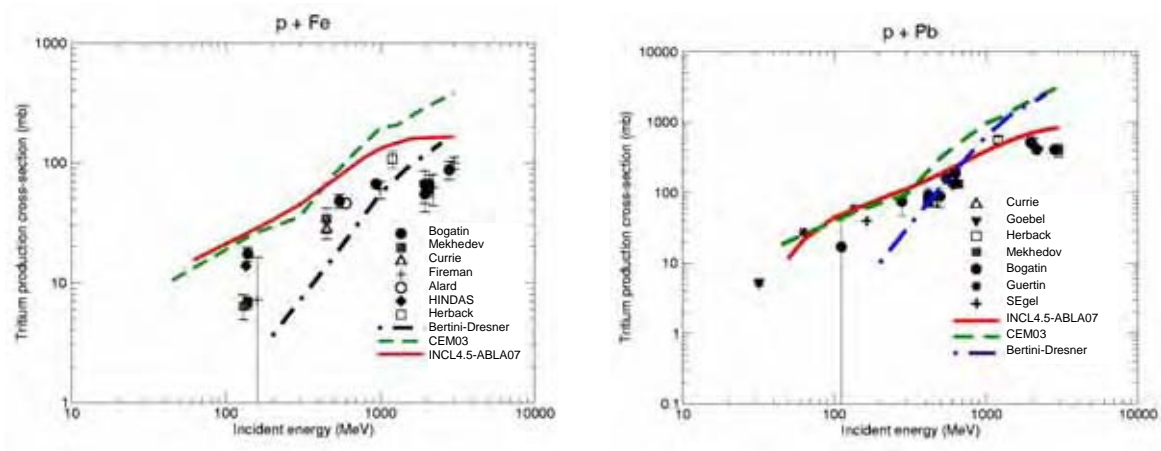INCL4.5/Abla07 is plotted as solid line, CEM03 is dashed and Bertini-Dresner is dotted. References on data in [14].

Figure 4: Helium excitation functions: Fe(p,xα)

INCL4.5/Abla07 is plotted as solid line for ^{4}He and as dashed line for ^{3}He. References on data in [14].
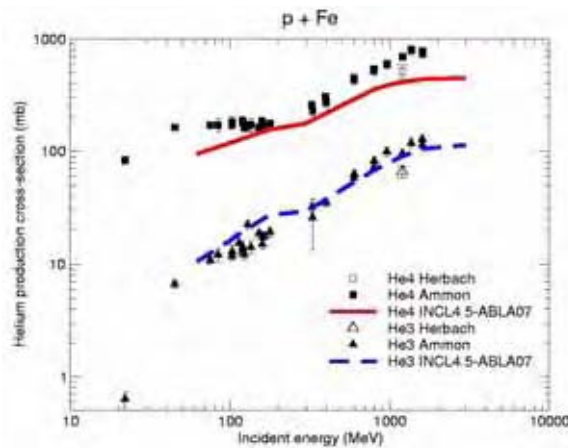

Figure 5: Charge distribution for the reaction Fe(1 GeV.u) + p

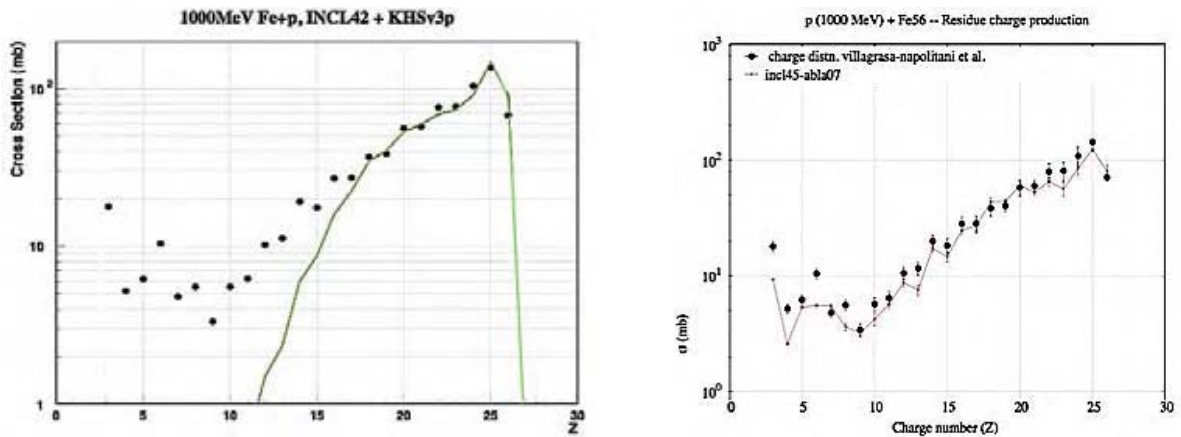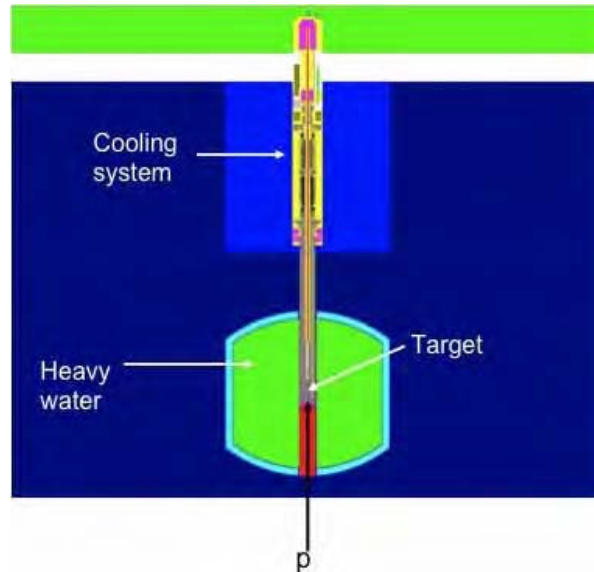INCL4.2-AblaV3p (left), INCL4.5-Abla07 (right). Data from [15].

**Figure 6: Main parts of the lead-bismuth eutectic (LBE) MEGAPIE target**

proton beam (575 MeV-0.947 mA) impinging the target surrounding by a water tank. Calculations on neutron flux and residue production in different places had been performed with several models like INCL4.2-AblaV3p available in MCNPX2.5 (more information in [4]). We show hereafter new results obtained in the target.

Several models calculated time evolution of the total activity in the target previously and results were almost the same. The only difference was after around 10 years of cooling due to the production of tritium. Figure 7 summarises the results with the two versions (left for the old one and right for the new one) and Bertini-Dresner as default option in MCNPX. It is clear that the tritium production was missing which is fixed now. Moreover the difference between Bertini-Dresner and INCL4.5-Abla07, about a factor 2, can be explained by Figure 3 (right part) where the INCL4.5-Abla07 model fits very well the experimental data while Bertini-Dresner underpredicts them in the MEGAPIE energy range, *i.e.* below 575 MeV.

Figure 7: Total activity of the LBE target as a function of cooling time after 123 days of irradiation with 575 MeV protons at 0.947 mA using INCL4.2-AblaV3p (left) and INCL4.5-Abla07 (right). Bertini-Dresner, as default option in MCNPX, is also used as the contributions from tritium.
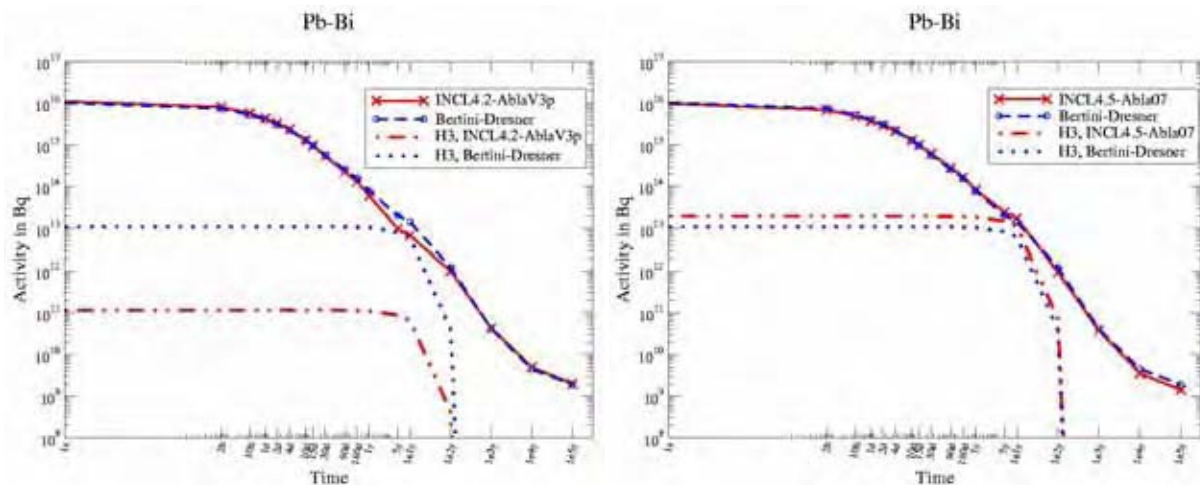
With Figure 8 we see importance of IMF emission. If fission fragment production has not changed, Ne (Z = 10) production has been significantly increased and the results obtained within the *Benchmark of Spallation Models* [16] give us confidence in these new predictions.

Figure 8: Quantity of volatiles (up to Xe) produced in the LBE target after 123 days of irradiation with 575 MeV protons at 0.947 mA using INCL4.2-AblaV3p (left) and INCL4.5-Abla07 (right). Bertini-Dresner, as the default option in MCNPX, is also plotted.
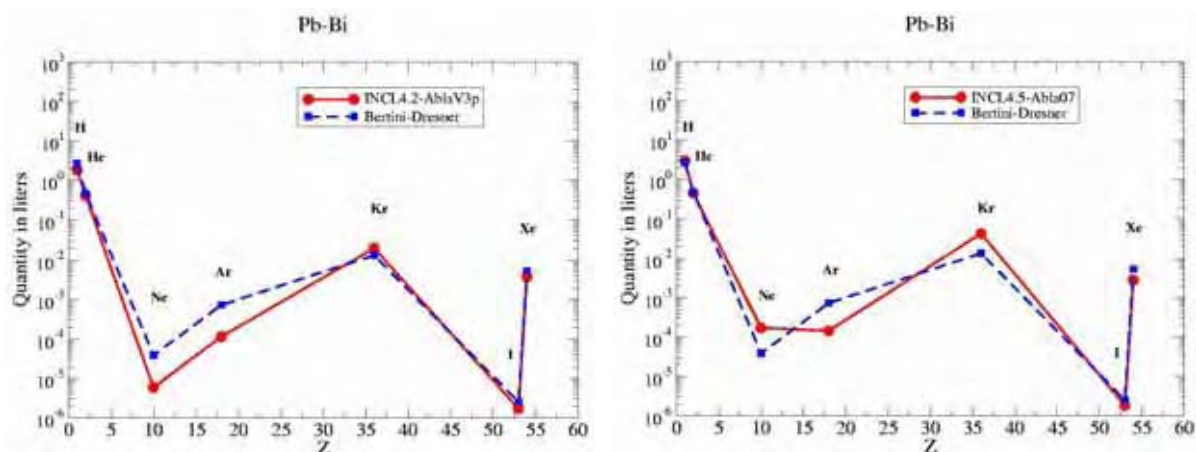
Conclusions

INCL4 and Abla have been considerably improved. Emission of composite particle, isospin and/or energy-dependence of the nucleon and pion potentials, extension to low-energy projectile, and other minor modifications in INCL4.2 led to the new version INCL4.5. As concerns Abla side, much more sophisticated inverse cross-section description and Coulomb barrier calculation for evaporation of all types of nucleons, light-charged particles and IMF are the main new ingredients included in AblaV3p to end up in Abla07.

These new versions lead to much better prediction in light-charged particle production, especially tritium and He, and in IMF prediction. This makes INCL4.5-Abla07 one of the most reliable model combinations to describe spallation reactions and then give more confidence when designing facilities like spallation neutron sources, accelerator-driven systems or radioactive ion beam facilities from the efficiency and safety points of view.

References

[1]   Boudard, A., *et al.*, *Phys. Rev.*, C 66, 044615 (2002).

[2]   Junghans, A.R., *et al.*, *Nucl. Phys.*, A 629, 655 (1998).

[3]   Pelowitz, D.B. (Ed.), *MCNPX User's Manual, Version 2.5.0*, LA-CP-05-0369, April 2005.

[4]   Zanini, L., *et al.*, *Neutronic and Nuclear Post-test Analysis of MEGAPIE*, PSI Bericht Nr. 08-04, ISSN 1019-0643, December 2008.

[5]   David, J-C., *et al.*, *Benchmark Calculations on Residue Production Within the EURISOL DS Project, Part I: Thin Targets*, CEA Saclay Internal report DAPNIA-07-04; David, J-C., *et al.*, *Benchmark Calculations on Residue Production Within the EURISOL DS Project, Part II: Thick Targets*, CEA Saclay Internal report DAPNIA-07-49, www.eurisol.org.

[6]   Pohorecki, W., *et al.*, "Thick Lead Target Exposed to 660 MeV Protons: Benchmark Model on Radioactive Nuclides Production and Heat Generation, and Beyond", *Proceedings of the International Conference on Nuclear Data for Science and Technology*, Nice, France, 22-27 April 2007, O. Bersillon, *et al.* (Eds.), EDP Sciences, pp. 1225-1228 (2008).

[7]   Ammon, K., *et al.*, *NIM*, B266, 2-12 (2008).

[8]   *Proceedings of the Joint ICTP-IAEA Advanced Workshop on Model Codes for Spallation Reactions*, ICTP Trieste, Italy, 4-8 February 2008. D. Filges, *et al.* (Eds.), IAEA INDC(NDS)-530, Vienna, August 2008, www-nds.iaea.org/reports-new/indc-reports/indc-nds/indc-nds-0530.pdf.

[9]   Cugnon, J., *et al.*, *Final Report and Code of an Improved Version of INCL4/ABLA*, FP7-EUROTRANS NUDATRA/W4.5, Deliverable D5.19 (2010).

[10]   Aoust, Th., *Amélioration du modèle de cascade intranucléaire de Liège en vue de l'étude de cibles de spallation pour les systèmes hybrides*, Ph.D. thesis, University of Liège (2007).

[11]   Mashnik, S.G., *et al.*, *CEM03.03 and LAQGSM03.03 Event Generators for the MCNP6, MCNPX, and MARS15 Transport Codes*, LA-UR-08-2931, Los Alamos (2008).

[12]   Bertini, H.W., *Phys. Rev.*, 131, 1801 (1963); Bertini, H.W., *Phys. Rev.*, 188, 1711 (1969).

[13]   Dresner, L.W., ORNL-TM-196 (1962).

[14]   Leray, S., *et al.*, *NIM*, B268, 581-586 (2010).

[15]   Villagrasa-Canton, C., *et al.*, *Phys. Rev.*, C 75, 044603 (2007).

[16]   International Atomic Energy Agency (IAEA), "Benchmark of Spallation Models", http://nds121.iaea.org/alberto/mediawiki-1.6.10/index.php/Benchmark:CalculRes.

Methodology to address radiation protection and safety issues in the IFMIF-EVEDA accelerator prototype

J. Sanz[1,2]**, P. Sauvan**[1,2]**, F. Ogando**[1,2]**, D. López**[1,2]**,
M. García**[1,2]**, A. Mayoral**[1,2]**, F. Ortíz**[1]**, V. Blideanu**[3]**, P. Joyer**[3]
[1]Dpto. de Ingeniería Energética, Escuela Técnica Superior de Ingenieros Industriales,
Universidad Nacional de Educación a Distancia, Madrid, Spain
[2]Instituto de Fusión Nuclear, Universidad Politécnica de Madrid, Madrid, Spain
[3]Commissariat à l'énergie atomique (CEA-Saclay, IRFU), Gif-sur-Yvette, France

Abstract

In the IFMIF-EVEDA accelerator prototype, deuterons (with energies up to 9 MeV) interact with the materials of the accelerator components due to beam losses and in the beam dump, where the beam is stopped. The productions of neutrons/photons together with radioactive inventories due to deuteron-induced reactions are some major issues for radiation protection and safety assessment.

Here, we will focus on the proposal of a computational approach able to simulate deuteron transport and evaluate deuteron interactions and production of secondary particles with acceptable precision. Current Monte Carlo codes, such as MCNPX or PHITS, when applied for deuteron transport calculation, use built-in semi-analytical models to describe deuteron interactions. These models are found to be unreliable in predicting neutron and photon generated by low-energy deuterons, typically present in the IFMIF-EVEDA prototype accelerator. In this context, a new computational methodological approach is proposed based on the use of an extended version of current MC codes capable of using evaluated deuteron libraries for neutron (and gamma) production.

The TALYS nuclear reaction code is found to be an interesting potential candidate to produce the evaluated data for double-differential neutron and photon emission cross-sections for incident deuterons in the energy range of interest for IFMIF-EVEDA applications. The recently-released deuteron TALYS-based Evaluated Nuclear Data Library, TENDL-2009, is considered a good starting point in the road to achieve deuteron data files of enough quality for deuteron transport problems in EVEDA.

Unfortunately, current Monte Carlo transport codes are not able to handle light ion libraries except for protons. To overcome this drawback the MCNPX code has been extended to handle deuteron (also triton, helion and alpha) nuclear data libraries. In this new extended MCNPX version called MCUNED, a new variance reduction technique has also been implemented for the production of secondary particles induced by light ion nuclear reactions, which allow reducing drastically the computing time needed in transport and nuclear response function calculations. Verification of these new capabilities for Monte Carlo simulation of deuteron transport and secondary product generation included in MCUNED is successfully achieved.

The existence of the MCUNED code allows testing for the first time the deuteron cross-section TENDL package by simulation of integral experiments. Some preliminary efforts are addressed to compare existing experimental data on thick target neutron yields for copper with those computed by the MCUNED code using TENDL cross-sections.

Introduction: IFMIF-EVEDA and radiation protection issues

The International Fusion Materials Irradiation Facility (IFMIF) [1] is one of the three projects of the broader approach toward fusion between Japan and the European Union, planned to be performed in parallel with the ITER project. The objective of IFMIF is to study the behaviour of materials and components under irradiation with conditions close to those in a nuclear fusion reactor. Engineering Validation and Engineering Design Activities (EVEDA) [2] is the first phase of the IFMIF project and was begun in mid-2007. Engineering activities include the three main parts of the future IFMIF facility: the accelerator, the target and the test facilities. A prototype of the IFMIF accelerator is under construction in Japan at the Rokkasho-Mura site. The accelerator sub-systems and components will be provided by the European team that is in charge of safety and radiation protection calculations for these equipments.

The IFMIF-EVEDA prototype will be a 9 MeV, 125 mA CW deuteron accelerator, identical to the low-energy section of one of the IFMIF accelerators. IFMIF will use two deuteron beam lines delivering each 125 mA @ 40 MeV. The prototype will be tested to verify the validity of the design before the launch of the IFMIF construction. It includes an ion source, a radiofrequency quadrupole (RFQ) cavity and the first module of a superconducting linac based on half-wave resonator (HWR) cavities. As no target is foreseen for the accelerated beam, a beam dump (BD) is required to stop it during commissioning and accelerator tests.

Deuterons in the accelerator prototype will interact with materials all along the beam line where deuterons are lost, and at the end of the beam line, in the beam dump where the whole beam is stopped. As a result of these deuteron interactions with the intercepting material and with the previous deuterons implanted in it, secondary neutrons and gammas as well as deuteron-induced activated products will be generated.

The generation of neutrons will induce: i) high neutron and gamma prompt dose rates during accelerator operation; ii) activation of the accelerator components as well as all the other materials inside the accelerator vault, including activation of air and corrosion products in the coolant; iii) decay gamma dose rates after accelerator shutdown. The deuteron-induced activation of the accelerating components and beam stop will result in decay gamma dose rates after accelerator shutdown. The production of tritium by interaction of deuterons with the previous implanted deuterium is also an issue to be considered.

The main elements of the methodology to address the above-mentioned radiation protection issues (presented in the second section) can be grouped into two general sets: i) computational tools and nuclear data for transport of particles and calculation of relevant response functions; ii) computational tools and nuclear data for activation calculations.

Here we will be focused on the transport activities, and in particular we will present the work done and final conclusions achieved within the IFMIF-EVEDA Accelerator System Group (ASG) regarding the computational methodology designed to carry out the simulation of deuteron transport and secondary product generation.

Firstly, we present the outcome from a benchmark [3] performed to assess the availability and quality of cross-section data for neutron generation due to incident deuterons. Calculations of excitation functions for deuteron reactions producing neutrons are performed using the nuclear models included in MCNPX [4] and PHITS [5], as well as the dedicated nuclear reaction code TALYS [6] and corresponding deuteron TALYS-based Evaluated Nuclear Data Library TENDL2009 [7]. The definition of the benchmark is provided in the second section and the discussion of the results in the third one. It is shown that some developments regarding computational tools and nuclear data are required in order to solve the problem arising from the fact that the built-in nuclear models included in current MC codes do not allow predicting with a reasonable accuracy the production of secondary particles and residuals from deuteron interactions in the energy range of interest of the EVEDA accelerator. The potential advantages of using deuteron transport cross-section data files produced by the dedicated nuclear model code TALYS in transport calculations, instead of using those built-in models included in the MC codes, is discussed in the third section.

The use of such tabulated data introduces the flexibility to easily change nuclear data used in the transport code when they need to be improved. Unfortunately, current Monte Carlo transport codes, such as MCNPX, PHITS or FLUKA [8], are not able to handle light ion libraries except for protons. To overcome this drawback the MCNPX code has been extended to handle deuteron, triton, helion and

alpha nuclear data libraries. In this new extended MCNPX version, called MCUNED [9], a new variance reduction technique has also been implemented for the production of secondary particles induced by light ion nuclear reactions, allowing a drastic reduction in the computing time for many applications. The main features of MCUNED will be presented in the fourth section, showing its utility in addressing EVEDA-like problems. The MCUNED code has been accepted by the ASG of IFMIF-EVEDA as the current MC transport option to use in addressing the deuteron transport problems in EVEDA.

The deuteron cross-sections generated by TALYS, and in particular the recently-released deuteron files of ENDL-2009, are considered a good starting point on the road to achieve deuteron data files of sufficient quality for deuteron transport problems in EVEDA and furthermore in IFMIF accelerators. The existence of the MCUNED code allows testing for the first time the deuteron cross-section TENDL package by simulation of integral experiments. In the fifth section we present some preliminary efforts [10] aimed to compare existing experimental data on thick target neutron yields for copper with those computed by the MCUNED code using TENDL cross-sections. Finally in the sixth section, the main conclusions of the work are presented.

General methodology for radiation protection calculations: Need for validated nuclear data and computational tools

The main elements of the methodology can be grouped in two general sets: *i)* computational tools and nuclear data for transport of particles and calculation of relevant response functions; *ii)* computational tools and nuclear data for activation calculations.

Different alternatives have been used in activation calculations for EVEDA applications. In all of them, the procedure followed is to use deuteron and neutron fluxes computed previously with transport codes as input to a dedicated activation code which will use activation cross-section and decay data libraries. MCNPX is used to transport the emitted gamma rays and compute flux and residual gamma dose rates. Some alternatives [11,12] are under discussion within IFMIF-EVEDA ASG regarding the activation codes and activation cross-sections to be used in EVEDA applications and the final agreement will be reached soon.

As far transport activities, the main items are the transport of deuterons, production and transport of secondary neutrons and gammas and finally the assessment of deuteron, neutron and gamma fluxes and prompt doses. The use of Monte Carlo transport codes has been the option considered for IFMIF-EVEDA applications. Different options have been proposed to address the problem of deuteron implantation profile [12-14], which is necessary to be known to compute the d-D neutron source and tritium production. These options are under discussion within IFMIF-EVEDA ASG and a final decision will be reached soon. Agreement has been already reached regarding the methodology to address the simulation of deuteron transport and secondary product generation. The presentation of the work done within this activity is the goal of this paper.

The Monte Carlo codes MCNPX and PHITS, widely used in radiation protection accelerator studies, were initially considered as candidates for EVEDA applications. These codes use built-in analytical models to deal with deuteron nuclear interactions. In some of the first EVEDA radiation protection studies aimed at the beam dump design, the applicability of MCNPX to predict neutron production with sufficient accuracy in the particular situation of 9 MeV deuterons impinging on the copper beam stop was found questionable [15]. As a consequence, a more extensive effort was planned in order to define a reliable methodology to calculate and make use of the deuteron cross-sections needed for EVEDA calculations. In this context, a benchmark [3] has then been proposed between both European home teams involved in safety and radiation protection calculations for IFMIF-EVEDA (UNED and CEA) in order to compare calculated cross-sections, using different MC transport codes and dedicated nuclear reaction codes, with experimental data available for different elements relevant to the IFMIF-EVEDA project.

These elements are: Cu, Ni, Fe, W, C, Cr and Nb. They are typical components of accelerator equipments (Cu for the beam dump, stainless steel for the vacuum chamber, Nb and W for other specific equipments such as the superconducting drift tube linac). The benchmark has been focused on the EVEDA phase and the energy has been set in the range 0 to 20 MeV.

The benchmark was then performed in three steps:

- In the first step, an inventory of the available experimental data in EXFOR [16] regarding the excitation functions of the deuteron reactions producing neutrons for these elements was undertaken.

- In the second step, the different cross-sections were calculated with the different nuclear models included in MCNPX and PHITS.

- In the third step, the different cross-sections were calculated with the dedicated nuclear reaction code TALYS.

The comparison of the results will allow us to test the MC codes regarding their capability to predict neutron production for EVEDA conditions and to test the capability of TALYS to generate neutron (and gamma) production data files for deuteron-induced reactions with sufficient accuracy. The results obtained are discussed in the following section.

Description of deuteron interactions in the transport process: Limitations of current MC codes and potential of the TALYS nuclear reaction code

Cross-sections calculated with MCNPX-2.6 (using INCL4/ABLA and ISABEL/Dresner/RAL model options) and PHITS (QMD model) show that for the majority of the reactions there are very strong disagreements concerning both energy dependence profile and values. For the other nuclear models included in MCMPX (such as CEM03 and LAQGSM) the situation is much worse. Thus, it was detrmined that the present versions of the nuclear models included in MCNPX and PHITS are not appropriate for dealing with deuteron-induced reactions in the energy range of EVEDA applications.

Figures 1, 2 and 3 are examples of reactions showing the bad behaviour of MCNPX and PHITS nuclear models. A strong disagreement with experimental cross-sections is observed not only in amplitude but also in shape.

As far MCNPX, it is seen that the INCL4/ABLA model is in general the one providing the best results for EVEDA applications. ISABEL/Dresner/RAL is the second one in performance, but it is totally unacceptable. All the models, except INCL4, are unable to compute neutrons for deuteron-incident energies below around 6 MeV, since as can be seen in the figures, unphysical very low values are assigned to the cross-sections below this energy. In the EVEDA accelerator, the production of neutrons by interactions by 5 MeV deuterons in copper is in terms of radiation protection implications an important aspect that should not be neglected [13,17].

The general behaviour of the TALYS-1.0 cross-sections obtained using the default-global set of parameters is also illustrated in the figures. It is seen than even if results obtained with TALYS-1.0 (with default-global parameters) are in most cases not much better in amplitude than those obtained with MCNPX and PHITS, they give a shape that fits rather well the shape of the experimental values. The utilisation of TALYS with appropriate adjusting parameters will be required to obtain a good reproduction of experimental cross-sections for safety and radiation protection calculations.

Several reactions, including those given in Figures 1, 2 and 3 (^{61}Ni(d,n)^{62}Cu, ^{65}Cu(d,2n)^{65}Zn and ^{64}Ni(d,2n)^{64}Cu, respectively), have been identified as examples of reactions for which a qualitative acceptable profile of the excitation function is obtained with TALYS-1.0 default-global parameters, but for which improvement in the fit to measurements is required.

For these problematic cases, TALYS offers the capability to adjust the parameters of the optical model potential (OMP) involved in the interactions between the incident particle and the nucleus. In order to show that these kinds of problems can be solved reasonably, we have chosen two cases. In the first, results of fitting using standard mathematical tools are presented. In the second, results obtained from using local parameters based on a sound physical approach are given.

The first case addresses deuteron reactions in ^{56}Fe. For this nuclide there are values in EXFOR for three different reactions: ^{56}Fe(d,n)^{57}Co, ^{56}Fe(d,2n)^{56}Co and ^{56}Fe(d,a)^{54}Mn. The TALYS-1.0 results (using default-global parameters) obtained for them show that they reproduce well the energy dependence of the cross-section defined by experimental data but that the quantitative fit is insufficient. Fitting calculations with standard mathematical tools were done by the UNED team for all the experimental

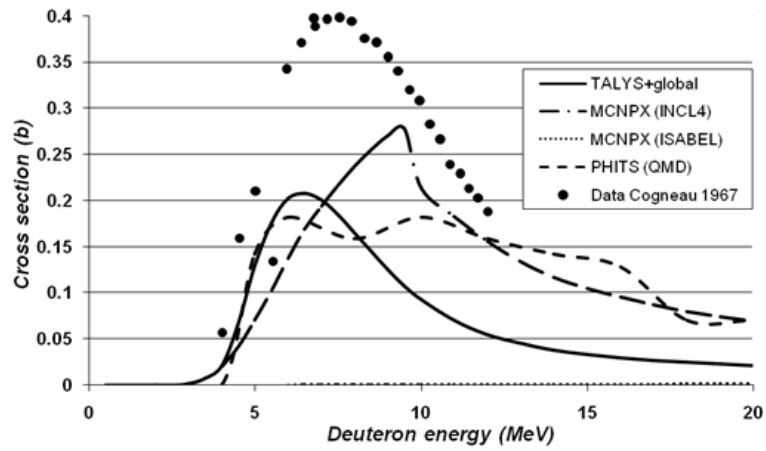**Figure 1: Cross-section for ^{61}Ni(d,n)^{62}Cu reaction – comparison of evaluated and measured data**

Figure 2: Cross-section for ^{65}Cu(d,2n)^{65}Zn reaction – comparison of evaluated and measured data

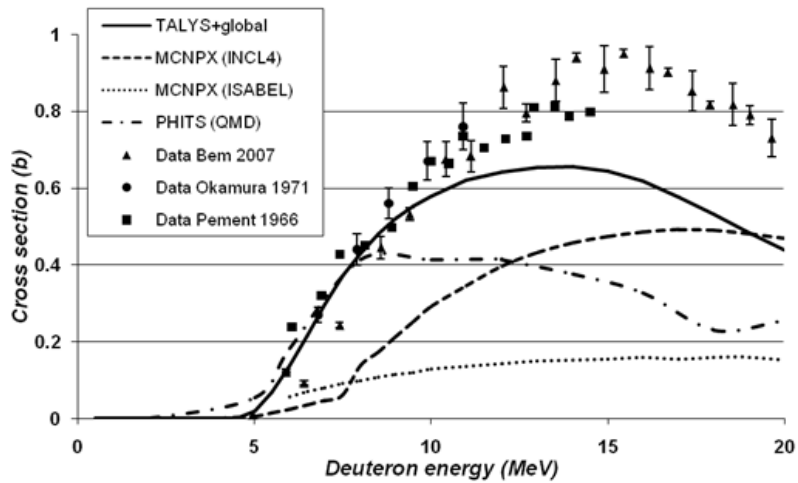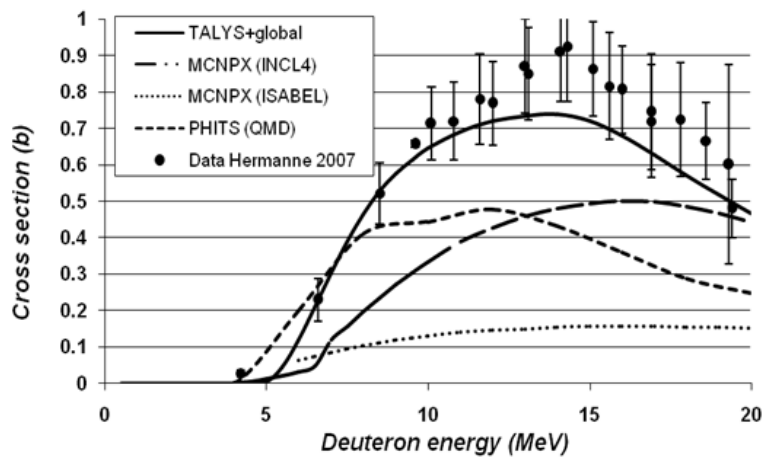**Figure 3: Cross-section for ^{64}Ni(d,2n)^{64}Cu reaction – comparison of evaluated and measured data**

values [3] and as a result a common set of parameters for the three reactions has been derived. Figure 4 shows the improvement performed for the reaction $^{56}Fe(d,n)^{57}Co$ using TALYS-1.0 with the fitting parameter set over the TALYS-1.0 results using the default-global parameters. With the selected parameter set, an improvement of $^{56}Fe(d,2n)^{56}Co$ and $^{56}Fe(d,a)^{54}Mn$ reactions – of interest for activation analysis – has also been achieved.

The second case refers to the $^{65}Cu(d,2n)^{65}Zn$ reaction for which Avrigeanu local OMP parameters derived from physical basis are used [18]. Improvement in the fitting is also observed (see Figure 5).

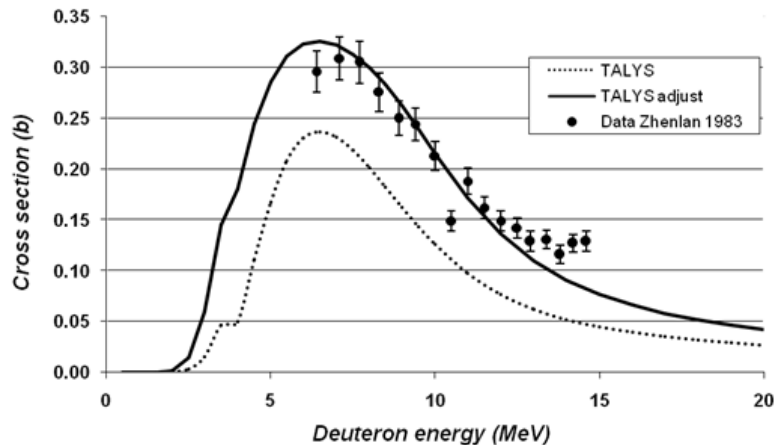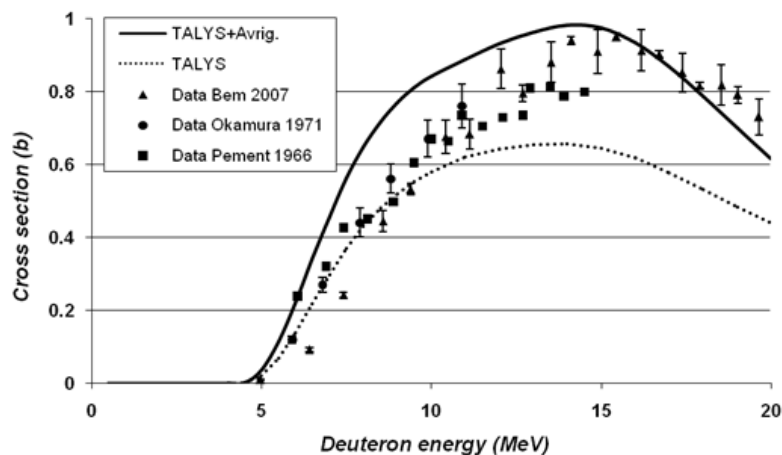**Figure 4: Improved cross-section for reaction $^{56}Fe(d,n)^{57}Co$ with TALYS and fitting OMP parameters**

Figure 5: Improved cross-section for reaction $^{65}Cu(d,2n)^{65}Zn$ with TALYS and local OMP parameters

Another critical issue with regard to neutron production is the emitted spectrum. It is worth mentioning that the one computed with MCNPX-2.6 and PHITS is not realistic at all because an unphysical high-energy tail is predicted. On the other hand, TALYS-1.0 predictions are always consistent with the kinematics of the reactions. An example of this is provided in Figure 6, which shows the angular integrated distribution for 9 MeV deuterons incident on natural copper computed by MCNPX-2.6 (INCL4/ABLA), PHITS and TALYS-1.0 (default-global parameters) The maximum physical energy of the emitted neutrons is about 15.7 MeV.

As a conclusion to this benchmark exercise, it was agreed within the ASG of IFMIF-EVEDA that the option to follow for addressing transport simulations and prompt dose calculations in EVEDA was the development of a computational procedure based on extending Monte Carlo codes to use external data files generated by TALYS, with appropriate adjusting of optical model potential parameters when necessary.

Figure 6: Probability distribution of emitted neutrons for ^{nat}Cu and 9 MeV incident deuterons
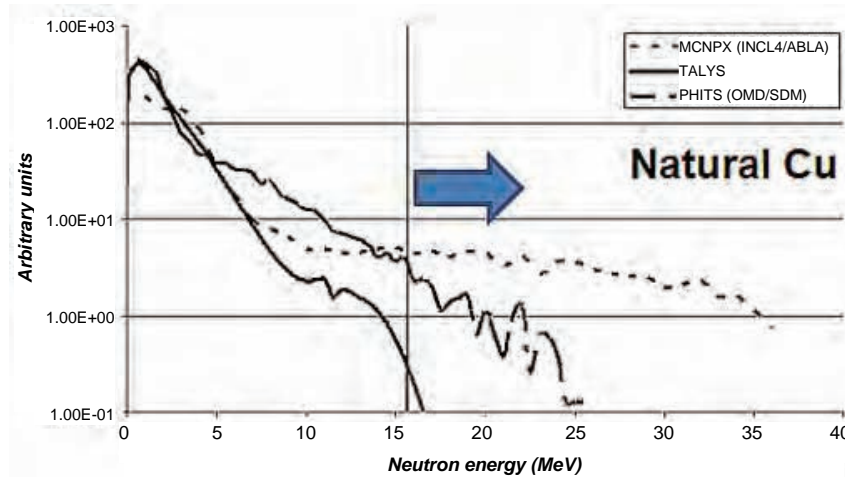
MCUNED: New capabilities for Monte Carlo simulation of deuteron transport and secondary product generation

MCUNED [9] is a new computational tool resulting from an extension of the MCNPX code, which significantly improves the treatment of problems where any secondary product (neutrons, photons, tritons, etc.) generated by low-energy deuteron-induced nuclear reactions could play a major role. The two singular features of MCUNED are: i) it handles deuteron-evaluated data libraries (residual production cross-sections and energy-angle distributions of all outgoing particles); ii) it includes a reduction variance technique for production of secondary particles by charged particle-induced nuclear interactions, which allows drastically reducing the computing time needed in transport and nuclear response calculations. A third feature is that MCUNED input is fully compatible with any MCNPX input and all the capabilities of the original MCNPX (like the flexibility in definition of the charged particle source, the definition of the geometry of the system, ptrac option, nuclear responses, etc.) are available in the MCUNED version. Moreover the responses of MCUNED simulations have not experienced any variation with the implementation of the new capabilities with respect to MCNPX responses. In the following we present some aspects of the two singular features of MCUNED.

Handling of deuteron libraries for transport calculation: Implementation in MCPNX and verification process

The MCNPX subroutines devoted to read and process proton nuclear cross-section from libraries have been modified and extended allowing the use of deuteron libraries. Subroutines dedicated to the sample of nuclear reactions have also been modified in order to use tables instead of models during the deuteron transport. The charged particle transport scheme remains the original from MCNPX.

A verification process has been defined in order to check that the modification of MCNPX subroutines allowing reading deuteron libraries is correct. The verification test is defined by a set-up consisting of 9 MeV deuteron pencil beam impacting onto a thin cylindrical ^{63}Cu target. Simulations are performed to obtain the neutron spectra emitted from the thin target at different angles with respect to the beam axis. The simulations are performed with MCUNED and the deuteron transport library is provided by the TENDL package [7]. Double differential neutron yields computed by MCUNED are straightforwardly converted to double differential cross-sections and compared with the double differential cross-section supplied by TENDL. The matching between both results was excellent. This outcome validates the management of deuteron cross-section tables in MCUNED.

Figure 7 shows the neutron emission double differential cross-section obtained from the ENDF format library and the cross-section calculated with MCUNED for four different angles, showing the excellent matching between both.

Figure 7: Neutron double differential cross-section for the reaction d-^{63}Cu and 9 MeV deuterons
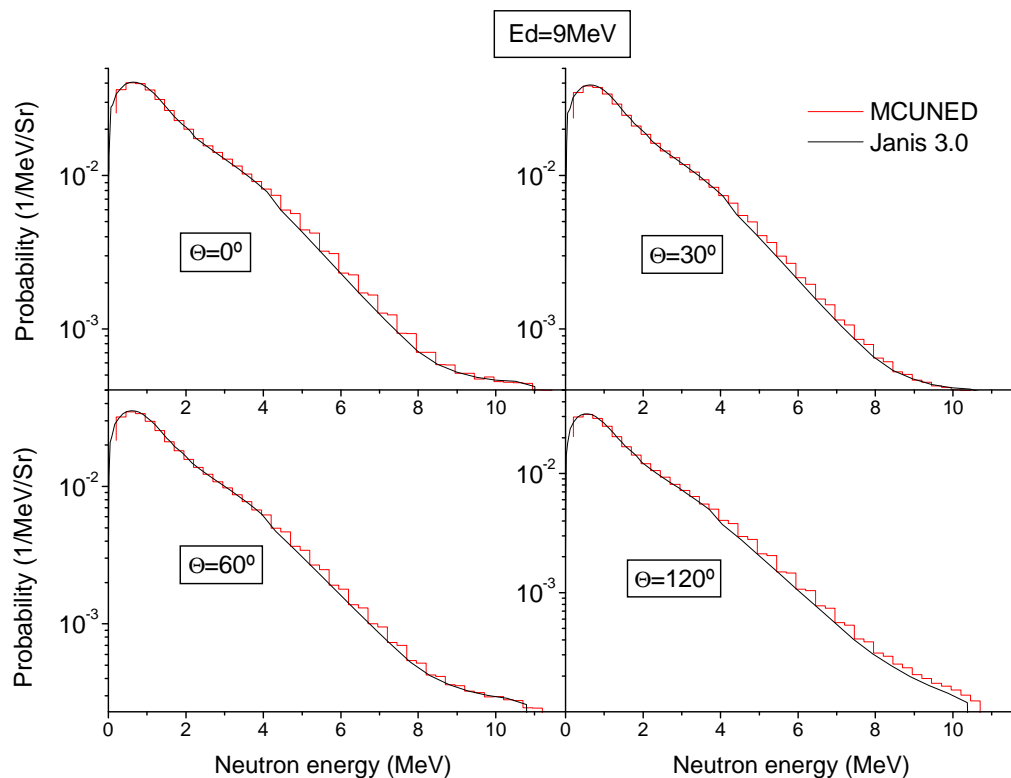
Variance reduction technique for generation of secondary product by light ions interaction: Basis and verification

Another important drawback of current Monte Carlo codes when applied to transport of low-energy light ions is the huge amount of computing time that can be required to address some important problems. This will take place in problems where one or several types of secondary products play a major role. A good example is the calculation of prompt dose rates outside the accelerator vault and corresponding shielding issues. The neutrons produced by deuteron interactions are the main responsible for these doses.

In this kind of problem the interest of the simulation is emphasised in the transport of secondary particles, and it is necessary to perform the calculation with a large number of secondary particle histories in order to reduce the statistical error in the response functions of interest (doses in shielding problems). Moreover, the secondary particle source has to be distributed adequately (energetically and spatially) with respect to the simulated primary particle source. Let us name "SH" as the desired number of secondary particles histories to achieve an acceptable statistical error. If we represent the production of secondary per primary particles by (s/p), then the number of needed primary particles histories PH can be written as SH*(s/p)$^{-1}$.

The problem arises when the production of secondary per primary particles (s/p) is very low. For example, if primary particles are low-energy ions, such as deuterons in the EVEDA (maximum energy is 9 MeV) where the number of produced neutrons per incident deuteron is about 10^{-4}, the problem highlighted above takes a real importance. This problematic of scarce secondary particle production has been successfully treated in [19] for a specific geometry and beam target set-up, but clearly the method is too restricted to be used in a general case.

At low energy, ions have short track lengths inside the material due to the slowing down of the particle. This short track associated with a relatively low absorption cross-section leads to a very low

production of secondary particles. In EVEDA the order of magnitude of the ratio (s/p) will be around 10^{-4}. This feature of low-energy light ion transport means wasting a lot of computing time in transporting primary particles that have no contribution in the calculation of the response functions associated to the production and transport of secondary particles.

The main idea of the new variance reduction technique [9] implemented in MCUNED, for the production of secondary particles from nuclear reaction with charged particles, is to always force the nuclear reaction, taking care of the correct transport of charged particle, giving rise to the absorption of the incident particle by the target nucleus for each charged particle history. The weight of the secondary particle produced is then multiplied by the probability of such nuclear absorption, in order to maintain the yield of secondary particle production. This variance reduction technique is valid for all kinds of ions, but it is not suitable for electron or positron because it does not take into account the bremsstrahlung effect, which is negligible for ions.

A comprehensive verification process has been undertaken [9] and the procedure to evaluate the benchmark test set for verification of the variance reduction technique is based on the following considerations:

- Simulations are run with MCNPX and MCUNED. The same input files are used in both simulations. The only differences will be the card in the MCUNED input setting active the option of variance reduction for generation of secondary particles, and the different number of primary particles histories used in running MCNPX and MCUNED.

- The number of initial primary particle histories in both simulations is adjusted to achieve the same (or very similar) statistical error in the tally results of interest.

- The variance reduction technique is considered correct if the relative error between MCNPX and MCUNED calculations is comparable to the statistical error of the tally values, that is:

$$\varepsilon_r = \frac{\left| \overline{X}_{MCNPX} - \overline{X}_{MCUNED} \right|}{\overline{X}_{MCNPX}} \leq max(\varepsilon_{MCNPX,}\varepsilon_{MCUNED})$$

where $\overline{X}_{MCNPX}$ is the mean value of a given quantity computed by MCNPX, $\overline{X}_{MCUNED}$ is the mean value of the same quantity computed with MCUNED with the variance reduction technique option active, and ε_{MCNPX} and ε_{MCUNED} are the statistical errors in MCNPX and MUNED calculations.

- Finally, in order to measure the benefit in using the variance reduction technique, we will compare the computing time necessary to perform the whole simulation with one processor computer when running MCNPX and MCUNED.

The conclusion of the verification process performed is that variance reduction technique leads to correct results and that it is useful when the production of secondary particle is low, and essential when the production rate of secondary particle is very low.

As an example of the kind of tests performed, we will refer to that in which a 10 MeV proton beam impacts onto a cylindrical copper target, 1 mm thickness and 1 cm radius. Simulations are performed with MCNPX and MCUNED to obtain neutron spectrum at different angles with respect to the beam axis, using in both simulations an external data library for proton reaction cross-sections.

The comparison between MCNPX and MCUNED calculations for the emitted neutrons from the thick target relative to spectral neutron yield, energy integrated angular distribution of neutron yield and neutron energy spectra at different emission angles show that the relative errors between MCNPX and MCUNED mean values are lower than the statistical errors (statistical errors are lower than 1% in most of the values). The good agreement between both simulations traduces the correct implementation of the variance reduction technique into the MCUNED code.

In Table 1 the number of histories used and results from both simulations are displayed to exhibit the benefit in using the variance reduction technique. It is seen that the reduction in computing time is in this case outstanding, being the time needed by MCNPX three orders of magnitude higher than with MCUNED simulation.

Table 1: MCNPX-MCUNED performance comparison of neutron emitted from copper thick target

The computing time is the time necessary to perform the whole simulation with one processor computer

	MCNPX	MCUNED
Number of histories	1E+10	1E+10
Computing time	1.37E+05 minutes	32 minutes
Produced neutron histories	5.59E+06	5.36E+06
Neutron/proton	5.589E-04	5.587E-04
Statistical error	0.04%	0.03%

An estimation of the ratio between the computing time used without (normal execution of MCNPX) and with variance reduction can be made straightforward. Taking T_p as the computing time it takes to calculate one primary particle history and T_s the time it takes to transport the secondary particles produced by the source particle nuclear reaction, then the time needed to produce and transport secondary particles without variance reduction will be $T_{withoutVR} = n*T_p + T_s$ (with $n = (s/p)^{-1}$), while with variance reduction the new time is $T_{VR} = T_p + T_s$. The time saving gain is then:

$$G = \frac{T_{withoutVR}}{T_{VR}} = \frac{n + T_s/T_p}{1 + T_s/T_p}$$

Since, for the low-energy deuterons present in EVEDA, the number of secondary neutrons per incident deuteron is in the order of 10^{-4} for 9 MeV deuterons, a very important gain higher than a factor 1 000 will be obtained for most of the applications.

Other tests have been performed [9] to check the ability of the variance reduction technique to reproduce in addition to the secondary neutron the photon production, neutron and photon fluxes, as well as response functions related to these quantities, such as the ambient equivalent dose produced by neutrons and photons in the surroundings of a thick target. The simulation set-up consists of a 100 mA proton current at 6.7 MeV impinging on a cylindrical nickel target of 1 mm thickness and 1 cm radius. This simulation has the characteristic parameters of the beam stop irradiation conditions of the LEDA accelerator. The results of the simulations have shown the positive verification of the implementation of the reduction variance technique for calculation of all kinds of response functions.

TENDL deuteron library benchmarking against integral experimental data: Applications to copper

We present the outcome of preliminary efforts [10] aimed to compare existing experimental data on thick target neutron yields for deuteron interactions on copper with those computed by the MCUNED code using TENDL-2009 deuteron cross-sections [7]. Experiments for incident deuteron energy up to 40 MeV have been collected.

The experimental and simulated results for the neutron yields are summarised in Tables 2 and 3.

Table 2: Total neutron yield (4π)

Ref.	E_d (MeV)	$E_n >$ (MeV)	Exp (n/d)	TENDL (n/d)	Yield frac.
20	10	0	8.81E-04	6.44E-04	1
21	33	0	1.81E-04	1.50E-02	1

Table 3: Neutron yield in the forward direction

Ref.	E_d (MeV)	$E_n >$ (MeV)	Exp (n/d)	TENDL (n/d)	Yield frac.
22	16	4	2.76E-04	5.94E-05	0.20
21	33	4	6.16E-03	7.49E-04	0.39
22	33	4	6.68E-03	7.49E-04	0.39

The measured total yield including all neutron energies is in reasonable agreement with the simulations. The major component of the discrepancy between experiments and simulations has to do with the neutron yield in the forward direction. Then, it can be said that TENDL underestimates neutrons emitted in the forward direction.

The neutron spectrum in the forward direction for two different energies is depicted in Figure 8. It can be seen that is not correctly reproduced by TENDL, increasing the discrepancies as deuteron energy increases.

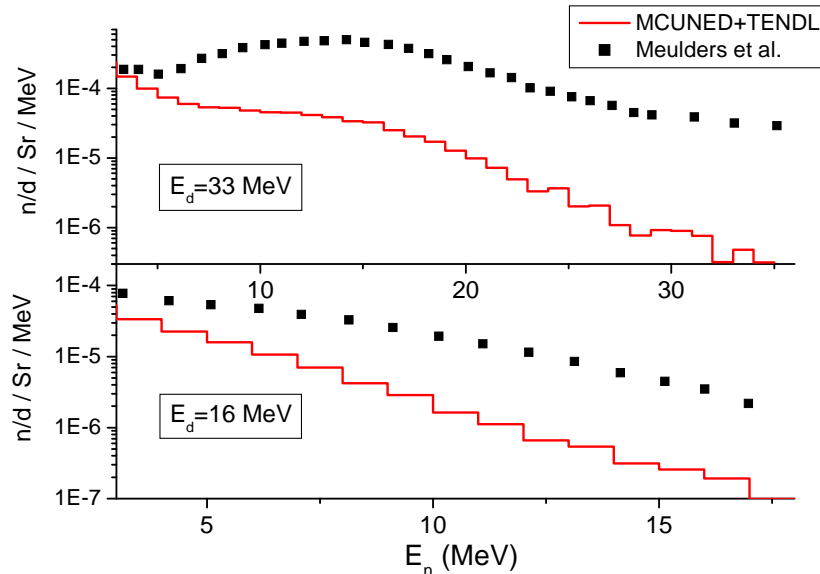**Figure 8: Spectra of neutrons emitted in the forward direction (experiments from Ref. [22])**

Figure 9 shows the neutron spectra at various emission angles for 33 MeV incident deuterons. This figure shows that up to 45° the simulated and experimental spectra do not match each other. For backward neutrons, from 45° and higher, the simulated and experimental spectra are in good agreement.

The angular distribution of produced neutron has been plotted in Figure 10 for two different energies. For both incident deuteron energies, the experimental and simulated angular distributions are similar for angles higher than 45°, while in the forward direction the experimental distribution has a stronger contribution, the discrepancies being much lower as deuteron energies decrease.

The differences existing between experimental and simulated spectra can be attributed to the deuteron break-up process during the nuclear reaction. The hump at 13 MeV in Figure 9 at 0° is the typical signature of the break-up process, which can be defined as having a projectile fragment emerging from the reaction in a relatively narrow peak centred close to the beam velocity and strongly directed toward forward angles. Since the break-up process is included in TALYS with a simple model, the TENDL deuteron library should reproduce this behaviour. Angular integrated neutron spectra produced by TALYS exhibit the break-up hump feature, but the code is not able to correctly reproduce the angular spectra. In fact, to produce the angular neutron spectrum, TALYS use the Kalbach [24] systematic. It is known that this systematic cannot satisfactorily reproduce the peaked forward angular distribution and instead of producing a pronounced break-up contribution to the forward angle, this systematic smoothes the break-up contribution over a large angular aperture. Very recently a new phenomenological model for projectile break-up reaction has been proposed [25]. In this model a peaked forward angular distribution is given to reproduce the angular distribution of the emitted fragment of the break-up reaction. Experiments recently performed [26] for copper in the energy range of interest for EVEDA will be extremely useful (since few experiments are available in this energy range) in evaluating and improving (if necessary) TENDL for EVEDA applications.

Figure 9: Neutron spectra produced by 33 MeV deuterons (experiments from Ref. [21])
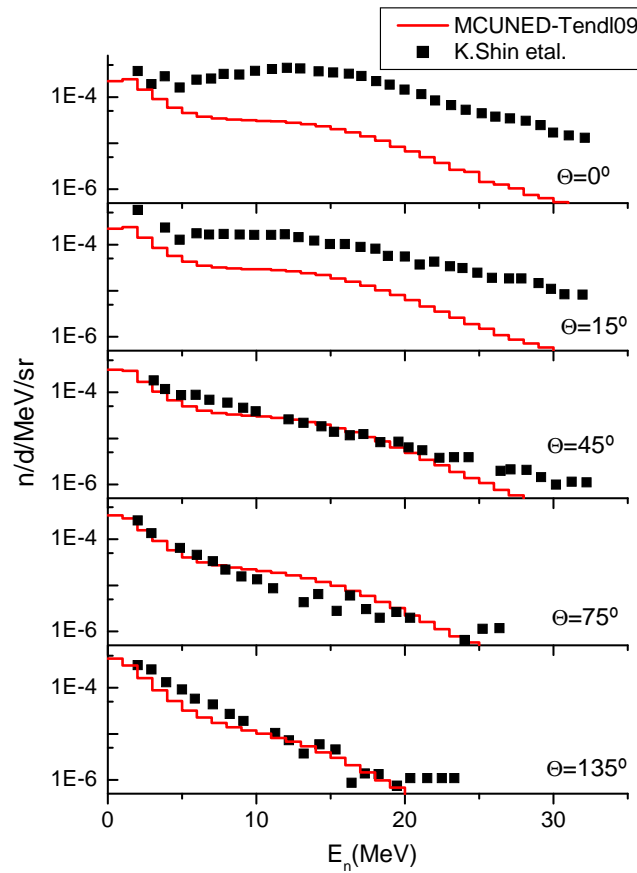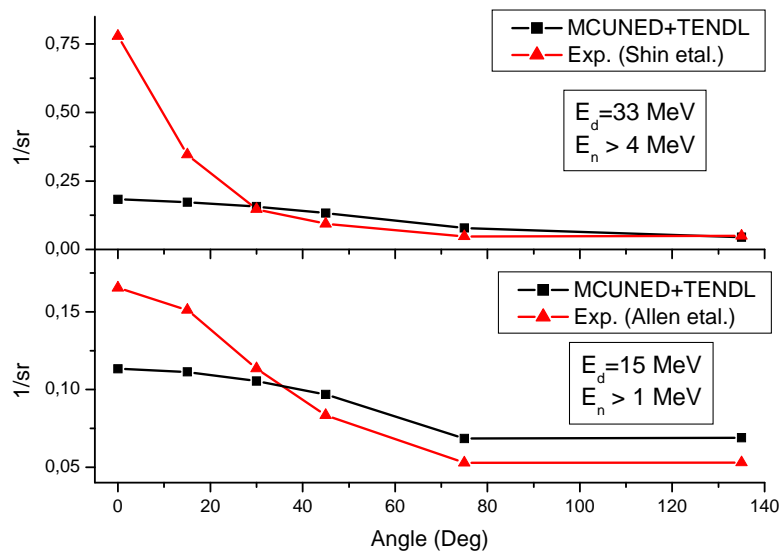

Figure 10: Normalised neutron angular distribution (experiments from Refs. [21,23])

Conclusions

The different computational elements required in addressing the radiation protection issues of the IFMIF-EVEDA accelerator prototype have been identified and several alternatives have been found for most of them. Some of the possible options are under discussion within IFMIF-EVEDA ASG regarding activation and deuterium implantation issues and a final agreement will be reached soon.

Regarding simulation of deuteron transport and secondary product generation the agreement about the computational methodology to be used has already been reached. It has been concluded that: *i)* the nuclear reaction models included in the transport codes (MCNPX, PHITS) should not be used in EVEDA radiation protection calculations; *ii)* the cross-sections for deuteron reactions should be calculated with the dedicated nuclear model reaction code TALYS, using when necessary appropriate adjusting OMP parameters to achieve a better description of the nuclear reactions of interest for EVEDA; *iii)* extensions of current transport Monte Carlo codes are needed in order to include the capability to use the deuteron evaluated transport data files generated by TALYS; *iv)* the MCUNED code, a MCNPX extended version, is the accepted response to this need.

The two singular features of MCUNED are: *i)* it handles deuteron-evaluated data libraries (residual production cross-sections and energy-angle distributions of all outgoing particles); *ii)* it includes a reduction variance technique for production of secondary particles by charged particle-induced nuclear interactions, which allows reducing drastically the computing time needed in transport and nuclear response calculations. Around a factor of 1 000 in saved computing time can be obtained with MCUNED for EVEDA applications. All MCUNED extensions to MCNPX have been verified with very positive results.

MCUNED-TENDL libraries shows a relevant superior performance versus current Monte Carlo simulation tools for deuteron transport in the EVEDA energy range, but this performance may be needed to be improved by adjusting deuteron-TENDL library cross-sections when required.

MCUNED is the only tool available to perform benchmarking of the TENDL evaluated deuteron cross-section against integral experiment.

Efforts are underway for benchmarking of TENDL-2009 against experimental data on thick target neutron yields for deuteron interactions on copper. Experimental values are compared with those obtained by simulation of the experiments using the MCUNED code and TENDL-2009 deuteron cross-sections. Experiments for incident deuterons in the range of energies of interest for EVEDA and IFMIF accelerators have been collected. Total neutron yields from simulations are in a reasonable agreement with experiments, but TENDL underestimates neutrons yields emitted in the forward direction. Angular distribution and spectrum of backward-emitted neutron is well reproduced by TENDL but the neutron spectra is not well reproduced for neutrons emitted in the forward direction.

Differences between experiments and simulations decreases as incident deuteron energy decreases, and a reasonable behaviour of TENDL library could be expected for EVEDA applications. Unfortunately few experiments exist for EVEDA applications. The simulation of those recently performed for 9 MeV deuterons on copper will be very useful in evaluating and improving (if necessary) TENDL for EVEDA applications.

Acknowledgements

References

[1] IFMIF International Team, *IFMIF Comprehensive Design Report*, International Energy Agency, Implementing Agreement for a Program of Research and Development on Fusion Materials, January 2004.

[2] Garin, P., M. Sugimoto, "Main Baseline of IFMIF/EVEDA Project", *Fusion Engineering and Design,* 84, 259 (2009).

[3] Blideanu, V., *et al.*, "Deuteron Cross Section Evaluation for Safety and Radioprotection Calculations of IFMIF/EVEDA Accelerator Prototype", *Proc. 14th ICFRM*, Sapporo, Japan, 6-11 September 2009.

[4] Pelowitz, D.B. (Ed.), *MCNPX: User's Manual, v2.6.0*, LA-CP-07-1473, April 2008, *http://mcnpx.lanl.gov*.

[5] Iwase, H., K. Niita, *PHITS: Particle and Heavy-ion Transport Code System Version2.08* (2006), *http://phits.jaea.go.jp*.

[6] Koning, A.J., S. Hilaire, M.C. Duijvestijn, "TALYS-1.0", *Proc. of the Int. Conference on Nuclear Data for Science and Technology (ND2007)*, Nice, France, 22-27 April 2007, O.Bersillon, *et al.* (Eds.), EDP Sciences pp. 211-214 (2008). See also *TALYS 1.2. User Manual* (2009), *www.talys.eu*.

[7] Koning, A.J., S. Hilaire, M.C. Duijvestijn, *www.talys.eu/tendl-2009*.

[8] Ferrari, A., *et al.*, *FLUKA: A Multi-particle Transport Code*, CERN 2005-10 (2005), INFN/TC_05/11, SLAC-R-773, *www.fluka.org/fluka.php*.

[9] Sauvan, P., J. Sanz, F. Ogando, "New Capabilities for Monte Carlo Simulation of Deuteron Transport and Secondary Products Generation", *Nucl. Inst. and Meth.*, A, 614, 323 (2010).

[10] Sauvan, P., *et al.*, "Computational Tools and Nuclear Data for Radioprotection Studies in Low Energy Light Ions Accelerators", *International Conference on Nuclear Data for Science and Technology (ND2010)*, JeJu, Korea, April 2010.

[11] Sanz, J., O. Cabellos, N. García-Herranz, *ACAB-2008: Activation Code V2008*, NEA-1839, OECD/NEA Data Bank (2008).

[12] Joyer, P., *et al.*, "IFMIF/EVEDA Accelerator Nuclear Safety Issues and Nuclear Data Needs", *Shielding Aspects of Accelerators, Targets and Irradiation Facilities (SATIF-9)*, Oak Ridge, TN, USA, 21-23 April 2008, OECD/NEA, Paris (2010).

[13] Sanz, J., *et al.*, "Neutron Induced Activation in the EVEDA Accelerator Materials: Implications for the Accelerator Maintenance", *Journal of Nuclear Materials*, 386-388, pp. 991–993 (2009).

[14] Mayoral, A., *et al.*, "Relevance of d-D Interactions on Neutron and Tritium Productions in IFMIF-EVEDA Prototype", *14th International Conference on Fusion Reactor Materials (ICFRM-14)*, Sapporo, Japan, 6-11 September 2009.

[15] Sanz, J., *et al.*, "First IFMIF/EVEDA Radioprotection Studies for the Preliminary Design of the Accelerator Beam Dump", *Fusion Science and Technology*, Vol. 56, No. 1, 273-280 (2009).

[16] *EXFOR Systems Manual*, IAEA-NDS-207 (BNLNCS-63330-00/04-Rev).

[17] García, M., *et al.*, "Decay Gamma Dose Rates in the EVEDA Accelerator: Impact of the Deuteron Losses Uncertainties in the Accelerator Maintenance", *Nuclear Technology*, Vol. 168, No. 1, pp. 132-138, October 2009.

[18] Avrigeanu, M., V. Avrigeanu, Fl. Roman, *Deuteron-induced Activation Cross Section Evaluation for Accelerator Materials*, Progress Report to the EURATOM-MEdC Association, Task: TW5-TTMI-004, Deliverable No. 6, December (2006).

[19] García, M., *et al.*, "Optimised Design of Local Shielding for the IFMIF/EVEDA Beam Dump", these proceedings.

[20] Smith, L.W., P.G. Kruger, "Thick Target Yields from (d,n) Reaction at 10 MeV", *Physical Review*, 83, 1137 (1951).

[21] Shin, K., *et al.*, "Neutron and Photon Production from Thick Targets Bombarded by 30-MeV p, 33-MeV d, 65-MeV 3He and 65-MeV α Ions: Experiment and Comparison with Cascade Monte Carlo Calculations", *Physical Review,* C 29, 1307 (1984).

[22] Meulders, J.P., *et al.*, "Fast Neutron Yields and Spectra from Targets of Varying Atomic Number Bombarded with Deuterons from 16 to 50 MeV", *Phys. Med. Biol.*, 2, 235 (1975).

[23] Allen, A.J., *et al.*, "Thick Target Fast Neutrons Yield from 15-MeV Deuteron and 30-MeV Alpha Bombardement", *Physical Review*, 81, 536 (1951).

[24] Kalbach, C., "Systematics of Continuum Angular Distributions: Extensions to Higher Energies", *Physical Review*, C 37, 2350 (1988).

[25] Kalbach, C., "Complete Phenomenological Model for Projectile-breakup Reactions", *www-nds.iaea.org/fendl3/docs/dBreakupRCM2.pdf* (2010).

[26] Shigyo, Nobuhiro, "Measurement of Deuteron Induced Thick Target Neutron Yields at 9 MeV", *International Conference on Nuclear Data for Science and Technology*, JeJu, Korea, April 2010.

Annex 1: List of participants

Belgium

STICHELBAUT, Frederic
Ion Beam Applications (IBA)
Louvain-la-Neuve

frederic.stichelbaut@iba-group.com

Czech Republic

PROKUPEK, Jan
Institut of Physics Academy of Science
Prague

prokupek@fzu.cz

France

DAVID, Jean-Christophe
Commissariat à l'énergie atomique
(CEA-Saclay)
Gif-sur-Yvette

jean-christophe.david@cea.fr

Germany

CHETVERTKOVA, Vera
Gesellschaft für Schwerionenforschung (GSI)
Darmstadt

v.chetvertkova@gsi.de

DITTRICH, Wolfgang
AREVA NP GmbH – Dep. PEPA-G
Erlangen

wolfgang.dittrich@areva.com

FEHRENBACHER, Georg
Gesellschaft für Schwerionenforschung (GSI)
Darmstadt

g.fehrenbacher@gsi.de

FERRARI, Anna
Institut für Sichereitsforschung &
Institut für Strahlenphysik
FZD Dresden-Rossendorf
Dresden

a.ferrari@fzd.de

LEUSCHNER, Albrecht
Deutsches Elektronen-Synchrotron (DESY)
Hamburg

Albrecht.Leuschner@desy.de

MARES, Vladimir
Helmholtz Zentrum Munchen
Neuherberg

mares@helmholtz-muenchen.de

MUELLER, Reinhold
Strahlenklinik University
Erlangen

reinhold.mueller@uk-erlangen.de

MUSTAFIN, Edil
Gesellschaft für Schwerionenforschung (GSI)
Darmstadt

e.mustafin@gsi.de

PIOCH, Christian
Helmholtz Zentrum Munchen
Neuherberg

christian.pioch@helmholtz-muenchen.de

STRASIK, Ivan
Gesellschaft für Schwerionenforschung (GSI)
Darmstadt

i.strasik@gsi.de

Iran

ESMAILI, Sasan
Azad University of Sanandaj
Sanandaj

sasan_esmaili@yahoo.com

Italy

MEAZE, A.K.M. Moinul Haque
Istituto Nazionale di Fisica Nucleare (INFN)
Bari

moinul.meaze@ba.infn.it

SALA, Paola
Istituto Nazionale di Fisica Nucleare (INFN)
Milano

paola.sala@cern.ch

SARCHIAPONE, Lucia
Laboratori Nazionali di Legnaro (LNL)
Istituto Nazionale di Fisica Nucleare (INFN)
Legnaro

lucia.sarchiapone@lnl.infn.it

ZAFIROPOULOS, Demetre
Laboratori Nazionali di Legnaro (LNL)
Istituto Nazionale di Fisica Nucleare (INFN)
Legnaro

zafiropoulos@lnl.infn.it

Japan

IWAMOTO, Yosuke
Japan Atomic Energy Agency (JAEA)
Tokai

iwamoto.yosuke@jaea.go.jp

IWASE Hiroshi
High Energy Accelerator Research
Organization (KEK)
Tsukuba

hiroshi.iwase@kek.jp

NAKAMURA, Takashi
Tohoku University/Shimizu Corporation
Koto-ku, Tokyo

nakamura.takashi@shimz.co.jp

NAKASHIMA, Hiroshi
Japan Atomic Energy Agency (JAEA)
Tokai

nakashima.hiroshi@jaea.go.jp

OGAWA, Tatsuhiko
University of Tokyo
Wako

tatsuhiko.ogawa@cern.ch

OISHI, Koji
Institute of Technology/Shimizu Corporation
Koto-ku, Tokyo

oishi@gakushikai.jp

SATO, Tatsuhiko
Japan Atomic Energy Agency
Tokai

sato.tatsuhiko@jaea.go.jp

SHIGYO, Nobuhiro
Kyushu University
Fukuoa

shigyo@kune2a.nucl.kyushu-u.ac.jp

UWAMINO, Yoshitomo
RIKEN
Wako

uwamino@riken.jp

Portugal

ROMANETS, Yuriy
Instituto Tecnológico e Nuclear (ITN)
Sacavém

yuriy@itn.pt

Saudi Arabia

ABDULLAH, Rasyieda
Saad Specialist Hospital
Al Khobar

aliciaadam7@gmail.com

Spain

ARROYO, Jose Manuel
Centro de Investigaciones Energéticas,
Medioambientales y Tecnológicas (CIEMAT)
Madrid

josemanuel.arroyo@ciemat.es

GARCIA, Mauricio
Universidad Nacional de Educación
a Distancia (UNED)
Madrid

maurigarciac@hotmail.com

SANZ GONZALO, Javier
Universidad Nacional de Educación
a Distancia (UNED)
Madrid

jsanz@ind.uned.es

Switzerland

KISELEV, Daniela
Paul Scherrer Institut (PSI)
Villigen

Daniela.Kiselev@psi.ch

United Kingdom

MALLOWS, Sophie
The University of Manchester
Manchester

sophie.mallows@cern.ch

SUBLET, Jean-Christophe
Culham Centre for Fusion Energy
Abingdon

jean-christophe.sublet@ccfe.ac.uk

United States

FASSÒ, Alberto
SLAC National Accelerator Laboratory
Menlo Park

fasso@slac.stanford.edu

GALLMEIER, Franz
Oak Ridge National Laboratory
Oak Ridge

gallmeierfz@ornl.gov

KIRK, Bernadette
Oak Ridge National Laboratory
Oak Ridge

kirkbl@ornl.gov

KOI, Tatsumi
SLAC National Accelerator Laboratory
Menlo Park

tkoi@slac.stanford.edu

MOKHOV, Nikolai
Fermilab
Batavia

mokhov@fnal.gov

RAKHNO, Igor
Fermilab
Batavia

rakhno@fnal.gov

WILLIAMS, Gail
Office of Naval Research
Arlington

gwilliams@ar-dc.com

International organisations

BOCCONE, Vittorio
European Organization for Nuclear
Research (CERN)
Geneva, Switzerland

Vittorio.Boccone@cern.ch

BRUGGER, Markus
European Organization for Nuclear
Research (CERN)
Geneva, Switzerland

markus.brugger@cern.ch

CHARITONIDIS, Nikolaos
European Organization for Nuclear
Research (CERN)
Geneva, Switzerland

charitonick@gmail.com

CHIN, Mary P.W.
European Organization for Nuclear
Research (CERN)
European Spallation Source (ESS)
Geneva, Switzerland

mary.chin@esss.se

DAMJANOVIC, Sanja
European Organization for Nuclear
Research (CERN)
Geneva, Switzerland

sdamjano@cern.ch

ENE, Daniela
European Spallation Source (ESS)
Lund, Sweden

daniela.ene@esss.se

FELDBAUMER, Eduard
European Organization for Nuclear
Research (CERN)
Geneva, Switzerland

eduard.feldbaumer@cern.ch

FERRARI, Alfredo
European Organization for Nuclear
Research (CERN)
Geneva, Switzerland

alfredo.ferrari@cern.ch

GULLIFORD, Jim
OECD Nuclear Energy Agency (NEA)
Issy-les-Moulineaux, France

Jim.GULLIFORD@oecd.org

JAEGERHOFER, Lukas
European Organization for Nuclear
Research (CERN)
Geneva, Switzerland

lukas.jaegerhofer@chello.at

LEBBOS, Elias
European Organization for Nuclear
Research (CERN)
Geneva, Switzerland

elias.lebbos@cern.ch

LOKHOVITSKIY, Arkady
European Organization for Nuclear
Research (CERN)
Geneva, Switzerland

Arkady.Lokhovitskiy@cern.ch

RICHTER, Herta
European Organization for Nuclear
Research (CERN)
Geneva, Switzerland

herta.richter@cern.ch

ROESLER, Stefan
European Organization for Nuclear
Research (CERN)
Geneva, Switzerland

Stefan.Roesler@cern.ch

SILARI, Marco
European Organization for Nuclear
Research (CERN)
Geneva, Switzerland

marco.silari@cern.ch

STEVENSON, Graham R.
European Organization for Nuclear
Research (CERN)
Geneva, Switzerland

gstevenson@wanadoo.fr

THEIS, Christian
European Organization for Nuclear
Research (CERN)
Geneva, Switzerland

christian.theis@cern.ch

TROVATI, Stefania
European Organization for Nuclear
Research (CERN)
Geneva, Switzerland

stefania.trovati@cern.ch

TRUMMER, Julia Brigitta
European Organization for Nuclear
Research (CERN)
Geneva, Switzerland

Julia.Trummer@cern.ch

VERSACI, Roberto
European Organization for Nuclear
Research (CERN)
Geneva, Switzerland

roberto.versaci@cern.ch

VINCKE, Heinz
European Organization for Nuclear
Research (CERN)
Geneva, Switzerland

Heinz.Vincke@cern.ch

VINCKE, Helmut
European Organization for Nuclear
Research (CERN)
Geneva, Switzerland

helmut.vincke@cern.ch

ZAJACOVÁ, Zuzana
European Organization for Nuclear
Research (CERN)
Geneva, Switzerland

zuzana.zajacova@cern.ch

Shielding Aspects of Accelerators, Targets and Irradiation Facilities – SATIF-10

Particle accelerators have evolved over the last decades from simple devices to powerful machines, and are having an increasingly important impact on research, technology and daily life. Today they cover a wide range of applications including material science and medical applications. In recent years, requirements from new technological and research applications have emerged while the number of accelerator facilities in operation, being commissioned, designed or planned has significantly grown. Their parameters (such as the beam energy, beam currents and intensities, and target composition) vary widely, giving rise to new radiation shielding aspects and problems.

Particle accelerators must be operated in safe ways to protect operators, the public and the environment. As the design and use of these facilities evolve, so must the analytical methods used in the safety analyses. These workshop proceedings review the state of the art in radiation shielding of accelerator facilities and irradiation targets. They also evaluate progress on the development of modelling methods used to assess the effectiveness of such shielding as part of safety analyses.